Time-Resolved Studies of Molecular Reaction Dynamics and Development of Experimental Methodology

Thesis by

Norbert Franz Scherer

In Partial Fulfillment of the Requirements
for the Degree of
Doctor of Philosophy

California Institute of Technology
Pasadena, California
1989

(submitted January 23, 1989)

ABSTRACT

The six research topics presented in the following chapters are concerned with several diverse problems of molecular reaction dynamics in isolated gas-phase environments. The scope of the studies ranges from performing direct measurements of bond-breakage on electronically dissociative potential energy surfaces, to monitoring the time-course of a restricted geometry bimolecular reaction. The common experimental method used in all of the studies has been a variant of pump-probe time-resolved spectroscopy. The underlying theme of the endeavors has been threefold: 1) To gain a better understanding of the role of intramolecular dynamics that precede or are commensurate with the reaction dynamics; 2) To begin to appreciatiate the observable manifestations of specific features of the reactive potential energy surface; and 3) To utilize the specific temporal behavior to elucidate quantitative information for the said potential surface.

The studies of molecular dissociation on repulsive electronic surfaces has lead to a quantification of the timescale for primary steps in reaction processes. Moreover, transform limited temporal/spectral studies have begun to focus on specific long-range reaction fragment interactions in a state-specific manner. The latter endeavor has identified a mechanism for the reaction-fragment(s) interaction in the near-asymptotic product region.

Predissociative reaction and intramolecular dynamical behavior has been studied on ground potential energy surfaces. Overtone excitation of the OH-stretch mode of hydrogen peroxide enables molecular ground state excitation and state-specific detection of the OH reaction product. These investigations point out the potential of this picosecond pump-probe method for directly elucidating the intramolecular energy redistribution process and the possibility for direct investigation of the long-range tail region of the free-radical recombination potential surface.

The investigation of a spatially oriented bimolecular reaction has conclusively shown that the IH-OCO reaction proceeds by way of the $[HOCO]^{\dagger}$ reaction complex species. The close proximity of the van der Waals bound reactants produces unique multi-body interactions not found in the gas phase but which may arise in condensed phases. Moreover, these investigations have obtained evidence for a unique reaction reasonance (which is analogous to a shape-resonance) feature. The presence of such a resonance in the reaction entrance channel region affects the temporal behavior and yield of product formation.

ACKNOWLEDGEMENTS

Many people have contributed to the learning and living environment at Caltech. I feel fortunate to have come to meet and know a large variety of people all with their particular qualities and personalities. The list of persons who have influenced my life, hence the content and quality of this thesis, is quite extensive. I would like to thank them all. A few individuals, however, deserve to be specifically acknowledged.

Firstly, my advisor, Ahmed Zewail, whose infectuous enthusiasm for research has made a significant impact on me from the very first day, which was also the first day in the lab. His ability to understand the significance of the results of an experiment was always impressive, and sometimes prophetic. I would wish to have only a small fraction of that insight for my own future work. His unwavering confidence in my ability to 'pull-off' the (impossible) experiment was instrumental in it actually happening. His generosity in funding the experiments which I was involved with was always considerable. I am also grateful for the enormous patience which he has exercised on my behalf. My eccentricities in doing research and stubborness in writing papers resulted in frustrations which he has not held against me. I am appreciative of his efforts to guide me personally as well as profesionally in times of difficulty. Even though I fell short of his recommended 22 hours per day schedule, I hope that he would take me again if the clock were reset and the circumstances were to be repeated. For my part, I would gladly choose to work with Ahmed again.

Professor Richard Bernstein, with whom I have had the opportunity to collaborate, has been more of a respected teacher to me than he could know. Our long discussion sessions were always very illuminating to me. His (apparently) endless enthusiasm for a wide range of scientific problems and considerable attention to detail has served to enhance my appreciation for experimental research in general and for our collaborative effort in particular. I will always recall these days of interaction with my most statesman-like 'post-doctoral' associate.

A few other people were instrumental in the success of much of what I have done here. Dr. Joseph Perry was my first labmate and my pseudo-mentor for the first $1\frac{1}{2}$ years. His excellent experimental ability, far ranging scientific interests and infinite patience served to accelerate my development in experimental research. Our collaborations over the years have been formative experiences. He showed me the value of holding an open mind about matters ranging from art to ethnic foods to scientific research. Prof. Joseph Knee was an exemplary role model for demonstrating the importance of attaining a balance between the pursuit and enjoyment of science and the possibility and importance of a well rounded personal life. His

uncomplicated manner and speech made every interaction interesting and refreshing. Dr. Lutfur Khundkar, a generous human being and my best friend at Caltech, also was the person whom I would frequently measure myself against. Our implicit competition served as a source of inspiration for myself. I always found his considerable abilities to understand the underlying physics of his (or my) research efforts both intimidating and imitable. Our constant interactions over the years helped me to become a more understanding person. My education here would have been much less complete and enjoyable without his teachings about chemical physics and life. I look forward to our future interactions with anticipation.

Other people have made my 'Caltech experience' one of (mostly) fond remembrances. I would like to thank Earl Potter, the (un-)fortunate inheritor of the apparatus which I helped to construct, for unselfishly providing assistance during my last experimental endeavor. His enthusiasm for 'doing whatever it takes' was instrumental in keeping my estimate of the time required for the last project to be off by only a factor of two. Dr. Jack Breen has brought the painfully honest but most enjoyable east-coast manner back to the group. Dr. Todd Rose showed me new ways of approaching research problems and life in L.A. Ed Sleva was a good friend to whom I would like to extend my encouragement for sucessfully completing his doctorate. I always admired David Semmes for his unpretentious attitude toward learning and pursuing life.

I should acknowledge Spencer Baskin for taking the time to help me to better undestand the idea of rotational coherence. Even though our views of doing experimental science were quite different, I would like to thank Christopher Sipes for his significant contributions to the work which is described in Chapters 4 and 7 of this thesis. The collaboration had a great deal of potential, and the fact that our differences caused much of this to go unrealized is a disappointment for me.

I would like to express my gratitude to the Caltech staff who expedited the research in a way which is only possible here. In particular I would like to thank Tom Dunn for the enthusiasm that came with every electronics project I saddled him with. Fran Bennett was always kind and helpful to me in spite of the number of 'rush orders' I placed with her. Finally, no matter how irresponsible I tried to be, Sandra Potter patiently (but firmly) managed to get me though my quarterly paperwork obligations.

I would like to thank Professor Graham Fleming, my postdoctoral research advisor, for his financial and scientific support while I was writing this thesis. He has shown considerable patience with my delaying the start of our joint efforts.

I would like to thank my parents who have had more to do with my getting to this point than anyone. They have provided me with all of the opportunities which they never had. I can never repay the many sacrifices which they make on

my behalf. My brother has also taught me to better understand myself by rejecting my career pursuits in favor of more adverturous goals; I respect him more than he could know. Collectively, their love and encouragement during the trying times has always helped me to perservere. I hope they know how important they have been and always will be in my life.

Finally, I would like to thank my fiancee, Dr. Seung-Eun (Susan) Choi, for her generous sacrifices in time and fingertips (for much of the typing). Her interest and devotion to help me overcome my deficiencies (which are numerous) has created an extra degree of stability in life and in our lives together. I constantly learn from her example; often I am humbled. She has provided the daily inspiration for me to complete this endeavor. I want to say how much I care for her in having made the last two years the most pleasant time of my life.

I would like to dedicate this work and all
that it means to me to my parents and my brother.
The realization of the present effort has been possible
only because of their love, devotion and affection.
This thesis is the fruition of the seeds of life,
which they planted in my heart and mind.
The care they give me and their teaching by word
and example are instrumental in providing me with
inner strength, peace of mind, and self-respect.

Prologue

"The lightning is his slave; heaven's utmost deep
Gives up her stars, and like a flock of sheep
They Pass before his eye, are numbered, and roll on!
The tempest is his steed, he strides the air;
And the abyss shouts from her depth laid bare,
Heaven, hast thou secrets? Man unveils me;
I have none."

P.B. Shelley
(from Prometheus Unbound)

".... What actually does give substance and reality to the efforts of a scientist in his desire to participate actively in the progress of his science to the best of his ability? And if I have to describe in one word what is the prime motive which underlies a scientist's work, I would say systemization. That may sound rather prosaic, but I think it approaches the truth. What a scientist tries to do essentially is to select a certain domain, a certain aspect, or a certain detail, and see if that takes its appropriate place in a general scheme which has form and coherence; and, if not, to seek further information which would help him to do that. This is perhaps somewhat vague, particularly, the use of the words "appropriate," "general scheme," "form," and "coherence." I admit that these are things which cannot be defined any more than beauty in art can be defined; but people who are acquainted with the subject have no difficulty in recognizing or appreciating it."

S. Chandrasekhar
(from Truth and Beauty)

TABLE OF CONTENTS

CHAPTERS

CHAPTER I.

Introduction

It has often been said that the status of a given scientific discipline is dictated by the level of technology which may be brought to bear to perform "state-of-the-art" experiments. The present thesis is a case in point, where the amalgamation of several distinct technologies has allowed for unprecedented experimental capability. The particular and unique technological advance described herein is the implementation of ultrashort-pulse lasers, and the associated pump-probe experimental method, to dynamical studies of isolated and ultracold molecules in free-jet expansions. The present thesis is a description of the experimental method by way of application to the time-resolved study of molecular reaction dynamics.

The complex experimental endeavors evolved from the desire to enhance the state of knowledge of elementary reaction behavior. A primary concern in developing an appreciation of reaction phenomena is to understand the intramolecular dynamical behavior that may lead to reaction. The initiation step for the salient reaction is, in the present case, optical excitation. The method of initial state preparation by optical projection from a ground-state level[1] directly affects the type of dynamical behavior that results. Intramolecular Vibrational energy Redistribution (IVR) is symantic with the constitution (i.e. superposition of modes) of the initial state vector. Several types of intramolecular dynamical evolution may occur:[2] 1) simple decay of the amplitude of the state vector; 2) coherent interferences and recurrences of the inital state vector; and 3) dissipative and nonrecurrent dynamics. The second point may be visualized as a classical type of quasi-periodic phenomenon while the last has been referred to as intrinsically exhibiting or quickly transitioning to chaotic behavior.[3] These diverse intramolecular behaviors may precipitate a specific reaction phenomenon for some molecular system and for the proper choice of experimental conditions. Clearly, the intramolecular dynamics preceeding the reaction may have a significant impact on the observable behavior. The short timescale of these intramolecular relaxation processes necessitates that the associated experimental apparatus have the capability of obtaining picosecond or femtosecond temporal response functions.

The achievement of the coupling of the necessary experimental methods has been an extensive evolutionary process. Molecular beam and crossed-molecular beams began to be employed by chemists in the 1950s and early 1960s.[4] The early work centered around the study of inelastic collisions and reactive collisions for well-defined center-of-mass relative velocities. These seminal endeavors have been acknowledged and reviewed by some of the principal participants.[5] The notion of crossed molecular beams has been extended to consider crossig a beam with high resolution lasers.[6] The latter advance has allowed for studying "half-collisional" reaction events in addition to the full collision dynamics of the crossed molecular beam methods.

Sensitive experimental detection methods, such as Laser Induced Fluorescence (LIF),[7] are required to study the small flux of reaction products obtained from crossed laser and molecular beam photo-induced unimolecular reactions. The distribution of energy among the different degrees of freedom of the reaction products is an important signature of the type of reactive potential energy surface (PES) features that most strongly affect the course of the reaction. The "pump-probe" methods (without sub-nanosecond time resolved capability), which have been developed for the study of energy partitioning to the product internal degrees of freedom, primarily involve fluorescence detection.[8] The translational motion of the fragments may be measured by Doppler spectroscopy.[9]

The dynamics of the photodissociation process are intrinsically dependent on the reactant(s) geometry, the behavior of the PES in some coordinate representation and the lifetime of the excted state. Implicitly, as mentioned above, intramolecular dynamics also play a role in the outcome of a reaction. Additionally, exit-channel interactons influence some observable properties of the final reaction. The development of more powerful methods for analysis of the fluorescence signal has allowed the determination of polarization or alignment properties of some types of collisional interactions and, in particular, photo-reactions.[8,10] Such observed alignment properties imply that the that the reaction product translational and rotational motions

are correlated with the photo-selected parent molecule transition moment direction. The simultaneous correlation of the anisotropy of these two product degrees of freedom with a common system vector implies that other vector correlations should also be obtained.[11]

The experimental and theoretical descriptions of the observable outcome of a reaction have, so far, focused on the post-reaction observables. The analyses are quite powerful in predicting the source of fragment excitations because of the intrinsic geometric properties of the reaction PES. The emphasis on the asymptotic quantities follows from insufficient temporal resolution to directly monitor the time course of the salient reaction. The study of emission from reactants thating are in the process of falling apart was the direction of initial attempts to better understand the actual course of the reaction prior to all the dynamical evolution having been concluded.[12]

The focus of this thesis is to demonstrate the utility and application of ultrafast pump-probe methods to the elucidation of reaction mechanistic behavior. The crossed laser and beam method was extended to the sub-nanosecond and picosecond timescale by prior efforts in the Zewail group.[13] The first application of ultarfast pump-probe methods to the investigation of intramolecular dynamics in the jet-cooled environment was demonstrated in the same research group.[14] The experimental methods have been applied to the seminal study of microcannonical rates of unimolecular electronic predissociation of NCNO in the jet-cooled environment.[15] The first demonstration of a time-resolved measurement of an isolated bimolecular reaction[16] shows the potential for the time-resolved study of an additional class of reaction phenomena.

Chapter 2 of this thesis qualitatively and quantitatively summarizes the basic concepts and considerations underlying the referenced endeavors. The considerations for the construction of a versatile ultrafast pump-probe apparatus are described. The specific design implemented in the experimental studies of the subsequent chapters of this thesis is explained in detail.

Chapters 3 and 4 describe investigations of the primary step of photo-induced dissociation of ICN and HOOH, respectively. Chapter 3 considers the time-resolved manifestation of bond-breakage and the direct measurement thereof. This investigation is significant in that it demonstrates that sub-picosecond laser pulse technology may be used to directly measure the evolution of the reactant in transition to products. (See reference 17 for further discussion of this last point) Chapter 4 considers the observable manifestations of long-range potential surface interactions. The transform limited temporal/spectral studies were optimized for the study of the near asymptotic region of the reaction PES. It is shown that fragment multipolar interactions cause rotational quantum number dependent perturbed OH fragment spectral broadening and transient absorption.

Chapters 5 and 6 consider the dynamics of vibrational predissocation of HOOH on the ground potential surface. One-photon overtone pumping provides the energy necessary to surmount the barrier to dissociation along the O-O coordinate. It is concluded for the case of pumping the fourth overtone level of the OH-stretching mode, that IVR does not compete effectively with the rate of molecular dissociation. Since the excitation is initially localized in the OH-stretch coordinate, it is clear that IVR preceeds the dissociation event. The observed quasi-biexponential rates of reaction may be ascribed to the complex distribution of initial state which arises from the finite laser bandwidth and thermal ground-state distribution. Chapter 6 demonstrates the feasibility of studying the long-range tail of the attractive portion of the PES following the more rapid IVR which results from fifth overtone pumping.

Chapter 7 is a study of the van der Waals force oriented parent bimolecular reaction dynamics of the system IH-OCO $+h\nu \rightarrow [HOCO]^{\dagger} \rightarrow$ OH+CO. The proximity of the oriented reactants lead to entrance channel interactions, which are shown to be important in determining the course and outcome of the reaction. It is demonstrated that the reaction proceeds through the $[HOCO]^{\dagger}$ intermediate configuration and that this intermediate survives for an unexpectedly long period of time for the assumed reaction energies. It is shown that entrance channel mult-body

interactions reduce the actual energy available for the HOCO to dissociate to the products. The contributions to the reaction product from the two reaction potential energy surfaces, which correlate to the product iodine $P_{3/2}$ and $P_{1/2}$ spin-orbit states, are observed in the dynamics of product formation. It is shown that the reaction dynamics that occur on the PES correlated to the $I(P_{3/2})$ product exhibit an energy defect of about $2000cm^{-1}$. By contrast, the dynamics that correlate to the excited iodine product do not exhibit a significant energy defect. However, the entrance channel portion of the PES correlated to $I(P_{1/2})$ sustains a reaction resonance feature. The evidence for this is the enhanced HOCO lifetime for the case of 240nm excitation and the enhanced reaction yield at the same energy.

Appendix A describes the observation of rotational coherence effects in pump-probe experiments of stilbene with multiphoton ionization detection. The effect becomes manifest by way of two-photon probing through a resonant intermediate level (e.g. S_4) and then to the ion continuum. The pump-probe method holds promise to develop a better understanding of the destruction of molecular coherences by way of vibrational predissociation of van der Waals complexes formed in the jet-cooled environment. This experimental effort summarizes and concludes several of the early endeavors in graduate research conducted by this author.

As is to be expected, the state-of-the-art in experimental capability is proceeding to ever shorter timescales[17] and to other types of unimolecular reaction processes.[18] These efforts leads ever further down a path of elucidating more of the significant features of the reactive potential energy surface.

This thesis should be read in conjunction with the thesis by L.R. Khundkar[19] because of the complementary research topics and background material presented therein. In particular, the kinetic model for pump-probe studies, which is developed in chapter 2 of reference 19, is relevant to obtaining a better appreciation of the types of considerations that go into the analysis of such experimental measurements. Also, the summary of statistical reaction models, which is presented in chapter 3 of the same reference, is helpful for gaining a better appreciation of the quality and

reliability of the predictions of such models. These predicted reaction rates serve as a useful calibration point against which to compare the measured rates of reaction.

REFERENCES

1. K.F. Freed and A. Nitzan, J. Chem. Phys., **73**, 4765 (1980); see also C. Rhodes in *Radiationless Transitions*, ed. S.H. Lin, Acad. Press, NY. (1980); A. Tramer and R. Voltz, in *Excited States, vol I*, ed. E.C. Lim, Academic Press, NY, (1979), p. 281
2. P.M. Felker and A.H. Zewail, Adv. Chem. Phys., **70**,265 (1988).
3. S.A. Rice, Adv. Chem. Phys., **47**, 117 (1981); D. Tannor and S.A. Rice, ibid, **70**, 000 (1988); S. Mukamel, J. Chem. Phys., **82**, 2867 (1985).
4. See the monograph by R.D. Levine and R.B. Bernstein, *Molecular Reaction Dynamics and Chemical Reactivity*, Oxford Univ. Press, NY (1987).
5. D.R. Herschbach, Angew. Chem. Int. Ed., **26**, 1221 (1987); Y.T. Lee, ibid., **26**, 936 (1987).
6. R.E. Smalley, L. Wharton and D.H. Levy, Acc. Chem. Res., **10**, 139 (1977).
7. R.N. Zare and P.J. Dagdigian, Science, **185**, 739 (1974).
8. C.H. Greene and R.N. Zare, Ann. Rev. Phys. Chem., **33**, 119 (1982);J. Chem. Phys., **78**, 6741 (1983).
9. J.L. Kinsey, Ann. Rev. Phys. Chem., **28**, 349 (1977)
10. U. Fano and J.H. Macek, Rev. Mod. Phys., **45**, 553 (1973); D.A. Case, G.M. McClelland and D.R. Herschbach, Mol. Phys., **35**, 541 (1978).
11. R.N. Dixon, J. Chem. Phys., 85, 1866, (1986).
12. H.C. Foth, J.C. Polanyi and H.H. Telle, J. Phys. Chem., **86**, 5027 (1982); D. Imre, J.L. Kinsey, A. Sinha and J. Krenos, ibid. **88**, 3956 (1984); R.R. Brooks, Chem. Rev., **88**, 407 (1988).
13. W.R. Lambert, P.M. Felker and A.H. Zewail, J. Chem. Phys.,**75**, 5958 (1981).
14. N.F. Scherer, J.F. Shepanski and A.H. Zewail, J. Chem. Phys., **81**, 2181 (1984).

15. L.R. Khundkar, J.L. Knee and A.H. Zewail, J. Chem. Phys., **87**, 77 (1987)

16. N. F. Scherer, L.R. Khundkar, R.B. Bernstein and A.H. Zewail, J. Chem. Phys., **87**, 1451 (1987).

17. M.J. Rosker, M. Dantus and A.H. Zewail, J. Chem. Phys., **89**, 6113 (1988); M. Dantus, M.J. Rosker and A.H. Zewail, ibid., **89**, 6128 (1988).

18. T.S. Rose, M.J. Rosker and A.H. Zewail, J. Chem. Phys., **88**, 6672 (1988); M.J. Rosker, T.S. Rose and A.H. Zewail, Chem. Phys. Lett., **146**, 175 (1988).

19. L.R. Khundkar, Ph.D. Thesis, *Microcannonical Rates of Unimolecular Reactions Studied by Time-Resolved Photofragment Spectroscopy*, Caltech 1988.

CHAPTER II.

Experimental Apparatus: Background Considerations and Design

2.1 GENERAL CONSIDERATIONS

The express intent underlying the range of studies pesented in this thesis is the attainment of unique information about the dynamics of Intramolecular Vibrational Energy Redistribution (IVR) and photoinitiated chemical reactions. The knowledge obtained through time-resolved measurements of the dynamical behavior will provide a complementary view to that inferred through more conventional "asymptotic" measurements.[1] The novelty of such experimental efforts is to probe the uni- or bi-molecular dynamics directly in time.[2] This ability allows for the possibility of directly viewing the time evolving reaction behavior. Measurement of the post-reaction observables[3] necessitates that these quantities be correlated and interpreted by way of models of the actual dynamics. Attaining the ability of performing direct measurement of the reaction dynamics requires the design of experiments allowing for unambiguous interpretation of the time-resolved observations. The present chapter will discuss the considerations that have defined the experiments and the specific instrumental design required for implementation of the stated goals.

Fulfilling the desire of directly measuring the progress of a chosen reaction requires experimental system time-resolution comparable to the timescale of the dynamical behavior of interest.[4] This implies generating a sufficiently short (temporal) system response function to observe dynamics within, perhaps, a molecular vibrational period, or at least on a timescale consistent with a statistical description of the reaction dynamics. In addition, it is desirable to have specificity in the probing process for different optically distinct fragment configurations along the coordinate from reactants to products. Finally, a high degree of state selectivity is necessary to elucidate particular aspects of the reaction dynamics.

The attainment of the high time resolution implied for these photo-initiated reactions requires implementation of short-duration laser pulse pump-probe methods.[4] The basic idea is to initiate the desired reaction with the femto- or pico-second laser pulse of the proper wavelength. The intensity level of some signal, which is

proportional to the transient population of the reactant or product or some species still in transition, is recorded as a function of the time delay between the excitation pulse and the second (e.g. probe) pulse. The probe pulse wavelength is chosen to afford discrimination between the reactant, products and transient intermediate-configuration species. In some experimental situations it will be possible to selectively probe the asymptotic (free) product species or the transient fragment (which is becoming the product) by simply tuning the wavelength of the probe pulse.

The types of pulsed probing methods to be discussed in this thesis are a variant of absorption spectroscopy. The absorption signal will be proportional to the population of the given moiety.[5] For example, the probe pulse may cause Laser Induced Fluorescence (LIF)[1] by being tuned to resonance with a reaction product ground to excited electronic state transition. To reiterate, the incoherent emission from the excited state will be proportional to the population initially present in the ground state. This emission is detected with a photosensitive device such as a photomultiplier tube (PMT). Alternatively, the product ground state (transient) population may be measured using single or multiple photon ionization (PI or MPI), with or without intermediate state resonant enhancement.[6,7] The actual, detected species will be the moiety positive ion as this species is electrostatically accelerated into a particle detector. The ion signal is proportional to the ground state population which is spectrally resonant with photon absorption through some intermediate state to the level of the ground electronic state of the ion. Electron detection from MPI is also possible and could yield the same or additional product state information.[6]

The evolution along the reaction path causes a temporal response to occur in the fraction of ground state molecules which fall within the laser spectral bandwidth for the resonant optical transition. It is this effect which, in principle,allows for the possibility of doing spectroscopy of the reaction while the targetted fragment resides in a transition state (TS) configuration. Such a conformation, which is neither reactant nor product(s), is of critical importance in determining (and measuring)

the course of the reaction.[2,3] It may be said that such ultrafast pump-probe time resolved spectroscopy is the only presently available means by which to directly follow the course of an isolated unimolecular or bimolecular reaction.

The following part of this section will be devoted to reviewing some of the physical concepts that underly the operation and design of short-pulse lasers and pulse compression schemes. This will be followed by a subsection devoted to the amplification of the traditionally low pulse intensity systems listed above. Thereafter, a range of schemes for obtaining tunable light and alternative (e.g. ultraviolet) operational wavelengths will be examined. Points of consideration of the experimental medium (e.g. isolated gas phase and ultracold free-jet expansion) will be described. Since many of the following chapters focus on probing the dynamics of hydroxyl radical formation, a description of some spectroscopically useful concepts will be given.

2.1.1 Time-Resolved Spectroscopy

The field of picosecond spectroscopy has been an area of active research for almost twenty years. Earlier research was focused more on problems in the condensed phase. The issue was one of practicality. The repetition rate of early laser systems was near 1Hz, which necessitated obtaining large signals by way of the high number density in condensed media. This earlier research has been reviewed by Eisenthal.[8]

Subsequent technological developments have led to the development of reliable laser systems with subpicosecond to a few femtosecond temporal resolution. A recent review of the applications in the area of chemistry may be found in Refs. 9 and 10. A discussion of the development of ultrashort pulse lasers and applications to problems of physics and chemistry is given in Ref. 11. The higher laser repetition rates and large peak pulse energies of the presently available laser/amplifier designs allow for the study of a much greater diversity of problems. The high peak powers are especially relevant to the context of this thesis, that is, extension to the study of dynamical phenomena in the gas phase.

The only type of experimental method currently available for taking full advantage of the temporal resolution offered by such short optical pulses are pump-probe optical gating methods.[12] Reference 12b is especially relevant to the topics discussed throughout this chapter and the remainder of this thesis. The model of pump-probe dynamics[12b] considers operationally practical issues in a quantitative manner. Various pump-probe techniques are described in references 8-11. Other implementations range from the scale of fully dedicated ultraviolet "spectrometers"[13] to low-pulse amplitude high repetition rate near shot noise limited transient absorption instruments.[14] However, along with the enhanced time resolution and added versatility intrinsic to pump-probe nonlinear optical spectroscopic experiments[15] comes the complications of coherent pump-probe interactions. Such matter-radiation interactions give rise to effects termed "coherent artifacts."[16] Further discussion of this topic will be defered to the individual chapters. A description will be given, where relevant, to explain the considerations given to ensuring that the measured data is not due to such effects.

2.1.2 Short Pulse Laser Oscillators

The creation of temporally short pulses has essentially taken two paths in technological development. The first is the conception and design of lasers that intrinsically produce pulsed outputs of picosecond or femtosecond duration. The second route involves pulse compression devices which are typically used extracavity. The discussion in this subsection will focus on the first concept.

Short pulse generation by way of gas and solid state lasers and synchronously pumped dye lasers begins with an active amplitude modulation device. This device modulates the Q of the laser in synchrony with the travel time of light, for a round trip time of 2L/c. The concept of synchronous modulation is termed active mode-locking. The ideal mode-locking device would be an optical shutter that opens for the duration of the desired pulse, but remains closed at other times. The devices more typically used employ an intracavity loss or phase modulator driven by a sinusoidal RF signal with period L/c. The general concept of the mode-locking process

is to convert the cw intensity of a laser running at a single frequency and induce addition FM sidebands onto the central frequency. The sidebands are quantized in units of the longitudinal mode spacing of c/2L; therefore, coupling of the RF with the laser at frequency ω_o gives two sidebands at $\omega_o \pm b$, where b=c/2L. As gain builds in the sidebands, the interaction of these lasing modes with the Rf may create additional sidebands at $\omega_o \pm 2b$, and so on. The sidebands persist provided the gain that can be extracted at the frequency $\omega_o \pm nb$ (where n=1,2,...) is large enough to overcome the gain threshold for lasing. Therefore, the upper limit on the value of n is defined by the laser medium (homogeneous) linewidth.

Since the laser modes are coupled in phase by the Rf signal, there tends to be contructive interference over a shorter and shorter portion of the cavity length for greater numbers of longitudinally coupled modes. It is illustrative to give a brief quantitative description of the mode locking process. Begin by assuming a sinusoidal modulation of the transmission of the acousto-optic device. This is given by[17] T=$(1+\delta \cos \Omega t)$ with modulation factor $\delta < 1$ and modulation frequency f=$\Omega/2\pi$=c/2L. The amplitude of the mth mode is[17]

$$\begin{aligned} A_m(t) &= \mathrm{T}\, A_o \cos \omega_m t \\ &= \left(\frac{A_o}{2}\right) \cdot (1 + \delta \cos \Omega t) \cos \omega_m t \end{aligned} \tag{2.1a}$$

or may alternatively be expressed as

$$\begin{aligned} A_m(t) = &\left(\frac{A_o}{2}\right) \cos \omega_m t \\ &+ \left(\frac{A_o\, \delta}{4}\right) \cdot \Big[\cos(\omega_m + \Omega)t + \cos(\omega_m - \Omega)t\Big] \end{aligned} \tag{2.1b}$$

If the modulation frequency $\Omega/2\pi$ equals the mode spacing, $\Delta\nu$ = c/2L, sideband amplitudes

$$A_{m\pm} = \left(\frac{A_o\, \delta}{4}\right) \cos \omega_{m\pm} t \tag{2.2}$$

are generated in the adjacent resonator modes denoted by $m\pm$. These modes are further amplified by stimulated emission.

The phases of these sidebands are determined by the phase of the carrier wave (Rf) and by the modulation phase. The three waves described by Eqns. (2.1b) and (2.2) are in phase at times $t_k = 2\pi k/\Omega$, $(k = 0, 1, 2, \ldots)$. Modulation of these modes generates new sidebands at $\omega_{2\pm} = \omega_2 \pm 2\Omega$. This process continues until all modes within the gain profile of the active medium oscillate with mutually coupled phases.

The bandwidth $\delta\nu$ of the gain profile will support 2p+1=$\delta\nu/\Delta\nu$ lasing modes. The superposition of these phase-coupled modes results in a total amplitude

$$A(t) = \sum_{-p}^{+p} A_m \cos(\omega_o + m\Omega)t \tag{2.3}$$

which describes the Fourier components of the resultant intracavity pulse. The total time-dependent laser intensity I(t) is proportional to $A^*(t) \cdot A(t)$ and is given by[17]

$$\mathrm{I}(t) = \frac{{A_o}^2 \sin^2\left[(2\mathrm{p}+1)(\Omega/2)t\right] \cos^2\omega_o t}{\sin^2\left[(\Omega/2)t\right]}. \tag{2.4}$$

The greater the number of modes which can be coupled via the frequency modulation, the greater the resultant coherently locked gain profile. The larger the number of frequency components that are in phase at time t_k, the shorter the associated temporal pulse duration. The pulse train will have a period of 2L/c.

Both the shape of the gain profile and the efficiency of the modulation have an effect on the resultant pulse shape and temporal width. The modulator in Ar ion (gas) and Nd:YAG (solid-state) lasers is achieved by an intracavity Acousto Optic (AO) modulator. The coupling of the Rf to the AO-modulator medium is achieved by bonding a piezoelectric transducer to a Bragg diffraction cell, which is typically constructed of quartz. The phonon propagation corresponds to the motion of a density wave which causes a periodic change in the index of refraction. The light

beam of the laser is partially diffracted from this refractive index gradient. Additionally, the Rf frequency is adjusted to be equal to the cavity mode spacing, $\Delta\nu$. The diffraction efficiency will have a direct bearing on the resultant pulse duration. It is possible to enhance this efficiency by producing a standing wave pattern in the quartz medium by tuning the modulator resonance to a resonance frequency of the cavity. The tuning is achieved by way of variation of the temperature of the acoustic cell. The resultant standing wave will be of frequency c/2L.

When the angle of incidence of the light beam onto the acoustic cell is optimized to the Bragg angle, the fraction of the light diffracted in a single pass through the cell is given by[18]

$$\frac{\mathrm{P_d}}{\mathrm{P_o}} = \pi^2\,\mathrm{M}\cdot\frac{l^2}{2{\lambda_o}^2}\cdot\frac{\mathrm{P_a}}{A} \tag{2.5}$$

where M is the acousto-optic figure of merit for fused quartz, l is the interaction length of the light and acoustic wave, λ_o=laser wavelength and $\mathrm{P_a}/A$ is the acoustic power density. (M=$1.51\times10^{-18}\,s^2/g$). The fractional amount of diffracted light expected for the Ar ion is about 0.03 for an input Rf power level of 0.4 watts. The Nd:YAG single pass diffraction efficiency is about 0.02 for 1.2 watts Rf power.

Actively mode-locked lasers may be used to synchronously pump cavity length matched dye lasers.[19] The first subpicosecond pulses from a synchronously pumped cavity were obtained by Heritage *et al.*[20] The pulsed output from these types of lasers may be temporally characterized by autocorrelation[12a] and cross-correlation[21] techniques. The cavity length matching properties have also been characterized[21,22] to better understand the mechanism of pulse formation from the noise burst model[23] substructure.

The method of pulse characterization is done by way of second harmonic generation in nonlinear optical crystals.[12,18a,24] The second harmonic signal is proportional to the autocorrelation function of the pulse intensity, I(t). The autocorrelation signal is given by

$$\mathrm{G}(\tau) = \frac{\langle\,\mathrm{I}(t+\tau)\cdot\mathrm{I}(t)\,\rangle}{\langle\,\mathrm{I}(t)^2\,\rangle} \tag{2.6}$$

where the brackets refer to performing a time average. The experimentally measured autocorrelation is more accurately represented by[26]

$$G(\tau) = G_p(\tau)\left[1 + G_n(\tau)\right] \tag{2.7}$$

where $G_p(\tau)$ is the autocorrelation function of the pulse envelope. The bracketed term is the autocorrelation of the Gaussian-noise pulse substructure. The widths of the pulse and the noise autocorrelations is given by $\Delta\tau_p$ and $\Delta\tau_n$, respectively. If $\Delta\tau_n \approx \Delta\tau_p$ then the laser is well mode-locked since the pulse is of the same duration as any underlying noise, hence the maximal number of longitudinal modes (for a fixed bandpass tuning element) are locked in phase. In the case of a Gaussian pulse,[23]

$$I(t) = \exp\left(-\frac{4\ln 2}{\Delta {t_p}^2}\cdot t^2\right) \tag{2.8a}$$

and

$$G_p(\tau) = \exp\left(-\frac{4\ln 2}{\Delta {\tau_p}^2}\cdot {\tau_p}^2\right) \tag{2.8b}$$

and $\Delta\tau_p/\Delta t_p = \sqrt{2}$. The autocorrelation is $\sqrt{2}$ wider than the actual pulse duration.

The mechanism of pulse formation in synchronously mode-locked lasers has been studied by Yasa *et al.*[25] It was found that the pulses tend to walk forward in time by preferential amplification of the pulse leading edge and decreased gain for amplification of the pulse trailing edge. This process occurs with each cavity round-trip. The relatively short pump pulse of 80ps FWHM defines a region of maximal gain in a window of less than 80ps duration. The leading edge of the window is defined by the time position where the gain rises above threshold. The window closes when sufficient gain is lost via stimulated emission such that the gain falls below threshold. These ideas are illustrated in Figure 1, which is adapted from Ref. (25).

By the reasoning just presented, it is expected that shorter pulses occur in association with higher transmission output couplers (i.e. greater loss) and lower total gain. The amount of gain, however, must be chosen to allow for obtaining

adequate amplitude stability to perform the desired experiments. The experimental characterization of the synchronously pumped dye laser and intrinsic sources of noise have been analyzed to understand their effect on pulse formation and the quality of mode-locking by von der Linde.[26]

The operational advantages of synch-pumped dye lasers has been recognized for some time.[27] The primary advantage is the ease of tunability of the laser wavelength. The bandwidth of these lasers may also be discretely adjusted by changing the cavity tuning elements (e.g. interference wedge, 1, 2, or 3 plate birefringent filters or intracavity etalon). A description of the operational properties of different intracavity tuning elements may be found in Refs. 5 and 18. Another advantage is the relatively uncomplicated cavity design, which facilitates alignment and operation. This last consideration is not trivial because many experiments require both time resolution of a few picoseconds and independently tunable pump and probe pulses.

Two independent synch-pumped dye lasers allow for versatility in the types of experiments that may be addressed. The operation of two such dye lasers will, however, restrict the experimentally obtainable two dye laser cross-correlation function. In the simplest form, the temporal width cross-correlation will contain three terms, where for Gaussian pulses and timing jitter, one obtains

$$\Delta\tau_{cc}{}^2 = \Delta t_{p_1}{}^2 + \Delta t_{p_2}{}^2 + \Delta t_j{}^2. \tag{2.9}$$

according to the previous convention for the terms. The jitter arises from the incomplete mode-locking of the two dye lasers. The timing jitter has been analyzed.[28] For $\Delta t_{p_1} = 2.2$ps, $\Delta t_{p_2} = 2.7$ps, the cross-correlation width is measured to be 3.8ps (FWHM). The best case condition in Ref. 28 gave a timing jitter width of 2.7ps. More typically the two dye lasers would have different gain/loss conditions. The different gain arises either from different pumping conditions for the two dye lasers or from running the two lasers at two different wavelengths. In the latter case each

dye laser stimulates emission from two different portions of the given dye (or separate dyes) gain curve. Such non-ideal experimental conditions are more typical and result in a value for the jitter measured[28] as 5ps (FWHM).

Synchronously pumped dye lasers with both gain and saturable absorber jets in the cavity are one method of achieving shorter pulse durations with reasonably simple cavity design. The addition of the saturable absorber medium makes the mode-locking both active and passive. The pulse duration of this dual mode-locked design is shorter than that obtained from simply synch-pumped lasers. However, the laser is less easily tunable because the pulse duration changes at operating frequencies which are somewhat removed from an optimal value. The optimal range is obtained from the specific choice of gain and absorber dyes and concentrations. The gain and saturable absorbers are typically organic dye molecules that flow from a nozzle to form a dye jet 50-200μm thick. Although not an absolute necessity,[29] these lasers typically contain two dye jets to separate the gain and absorber media.[30]

Since the pulse durations of such lasers is in the range of 200fs, new effects such as group velocity dispersion (GVD) can degrade the pulse quality from the optimal. Introduction of a series of intracavity prisms[31a] allows for independent adjustment of the four main parameters in pulse formation: gain, loss, saturable absorption (for passive mode-locking) and compensation for dispersion. Pulse broadening due to group-velocity dispersion (GVD) is always present when a pulse of finite frequency passes through a material wherein the value of the index of refraction has a frequency dependence. The time delay τ_d between two components of the pulse optical field separated by an angular frequency difference $\Delta\omega$ is given by

$$\tau_{\mathrm{d}} = -\mathrm{L}\ \Delta\omega \cdot \frac{\partial^2 \mathrm{n}}{\partial \omega^2} \tag{2.10}$$

where L is the length of the medium, n is the index of refraction, and ω is the laser angular frequency. Passive mode-locking by way of saturable absorption is a type of pulse shaping method whereby the thin absorber jet or cell is bleached by

the leading edge of the circulating intracavity pulse. The gain jet, however, acts to preferentially amplify the leading edge of the intracavity pulse. The balance of the saturable absorption and saturable gain dynamically shapes the pulse, and, under the proper conditions, significantly shortens the nominal pulse duration. The absorber concentration is typically adjusted to optimize short pulse formation by preventing longer-duration lower-peak power pulses from lasing. The operational characteristics of these types of lasers have recently been presented.[31b]

The colliding pulse ring dye laser was the first reliable and stable type of sub-picosecond/femtosecond dye laser.[32] The laser operates on the principle that interference of two counter propagating pulses in the saturable absorber jet enhances the effectiveness of the saturable absorption. The ring is configured such that the gain and absorber are separated by one quarter of the cavity round trip. This allows each pulse to extract equal amounts of gain every round trip. The gain is continuously created by a cw-Ar ion pump laser as opposed to the aforementioned synchronously pumped designs. The interference between the two pulses creates a standing wave in the saturable absorber, which acts to reduce the energy required to saturate the absorber. The idea of intracavity adjustable GVD with four prisms was originally applied to such colliding pulse mode-locked (CPM) dye lasers.[33] The introduction of the prisms compensates for self-phase modulation (SPM) resulting from the nonlinear response of the dye solvents or the time-dependent saturation of the laser dyes.[33] These laser have produced the shortest pulses directly obtained from an oscillator to date. However, these lasers are not tunable and essentially operate at a single fixed frequency related to the choice of the gain and absorber dyes.

The last type of laser oscillator is a hybrid of the linear cavity dual jet and the CPM designs. The end mirror on the dual jet linear cavity is replaced by a small ring. The saturable absorber dye jet is located at the midpoint of the ring to achieve the CPM effect. This hybrid ring design is termed an antiresonant ring laser.[34] The cavity configuration is synchronously pumped by a mode-locked

Nd:YAG[35a] or a mode-locked Ar laser.[35b] The output pulse durations are typically less than 100fs but are again not spectrally tunable. Intracavity prisms allow for compensation of intracavity dispersion.[35c] The synchronously pumped design allows for high repetition rate synchronous amplification.

2.1.3 Optical Pulse Compression

Having considered the types of short pulse dye laser designs that currently exist and the various advantages and/or trade-offs inherent in each design, it is useful to examine another approach to short pulse generation. The underlying idea for extracavity pulse compression is to allow light to interact with a medium which will increase the frequency spectrum. The pulse frequency broadening must occur in a fashion such that the pulse can be compressed down to near the minimal value of the temporal-spectral transform relation.

The spectral broadening is achieved by injecting a pulse into an optical fiber (with a 4μm core diameter) and obtaining SPM. The SPM effect arises from the intensity dependence of the index of refraction of the fiber. It has been shown that the instantaneous frequency is given by[36]

$$\omega' = \omega_o - \frac{\omega_o}{c} \mathrm{L} \frac{\mathrm{n}_2}{2} \cdot \frac{\partial \mathrm{E}^2}{\partial t} \tag{2.11}$$

where ω_o is the carrier frequency, n_2 is the nonlinear index of refraction, E is the electric field amplitude and L is the propagation length. The frequency modulation arising from SPM results in a linear frequency spread (chirp) to be created across the temporal profile of the pulse. The GVD described by Eqn. (2.10) also occurs in the optical fiber but this does not create a greater frequency bandwidth in the manner of SPM.

By contrast, Treacy[37] has shown that the diffraction of a pulse of light off a pair of gratings will result in a pulse whose phase function is given by

$$g(t) = \omega t + \frac{1}{2}\beta t^2 + O(t^3). \tag{2.12}$$

If terms of order t^3 can be neglected, the chirp is linear, $\dot{g}(t)(\equiv \partial g(t)/\partial t) = \omega + \beta t$ and β is identified as the frequency-sweep rate. The exact expression for the grating will not be given, but rather it suffices to say that the linear-chirp of Eqns. (2.10) and (2.11) and that for Eqn. (2.12) are of opposite sign. It is therefore possible to recompress the optical pulse that has passed through an optical fiber with a pair of diffraction gratings.

This scheme has been implemented for the compression of optical pulses from synch-pumped dye lasers,[38] and from CPM lasers.[39] The cavity dumped output pulse of a simple synch-pumped laser was reduced from 5.4ps to 450fs with such a fiber/grating scheme[38]; the compressed CPM pulse reached a temporal duration of 30fs.[39] This method appears to be a useful way of extending the experimental pulse duration from the picosecond to the sub-picosecond domain and yet maintain wavelength tunability.[40]

A limitation of the fiber/grating pulse compression method is the need for including terms for the phase description of the pulse which are higher than quadratic.[41] The need to account for the cubic contribution to the instantaneous phase (or frequency) of the chirped pulse has been recognized by Shank and coworkers.[42] The solution is to use prisms as well as gratings to compensate for quadratic and cubic contributions to the instantaneous phase of the pulse. This extra compensation has allowed for the generation of 6fs pulses.[42]

Pulse compression methods are the only means by which to make the transition from a few tens of femtosecond pulses to less than 10fs. An alternative use of pulse compression is to shorten the pulse that pumps the synch-pump dye laser. Such pulse compression has been successfully demonstrated for cw-mode-locked Nd:YAG lasers.[43] The shorter excitation pulse duration serves to reduce the synchronously pumped dye laser output.

The general conclusions from this subsection are several. First, various laser systems have been developed which collectively span the 100ps to 10fs temporal range. Second, in addition to the temporal trade-offs of the different designs, the

ease of wavelength tunability is perhaps an equally important point for consideration. Each laser system described above has distinct advantages and disadvantages. Therefore, the choice of laser system depends on the practical considerations of the chosen experimental study.

2.1.4 Short Pulse Amplification

The pulse energies from the laser oscillators described above are of the order of 1nJ. Such low pulse energies are not suitable for generating other optical frequencies to undertake the experiment of interest. A wide variety of optical mixing techniques exist to expand the range of the aforementioned dye laser.[44] However, such optical nonlinear methods are highly peak-intensity dependent (e.g. I^2, I^3, etc.). The desire is, therefore, to amplify the pulse energy by three to six orders of magnitude, depending on the associated pulse repetition rate.

Since the theory of pulse amplification has been extensively treated,[24,45,46] only a brief summary of the essential aspects will be presented here. Experimental considerations in the amplification of short optical pulses have been described and reviewed in Refs. 47 and 48, respectively.

An optical dye amplifier typically consists of a pump laser (excitation) source, a dye cell or jet as the gain medium and an optical arrangement for manipulation of the transverse mode profile of the beam to be amplified. The energy is stored by optical excitation of the dye chromophore and relaxation of the dye and surrounding solvent medium to a steady-state population inversion condition. The loss from the steady state arises from spontaneous emission. Efficient energy extraction from the optical amplifier occurs when the pulse energy density is comparable to the gain saturation limit. This is intuitively obvious because the amplifier increases the pico- or femtosecond pulse energy by way of stimulated emission. Gain saturation corresponds to the level at which the seed pulse energy density exceeds the value necessary to deplete all the available gain. Additionally, the Rabi pulsation period may become shorter than the pulse duration.[49]

Gain saturation, therefore, necessarily implies temporal broadening of the pulse to be amplified. Other problems also arise at these high energy densities, which are of the order of $10^{10}\,W/\mathrm{cm}^2$ and above. Nonlinear nonresonant interactions with the medium can result in SPM and the associated effect of self-focusing. The former causes spectral broadening which may be difficult to compensate for. The latter effect, which is related to the optical Kerr effect,[44,24] will irreversibly alter the transverse mode profile and distort the pulse temporal profile. A pulse that propagates through a dense medium encounters group velocity dispersion and becomes temporally broadened. This dispersive effect may, however, be readily corrected.

Operationally, these issues have been addressed in Refs. 47 and 48. The distortions that cause linear chirps can be compensated with prisms or gratings, as described in the previous subsection. Also the optical path length of the amplifier should be minimized. Saturable absorber jets can be inserted into the amplifier to deal with the gain saturation, which tends to preferentially broaden the leading edge of the pulse. Another partial solution is to divide the amplifier into several stages and adjust the gain and gain density in each state to more closely match the energy density of the ultrashort pulse.

In general, the overall energy extraction efficiency, defined as total amplified pulse energy divided by the pump pulse energy, decreases with input pulse width. The shorter pulse durations imply higher peak pulse energy for a given average power. One way around this problem is to do "chirped pulse amplification,"[50] where the pulse is temporally stretched and the broadened pulse is subsequently amplified. The longer pulse duration allows for obtaining a higher extraction efficiency. The linear chirp imparted in the broadening step may be reversably (re)compensated. Subsequent pulse recompression will ideally result in an output pulse that is approximately of the same temporal duration as the input pulse but of significantly higher peak energy than could have been obtained with a typical amplification scheme.

The following description of gain extraction from an optical amplifier will follow the treatment of Ref. 46. The short oscillator pulse is assumed to travel through

the dye amplifier after the pump pulse and once the steady state is reached. The short pulse travels along the x^+ longitudinal direction. The propagation equation is[46]

$$\left(\frac{\partial}{\partial \mathrm{x}} + \frac{n}{c}\frac{\partial}{\partial t}\right) \mathrm{I}_l(\mathrm{x},t) = \left[(\sigma_l + \sigma_a)\,\mathrm{N}_1(\mathrm{x},t) - \sigma_a \mathrm{N}\right] \mathrm{I}_l(\mathrm{x},t) \tag{2.13}$$

where $\mathrm{I}_l(\mathrm{x},t)$ is the intensity of the pulse at location x at time t. The emission and absorption cross sections at the wavelength of the pulse is give by σ_l and σ_a, respectively. The population in the excited state, S_1, of the dye molecules is given by $\mathrm{N}_1(\mathrm{x},t)$. The rate equation for the population in S_1 is

$$\frac{\partial \mathrm{N}_1}{\partial t} = \left[-(\sigma_l + \sigma_a)\,\mathrm{N}_1 + \sigma_a \mathrm{N}\right] \mathrm{I}_l. \tag{2.14}$$

which ignores the contribution from spontaneous emission. The stored energy of the amplifier is defined as

$$\mathrm{E}_{\mathrm{st}} = 4\,\mathrm{r}^2 \int_0^{\mathrm{L}} \mathrm{N}_1(\mathrm{x})\; d\mathrm{x} \tag{2.15}$$

where L is the length of the amplifier medium and $\mathrm{E}_{\mathrm{st}} = 4\mathrm{r}^2\,\mathrm{N}_{\mathrm{st}}$. The saturation energy level is defined as $\mathrm{E}_{\mathrm{sat}} = (\sigma_l + \sigma_a)^{-1}$ and the input energy $\mathrm{E}(0,t)$ is normalized to this value, $\bar{\mathrm{E}}(t') = \mathrm{E}(\mathrm{x}',t')/\mathrm{E}_{\mathrm{sat}}$. The normalized stored energy is given by

$$\mathrm{Z} = (\sigma_l + \sigma_a)\,\mathrm{N}_{\mathrm{st}} - \sigma_a\,\mathrm{N}\,\mathrm{L} \tag{2.16}$$

Defining the pulse intensity at (x',t') by the energy, $\mathrm{E}(\mathrm{x}',t') = \int_{-\infty}^{t'} \mathrm{I}_l(\mathrm{x}',t')\; dt$ results in an expression for the output pulse intensity, which may be written as[46]

$$\mathrm{I}_l(\mathrm{L},t') = \frac{\exp(\mathrm{Z})\,\exp\left[\bar{\mathrm{E}}_o(t')\right]}{1 + \left[\exp \bar{\mathrm{E}}_o(t') - 1\right] \cdot \exp(\mathrm{Z})} \cdot \mathrm{I}_l(0,t'). \tag{2.17}$$

The total energy gain of the amplifier stage is given by

$$\bar{g} = \frac{\bar{\mathrm{E}}_{\mathrm{L}}(t = +\infty)}{\bar{\mathrm{E}}_o(t = +\infty)} \tag{2.18a}$$

while the conversion efficiency is given by

$$\varepsilon = \frac{\bar{E}_L(+\infty) - \bar{E}_o(+\infty)}{Z}. \qquad (2.18b)$$

In the limit of small input energy, $\bar{E}_o(t') \ll \exp(-Z)$, $\bar{E}_L(t') = \exp(Z) \cdot E_o(t')$, $\bar{g} = \exp(Z)$ and $\varepsilon = \bar{E}_o(+\infty) \cdot \exp(Z)/Z$. For the limit of deep saturation $\bar{E}_L(t') \sim Z + \bar{E}_o(t')$ and virtually all the stored energy is transferred to the amplified pulse, but the amplified pulse will be severely broadened.

Under more typical operating conditions of $\exp(-Z) \ll \bar{E}_o(+\infty) \ll 1$ one obtains $E_L(t') = Z + \ln \bar{E}_o(t')$, $\bar{g} \sim Z/\bar{E}_o(t')$, and $\varepsilon \sim 1 + [\ln \bar{E}_o(+\infty)/Z]$. The pulse shape distortion can be analyzed by considering the change in shape for the typical amplification conditions. Amplification of a pulse with an exponential trailing wing causes the width to narrow. Amplification of a pulse with a trailing wing results in temporal broadening.

2.1.5 Nonlinear Techniques

The wavelength of the light available directly from the laser oscillator and amplifier may not be of precisely the correct wavelength to conduct the specific experiment. In particular, all of the studies described in the subsequent chapters required generation of UV light in the 388-210nm range for the excitation and probe pulses. The amplification described in the previous subsection facilitates the nonlinear mixing processes necessary to obtain the desired wavelength. A range of techniques have been employed to obtain UV light which is of a fixed, discretely adjustable or continuously adjustable frequency. Some methods will be briefly described below.

The most straightforward method of obtaining UV wavelengths is second harmonic generation. In the case of tuning to a resonance transition in the pump or probe beam the dye laser wavelength would be adjusted such that the second harmonic of this fundamental is at the appropriate frequency. The method of second harmonic, sum frequency and difference frequency generation, are all described

by a formalism wherein the desired output wavelength arises from the second order nonlinear susceptibility tensor matter-radiation interaction.[51] These processes require the use of uniaxial media (*e.g.* KDP, $LiIO_3$, KTP, β-BBO) wherein the nonlinear index of refraction differs along two distinct crystaline axes. The proper phase matching condition follows from momentum and energy conservation for the two input and single output beams.

Stimulated Raman Scattering (SRS) in vapors[17] has also been employed to generate wavelengths of frequency $\nu_o \pm n \cdot \nu_{RS}$, where ν_o is the input laser frequency, ν_{RS} is the frequency of the chosen molecules Raman active vibrational mode(s) and n=1,2,... . The laser light is softly focused into a high pressure gas cell (100-200 psi) filled with the appropriate gas. It is necessary to focus the input light to achieve the large pulse intensities necessary to drive the $\chi^{(3)}$ process. The long focal length lens allows for a long interaction length in the crystal with uniform **k**-vector conditions. The long path phase matching conditions allow for converting 3-5% of the incoming light to the Stokes shifted frequency and 2% to the anti-stokes shifted frequency. The gas of choice was CH_4 because of its large Raman cross-section (about 8 times larger than N_2) and the convenient frequency shift of $2914cm^{-1}$. The light exiting the Raman cell is recollimated with a 0.5m lens. A nonlinear mixing crystal is placed after this lens to generate the second harmonic of a selected Raman order (for n=1) or to generate the sum frequency of the transmitted laser fundamental and the chosen Raman order.

The dye oscillator operates at continuously tunable wavelengths in the range of 620-560nm. Second harmonic light converts these wavelengths to 310-280nm, respectively. Mixing the fundamental with the Raman light gives a continuous range from 284-259nm and 340-305nm for the Antistokes and Stokes orders, respectively. A separate mixing process involving the amplified fundamental and the 1.064μm fundamental of the Q-switched Nd:YAG, which pumps the dye amplifier, achieves the 392-366nm range. Another mixing scheme is of the second harmonic of the dye laser output plus the 1.064μm light. This is done in two separate processes

placed in series and achieves tuneable light in the range 240-220nm. Several of these mixing techniques were applied and described more fully in the specific context of the experimental work of Khundkar and coworkers.[52]

Another versatile method for frequency generation is the production of a white light optical continuum.[53] The spectral continuum is produced from the interaction of an intense picosecond[54] or femtosecond pulse[55] with water, ethylene glycol, or other materials.[24] The continuum frequency band spans the visible spectral range, especially in the case of femtosecond pulse continuum generation. Several mechanisms contribute to the effect. The underlying mechanism of continuum generation for pulses longer than 10ps in duration appears to be a four photon parametric process.[53] The main mechanism driving the process on the femtosecond timescale is self-phase modulation. For pulses of intermediate duration both processes contribute in some proportion.

The spectral continuum is ideally suited for performing pump-probe transient absorption experiments with multiple wavelength parallel detection schemes. Such two-dimensional spectroscopy (time and frequency) is a powerful method for following some portion of a molecular reaction,[57] for example. Alternatively, narrow bandwidth portions of the continuum light could be selected using interference filters or the spectral/temporal filtering method described in the following section. This spectrally continuously tunable light source could be used in place of a second synchronously pumped dye laser, for example. The clear advantage of this method is removing the jitter contribution from the pump-probe cross-correlation. The capability of independent tunability would still be maintained.

Assume that the mechanism for continuum formation arises from the quadratic expression for SPM. Then, a quadratic pulse compressor could, in principle, reduce the pulse duration of the continuum pulse to within $\pm 3000 \mathrm{cm}^{-1}$ of the central frequency.[58] This is seen in the expression for the instantaneous frequency

$$\omega(t) - \omega_{\mathrm{L}} = -\left(\frac{\omega_{\mathrm{L}}\, l}{\mathrm{c}}\right) \cdot \frac{\partial(\mathrm{n}_2\, \mathrm{E}^2)}{\partial t} \tag{2.19}$$

where ω_L is the incident laser central frequency, l is the sample length, and n_2 is the nonlinear intensity dependent index of refraction and $E(t)$ is the laser pulse electric field. An implementation of this idea will be described in the following section. Amplification of a spectrally selected portion of the optical continuum is a practical method of producing high intensity tunable pulses to serve as the pump or probe beam.

A variety of second (and higher) order nonlinear frequency mixing methods may be used to generate the appropriate wavelengths to carry out a large variety of experiments. The versatility and diversity of the methods described allows for obtaining (in principle) complete spectral coverage from 700 to 200nm and perhaps beyond.

2.1.6 Collisionless and Jet-Cooled Reaction Conditions

All of the studies of gas phase reaction dynamics presented in this thesis were performed under isolated molecular conditions. The observed dynamics are due to intramolecular dynamics and are not perturbed by intermolecular interactions on the timescale of the experiment. The study of dynamical processes under thermal (300K) conditions is intrinsically complicated by the distribution of initial conditions of the excitation. This results from the finite width of the Boltzmann distribution(s) of the reactant ground state modes.

By contrast, supersonic jet expansion techniques produce effectively isolated molecules[59] with substantially reduced rotational and vibrational temperatures.[60] The partition function, which describes the populations of the rotational, vibrational and translational degrees of freedom, does not correspond to a true Boltzmann distribution. Typically, the vibrational degrees of freedom maintain the highest effective temperature. This is intrinsically due to the larger energy quantum transitions associated with vibrational as opposed to rotational and translational motions.[61]

The dissertations of two previous students of Prof. Zewail have summarized the hydrodynamic description of free-jet expansions[62] and analyzed a microscopic

picture[63] of the collision processes involved. A brief synopsis of the salient considerations will be presented here.

The jet expansion consists of a carrier gas, which is usually a monatomic system (e.g. He, Ne, Ar), and the dilute seed molecule (e.g. CH_3I,[52] NCNO,[52] HI:CO_2, or *t*-stilbene). The seed is entrained in the carrier gas flow and typically is of 1 part in 1000 concentration. (For an exception to this dilution factor see Chapter 7). As the gas mixture (here assumed very dilute, essentially one component hydrodynamics) expands from the nozzle orifice into a vacuum with a pressure differential of at least 10^3, intermolecular (or atom-molecule) collisions cause relaxation of the equation of state. As noted above, the new thermodynamic state may not necessarily be fully equilibrated for all the degrees of freedom. The convergence of the cooling dynamics is slower than the rate of reduction in the number of cooling collisions. In other words, the axial vector of the expanding gas reaches a position of a certain distance from the source aperture where the collisions do not equilibrate the molecular degrees of freedom, including translation. The position, termed the freeze-in distance, in defined by the expression[64]

$$x_c = \frac{D \cdot (n_s Q D)^{1/\gamma}}{\gamma} = \left(\frac{D}{\lambda_s}\right)^{1/\gamma} \tag{2.20}$$

where D is the orifice (nozzle) diameter, n_s is the molecular density of the source, Q is the collisional cross-section for momentum transfer averaged over the Maxwellian velocity distribution, $\gamma = C_p/C_v$ is the ratio of heat capacities, and γ_s/D is termed the Knudsen number.

Since the momentum of the individual molecules is essentially not disturbed beyond this distance, the path of the molecules is along collisionless streamlines. The flow is finally interrupted by accumulated collisions with the ambient gas of the vacuum chamber. The entrained gas produces an axial shock front, termed the Mach disk, at a distance[59]

$$x_m = \frac{2}{3} D \left(\frac{P_o}{P}\right)^{1/2} \tag{2.21}$$

where P_o is the nozzle (backing) pressure and P is the chamber pressure.

The isentropic core is the term given to the spatial region defined axially by the freeze-in distance and the position of the Mach disk. The radial boundary defining the isentropic core is another shock front; sometimes termed the barrel shock. The isentropic core is pertinent to the present study since this constitutes the region of optimal cooling and isolation.

The temperature at a given position of the expansion within the isentropic core is given by[59,60]

$$T = T_o \left[1 + \frac{1}{2} (\gamma - 1) M_{eff}^2 \right]^{-1} \tag{2.22}$$

where T_o is the source temperature and M_{eff} is the local Mach number. The number density at the position in the expansion is given by[59,65]

$$n = n_2 \left[1 + \frac{1}{2} (\gamma - 1) M_{eff}^2 \right]^{-1/(\gamma-1)} \tag{2.23}$$

where the terms have been defined above. The collision rate at the same position in the expansion is given by[60]

$$z_c = \sqrt{2}\, n\, \sigma \bar{\nu}_o \left(\frac{T}{T_o} \right)^{1/2} \tag{2.24a}$$

which can be rewritten using Eqns. (2.22) and (2.23) as

$$z_c = \sqrt{2}\, n_s\, \sigma \bar{\nu}_o \left[1 + \frac{1}{2} (\gamma - 1) M_{eff}^2 \right]^{-\frac{(\gamma+1)}{2(\gamma-1)}} \tag{2.24b}$$

where σ is the hard sphere collisional cross-section and $\bar{\nu}_o$ refers to the mean of the Maxwellian velocity distribution $\sqrt{\frac{8kT}{\pi M_{eff}}}$. The local Mach number is an empirical quantity, which has been shown to correspond to[59]

$$M_{eff} = 3.26 \left(\frac{x}{D} - 0.075 \right)^{0.67} - 0.61 \left(\frac{x}{D} - 1.075 \right)^{-0.67} \tag{2.25a}$$

for a monoatomic gas and to

$$M_{eff} = 3.65\left(\frac{x}{D} - 0.40\right)^{0.40} - 0.82\left(\frac{x}{D} - 0.40\right)^{-0.40} \qquad (2.25b)$$

for a diatomic gas.

Vibrational cooling may occur by way of formation and dissociation of van der Waals (vdW) complexes in addition to the V-T mechanism, which is the limit of description afforded by hydrodynamic modelling. The low translational temperatures, thereby indicating small relative (i.e., center mass) impact energies, allows for soft collisions that may produce vdW species. Differing mechanisms exist for the intra-complex dynamics[66,67] but the dissociation process is certainly V-T energy transfer. Such ideas may account for the observed[61] inverse temperature dependence for the efficiency of vibrational cooling. Clearly, the formation of vdW complexes in the higher collision freeze-in zone exist and persist in the isentropic core.[68] Ref. 63 contains a clear presentation of the microscopic dynamics, which result in the cooling of the translational motion, and the collisional dynamics, which cause flow along streamlines in the region of the isentropic core.

Having considered some of the desired factors for directly measuring time-dependent reaction dynamics, it is worthwhile to elaborate on the experimental apparatus and the principles of operation. The subsequent sections will make use of the general discussion and background presented herein to specifically outline the experimental system employed in the study of gas phase molecular reaction dynamics. The detailed investigations are presented in the subsequent chapters. The course of the discussion of this section has considered the several essential or fundamental principles which will guide the construction of a generally applicable laser/molecular beam apparatus. This device will be used to carry out time-resolved studies of many different reactions.

2.2 SYSTEM DETAILS

The focus of this section is to provide a detailed description of the femto/-picosecond laser apparatus, which has been used to conduct the experiments described in the subsequent chapters of this thesis. Some motivating factors for the individual components of the apparatus were presented in the previous section. The conceptual and theoretical ideas presented therein will be freely referred to in the current section. The remaining portion of this chapter may be viewed as a systematic presentation of the operational details of the laser/molecular beam apparatus and the support equipment. The general character of the apparatus described herein is relevant to the experimental efforts described in L. R. Khundkar's recent dissertation.

The experimental apparatus may be divided into several component sections: 1) the laser system for short pulse generation and the associated temporal and spectral diagnostics; 2) wavelength generation and the traveling delay line configuration, including the various nonlinear mixing schemes implemented in different experimental efforts; 3) the molecular beam apparatus, including the chamber, vacuum apparatus, pulsed valve and controller, detection methods and beam characterization; 4) the collisionless environment, ambient temperature gas cell; 5) the detection electronics and signal processing apparatus. Finally, a brief overview of the nonlinear least squares data analysis routines will be presented.

2.2.1 Specific Design Considerations

The laser apparatus is conceived to provide a reasonable (if not optimal) balance between several offsetting or conflicting design parameters. Firstly, the essential motivation is to construct an apparatus that has sufficiently good temporal resolution to directly monitor the detailed reaction dynamics through the chosen observable (e.g. LIF, MPI, etc). Secondly, independent wavelength tunability of the pump and probe beams will make possible a variety of experimental measurements, thereby allowing for comprehensive study of the salient reaction. Thirdly,

the temporal resolution is to be balanced with the need for a restricted laser bandwith, which makes possible a greater degree of state specificity in the products, and perhaps also in the reactants. Finally, amplification of the laser pulses to sufficiently high per pulse energies will facilitate efficient and various nonlinear mixing schemes. The latter facilitates the creation of (essentially) continuously tunable pump and/or probe wavelengths from 700-220nm.

Mutual attainment of the first and third desired objectives are restricted to obeying the Heisenberg uncertainty relation $\Delta t \Delta \nu \sim 0.441$ for Gaussian pulses. The spectral resolution necessary to satisfy the state selectivity requirement is dictated by the spacing of, for example, the electronic transitions for adjacent values of the rotational quantum number for the ground state product. Concentrating on CN and OH reaction products for the moment, an estimate for the upper limit of the frequency bandwidth is about 8cm^{-1}. In the case of Gaussian pulse shapes, this allows for 1.8 ps pulse durations (Gaussian FWHM).

Considerations for the optimal compromise in performing pump-probe studies, wherein the desire is to probe the reaction product in a state-specific manner, arise from a spectral limiting requirement. The following chapters are primarily concerned with the probe detection of the hydroxyl radical by way of LIF. A brief description of the spectroscopy of OH would dramatize this spectral consideration for the laser and molecular beam designs.

The LIF detection method is a conceptually simple idea and of high sensitivity. The method follows from irradiating the desired molecular (or radical) species with light from a tunable dye laser source. Scanning the frequency of the laser light changes the probability of observing emission in conjunction with tuning into resonance with a ground to excited electronic state transition. Furthermore, the transition occurs only if the ground (initial) state of the electronic transition is populated. A photomultiplier tube is used to detect fluorescence emission from the excited electronic state. The observed linewidth(s) will be a convolution of the laser spectral width and the intrinsic absorption linewidth. The intensity of the total

fluorescence is monitored as a function of the laser frequency, thus mapping out an excitation spectrum that reflects the relative populations of the initial quantum states.

The hydroxyl radical is a good choice for conducting LIF probing, for several reasons. Firstly, the resonance frequency for the $A\,^2\Sigma^+ \leftarrow X\,^2\Pi$ transition[69] is centered near 308nm, which is a wavelength readily obtainable with current laser technology. Secondly, the upper state fluorescence quantum yield is unity under collisionless experimental conditions (on the timescale of several microseconds). Thirdly, the absorption and fluorescence spectral and temporal properties have been analyzed. Finally, the relative line strength factors for the transitions have been measured.[70] A difficiency of the OH probing is that the $\nu = 2, 3$, and higher vibrational levels of the $^2\Sigma^+$ state predissociate. The rate of predissociation is larger than the rate of emission and prevents the detection of fluorescence emission from these levels. The predissociation follows from a curve crossing of the $^2\Sigma^+$ and $^4\Sigma^-$ electronic surfaces.

The spectroscopy of the $A - X$ band of OH has been characterized by Dicke, et al.[69] Angular momentum coupling in the $X\,^2\Pi$ ground state of OH gives rise to spin-orbit splitting and Λ-type doubling of the energy levels. The $X\,^2\Pi$ state is intermediate between Hund's coupling case (a) and Hund's case (b). Following the notation of Ref. 71, Hund's case (a) describes the most significant interaction to be the coupling of the electron spin and orbital angular momenta individually to the molecular axis because of electron correlation. The projection of $\vec{L}$ on the axis is denoted by $\vec{\Lambda}$, the projection of $\vec{S}$ is $\vec{\Sigma}$, and the resultant sum is $\vec{\Omega} = \vec{\Lambda} + \vec{\Sigma}$. The molecular rotational angular momentum $\vec{N}$, which is perpendicular to the molecular axis, couple to $\vec{\Omega}$ such that $\vec{N} + \vec{\Omega} = \vec{J}$. Case (b) is an adequate description when $|\Lambda| = 0$ but $|S| \neq 0$ in a diatomic molecule. Here, $\vec{S}$ does not couple to the internuclear axis, rather the electron spin remains in a fixed orientation in space while the molecule rotates. The good quantum numbers are S and J, where J takes the values $|N + S|$ to $|N - S|$ and is split into 2S+1 components. The coupling

gradually changes from case (a) to (b) with increasing nuclear rotational angular momentum, $\vec{N}$.

The $A\,^2\Sigma^+$ first excited electronic state is of Hund's case (b) and exhibits the splitting due to coupling of the electron spin with nuclear rotation. Figure 2 schematically shows the energy levels of the $A\,^2\Sigma^+ - X\,^2\Pi$ system and the notation shown is of case (b) designation for both states. In this notation, J is the quantum number for the total angular momentum and N is the quantum number for J-S. F_1 and F_2 represent the two spin components of the upper state (since S=1/2, 2S+1=2). The terms f_1 and f_2 represent the two spin components of the ground state. The subscripts 1 and 2 are defined such that J=N+1/2 for F_1 and f_1 while J=N-1/2 for F_2 and f_2. Primes on f_i indicate the upper Λ-state.

The general selection rule for transitions between the two electronic states is $\Delta J = 0, \pm 1$. For states corresponding to Hunds case (b) the additional selection rule $\Delta N = 0, \pm 1$ occurs. Transitions which satisfy both selection rules form strong branches and those that violate the ΔN rule are weak. The exception to the latter point occurs for small N. Additionally, the even$\rightarrow$odd and odd$\rightarrow$even ($+ \rightarrow -$; $- \rightarrow +$) symmetry selection rule must be satisfied.

The transition branch types (O,P,Q,R,S) are defined according to their change in N (e.g. ΔN=2 implies O-branch and ΔN=-2 implies S-branch). The subindices refer to the subindices of the final and initial levels, respectively, where, for example, $Q_{21}(N) = F_2(N) - f_1^1(N)$. If both indices are the same, the branch is termed a main branch and is given only one sub-index. The branches with two subindices are termed satellite branches. Figure 2 shows transitions from the various branches with labels. The main branches Q_1, Q_2, R_1, P_2 have a satellite branch which originates from the same level in the $^2\Pi$ state and transitions to a different spin component in the upper state (c.f. $Q_1(2)$ and $Q_{21}(2)$). In the case of LIF mesurements, a branch and its satellite branch represent redundant information about the population of the level of origin.

The OH rotational constant B has a value of $18.515cm^{-1}$ in the $\nu = 0\ ^2\Pi$ state and $16.961cm^{-1}$ in $\nu = 0$ of $^2\Sigma^+$ state. The energy splitting between the $Q_1(1)$ and $Q_1(2)$ transitions is calculated to be $7.8cm^{-1}$. This transition energy difference establishes the maximum value for the probe laser bandwidth. Operationally, it would be desirable to have a bandwidth which is less than half of this value.

2.2.2 Laser Apparatus: Pulse Generation and Amplification

The presently employed laser system is not uniquely indigenous to this thesis, but has been uniquely coupled with the molecular beam apparatus to allow for a high degree of initial and final state specificity in rotational, vibrational, and in the case of the oriented bimolecular reaction of Chapter 7, the relative translational motion of the reactants.

The aforementioned restriction on the probe laser bandwidth and the implicit desire to have an easily tunable laser system limits the choice to the synchronously pumped dye laser discussed in the previous section. The dual jet synch-pumped actively/passively mode-locked dye laser was excluded due to added complexity without being able to take full advantage of the significantly shorter pulse durations inherent in this design.

The pump laser source was either an acousto optically mode-locked Ar ion or Nd^{+3}:YAG laser (Spectra Physics model 342A-01 acousto-optic mode-locker). Both lasers produce relatively stable trains of pulses, and are a convenient pump energy source for the dye laser. The Ar ion laser pulse duration is typically 120ps FWHM Gaussian for an output at 5145Å and 0.9 watts average power. The Ar laser has barely sufficient peak pulse energy to effectively pump two dye lasers in tandem. Moreover, the Ar laser suffers from significant amplitude and phase noise, which ranges from near DC to 4MHz (see Ref. 26 and references therein). The cross-correlation jitter for two optimally aligned synch-pump dye lasers being pumped by an Ar ion laser has been measured to be 6-7ps (Gaussian).[72] The dye laser pulses for a linear cavity laser pumped by an Ar laser have a Lorentzian temporal profile.[23]

A mode-locked Nd:YAG pump laser produces considerably improved jitter responses for two synchronously pumped dye lasers.[28] This results in part from the 80ps FWHM Gaussian pulses. Photographs of oscilloscope traces of the YAG fundamental, 532nm and dye laser pulses (and convoluted electronic response) are shown in Figure 3a. Another contribution to the better jitter characteristics is the reduced amount of amplitude noise in the 100KHz to 4MHz range. Phase and amplitude noise in this frequency range is readily apparent in poorer quality mode-locked pulses. Figure 3b shows oscilloscope traces of the noise spectrum of the Nd:YAG laser.

Pumping only one cavity length matched dye laser and deriving the second, independently tunable, pulse from the first eliminates the jitter contribution to the laser system response function. This benefit is obtained at the expense of additional complexity in the generation of the second tunable light source. The remainder of this subsection will focus on the description of a single amplified dye laser pulse that generates the pump pulse fundamental via continuum generation.

The Nd^{+3}:YAG laser (Spectra Physics Model 3000) is mode-locked with a prism/transducer acousto-optic modulator (Spectra Physics Model 342A-01). The Rf frequency (near 41MHz) is derived from an ultra stable frequency synthesizer/Rf amplifier unit (S.P. Models 451, 452). A servo loop (S.P. Model 453) monitors the phase of Rf reflected from the transducer and adjusts the Rf intensity to optimize the resonance lock by changing the temperature, hence the resonance frequency, of the acoustic cell. The last device also amplifies the Rf to provide up to 1.5 watts of power to the transducer. The YAG laser is a stable resonator design with a symmetrically placed rod. The AO-modulator is near the high reflector and the output coupler is 10% transmissive.

The 1.064μm output is focused into a $3 \times 3 \times 5$mm KTP cyrstal. The 5320Å output is separated by dichroic beam splitters from the fundamental. The output pulses of 10nJ energy, 82MHz repetition rate and 600-900mW power are used to pump a single cavity length matched dye laser. The 80ps pump pulses with

900mW power are also of sufficient energy to simultaneously pump two dye lasers (c.f. Chapter 5 and Ref. 52). A schematic of the YAG and dye oscillators and the amplifier arrangement is shown in Figure 4.

The cavity length matched dye laser (ΔL=+1 to +3μm) is used with a range of dye (R560, R590, DCM, LDS-698, etc.) to obtain the desired fundamental frequency. Most experiments employ the dye R6G (R590) in ethylene glycol at about 1×10^{-3}M concentration. The dye jet is a 200μm thick stream of the dye/glycol solution. The dye-jet is formed by flowing the solution, at 40psig, through a flattened stainless steel nozzle. The surface tension of the liquid maintains a smooth stream and flat surfaces following the nozzle. The design produces two interferometrically flat parallel faces on the dye stream. (A strong interference pattern is obtained from the spatially overlapped portions of the front and back surface Brewster angle reflections.) The dye laser timing element consists of two or three crystaline quartz birefringent plates, which are fixed at Brewster's angle in the path of the cavity. The two-plate birefringent filter (BRF) resulted in a lasing bandwidth of 7.5-9.0cm^{-1} FWHM Gaussian. In the case of a three-plate BRF the third plate could be rotated with respect to the other two to narrow or broaden the lasing bandwidth. The bandwidth range for the 3-plate BRF is discretely adjustable from 2.0cm^{-1} to 7.0cm^{-1} and produces nearly transform limited pulses. The step size for the adjustment depends upon the spectral rotation orders of the 3rd plate and is about 0.5cm^{-1} on average. Typically, the higher the rotation order the narrower the resultant laser bandwidth.

Finally, the three mirror cavity is an astigmatically compensated design, although the beam waist in the jet is astigmatically distorted. Operationally, the dye laser was run in a fashion that restricted the temporal pulse duration by the limited spectral bandpass of the tuning element. The combination of restricted laser bandwidth, well mode-locked less than 80ps pump source and cavity length matching (and stability) are desirable conditions for obtaining extensive mode competition

and transform limited operation. The mode competition follows from the establishment of a balanced gain modulation - nominal loss condition which minimizes the laser (longitudinal mode) pulse substructure. The gain/loss balance of the dye laser was adjusted to obtain stable and reproducible pulses that were essentially transform limited. Choosing an output coupler of 30% transmissivity provides considerable loss and allows the gain to be balanced by adjusting: (i) the incident pump power, (ii) size of the focused excitation light in the jet, and (iii) the R6G and DQOCI concentrations.

These oscillator pulses were monitored on a continuous basis with a spinning-block home-built autocorrelator. The design is schematically depicted in Figure 5. The broader (homogeneous) gain profile of the dye medium allows for obtaining minimum autocorrelations of 3ps FWHM, as measured by autocorrelation. The realization of stable 2.1ps (assumed Gaussian shape) pulse generation is facilitated by having only a 1-3μm cavity length mismatch between the YAG and dye cavities and the use of a two-plate birefringent filter as the cavity tuning element. The typical satellite pulsing obtained near optimal cavity length match is minimized by adding the saturable absorber DQOCI to the gain medium. The pulsewidth is dictated by the number of modes in the bandpass remaining above the lasing threshold and locked in phase.

The autocorrelator functions as a continuously variable delay Michelson interferometer. The delay originated from a spinning 3/4″ thick glass block. A beam splitting cube separates the incoming light into the two arms of the interferometer and both beams pass through the glass block. The lengths of the arms are adjusted and the beams are aligned to have the t=0 position occur for a block orientation of $\theta_o = 45°$ to both incident beams. The orientation of the laser polarization is of P-polarization with respect to the block face. The retroreflecting design of the interferometer compensates for refraction in light traversal through the glass block. The useful autocorrelator range is about 30ps as measured by adjusting the delay of one arm and observing the signal on a synchronized (at 60Hz) oscilloscope. For

small deviation of the orientation of the block from 45° the delay is a nearly linear range described by

$$\tau_d = n\,L \cdot (\sin\theta_1 - \sin\theta_2) \cdot 33.3\text{ps/cm} \tag{2.26}$$

where n≃1.5 in the index of refraction of glass, L=1.90cm, θ_1 and θ_2 are the angles of incidence of the two beams. It is seen that the useful angular range is about ±8 degrees.

The necessity for amplifying the dye pulses arises from the need to obtain higher peak powers to sucessfully employ more versatile frequency generation methods and thereby allow for the generation of the desired pump and probe wavelengths. Many amplification methods exist but all obtain approximately the same average power of 10-100mW. Operationally, the choice becomes one of trading-off high peak power for higher repetition rate in the amplification process. The requirements of some of the experimental efforts described in the next chapters and in L.R. Khundkar's thesis[52] have required high peak power pulses to ensure success.

The main portion of the dye laser beam was injected into a four-stage pulsed dye amplifier pumped by a 20Hz, 300mJ/pulse (532nm) Q-switched YAG laser (Quanta Ray Model DCR-2A). The synchronization of the firing of the Q-switched pump to the dye laser output was obtained by monitoring the Rf signal fed into the piezo transducer of the cw-YAG. The time delay was electronically controlled. The 3ns pulse duration of the Q-switched YAG eased the electronic jitter requirements (to about ±1ns) and allowed for an amplifier design with only approximately equivalent (±5cm) optical path delays for pumping each stage of amplification. The first three amplifier stages were pumped in a transverse fashion with 6, 15, and 25% of the pump energy going to the first, second, and the third stages, respectively. The amplifier design is shown in Figure 4.

The first two stages were optically separated by either a spatial filter or a 200μm thick dye jet of 4×10^{-4}M malachite green or DQOCI in ethylene glycol.

The second and third stages were separated by a 50μm diameter diamond pinhole spatial filter. The primary purpose of the spatial filters is to reduce the amount of amplified spontaneous emission (ASE) intrinsic to pulsed dye-amplifier designs wherein the pump pulse is of much longer duration than the pulse to be amplified. The lenses that focused the beam into the spatial filters also increased the beam diameter in each subsequent amplification stage from initially 0.5mm to a final size of 1cm diameter. The fourth stage was longitudinally pumped by the remaining 50% of the 532nm beam and the 1cm diameter was matched to the size of the YAG transverse beam diameter. The amount of gain extracted from the four stages was 250, 125, 3, and 10, for an increase from the input pulse energy of 0.5nJ to 0.5mJ. The path length in the first two stages is about 2cm and increases to nearly 3cm in the last two stages.

The amplifier design is generally similar to that presented in Ref. 47. The present design is optimized for the amplification of a wide spectral range. This facilitates the production of continuously tunable amplified picosecond pulses. The primary enabling requirement is to avoid the need for saturable absorber jets between the gain stages. The diamond pinholes (Fort Wayne Wire Dye) adequately isolate the stages. This is done without discriminating against wavelength tunability. Comparable flexibility is not obtained with saturable absorber jets where the dye concentration or the saturable absorber dye must be reoptimized at every wavelength.

The optical train produces infinitely conjugate ratio beams between each stage. The increase in the beam diameter from stage to stage allows for full transverse Fourier mode evolution. All the optics of the apparatus are positive lenses and are arranged sequentially from shorter to longer focal length. Negative lenses, which can change the inverse transform function, are not used. Astigmatism is avoided by passing essentially collimated beams through the dye cells. This is necessary because the cells are angled to prevent ASE from reflecting and hence oscillating between two stages.

The autocorrelation of an amplified pulse is shown in Figure 6a. The 6.6ps FWHM Gaussian pulse shape, shown with the fitted Gaussian, does not exhibit a coherence-spike feature, indicating that the pulse originates from a well mode-locked dye laser. The broad temporal width comes about because of the narrow dye laser bandwidth (of $2.5cm^{-1}$), which is selected by the tuned (i.e. aligned optical axes of the) 3-plate BRF.

Amplification of short duration pulses requires that the gain bandwidth is spectrally broader than the laser pulse bandwidth. This requirement is especially important for femtosecond pulse amplification where the pulse bandwidth could be as large as several hundred wavenumbers. Optimization of the gain curve in each dye state to optimally match the laser pulse bandwidth may require the use of different dyes in successive states.[47] Figure 7 shows a plot of the amplified pulse (as opposed to autocorrelation) width for different ultimate final pulse energies. The figure also shows the temporal behavior of the coherence spike that reflects the substructure underlying the pulse. It is seen that the pulse broadens but the pulse coherence time is not affected. The pulse has been intentially poorly mode locked with a tuning wedge in the cavity - the mode locking is not sufficient to maintain phase coherence over the entire bandpass envelope.

The saturable absorber was used for two reasons. Firstly, amplification of 0.3 to 2.0ps duration pulses without the saturable absorber and only the spatial filters tends to broaden the pulse duration to 1.5 to 2.5ps, respectively, for 0.5mJ output pulse energies. The absorber reduced this broadening by at least 50%. Even less pulsewidth broadening could be obtained for lower amplification gain factors. Secondly, the saturable absorber was also somewhat more effective in reducing the ASE which originates in the first stage than the spatial filter. The dye in the amplifier stages was a mixture of R640/CV670 in about a 10-15:1 ratio when the experiment involved OH probing. The solvent was methanol in all stages, with the concentration of the dye being 2×10^{-4} M in the first two stages and 5×10^{-5} in the last two. The dye mixture was used in an energy transfer mode to obtain enhanced

gain near 619nm when the $Q_1(6)$ transition was probed. The R640/methanol alone gives little gain at this wavelength. Other dyes such as LDS-698, DCM, KR620, R610, R590, R560 have been used in the amplifier to produce amplification over the 700-560nm range of the dye laser output.

An alternative scheme was required for the experiments of Chapter 3. A fiber/grating pulse compression scheme was used to reduce the pulsewidth to approximately 0.4ps.[38] The compression required a 20-30nJ 5.5ps pulse for sufficient peak intensity to obtain adequate SPM and the concomitant spectral bandwidth in the optical fiber. A DQOCI saturable absorber dye jet was inserted after the second amplifier stage, with a dye concentration of about 5×10^{-4}M. The grating double-pass separation was also used to pre-compensate for the quadratic (GVD) dispersion which arises from passing through the amplifier. Figure 6b shows the amplified pulse, fitted with a Lorentzian shape to 0.42ps. The broadening from 0.36 to 0.42 is not an unusually large amount. The small degree of broadening arose from saturable absorption, which preferentially removes part of the broadened pulse leading edge. The small broadening also resulted from the chirp pre-compensation, which may be done by extending the grating-pair separation beyond the amount necessary to simply optimize the pulse duration out of the compressor. Finally, limiting the gain factor to only obtain 150μJ pulse energy, in turn limits the amount of gain saturation which occurs in the amplification. The ubiquitous "pedistal"[38] feature, which arises from the cubic contribution to the instantaneous pulse phase (or frequency)[42] was eliminated, or at least significantly reduced. It is believed that this resulted from the combination of chirp pre-compensation and the threshold break-through operating condition of the saturable absorber, with the rapid ground state recovery time.

2.2.3 Continuously Tunable Synchronized Pulse Generation

The amplified picosecond pulse is split by an 80% reflectance beam splitter, where the transmitted 20% of the beam will be frequency doubled and used as the probe beam. The majority of the light is focused into a cell of nanopure water

and results in the creation of an optical continuum.[53-56] The spectral continuum is produced to allow for good pump-probe laser pulse synchronization with a minimum of relative timing jitter. The continuous frequency light source is to be used as the seed light pulse for a second amplifier. This (re)amplified continuum light is to serve as the source of the fundamental light frequency that becomes the tunable pump beam. Extensive optical manipulation of this light source is required for spectral bandpass selection, limited pulse shaping and amplification to the 0.1-0.25mJ level. For more extensive discussions of pulse shaping, see Refs. 74 and 75.

The spectral continuum is obtained when the intense optical pulse from the first amplifier interacts with an appropriate medium for efficient conversion. A half-waveplate rotates the plane of polarization of the entrant light source to the horizontal to enhance the efficiency of the optics which are to follow. An 8cm lens focuses the beam into a 2cm cell of water. The optical continuum beam is recollimated with a 6cm achromat lens and is analyzed with a polarizer, which is set to transmit only horizontally polarized light. Self phase modulation (SPM), observed to be a significant mechanism in continuum generation,[54-56] should maintain the same polarization of light as the entrant beam. Figure 8 shows a semilog plot of the spectral intensity distribution of the continuum.

Following the polarizer, the beam is diffracted off an 1800 lines/mm ruled diffraction grating, is directed into a cylindrical lens (f=15cm) placed 20cm after the grating face and onto a variable aperture slit positioned at the focal plane of the cylindrical lens. A retroreflecting mirror immediately follows the slit and passes the spectrally selected beam back onto the grating but displaced ~2cm below the entrant beam. This optical scheme is depicted in Figure 9a. The retroreflected beam is vertically displaced. The grating is blazed at 600nm and has a better diffraction efficiency for p-polarized light for wavelengths shorter than the designed blaze. The first order diffracted beam is used in the current arrangement. A more elaborate quadrupal pass arrangement is shown in Figure 9b. The arrangement obtains twice the dispersion and also eliminates the spectral chirp of the transverse mode profile,

which occurs with a double pass arrangement. The double pass may also produce a horizontally elongated mode, as suggested in the second-pass of Figure 9b, which may result in temporal broadening.

Martinez[76] has shown that the introduction of a lens of focal length longer than its separation from the grating face will allow for the introduction of position group velocity dispersion (GVD) on the exiting beam, causing a positive linear chirp to be introduced in the pulse temporal behavior. Treacy[37] has shown that a grating pair arrangement introduces negative GVD. This latter arrangement has been applied to pulse recompression following dispersion in an optical fiber.[38,39] This arrangement introduces negative GVD and acts to compensate for approximately 0.5ps of pulse broadening by quadratic dispersion. Such temporal broadening arises from the dispersion of the index of refraction in the glass, suprasil, and the dye medium of the amplifier. In particular this negative GVD will offset some of the positive GVD introduced by the second amplifier.

The resultant spectrally selected pulse, with a 3Å bandwidth, has approximately the same temporal pulse duration as the pulse entrant on the continuum cell. This narrow bandwidth gives only a small amount of spectral transverse chirp and does not measurably affect the duration of the continuum pulse. The pulse energy of this spectrally selected portion of the optical continuum varies from about 25nJ near the center frequency to about 0.5nJ at 470nm. These pulse energies are sufficient to be injected into and serve as a seed for a second dye amplifier. This second amplifier was pumped with either the second or third harmonic of the Q-switched YAG laser. The three stage amplifier, with the last state being longitudinally pumped, could obtain amplification factors of $\sim 2 \times 10^4 - 5 \times 10^5$ depending on the pump wavelength, amplifier dye and initial picosecond pulse energy.

Figure 10 shows the cross-correlation (sum frequency generation) of the pulse that gave rise to Figure 6a and the 530nm amplified continuum pulse. The cross-correlation $G(\tau_p)$, with width, $\Delta\tau_p$, was fit to an 8.5ps FWHM Gaussian. The

continuum (assumed Gaussian) pulse width may be obtained by Gaussian deconvolution where

$$\Delta\tau_p{}^2 = \Delta t_1{}^2 + \Delta t_{cont.}{}^2 \tag{2.27}$$

and Δt_1 from Figure 6a is 6.6ps. This yields a 5.3ps FWHM Gaussian pulse width for the spectrally selected optical continuum pulse. The high order of the continuum generation process and the pulse chirping with the grating/lens arrangement has obtained a temporally shorter continuum pulse than the generating pulse.

The experimental studies of Chapters 4, 6, and 7 used this synchronized pump-probe pulse scheme. The work of Chapter 6 directly utilized the output from the second dye amplifier. Amplification of 532-474nm light with the 355nm pump and several dyes (coumarins: 522, 500, 481, 480, 460; Exciton Chemicals)[77] in polar and nonpolar solvents (ethanol, hexane, cyclohexane) obtained 0.2mJ pulse energies throughout this range.

The time-resolved experimental studies of Chapters 4 and 7 were performed over the wavelength range 265-230nm. Continuous coverage of wavelengths 265-237nm is obtained from second harmonic generation of the amplified output. The frequency doubling was performed in a 4mm β-borate (β-BBO; CSK Co.) crystal[78] placed slightly after the beam waist of a 1m focal length lens. This second harmonic light was used as the experimental pump beam and initiated a bimolecular reaction by causing the HI moiety to dissociate. Alternatively, the 266nm picosecond pulse was used to photolyze HOOH. Amplification of wavelengths in the 620-580nm range was also demonstrated. The only complication for this wavelength range is the proximity to the ASE spectral band from the first amplifier. Narrow pass interference filters (Corion Model P10-620) or the saturable absorber jet in the first amplifier minimized the problem with reamplified ASE.

Attempts were made to obtain better energy extraction without pulse distortion from the second amplifier by introducing a large positive GVD chirp.[50] However, the narrow spectral width of the selected continuum light and the space restrictions for the lens/grating pulse processing device (confined to a 1.5 sq.ft. region) limited

the amount by which the pulses could be temporally broadened. These constraints precluded the attainment of sufficiently broad pulses, and the associated increased amplification energy extraction efficiency, to overcome the additional power losses occuring from double-passing off of another optical grating arrangement. The second grating arrangement, with the inverse (negative) GVD properties as that used for pulse broadening, could, in principle, be implemented to recompress the high intensity pulse.

As mentioned above, the 20% remainder of the beam from the first amplifier is used to form the probe beam. The visible pulse propagates through a variable delay line (stepper motor/worm gear translation stage) 10μm/step resolution to obtain the timing delay between the pump and probe pulses. The beam is then focused (f=40cm) into a 1mm KDP crystal, recollimated with a 25cm suprasil lens and sent toward the molecular beam apparatus. By focusing into the thin nonlinear crystal, and in particular placing the crystal within a confocal length of the position of the beam waist, causes the second harmonic transverse profile to become much less structured than the entrant fundamental beam. This pulse, with a narrow spectral bandwidth is used as the probe pulse (for OH LIF) in most of the following chapters.

The experiment of Chapter 7 and experiments of reference (52) are performed in a molecular beam apparatus. The pump and probe beams are independently focused into the molecular beam apparatus. A 150μm diamond pinhole inside the chamber and on the axis with the molecular beam, but positioned orthogonal to the direction of the jet expansion, is used to overlap the pump and probe light beams. Typically, a 0.75m plcx lens is used to focus the pump beam and a 1m plcx lens focuses the probe light. This arrangement allows the beam waists of the pump and probe light to be independently adjusted and matched to the molecular beam axis. Both beams show significant diffraction from the 150μm pinhole. The pump and probe beams are combined by a dichroic reflector (coated to allow for 80-90% transmission of the probe light) and propagate collinearly through the molecular

beam apparatus. The pump pulse energy is 5-10μJ, and the probe pulse energy is attenuated to be $\leq 1\mu$J.

2.2.4 Molecular Beam Apparatus

The molecular beam apparatus consists of a pulsed nozzle, a vacuum chamber, a pumping unit and an electronics unit. The last component subsystem provides an electrical pulse to the valve in synchrony with the Q-switched laser firing. A partial cut-away drawing of the molecular beam apparatus is presented in Figure 11. The laser beams may enter the LIF or MPI ports. These beams are oriented orthogonal to and directed into the plane of the page. The vacuum chamber consists of two cylindrical chambers (10″ and 8″ diameters, 1/8″ stainless steel wall) separated by a 1.5inch tall 1.3mm opening tapered cone Ni electroformed skimmer (Beam Dynamics). The skimmer allows for differential pumping of the two chambers, nominal experimental pressures of 2×10^{-4} torr and 4×10^{-6} torr exist in the primary and secondary chambers, respectively. Each volume is evacuated with a 6″ diffusion pump (Varion VHS-6). The chambers are isolated from the pump via LN_2 cryobaffles. The baffles effectively eliminate backstreaming of pump oil. The primary chamber, which handles greater than 95% of the gas load, is arranged with the axis of the expansion, the laser entrance and exit (light baffle) ports, and the LIF collection optics and 150μm pinhole on three mutually orthogonal axes. The second chamber also has three such mutually orthogonal axes; one defined by the now skimmed molecular beam, the second contains the entrance and exit optical ports for the laser light (used in reference (52) and Appendix A), and the third consists of an electron ionization time of flight mass spectrometer (EI-TOFMS), described below.

The pulsed nozzle assembly is of Kel-f and Teflon-coated metal construction. The valve design has been described before,[79] so the elaboration here will be brief. The valve is a solenoid-plunger design, wherein a current pulse energizes the solenoid coil. This induces a metal piston to be retracted and pull the Vespel plunger (with a Viton tip) to expose the orifice opening. The valve is closed by the action of a

small spring which forces the Vespel/Viton plunger to seal the opening. All of the exposed metal surface have been coated with a 2/1000″ layer of Teflon to prevent the experimental gases (e.g. HI) from decomposing or reacting in the nozzle plenum just prior to expansion. The nozzle orifice is created by a 1/16″ thick strainless steel disk (held to the Kel-f nozzle body by a screw-on cap) with a 500μm hole. The screw cap contains a 60° conical aperture centered on the orifice position. The 2mm deep conical extension slightly confines the jet during the early collisional (i.e. cooling and clustering) portion of the expansion. Such a shaped orifice is thought to aid in the formation of molecular clusters.

The nozzle open-time is controlled by the voltage and pulse duration of the electrical pulse applied to the solenoid (120V, 550-600μsec). The resultant open-time, as measured by the EI-TOFMS varies from 600-800μsec. The time-delay of the firing of the electric pulse and the laser firing is adjusted to optimize the amount of the desired cluster present at the arrival time of the laser pulses. The pulsed nozzle controller is triggered by a TTL signal from the Q-switched YAG. This trigger pulse arrives 3.3 msec prior to laser Q-switching. The controller generates an appropriate internal timing delay. The delay time is adjusted by optimizing the 1+1 molecular complex ion signal.

The second vacuum chamber contains the EI-TOFMS, which consists of a pulsed electron gun juxtaposed with several voltage grids, a TOF field-free drift region (1 meter) a grounding grid and the ion detector (EMI-9642/3B). This apparatus is depicted in detail in Figure 12. The positive ions generated in the interaction region by photoionization via electron impact ionization are electrostatically accelerated toward the detector. Ideally, all the ions receive the same amount of kinetic energy, but because of mass differences, the heavy ions achieve a lower terminal velocity. The velocities scale inversely with the square root of the ion mass. The field-free drift region acts to spatially separate the fragments, hence their arrival time. The linear equation for the arrival times, obtained with two calibration

masses (to obtain the slope and intercept), directly defines the square root of the ion masses.

The electron gun consists of a filament in a Faraday cup and an extraction (gate) grid. The filament is clamped to a Macor base which is, in turn, supported in a stainless steel cup. The gate plate is supported on Macor insulating spacers and is linked to a separate bias supply. The electrical connections for the filament bias and filament current supply and return and the gate bias are made via vacuum electrical feedthrough elements. These insulated connections pass through the base of the rotatable stainless steel vacuum flange. The same flange supports the entire mechanical structure of the electron gun. A bridged rectifier DC power supply provides 3.5-4.0 amps of current to the coiled tungsten wire (0.005″) filament. The room temperature voltage drop occurs across the 1Ω filament resistance. The Faraday cup is held at the potential of the low-side of the filament, which (along with the covering extraction grid) "stores" the electrons. The gate grid is held several volts below the filament potential, and is pulsed +20 to 30 V above the filament potential for about 1μsec to extract the electrons. The electrons pass through two additional slotted steel plates which act to better define the electron beam by serving as a crude Einsel lens. The bias on these plates is the same as that on the gate. The electron beam is subsequently accelerated to 30 to 50 eV energy, which is the potential difference between the filament and repeller/accelerator grids.

The electron beam current reaching the repeller grid is about a 5 to 10μA/pulse at 20 Hz and 3.5 Amp filament current. The gate pulse duration is the nominal 1μsec value. It may be infered that a significant amount of electron storage occurs in the Faraday cup surrounding the filament. This conclusion comes from comparing the efficiency of this emission intensity with the duty cycle for the electron beam and taking account of the maximal 1% emissivity of the untreated tungsten filament.

The repeller grid is pulsed to the accelerator voltage about 0.75 μsec before the beginning of the gate pulse and returned to 150 V above the accelerator grid voltage 0.25 μsec following the end of the gate pulse. This creates a field-free region between

the repeller and accelerator grids; that is, the crossing-region of the electron and molecular beams. Four symmetrically positioned cylindrical permanent magnets (not shown in the figure) surround the electron gun. The magnets extend vertically to the region between the repeller and accelerator grids. These magnets are oriented to reduce the divergence of the electron beam and increase the electron beam density in the interaction region. The addition of the magnetic field increases the intensity of the detectable mass peaks by about a factor of 5.

The electron gun drive electronics, which produce the gate pulse and pulse the voltage of the repeller grid, is based on a discrete transistor design. A schematic circuit diagram is shown in Figure 3.4 of reference (52). Briefly stated, the trigger for the drive electronics is produced by a Wavetek pulse generator (model 802),which in turn is triggered by the electrical output of an H.P. fast photodiode. The photodiode monitors the Q-switched Nd:YAG laser pulse. This allows for producing the electrical pulse in time synchrony with the optical pulses (and spectroscopic experiment). The trigger pulse, which is 2 μsec in duration, is an input for the two electronic control circuits. In the case of the gate circuit, the amplified trigger pulse is used to rapidly ($\sim$25nsec = risetime) switch, via a high voltage capable MOSFET (Motorola model MPT-1N60), a 30-40V pulse into a 2μF, 600V rated capacitor. The capacitor induces the 30 to 40V pulse onto the nominal DC voltage of the gate.

The circuit for the repeller pulse is similar in design (c.f. Figure 3.4 of reference 52) except that the pulse feature (2μsec duration, 150V amplitude) is subtracted from the nominal 550V bias of the repeller. This is caused by switching a simple MOSFET of the same design. This discrete device can hold-off 600V, and with the present circuit design is able to transiently switch $\sim$180V. This switching action connects the repeller DC bias to a 47Ω drop to ground.

The repeller, accelerator and ground grids are located directly above the electron gun, and all of the grid spacings are about 3 cm. All of the grids, including

the electron gun, consist of a Ni electroformed mesh that is 90% transmissive. Proceeding vertically up toward the detector, the grounding grid is followed by two parallel, vertically oriented electrodes. One of the plates is grounded and the other, when properly biased, deflects the ions of a given mass-range toward the detector. These deflection plates serve to remove the transverse velocity component of the ions, which arises from the translational velocity of the molecules in the skimmed expansion. A second grounded grid, located 1 meter above the first, defines the end of the field-free region of the TOF drift tube. The ion detector cathode, at -3200V, follows the grounding grid, and accelerates the ions to energies sufficient to initiate the electron cascade through the 18 dynode detector, with about 20% quantum efficiency. The TOF-MS is of standard design[80], although the detector is not. The present design for the electron gun was inspired by the more elaborate system of reference (81).

The mass resolution ability using either of the data acquisition methods described in the following subsection, especially in the boxcar detection scheme, is approximately 4 amu at 127 amu. The detection resolution at the mass of the desired complex, m/e=172, is about 6-8 amu for good peak separation. Figure 14 shows an EI-TOF mass spectrum of an expansion of 94.5% He, 4% CO_2 and 1.5% HI at 1800torr though a 0.5mm orifice. Selected ion peaks are labeled for reference. The mass spectral features for the complex are sometimes seen convolved with the $(CO_2)_4$ species - four mass units larger. A slightly too rich CO_2concentration results in a broadened feature, with two discernable peaks, at 172 and 176 m/e positions.

A large dynamic range for the signal detection is required to observe the 1:1 complex and the even more evanescent signal corresponding to the higher mass (undesired) clusters at the few-millivolt level. This implies that the HI signal level is about 100 mV, the CO_2 level is 300-400mV and the helium peak is saturating the detection/amplification system at a level of in excess of 2V.

Similar EI-TOFMS devices can achieve unit mass resolution at m/e=128.[81] One essential difference between the designs lies in the method of pulse generation and

the applied acceleration voltages. The time duration of the rising edge of the repeller pulse has a large effect on the system time, hence the mass, resolution. The present design limits the rise time (trailing edge) of the repeller pulse to $\tau(1/e)$ ~150nsec. The design of reference (81), employing high speed pulse generators instead of the present MOSFET arrangement, accounts for much of the ×5 better m/e resolution. The electrical pulse generating system described above is much more inexpensive than the system of reference (81), at the expense of poorer mass resolution. The poorer resolution also arises from the large (3cm) grid spacings, low grid voltages and relatively small E-fields. The ×2 larger overall acceleration voltage and 2-5 times larger potential gradients for the repeller-accelerator-ground grid arrangement (1cm vs. 3cm grid spacings) is a better approximation to the ideal limits of first order space charge focusing.[82]

The latter effect has been described by Willey and McClaren.[82] The need for first order charge focusing stems from the condition that an ion that is initially closer to the detector acquires less kinetic energy, and therefore, takes more time to pass through the field-free region. The focusing effect requires choosing the repeller-acceleraator grid spacing, $2s_0$, the accelerator grid separation, d, and the drift region, D. The respective E-fields, E_s and E_d are then optimized to focus the initial spatial distribution of ions in the interaction region at the detector plane. The relationship between the fixed positions and the adjustable parameters is[82]

$$D = 2s_o k_o^{3/2} \cdot \left[1 - \left(\frac{1}{k_o + \sqrt{k_o}} \cdot \frac{d}{s_o} \right) \right] \tag{2.28}$$

where $k_o = (s_o E_s + qdE_d)/(s_o E_s)$, and q is a unit of charge. In practice, this expression may be rewritten to allow a clearer presentation of the voltages that are necessary for fixed values of $2s_o$,d and D. Equation (2.28) dictates the relative voltages on the respective potential grids, and optimizes the length dimensions to obtain the least temporal spread in the ion flux for the individual ion masses at the detector. It may be seen that larger bias values, along with smaller grid

spacings, hence larger potential gradients, are desirable in simulating the asymptotic conditions appropriate for this expression.

2.2.5 Signal Detection

The 50Ω terminated output of the detector is fed into a 500MHz (PAR model 115) ×10 wide-band amplifier. The output is entrant on a Boxcar integrator and averager unit (PAR model 164, 162 averager), which produces an output voltage proportional to the current observed in the 50nsec integrator gate width. The voltage output is fed to a voltage-to-frequency (VFC) converter, and the signal is stored in a multichannel analyzer (MCA, Tracor Northern models TN-1706 & Tn-1314). The time delay position of the boxcar gate may be swept in time to scan a mass-spectrum, higher mass species arriving at the detector later in time than the lighter ions.

Alternatively, the output of the ×10 amplifier is fed into a 100MHz transient digitizer (LeCroy model TR8818). The device simultaneously samples 1000 sequential 40 or 80 nsec time intervals and digitizes the analog voltage signal of the entire mass-spectrum (or a selected portion thereof) for every laser shot. This parallel data collection expedites the diagnostic exercise. The transient digitizer is hard-wired (direct memory access, DMA) into an LSI 11/23 minicomputer for storage of the 1000 channel signal every shot. This method, however, has poorer ultimate temporal resolution than the Boxcar gated integrator described above.

The experimental signal is monitored by LIF of the OH product with the probe laser tuned to the $X^2\Sigma \leftarrow A^2\Pi$ electronic transition. The fluorescence emission is monitored, as mentioned above, at right angles to the laser and molecular beam axes. The laser, focused to a 150 μm beam waist diameter, intersects the molecular beam at x/D=40-45, which is 40-45 nozzle diameters downstream. It is expected that the turbulent flow (collisional) region ends by x/D=25 or less for the experimental conditions. The emission is collected by a 2″ diameter planoconvex f/1 suprasil lens. The lens is positioned to collimate the emission. This now collimated emission

passes through a 2″ diameter 3/8″ thick suprasil window which forms the vacuum seal along this optical path.

The collimated light next passes through a 12nm FWHM bandpass interference filter (Andover) centered at 308nm. Another plano-convex lens (f/1.5, 2″ diameter) focuses the entrant light onto an adjustable slit, which is set to maximize the signal throughput and minimize any scattered laser light. Since resonance fluorescence is being probed, light scattered from other portions of the chamber is preferentially discriminated against. Filters in addition to or instead of the interference filter are placed between this f/1.5 lens and the slit to minimize the amount of filter fluorescence (from these cut-off or bandpass filters Schott WG-320 and UG-11, respectively) that could reach the detector. Another f/1.5 lens recollimates the emission which passes through the slit, and a final f/1.5 lens, which is permanently mounted inside the PMT housing, focuses the emission onto the photocathode of a signal photon counting PMT (Amperex XP2020). The PMT is mounted in a thermoelectrically cooled housing (Products for Research model TX-104-RF).

Figure 14 shows the arrangement of the electronic components for TOF and LIF detection. In the case of LIF single photon counting detection, the nominally 50Ω terminated output is amplified in a wide band amplifier (PAR model 115, DC-500MHz) and sent to a constant fraction differential discriminator (Ortec 583). The discriminated pulse is fed to the stop input of a Time to Amplitude Converter (TAC, Ortec 457). The start pulse for the TAC is obtained from a fast photodiode, which monitors the Q-switched YAG laser pulse, and is amplified and inverted in a 1.3GHz bandwidth amplifier (H.P. model 84470), then fed to a constant fraction discriminator (PAR model 473-A). The fast negative voltage pulse becomes the start pulse for the TAC. The TAC output is passed to the MCA, which accumulates the signal in synchrony with the stepper motor (i.e. delay line) advance. This signal detection arrangement is appropriate for single photon counting detection. The MCA stores one count for every detected photon event, and since channel position of the MCA is synchronized to the delay line step advance, the pump-probe

relative time delay transient is collected. Typical accumulation times are 3 seconds per channel and the scans are repeated a sufficient number of times to obtain the desired S/N ratio. The accumulation time depends on the signal level, the intrinsic amplitude fluctuations, and the enhancement over the one beam alone background signals.

2.2.6 Laser System Response Function

A necessity for complete analysis of time-resolved, and especially pump-probe experiments, is accurate knowledge of the system temporal response function. Measurement of the cross-correlation allows for determination of the waveform (shape and width) of the (de-)convolution function and the experimental time zero. The most useful and versatile method for obtaining the cross-correlation is by way of sum frequency[12,28] or difference frequency[83] generation. The former process was used in obtaining the auto- and cross-correlations shown in Figures 6a and 10, respectively.

Sum frequency generation for UV pump and probe beams is not always feasible due to absorption in the nonlinear optical material, or limitations of the momentum conservation (phase matching angle) conditions. Difference frequency generation is a feasible alternative method provided that the pump and probe wavelengths are sufficiently separated. Limitations are imposed by the range of detectors (e.g. Si, Ge, InPs, etc.) that are required to detect the visible, near and far infrared difference frequency beam. Material limitations also arise because of IR absorption within the nonlinear material.

An alternative method for the measurement of 1+1 pump-probe cross correlations was first developed for the research described in chapter 3. The 1+1 two-photon (pump-probe) ionization signal was used to follow the time evolution of a long-lived resonant intermediate level. The ionization is performed in a gas cell with the anode being a wire positioned parallel and below the laser axis. The cathode is a curved stainless-steel hemi-cylindrical sheet that has the cathode as the axis of symmetry. The arrangement allows for efficient electron collection and electron-molecule collisions result in a cascade of secondary mechanism electron

formation, and thereby amplification. The signal is detected and amplified with a charge-sensitive preamp (Ortec 109PC and 115 power supply). The output signal is connected to the Boxcar integrator input.

The temporal profile for population relaxation of such resonant intermediate levels, as monitored by the total ion signal, is a convolution of the pump and probe pulses with a Heavyside step function,

$$S_{cc}(t) = \int_{-\infty}^{t} dt' \int_{-\infty}^{\infty} I_{pump}(t'')\, H(t')\, I_{probe}(t'')\, dt'', \qquad (2.29)$$

where $H(t') = 0$ for $t' \leq 0$ and $H(t') = 1$ for $t' > 0$, and I_i are the pulse intensity profiles. The normalized form of this expression is the integral of the cross-correlation discussed in the previous section and subsection.

Two requirements must be satisfied to implement this method of measuring the response function. Firstly, the selected molecule must have an absorption at the wavelength of the pump pulse. Secondly, the ionization energy of the same molecule must be sufficiently low to enable a single probe photon to reach the ionization threshold. Several substituted aniline compounds satisfy these conditions in the case where the the pump wavelengths range from 310-220nm and the probe wavelengths are near 388 and 308nm. Table 1 presents a short list of the compounds that have been investigated as candidate systems for measuring 1+1 response functions.

The p-n butyl aniline 1+1 ionization scan of Figure 15 shows a long-lived S_1 state. Expression (2.29) is valid only if the state lifetime is much longer than the temporal duration of the integrated cross-correlation. If this condition is not met then the state lifetime contribution to the response function rise must be eliminated by deconvolution. The 810ps lifetime for the 235nm excitation wavelength makes this system a candidate for use in obtaining the response function for experiments that are to occur on a less than 50ps timescale.

It is of interest to compare the decay curve and measured lifetime of the ionization signal in Figure 15 to the dynamical behavior observed by monitoring fluorescence emission following excitation to the 815cm^{-1} level in S_1 as reported in reference (88). Contrary to the dynamics observed here, the fluorescence studies show a pronounced biexponential decay of the fluorescence signal. The prompt decay, in the case of fluorescence detection, is attributed to dissipative IVR, while the long component decays on a timescale of approximately a few nanosecond. Although the excitation wavelengths for the two experiments are different, it is plausible to assume that the ionization experiment for 1-photon probing does not exhibit explicit sensitivity to the IVR process. The fluorescence detection studies have sensitivity to the evolution of the initially prepared state vector and population relaxation, while the 1-photon ionization probe appears to have sensitivity for only population relaxation.

It could perhaps be argued that the Franck-Condon factors for the $S_{IP} \leftarrow S_1$ transition do not provide selectivity to the change of the vibrational state vector from the initially prepared configuration. It suffices to say that the response behaves as if the excitation of the thermal bulb sample at 235nm is to a single state in S_1, which lives for 810ps.

Another complication must be taken into account before the 1+1 ionization signal may be considered to be the integral of the pump-probe cross-correlation. It is possible that the additional physical relaxation process of rotational coherence[89] and rotational coherence detected by MPI[90] may contribute to the t=0 behavior. Figure 16a shows the parallel and perpendicular pump-probe polarization 1+1 ionization responses of N,N-diethyl aniline (DEA). It is seen that the signal from the case of perpendicular relative polarizations rises more promptly than that for parallel pump-probe relative polarizations. The signal arising from the perpendicular polarization case is plotted as a solid line in the figure. This type of behavior is indicative of ($\parallel$, $\perp$) transition moments[89] for ($S_1 \leftarrow S_0$, $S^+ \leftarrow S_1$) optical pumping to the ion.[90] The effect is reinforced in Figure 16b, which shows a plot

of the pump-probe anisotropy, r(t),[90] which is also consistent with having orthogonal transition moments for the two transitions. For the case of room temperature studies, the decay (rise) of r(t) to the asymptotic value, r(t)$\approx$ 0, occurs in less than 1ps.[89] The experimental r(t) data shows that the rotational coherence effect is manifest on the 0.5ps timescale. The temporal width at half maximum for the rise of r(t) is $\Delta t \approx 0.7$ps, as obtained from a simple Gaussian deconvolution with the 0.65ps system response function. These rotational coherence contributions to the 1+1 ionization response must be carefully considered in any data analysis (*e.g.*, time-dependent alignment studies) or deconvolution proceedures.

The final figure of this chapter, number 17, compares the prompt electronic dissociation of hydrogen peroxide and appearance of the hydroxyl radical product, as detected by LIF, with the 1+1 ionization signal of p-n butyl aniline. The 4ps response function obtained for 241nm and 308nm pump and probe pulses, respectively, limits the temporal sensitivity to the rapid rotational coherence dynamics. The two scans, taken under identical experimental conditions and time-zero delays, show that the HOOH dissociation dynamics and the 1+1 ionization signal, for parallel pump-probe polarizations, exhibit the same dynamical behavior for the signal rise.

2.2.7 Data Fitting and Analysis

The nonlinear least-squares fitting incorporate the algorithm developed by Marquardt.[91] All of the computer data fitting routines have a common root section and require specified I/O sections and the proper data fitting function and its derivative for operation.

REFERENCES

1. For examples of these asymptotic quantities, see C.H. Greene and R.N. Zare, Annu. Rev. Phys. Chem. **33**, 119 (1982); J. Chem. Phys. **78**, 6741 (1983); J.L. Kinsey, Annu. Rev. Phys. Chem. **28**, 349 (1977).

2. A.H. Zewail, Ber. Bunsenges. Phys. Chem. **92**, 373 (1988).

3. H.J. Foth, J.C. Polanyi and H.H. Telle, J. Phys. Chem. **86**, 5027 (1982); P.R. Brooks, Chem. Rev. **88**, 407 (1988).

4. G.R. Fleming, *"Chemical Applications of Ultrafast Spectroscopy,"* Oxford Science Publications, Oxford 1986.

5. W. Demtröder, *"Laser Spectroscopy,"* Springer-Verlag, Berlin 1982; also see D.P. Millar, Ph. D. Thesis, Caltech 1982, Chapter 3.

6. J. Berkowitz, *"Photoabsorption, Photoionization and Photoelectron Spectroscopy,"* Academic Press, New York 1979; S.H. Lin, Y. Fujimora, H.J. Neusser and E.W. Schlag, *"Multiphoton Spectroscopy of Molecules,"* Academic Press, New York 1984.

7. For an experimental application of MPI to reaction product detection, see Z. Xu, B. Koplitz and C. Wittig, J. Chem. Phys. **87**, 1062 (1987) and references therein.

8. K.B. Eisenthal, Annu. Rev. Phys. Chem. **28**, 207 (1977); see also G.R. Fleming, Adv. Chem. Phys. **49**, 1 (1982).

9. G.R. Fleming, Annu. Rev. Phys. Chem. **37**, 81 (1986), see also Ref. 4.

10. A. Migus, A. Antonetti, J. Etchepare, D. Hulim and A. Orszag, J. Opt. Soc. Am. B **2**, 584 (1985).

11. C.V. Shank, Science **233**, 1276 (1986).

12. E.P. Ippen and C.V. Shank, in *" Ultrashort Light Pulses"*, S.L. Shapiro, ed., Vol. 18 of Topics in Applied Physics (Springer-Verlag, Berlin, 1977); (b) L.R. Khundkar, Ph. D. Thesis, Caltech (1988), Chapter 2.

13. J.H. Glownia, J. Misewich and P.P. Sorokin, J. Opt. Soc. Am. B **3**, 1573 (1986).

14. (a) D.H. Waldeck, W.T. Lotshaw, D.B. McDonald and G.R. Fleming, Chem. Phys. Lett. **88**, 297 (1982); T.L. Gustafson and D.M. Roberts, Opt. Commun. **43**, 141 (1982). (b) L. Andor, A. Lörincz, J. Siemion, D.D. Smith and S.A. Rice, Rev. Sci. Instrum. **55**, 64 (1984); E.L. Quitevis, E.F.G. Templeton and G.A. Kenny-Wallace, Appl. Opt. **24**, 318 (1985).

15. See, for example, M.D. Levenson, *"Introduction to Nonlinear Laser Spectroscopy,"* Academic Press, New York (1982).

16. S.L. Palfrey and T.F. Heinz, J. Opt. Soc. Am. B **2**, 674 (1985).

17. (a) A. Yariv, *"Quantum Electronics,"* 2nd ed., John Wiley and Sons, New York (1975); (b) M. Sargent III, M.O. Scully and W.E. Lamb, Jr., *"Laser Physics,"* Addison-Wesley Publishing, London (1974).

18. P.W. Smith, Proc. IEEE, **58**, 1324 (1970); see also "Spectra Physics Product Manual"

19. (a) B.H. Soffer and J.W. Linn, J. Appl. Phys. **39**, 5859 (1968); (b) C.K. Chan and S.O. Sari, Appl. Phys. Lett. **25**, 403 (1974).

20. J.P. Heritage and R.K, Jain, Appl. Phys. Lett. **32**, 101 (1978).

21. D.B. McDonald, D.H. Waldeck and G.R. Fleming, Opt. Commun. **34**, 127 (1980).

22. D.P. Millar and A.H. Zewail, Chem. Phys. **72**, 381 (1982); D.M. Kim, J. Kuhl, R. Lambrich and D. von der Linde, Opt. Commun. **27**, 123 (1978).

23. H.A. Pike and M. Hersher, J. Appl. Phys. **41**, 4562 (1970).

24. A.E. Siegman, *"Lasers,"* University Science Books, Mill Valley, California (1986).

25. Z.A. Yasa, Appl. Phys. B **30**, 135 (1983); for a numerical simulation of pulse formation from noise, see Z.A. Yasa and O. Teschke, Opt. Commun. **15**, 169 (1975).

26. D. von der Linde, Appl. Phys. B **39**, 201 (1986)

27. R.K. Jain and J.P. Heritage, Appl. Phys. Lett. **32**, 41 (1978).

28. J.M. Clemens, J. Najbar, I. Bronstein-Bonte and R.M. Hochstrasser, Opt. Commun. **47**, 271 (1983).

29. G.A. Mourou and T. Sizer II, Opt. Commun. **41**, 47 (1982)

30. E.P. Ippen and C.V. Shank, Appl. Phys. Lett. **27**, 488 (1975); Z.A. Yasa, A. Dienes and J.R. Winnery, Appl. Phys. Lett. **30**, 24 (1977); P.M.W. French and J.R. Taylor, IEEE J. Quant. Elect. **22**, 1162 (1986); M.A. Kahlow, W. Jarzeba, T.P. Dubruil and P.F. Barbara, Rev. Sci. Instrum., **59**, 1098 (1988).

31. (a) M.D. Dawson, T.F. Boggess, D.W. Garvey and A.L. Smirl, Opt. Commun. **60**, 79 (1986); (b) M.D. Dawson, D. Maxson, T.F. Boggess and A.L. Smirl, Opt. Lett. **13**, 126 (1988); D. Kühlke, U. Herpers and D. von der Linde, Appl. Phys. B **38**, 233 (1985).

32. R.L. Fork B.I. Greene, and C.V. Shank, Appl. Phys. Lett. **38**, 671 (1981); R.L. Fork, D.V. Shank, R. Yen and C.A. Hirlmann, IEEE J. Quant. Elect. **QE-19**, 500 (1983).

33. R.L. Fork, O.E. Martinez and J.P. Gordon, Opt. Lett. **9**, 150 (1984); J.A. Valdmanis, R.L. Fork and J.P. Gordon, Opt. Lett. **10**, 131 (1981).

34. A.E. Siegman, IEEE J. Quant. Elect. **QE-9**, 247 (1973); Opt. Lett. **6**, 334 (1981).

35. (a) T. Norris, T. Sizer and G. Mourou,J. Opt. Soc. Am. B **2**, 613 (1985); (b) H. Vanherzeele, R. Torti and J.C. Diels, Appl. Opt. **23**, 4182 (1984); (c) J.C. Diels, N. Jamasbi and L. Sarger, in *"Ultrafast Phenomena V,"* G.R. Fleming and A.E. Siegman eds., Springer-Verlag, Berlin (1986).

36. R.H. Stolen and C. Lin, Phys. Rev. A **17**, 1448 (1978).

37. E.B. Treacy, IEEE J. Quant. Elect. **QE-5**, 454 (1969).

38. H. Nakatsuka and D. Grischkowsky, Opt. Lett. **6**, 13 (1981); B. Nikolaus and D. Grischkowsky, Appl. Phys. Lett. **42**, 1 (1983); D. Grischkowsky and A.C. Balant, *ibid.*, **41**, 1 (1982).

39. C.V. Shank, R.L. Fork, R. Yen, R.H. Stolen and W.J. Tomlinson, Appl. Phys. Lett. **40**, 761 (1982); A more in depth analysis of the compression process has been given by W.J. Tomlinson, R.H. Stolen, and C.V. Shank, J. Opt. Soc. Am. B **1**, 139 (1984).

40. Y. Ishida and T. Yajima, Opt. Commun. **58**, 355 (1986)

41. W. Zhao and E. Bourkoff, IEEE J. Quant. Elect. **QE-24**, 365 (1988).

42. R.L. Fork, C.H. Brito Cruz, P.C. Becker and C.V. Shank, Opt. Lett. **12**, 483 (1987); C.H. Brito Cruz, P.C. Becker, R.L. Fork and C.V. Shank, Opt. Lett. **13**, 123 (1988).

43. H. Roskos, A. Seilmeier, W. Kaiser and J.D. Harvey, Opt. Commun. **61**, 81 (1987); A.S.L. Gomes, U. Osterberg, W. Sibbett and J.R. Taylor, *ibid.*, **54**, 377 (1985).

44. Y.R. Shen, *"Principles of Nonlinear Optics,"*, John Wiley, New York 1984

45. T.L. Koch, L.C. Chiu and A. Yariv, J. Appl. Phys. **53**, 6047 (1982); Opt. Commun. **40**, 364 (1982); A.A. Hnilo and O.E. Martinez, *ibid.*, **60**, 87 (1986).

46. A. Migus, C.V. Shank, E.P. Ippen and R.L. Fork, IEEE J. Quant. Elect. **QE-18**, 101 (1982).

47. R.L. Fork, C.V. Shank, and R. Yen, Appl. Phys. Lett. **41**, 223 (1982).

48. W.H. Knox, IEEE J. Quant. Elect. **QE-24**, 388 (1988).

49. R.W. Loudon, *"Quantum Theory of Light,"*, 2nd ed., Oxford, Oxford 1987.

50. P. Maine, D. Strickland, P. Bado, M. Pessot and G. Mourou, IEEE J. Quant. Elect. **QE-24**, 398 (1988).

51. A. Yariv and P. Yeh, *"Optical Waves in Crystals,"*, John Wiley, New York 1984.

52. L.R. Khundkar, Ph.D. Thesis, Caltech (1988).

53. R.R. Alfano and S.L. Shapiro, Phys. Rev. Lett. **24**, 584, 592, 1217 (1970.

54. Q.X. Li,T. Jimbo, P.P. Ho and R.R. Alfano, Appl. Opt. **25**, 1869 (1986); T. Jimbo, V.L. Caplan, Q.X. Li, Q.Z. Wang, P.P. Ho and R.R. Alfano, Opt. Lett. **12**, 477 (1987).

55. R.L. Fork, C.V. Shank, C. Hirlmann, R. Shen and W.J. Tomlinson, Opt. Lett. **8**, 1 (1983).

56. G. Yang, and Y. R. Shen, Opt. Lett. **9**, 510 (1984); J. T. Manassah, M.A. Mustafa, R.R. Alfano and P.P. Ho, IEEE J. Quant. Elect. **QE-22**, 197 (1986).

57. J. Misewich, J.H. Glownia, J.E. Rothenberg, and P.P.Sorokin, Chem. Phys. Lett. **150**, 374 (1988); J.H. Glownia, J. Misewich and P.P. Sorokin, J. Opt. Soc. Am. B, **3**, 1573 (1986).

58. N.F. Scherer, Proposition Report, Caltech (1988).

59. D.M. Lubman, C.T. Rettner and R.N. Zare, J. Phys. Chem. **86**, 1129 (1982).

60. J.B. Anderson, R.P. Andres and J.B. Fenn, Adv. Chem. Phys. **10**, 275 (1965); J.B. Anderson in *"Molecular Beams and Low Density Gas Dynamics,"*, P.P. Wegener, ed., Marcel Deccer, New York 1974; A. Kantrowitz and J. Grey, Rev. Sci. Instrum. **22**, 328 (1951); also see R. Campargue, J. Phys. Chem. **88**, 4466 (1984).

61. G.M. McClelland, K.L. Saenger, J.J. Valentini and D.R. Hershbach, J. Phys. Chem. **83**, 947 (1979).

62. Wm.R. Lambert, Ph.D. Thesis, Caltech (1983).

63. P.M. Felker, Ph.D. Thesis, Caltech (1986).

64. J.B. Anderson and J.B. Fenn, Phys. Fluids **8**, 780 (1965).

65. H. Ashkenas and F.S. Sherman, in *"Rarified Gas Dynamics,"*, Fourth Symposium, Vol. II, J.H. deLeeuw, ed., Academic Press, New York 1966.

66. W. Sharfin, K.E. Johnson, L. Wharton and D.H. Levy, J. Chem. Phys. **71**, 1292 (1979).

67. G. Ewing, Chem. Phys. **29**, 253 (1978); J.A. Beswick and J. Jortner, Adv. Chem. Phys. **48**, 323 (1981).

68. D.H. Levy, Adv. Chem. Phys. **48**, 323 (1981).

69. G.H. Dicke and H.M. Crosswhite, J. Quant. Spect. Radiat. Trans. **2**, 97 (1962).

70. W.L. Dimpfl and J.L. Kinsey, J. Quant. Spect. Radiat. Trans. **21**, 223 (1979); D.R. Crosley and I.L. Chidsey, *ibid.* **23**, 187 (1980).

71. J. Hougen, *"The Calculation of Rotational Energy Levels and Rotational Line Intensities in Diatomic Molecules,"* NBS Monograph 115, US Government Printing Office, Washington DC, 1970; G. Herzberg, *"Molecular Spectra and Molecular Structure, Vol. I: Spectra of Diatomic Molecules,"* Van Nostrand Reinhold, New York 1950.

72. J.W. Perry, National Bureau of Standards, private communication (1985).

73. M. Bron and E. Wolf, *"Principles of Optics,"* McMillian, New York 1964.

74. R.N. Thurston, J.P. Heritage, A.M. Weiner and W.J. Tomlinson, IEEE J. Quant. Elect. **QE-22**, 682 (1986); A.M. Weiner, J.P. Heritage, and E.M. Kishner, J. Opt. Soc. Am. B. **5**, 1563 (1988).

75. For example, see W.S. Warren, Science **242**, 878 (1988) and references therein.

76. O.E. Martinez, IEEE J. Quant. Elect. **QE-23**, 59 (1987); *ibid.*, **QE-24**, 2530 (1988).

77. D.M. Guthals and J.W. Nibler, Opt. Commun. **29**, 322 (1979). The agent DABCO, which does not absorb 355nm light, was mixed in the dye solution to scavenge the singlet oxygen (from ozone photolysis). The oxygen atom otherwise reacts with the triplet state of the dye to form a useless photoproduct.

78. Y. Ishida and J. Yajima, Opt. Commun. **62**, 197 (1987).

79. B.W. Keelan, J.A. Syage, J.F. Shepanski and A.H. Zewail, Proc. Int. Conf. Lasers, (STS, McLean, VA, 1985) p. 718

80. D.M. Lubman and R.M. Jordan, Rev. Sci. Instrum., **56**, 373 (1985); R.B. Opsal, K.E. Owens and J.P. Reilly, Anal. Chem., **57**, 1884 (1985); see also U. Boesl, H.J. Neusser, R. Weinkauf and E.W. Schlag, J. Phys. Chem., **86**, 4857 (1982).

81. J.E. Pollard and R. Cohen, Rev. Sci. Instrum., **58**, 32 (1987).

82. W.C. Wiley and I.H. McLaren, Rev. Sci. Instrum., **26**, 150 (1955).

83. N.F. Scherer, J.W. Perry, F.E. Doany and A.H. Zewail, J. Phys. Chem.,**89**, 894 (1985).

84. T.G. Dietz, M.A. Duncan, M.G. Liverman and R.E. Smalley, Chem. Phys. Lett., **70**, 246 (1980).

85. D.E. Powers, J.B. Hopkins and R.E. Smalley, J. Chem. Phys., **72**, 5721 (1980).

86. *Handbook of Chemistry and Physics*, 59th Edition, CRC Press (1978).

87. H. Tsubomura and T. Sakata, Chem. Phys. Lett., **21**, 511 (1973); K. Fuke and S. Nagakura, J. Mol. Spect., **64**, 139 (1977); J.A. Woodworth, T.A. Green and C.A. Frost, J. Appl. Phys., **57**, 1648 (1985).

88. J.S. Baskin, M. Dantus and A.H. Zewail, Chem. Phys. Lett., **130**, 473 (1986).

89. P.M. Felker and A.H. Zewail, J. Chem. Phys., **86**, 2460 (1987);J.S. Baskin, P.M. Felker and A.H. Zewail, ibid., **86**, 2483 (1987).

90. N.F. Scherer, L.R. Khundkar, T.S. Rose and A.H. Zewail, J. Phys. Chem., **91**, 6478 (1987); and Appendix A of this thesis.

91. D.W. Marquardt, *SIAM*, **11**, 431 (1964); D.P. Millar, Ph. D. Thesis, Caltech 1982, Appendix II; W.H. Press, B.H. Flanery, S.A. Teukulsky and W.T. Vetterling, *Numerical Recipes*, Cambridge University Press, Cambridge 1986.

Table 1.

Time-Resolved Studies of 1+1 Resonance Enhanced Ionization of Several Molecules With Low-Lying Ionization Potentials

Compound	$\lambda_{S_1-S_0}$ (Å)	IP (eV)	1+1 λ_{pump} (nm)	Ionization λ_{probe} (nm)	Conditions τ_{S_1} (ps)
Aniline	2938 (84)	7.70 (84)	235	308	60 ± 5
p-Ethyl Aniline	3006 (85)	~7.4 (86)	235	308	120 ± 10
p-n-Butyl Aniline	3007 (85)	~7.3 (86)	235	308	810 ± 80
n,n-Dimethyl Aniline	≥3000 (85,86)	7.12 (86)	235	308	84 ± 10
Acetophenone	2430 (86)	9.27 (86)	235	308	75 ± 10
n,n-Diethyl Aniline	≥3003 (87)	6.99 (86)	308	388	>200

FIGURE CAPTIONS AND FIGURES

1. Time dependance of the intracavity gain in a synchronously pumped dye laser. The dye pulse follows the peak of the pump pulse envelope. The gain is depleted below threshold (RG=1) by stimulated emission by the dye pulse. The gain may pass above the RG=1 value at time τ_s and produce secondary pulses in the same oscillator.

2. Schematic diagram of the OH $A^2\Sigma^+ - X^2\Pi$ energy levels and the associated optical transitions. The notation is described in the text.

3a. Temporal images of the 1.064μm, 532nm and 5ps dye pulses. The horizontal scale is 100ps/div. The lower photo shows the oscilloscope and sampling head (Tektronix 7904, S1) combination with Spectra Physics Ultrafast Diode (model 403B). The photographs indicate approximately 100 and 80ps pulse durations for the first two traces, respectively.

3b. Noise spectral analysis of the mode locker rf output, the 1.064μm andd 532nm pulses for two different frequency ranges (200Hz/div and 20kHz/div). The majority of the noise occurs at low frequency. Some of the noise originates from the rf-source and other noise arises from instabilities in the lamp discharge, transient cavity misalignment and other fluctuations which are intrinsic to other optical components.

4. The laser oscillators and pulsed dye amplifiers are shown as layed out on a single $4' \times 10'$ optical table. The path of the light beams are indicated. The position of the continuum generation optical arrangement is also indicated. Refer to the text for more details.

5. A schematic diagram of the second experimental optical table, which contains the scanning delay line interferometer, nonlinear frequency generation configurations, the spinning block autocorrelator and the low scattered-light gas sample cell. See the text for further descriptions of the use of each item.

6a. The autocorrelation of the amplified pulses is shown. The solid line superimposed on the data points (circles) is the fitted 6.6ps Gaussian FWHM pulsewidth. The associated autocorrelation width, actually shown in the figure, is $\sqrt{2}$ larger. The pulses orginate from an optimal cavity length matched ($\Delta l \approx 1\mu$m) dye laser and a 3-plate intracavity tuning element.

6b. The autocorrelation of the amplified 350fs Lorentzian pulses obtained from a fiber/grating pulse compressor. The input to the compressor is a 5.5ps Gaussian pulse from a cavity dumped synchronously pumped dye laser system. The fitted pulse duration which results in the displayed solid fitted line is 420fs with a Lorentzian pulse shape.

7. Plot of the amplified pulse temporal width vs output power. A power of 10mW corresponds to 0.5mJ energy per pulse. The oscillator pulse has been improperly mode-locked to also allow for examination of the effect of output power on the coherence-spike feature. The pulse width but not the coherence width increases with extracted energy.

8. A semi-log plot of the wavelength dependance of the optical continuum generated by focusing a 5ps Gaussian pulse into a cell of water. The continuum light has passed through a polarizer, as described in the text. The sharp spike feature is the unconverted original dye laser light and the hump to shorter wavelengths is the ASE which arises from the amplification process using R640/CV670 in methanol.

9a. A double-pass diffraction grating/cylindrical lens and slit arrangement to allow for spectral selection of a frequency bandpass from the optical continuum. The separation of the lens and grating relative to the focal length of the lens may be adjusted to alter the sign and magnitude of the linear chirp imparted on the spectrally selected pulse.

9b. A quadruple-pass optical arrangement that serves the same function as that described in 9a. The added feature of this design, obtained at the expense of the through-put efficiency, is to remove the transverse-mode frequency sweep whichis incured from the design of Figure 8a.

10. A cross-correlation of the 616nm amplified dye pulse and the 530nm amplified continuum. The cross-correlation is obtained for the pulses of Figure 6a. The measured cross-correlation width of 8.5ps yields a gaussian pulse width of 5.3ps for the chirp-precompensated amplified continuum light.

11. The molecular beam apparatus. The dual-chamber differentially pumped aspect of the design is indicated. The cut-away view allows for visualizing the LIF collection optics and detection scheme and the EI-TOFMS arrangement in the second chamber.

12. This schematic of the EI-TOFMS shown in the previous figure provides additional details of the design. Refer to the text for the operating parameters.

13. EI-TOF mass spectrum for a supersonic jet expansion of a He:CO_2:HI mixture. The relative compositions are 95.5:4:1.5. The deflection plate voltage is adjusted to optimize the detection sensitivity of the 120-200amu mass range. This tends to discriminate against the lower mass species, especially He and CO_2. The electron impact energy is 30eV, the repeller voltage is 550V, accelerator is set at 400V and the filament is biased at 370V.

14. This schematically outlines the arrangement of the detection electronics for the LIF and TOF signals.

15. 1+1 ionization signal for p-N Butyl Aniline. The pump-probe scan shows the decay of the signal level over the displayed range and shows the fitted single exponential lifetime of 810ps. See the text for additional discussion on the significance of the single exponential decay.

16a. Comparison of parallel and perpendicular 1+1 ionization temporal scans of N,N Diethyl Aniline. The perpendicular scan is the more sharply rising feature. The scans were obtained for the save pump-probe relative time delay. The pump and probe wavelengths are 306nm pump and 388nm probe, respectively.

16b. Plot of the rotational anisotropy, r(t), of the DEA data of Figure 16a. The two figures are plotted on the same timescale and for the same t=o position. The data were obtained at room temperature. A solid line connects the data points.

17. Comparison of p-n butyl aniline "response" vs HOOH direct dissociation at 241nm pump and 308nm probe. The HOOH pump-probe LIF detection data are the open circles and the ionization signal is the solid line. The two curves are essentially identical in the temporal characteristics. The data are obtained for parallel pump-probe polarizations.

Figure 1.

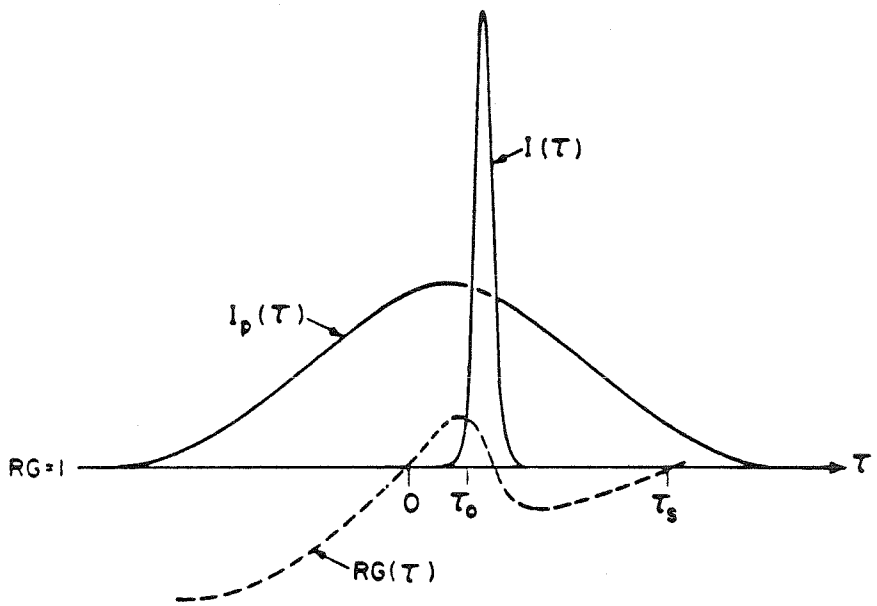

Figure 2.

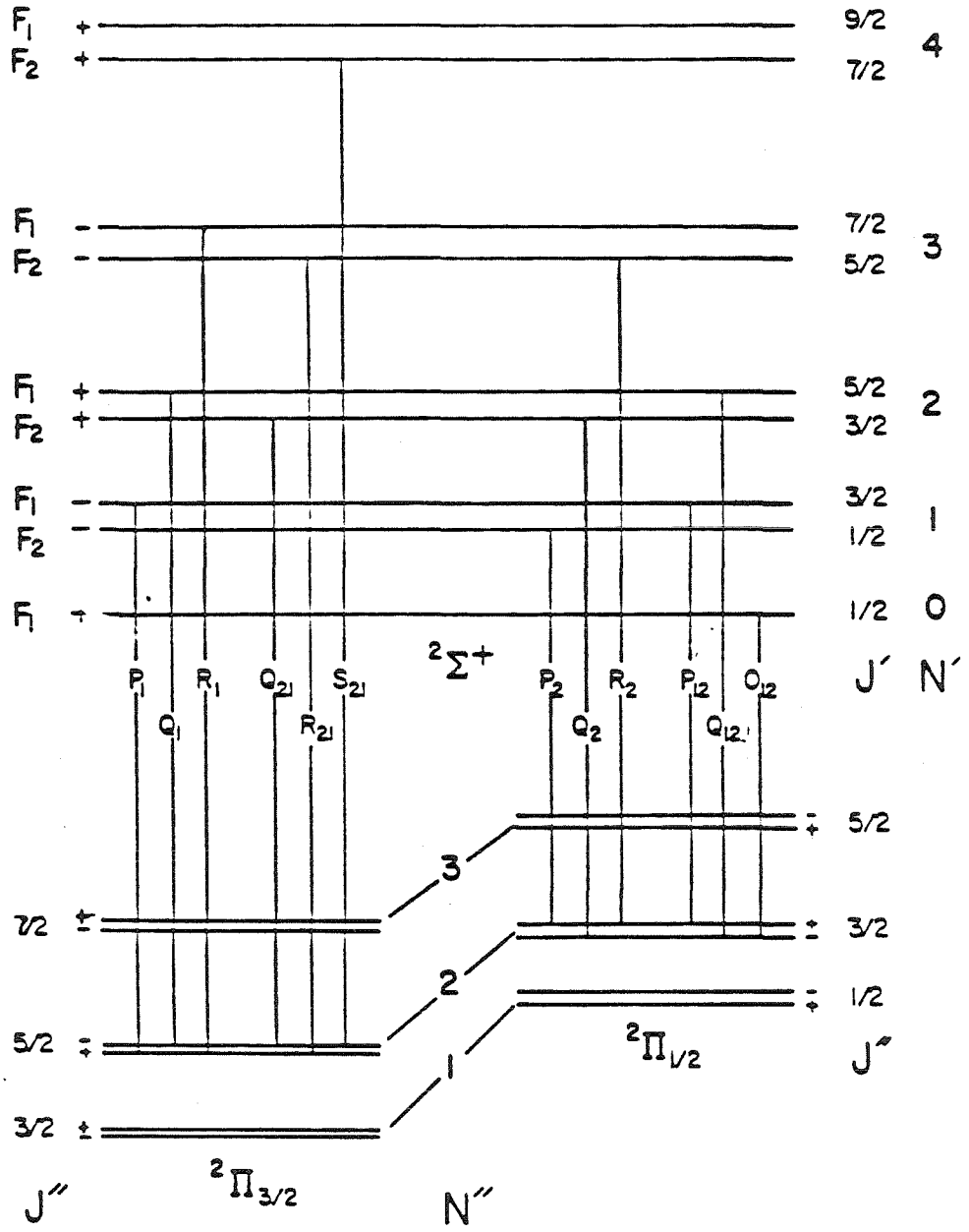
F1 +
F2 +
9/2
7/2
4
F1 -
F2 -
7/2
5/2
3
F1 +
F2 +
5/2
3/2
2
F1 -
F2 -
3/2
1/2
1
F1 +
1/2
0
P1 Q1 R1 Q21 R21 S21
2Σ+
P2 Q2 R2 P12 Q12 O12
J' N'
5/2
3/2
1/2
7/2
5/2
3/2
3
2
1
2Π1/2
J''
2Π3/2
N''

Figure 3a.

1.064

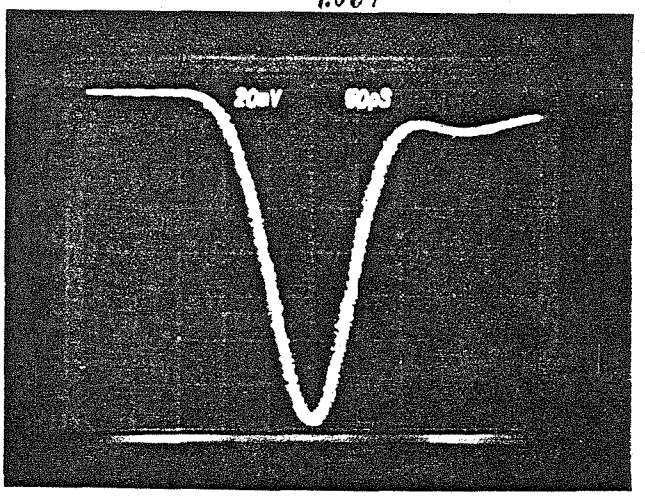

532

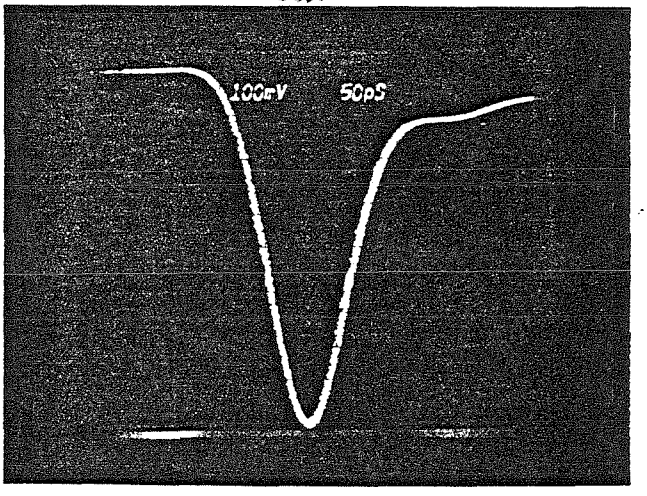

Dye

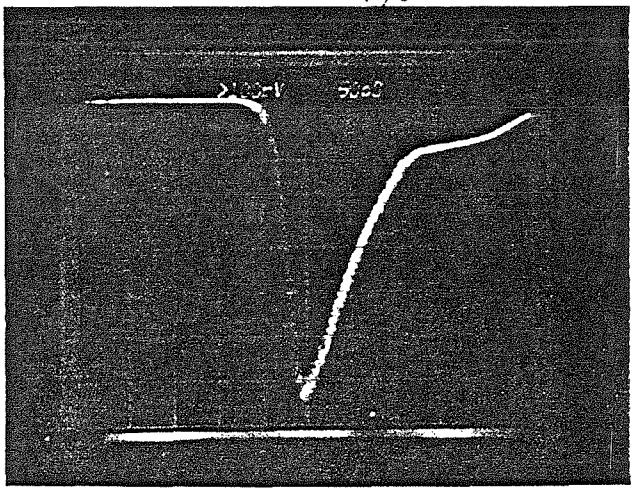

Figure 3b.

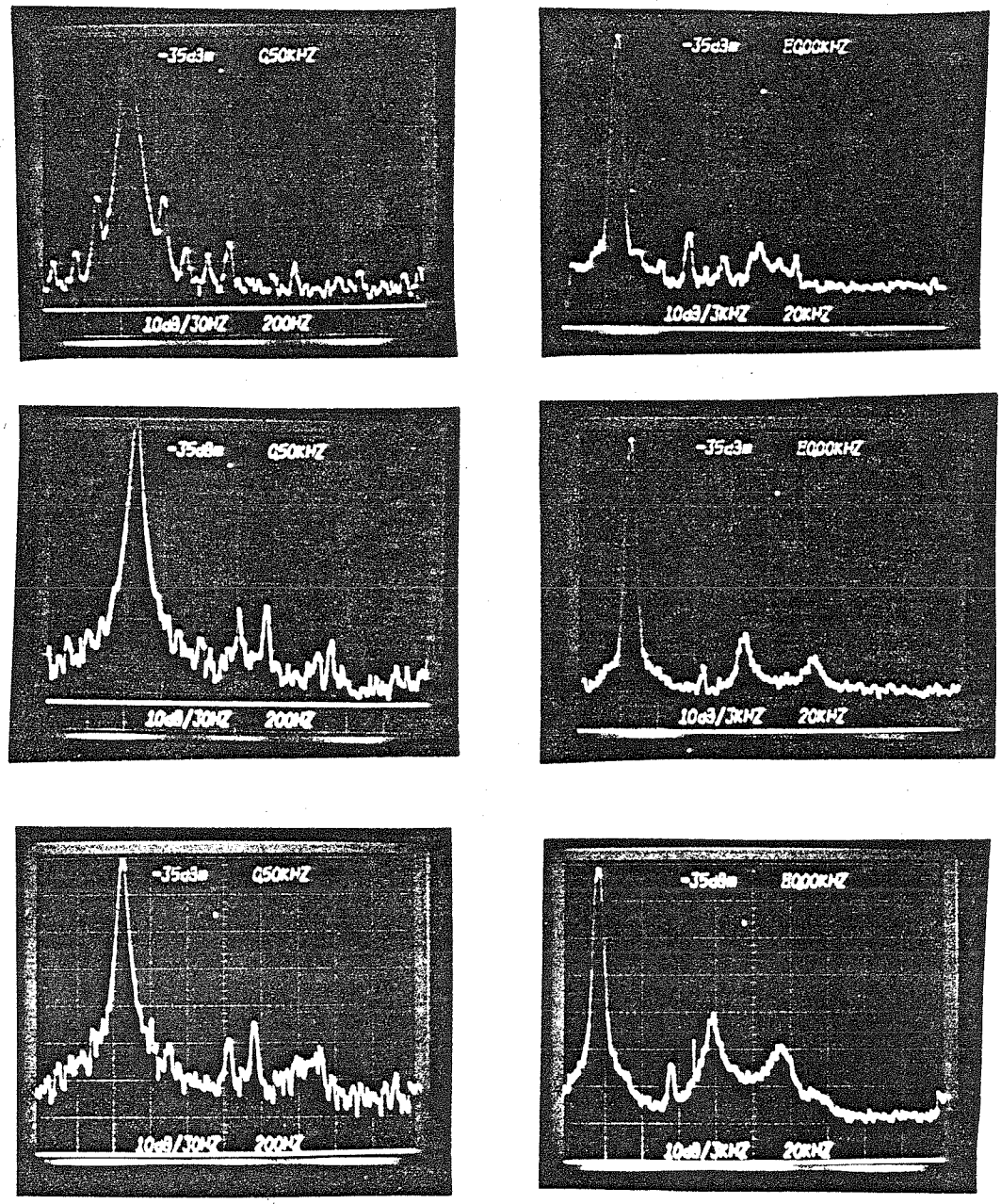
-35dBm 650KHZ
10dB/30HZ 200HZ
-35dBm 8000KHZ
10dB/3KHZ 20KHZ
-35dBm 650KHZ
10dB/30HZ 200HZ
-35dBm 8000KHZ
10dB/3KHZ 20KHZ
-35dBm 650KHZ
10dB/30HZ 200HZ
-35dBm 8000KHZ
10dB/3KHZ 20KHZ

Figure 4.

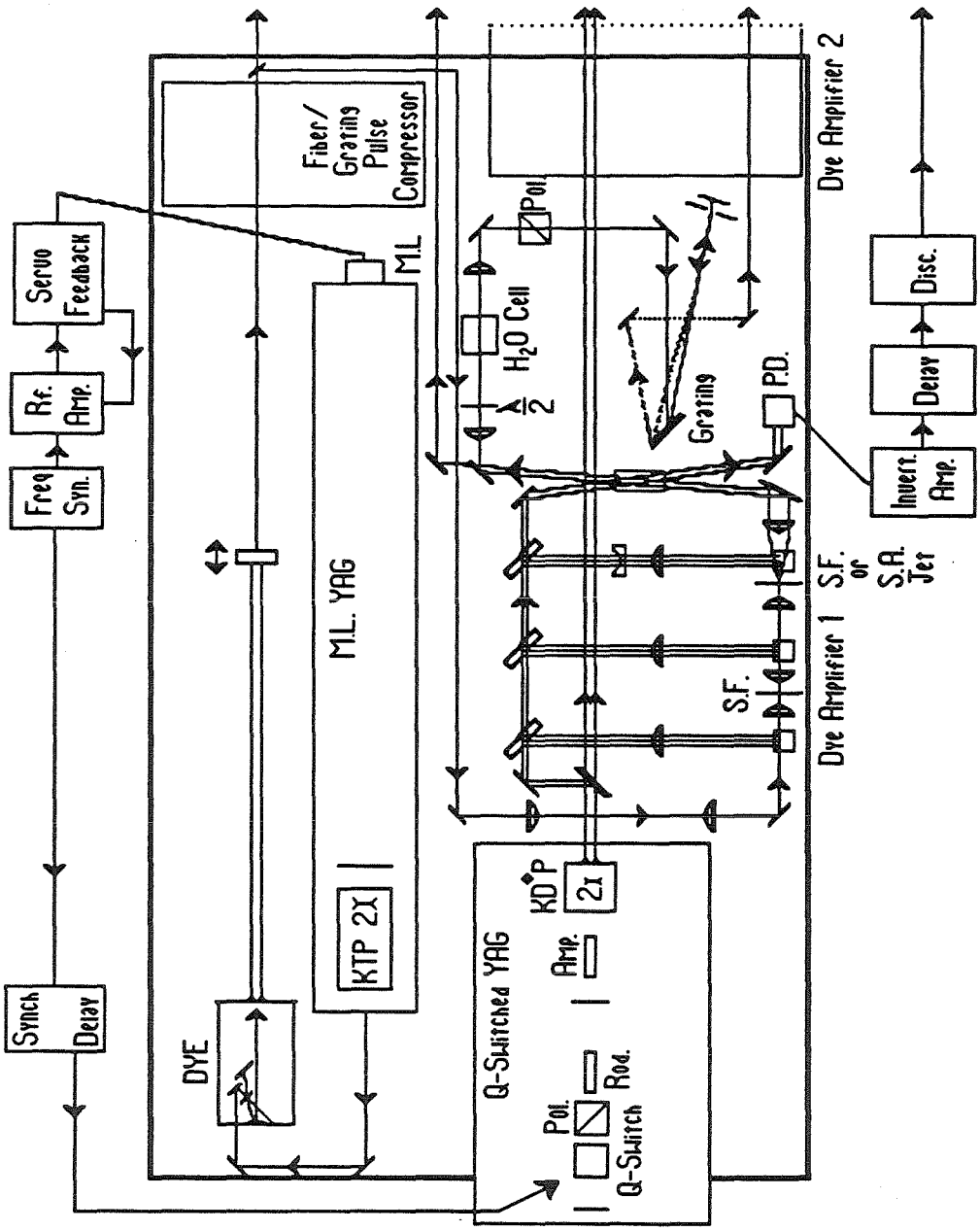
Fiber/
Grating
Pulse
Compressor
Dye Amplifier 2
Servo
Feedback
M.L
Pol.
Rf.
Amp.
H2O Cell
λ/2
Grating
P.D.
Disc.
Delay
Freq
Syn.
Invert.
Amp.
M.L. YAG
S.F.
or
S.A.
Jet
Dye Amplifier 1
S.F.
KTP 2X
KD*P
2ω
Amp.
Synch
Delay
DYE
Q-Switched YAG
Pol.
Rod.
Q-Switch

Figure 5.

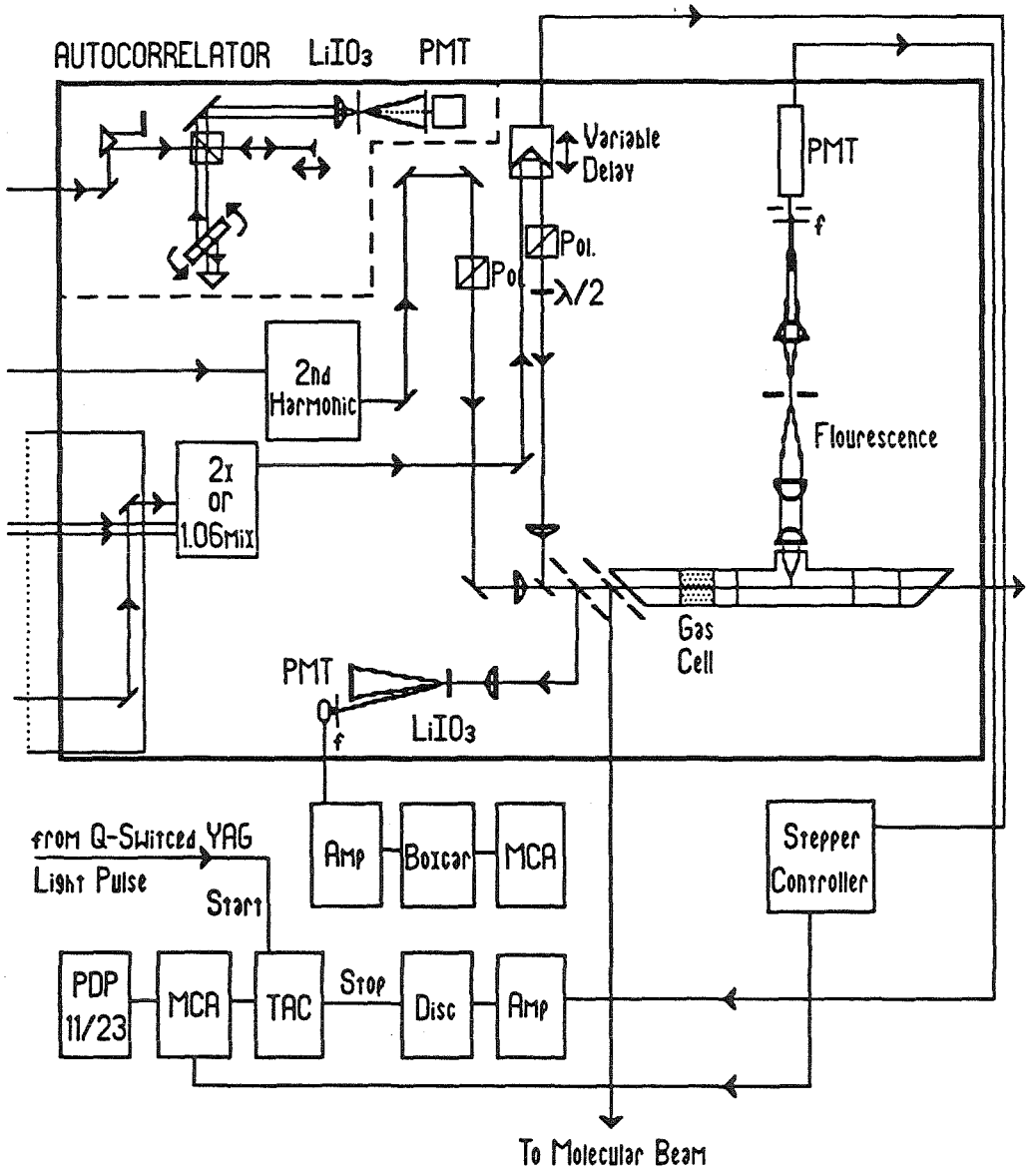
AUTOCORRELATOR
LiIO3
PMT
Variable Delay
PMT
f
Pol.
Pol.
λ/2
2nd Harmonic
2x or 1.06mix
Flourescence
Gas Cell
PMT
f
LiIO3
from Q-Switced YAG
Light Pulse
Start
Amp
Boxcar
MCA
Stepper Controller
PDP 11/23
MCA
TAC
Stop
Disc
Amp
To Molecular Beam

Figure 6a, 6b.

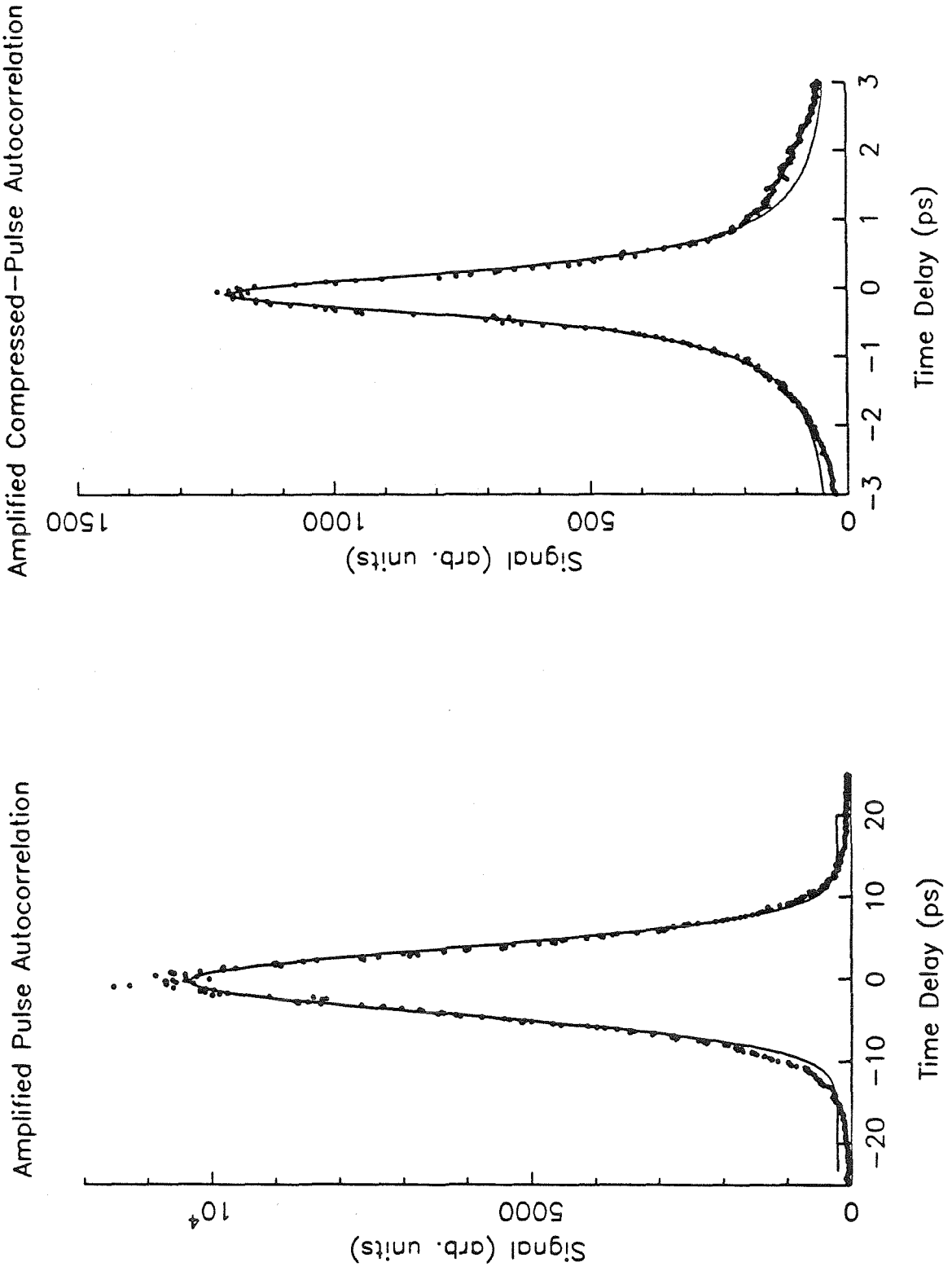
Amplified Compressed–Pulse Autocorrelation
Signal (arb. units)
0
500
1000
1500
Time Delay (ps)
−3
−2
−1
0
1
2
3
Amplified Pulse Autocorrelation
Signal (arb. units)
0
5000
10⁴
Time Delay (ps)
−20
−10
0
10
20

Figure 7.

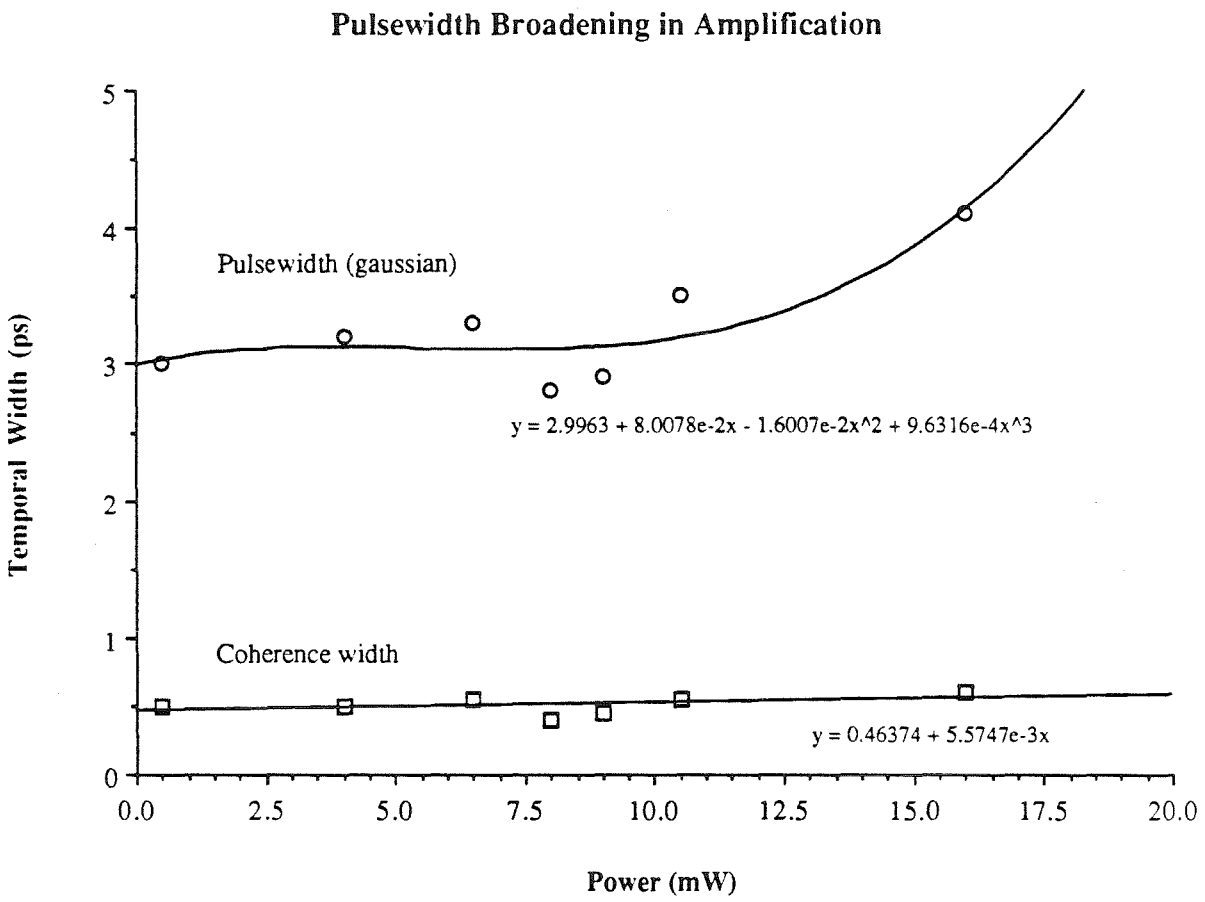
Pulsewidth Broadening in Amplification
Temporal Width (ps)
Power (mW)
Pulsewidth (gaussian)
y = 2.9963 + 8.0078e-2x - 1.6007e-2x^2 + 9.6316e-4x^3
Coherence width
y = 0.46374 + 5.5747e-3x
0
1
2
3
4
5
0.0
2.5
5.0
7.5
10.0
12.5
15.0
17.5
20.0

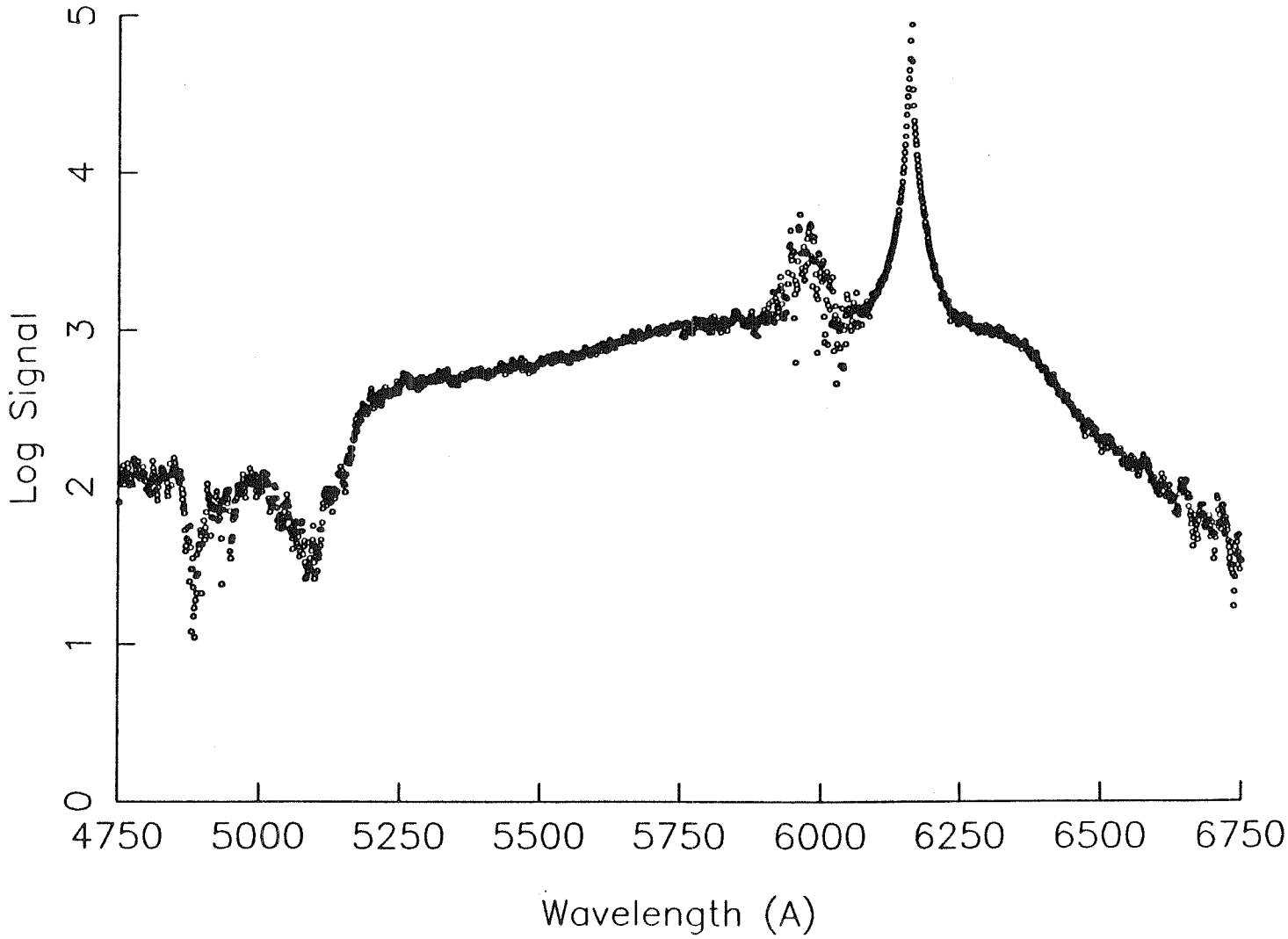
Optical Continuum Spectral Density
Log Signal
0
1
2
3
4
5
4750
5000
5250
5500
5750
6000
6250
6500
6750
Wavelength (A)

Figure 8.

Figures 9a, 9b.

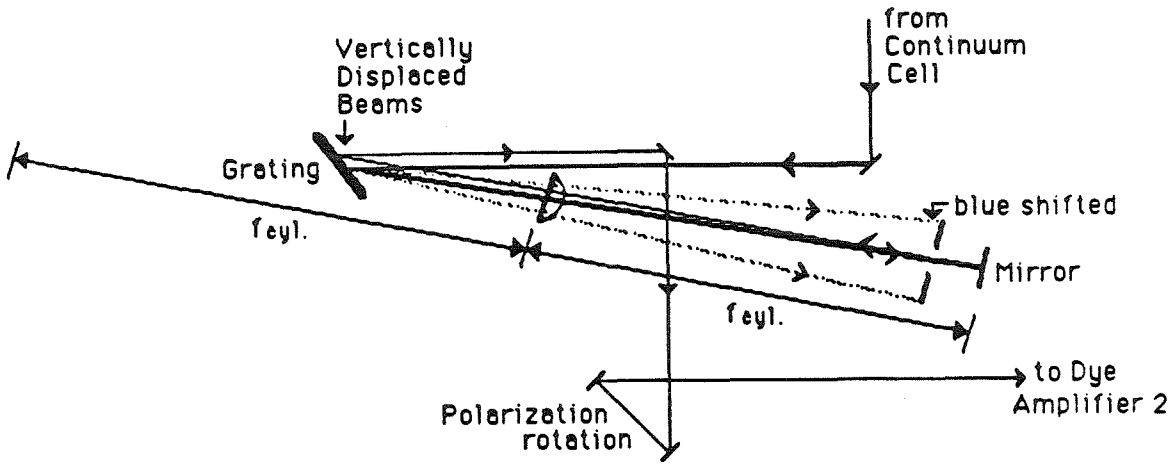

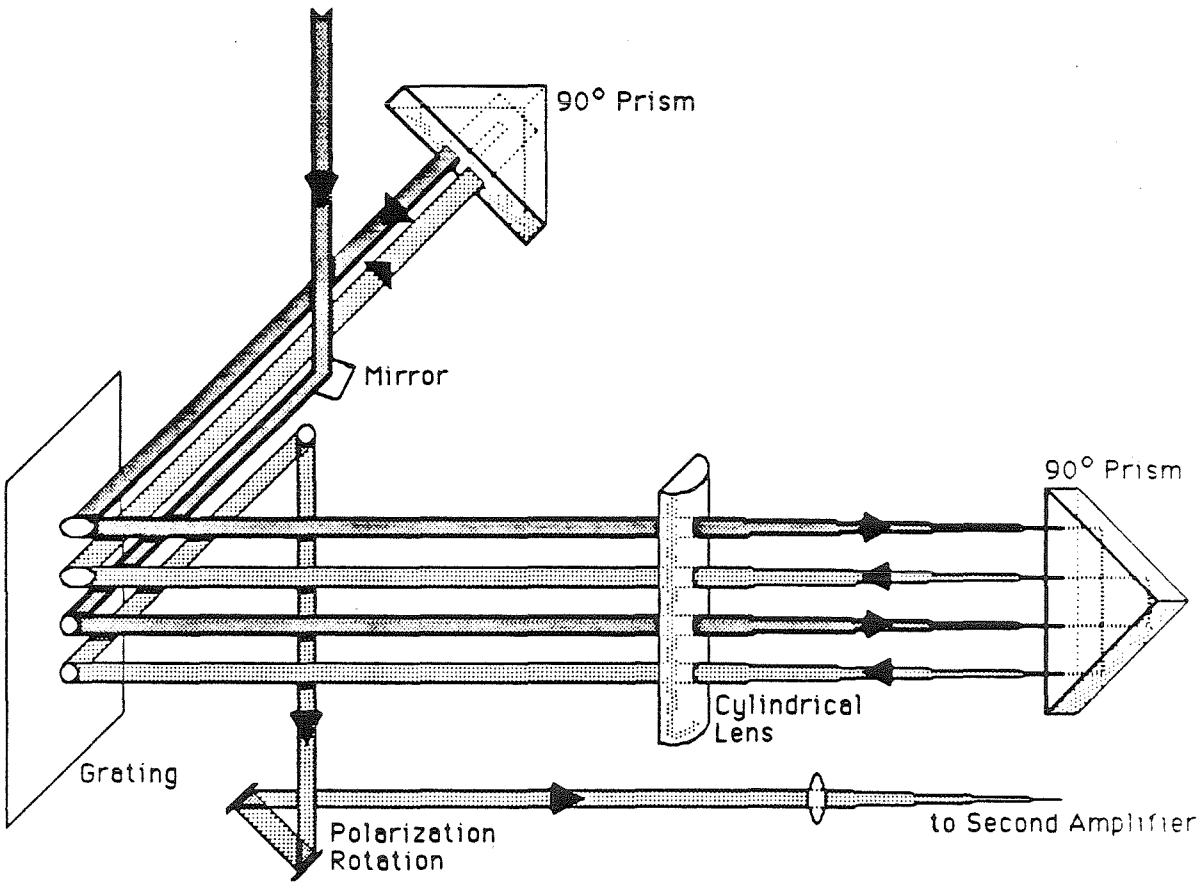

Figure 10.

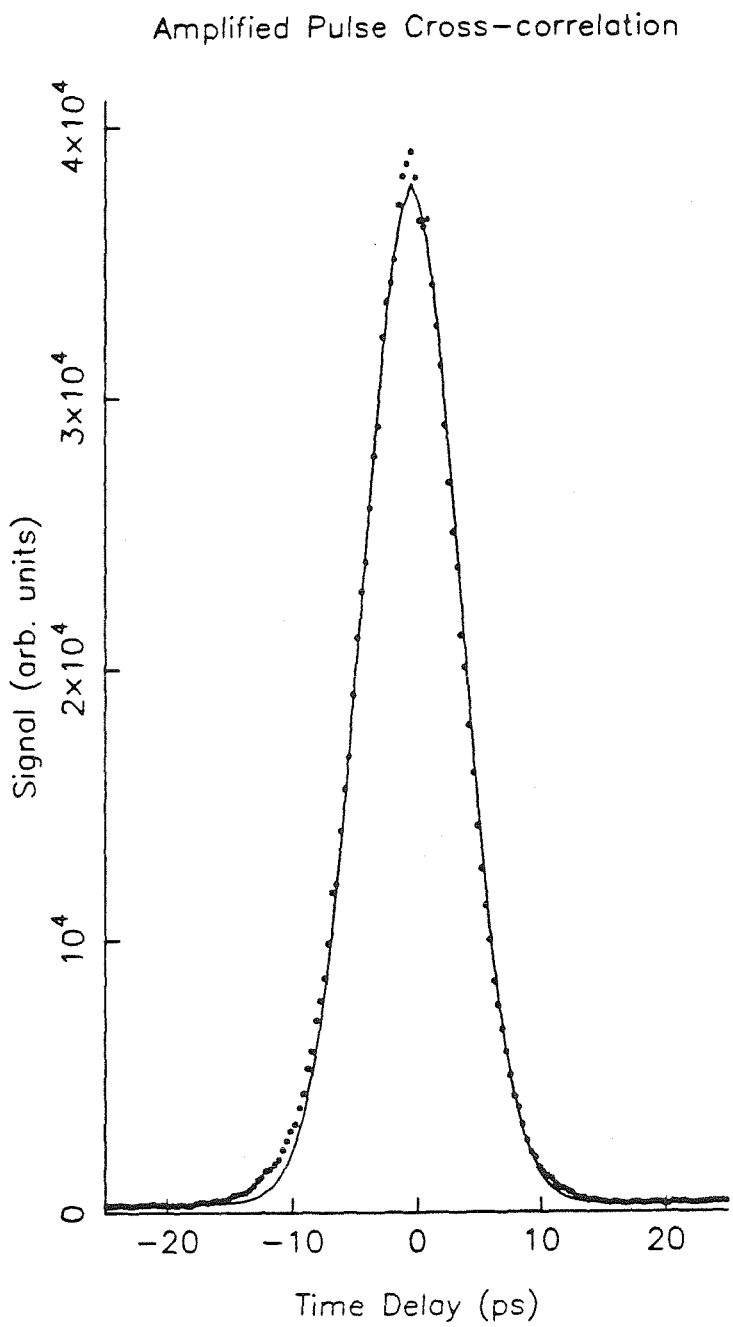
Amplified Pulse Cross-correlation
Signal (arb. units)
0
10^4
2×10^4
3×10^4
4×10^4
−20
−10
0
10
20
Time Delay (ps)

Figure 11.

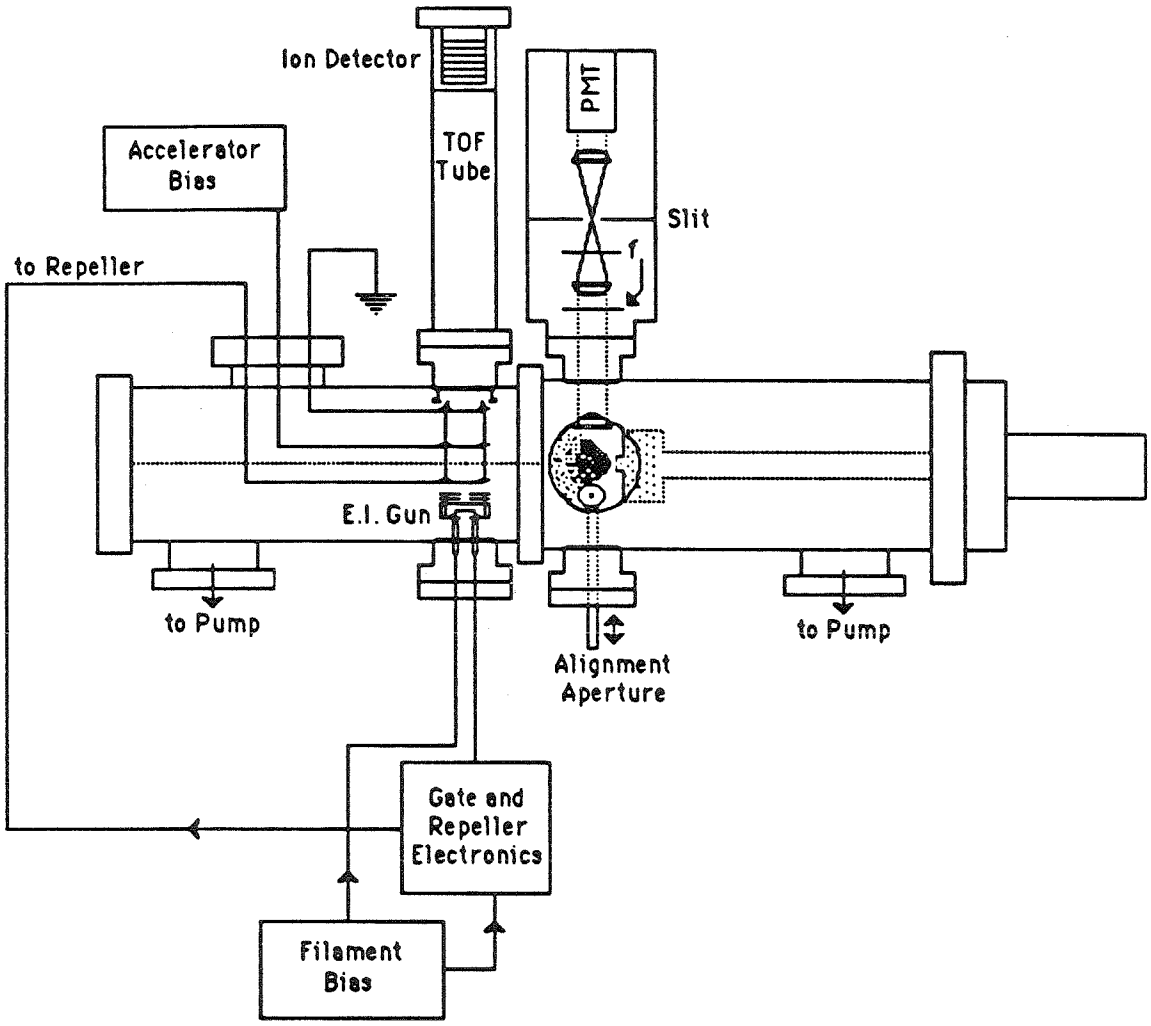
Ion Detector
PMT
TOF Tube
Accelerator Bias
Slit
f
to Repeller
E.I. Gun
to Pump
to Pump
Alignment Aperture
Gate and Repeller Electronics
Filament Bias

Figure 12.

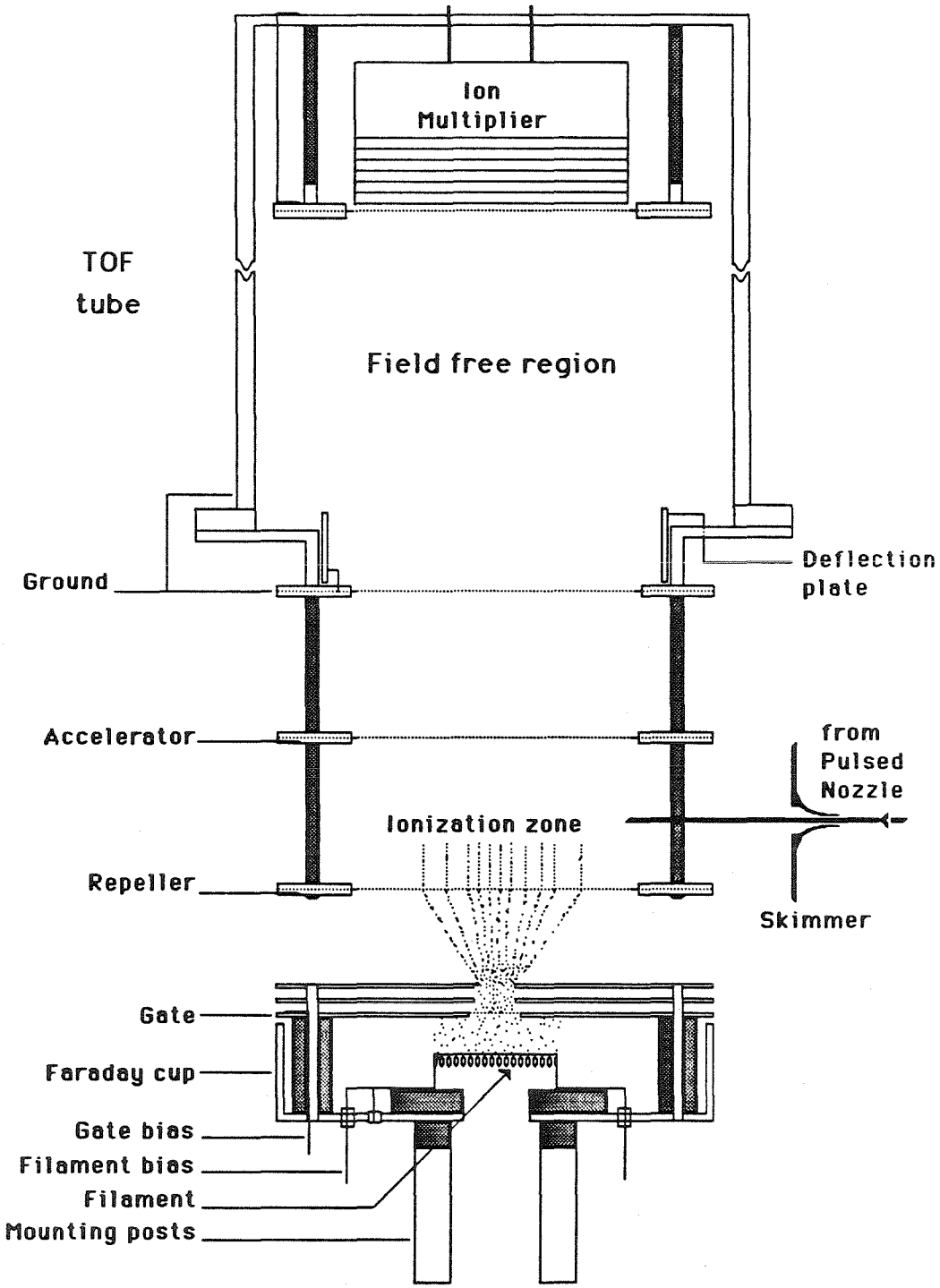
Ion
Multiplier
TOF
tube
Field free region
Ground
Deflection
plate
Accelerator
from
Pulsed
Nozzle
Ionization zone
Repeller
Skimmer
Gate
Faraday cup
Gate bias
Filament bias
Filament
Mounting posts

Figures 13a, 13b.

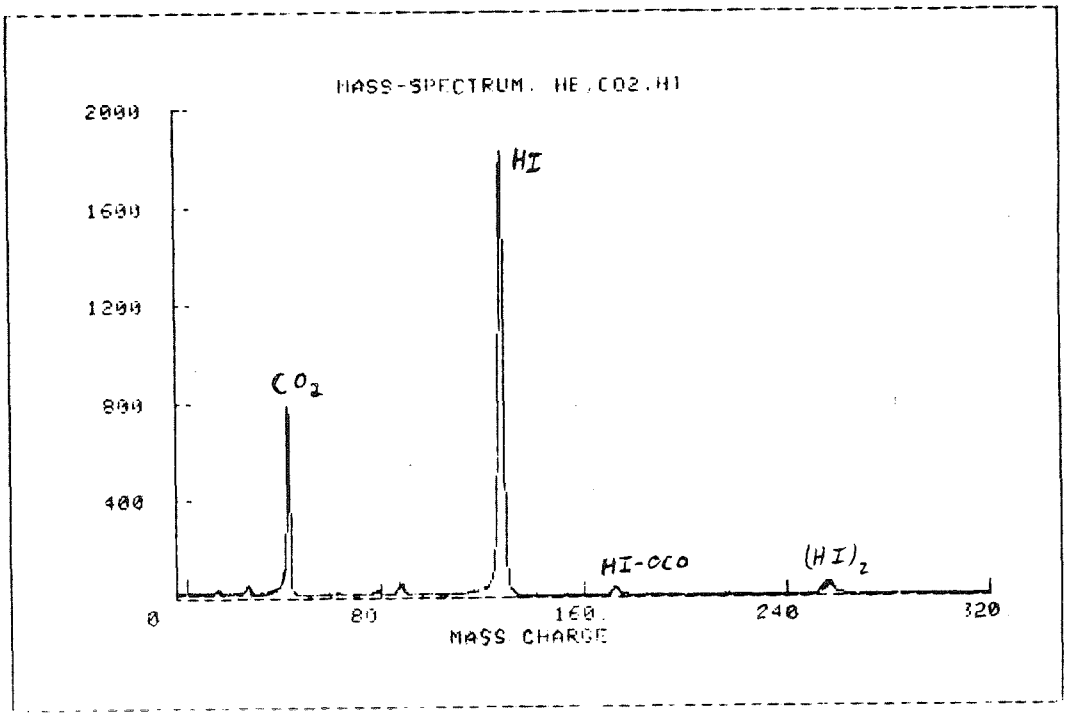

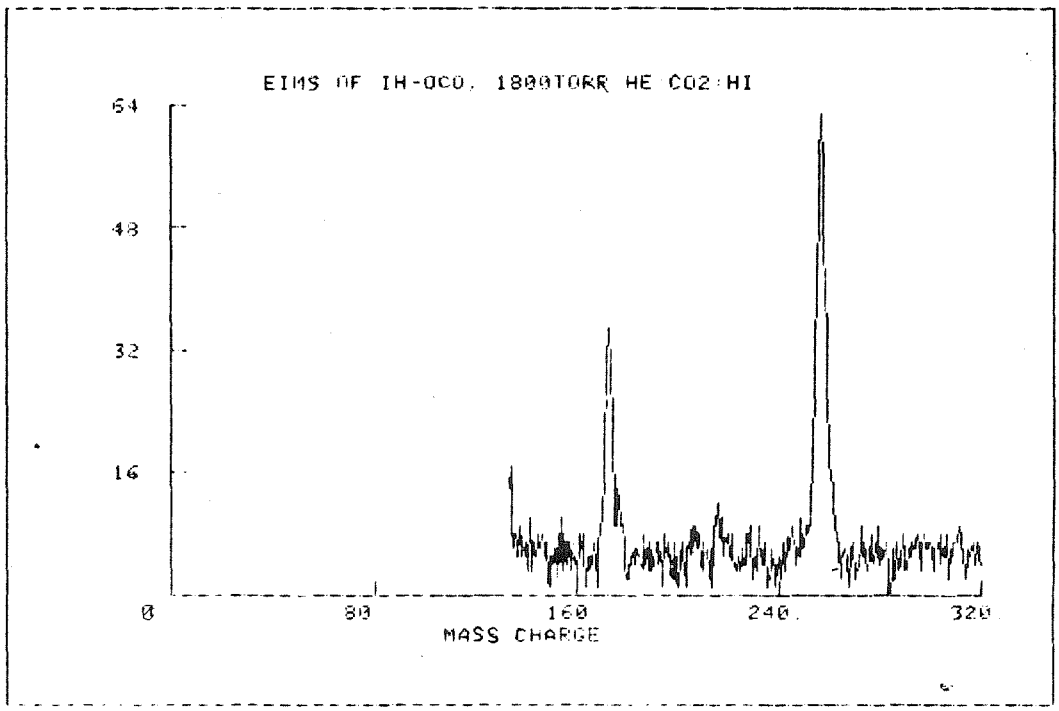

Figure 14.

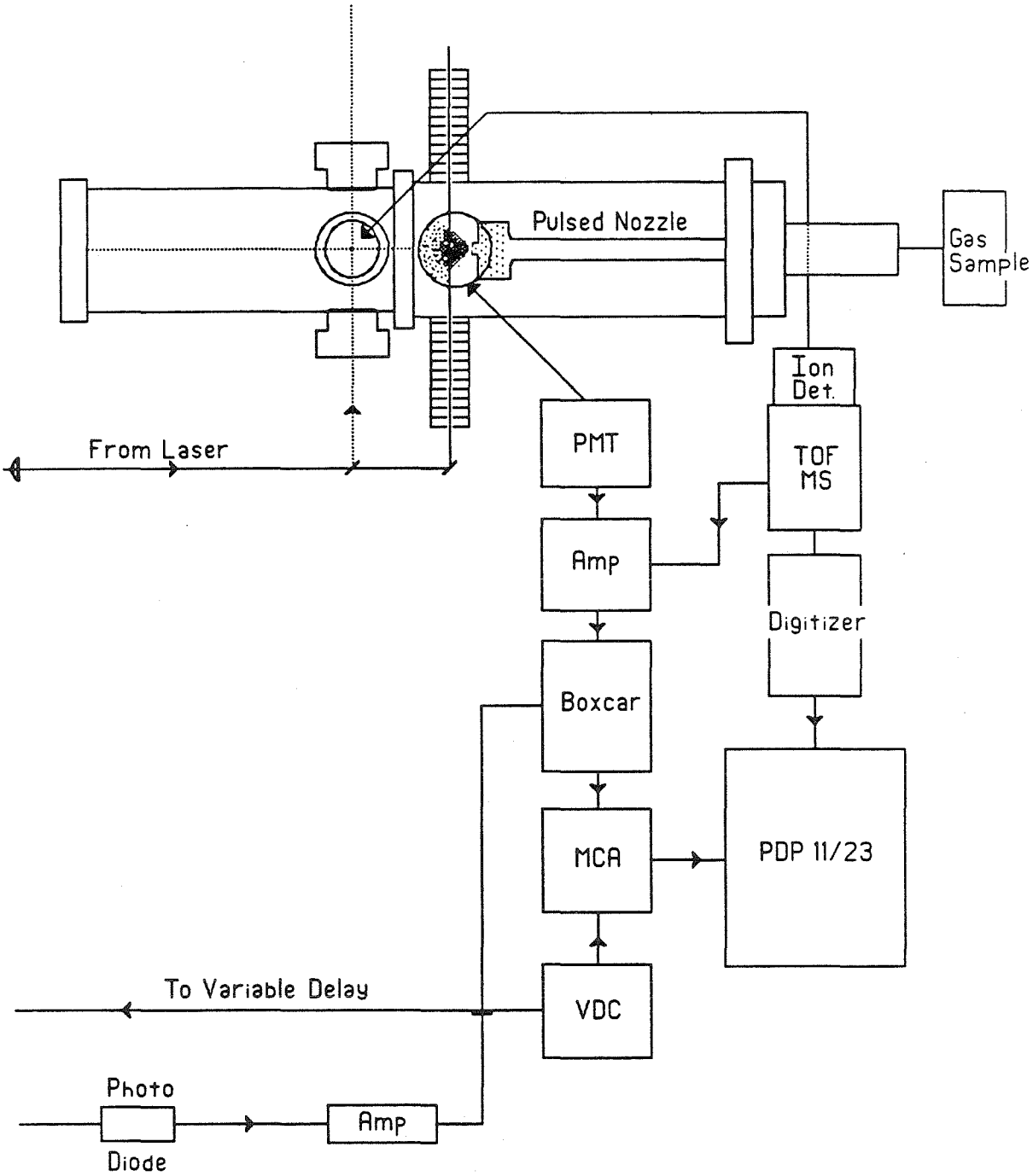
Pulsed Nozzle
Gas Sample
Ion Det.
From Laser
PMT
TOF MS
Amp
Digitizer
Boxcar
MCA
PDP 11/23
To Variable Delay
VDC
Photo Diode
Amp

Figure 15.

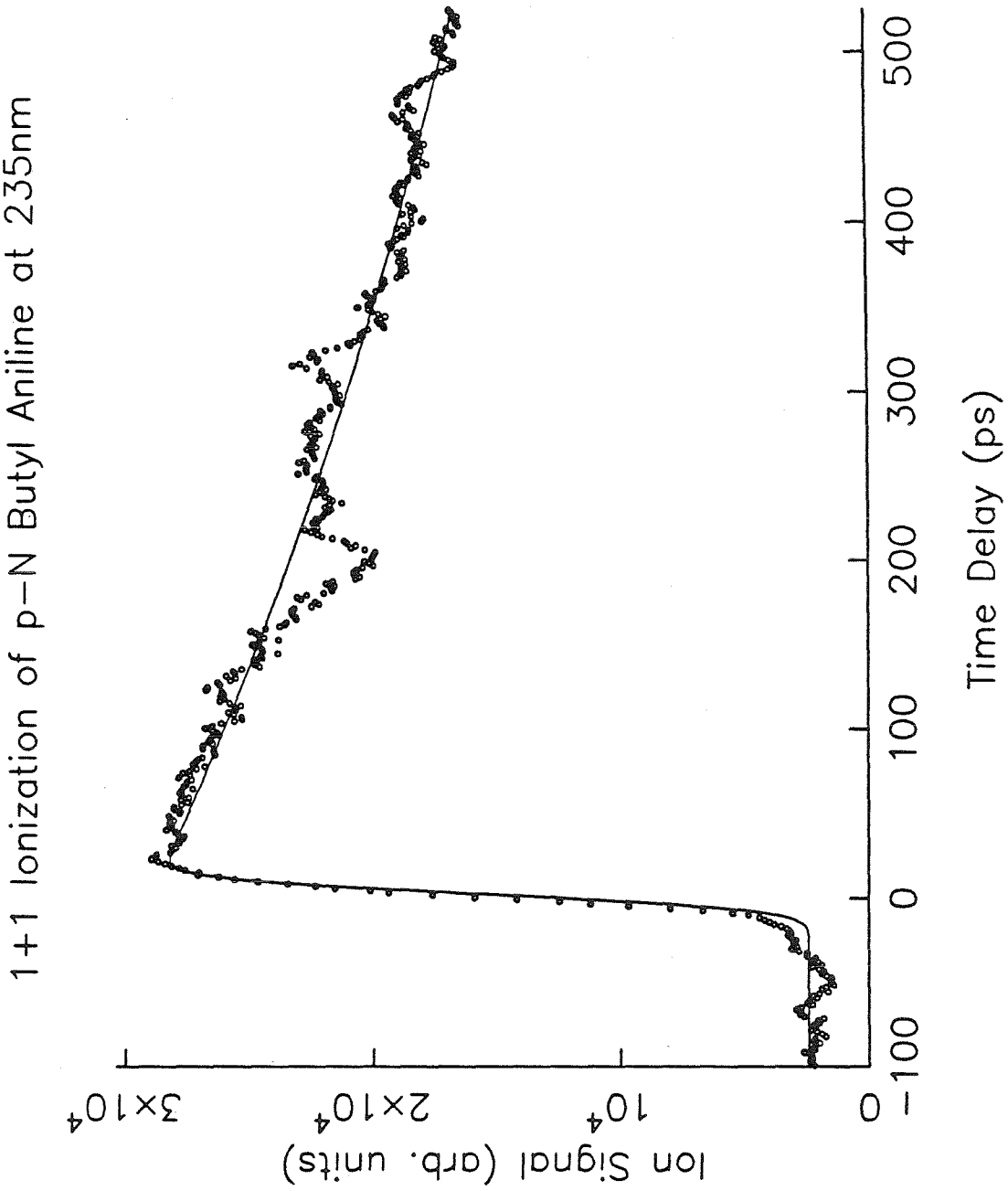
1+1 Ionization of p−N Butyl Aniline at 235nm
Ion Signal (arb. units)
0
10⁴
2×10⁴
3×10⁴
−100
0
100
200
300
400
500
Time Delay (ps)

Figure 16a, 16b.

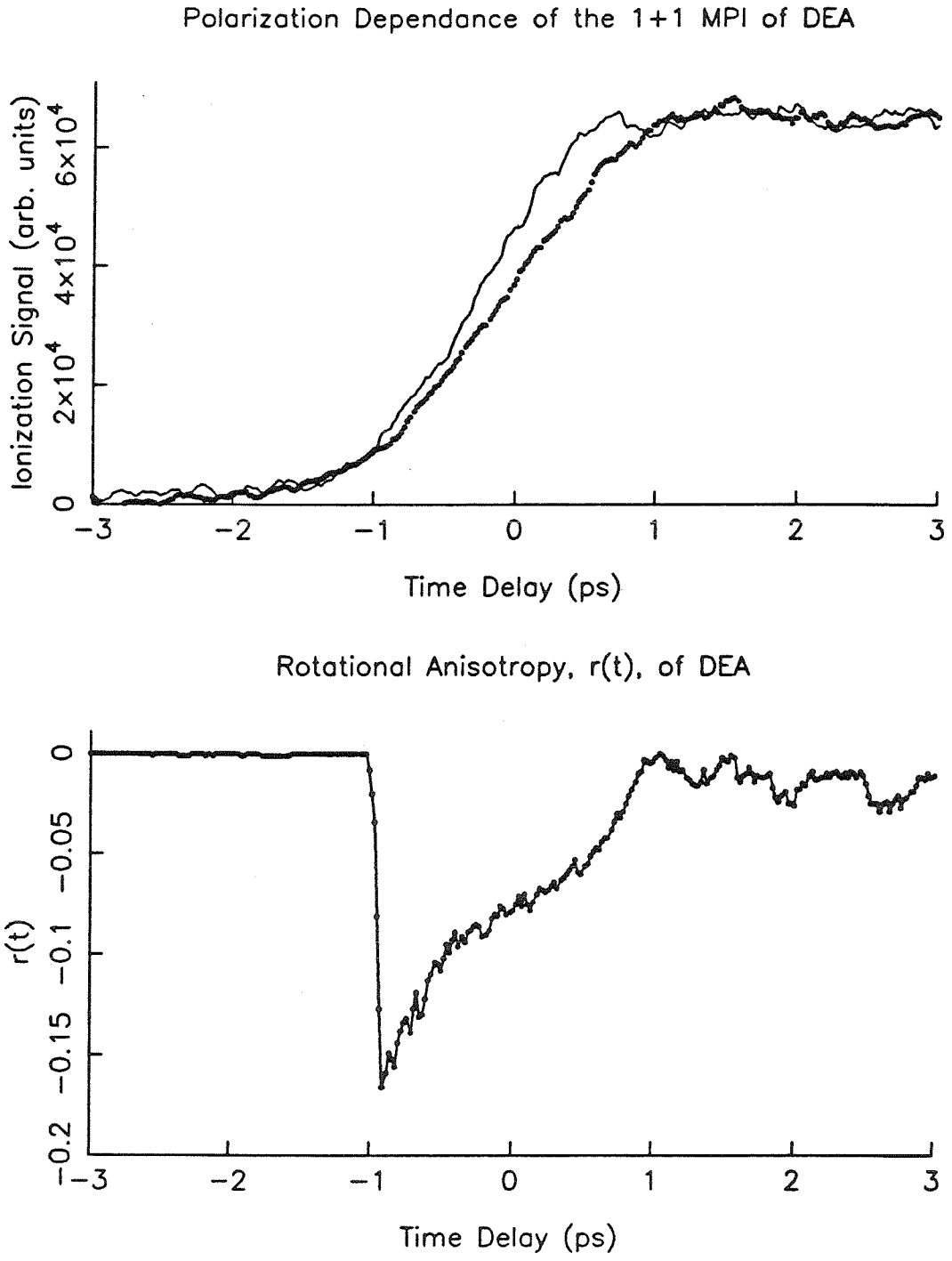

Figure 17.

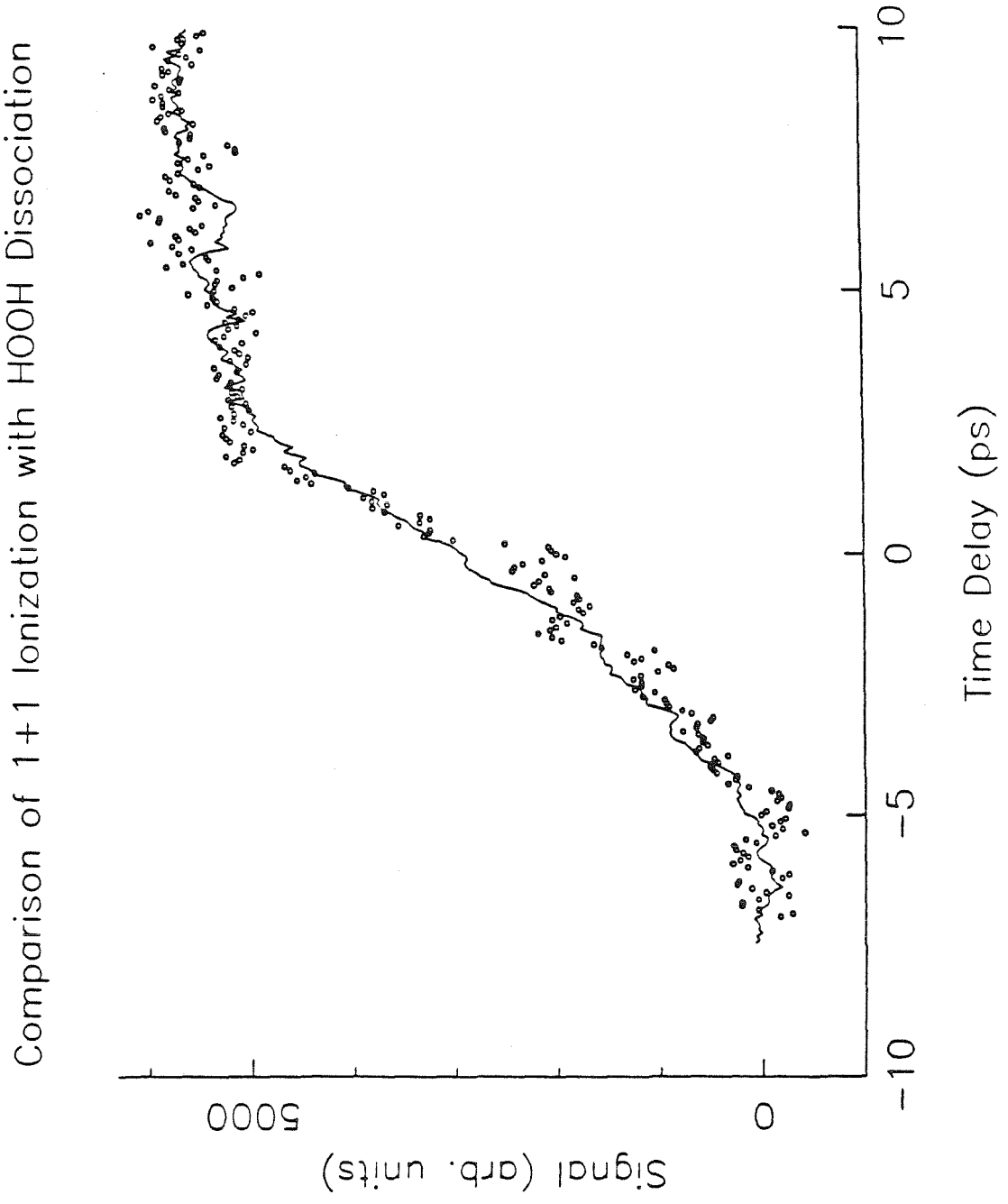
Comparison of 1+1 Ionization with HOOH Dissociation
Signal (arb. units)
5000
0
-10
-5
0
5
10
Time Delay (ps)

Published in The Journal of Physical Chemistry **89, 5141 (1985).

*Recipient of the Proctor and Gamble Award of the American Chemical Society (1986), for the work presented in this chapter.

CHAPTER III.

Femtosecond Photofragment Spectroscopy: The Reaction ICN → CN + I

N. F. Scherer,* J. L. Knee, D. D. Smith,† and A. H. Zewail‡

A. A. Noyes Laboratory of Chemical Physics,§

California Institute of Technology Pasadena, California 91125

---

† Permanent Address: Deparment of Chemistry, Purdue University West Lafayette, IN 47907

‡ Camille and Henry Dreyfus Foundation Teacher-Scholar

§ Contribution No. 7308

ABSTRACT

In this letter we report our first results on femtosecond photofragment spectroscopy. The reaction studied is: I-CN $\rightarrow$ [I$\cdots$CN] $\rightarrow$ I + CN. *A photolysis-and-probe scheme is used to measure the rate of the primary photodissociation of* ICN *under collisionless conditions. The* CN *build-up time is measured from these preliminary results to be 600$\pm$100fs. These direct measurements for the time of bond breakage in* ICN *are discussed in relation to the dynamics of the recoil process of the reaction.*

3.1 INTRODUCTION

Studies of the dynamics of primary photofragmentation processes offer new opportunities for the direct viewing of the process of bond breakage, its dependence on the nature of the transition state, and the resultant internal states of the products. Information about (average) photodissociation lifetimes, $\overline{\tau}$, has in the past been obtained from knowledge of the product angular distribution(s) and from the calculated average rotational period of the parent, $\overline{\omega}$, as is illustrated, for the case of ICN, in the pioneering work of Ling and Wilson.[1] To obtain $\overline{\tau}$, however, one must assume a model for the sharpness of the angular distribution and rely on the classical model for relating $\overline{\tau}$ and $\overline{\omega}$ to the spatial anisotropy, β, of the reaction. Picosecond and femtosecond photolysis-and-probe techniques allow one to obtain τ directly and test the validity of the models involved in the description of the rotation of the parent and the recoil process. Comparison of the direct time-resolved results with steady-state angular distribution measurements can then be made.

In recent work from this laboratory we have reported on the picosecond photolysis-and-probe monitoring of chemical reactions in molecular beams.[2-4] The primary process of alkyl iodide, RI, bond fragmentation to R and I was not, however, resolved because the fragmentation, in this case, is on a repulsive surface and the time scale for dissociation is shorter than the picosecond resolution of our experiment.

In this Letter we wish to report our first results on the femtosecond time-resolution of the primary photofragmentation (on the repulsive surface) of the reaction

$$\text{I-CN} \rightarrow [\text{I}\cdots\text{CN}] \rightarrow \text{I} + \text{CN}$$

In these experiments, as outlined in Figure 1, a femtosecond pulse (photolysis pulse) initiates the dissociation by exciting ICN (with a well defined *E*-field polarization direction in the laboratory frame) to the continuum absorption of the repulsive $\tilde{A}$ state with 306-nm light. The second pulse (probe pulse) monitors the recoiled CN at 388 nm (with its *E*-field orientated parallel or perpendicular to that of the photolysis pulse polarization). By observing the laser-induced-fluorescence of the rotationally excited CN fragment as a function of the time delay between the photolysis and probe pulses we measure the build-up (rise) time for the formation of the CN photoproduct. These experiments provide a direct view of the process of bond breakage and illustrate some of the difficulties inherent in the earlier indirect methods.

3.2 EXPERIMENTAL SECTION

3.2.1 Apparatus

The two femtosecond pulses (306 and 388 nm) were generated by using the following arrangement: A mode-locked argon ion laser synchronously pumps a cavity dumped dye laser (pulse width 5ps, 612nm), the output of which is compressed in a fiber optic/grating double-pass arrangement. The compressed pulse autocorrelation is typically 350-400 fs in duration. These pulses are amplified in a three stage dye amplifier which is pumped by the second harmonic of a Nd:YAG laser. The first two gain stages are isolated from each other by a spatial filter, while the second two are optically separated by a dye jet of the saturable absorber DQOCI. The resultant amplified pulses have typical energies of 150μJ and are usually 400fs in duration.

The pulse compressor is adjusted to precompensate for the dispersion encountered in the amplifier which, along with the saturable absorber jet, serves to prevent any significant pulse broadening. Mixing the amplified pulse in a nonlinear crystal with the 1.06μm YAG fundamental produces the 388-nm probe light, while the 306-nm light is the second harmonic of the amplified fundamental. This method of light generation produces pump-and-probe pulses with an insignificant amount of relative timing jitter. We have also taken care to ensure that we are able to phase-match the entire frequency bandwidth to minimize the extent of pulse broadening in the two mixing processes.

The 306- and 388-nm pulses traverse seperate arms of a Michelson intrferometer, one beam path containing a fine-resolution variable delay. The relative polarization is adjusted with a Soleil-Babinet compensator/thin film polarizer combination in the 388-nm arm. The beams are recombined and adjusted to travel collinearly through the experimental (ICN) and response function cells. The ICN cell is extensively baffled to reject scattered laser light and allow straightforward detection of the resonance laser induced fluorescence from the CN fragment. The response function of the system is obtained by replacing the ICN-LIF cell with an ionization cell of N,N-diethylaniline (DEA) and generating a resonance enhanced 1+1 ionization transient. The cell repositioning is done without changing any of the overlap adjustments or adding neutral density filters, therefore, a calibrated set of data (ICN transient, DEA REMPI response) is obtained. Calibration of the ICN transient against the REMPI response allows us to measure the rise and the "t=0 shift" for the 306/388 nm pulse excitation instead of relying on the autocorrelation of the dye laser pulses. Finally, the handling of ICN and the signal processing are straight forward and have been described elsewhere.[4]

3.2.2 Treatment of the Data

Figure 2 displays the apparent rise and shift observed in these femtosecond photoysis-and-probe experiments. This form of the delayed rise is similar to the observation made by Smith et al.[5] on the picosecond time scale. To obtain τ

from our measurements we have treated the data in the following way. We used the REMPI transient as the response function of the system for fitting the ICN transient using a non-linear least squares single exponential fitting routine. This gave $\tau = 600 \pm 100$ fs.

The REMPI transient rises and becomes flat with no indication of any decay components. This indicates that the resonant intermediate is long lived (ns) and that the observed REMPI is the response function for the 306/388 nm experiment. We have also considered the possibility that the intermediate state of DEA has an additional fast decay component due to off-resonant ionization and/or IVR processes.[6] In this case a biexponential decay is the expected behavior and the fast component can result in further sharpening of the response function, leading to an apparent shift from the actual system response. We have modeled the observed rise by convoluting a gaussian pulse (the integration of which gives the ICN transient) with a decaying biexponential function, fixing the long component at 8 ns decay and the fast component as pulse width limited (to be of the order of the pulse). It is found that the experimentally observed shift cannot be obtained while simultaneously maintaining the shape of the REMPI transient. When the experimental shift is matched the modelled REMPI response shows a pronounced decay component, which is inconsistent with the experimental observation. We found that by making the fast component much shorter (< 10 fs) we could, in principle, reproduce the shift but with the ratio of the fast to slow component being unphysically large (> 50).

The above treatment of the data confirms that the REMPI transient is the system response and that the observed shift is due to the finite τ of 600 ± 100fs. This is consistent with several experimental facts: (1) We observe similar temporal behavior when the polarization of the probe is perpendicular to that of the photolysis pulse. (2) The temporal behavior is not sensitive over a range of pulse energies, and the ion signal is linear in the probe intensity. (3) The pump wavelength is on

resonance with the absorption of DEA, which at room temperature is continuous at 306 nm.[7]

Finally, to reiterate, the fitting of the ICN rise (600 ± 100fs) was a convolution of the measured response function with a single exponential build-up, reflecting the prompt photodissociation process on the repulsive surface(s).

3.3 RESULTS AND DISCUSSION

ICN is a prototypical triatomic molecule for the study of the dynamics of axial recoil.[8-11] The photofragmentation spectroscopy of the $\tilde{A}$ continuum of ICN (maximum ~255nm)[12] has been extensively studied, a summary of which is found in the recent article by Nadler et al.[13] Our interest in this problem stems from a desire to directly measure the the photodissociation lifetime to obtain a better understanding of dynamics on repulsive surfaces . The reaction on this repulsive surface(s) produces CN radicals and iodine in its ground (I) and excited (I*) spin-orbit states. The CN is produced in the $X^2\Sigma^+$ ground state with essentially no vibrational excitation. On the other hand, there is extensive rotational excitation of the CN which is produced, and the distribution is known. Moreover, recent studies by Wittig's group[13] indicate that the spatial anisotropy parameter, β, is quite large for this reaction (1.3-1.6), which is slightly less than the maximum expected value of 2.0. Their values of β, which were obtained for 266 nm photolysis, should be compared with the values obtained earlier by Ling and Wilson (1.02 and 1.4). Knowledge of β can give an average photodissociation lifetime, $\overline{\tau}$, assuming a simple classical model for relating the average rotational period of ICN, $\overline{\omega}$, and $\overline{\tau}$ to β. This model assumes that the "loss" of the anisotropy is solely determined by the rotation of the parent, and that no other channels, such as surface crossing or transverse recoil, are involved. Assuming that the decrease in the value of β is only due to the rotation of the parent both Ling and Wilson and Nadler et al. infer that the average photodissociation time is 100-200 fs.

Figure 2 shows results obtained when monitoring the CN photoproduct with the femtosecond photolysis-and-probe scheme in a parallel configuration of the laser polarizations. Similar transients were obtained for the perpendicular configuration. The measured rise is the time required for the recoiled CN fragment to seperate from ICN following the photolysis pulse excitation. With this information we would like to address the point (supra vide) about relating this directly measured τ to the dynamics of the recoil process.

In a simple classical model for this axial recoil, our measured τ can be related to β using the relationship for the spatial distribution of the reaction products advanced by Zare, Herschbach, Bersohn, Wilson, Jonah and others.[15] For a parallel-type transition and for recoil along the internuclear axis in a center of mass coordinate system,

$$\beta/2 = [1 + (\omega\tau)^2][1 + 4(\omega\tau)^2]^{-1}.$$

The values of ϖ at 300 K and 337 K have been computed to be 1×10^{12} rad s^{-1} [13] and 1.89×10^{12} rad s^{-1} [1], respectively. Using our τ and these values of ϖ we obtain β= 1.1 and 0.7 for the two cases. Furthermore, our results indicate that the angle of rotation of the parent is 34° and 65°, respectively. In other words, the parent ICN molecule rotates, on the average, 30-60° prior to dissociation.

It is interesting to compare the range of β values of 0.7 to 1.1 (depending on the value of ϖ choosen) obtained here to the measured range of β's (1.2-1.6 [13] and 1.-1.4 [1]) for 266 nm photolysis. There are a number of considerations that must be taken into account in comparing these time resolved measurements to previous "CW" photofragmentation results. First, the photolysis wavelength may have an effect on τ, as these experiments were performed by pumping at 306 nm, considerably to the red of the 266 nm pumping used in the other studies.[1,13] Second, the β's in references 1 and 13 were obtained from the classical formula given above which neglects level crossing, transverse recoil and orbital angular momentum. It also assumes that the optical transition is purely parallel in this case. Inclusion of these dynamical effects is essential to the understanding of the recoil process, and we hope

to be able to isolate their seperate influences on the dynamics by these femtosecond time resolution experiments. We also plan experiments with shorter time pulses and at lower temperatures (beams) to separate these effect.

In conclusion, this work shows that the femtosecond photofragment spectroscopy of reactions is experimentally feasible and can directly measure the rate of formation of products in given states. It is our hope that these experiments, when completed, will provide the details of the transition state involved in the recoil process. Since the recoil velocity of this reaction is $\sim 2 \times 10^5$cm/s, the fragment separation is $\sim$10Å on the time scale of the experiment ($\sim$500fs). With this time resolution we must therefore consider the proximity of the fragments at the time of probing, i.e. the evolution of the transition state to final products. There is a wealth of experiments to be done on this (ICN) and other systems to directly elucidate the dynamics of photofragmentation under collisionless conditions.

Acknowledgements. This research was supported by the National Science Foundation. We thank Prof. C. Wittig for his interest in this work and useful discussion on ICN.

REFERENCES

1. J.H. Ling and K.R. Wilson, J. Chem. Phys. **63**, 101 (1975).
2. J.L. Knee, L.R. Khundkar, and A.H. Zewail, J. Chem. Phys. **82** 4715, (1985).
3. J.L. Knee, L.R. Khundkar and A.H. Zewail, J. Chem. Phys. **83**, 1996 (1985).
4. L.J. Knee, L.R. Khundkar and A.H. Zewail, J. Phys. Chem. **89**, 4659 (1985).
5. D.D. Smith, A. Lrincz, J. Siemion and S.A. Rice, J. Chem. Phys. **81**, 2295 (1984).
6. (a) N.F. Scherer, J.W. Perry, F.E. Doany and A.H. Zewail, J. Phys. Chem. **89**, 894 (1985). (b) J.W. Perry, N.F. Scherer and A.H. Zewail, Chem. Phys. Lett. **103**, 1 (1983). (c) N.F. Scherer, J.F. Shepanski and A.H. Zewail, J. Chem. Phys. **81**, 2181 (1984).
7. K. Kimura, H. Tsubomura and S. Nagakura, Chem. Soc. Jpn. **37**, 1336 (1964).
8. (a) R.N. Zare and R.B. Bernstein, Phys. Today **33**, 43 (1980). (b) R.D. Levine and R.B. Bernstein, *"Molecular Reaction Dynamics"*, (Oxford Press, New York, 1979).
9. (a) R. Bersohn, J. Phys. Chem. **88**, 5145 (1984). (b) J.P. Simons, J. Phys. Chem. **88**, 1287 (1984). (c) S. Leone, In *"Dynamics of the Excited State"*, K.P. Lawley ed., (Wiley, New York, 1982), p 255.
10. (a) M. Shapiro and R. Bersohn, J. Chem. Phys. **23**, 3810 (1980). (b) K.F. Freed and Y.B. Band, *"Excited States 3"*, E. Lim ed., (Academic Press, New York, 1978), p 104. (c) W.M. Gelbart, Annu. Rev. Phys. Chem. **28**, 323 (1977).
11. (a) E.J. Heller, Acc. Chem. Res. **14**, 368 (1981); E.J. Heller, J. Chem. Phys. **76**, 3035 (1982). (b) D. Imre, J.L. Kinsey, A. Sinha and J. Krenos, J. Phys. Chem. **88**, 3956 (1984).
12. (a) G.W. King and A.W. Richardson, J. Mol. Spect. **21**, 339 (1966). (b) J.W. Rabalais, J.R. McDonald, V. Scherr and S.P. McGlynn, Chem. Rev. **71**, 73 (1971).
13. I. Nadler, D. Mahgerefteh, H. Reisler and C. Wittig, J. Chem. Phys. **82**, 3885 (1985).
14. Parallel ($\parallel$) and perpendicular ($\perp$) refer to the orientation of the polarization of the photolysis pulse to the probe pulse.
15. (a) R.N. Zare and D.R. Herschbach, Proc. IEEE **51**, 173 (1963). (b) J.L. Kinsey, J. Chem. Phys. **80**, 2589 (1984). (c) S. Yang and R. Bersohn, J. Chem. Phys. **61**, 4400 (1974). (d) C. Jonah, J. Chem. Phys. **55**, 1591 (1971). (e) C.H. Greene and R.N. Zare, Annu. Rev. Phys. Chem. **33**, 119 1982

FIGURE CAPTIONS

1. Schematic representation of the ICN state structure relavent to the photodissociation processes being considered. The femtosecond photolysis pulse excites the ICN to the $\tilde{A}$ state contiuum. Product CN radicals are detected with the probe pulse by laser-induced fluorescence.

2. The leftmost transient is the system response function. The right-shifted transient is the ICN photofragmentation taken under identical conditions of overlap and time-delay. The shift and change of slope between the transients is quite evident. The solid line which passes through the points of the ICN transient are a convolution of the measured response function (REMPI transient) with a 600-fs exponential buildup, which agrees with a nonlinear least squares fit of the same.

Figure 1.

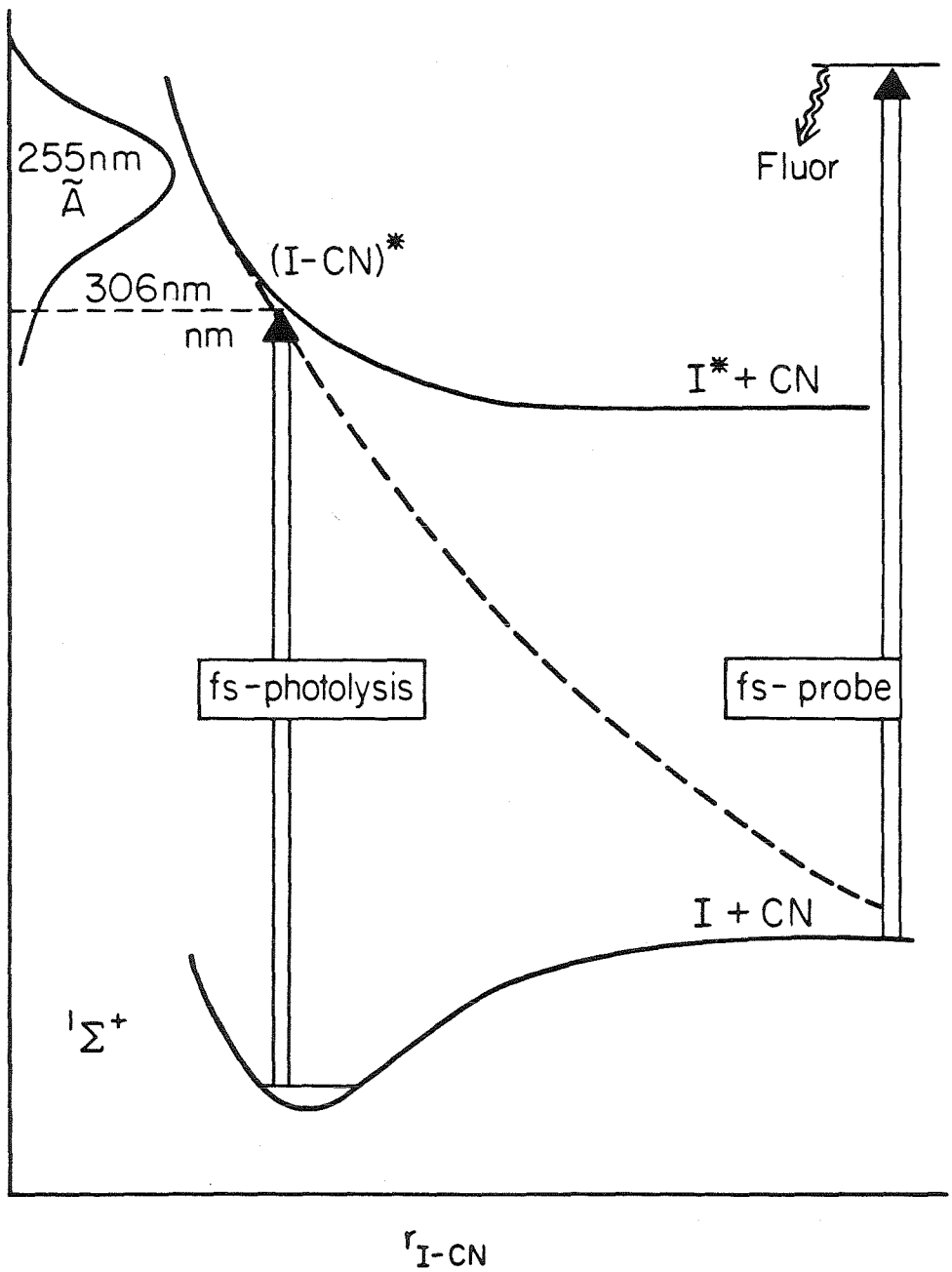
255nm
Ã
306nm
nm
(I-CN)*
Fluor
I* + CN
fs-photolysis
fs-probe
I + CN
$^1\Sigma^+$
r_{I-CN}

Figure 2.

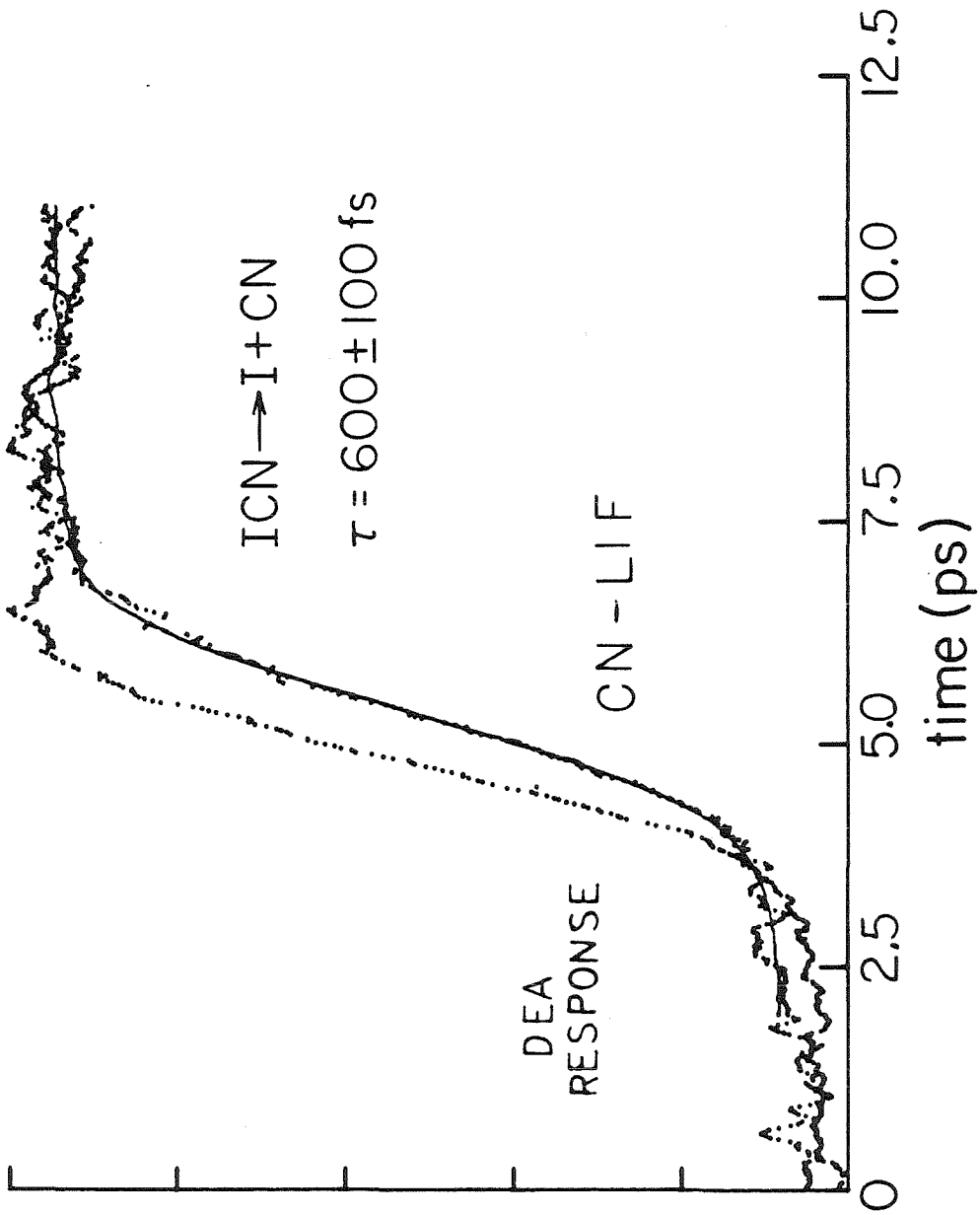
ICN⟶I+CN
τ = 600±100 fs
CN-LIF
DEA
RESPONSE
0
2.5
5.0
7.5
10.0
12.5
time (ps)

CHAPTER APPENDIX A

The work reported in Chapter 3 and the publication of the same material[1] has had a catalyzing influence on further studies which directly time-resolve molecular bond breakage. Zewail and coworkers [2-6] have begun to establish a foundation for extracting information about the reactive potential energy surfaces from femtosecond timescale dynamical studies. This appendix offers additional information about the polarization properties of the titled reaction in measurements performed in 1985. The implications of the dynamical effects to be presented were only realized after the formulation of other studies of Femtosecond Transition-State Spectroscopy (FTS).[2,4]

The conceptually difficient notion implemented in the data analysis of the preceeding chapter was the assumption that the appearance of the nascent CN reaction product occurs beginning at the t=0 position. In other words, the process of dissociation is not instantaneous even on the present experimental timescale. The previous analysis, therefore, incorrectly assumed that the proper model for data analysis is the convolution of a single exponential function with the measured response function and originating at the t=0 position of the response. A more correct model analysis would take into consideration the finite temporal delay prior to product appearance. The delay, $\Delta\tau$, arises from the fact that the incipient CN fragment must proceed to within a position of internuclear separation for which the remaining reaction potential energy is the same as the probe laser bandwidth. This is an overly simplified description which does, however, contain the essence of the proper physical picture of the dynamics.

The initiation of the dynamical process of electronic dissociation of a molecular species occurs by absorption of a photon of light. The Franck-Condon then implies that the state initially prepared on the excited electronic surface is the projection of the ground-state wavefunction, which is a Gaussian wavepacket. The wavepacket is not an eigenfunction of the excite potential surface and will, therefore, evolve.

The evolution may be described as motion of the center of the wavepacket, which is proportional to

$$\frac{\partial V}{\partial R}\Big|_{R(t)}$$

and spreading of the wavepacket , which is proportional to

$$\frac{\partial^2 V}{\partial R^2}\Big|_{R(t)}.$$

From this description of the dynamical motion it is, moreover, not obvious why the rise in the nacent reaction product population should correspond to an exponential function. The integral of the spreading Gaussian wavepacket, hence the integral of a gaussian function, is perhaps physically more realistic.

Another concern about the reasonableness of the 1+1 ionization method being a good technique for measuring the laser pump-probe cross-correlation was addressed in section 2.2.6 of the preceeding chapter. The finding from Figures 16a and 16b of chapter 2 is that rotational coherence effects are manifest in the ionization signal of parallel vs. perpendicular pump-probe polarizations. A plot of the rotational anisotropy in Figure 16b of chapter 2 undergoes dynamical evolution on a 0.5-1ps timescale.

All these reservations not withstanding, a re-analysis of the data presented in Figure 2 of this chapter would be useful. In particular, the analysis of the previously measured ionization and ICN photodissociation dynamics for perpendicular relative pump-probe polarizations will also be analyzed. Figure A1a shows the ICN photodissociation reaction data (open circles) as a rising function to an asymptotic value. The dots temporally preceeding the ICN data are from the 1+1 ionization of p-N Butyl Aniline (PBA). Both sets of data were obtained from the the same temporal delay (i.e. t=0) values and for parallel relative pump and probe E-field polarizations. The data set is the same as that shown and analyzed in Figure 2 of the present chapter. The solid line that passes through the ICN data is the best-fit convolution of a single exponential function with the PBA response, and includes

a time shift parameter. The results of this fitting give $\tau_{ICN,\parallel} = 0.35 \pm 0.1$ps and $\Delta\tau = 0.2 \pm 0.07$ps. Figure A1b shows the same data for perpendicular relative polarizations. The best fit values, obtained by minimizing the sum of the squares of the deviations between the data and the fitting curve, are $\tau_{ICN,\perp} = 0.19 \pm 0.1$ps and $\Delta\tau = 0.48 \pm 0.1$ps. The significant difference from the results presented in the chapter shows that the fitted lifetime for bond-breakage decreases if a temporal shift is included.

Considering the aforementioned limitations of the analysis just presented, the fitted reaction times (and functional forms) can only be said to give an approximation of the actual dynamics. The large temporal shift for the perpendicular data, as opposed to the parallel data, is a manifestation of the rotational coherence effect discussed above.

A similar plot of the rotational anisotropy of the ICN data would be of interest. Figure A2a shows the rise of the CN LIF signal as a function of the relative time-delay. The t=0 position has been obtained from the parallel PBA data. The temporal conditions for the parallel (solid line) and the perpendicular (open circles) are again identical so the rotational anisotropy may be evaluated without ambiguity. Figure A2b shows the magnitude of r(t) plotted aganst time. A non-zero, in particular a positive value for r(t), occurs for the early portion of the near t=0 temporal region. This occurs when the amplitudes of the parallel and perpendicular scans are normalized to a common value at negative time delays and at long time delays. The probe polarization was held fixed with the E-field directed at the photomultiplier detector. The normalization of the files long before and after time zero eliminates any contribution to the anisotropy from a static alignment (asymptotic alignment of the CN rotational angular momentum with the ICN transition moment). The r(t) plotted in Figure A2b arises from a transiently changing alignment of the fragments duing the time of separation.[6]

The last point may be justified because of two characteristics of the experimental conditions. Firstly, the probe laser wavelength is centered near the R-branch

band-head region of the CN($\upsilon = 0$) electronic absorption region. However, the red edge of the 150cm^{-1} bandwidth extends beyond the band-head absorption. Secondly, it is known that the fiber/grating pulse compression scheme does not produce transform limited pulses. In the case of ideal recompression, the passage of the spectrally broad pulses through any medium with positive group velocity dispersion would tend to produce a chirp whereby the red portion of the pulse would temporally lead the blue portion. (The latter point has not been experimentally quantified) This combination of effects could explain the transient anisotropy observed at time-delays with values slightly less than zero.

Several conclusions arise from these additional analyses of the temporal data of ICN photofragmentation. Firstly, the evaluation of time-zero and the system response function must be done with care for the 1+1 ionization of molecular species. Secondly, the temporal fitting procedure should include a (physically reasonable) temporal shift because of the time required for the perturbed CN fragment to become resonant within the probe laser bandwidth. Finally, transient anisotropies are observable for CN fragment absorption which is to the red of the nascent CN absorption wavelengths. These transient anisotropies may reflect angular potential interactions that occur in the tail of the reaction potential energy surface.[7]

REFERENCES

1. N.F. Scherer, J.L. Knee, D.D. Smith and A.H. Zewail, J. Phys. Chem., **89**, 5141 (1985).

2. M.J. Rosker, M. Dantus and A.H. Zewail, J. Chem. Phys., **89**, 6113 (1988); M.Dantus, M.J. Rosker and A.H. Zewail, ibid, **89**, 6128 (1988).

3. R. Bersohn and A.H. Zewail, Ber. Bunsenges. Phys. Chem., **92**, 373 (1988); R.B. Bernstein and A.H. Zewail, J. Chem. Phys., in press (1989).

4. T.S. Rose, M.J. Rosker and A.H. Zewail, J. Chem. Phys., **88**, 6672 (1988); M.J. Rosker, T.S. Rose and A.H. Zewail, Chem. Phys. Lett., **146**, 175 (1988).

5. L.R. Khundkar, Ph.D. Thesis, Caltech (1988).

6. A.H. Zewail, Farad. Disc. Chem. Soc., to be published.

7. M.A. O'Halloran, H. Joswig and R.N. Zare, J. Chem. Phys., **87**, 303 (1987).

FIGURE CAPTIONS

A1a. Pump-probe time resolved formation of the CN product following the photofragmentation of ICN. The ICN data are the open circles, the 1+1 ionization response of p-N Butyl Aniline is given by the solid points. The best fit exponential, convolved with the ionization response function, and including a small time-shift is the solid line through the data points. The pump and probe are polarized parallel to one another.

A1b. Same as in A1a except that the relative polarization of the pump and probe beams is perpendicular. See the text for more discussion.

A2a. Plot of the parallel and perpendicular ICN photofragmentation signals. The signal amplitudes are set equal at long negative and positive time delays.

A2b. Plot of r(t) for the data and temporal delay of Figure A2a. The transient anisotropy occurs slightly before zero time-delay. The cause of transient r(t) behavior and the explanation of the temporal position of the effect are elaborated in the text.

Figure A1.

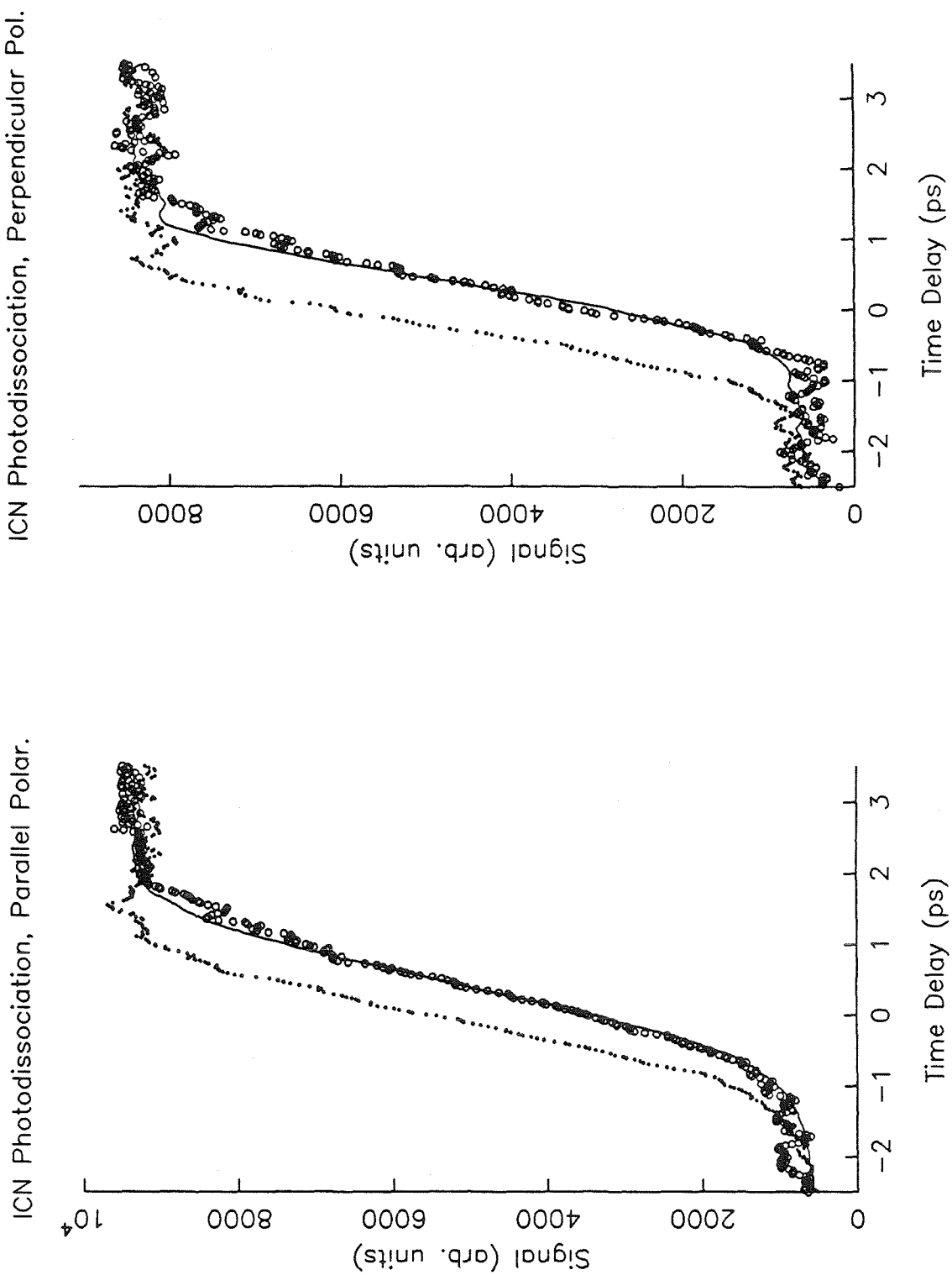
ICN Photodissociation, Perpendicular Pol.
Signal (arb. units)
0
2000
4000
6000
8000
Time Delay (ps)
−2
−1
0
1
2
3
ICN Photodissociation, Parallel Polar.
Signal (arb. units)
0
2000
4000
6000
8000
10⁴
Time Delay (ps)
−2
−1
0
1
2
3

Figure A2.

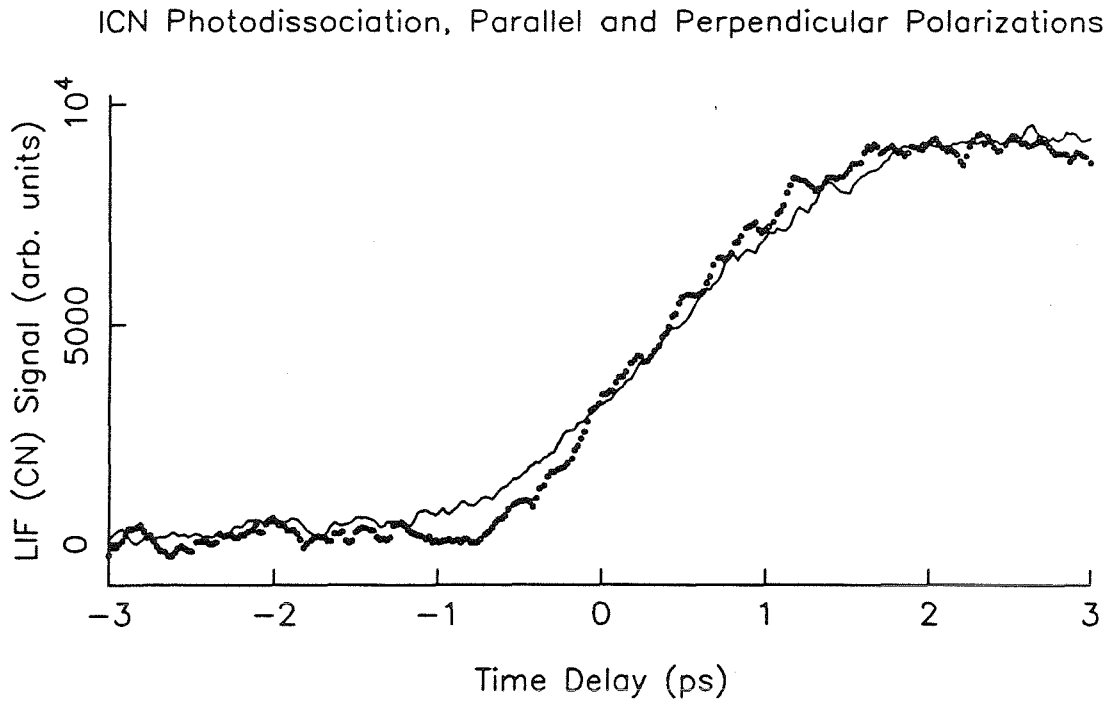
ICN Photodissociation, Parallel and Perpendicular Polarizations
LIF (CN) Signal (arb. units)
10^4
5000
0
−3
−2
−1
0
1
2
3
Time Delay (ps)

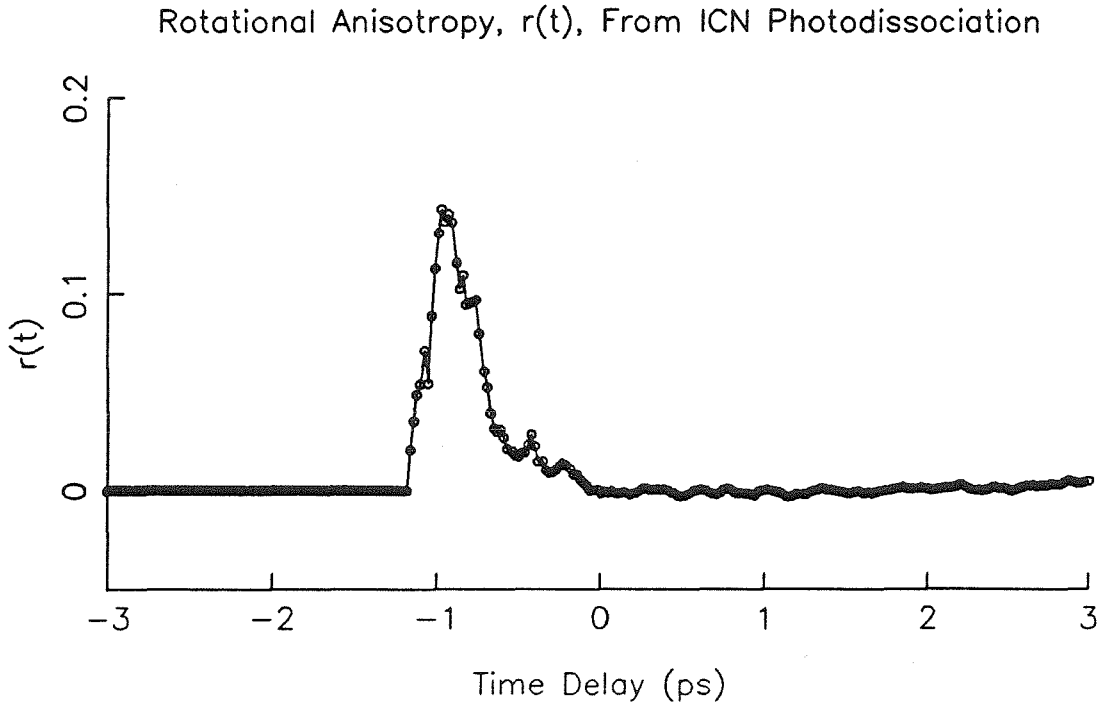
Rotational Anisotropy, r(t), From ICN Photodissociation
r(t)
0.2
0.1
0
−3
−2
−1
0
1
2
3
Time Delay (ps)

CHAPTER IV.

Temporal and Spectral Studies of the Perturbed OH Product Fragments Obtained from the Photoinitiated Direct Dissociation of HOOH

4.1 INTRODUCTION

Interest in the dynamical behavior of molecular photo-dissociation arises, in part, from the concept that this chemical event may be thought of as the second half of a reactive collision. The photodissociation dynamics (typically) occur on the final electronic surface of the more global and relevant reaction Potential Energy Surface (PES). The study of the progression of such unimolecular reactions may be done with much more selective initial conditions than are obtainable in the full collisional reaction. Traditional studies of such half-collisions have primarily sought to quantify the reaction mechanism by way of asymptotic observables which are of a scalar[1-3] or vectorial[4-8] nature. The scalar quantities refer to detection of the partitioning of energy into translation, vibration and rotation and the measurement of specific product state populations. The vector measurements are of correlations of intrinsic molecular or dynamic geometric quantities. The vector correlations are of product angular distributions, velocity and directional or velocity and rotational correlations or other alignment (orientational) factors which relate to the intrinsic dynamics (kinematic, angular forces, planar or non-planar dissociation) of the dissociation process.

The previous quantities were referred to as asymptotic because the properties manifest aspects of the half-collision dynamics but do not explicitly monitor the quantities during the course of reaction. Rather, the asymptotic quantities are measured once the product fragments no longer interact and therefore the product populations and dissociation kinematic effects are "locked-in." The range of expected dynamical behaviors as reported for both experimental and theoretical endeavors is summarized in the articles of Ref. 9.

Several research groups have tried to extend the spectrally resolved measurement methods to the domain of the dissociation reactions wherein the reaction fragments (incipient products) are transitioning between reactants and products. The concepts have centered around the idea of monitoring the small amount of photoemission which is obtained from the separating fragments. This type of spectroscopy

attempts to infer the temporal evolution of the dissociation process from the relative intensity of the emission features.

Polanyi and coworkers[10] have studied the wing-emission from the perturbed fragments of (photo-dissociating or bimolecular collisional) simple reactant species. The study of diatomic dissociation, in particular NaI, allows for reconstruction of potential surface difference features in a type of RKR inversion procedure. The Na emission results from the photoinduced dissociation of NaI which produces electronically excited Na. The primary wing emission occurs to the longer wavelength side of the Na D-line, and it is reasoned that this emission arises from incipient Na atoms being perturbed by the iodine photofragment partner. In the case of this direct dissociation process, the emission could, in principle, obtain from all nuclear configurations through which the system passes during the transition from reagents to separated fragments. The (exponentially) increasing separation of the relevant spectroscopic potential surfaces can explain for the red wing-emission. However, these authors also report a smaller amplitude blue wing-emission feature. This point will be addressed in some detail below.

Other researchers have utilized the Raman emission from dissociating molecules to aid in the determination of the ground electronic PES and the intramolecular dynamics which accompany photodissociation in polyatomic species. An investigation of the continuum resonance Raman scattering of I_2 reported the measured spectrum for projection onto the ground PES.[11] This work also evaluated the associated overlap integrals for the continuum to bound optical transition. By contrast, Imre et al.[12] studied the continuum-bound Raman spectrum of a polyatomic system, CH_3I. The analyzed spectrum shows emission features consistent with projection onto the CH_3-I stretch coordinate. The measured spectrum also contains additional combination bands associated with the CH_3 symmetric bending motion.

The Raman spectral results have been compared with the semi-classical calculation results from a Gaussian wavepacket analysis of the dynamical evolution. The idea, as formulated by Heller and coworkers,[13] consists of a constant Franck-Condon (FC) projection of the amplitude (Gaussian wavepacket) of the ground vibrational

state in the bound electronic level onto the dissociative electronic level. Subsequent wavepacket evolution on this excited surface allows for projection, via the radiation field, back onto the ground electronic surface. The projection amplitude onto specific vibrational levels of the ground state varies with time. The total Raman intensity at a given spectral frequency is the projection amplitude integrated over the time course of the dissociation process. The spectral features, therefore, contain information of the ground state vibrational levels. This discrete frequency information is convoluted with the dynamical evolution (i.e., center-of-mass motion, spreading and possibly bifurcation) of the initially prepared Gaussian wavepacket. Such numerical calculation results closely simulate the measured photodissociation emission spectrum.[14,15]

Other frequency resolved studies of photo-assisted dynamical processes such as association[16] or bimolecular reactions have been reported.[17] The emphasis of these studies is to better understand the PES features which influence the course of the reaction. The goal is performing spectroscopic measurements in the transition state region of the reaction. The subject of spectroscopic studies of molecules during reaction has recently been reviewed.[18]

Alternatively, the idea of performing time-resolved measurements of the dynamics of bond-breakage[19] and spectroscopy of the reactant becoming a product has been pioneered by Zewail and coworkers.[20–23] The idea of these experiments is to observe the dynamics of the photodissociation process directly in time and to monitor the time dependence of the complete bond breakage[19,20] Furthermore, it is possible to monitor the transient evolution of the initially prepared wavepacket through spectrally targeted portions of the relevant PES. These targeted regions may correspond to configurations of no return[20,22] or quasi-bound (predissociative) resonant levels of the excited PES manifold.[21] In all cases the experiment is of a pump-probe nature wherein a spectrally tunable pico- or femto-second pulse resonantly prepares the molecule on the reactive PES. The application of the pump-probe method in the study of unimolecular dissociation dynamics is illustrated in Figure 1. The probe pulse is of a similar temporal duration and may be (frequency)

tuned into the nascent product electronic transition(s). The probe may also be tuned off the nascent product resonance(s) to observe the transient evolution of the dynamics while the partner product species still perturbs the spectroscopically observable species. The signal detection is via Laser Induced Fluorescence (LIF) or Multiphoton Ionization (MPI).[22] It is in principle possible to extract information about the optically relevant potential surfaces by inversion methods.[23]

Finally, another recent experiment has directly probed the spectrally evolving dynamics of dissociation of TlI.[24] The detection method used herein is absorption of a continuum probe beam and measures the evolution of this absorption spectrum for different pump-probe delay periods. These authors observe wing absorption to the red of the Tl ($7S_{1/2} \leftarrow 6P_{1/2}$) resonance line. This would be expected from the previous discussion. However, a negative absorption is observed in the blue-wing region, which cannot be explained without explicit consideration of the optical coherence produced by the probe pulse. In other words, the effectively two-level Tl system is quickly excited to a coherence superposition state via the probe pulse excitation, thereby creating a polarization. The blue-shifting of the evolving product absorption band with increasing reaction time (pump-probe delay) causes the atomic polarization to constructively interfere with the probe light. Consequently, more light with a wavelength within the blue portion of the probe frequency band is projected toward the detector.

From this extensive introduction it becomes possible to surmise that an ideal experimental situation would be to simultaneously have good temporal and spectral resolution. The limit of this condition is the Heisenberg uncertainty principle, which restricts Gaussian laser pulses to $\Delta\nu\Delta\tau$=0.441.[25] This intrinsic experimental limitation dictates that the operational choice of the laser pulse spectral width will be determined by the resolution required to observe the product features of interest. The temporal pulse duration will be minimized accordingly.

The present experimental endeavor is for the reactant system HOOH, and yields two OH radicals for photofragmentation products. A schematic representation of the experimental concept is presented in Figure 1. The one-dimensional PES for the

dissociation process is described by an exponentially decreasing function. Pulsed excitation is to this upper repulsive PES. The OH rotational state populations are monitored by the probe pulse, which may follow the dynamical evolution to the nascent product configuration. Variation of the pump-probe time delay maps out the rate of product formation. The unique capability exercised in the present study is the ability to tune the probe pulse to the red or blue of nascent product absorptions. This allows for simultaneous temporal and spectral studies of the dynamical evolution on the near asymptotic tail of the repulsive HOOH ^1A_u PES.[26]

The hydrogen peroxide system has been chosen for several reasons: Firstly, the excitation and probe wavelengths are readily obtainable. Secondly, many studies of the scalar and vector asymptotic properties of the dissociation process have been measured. Thirdly, the dissociation process occurs primarily on the ^1A_u surface and results in $\leq$85% of the available energy going into translation with almost all of the remainder populating the rotational degrees of freedom of the OH product. Finally, the multipole moments of the OH product have been measured and calculated to the order relevant to the experiment at hand. These issues will be reexamined below.

The following section of this chapter will outline the experimental method employed in the current work. This will be followed by a section that will review the spectroscopy of HOOH and the electrostatic properties of the OH radical. The results section will present the experimental measurements of on- and off-resonance transient waveforms and the spectra observed from discrete temporal and frequency tuned studies. These findings will be compared to the expectation from a classical model for the dynamics of dissociation.[23] The data will also be compared to a second model which explicitly evaluates the spectral profile for fragment absorption during dissociation. The discussion section will be concluded by posing a third model, which considers the expected spectral evolution for OH-OH interactions via the permanent dipole and quadrupole moments. It will be shown that this third interpretation is in reasonably qualitative agreement with the experimental results. The conclusion section will consider the extensions to the electrostatic interaction

model which will allow for making a better quantitative comparison with the present experimental results.

4.2 EXPERIMENTAL SECTION

The laser and gas cell apparatus have been described in the Chapter 2. A brief synopsis of the overall experimental arrangement with additional elaboration on the more essential aspects will suffice. The experimental apparatus consists of three distinguishable parts: (1) the amplified picosecond pulse apparatus; (2) the nonlinear frequency mixing crystals, variable delay line and the flowing gas cell; and (3) the photodetection electronics and signal processing equipment.

The picosecond laser pulses are obtained from a mode-locked Nd:YAG laser synchrously pumping a cavity-length matched dye laser. The dye jet combines a gain medium of rhodamine-6G and saturable absorber DQOCI in ethylene glycol. The rapid ground state recovery time of the DQOCI quenches the gain in the dye jet before secondary pulses form in the laser cavity. These wing features would otherwise appear for a cavity length adjusted within $+3$ to -1μm of the optimal value. The dye laser bandwidth, and hence the minimum obtainable temporal pulse width, is controlled by a three-plate birefringent filter. The second harmonic of the synch-pumped dye laser light is used as the probe pulse. The dye laser cavity length adjustments are monitored with a home-built spinning block autocorrelator.

The output of the dye laser is injected into a Nd:YAG laser pumped four-stage dye amplifier. The dye medium is R640/CV670 in methanol in all the stages. The absolute and relative dye concentrations (R640/CV670) are adjusted to avoid pulse broadening effects from peak pulse energy saturation or restriction of the picosecond bandwidth profile. The overall gain factor from the amplifier is 1×10^6, to a per pulse energy of 0.4nJ. The temporal duration of the entrant pulse was 5ps and the exiting pulse is measured to be 5.5ps FWHM Gaussian.

The probe beam is obtained by focusing 20% of the amplified dye laser pulse into a 1mm KDP crystal with a f=40cm lens. The resultant second harmonic

beam is somewhat less structured in the transverse spatial profile. The probe pulse bandwidth is measured to retain a nearly constant value of 4.2cm^{-1} across any given spectrally tuned range. The probe pulse temporal duration is determined to be 3.8ps FWHM Gaussian by difference frequency generation cross-correlation measurements.

Spectral tuning studies were performed in the range of 305 to 309nm. The tuning of the probe laser frequency is accomplished over several overlapping 2.5Å intervals. The 2.5Å tuning range is sufficiently small that the dye laser temporal duration is not measurably affected. The amplified output also remains constant to within $\pm 5\%$ over the scan interval. This is because the amplifier dye mixture is adjusted to yield only a maximal 25% intensity change over the 304.5-309.5nm range. The spectral tuning is done by a geared-down (10:1) stepper motor (200steps/rev.) attached to the micrometer actuator of the birefringent filter rotation mount. The system frequency repeatability is better than 0.25Å provided that the frequency scan hysteresis is adequately removed by always approaching the scan initial position from the same direction and with an adequate number of pre-scan steps.

The remaining 80% of the output of the first amplifier is focused into a 1.5cm cell of nanopure water to generate an optical continuum. The continuum is analyzed with a polarizer to remove light with a polarization orthogonal to that of the entrant dye laser light. The continuum beam is double passed through a diffraction grating/cylindrical lens/0.5mm slit combination. The idea of this optical arrangement is two-fold. Firstly, the 1800 l/mm grating disperses the continuum frequencies, the f=15cm cylindrical lens creates a focal plane of the spectrally dispersed light and the adjustable opening plane-parallel slit selects a spectral bandpass centered at a specific frequency. A mirror immediately after the variable aperture slit retroreflects the selected bandpass back along the same path but vertically displaced by 1.5cm from the original beam spot on the grating face. Secondly, the position of the lens from the plane of the grating will determine whether the described optical arrangement imparts positive, negative, or no frequency chirp on the spectrally selected pulse. If the separation between the grating face and the lens is less than

the focal length of the lens, then the arrangement imparts a positive frequency chirp (i.e., red leading blue) on the temporal pulse profile.[27] If the lens is further removed than its focal distance, then a negative chirp condition is obtained. The present arrangement placed a f=15cm cylindrical lens 20cm from the grating face to introduce approximately a 3-4cm^{-1}/ps negative frequency chirp. The idea is to compensate for any previously accumulated positive group velocity dispersion from the continuum generation process and the anticipated dispersion from the second amplifier.

The spectrally selected 3Å near Gaussian band pass at 5320Å is injected into a three stage dye amplifier. The third harmonic of the Q-switched Nd:YAG laser pumps a dye solution of coumarin 522 in ethanol to provide gain at 532nm. The spatial mode profile is near TEM_{00} with some small and randomly distributed intensity variations, probably resulting from self-focusing and filament creation in the continuum generation process.[28] The amplification process obtains a gain factor of about 1×10^5 for an output of 250μJ/pulse.

This amplified spectrally selected continuum pulse is focused with a 1meter lens into a 4mm long β-BBO crystal. The resultant 266nm pulse has 21cm^{-1} spectral bandwidth and a temporal duration of 4.5ps as determined from cross-correlation studies. It may be judged that the chirp (pre-) compensation scheme is of some utility in preventing additional severe pulse broadening for the pump pulse.

The probe pulse passed through the scanning delay arm of the variable delay interferometer. The pump beam passed through a fixed delay. Both beams are combined in a collinear geometry with a dichroic reflector for 266nm. The pump and probe beams were independently focused with 0.8 and 1.0 meter lenses, respectively. The beam waists were within 10% of the same 150μm diameter and the axial positions of the beam foci were independently adjusted to match at the position of the collection optics. The pump beam had an energy of about 20μJ/pulse and the probe was attenuated to less than 1μJ/pulse.

The gas cell is designed to allow for continuous flow of the HOOH sample. The pressure is monitored by a Baratron capacitance nanometer and is typically

adjusted to be 100mtorr. The gas cell is of glass and quartz construction. The amount of scattered light which may be detected by the photomultiplier tube is minimized by the introduction of several axially symmetric black Teflon light baffles placed within the tube.

The fluorescence collection system is of 2″ diameter $f/1$ design. The only filter placed between the gas cell and the single photon counting photomultiplier tube (spc-pmt) is a Corning 7-54, which rejects the visible spectral region but allows the OH resonance fluorescence to be monitored with a 90% transmission efficiency. Scattered light resulting from the 266nm excitation is attenuated by more than a factor of ten with the same filter. The spc-pmt is employed because of its superior performance characteristics. The pmt gain is of the order 10^7 and the pulse height distribution is narrower than for conventional high gain photomultiplier tubes. Moreover, photon counting tube is optimized to produce substantial peak currents but has low capacitance so that the available average output current is rather low. However, considering that the current experiment is performed at a 20Hz repetition rate and that the OH lifetime is about 1μsec, the experimental duty cycle is only 2×10^{-5}. Therefore, the larger dynamic range of the spc-pmt and the superior S/N characteristics make it the photodetector of choice.

The pmt anode current is terminated at 50Ω and obtains a $\times 10$ gain in a wideband amplifier. This signal is the input to a boxcar integrator (PAR 162, 164, 165) where the signal in a 300μsec gated interval is averaged. The output 0-10V signal is converted to a proportional frequency in a Voltage-to-Frequency Converter (VFC). The frequency signal is monitored by a Multichannel Analyzer (MCA) operated in multichannel scalar mode. The channel advance of the MCA is synchronized to the step advance of the variable delay line and is used to accumulate the repetitively averaged temporal signals. The same signal detection, processing and accumulation equipment, was used for the spectral scans. The only significant change is that the MCA channel advance was synchronized to the stepper motor which advanced the birefringent filter.

Data analysis was performed by adapting the nonlinear least squares Marquardt algorithm[29] to lineshape analysis and exponential combined rise and decay analysis. The essential changes to the standard programs (Ref. 29c) is in incorporating numerical evaluation of the fitted function and its derivative. A new recursion relation is used to evaluate the fitting function and derivative in the case of the combined exponential build-up and decay results.

4.3 SPECTROSCOPIC STUDIES OF HOOH

The absorption spectrum of the gas phase $S_o \rightarrow S_1$ ($n \rightarrow \sigma^*$) transition of ^1A_g to ^1A_u symmetry[26] has been recorded.[30] The OH product state populations have been examined for excitation wavelengths shorter than 193nm,[31] 193nm,[32,37] 248nm[32,38] and at 266nm.[34,35,39,40] Excitation at wavelengths shorter than 172nm yields electronically excited OH ($A^2\Sigma^+$) photoproduct. Product electronic excitation does not occur at 193nm or lower energy excitation. Another reaction channel leading to H-atom formation has been observed at 193nm.[37] The studies of Refs. 32-37 may be summarized by saying that the photodissociation dynamics at this energy conclude that two (or more) electronic surfaces are involved in the dissociation process and that the transition moments of these states (^1A_u, ^1B_g) are orthogonal. Moreover, the $S_o \rightarrow S_1$ transition moment is orhtogonal to the O-O internuclear axis.

The experimental studies performed at 266nm indicate[34] that a large fraction (cf. 80%) of the OH rotational energy is induced by torsional motion excitation during the early portions of the O-O bond dissociation. The remaining 20% obtains from bending-like motion, which results from axial dissociation and repulsion at a point not equivalent to the OH center of mass. Excitation at 266nm is believed to involve only the first excited singlet level (^1A_u state). Measurements of the product angular distribution estimate that the time interval over which significant angular "deflections" of the OH products from the initial dissociation axis occur. The estimated reaction time interval is 50-70fs.[34]

Several theoretical studies are also of relevance to the present experiment. Efforts have been made to calculate the energies of the excited states of HOOH.[26,41] The calculations do predict that only one excited state is involved in the dynamics for 266nm excitation.

A classical dynamics study[42] of the dissociation of HOOH shows that the rotational excitation is induced by a small torque exerted by the repulsive O-O force around the center of mass of the OH radicals. This, in turn, leads to the conclusion that the rotational state distribution resulting from a given model PES was not very dependent on the photon energy. (Each surface is approximately linear in the Franck-Condon region.) However, the use of a steeper potential gave rise to more rotational excitation. It was concluded that the steep portion of the PES generates the fragment angular momentum. These authors[42] also included the effects of dipole-dipole interactions and observed that the added angular potential resulted in the joint probability distribution function, $P(N_1, N_2)$ where $\mathbf{N}$ is the nuclear rotational angular momentum of the OH product, giving $N_1 < N_2$ or $N_1 > N_2$. This is opposed to the trend observed without the dipolar interaction where $N_1 \approx N_2$.

Finally, another classical dynamics study[43] shows good agreement with the scalar and vector properties observed in the 193nm experiments. Some disagreement exists for calculations at 266nm, where the inclusion of hot band excitations are more important. However, these studies show that the torsional dependence of the excited state potential is the most significant source of fragment rotational excitation. It is noted[43] that this disagrees with the calculations of Ref. 42. The source of the disagreement is attributed to a deficiency in the potential used in Ref. 42.

The extensive range of measurements of the product state distribution, product angular distribution, Doppler-shift of the recoiling fragments and alignment studies of the OH fragment following the photolysis of HOOH at 266nm provides a solid basis upon which to develop an interpretation of the present experimental results. The product state distribution[40] results display a narrow rotational distribution. Doppler measurements[40] show, in the absence of any measurable amount of product

vibrational excitation,[40] that the energy available for translation is $2 \times 10^4 \pm 1 \times 10^3 cm^{-1}$, and 90% of this energy is apportioned to translation.

A recent description of the photodissociation product vector correlations has been presented.[40b] The traditional A_0^2 alignment parameter[4,5] description has been rigorously advanced to the level of determination of the bipolar moments.[40b] The important product vector correlation for the present analysis is the correlation of velocity and total angular momentum (v,J). The (v,J) correlation corresponds to the $\beta_0^0(22)$ bipolar moment. This quantity has been analyzed from the Doppler studies.[40] Moreover, the product pair correlation $P(N_1,N_2)$ has been obtained.[36] The value of $\beta_0^0(22)$ was found to be close to its limiting value and became closer for larger J_{OH}. This result was interpreted to mean that the OH product fragments exhibited a desire to align $\vec{J}_{OH}$ parallel to the recoil velocity, $\vec{v}$. In other words, the dissociation produces products in which the planes of product rotation are mutually parallel but perpendicular to the O-O dissociation axis.

Klee et al.[40] explain this result by saying that the rotational angular momentum of the fragments arises from a strong torsional dependence for the ^1A_u excited electronic surface. The O-O bond dissociation is accompanied by excitation of the HO-OH torsional motion.[43] They concluded that the initial thermal excitation of ^1A_g ground state does not have a significant effect on the observed correlations. It is found, via the breakdown of the N_1=N_2, complete correlation of the two OH products[36] that the recoil along the O-O bond (slightly separated from the centers of mass) will produce some torque and rotational excitation. Also, the OOH bending mode dependence of the ^1A_u PES will create some rotational excitation. The latter two motions produce rotational momentum where $\vec{J}_{OH} \perp \vec{v}$ and $\vec{J}_{OH} \parallel \vec{\mu}$, where $\vec{\mu}$ represents the $S_1 \leftarrow S_0$ transition moment. These authors estimate that the rotational excitation for the non-torsional processes contributes about 25% of the total rotational energy. Finally, the product correlations have the largest deviation from $N_1 = N_2$ when N=1, and $N_1 = N_2$ is obtained for N=6.[36]

As was discussed above, the strong repulsion of the valence electrons in the σ^* orbital dominate the R_{O-O} <4Å range.[42] The ^1A_u surface is described by

Eqn. (5.4) for the O-O coordinate. The shape of the B_u surface which correlates with the electronically excited ($^2\Sigma$) OH product[26] is presently not known except at the equilibrium geometry of the ground state.[41] Assuming that the B_u state is either more steeply repulsive than the ^1A_u surface or is described by a form approximately equivalent to Eqn. (5.4) yields an exponential separation of the two potential surfaces. Consequently, it is expected that a red-wing absorption would result.[23] (It is probably a reasonable assumption to say that the B_u and ^1A_u surfaces behave in a similar fashion in the large O-O separation region, because the $^2\Sigma$ and $^2\Pi$ OH states exhibit nearly equivalent geometries.) Bersohn et al.[42] position the center position of a dipole-dipole interaction at 4Å O-O separation and turn the interaction off at smaller internuclear separations. Eqn. (5.4) gives value of V_1=1.7cm^{-1} at R=4Å. Although it is not known, the B_u surface is presently assumed to have a similar asymptotic approach to zero interaction potential energy. Therefore, the internuclear separation at and beyond 4Å will be dominated by long-range electrostatic interactions.

The spectroscopy of the OH radical was most fully treated by Dieke and Crosswhite.[44] The notation of Ref. 44 follows the conventions for Hund's case (b), which assumes that the spin is only weakly coupled to the internuclear axis. Hund's case (b), which is applicable to the $^2\Sigma$ levels (e.g. Λ=0), implies a coupling of the electronic spin and the nuclear rotational angular momentum **N**. Each value of N in $^2\Sigma$ manifold is split into two levels where J=N$\pm\frac{1}{2}$. For higher rotational states, case (b) may also be applied to the ground electronic state of OH radical, where $\Lambda \neq 0$. In such case, the resultant angular momentum **K**, formed by Λ+**N**, interacts with the spin **S** to form **J** (e.g., **J**=**K**+**S**). For the $^2\Pi$ electronic state the total angular momenta $\{J_{OH}\}$ is, thus, expressed as $K + \frac{1}{2}$ and $K - \frac{1}{2}$. (In the present experiment the Λ-doubling will not be resolved.)

However, for the low rotational level N ($1 \leq N \leq 6$) the angular momentum coupling is better approximated by Hund's case (a), in which the electronic orbital and spin angular momenta, denoted by Λ and **S**, respectively, couple strongly to the internuclear axis. Namely, the resultant electronic angular momentum, Ω, which

is formed by Λ+**S**, interacts with the nuclear rotational angular momentum **N** to form the total angular momentum (e.g., **J**$\equiv$ **Ω**+**N**). Λ-doubling splits each N level into two, but J remains the same for both levels. Although **K** is not defined in Hund's case (a), one can formally assign K values to be $J \pm \frac{1}{2}$ for $^2\Pi$ electronic state. Furthermore, the selection rules for the $^2\Sigma^+ \leftarrow {}^2\Pi_\Omega$ (where $\Omega = \frac{3}{2}, \frac{1}{2}$) transitions are $\Delta J = 0, \pm 1$ and $+ \leftrightarrow -$ (referring to the symmetry of the spin-rotation interaction: Λ-doublet). For case (b) systems, $\Delta K = K' - K'' = 0, \pm 1$. Transitions that satisfy both the ΔJ and ΔK rules constitute main branches. Transitions that violate the ΔN rule are satellite branches.

For large K, where Hund's case (b) is a good approximation, the satellite intensities become small compared to the main branch line intensities. P, Q, and R branches are obtained for ΔK=1,0, and -1, respectively. $Q_1(2)$ refers to ΔK=0 transition for K=2 level in the $^2\Pi_{3/2}$ manifold. The satellite transitions change J differently than the main branch transition. $Q_{21}(2)$ implies $\Delta N = 0$, $\Delta J = -1$, but the transition originates from the same state as $Q_1(2)$. Therefore, the main and satellite branch transitions probe the same $^2\Pi$ population. The transition radiative lifetimes have been tabulated in Ref. 45.

4.4 RESULTS

The photolysis pump and OH-LIF probe scheme has been described above. A schematic diagram of the relevant potential surfaces (not to scale) and the excitation and probe conditions are presented in Figure 1. The expectation is that on-resonance OH detection would yield a monotonic rise to a maximal signal (population) and remain at a constant value for the less than 100ps timescale of the present experiments.

Figure 2a shows the on-resonance temporal dependence of the OH-LIF signal. The rising portion of the figure corresponds to the region of the temporal pump-probe pulse convolution. The method for obtaining the pump-probe pulse convolution that is the system response function, is described below. The pulse

cross-correlation is convolved with a 0.46ps single exponential rise to obtain the solid line through the data points. The fact that the response function is obtained by way of two deconvolutions and a convolution means that any information about the experimental t=0 is not maintained. The fitted curve is, therefore, only an approximation of the actual dissociation dynamics. However, the temporal position of Figure 2d has been used as dictating the t=0 point for the response functions. The fit also obtains a value to the time-shift of $\Delta\tau$=0.78ps. The inverse rate (life-time) parameters in the fitting process are determined by minimizing the sum of the squares of the deviations between the experimental data points and the fitted curve.

Tuning the probe laser 2.6cm^{-1} to the red of the $Q_1(1)$ resonance probing of Figure 2a yields the result presented in Figure 2b. An additional transient feature is manifest in the figure but the longer-time temporal behavior is unchanged from the on-resonance process. The probe laser bandwidth is measured to be 3.5cm^{-1} FWHM Gaussian, which implies that the on-resonance signal is reduced to less than 1/3 of the value when the probe is tuned fully on-resonance. The same 7.2ps FWHM value for the system response function is obtained for Figures 2a-d. This value for the response is used to fit the data of Figure 2b with the functional form

$$\mathrm{I_{OH}}(t) = \int_{-\infty}^{t} dt' \int_{-\infty}^{\tau} d\tau'\ \mathrm{R}(\tau' - \tau_o) \cdot \Big[a_1 \exp\{-k_2(t' - \tau')\} + a_2\{1 - \exp\{-k_2(t' - \tau')\}\}\Big] + \Delta\tau_s \quad (4.1)$$

which involves convolution of the system response function to a form which is the molecular response. The molecular dynamical behavior is assumed to correspond to a transient resonant feature that decays away with a time constant k_1 and an exponential rise to an asymptotic value with rate k_2. Such dynamics are represented by a simple kinetic scheme

$$\mathrm{A} \xrightarrow{k_1} \mathrm{B} \xrightarrow{k_2} \mathrm{C} \quad (4.2)$$

where B and C are detected off-resonance and essentially only C is detected on-resonance. Eqn. (4.1) is obtained when $k_1 \ll k_2$. The fitted inverse rate of Eqn (4.1) to the data of Figure 2b give $1/k_2$=0.48ps and $\Delta\tau$=0.61ps. The fraction F($\equiv \frac{a_1}{a_1+a_2}$), is 0.79.

The data of Figure 2c is measured for a spectral detuning of 4cm^{-1} to the red of the $Q_1(1)$ resonance. This shows a more pronounced transient feature than Figure 2b. The temporal data is fit to Eqn. (4.1) where R(τ') is a 7.2ps FWHM Gaussian pulse. The solid line through the data is for $1/k_2$=0.50 and F=0.95 and $\Delta\tau$=0.4ps. Finally, Figure 2d shows a temporal response which is almost exclusively a transient feature. The temporal behavior is well approximated by a Gaussian pulse with a FWHM characteristic parameter of 5.35±0.25ps. The previously stated characteristic inverse rates all have fitting errors of about ±0.5ps. The reported lifetimes are, therefore, able to ascertain only that the dissociation dynamics always occur in less than about 1ps.

Apart from the issue of having the correct functional form for the response function is the uncertainty of the t=0 point. The shift value, $\Delta\tau_s$, of Eqn. (4.1) is varied to minimize the χ^2 value. The method for using the Figure 2d data to establish the t=0, and hence the $\Delta\tau_s$, values. Therefore, the uncertainty in the fitting results is significant for the magnitude of the observed effects.

The reason for the uncertainty in the measurement of the experimental t=0 and the response function is due to the instability of the multiphoton ionization method described in Chapter II of this thesis. The signal instability arises from the deposition of an insulating dielectric film on the cell electrodes. The film is either the p,N-butyl aniline or some photoproduct therefrom. The uncertainty in the t=0 position results from the necessity to attenuate the 266nm beam, thereby introducing an indefinite amount of additional optical delay in the pump beam path. Chapter II presented results of the λ=241nm photolysis of p,N-butyl aniline and the $Q_1(1)$ on-resonance hydrogen peroxide photolysis - OH LIF signal build-up. The two curves have nearly identical shapes, as can be discerned within the resolution of the pump-probe approximately 7.2ps response function. A more desirable method

for cross-correlation measurement would be difference frequency generation in a nonlinear medium. It was, however, not possible to detect this wavelength at the time of these experimental studies.

An alternative method was used to measure the system response function. The 1+1 ionization signal of p,N-butyl aniline was compared to the square of the 616:532nm cross-correlation obtained by sum frequency generation. Provided that the fundamental (wavelength) pulse is not frequency chirped and that the conversion efficiency of producing 308 and 266nm light is not in a saturation regime, the square of the cross-correlation of the fundamental beams should have the same temporal behavior as the cross-correlation of the two second harmonic pulses. This supposition is verified by the essentially identical temporal behavior observed in Figure 3a for the 1+1 ionization and the integrated square of the visible pulse cross-correlation. The sum frequency generation visible pulse cross-correlation may, therefore, be converted to the system response function. However, the fact that the visible and UV beams encounter different values for the refractive index in the dispersive optics in the beam path (i.e., lenses, beam recombiner, filters) the visible-visible t=0 differs from the t=0 for the HOOH studies. The response function of Figure 3a is well simulated by a symmetric Gaussian pulse of 5.15ps FWHM duration. This is in good agreement with the transient response of Figure 2d.

Further analysis of the data of Figure 2 requires obtaining better insight into the probable cause of the transient effect. It may be seen from examination of Figures 2a-d that the transient signal has an amplitude which appears to be only weakly dependant on the amount of detuning from resonance. This would not be expected if the transient feature obtained from a non-linear matter-radiation interaction. In such a situation the detuning from resonance would dictate that the amplitude of the feature scales inversely with the magnitude of the detuning. In other words, a virtual state decays with a time constant directly related to the detuning. If the signal were due to enhanced transient scattering of the probe light, then this Raman-like effect would be observed as a transient spike in the output of the photon counting pmt. Moreover, such a spike would come on the leading edge of

the monitored OH-LIF signal. Since the boxcar gate is delayed 200ns following the pump and probe pulses such a transient spike would, in any event, not be recorded.

Furthermore, a probe power dependence study could also elucidate the intrinsic nature of the effect. Figure 3b gives a log-log plot of the pump-probe signal at t=0 delay, t=25ps delay and $t = -15$ps delay. These three time delay positions monitor the transient signal, the on resonance signal and the probe-alone (1+1 pump and OH-LIF) signal. The appropriate background signal levels and, in the case of the first two power dependences, the probe-alone backgrounds are removed. The scale on the abscissa is the log of the measured probe beam intensity that is transmitted. The method of probe beam attenuation is rotation of the polarization of the probe beam with a half-wave plate and to analyze the rotated polarization with a Glan-Taylor polarizer to allow only a fixed polarization of light to be transmitted. The attenuation of this arrangement is close to the $\cos 2\theta$ value anticipated. A linear power dependence with unit slope implies a one photon process whereas a slope of two indicates a two photon process. Figure 3b shows that the t=+25ps pump-probe delay has a slope of 0.93, which is close to the value of unity, which is expected for a probe process where one photon causes the product LIF. The near unity value also indicates that the $Q_1(1)$ transition is not being saturated in the probing process. The $t = -15$ps delay results have a slope of 1.88, which is close to the value of two expected for a one 308nm photon dissociation and one 308nm photon to cause LIF. The near ideal value also indicates that the probing process is not exhibiting saturation of the optical transition. Finally, the t=0ps delay data is fit with a slope of 1.11. The deviations of the t=0 and t=+25ps delay probe power dependences may in part be due to slight changes in the pump and probe beam overlap. The nonideality in the spatial overlap may be caused by slight beam displacements that occur as the half-waveplate is rotated. The power dependence data have been taken for the detuning conditions which give rise to Figure 2c.

Taking the spectral tuning idea of Figure 2 somewhat further, it could be seen if the detuning behaviors persist for both blue and red-shifted probe frequencies. Figure 4 shows the result of this exercise. The on $Q_1(1)$ resonance probing, $\Delta\nu = 0.0$,

shows only a monotonic rise to the asymptotic OH-LIF signal level. The vertical bars are drawn to guide the eye in following a given curve and comparing the differing amplitudes. Small detunings of the 3.8-4.2cm^{-1} FWHM Gaussian probe pulses already show evidence for the presence of a transient feature. Since the transient feature appears to both sides of the resonance, it is possible that the abrupt appearance of the transient feature results from the idea that a given OH radical may be spectrally perturbed both to the blue and the red. It also appears that the transient feature maintains a fairly constant amplitude through the range of detunings. The scan amplitudes are normalized to each other by considering both the pump and probe intensities and the number of scans and removing the negative time (probe alone) signal. Finally, it appears in all cases that the transient feature temporally appears before the on-resonance scan. The maximal transient amplitude appears at approximately the inflection point of the on-resonance rise. This observation is consistent with the dynamical behavior expected from the sequential kinetic scheme of Eqn. (4.2).

A simple estimate for the time for which the spectrally perturbed OH fragment exists may be useful to visualize the dynamics. The amplitude of the spectrally perturbed fragment is about 1/10 of the nascent OH product amplitude. It may be argued that the spectrally perturbed OH fragment has the same magnitude transition moment as the nearby nascent OH resonant transition. The last point is valid provided that the nature of the perturbation arises from effects other than exchange repulsion or electron correlations.[46] In other words, OH* is more like OH than HOOH (^1A_u). It may be further postulated that the spectrally defined perturbed fragments live with a given lifetime in the same sense that a species in a predissociative state has a finite lifetime. The simple estimate for the lifetime of the blue-shift, i.e. -5cm^{-1}, perturbed fragments follows from

$$\mathrm{R} = \exp\left(-k \cdot \Delta t_p\right) \tag{4.3}$$

where the ratio of the transient spike to the on-resonance signal has, in this case, a value of 0.1. The state decay rate is given by k and Δt_p is the 5ps pulse duration. The state lifetime is, therefore, $1/k$=0.44ps.

The transition may be made to study the spectral evolution at discrete time delay positions. In particular, the transient behavior at t=0 may be contrasted with the asymptotic signal at t=+25ps delay. The temporal evolution is complete at t=+25ps; moreover, the measured spectrum should correspond to the nascent product spectrum monitored in the nanosecond product state distributions reported in Refs. 39 and 40. Figure 5a displays the spectral scan results for the t=0 delay with the t <0 probe alone background removed. Figure 5b shows the nascent $Q_1(2)$, $Q_1(1)$, and $R_2(3)$ spectral lines. The two scans were obtained under identical experimental conditions. Four separate scans have contributed each figure and the individual scans were obtained in an alternating fashion. Figure 5c shows the result of subtracting Figure 5b from Figure 5a. When comparing Figures 5a and 5b, it becomes apparent that more signal remains between the peaks of 5a. Visually, the region between the peaks is where the perturbed spectral effects are expected to be most noticeable. The difference spectrum, 5c, shows wing features that extend to the red (lower energy). The shape of the red-wing features infers that the spectrum has its origin with a specific resonance transition. It is not obvious whether blue-wing features are being produced.

Figure 5d shows the difference between Figure 5a and the quantity (0.5×Figure 5b). The idea of this figure is to eliminate only the nascent resonant absorption contribution to Figure 5a. The result should be the perturbed spectral shapes convolved with the 3.8cm^{-1} probe pulse spectral width.

One question remains to be addressed before the spectral data fitting can be implemented. It must be decided whether any blue-wing perturbed spectral features are observable in HOOH photodissociation or if the spectral and transient features observed in Figure 5 originate from red-wing absorption from the immediately adjacent blue resonant transition. This problem can be unambiguously solved only if no additional nascent resonant OH transitions complicate the spectrum of

the bluest absorption peak. These conditions are met by measuring the t=0 and t=+25ps spectra at energies greater than the R-branch bandhead region. Figure 6a gives the t=0 spectrum beginning at half of the maximal on-resonance signal of the $R_1(9)$-$R_1(11)$ group of transitions. The t=+25ps delay scan is presented in Figure 6b and begins from the same spectral position as 6a. Figure 6c gives the difference spectrum of Figure 6a minus the quantity (0.55×Figure 6b). A blue-wing absorption feature is clearly observed in this figure. However, normalization of the amplitude of the blue-wing feature to the on-resonance intensity and comparing to the normalized intensity in Figure 5d indicate that the blue-wing absorption is about 30% as intense as the value observed at the smaller rotational quantum numbers.

A nonlinear least squares fitting of the t=0 data for the $Q_1(6)$-$Q_1(1)$ and $R_2(3)$ and $R_2(4)$ transitions and band-head region is performed. The solid lines through the data points are obtained by fitting the experimental results with the form

$$S(\nu) = \sum_{\nu_i'} \int_{-\infty}^{\nu} d\nu''' \int_{-\infty}^{\nu'''} \Big[a_1 \; \delta(\nu''' - \nu_i') \cdot R(\nu'') + a_2 \; \delta(\nu''' - \nu_i') \cdot R(\nu''') \cdot R(\nu'') \Big] \, d\nu'' \qquad (4.4)$$

The delta function expression defines the spectral line position, $R(\nu'')$ is the measured probe pulse bandwidth, and $P(\nu'')$ is the spectrally perturbed lineshape and width. The first term represents the nascent spectral contribution to the t=0 spectrum and the second term represents the perturbed spectral portion of the signal. The relative amplitude of the on-resonance signal to the spectrally perturbed value is found to be about 5:1 at the resonance frequency.

The perturbed fragment spectrum of Figure 5b is fitted with the single-sided Gaussian functions. The results of this proceedure is shown in Figure 7. In the case of the these three perturbed spectral transitions (and others not shown) the single-sided fitting proceedure yields a reasonable approximation for the blue-shifted spectral features. It is visually noticeable that the blue-wing is broader in the case of the $Q_1(2)$ transition as compared to the $Q_1(1)$ transition.

The results of the spectral fitting procedure are presented in Table 1. The functional forms used for $P(\nu''')$ were single-sided Gaussian lineshapes. The positions of the fitted lineshapes were obtained from the known frequencies for the relevant OH transitions. The origin for the perturbed spectral shape was centered at the value of the transition frequency of nascent OH. The general trend observed from the data in Table 1 is that the low N-value transitions have narrower spectrally perturbed linewidths. The Gaussian blue-shifted wing increases in width from from $7cm^{-1}$ to $15cm^{-1}$ for a change of N=1 to N=6. The perturbed spectrum broadens as the monitored OH product acquires more rotational angular momentum.

The choice of an asymmetric Gaussian fitting form follows from visual inspection of the data plotted in Figure 5d. The choice for the relative amplitudes for the t=0 and t=25ps data used in obtaining Figure 5d stems from setting the points between $R_2(3)$ and $Q_1(1)$ and also $Q_1(1)$ and $Q_1(2)$ close to zero. This was decided such that the relative amplitudes result in a consistant presentation of the perturbed spectral data. Removal of too much of the long-delay signal results is significant amounts of "negative" amplitude and obvious distortions of the resulting spectrum. Conversely, removal of too little of the t=+25ps component diminishes the asymmetric character. The value of 0.5 for the amplitude of the t=+25ps data contribution does follow if it is considered that the t=0 signal is monitored at the inflection point of the rise of the on-resonance signal. The data for Table 1 are all obtained from difference spectra with the long-delay data amplitude being 0.5 times the asymptotic value.

The form and shape of the difference spectra are a sensitive function of the channel shift of each of the constituent spectra. Spectral drift was measured before and after each set with a 0.75m monochrometer. If any significant (measureable) drift occured (within a precision of about $0.5cm^{-1}$) the data did not contribute to the results presented in Table 1. Furthermore, the significance of any minor drift was minimized by acquiring the results in an ABBAA... fashion.

Table 1 also shows that the spectral response function increases slightly with increasing wavelength. This results from the operation of the dye amplifier in diminishing gain conditions. The amplifier must be run somewhat more into gain saturation conditions to achieve adequate amplification. The relatively small increase in the pulse spectral bandwidth is not enough to account for the significantly greater increase in the OH perturbed spectral widths for increased values of rotational angular momentum.

Figures 8-10 are comparisons of scans in which the pump and probe beam $\vec{E}$-field polarizations were oriented parallel and perpendicular to each other. Figure 8a compares the dynamical evolution in the case of the probe being tuned to the $R_2(3)$ OH electronic transition. The negative-time tails and the asymptotic signal magnitudes have been matched. It may be noticed that the two curves closely match each other over the entire displayed time window. Figure 8b shows the results of plotting

$$r(t)\frac{S_{\parallel}(t) - S_{\perp}(t)}{S_{\parallel}(t) + 2S_{\perp}(t)}$$

for $S_{\parallel}(t)$ and $S_{\perp}(t)$ obtained from Figure 8a. The values of r(t) prior ro a time delay of 4ps have been suppressed because of the extremely large (seemingly) uncorrelated fluctuations of r(t) prior to this point. For the r(t) data plotted it is seen that the result is at best a small positive deviation from a value of zero. In summary, the (normalized) anisotropy for on-resonance probing is nearly zero, and especially so for pump-probe time delays longer than the system response function.

Figure 9a shows the results for experimental polatization studies when the probe pulse is spectrally detuned to the blue of the $R_2(3)$ transition by 0.5Å. The negative-time tails and the asymptotic signal values are matched. Deviations in the signal amplitudes occur for the time delay range of 3-15ps. Figure 9b emphasizes these results. In particular, it is seen that the perpendicularly polarized signal is of greater magnitude is this temporal range and hence a negative anisotropy is obtained.

Finally, Figure 10a shows the results of the polarization dependent transients for a probe pulse spectrally detuned by 0.5Åto the red of the $Q_1(1)$ transition (the

blue-wing for the $Q_1(2)$ transition). The parallel polarization results are given by the solid line. The same signal normalization conditions as above are implemented. Figure 10b shows the time-dependent evolution of the anisotropy. In this case r(t) is positive in the range of 2-15ps, in contrast withe the results of Figure 9b. In Figures 9b and 10b the anisotropy decays to a value of zero approximately during the temporal convolution of the pump and probe pulses.

The essential point to be made is that the temporal behavior of the anisotropy exhibits sign changes for perturbed spectral features arising from R-branch versus Q-branch transitions. This effect will be examined further in the following section. Arguments will be made for the implication which these observed results have for the mechanism of the dissociation.

As a note, the data of Figures 8-10 were obtained by rotating the polarization of the probe beam and holding the polarization of the pump fixed and directed at the detector.

4.5 DISCUSSION

The results presented in the previous section show the utility of performing both temporally and spectrally resolved measurements of photodissociation reactions. Even though both the temporal and spectral resolution is necessarily compromised, the chosen characteristics are most appropriate for doing spectroscopy of incipient reaction fragments. This discussion section addresses the physical origin of the previously described experimental results.

The discussion will focus on considering three interrelated interpretations of the temporally and spectrally observable effects. An explanation will be provided for the transient (pulsed) feature, which manifests in measurement of the dynamics of OH formation. Any explanation will have to account for both the red and blue-wing absorption features. Finally, the observation that the magnitude of the perturbed fragment linewidth decreases with increasing rotational angular momentum must also be explained.

The most straightforward view of the dynamics of photodissociation results from the understanding that the state vector evolution is driven primarily by the sudden system perturbation. The drastic perturbation arises from the photoinduced electron promotion and the associated change of the electronic PES from being strongly attractive to being purely repulsive. Bersohn and Zewail[23a] have described the temporal evolution of the incipient reaction product absorption spectrum following (or convolved with) photoexcitation. Their model treats the dynamics in a classical fashion. The relevant generic repulsive surfaces may be described by[23a]

$$V_1(R) = V_{10} \exp(-R/L_1) \tag{5.1}$$

and

$$V_2(R) = V_{20} \exp(-R/L_2) + \hbar\omega_2^{\infty} \tag{5.2}$$

where $\hbar\omega_2^{\infty}$ is the transition energy to a specified final state for the asymptotically separated (free) fragments. The probe pulse of a given frequency, $\hbar\omega_{\text{probe}}$, will be tuned into resonance with an excited state of the $S_2 \leftarrow S_1$ transition, for example. The perturbed fragment absorption occurs at given internuclear (reaction coordinate) separations $R \cong R^*$ when $\hbar\omega_1^{\text{ex}} < \hbar\omega_{\text{probe}} < \hbar\omega_2^{\infty}$. This is the case for pulsed excitation with photon energy $\hbar\omega_1^{\text{ex}}$ from an initial bound ground state. In the case where the upper repulsive potential is flat, that is, $L_2 \rightarrow \infty$, the expression for the time dependence absorption spectrum becomes[23a]

$$A(t) = C\left\{ \gamma^2 + \left[E \cdot \left\{ \text{sech}^2\left(\frac{vt}{2L_1}\right) - \text{sech}^2\left(\frac{vt^*}{2L_1}\right) \right\} \right] \right\} \tag{5.3}$$

where a Lorentzian of half width γ describes the probe pulse energy distribution. This expression does not include the convolution with the pump-probe system response function, which is, however, presented in Ref. 23a.

In the present case, the value of E, which is the terminal kinetic energy, is much larger than γ and γ^2 (i.e., $E=\hbar\omega_1^{\text{ex}} - D_o = 2 \times 10^4 \text{cm}^{-1}$ vs. $\gamma^2 \cong 12.5 \text{cm}^{-1}$). If the assumption of $L_2 \rightarrow \infty$ is applied to the interpretation of the present experiment,

then the amount of potential energy remaining is only of the order less than $20cm^{-1}$. The authors of Ref. 23a have plotted Eqn. (5.3) for a series of values of the fractional portion of the remaining energy (compared to the initial potential energy). They observe curves similar to Figures 2b, 2c, and 2d when the remaining fraction of the initial potential energy is 0.01, 0.05, and $\geq$0.10, respectively. Clearly, there is discrepancy between the present measurements of the spectral and temporal dynamics and the calculation conditions necessary to qualitatively simulate the temporal behavior.

The notion that the present experimental observations do not originate simply from the exponential spreading of the V_1 and V_2 potential surfaces may be reinforced. It may be noted that the V_1 surface for HOOH, ignoring the torsional interactions, has been reported[42] as

$$V_1 = 705eV \cdot \exp(-R/0.266Å) \tag{5.4}$$

Values of t^* for Eqn. (5.3) as large as 0.1-1ps and OH asymptotic fragment velocities in excess of v=3.5Å/ps[40] result in a value of $\mathrm{sech}^2(vt^*/2L_1)$ to be small compared to unity. These conditions imply that the present picosecond probing process is sampling the near asymptotic region of the potential surface. This idea is consistent with the small spectral detuning of the experiments. However, the large value expected for $vt/2L$ (i.e., >5) implies that the observed dynamical evolution of the time-resolved signal does not obtain from the exponential separation of the two potential surfaces connected via probe excitation. See Figure 2 of Ref. 23a for further information about the timescales necessary to measure the repulsive dynamical evolution.

The method of Ref. 23a also cannot explain the presence of blue-shifted wing absorption observed in the present study. The model has been extended, however, to give an accounting of a physical basis for the blue absorption.[23b] Even this extended model does not account for the dependence of the width of the perturbed spectral line on the degree of rotational excitation.

Khundkar et al.[47] have formulated a more inclusive theory, which describes the temporal dynamics of photodissociation and extend the description to more explcitly treat spectral domain data. In certain cases, this model reduces to the model of Ref. (23a). The results of Ref. 45 demonstrates the effect the spectral and temporal widths of the pulses (especially the probe) have on the observable quantities of a pump-probe experiment. Figure 7B.4 of Ref. 47 shows the wing absorption expected from the convolution of Eqn. (5.3) with the system response function by integrating from $-\infty$ to ∞. As previously stated, the wing is only red-shifted in time. No blue-shifted wing is obtained. The main result of Ref. 47 is an expression for (a simulation of) the measured spectrum

$$\tilde{m}(-\xi) = \left[2\xi \cdot \sqrt{1 + (\sigma_s \xi / E)}\right]^{-1} + erfc(t_\infty/\sigma_t) \cdot \delta(0) \qquad (5.5)$$

where ξ is the energy of detuning from resonance in the interval (0,E), and σ_s is the spectral width of the probe pulse in units of energy. The temporal width of the response function, σ_t, is given in units of $v/2L_1$. Eqn. (5.5) must be convoluted with the probe bandwidth spectral response function for direct comparison with the experiment.

A crucial assumption for the derivation of Eqn. (5.5) is that the absorption at a given spectrally defined energy is proportional to the amount of time the system spends in that spectral/coordinate region. It is noted in Ref. (47) that expression (5.5) predicts a tail absorption feature that diminishes in amplitude as the reciprocal of the energy detuning near the resonance. The difference spectra, obtained by way of this formalism, do show red and blue shifted spectral wings. Even though the qualitative aspects of Figures 6c, 6d, and 7c may be explained by this formalism, quantitative differences remain. Firstly, the amplitude of observed perturbed spectral features in Figure 8 is 10-20% of the on resonance peak amplitude. By contrast, the simulated result via Eqn. (5.5) shows only a 1-2% spectrally perturbed amplitude. Secondly, the measured ratio of the red to blue wing amplitudes is about 3:1 whereas the amplitude ratio in the simulations is about half of that.

Finally, the experimentally observed red and blue wings appear to have about the same spectral width, whereas the simulations show that the red-wing is about an order of magnitude broader than the blue wing.

The discussion up to this point has concluded that the spectrally perturbed lineshapes and perturbed fragment induced transient (absorption) features originate from dynamics occuring in the near asymptotic region of the repulsive ^1A_u PES. It also appears that exponential separation of the two electronic surfaces connected by the probe beam cannot alone explain the effects described in the previous figures of this chapter. A more intuitively satisfying explanation of the dynamical features may be given by considering the effects that long-range, weak (*e.g.*, dispersive or electrostatic) interactions may have on the temporal and spectral data.

Buckingham[48] has described the long-range van der Waal interactions[49] of two dipolar fragments. The expression for the radial and angular potential interaction energy V(R,θ) for two such fragments is given by[48]

$$\begin{aligned} V(R,\theta) = {} & \mu_1\mu_2 R^{-3}\cdot(2\cos\theta_1\cos\theta_2 + \sin\theta_1\sin\theta_2\cos\phi) \\ & + \frac{3}{2}\mu_1\Theta_2 R^{-4}\left[\cos\theta_1(3\cos^2\theta_1 - 1) + 2\sin\theta_1\sin\theta_2\cos\theta_2\cos\phi\right] \\ & + \left[\frac{3}{4}\Theta_1\Theta_2 R^{-5}(1 - 5\cos^2\theta_1 - 5\cos^2\theta_2 + 17\cos^2\theta_1\cos^2\theta_2\right. \\ & \left. + 2\sin^2\theta_1\sin^2\theta_2\cos^2\phi + 16\sin\theta_1\cos\theta_1\sin\theta_2\cos\theta_2\cos\phi)\right] \\ & + \text{higher order terms.} \end{aligned} \tag{5.6}$$

Here, $\phi = \phi_1 + \phi_2$ is the rotation about the O-O internuclear axis. The value of θ_1 is specified as the angle each OH dipole makes with respect to the O-O axis, namely, the OOH bend angle.

The primary mechanism of rotational excitation in photofragmentation was postulated by Klee et al.[36,40]; the fragment rotational angular momentum arises from the torsional dependence of the ^1A_u surface. This conclusion will lead to significantly different values for the multipolar interaction potential than for the orthogonal projection of the angular momentum resulting from bending motion and

an orthogonal torque applied during the HOOH photodissociation. It is expected that the degree of $P(N_1, N_2)$ fragment correlation observed will allow for a given OH (N_1=1) fragment to effectively sample different orientational potentials than OH(N_1=6).

An *ab-initio* concern is that off-resonance wing absorption due to the probability of the targeted fragment sampling different configurations may be masked by the wing absorption. The latter arises from the simple exponential separation of the relevant potential surfaces. It is expected, however, that the long red-wing absorption resulting from this later process will have a smaller transition moment than absorption which originates in the nearly asymptotic region of the $^1A_u \rightarrow {}^2\Pi$ potential. This intuitive conclusion arises from the large difference between the magnitude of the transition moments for HOOH $^1A_u \leftarrow {}^1A_g$ excitation ($\sim 10^{-20}$cm^2).[50] The fragments in the near asymptotic region are expected to more closely resemble free OH than HOOH. At closer internuclear separations the incipient fragments more closely resemble HOOH than OH. In addition, the fragments at smaller internuclear separations exist in a spectroscopically selected region for a shorter period of time than in the asymptotic region, so the wing absorption strength will also be reduced on this basis.

The analysis of the long range interactions may be undertaken by assuming that the dissociation process yields two groups of products. The first group arises from the torsion excitation and it will be assumed that those hydroxyl radicals that obtain angular momentum from this mechanism do so with a maximal alignment of J_{OH} with $\vec{v}$. The second type of fragment interactions will be for the extreme case of $\vec{J}_{OH} \perp \vec{v}$.

Gericke et al.[40] have considered the three limiting orientations of $\vec{J}_{OH}$ relative to $\vec{\mu}_{HOOH}$ and $\vec{v}_{OH}$. In their coordinate system the O-O recoil axis is $\hat{x}$ and the orientation of $\vec{\mu}_{HOOH}$ is orthogonal to $\hat{x}$ along $\hat{z}$. The first limiting orientation is $\vec{J}_{OH} \perp \{\vec{\mu}_{HOOH}, \vec{v}_{OH}\}$, and is therefore along $\hat{y}$. Second, $\vec{J}_{OH} \parallel \vec{\mu}_{HOOH}$ thus along $\hat{z}$. Third, $\vec{J}_{OH} \parallel \vec{v}_{OH}$ and along $\hat{x}$. From experimental evaluation of the $\beta_0^0(22)$ (cf. $\vec{J}_{OH} \parallel \vec{v}$) and $\beta_0^2(02)$ (cf. the second correlation) and $\beta_0^2(20)$ (cf. the $\vec{\mu} \parallel \vec{v}$

correlation) they conclude[40] that the expectation value of the square of the angular momentum components are

$$\langle J_x{}^2 \rangle \sim 0.61\, J(J+1) \tag{5.7a}$$

$$\langle J_y{}^2 \rangle \sim 0 \tag{5.7b}$$

$$\langle J_z{}^2 \rangle \sim 0.39\, J(J+1) \tag{5.7c}$$

In a separate calculation they find that the energy for rotational motion parallel, $E_{\|}$, and perpendicualr, $E_{\perp}$, to $\hat{z}$ is

$$\langle E_{\|} \rangle = (450 \pm 25)\text{cm}^{-1} \tag{5.8a}$$

and

$$\langle E_{\perp} \rangle = (615 \pm 25)\text{cm}^{-1}. \tag{5.8b}$$

The wave function of a rigid rotor is characterized by the total angular momentum $\vec{J}$ and its projection M on the space-fixed axis (e.g. $\hat{z}$) of quantization, given in representation $| JM \rangle$. The explcit form is

$$| J\,M \rangle = Y_{JM}(\theta, \phi) = Y^J_M(\theta, \phi)$$

The probability for finding the rotor oriented along the solid angle element $d\Omega = \sin\theta\, d\theta\, d\phi$ for state $| J\,M \rangle$ is

$$P_{JM}(\theta) = \int_0^{2\pi} | Y^J_M(\theta, \phi) |^2 \, \sin\theta \cdot d\phi.$$

The two quantization conditions of interest, along $\hat{x}$ and $\hat{z}$ respectively are for Y^J_J and Y^J_0 and the probability weighting given by Eqns. (5.7). Therefore the present assumption of quantization about these two axes may be done with some justification.

Margenau[49] has described a method for the calculation of the resonance energies for rigid linear dipoles and quadrupoles. The two OH incipient fragments are in states characterized by the quantum number $j_1\, m_1$ and $j_2\, m_2$. The state function that represents the two species interacting in their unperturbed condition is the product of spherical harmonics (or Legendre polynomials)[49], namely,

$$\psi_k = \psi(j_1\, m_1,\, j_2\, m_2) = P(j_1\, m_1,\, \cos\theta_1) \cdot P(j_2\, m_2,\, \cos\theta_2) \cdot \exp i(m_1\phi_1 + m_2\phi_2) \tag{5.9}$$

The degeneracy of the state vector implies that the resonance values are obtained by solution of the determinant[47]

$$| \langle j_1\, m_1\, j_2\, m_2 \mid V \mid j_1\, m_1'\, j_2\, m_2' \rangle - \Delta E \cdot \delta_{m'm} | = 0 \tag{5.10}$$

However, all of the matrix elements of V_{ij} are zero so there is no first order effect. The nonzero second order effect is of the order of $| V_{ij} |^2$ and will not be considered here. The calculation of the quadrupole-quadrupole interaction involves solving the quantity $\langle j_1\, m_1 j_2\, m_2 \mid V_{\Theta\Theta} \mid j_1\, m_1 j_2\, m_2 \rangle$, and this will be done below.

The symmetry of the second and third terms (dipole-quadrupole) of Eqn. (5.6) may also eliminate those terms from consideration. Coordinate inversion of (θ_i, ϕ_i) gives $(\pi - \theta_i, \pi - \phi_i)$. The coordinate inversion changes the sign of the second and third terms of Eqn. (5.6) (as well as the first term as implicitly noted in the preceeding paragraph). The integration of V_{ij} over all space yields zero values for these two terms since the expressions are even functions. The fourth term for $V_{\Theta\Theta}$ is non-zero. The quadrupole term of Eqn. (5.6) may be rewritten in terms of spherical harmonics expressions.[51,52] In this formulation $\cos^2\theta_i = \frac{1}{3}\left[\sqrt{16\pi/5}\, Y^2_0(i)+1\right]$, and $\sin^2\theta_i = -\frac{1}{3}\left[\sqrt{16\pi/5}\, Y^2_0(i) - 2\right]$, where $Y^j_m(i) = Y^j_m(\theta_i, \phi_i)$ and i=1,2. Therefore

the quadrupole interaction term becomes

$$
\begin{aligned}
V_{\Theta\Theta} = 1 &- \frac{5}{3}\left\{\left[\sqrt{\frac{16\pi}{5}}\,Y_0^2(1) - 1\right] + \left[\sqrt{\frac{16\pi}{5}}\,Y_0^2(2) + 1\right]\right\} \\
&+ \frac{17}{9}\left[\sqrt{\frac{16\pi}{5}}\,Y_0^2(1) + 1\right]\left[\sqrt{\frac{16\pi}{5}}\,Y_0^2(2) + 1\right] \\
&+ \frac{1}{9}\left[2 - \sqrt{\frac{16\pi}{5}}Y_0^2(1)\right]\left[2 - \sqrt{16\pi/5}Y_0^2(2)\right] \\
&+ \frac{8\pi}{15}\Big\{\left[Y_2^2(1) + Y_{-2}^2(1)\right]\left[Y_2^2(2) + Y_{-2}^2\right] \\
&\qquad + \left[Y_2^2(1) - Y_{-2}^2(1)\right]\left[Y_2^2(2) - Y_{-2}^2(2)\right]\Big\} \\
&+ \frac{32\pi}{5}\Big\{\left[Y_{-1}^2(1) - Y_1^2(1)\right]\left[Y_{-1}^2(2) - Y_1^2(2)\right] \\
&\qquad + \left[Y_{-1}^2(1) + Y_1^2(1)\right]\left[Y_{-1}^2(2) + Y_1^2(2)\right]\Big\}
\end{aligned}
\tag{5.11}
$$

The above equation appears more formidible than the quadrupole term of Eqn. (5.6) but this form becomes easier to manipulate and evaluate. The spherical harmonic addition theorem[51] may be used to evaluate the spatial integrals of the form

$$
\begin{aligned}
&\int_0^{2\pi}\int_0^{\pi} Y_{j_1 m_1}(\theta_1,\phi_1)\, Y_{j_2 m_2}(\theta_2,\phi_2)\, Y_{j_3 m_3}(\theta_3,\phi_3)\, \sin\theta \mathrm{d}\theta\, \mathrm{d}\phi = \\
&\qquad \left[\frac{(2j_1+1)(2j_2+1)(2j_3+1)}{4\pi}\right]^{1/2} \cdot \begin{pmatrix} j_1 & j_2 & j_3 \\ 0 & 0 & 0 \end{pmatrix} \begin{pmatrix} j_1 & j_2 & j_3 \\ m_1 & m_2 & m_3 \end{pmatrix}
\end{aligned}
\tag{5.12}
$$

It is known that the normalized eigenfunction Y_{jm} has the property

$$
Y_{j\,-m}(\theta,\phi) = (-1)^m\, Y_{jm}{}^*(\theta,\phi) \tag{5.13}
$$

This property allows the evaluation of a form of Eqn. (5.12), which is useful for solution of the above potential interaction. In particular, for the quantization m=j

$$\int_0^{2\pi}\int_0^{\pi} Y_{j\,j}{}^{*}\, Y_{2\,m}\, Y_{j\,j}\, \sin\theta d\theta\, d\phi$$
$$= (-1)^{j} \int_0^{2\pi}\int_0^{\pi} Y_{j\,-j}\, Y_{2\,m}\, Y_{j\,j}\, \sin\theta d\theta\, d\phi$$
$$= (-1)^{j} \left[\frac{5\,(2j+1)^2}{4\pi}\right]^{1/2} \cdot \begin{pmatrix} j & 2 & j \\ 0 & 0 & 0 \end{pmatrix} \begin{pmatrix} j & 2 & j \\ -j & m & j \end{pmatrix}. \qquad (5.14)$$

The relevant formulation of the Wigner 3-j symbols gives[51]

$$\begin{pmatrix} j & 2 & j \\ 0 & 0 & 0 \end{pmatrix} = (-1)^{j+1} \cdot \frac{2j\,(j+1)}{\left[(2j+3)(2j+2)(2j+1)\,2j\,(2j-1)\right]^{1/2}} \qquad (5.15)$$

and

$$\begin{pmatrix} j & 2 & j \\ -j & m & j \end{pmatrix} = \delta_{m\,0} \cdot 2 \left\{ 3j^2 - \frac{j\,(j+1)}{\left[(2j+3)(2j+2)(2j+1)\,2j\,(2j-1)\right]^{1/2}} \right\} \qquad (5.16)$$

Combining these expressions gives a simplified form for Eqn. (5.14)

$$\int_0^{2\pi}\int_0^{\pi} Y_{j\,j}{}^{*}\, Y_{2\,m}\, Y_{j\,j}\, \sin\theta d\theta\, d\phi = \langle Y_{j\,m} \rangle$$
$$= \delta_{m\,0} \cdot (-1)\sqrt{\frac{5}{4\pi}} \cdot \frac{j}{2j+3}. \qquad (5.17)$$

This expression is evaluated twice to obtain the full spatially arranged potential interaction energy for the two hydroxyl radicals,

$$\langle V \rangle = 6\,\Theta_1\,\Theta_2\,R^{-5} \cdot \frac{j_1\,j_2}{(2j_1+3)(2j_2+3)} \qquad (5.18)$$

Evaluation requires substitution of the OH ground or excited quadrupole moments, the relevant rotational angular momentum quantum numbers.

Before proceeding with evaluation it should be made clear that the present method of obtaining the quantity

$$\langle j_1\, m_1\, j_2\, m_2 \mid V \mid j_1\, m_1\, j_2\, m_2 \rangle$$

has been adapted from the analogous problem of calculating the linewidths of pressure broadened spectral lines as developed by Anderson.[53] A review of the subject[54] has clarified the treatment of Ref. (53). The subject of collision induced broadening is closely related to the present study of perturbed fragment spectra following photodissociation. The subject of collision induced absorption has seen considerable activity in far infrared gas phase absorption[55] and in transiently induced polarizabilities in liquids.[56]

The dipole and quadrupole moments of $^2\Pi$ and $^2\Sigma$ OH have been evaluated by way of ab-initio CI methods.[57] The same quantities as well as microwave measurements of the rotational levels for the $^2\Pi$ [58a,b] and $^2\Sigma$ [58b] states have been measured[58b] and tabulated.[58b] The quadrupole moments at the OH equilibrium internuclear separation of $R_e = 1.84 a_o$ [57] are $\Theta = 1.82 \times 10^{-26}\, esu \cdot cm^2$ for the $^2\Pi$ state and $\Theta = 4.05 \times 10^{-26}\, esu \cdot cm^2$ for the $^2\Sigma$ level.

The transition energy for a given transition is obtained by evaluating Eqn. (5.18) for the two potential surfaces and for the appropriate values of j. For the case of a transition where $\Delta j=0$ and $\Delta m=0$, the expression for the interaction energy difference is

$$\begin{aligned} \Delta E_{pert} &= 6\left[\Theta_1\Theta_2(^2\Sigma) - \Theta_1\Theta_1(^2\Pi)\right] \cdot R^{-5} \cdot \frac{j_1 j_2}{(2j_1+3)(2j_2+3)} \\ &= (1.2 \times 10^5 cm^{-1}\, Å^5) \cdot R^{-5} \cdot \frac{j_1 j_2}{(2j_1+3)(2j_2+3)}. \end{aligned} \tag{5.19}$$

Some values of this function are presented in Table 2. The most notable trend is the positive value of the (net) interaction energy. This, in turn, means that the associated absorption spectral feature is shifted to higher energy. The blue-shift is seen to decrease with decreasing values of $j_1 (\equiv N_1)$. This is a trend that would be observed

as a decrease in the width of the blue wing in the experimentally measured spectral (t=0) scans. The average correlated j_2 value, $\langle j_2 \rangle$, is obtained from Ref. (36). The torsional excitation would lead to the condition $j_1 = j_2$. The experimentally observed perturbed spectral features, especially the blue-wing absorption, is seen to be very similar to the trend expected from product rotational excitation, which results from a torsional dependance for the upper potential surface. The agreement also appears to be more than just qualitative.

As indicated in the above discussion, a significant fraction (approximately 0.4) of the total rotational energy is associated with the OH fragments wherein $\vec{J}_{OH} \perp \vec{v}$.[36,40] It is useful to determine the type of perturbed energy which would arise from these alternative dissociation mechanisms and OH-OH fragment interactions. The method of the calculation will be similar to that presented above. The quantity to be evaluated in the interaction energy is given by

$$\langle j_1\, 0\, j_2\, m_2 \mid V \mid j_1\, 0\, j_2\, m_2 \rangle. \tag{5.20}$$

The measurements of Gericke et al.[35] show that the expected correlation are $j_1 < j_2$ for small j_1 and $j_1 > j_2$ for $j_1 \geq 7$. It is also expected that the relative alignment of fragments 1 and 2 will be orthogonal. Furthermore, it will be assumed that fragment 1 will have m_1=0 while for fragment 2 $m_2 = j_2$.

The utilization of the spherical harmonic addition theorem and implicitly the Wigner-Eckart theorem and the proper definitions for the 3-j matrices will yield the single particle orientational distribution. This is given by

$$\langle j_1\, 0 \mid Y_{2\,0} \mid j_1\, 0 \rangle = \delta_{m\,0} \cdot \sqrt{\frac{5}{4\pi}}\, \frac{j_1\,(j_1+1)}{(2j_1+3)(2j_1-1)}. \tag{5.21}$$

This expression may be used in the expression for the quadrupole interaction to evaluate the total interaction energy. After some algebra, one obtains

$$\begin{aligned}
&\langle\, j_1\, 0\, j_2\, m_2 \mid V \mid j_1\, 0\, j_2\, m_2 \,\rangle \\
&\quad = \Theta_1\Theta_2\, R^{-5} \cdot \left\{ \frac{-64j_1^2j_2 - 64j_1j_2 + 30j_2 + 8j_1^2 + 8j_1 + 39}{\left[3(2j_1+3)(2j_1-1)(2j_2+3)\right]} \right\} \\
&\quad = \Theta_1\Theta_2\, R^{-5} \cdot E_{12}
\end{aligned} \tag{5.22}$$

The perturbation energy for $\Delta j=0$ and $\Delta m=0$ transitions is given by

$$\begin{aligned}
\Delta E_{pert} &= \left[\Theta_1\Theta_2(^2\Sigma) - \Theta_1\Theta_2(^2\Pi)\right] \cdot R^{-5} \cdot E_{12} \\
&= (2.0 \times 10^4\, cm^{-1}\text{Å}^5) \cdot R^{-5} \cdot E_{12}.
\end{aligned} \tag{5.23}$$

Table 3 contains the calculated value of this expression for j_1, correlated average $j_2 = \langle j_2 \rangle$ and 4Å, 5Å and 6Å values for the O-O separation. The terms in Table 3 are negative in value, meaning that they will contribute to a red-shifted wing absorption in contrast to the dynamics that produced the data of Table 2. Also, it is seen that the magnitude of the interaction energy decreases.

The polarization data and anisotropies observed in Figures 8-10 should also be explained. To recall, the anisotropy of the perturbed spectral feature associated with the $R_2(3)$ transition is negative during the pump-probe pulse overlap. By contrast, the anisotropy associated with the $Q_1(2)$ transition decayed fron a positive value during the pump-probe pverlap. Different Λ-doublet levels are probed by the R and Q-branch transitions. The Q-branch probes those transitions for which the lone electron p-orbital is in the O-H plane of rotation (Λ^-): $\vec{J}_{OH} \perp \hat{\mu}_Q$. The R-branch transitions then probe $\vec{J}_{OH} \parallel \hat{\mu}_Q$. The torsional mechanism for the dissociation is associated with the $\vec{J}_{OH} \parallel \vec{v}$. correlation. Since $\vec{v} \perp \hat{\mu}_{HOOH}$ for this mechanism then the Q-branch transitions would monitor the correlation $\hat{\mu}_{HOOH} \parallel \hat{\mu}_Q$. The R-branch transitions would monitor the $\hat{\mu}_{HOOH} \perp \hat{\mu}_R$ correlation.

Hence, if the torsional mechanism is the primary cause of the blue-shifted perturbed spectral lineshape then it may be naively assumed that the anisotropy would

reflect a positive correlation for the Q-branch transitions and an anti-correlation for the R-branch transitions. This is indeed observed in Figures 8-10. Because the asymptotic values for the parallel and perpendicular data are made equal the anisotropy decays to zero. In actuality, the magnitude of the difference for the data sets would yield the previously measured asymptotic alignment.

4.6 CONCLUSIONS

The simultaneous spectral and temporal studies of the photodissociation of hydrogen peroxide and monitoring the formation of the OH product have been shown to be uniquely sensitive to the long-range fragment interactions. The sacrifice in temporal resolution is necessary to be able to spectrally resolve the wing-absorption features associated with each hydroxyl rotational quantum state. The long system response function, compared to the initial portion of the dissociation reaction (inferred to be about 60fs), selectively gates the observable features to the tail region. The small spectral detunings also do not probe the initial portion of the reaction dynamics.

The temporal measurements, performed in a manner that allows for self-consistent checks of the temporal response function and an estimate of the reaction time-zero, show that the reaction occurs in less than 1ps. The spectral measurements made at time-zero show enhanced absorption between the nascent OH resonances. The t=+25ps delay studies show only the behavior expected for convolution of the spectral response function with the nascent OH resonance features. Removal of the on-resonance contribution to the t=0 lineshapes results in the clear appearance of sharply blue-shifted wing absorption features. The widths of the absorption features are analyzed by an asymmetric Gaussian lineshape fitting procedure. The nearly baseline separation of the spectral features and the previous removal of the unperturbed contribution to the t=0 signal also makes possible a simple Gaussian deconvolution for the probe pulse spectral response function. The widths of the

wings are seen to broaden with increasing rotational angular momentum of the spectrally targeted OH rotational angular momentum.

Analysis of the perturbed lineshape to the blue of the R-branch band-head region confirms that the spectrally broadened features exhibit blue-wing absorptions. Read-wing absorption features cannot be totally ruled out, but it appears that the magnitude of any red-wing feature is dominated by the overlapping blue-wing absorption from the neighboring transition.

studies in which the relative pump-probe polarizations are made parallel and perpendicular can give additional information about the dynamics of the reaction. Analysis of the polarization dependent temporal curves by way of plotting the temporal evolution of the anisotropy, and doing so for both the Q-branch and R-branch transitions shows the $\hat{\mu}_{\mathrm{HOOH}}$ and $\hat{\mu}_{\mathrm{OH}}$ angular correlation. Probing the dynamics while tuned into the perturbed spectral wing feature yields geometrical information on the direction of the motions (hence forces) which result in the perturbed fragment spectrum. Such transient alignment effects are not readily observable using traditional (nanosecond) alignment methods. Moreover, the type of transient alignment observed clearly and straightforwardly demonstrates the importance of the torsional excitation mechanism to the dynamics of the electronic dissoccciation of hydrogen peroxide.

Determination of the physical interactions that may contribute to the net interaction in the region of large internuclear separation could be insightful in elucidating both the type of long range interaction that is operative and the validity of the fragment $\langle \mathrm{J}|v\rangle$ correlation.[36,40]. The model for the dynamics involves evaluating the interaction energies for the electrostatic permanent-moment fragment interactions. The analysis shows that the quadrupole-quadrupole interaction is the lowest order interaction that gives a non-zero value after performing the angular averaging. Quantitative evaluation of the interaction energy requires evaluation of the angular distribution function. The $\vec{\mathrm{J}} \parallel \vec{v}$ and $\vec{\mathrm{J}} \perp \vec{v}$ correlations have net interaction energies which are of opposite sign. In effect, the parallel correlation is repulsive in nature while the orthogonal interaction is attractive. Moreover, since the magnitude of the

quadupole moment in the excited $^2\Sigma$ OH state is larger than that in the ground state at the equilibrium bond-length, the $\vec{J}_{OH}\|\vec{v}$ correlation results in a blue-wing absorption feature that increases with rotational quantum numbers.

The surprise is the absence of, or at least severely reduced, red-wing absorption features. This may arise from the parallel pump-probe polarizations of the present study and the probe polarization directed at the detector. The HOOH and OH transition moments are aligned with large projections in a parallel (or anti-parallel) fashion for $\vec{J}_{OH}\|\vec{v}$.

The direct extension of this work is to perform the same experiment in a jet-cooled environment where the thermal contributions to the product rotational excitation are minimized. Alignment studies could also be performed which may tend to more-favorably select the photofragments which arise from the perpendicular vector correlation.

The integration of the classical equations of motion along with expression (5.19) and taking account of the probe laser bandwidth, etc., would allow for obtaining the perturbed spectral lineshape from this type of multipolar interaction. An even more rigorous treatment would involve obtaining the perturbed fragment absorption spectrum while performing Gaussian wavepacket calculations of the temporal evolution of the dissociation process. Preliminary efforts along the lines of the last two concepts is already in progress.

REFERENCES

1. R. Bersohn, J. Phys. Chem. **88**, 5145 (1984); R. Bersohn, IEEE J. Quant. Elect., **QE-16**, 1208 (1980).

2. See for example D.H. Parker in *"Ultrasensitive Laser Spectroscopy"*, D.S. Kliger ed., Academic Press, New York, (1983), p.235.

3. See for example H.W. Crose, P.J. Dagdigian and R.N. Zare, Fara. Disc. Chem. Soc. **55**, 277 (1973); J.L. Kinsey, Annu. Rev. Phys. Chem. **28**, 349 (1977); M.A.A. Clyne and I.S. McDermid, Adv. Chem. Phys. **50**, 1 (1982).

4. U. Fano and J.H. Macek, Rev. Mod. Phys. **45**, 553 (1973).

5. C.H. Greene, R.N. Zare, Annu. Rev. Phys. Chem. **33**, 119 (1982); P.L. Houston, J. Phys. Chem. **91**, 5388 (1987).

6. R.N. Zare and D.R. Hershbach, Proc. IEEE **51**, 173 (1963); C. Jonah, J. Chem. Phys. **55**, 1915 (1971); S. Yang and R. Bersohn, J. Chem. Phys. **61**, 4400 (1974); J.H. Ling and K.R. Wilson, J. Chem. Phys. **65**, 881 (1976); R.L. Dubs, V. McKoy and S.N. Dixit, J. Chem. Phys. **88**, 968 (1988).

7. J.L. Kinsey, J. Chem. Phys. **66**, 2560 (1977); E.J. Murphy, J.H. Brophy and J.L. Kinsey, J. Chem. Phys. **74**, 331 (1981); R. Schmiedl, H. Dugan, W. Meier and K.H. Welge, Z. Phys. A. **304**, 137 (1982); Z. Xu, B. Koplitz and C. Wittig, J. Chem. Phys. **87**, 1062 (1987).

8. P. Andresen, G.S. Ondrey, B. Titze and E.W. Rothe, J. Chem. Phys. **80**, 2548 (1984).

9. J.P. Simons, J. Phys. Chem. **88**, 1287 (1984); K.F. Freed and Y.B. Band, in *"Excited States"*, vol. 3, E.C. Lim ed., (1978), p.109; M. Shapiro and R. Bersohn, Annu. Rev. Phys. Chem. **33**, 409 (1982); G.G. Balint-Kurti and M. Shapiro, Adv. Chem. Phys. **60**, 403 (1985).

10. J.C. Polanyi and R.J. Wolf, J. Chem. Phys. **75**, 5951 (1981); J.H. Foth, J.C. Polanyi and H.H. Telle, J. Phys. Chem. **86**, 5027 (1982); H.R. Mayne, R.A. Poirer and J.C. Polanyi, J. Chem. Phys. **80**, 4025 (1984).

11. D.L. Rousseau and P.F. Williams, J. Chem. Phys. **64**, 3519 (1976).

12. D. Imre, J.L. Kinsey, A. Sinha and J. Krenos, J. Phys. Chem. **88**, 3956 (1984); D. Imre, J.L. Kinsey, R. Field and K. Katayama, J. Phys. Chem. **86**, 2564 (1982); M.O. Hale, G.E. Galica, S.G. Glogover and J.L. Kinsey, J. Phys. Chem. **90**, 4997 (1986).

13. E.J. Heller, Acc. Chem. Res. **14**, 368 (1981); S.Y. Lee and E.J. Heller, J. Chem. Phys. **76**, 3035 (1982); *ibid.* **71**, 4777 (1979); E.J. Heller, R.L. Sundberg and D.J. Tannor, J. Phys. Chem. **86**, 1822 (1982). See also S.O. Williams and D.G. Imre, J. Phys. Chem. **92**, 3363 (1988).

14. R.L. Sundberg, D. Imre, M.O. Hale, J.L. Kinsey and R.D. Coalson, J. Phys. Chem. **90**, 5001 (1986); see also R.D. Coalson and J.L. Kinsey, J. Chem. Phys. **85**, 4322 (1986).

15. See also S. Kanfer and M. Shapiro, J. Phys. Chem.**88**, 3964 (1984).

16. J.K. Lu, D.W. Setser and D. Oba, Chem. Phys. Lett. **109**, 429 (1984).

17. T.C. Maguire, P.R. Brooks, R.F. Curl, J.H. Spence and S. Ulvick, J. Chem. Phys. **85**, 844 (1986).

18. P.R. Brooks, Chem. Rev. **88**, 407 (1988).

19. N.F. Scherer, J.L. Knee, D.D. Smith and A.H. Zewail, J. Phys. Chem. **89**, 5141 (1985).

20. M. Dantus, M.J. Rosker and A.H. Zewail, J. Chem. Phys. **87**, 2395 (1987); *ibid.* **89**, 6128 (1988); M.J. Rosker, M. Dantus and A.H. Zewail, *ibid.* **89**, 6113 (1988).

21. T. Rose, M.J. Rosker and A.H. Zewail, J. Chem. Phys. **88**, 6672 (1988); M.J. Rosker, T. Rose and A.H. Zewail, Chem. Phys. Lett. **146**, 175 (1988).

22. L.R. Khundkar and A.H. Zewail, Chem. Phys. Lett. **142**, 427 (1987).

23. (a) R. Bersohn and A.H. Zewail, Ber. Bunsenges. Phys. Chem. **92**, 373 (1988); (b) R.B. Bernstein and A.H. Zewail, J. Chem. Phys., in press 1988.

24. J. Misewich, J.H. Glownia, J.E. Rothenberg and P.P. Sorokin, Chem. Phys. Lett. **150**, 374 (1988).

25. E.P. Ippen and C.V. Shank, in *"Ultrashort Light Pulses"*, S.L. Shapiro ed., Springer-Verlag, Berlin, 1984 2nd edition, p.88.

26. E.M. Evleth, J. Am. Chem. Soc. **98**, 1637 (1976).

27. O.E. Martinez, IEEE J. Quant. Elect. **QE-23**, 59 (1987); see also O.E. Martinez, *ibid.* **QE-24**, 2530 (1988).

28. See A.E. Siegman, *"Lasers"*, University Science Books, Mill Valley, California (1986).

29. (a) D.W. Marquardt, J. Soc. Ind. Appl. Math. **11**, 431 (1963); (b) P.R. Bevington *"Data Reduction and Error Analysis for the Physical Sciences"*, McGraw-Hill, New York, (1969); (c) D.P. Miller, Ph.D. Thesis, Caltech, 1982.

30. (a) C.L. Lin, N.K. Rohatgi and W.B. Demore, Geoph. Res. Lett. **5**, 113 (1978); L.T. Molina and M.J. Molina, J. Phtochem. **15**, 97 (1981); (b) P.A. Giguerre, J. Chem. Phys. **30**, 322 (1959), D.L. Bauch J. Phys. Chem. Ref. Data **9**, 295 (1980).

31. M. Suto and L.C. Lee, Chem. Phys. Lett. **98**, 152 (1983); H. Golzenleuchter, K.H. Gericke, F.J. Comes and P.F. Linde, Chem. Phys. **89**, 93 (1984).

32. G. Ondrey, N. Van Veen and R. Bersohn, J. Chem. Phys. **78**, 3732 (1983).

33. A.U. Grunewald, K.H. Gericke and F.J. Comes, Chem. Phys. Lett. **132**, 121 (1986); A. Jacobs, M. Wahl, R. Weller and J. Wolfrum, Appl. Phys. B **B-42**, 173 (1987).

34. F.J. Comes, K.H. Gericke, A.U. Grunewald and S. Klee, Ber. Bunsenges. Phys. Chem. **92**, 273 (1988).

35. K.H. Gericke, A.U. Grunewald, S. Klee and F.J. Comes, J. Chem. Phys. **88**, 6255 (1988).

36. A.U. Grunewald, K.H. Gericke and F.J. Comes, J. Chem. Phys. **89**, 345 (1988).

37. U. Gerlach-Meyer, E. Linnebach, K. Kleinermanns and J. Wolfrum, Chem. Phys. Lett. **133**, 113 (1987).

38. M.P. Docker, A. Hodgson and J.P. Simons, Chem. Phys. Lett. **128**, 264 (1986); Fara. Disc. Chem. Soc. **82**, 25 (1986).

39. R. Schmiedl, H. Dugan, W. Meier and K.H. Welge, Z. Phys. **A304**, 137 (1982).

40. (a) S. Klee, K.H. Gericke and F.J. Comes, J. Chem. Phys. **85**, 40 (1986); K.H. Gericke, S. Klee, F.J. Comes and R.N. Dixon, J. Chem. Phys. **85**, 4463 (1986); S. Klee, K.H. Gericke and F.J. Comes, Ber. Bunsenges. Phys. Chem. **92**, 429 (1988); (b) R.N. Dixon, J. Chem. Phys. **85**, 1866 (1986).

41. C. Chevaldonnet, H. Cardy and A. Dargelos, Chem. Phys.**102**, 55 (1986); E.A. Reinsch, Chem. Phys. Lett. **141**, 369 (1987).

42. R. Bersohn and M Shapiro, J. Chem. Phys. **85**, 1396 (1986).

43. R Schinke and v. Staemmler, Chem. Phys. Lett. **145**, 486 (1988).

44. (a) G.H. Dicke and H.M. Crosswhite, J. Quant. Spect. Radiat. Trans. **2**, 97 (1962); see also J.A. Coxon, Can. J. Phys. **58**, 933 (1980); *ibid.*, **60** 41 (1982); **57**, 619 (1979); (b) M.H. Alexander and P.J. Dagdigian, J. Chem. Phys. **80**, 4325 (1984).

45. W.L. Dimpfl and J.L. Kinsey J. Quant. Spect. Radiat. Trans. **21**, 233 (1979); I.D. Chidsey and D.R. Crosley, *ibid*, **23**, 187 (1980).

46. G.C. Maitland, M. Rigby, E.B. Smith and W.A. Wakeham, *"Intermolecular Forces"* (Oxford, Oxford 1987).

47. L.R. Khundkar, Ph.D. Thesis, Caltech 1988, Chapter 7B, pp.148-170.

48. A.D. Buckingham, Adv. Chem. Phys. **12**, 107 (1967); Fara. Disc. Chem. Soc. **40**, 232 (1965).

49. H. Margenau, Rev. Mod. Phys. **11**, 1 (1939); A. Krishnaji and V. Prakash, *ibid*, **38**, 690 (1966).

50. G. Herzberg, *"The Spectra and Structures of Simple Free Radicals"*, Cornell University Press, Ithica, New York (1971).

51. A.R. Edmonds, *"Angular Momentum in Quantum Mechanics"*, 2nd ed., Princeton University Press, Princeton, New Jersey (1960); R.N. Zare, *"Angular Momentum"*, Wiley, New York (1988).

52. U. Fano and G. Racah, *"Irreducible Tensorial Sets"*, Academic Press, New York (1959).

53. P.W. Anderson, Ph.D. Thesis, Harvard University (1949); Phys. Rev. **76**, 647 (1949).

54. C.J. Tsao and B. Curnutte, J. Quant. Spect. Radiat. Trans. **2**, 41 (1962).

55. M. Moon and D.W. Oxtoby, J. Chem. Phys. **84**, 3830 (1986); **75**, 2674 (1981); M. Moraldi and R. Vallauri, Chem. Phys. Lett. **114**, 82 (1985); A.Z. Devdariani, U.N. Ostroskii and A. Niehaus, J. Phys. B. **18**, L161 (198); J.D. Poll and J.L. Hunt, Can. J. Phys. **59**, 1448 (1981) and references therein.

56. G.G. Gray and K.E. Gubbins, *" Theory of Molecular Fluids, Vol. 1: Fundamentals"*, Oxford Science Publications, Oxford 1984; C.H. Wang, *"Spectroscopy of Condensed Media"*, Academic Press, New York 1985.

57. S.I. Chu, M. Yoshimine and B. Liu, J. Chem. Phys. **61**, 5389 (1974). See also V.P. Krishnaji, Rev. Mod. Phys. **38**, 690 (1966).

58. (a) D. Yaron, K. Peterson and and W. Klemperer, J. Chem. Phys. **88**, 4702 (1988); (b) Landolt – Bornstein; *Numerical Data and Functional Relationships in Science and Technology*, K.H. Hellwege, vol. 14, subvol. b, pp. 2-383, Springer-Verlag, Berlin 1983.

TABLE 1.

Perturbed Hydroxyl Spectral Lineshapes from the Photodissociation of HOOH

Transition	Gaussian Fit (asymmetric) (Å)	Spectral Response (symmet. Gaus.) (Å)
$Q_1(1)$	0.75[a]	0.38
$Q_1(2)$	0.82	0.43
$Q_1(3)$	0.92	0.40
$Q_1(4)$	1.07	0.43
$Q_1(5)$	1.2	0.45
$Q_1(6)$	1.3	0.45
$P_1(2)$	0.7	0.39
$R_2(3)$	0.9	0.41
$R_2(4)$	1.0	0.40
$\langle R_2 \rangle$=10	1.5	0.40

[a] Corresponds to 7.9cm^{-1} HWHM.

TABLE 2.

Quadrupolar Interaction Energy for $\vec{j}_1 \parallel \vec{v}$

Transition	j_1	$\langle j_2 \rangle$	$\Delta E(cm^{-1})$		
			R_{O-O}=4Å	R_{O-O}=5Å	R_{O-O}=6Å
$Q_1(1)$	1	1	4.7	1.5	0.62
$Q_1(2)$	2	2	9.6	3.1	1.3
$Q_1(3)$	3	3	13.0	4.3	1.7
$Q_1(4)$	4	4	15.5	5.1	2.0
$Q_1(5)$	5	5	17.3	5.7	2.3
$Q_1(6)$	6	6	18.8	6.1	2.5

TABLE 3.

Quadrupolar Interaction Energy for $\vec{j}_1 \perp \vec{v}$

Transition	j_1	$\langle j_2 \rangle$	$\Delta E(cm^{-1})$		
			R_{O-O}=4Å	R_{O-O}=5Å	R_{O-O}=6Å
$Q_1(1)$	1	5	-47	-15.4	-6.2
$Q_1(2)$	2	5	-42	-13.8	-5.5
$Q_1(3)$	3	6			
$Q_1(4)$	4	6			
$Q_1(5)$	5	6			
$Q_1(6)$	6	7			

FIGURE CAPTIONS AND FIGURES

1. A schematic drawing of the pump-probe as applied to the study of direct (electronic) dissociation. The excitation pulse to projects the ground-state wavefunction to the excited state. This picture is valid only for excitation pulse durations (and associated spectral frequency bandwidths) shorter (larger) than the intrinsic dynamical evolution (width of the absorption spectrum). The nascent product probing occurs in the limit of large fragment separations.

2a. The three plotted curves are: i) the HOOH on $Q_1(1)$ data (large data points); ii) the integral of the square of the 532nm and 616nm cross-correlation measurement with the t=0 point determined from figure 2d (smooth dotted curve); and iii) convolution of a 0.46ps exponential convolved with the displayed response and including a 0.78ps time-shift (solid curve).

2b. Shows the transient which is obtained for $2.6cm^{-1}$ detuning to the red of the $Q_1(1)$ resonance. The solid line is the best fit curve with response shown in Figure 2c and convolution with both a rising and decaying exponential functions. See the text for more details.

2c. The smooth dotted line is the system response function which leads to the smooth dotted curve in Figure 2a. The data is obtained for a $4cm^{-1}$ red-shifted detuning.

2d. A $5.5cm^{-1}$ red-shifted detuning results in almost no long-time tail signal for the $3.4cm^{-1}$ probe polse bandwidth.

3a. Comparison of the 1+1 ionization signal from p-N butyl aniline and the integral of the square of the visible-visible cross-correlation. The time-shift of the curves is varied to see if they show the same temporal dependance. If may be seen that the two curves have nearly superimposable shapes on the present timescale where the ionization signal perhaps rises slightly more slowly.

3b. Log-Log plot of the probe pulse power dependence obtained by measuring the OH-LIF signal at t=0 and t=+25ps delay. The slopes are nearly unity. The power dependance of the probe-alone signal shows a slope closer to two.

4. Composite of several pump-probe time-dependent curves at the indicated detunings where a positive detuning indicates a blue-shift.

5a. Spectral tuning data for the pump-probe delay set at t=0. The displayed transitions are, from left to right, $R_2(3)$, $Q_1(1)$, and $Q_1(2)$, respectively.

5b. Nascent spectrum for the same range taken for t=+25ps delay. The laser bandwidth is measured to be $3.5cm^{-1}$.

5c. Difference spectrum resulting from subtracting the spectrum of Figure 5b from the spectrum of Figure 5a. The signal level remains positive between the resonance positions and dips to negative values at the resonance positions.

5d. Difference spectrum obtained by removing only half the amplitude of Figure 5b from 5a. The resulting peaks are noticeably asymmetric in shape with the larger asymmetric portion extending to the blue in all cases; the so called blue-wing absorption.

6a. Analogous to Figure 5a but for spectral tuning to the blue (high energy) side of the R-branch bandhead region.

6b. The t=+25 tuning curve.

6c. This is the difference curve which results when half the amplitude of Figure 6b is subtracted from Figure 6a to remove the "on-resonance" contribution to the signal. This leaves only the perturbed spectral lineshape.

7. Asymmetric Gaussian fitting to perturbed spectral scan of Figure 5d. The perturbed spectra are for the $R_{@}(3)$, $Q_1(1)$, and $Q_1(2)$ transitions in going to longer wavelength. These fitted curves yield the results of Table 1.

8a. Parallel (solid line) and perpendicular pump-probe scans while tuned on-resonance to the $R_2(3)$ probe transittion. The two scans are matched in amplitude at negative and also at large positive delays.

8b. Time-dependence of the anisotropy abtained from Figure 8a. The early time values were set equal to zero up to a point where the sign flluctuations cease to occur; that is, the magnitude of the actual signal increases above the noise.

9a. Parallel (solid line) and perpendicularly polarized HOOH dissociation transients for the probe tuned 0.5Åto the blue for the $R_2(3)$ transition. The amplitudes are adjusted as in 8a.

9b. Time dependence of the anisotropy for the data of Figure 9a. The anisotropy shows a negative amplitude during the period of the pump-probe temporal overlap.

10a. As Figure 9a but for the probe tuned 0.5Åto the red of the $Q_1(1)$ transition.

10b. Time-dependence of the anisotropy for the data of 10a. The anisotropy shows a positive amplitude during the period of pump-probe temporal overlap

Figure 1

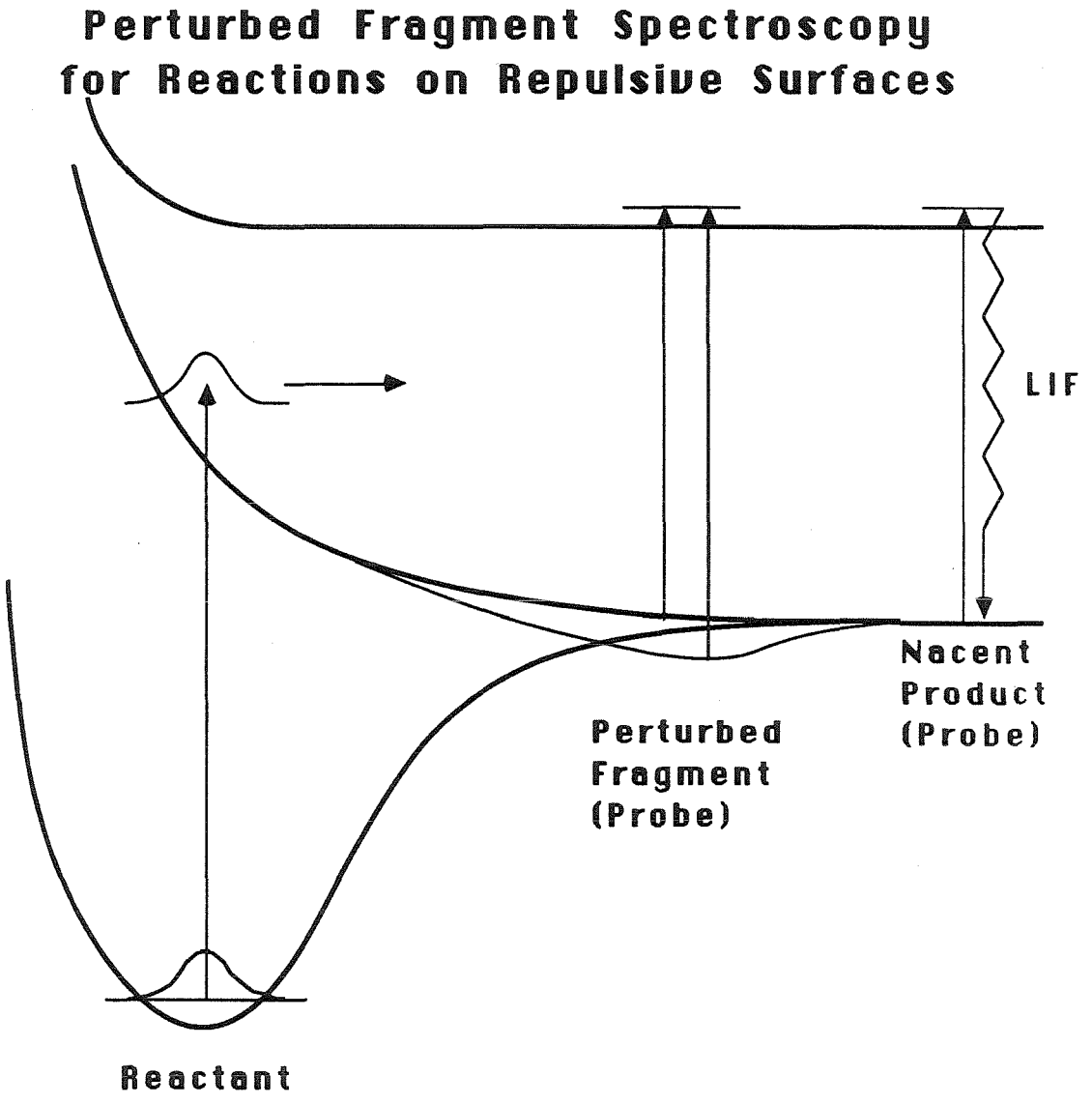
Perturbed Fragment Spectroscopy
for Reactions on Repulsive Surfaces
LIF
Nacent
Product
(Probe)
Perturbed
Fragment
(Probe)
Reactant

Figures 2a, 2b

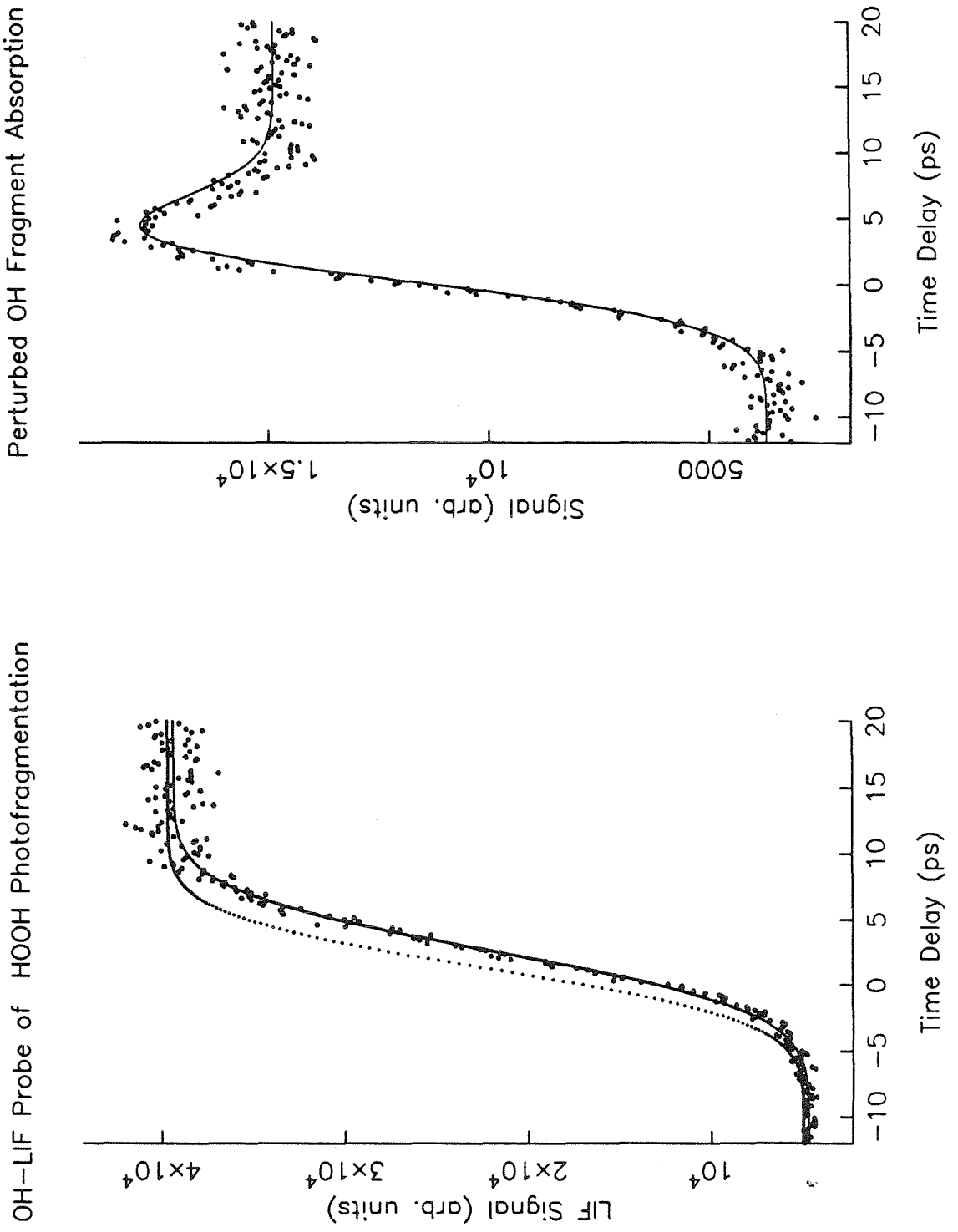

Figures 2c, 2d

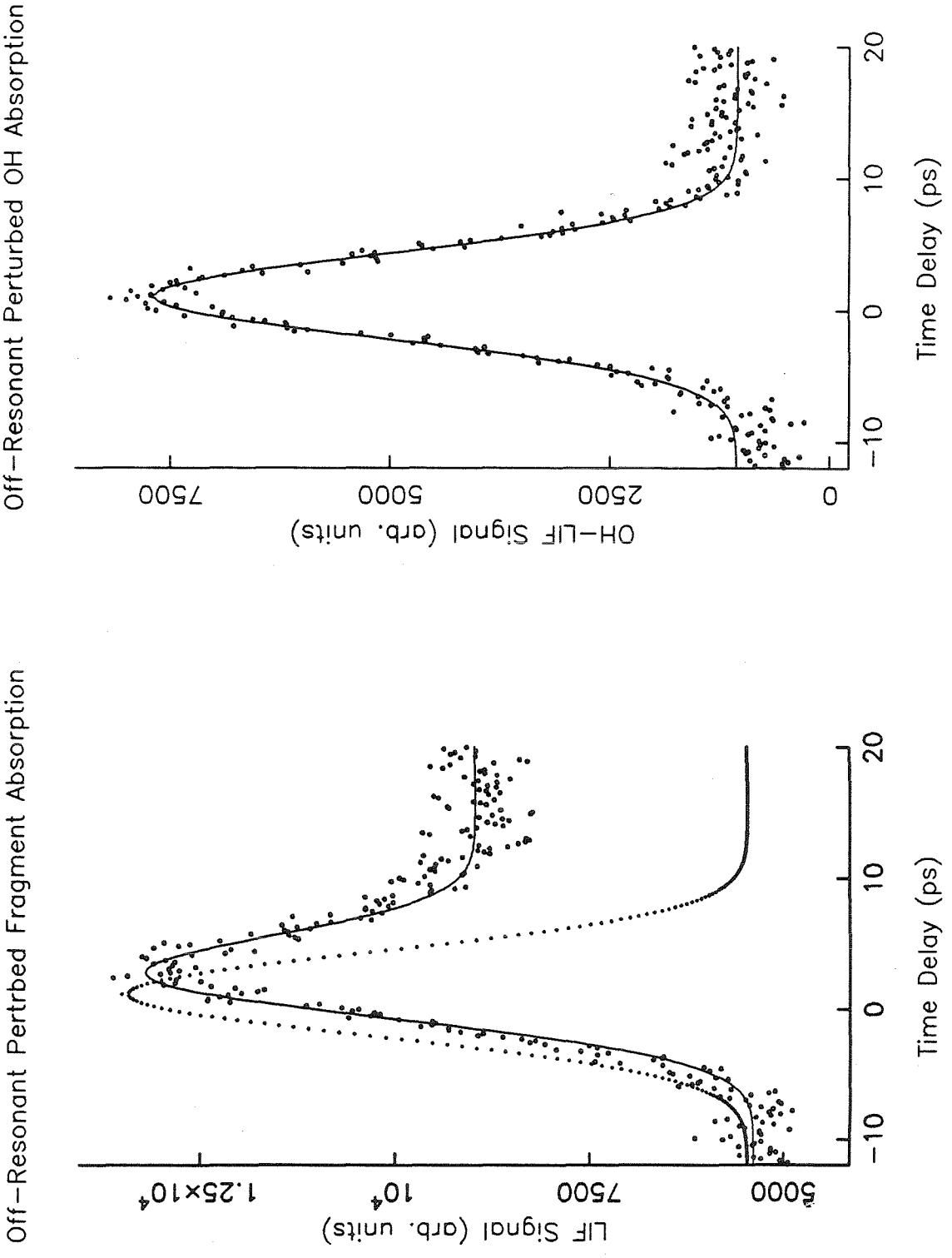

Figures 3a, 3b

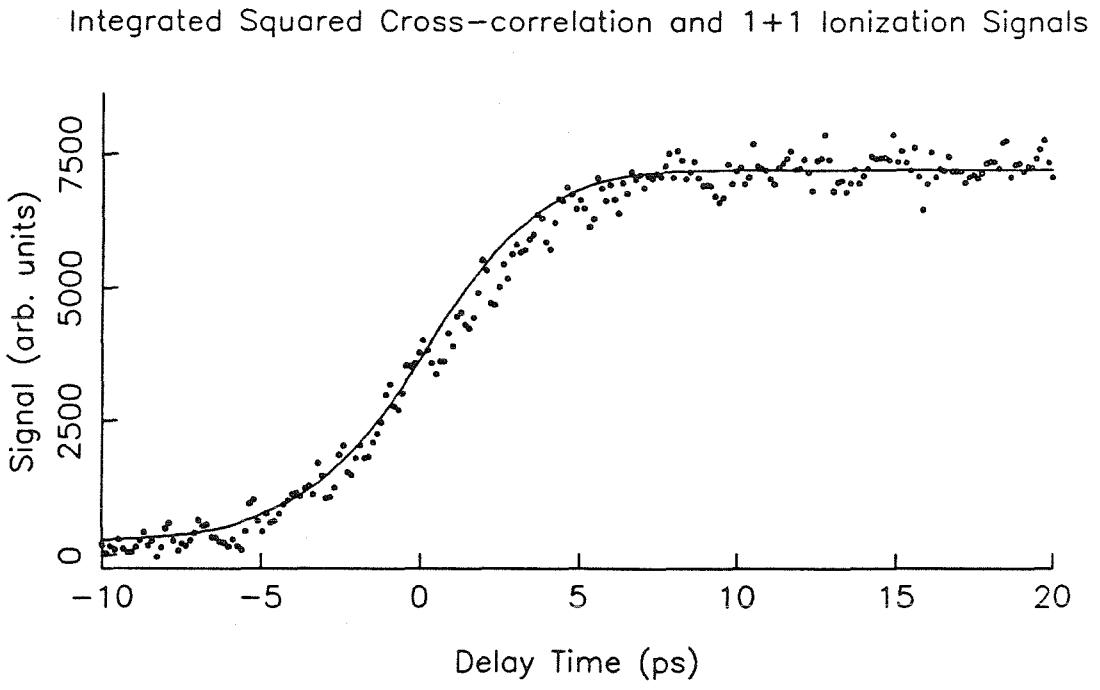

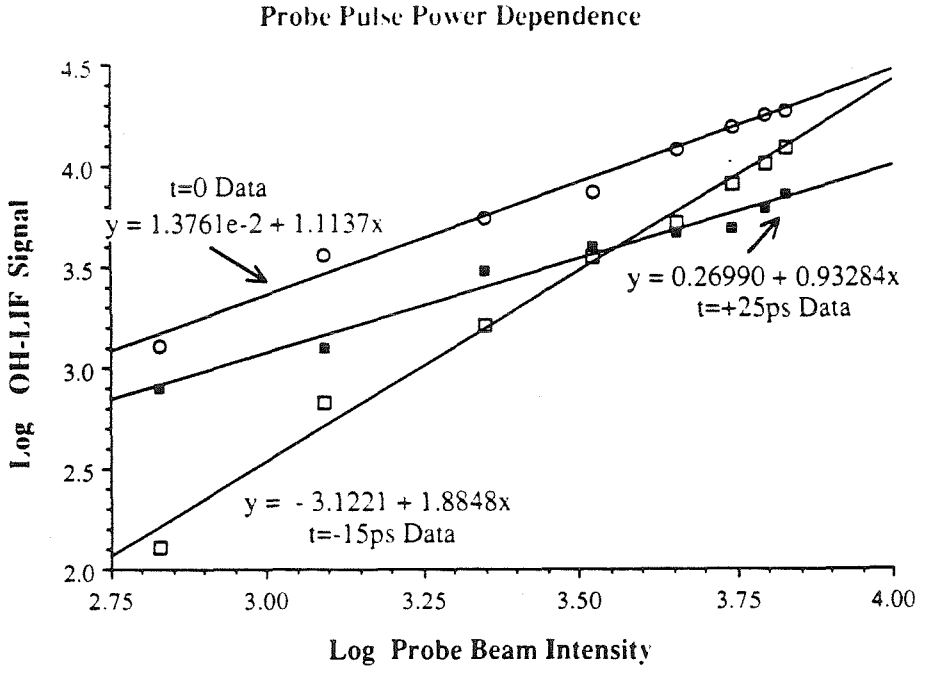

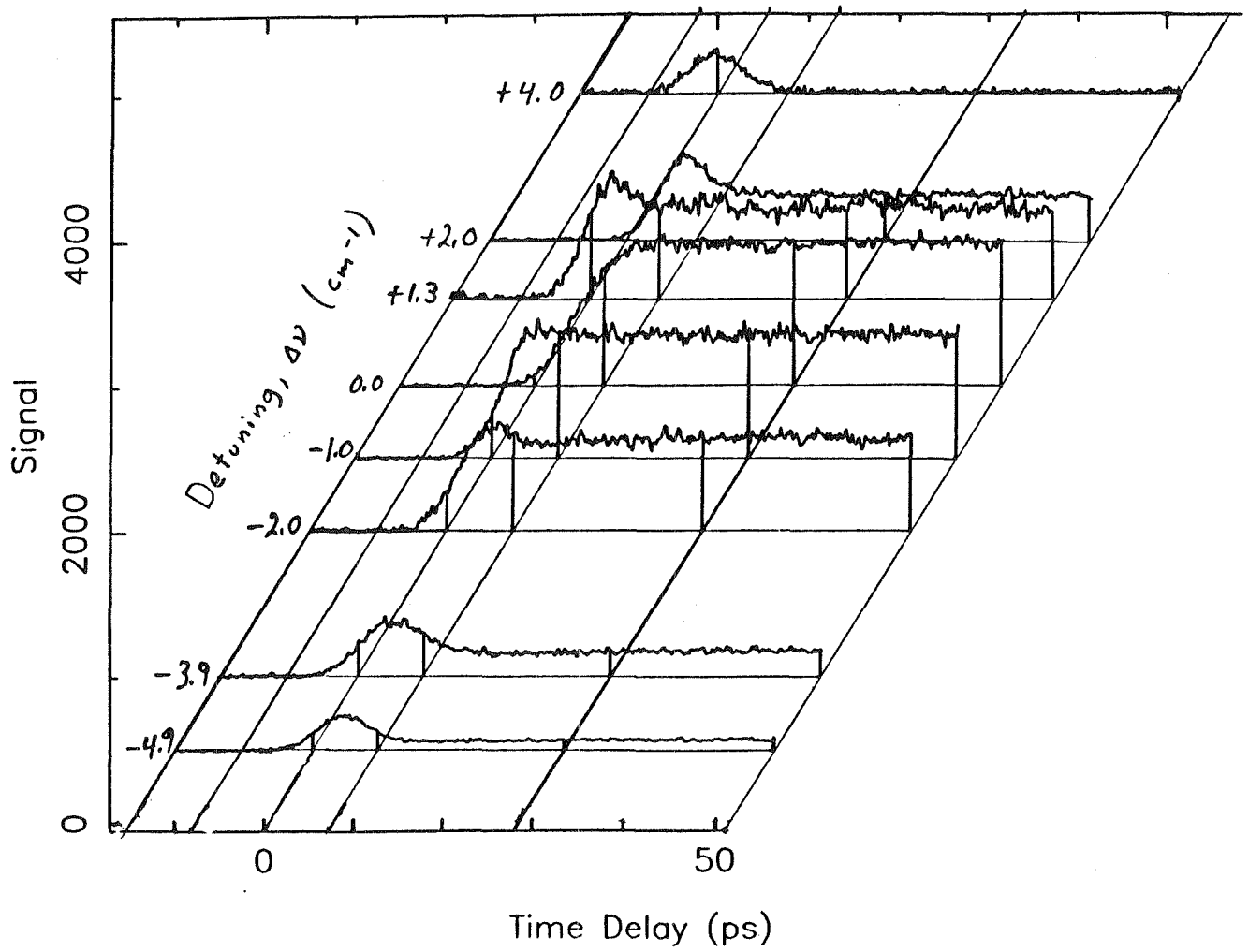
Time Delay Curves at Various Relative Detunings, HOOH Q1(1)
Signal
0
2000
4000
Detuning, Δω (cm⁻¹)
+4.0
+2.0
+1.3
0.0
-1.0
-2.0
-3.9
-4.9
0
50
Time Delay (ps)

Figure 4

Figures 5a, 5b

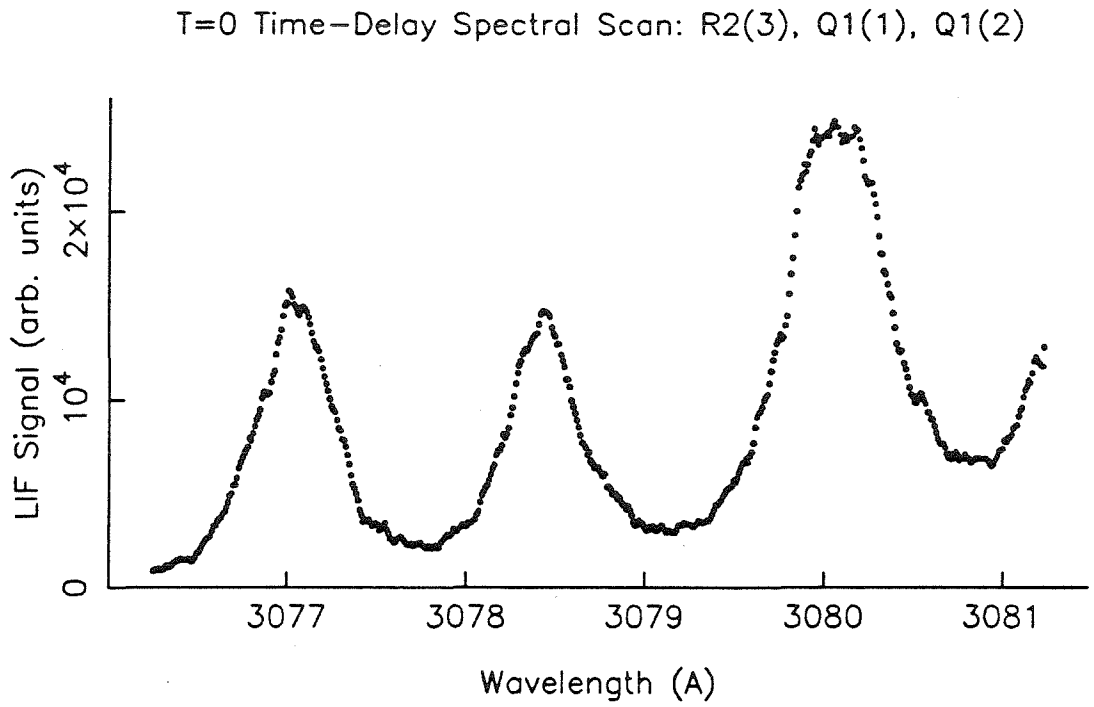

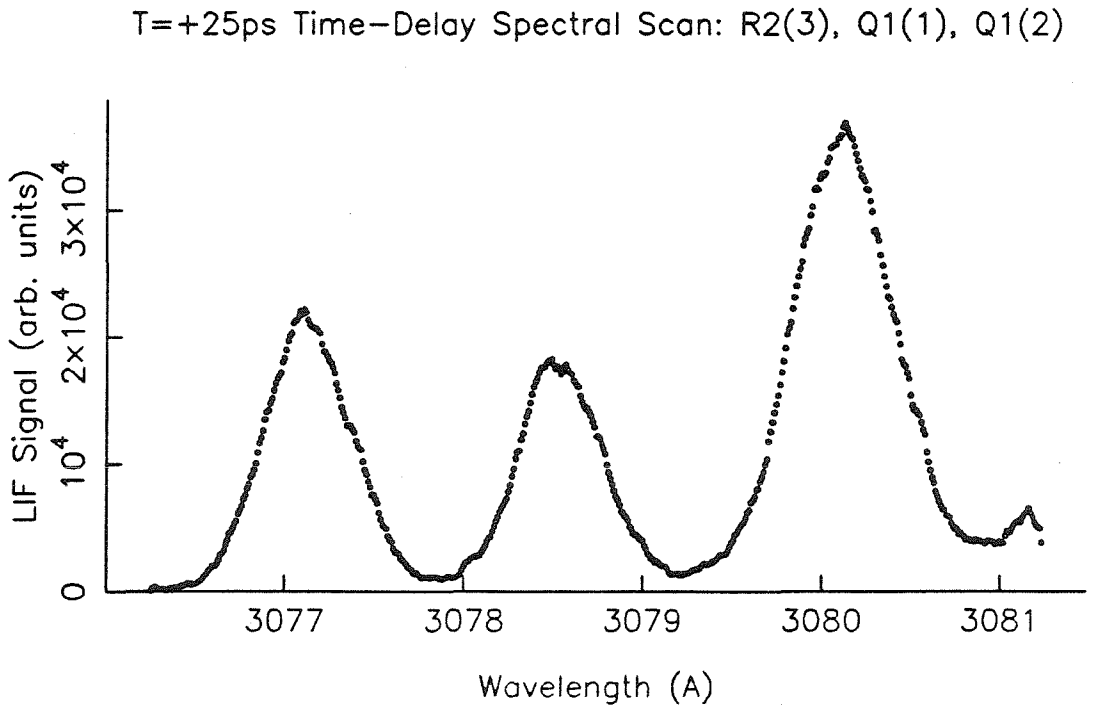

Figures 5c, 5d

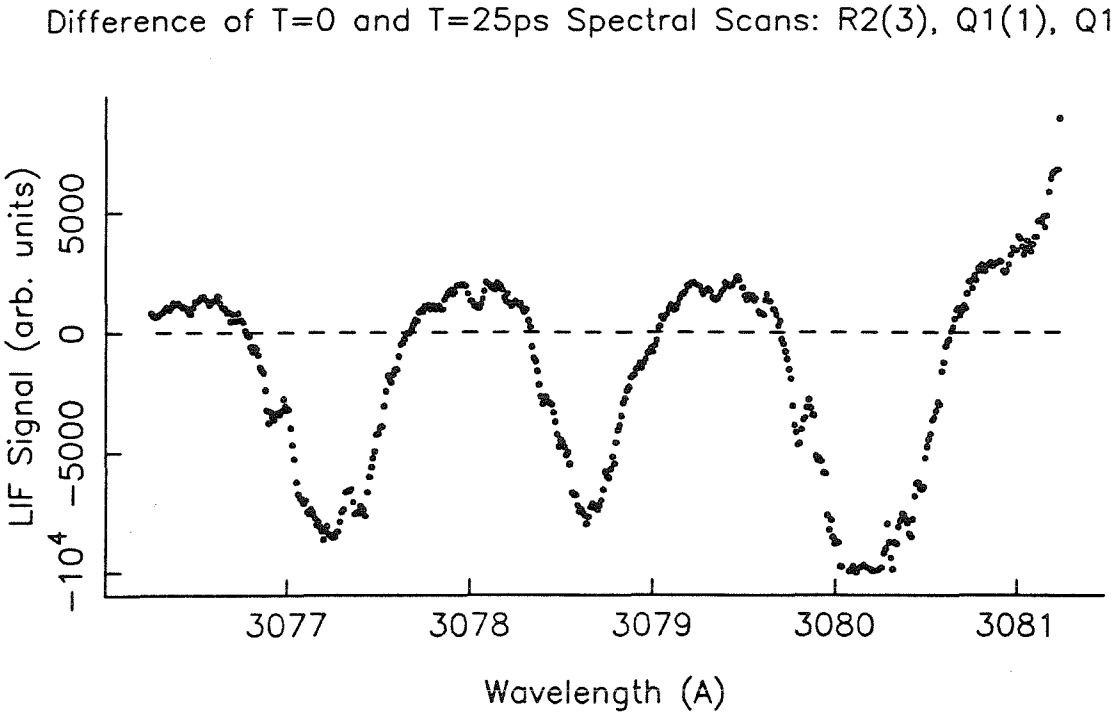

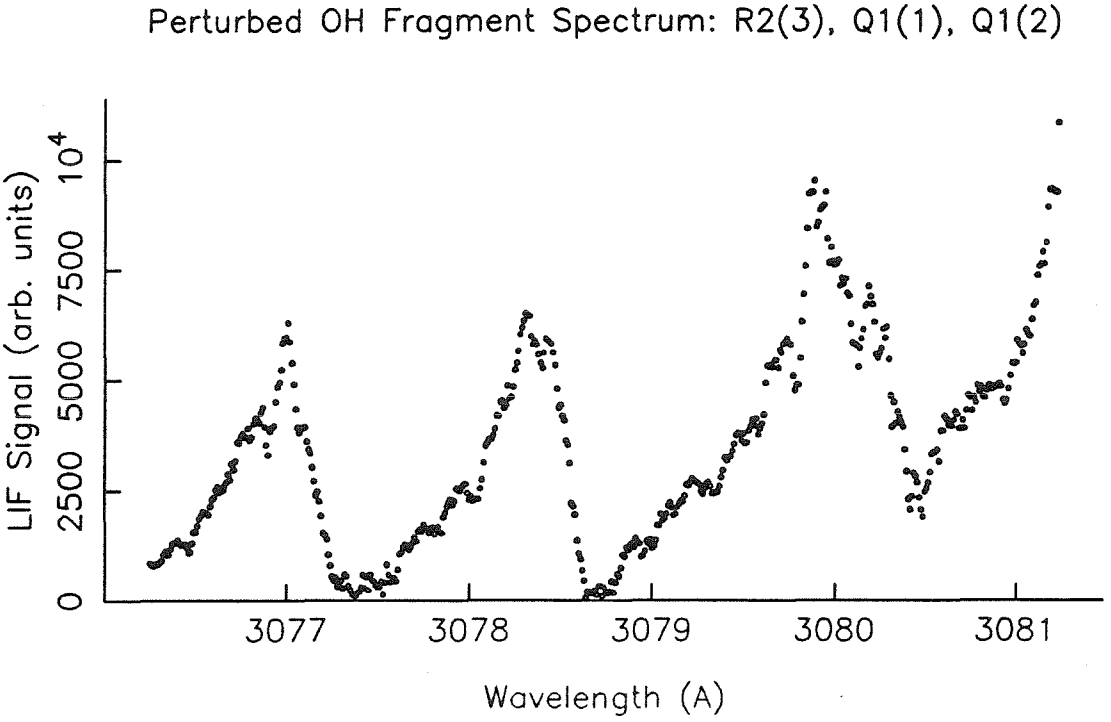

Figures 6a, 6b

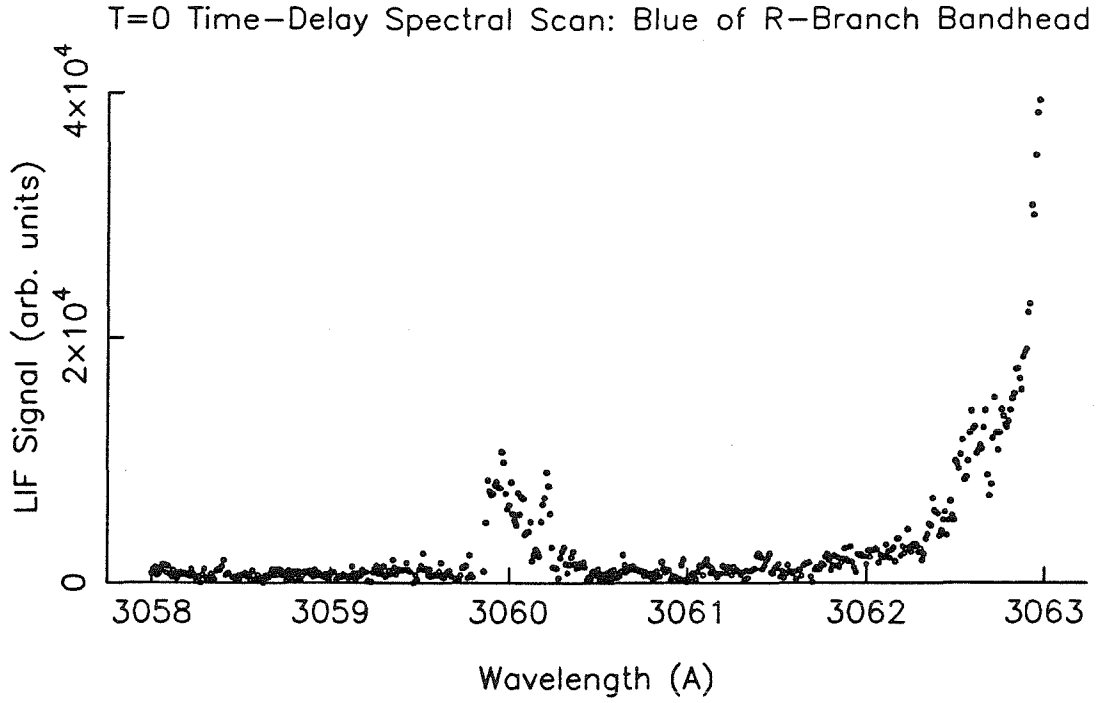

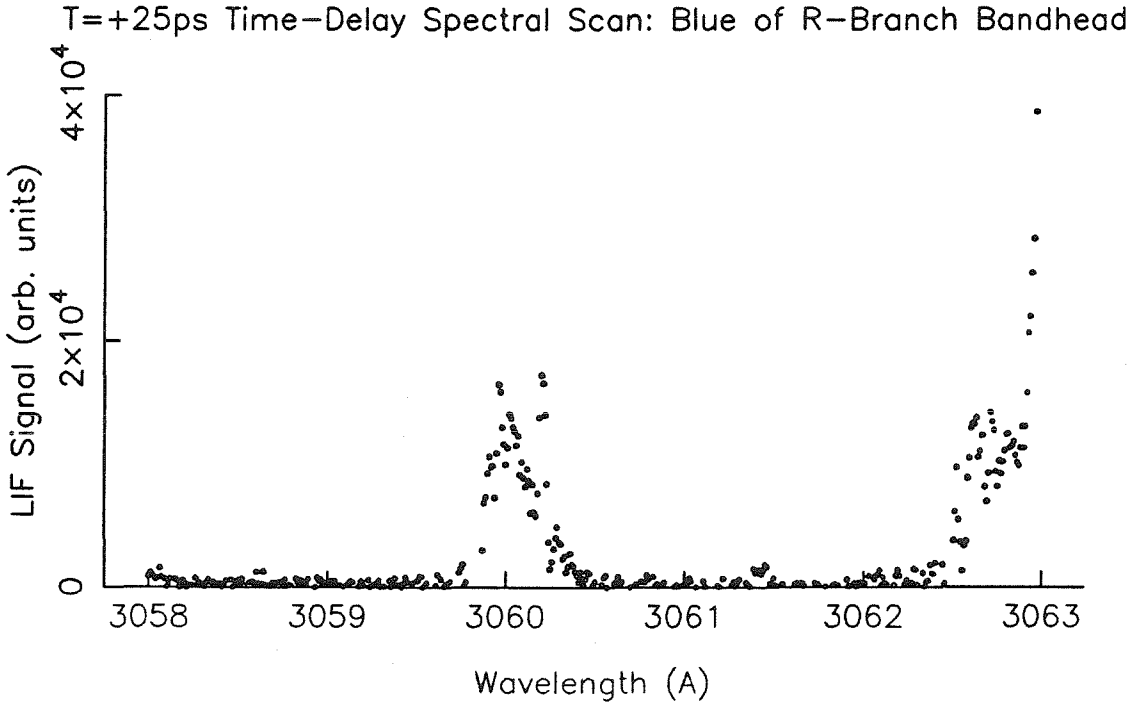

Figure 6c.

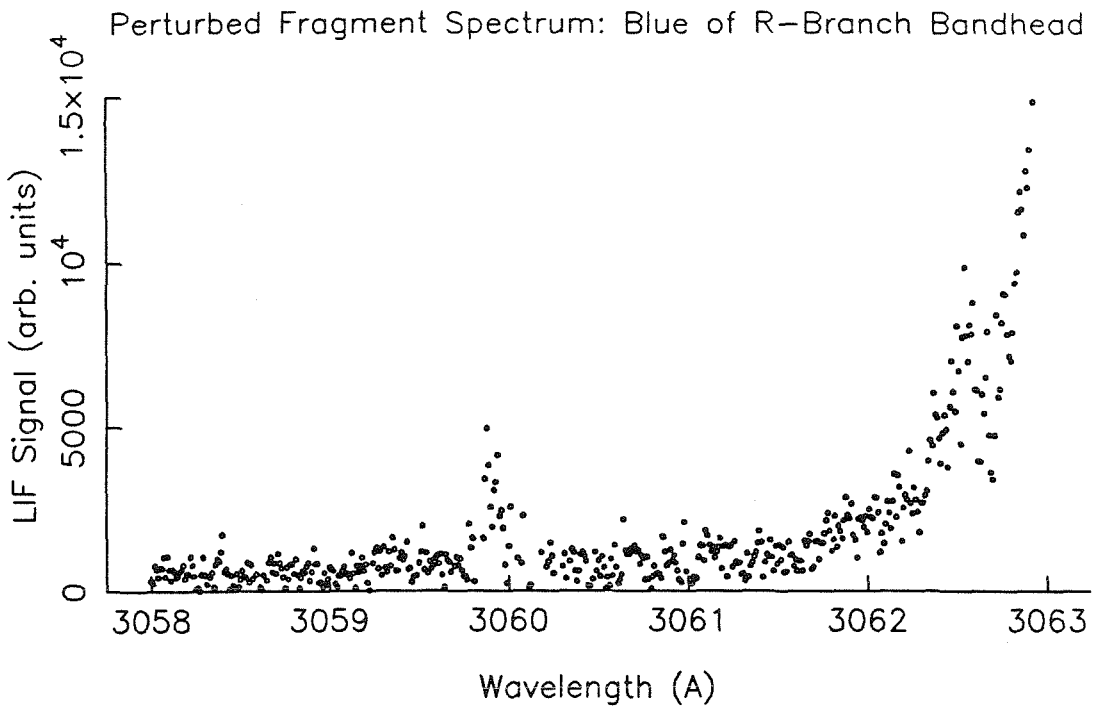
Perturbed Fragment Spectrum: Blue of R−Branch Bandhead
LIF Signal (arb. units)
0
5000
10^4
1.5×10^4
3058
3059
3060
3061
3062
3063
Wavelength (A)

Figure 7.

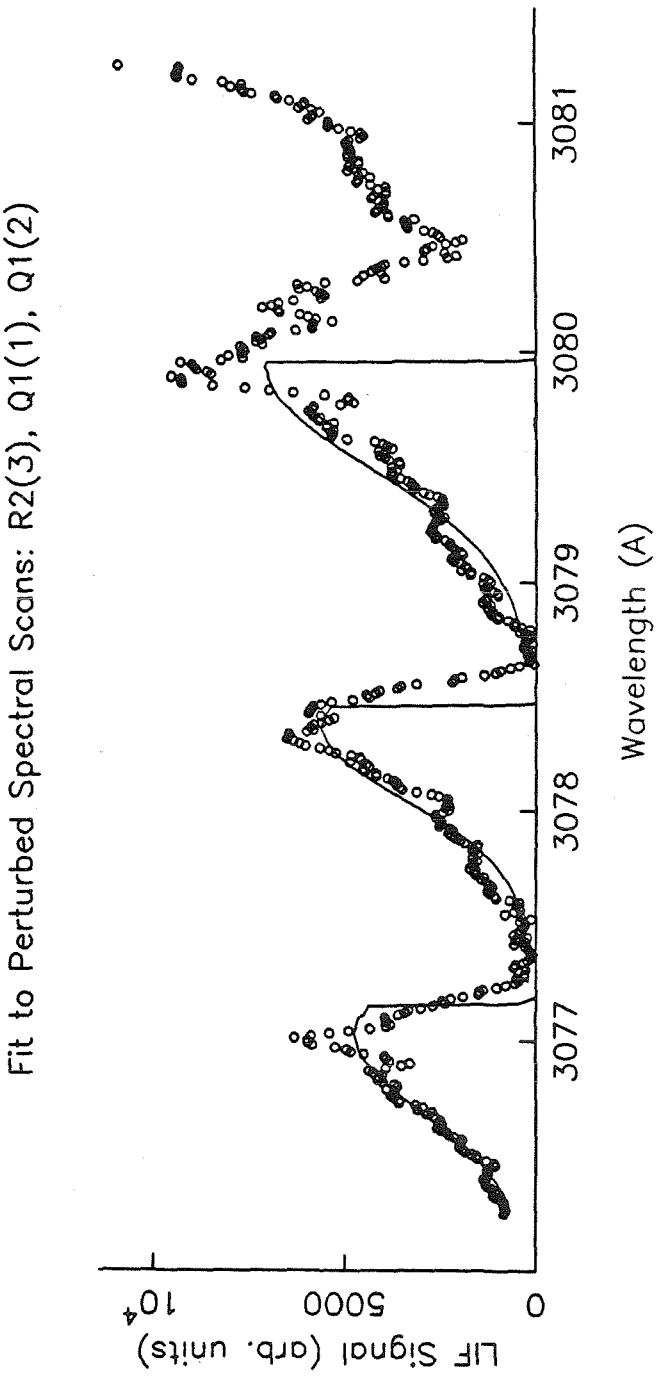
Fit to Perturbed Spectral Scans: R2(3), Q1(1), Q1(2)
LIF Signal (arb. units)
0
5000
10^4
3077
3078
3079
3080
3081
Wavelength (A)

Figures 8a, 8b.

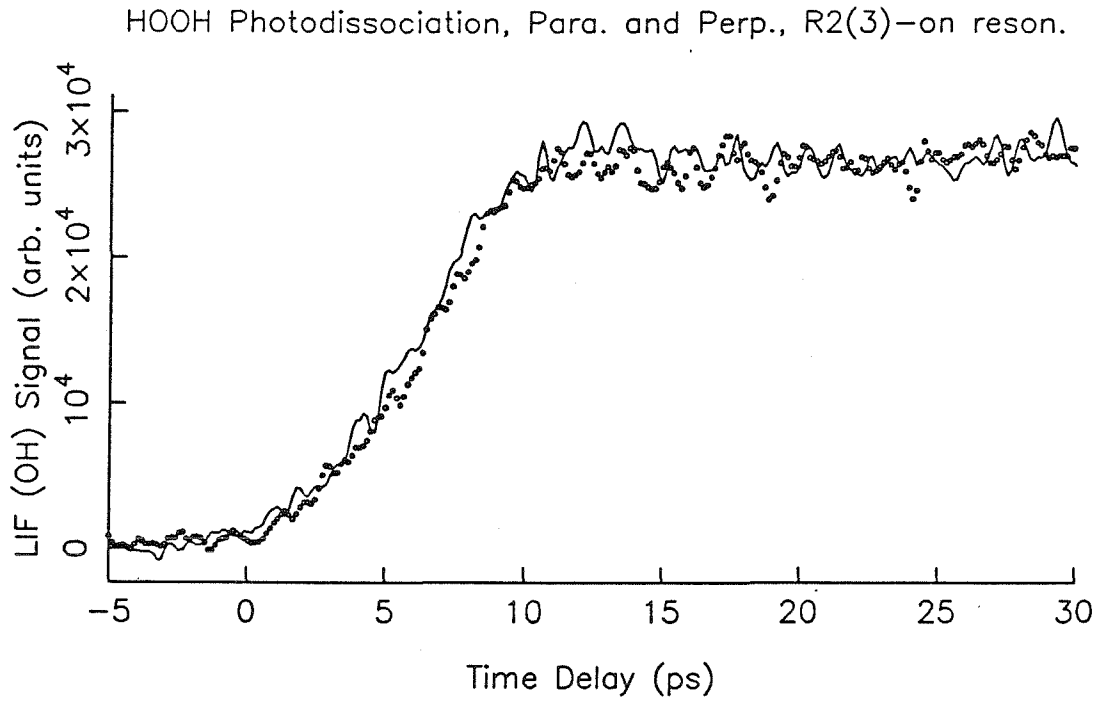

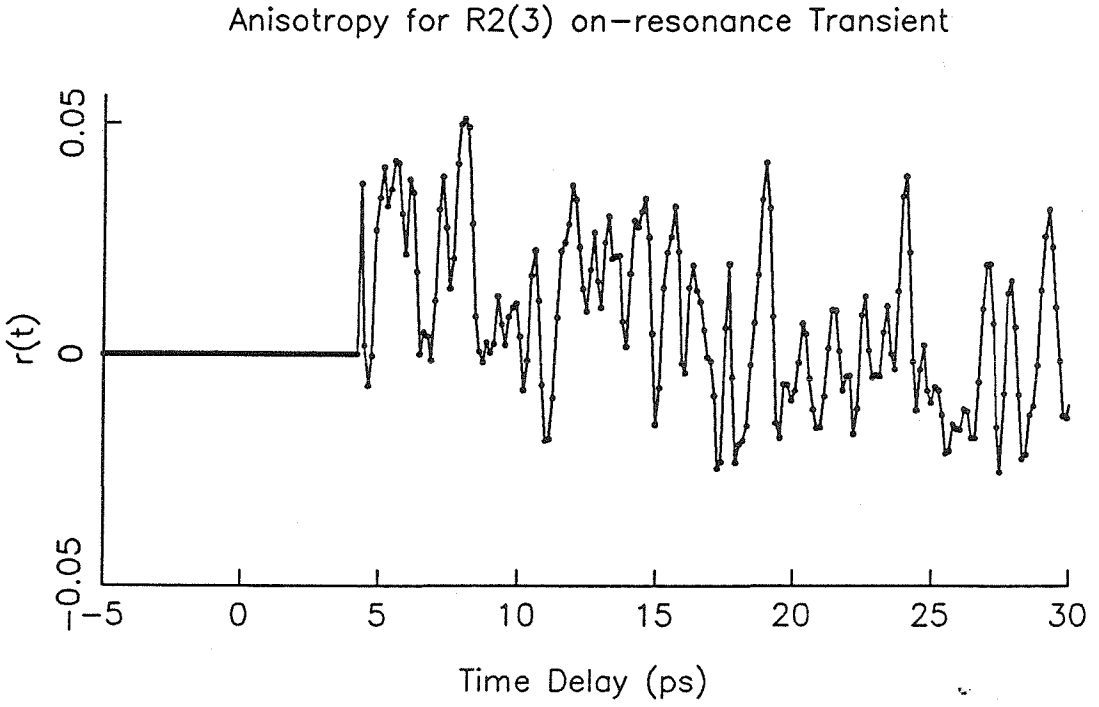

Figures 9a, 9b.

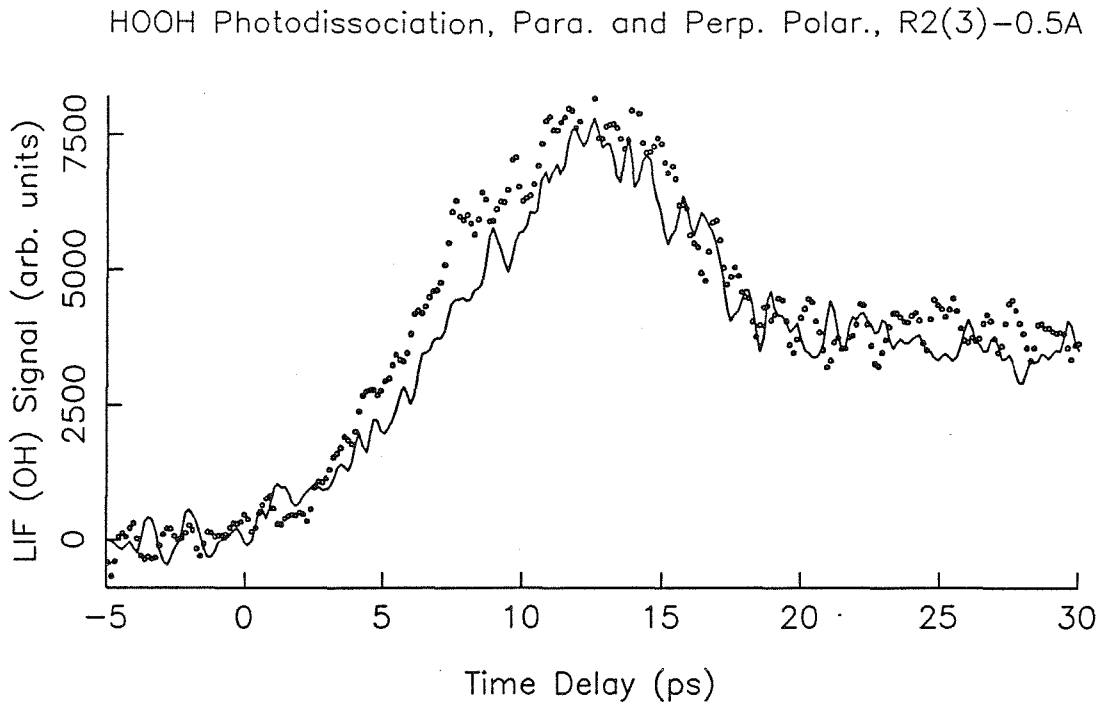

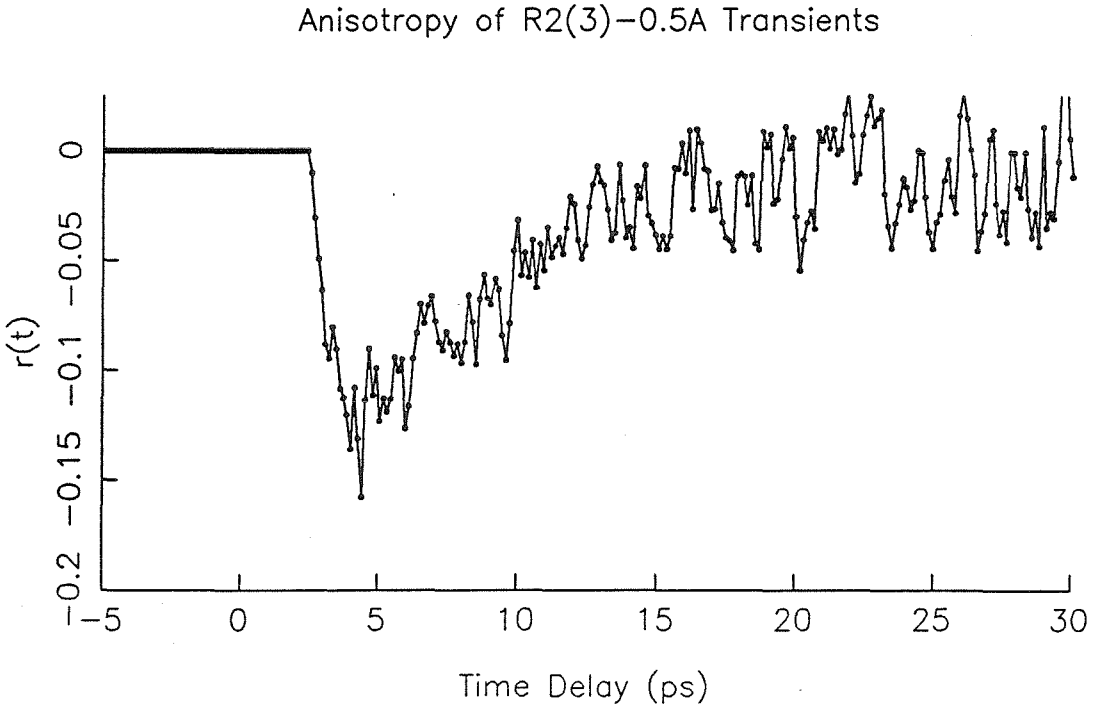

Figures 10a, 10b.

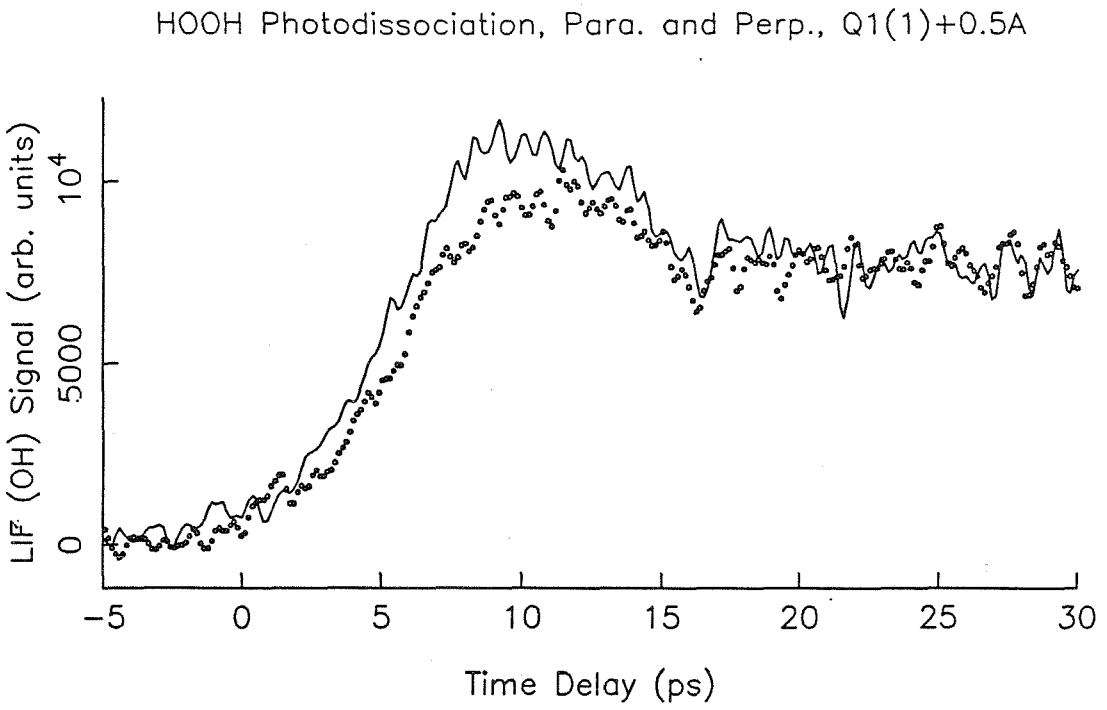

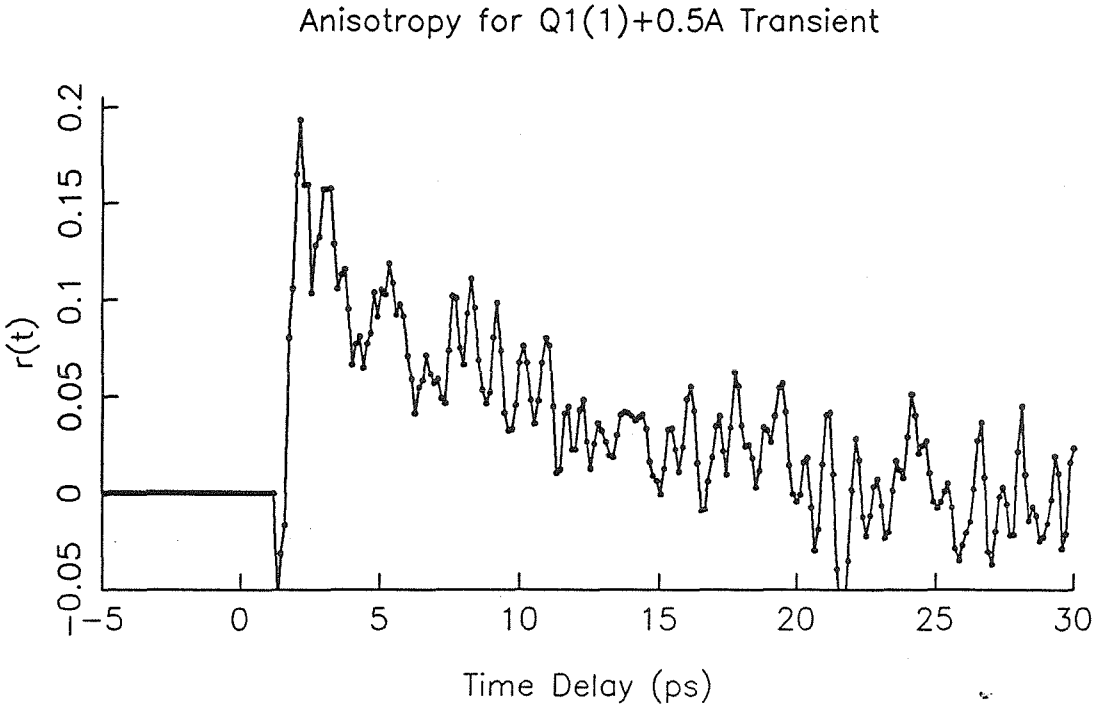

*Published in The Journal of Chemical Physics 87, 97 (1987).

CHAPTER V.

Picosecond Photofragment Spectroscopy II. The Overtone Initiated Unimolecular Reaction $H_2O_2(\nu_{OH}=5) \rightarrow 2OH$

Norbert F. Scherer and Ahmed H. Zewail

A. A. Noyes Laboratory of Chemical Physics,[a)]
California Institute of Technology Pasadena, California 91125

[a)] Contribution No. 7514

Picosecond photofragment spectroscopy. II. The overtone initiated unimolecular reaction $H_2O_2(v_{OH}=5)\rightarrow 2OH$

Norbert F. Scherer and Ahmed H. Zewail
Arthur Amos Noyes Laboratory of Chemical Physics,[a] *California Institute of Technology, Pasadena, California 91125*

(Received 9 December 1986; accepted 11 February 1987)

This paper, second in the series, reports on the picosecond time-resolved photofragmentation of the overtone ($v_{OH}=5$) initiated reaction: HOOH + $h\nu\rightarrow$2OH. The hydrogen peroxide is initially excited by way of a picosecond laser pulse to the fourth overtone level of the OH-stretch local mode. The subsequent unimolecular reaction behavior is obtained by monitoring the laser-induced fluorescence, caused by the picosecond probe–pulse electronic excitation of the OH radical photoproduct (in a given rotational state). The two pulses are scanned relative to one another in time thereby mapping out the product yield for the given delay-time interval. The resultant product formation behavior is found to be nonexponential, and may be modeled as a biexponential rise. Furthermore, the quasibiexponential behavior is sensitive to the exact excitation wavelength—slight variations of which result in large changes in the two time constants and the relative amplitudes of the fast and slow components. These experiments give direct evidence for the inhomogeneous nature of the overtone transition on the picosecond time scale, and provide the dissociation rate contribution to the homogeneous width (0.05–0.15 cm^{-1}). The apparent width for the main band feature is about 200 cm^{-1}. The rate of product formation (magnitude and form) is interpreted in terms of *statistical* and *nonstatistical* theories. The limitations of the applicability of each model is discussed. The fluctuations of the fitting parameters as a function of excitation wavelength may be simulated by a statistical model which considers all possible discrete optical transitions within the simulated laser bandwidth and the details of product formation from each state. For a nonstatistical interpretation, the biexponential form reflects a division of the vibrational phase space, and this is discussed in the spirit of a kinetic model. Finally, experimental results are reported for direct UV initiated photofragmentation. The observed dynamics indicate that a very different type of potential surface (repulsive) is involved, in contrast to the overtone initiated dissociation, which takes place on the ground state surface.

I. INTRODUCTION

The highly state-selective nature of optical overtone excitation encourages the possibility of the study of state-to-state reaction dynamics and bond-selective chemistry.[1] The specificity in the initial state creation results from rigorous transition selection rules in the excitation process. In contrast to unimolecular reactions which proceed via mechanisms involving internal conversion or intersystem crossing (see e.g., Ref. 2), local-mode (LM) excitation[3] of CH or OH oscillators provide a "site selective" method of depositing the energy in a given bond on the ground potential energy surface. Such a well defined initial state should allow for the detailed examination of the effect of intramolecular vibrational energy redistribution (IVR), from the LM into the reaction coordinate, on the dynamics of reaction. The trying aspect of such experimental studies stems from the small absorption cross sections ($\sigma<10^{-23}$ cm^{-2}) for transitions to those overtone levels (e.g., fourth, fifth, or higher) which are sufficiently energetic to obtain molecular dissociation (typically 40–60 kcal/mol). The consequent small excited molecule population makes the study of intramolecular dynamics and reaction rates difficult.

Following the spectroscopic measurements of the linewidth of LM states (typical 100–150 cm^{-1} in large molecules), it became clear that time-resolved study of the (picosecond) dynamics of such states are necessary. The need for direct measurements of the time evolution stems from the realization that the linewidth of LM states may not be directly related to the true rate(s) of energy relaxation and/or reaction out of such states. This is because dephasing and inhomogeneous broadening could contribute significantly to the linewidth.[4] Many attempts were made in this laboratory to measure the picosecond dynamics of LM states but without success. Our recent report[5] on the overtone initiated dissociation of hydrogen peroxide is the first successful picosecond time-resolved overtone experiment to directly obtain such information. The reaction studied is

$$HOOH(v_{OH}=5 \text{ excitation})\rightarrow 2OH.$$

The method, as depicted in Fig. 1, may be briefly described as a picosecond laser pulse exciting the molecule to the fourth overtone ($v_{OH}=5$) while a second (ps) pulse interrogates the OH radical reaction product formed in a specific rovibrational state. The OH laser-induced fluorescence (LIF) signal is monitored as a function of the relative

[a] Contribution No. 7514.

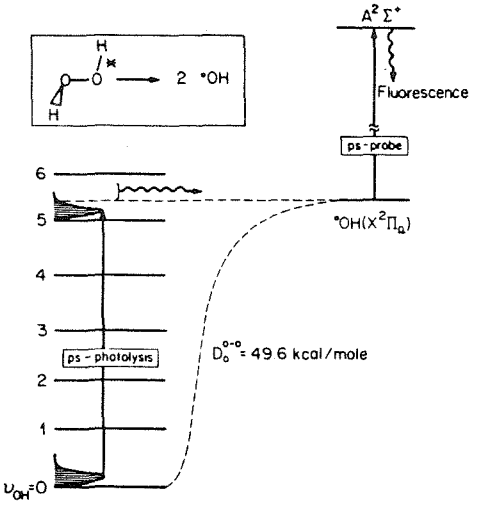

FIG. 1. The schematic of the picosecond overtone pump/OH LIF probe method. A picosecond pump pulse prepares the HOOH in the fourth overtone level of the OH stretching mode. Only states in the tail of the thermal distribution are energetic enough to dissociate. Intramolecular energy redistribution transfers the excitation + thermal energy to the reactive coordinate. The subsequent dissociation forms the OH radical product in various rotational states. A picosecond probe pulse excites the OH radical via the $^2\Sigma \leftarrow {}^2\Pi$ electronic transition. The resultant OH-LIF signal is proportional to the amount of ground state OH product in the specific state probed by the laser. The pump and probe laser pulses are scanned in time.

delay between the excitation and probe pulses. This development has afforded us with the capability to directly monitor the unimolecular reaction rates. The rates, taken in conjunction with the previously determined product state distributions,[6] should provide critical tests for theories of unimolecular reaction dynamics. Since the initial excitation is of the LM of the OH stretch and the reaction involves another coordinate, i.e., breaking the O–O bond, this motion of the internal energy implies that these studies are relevant to the IVR process and to the dynamics of the (ro-) vibrational phase space. The measured rate of reaction provides, by way of the Fourier transform, the contribution of the unimolecular dissociation to the homogeneous linewidth of the given transition. The apparent width[6] for this fourth overtone level is approximately 200 cm^{-1}.

The aesthetic appeal of the HOOH system results, in part, from it being a tetraatomic species for which there are few enough degrees of freedom such that the potential exists for making detailed theoretical/experimental comparisons. Also, prior to our work, there exist the results of numerous spectroscopic[7] and structural[8] investigations of hydrogen peroxide which are valuable to the present study. The types of studies which are most salient to the present work include elucidation of the (OH-stretch) ground state torsional potential,[9] some spectral assignments of the fourth overtone predissociation features by Crim's group,[6(b)] and photodissociation studies of the higher lying (repulsive) electronic states by Bersohn's group and by Klee *et al.*[10] There is an implicit simplification in coming to understand the dynamics of overtone-initiated reactions since the dissociation proceeds exclusively on the ground electronic surface and correlates to the lowest electronic configuration of the OH radical products.[11] Surface crossing and the associated non-Born–Oppenheimer wave functions are not an added complication to the interpretation of experimental results. Classical trajectory studies by Uzer, Hynes, and Reinhardt[12] have provided an enlightening description of a method by which energy redistributes from the LM to the reaction coordinate on the ground state surface of HOOH.

A practical appeal has to do with the reasonably low electronic ground state dissociation energy ($D_0 = 49.6$ kcal/mol),[13] which allows direct overtone pumping of the OH stretching mode facilitating studies of the ensuent reaction. Such excitation energies are readily accessible to amplified picosecond laser systems, thus enabling the measurements to be made. The product states of $OH(X\,^2\Pi_\Omega)$ fragment can also be probed using amplified picosecond pulses at UV wavelengths.

The remainder of this paper is structured in the following manner. A detailed description of our method for extension of the time domain for the overtone-pump LIF-probe technique and its application to the HOOH system is given in Sec. II. This will be followed by a presentation of some spectroscopic phenomenology (Sec. III) and the experimental results in Sec. IV which manifest the effect of the variation of the initially prepared state(s) on the subsequent reaction dynamics. Finally, in Sec. V we discuss the significant experimental observations of the product quasibiexponential buildup and the nonmonotonic behavior of the rate of molecular dissociation with respect to laser excitation energy. The results will be compared with statistical rate calculations and nonstatistical reaction theories. This will include an elaboration on the implications of conformity of the calculated results to the room temperature experimental data.

II. EXPERIMENTAL

The experimental arrangement essentially consists of four parts: (A) picosecond pulse generation, amplification and characterization; (B) the optical interferometer, gas cell, and laser induced fluorescence (LIF) detection scheme; (C) the HOOH sample and OH resonance calibration; and (D) the details of the methods used for signal acquisition and averaging, and data (also called transient) processing.

A. Two-color picosecond pulse generation and characterization

The picosecond pulses used in this study are produced by the synchronously pumped dye laser system depicted schematically in Fig. 2. The pulse initiation source is a Nd:YAG laser which is mode locked using a stabilized[14] acousto-optic modulator as the loss modulation element. The 532 nm output of the YAG laser (82 MHz rep. rate, < 80 ps pulses, 800 mw power, 10 nJ/pulse) synchronously pumps two cavity-length matched R6G dye lasers. The first dye laser (DL1) contains a three-plate birefringent filter as the tuning element, while the second dye laser (DL2) utilizes an identical three-plate birefringent filter as well as a

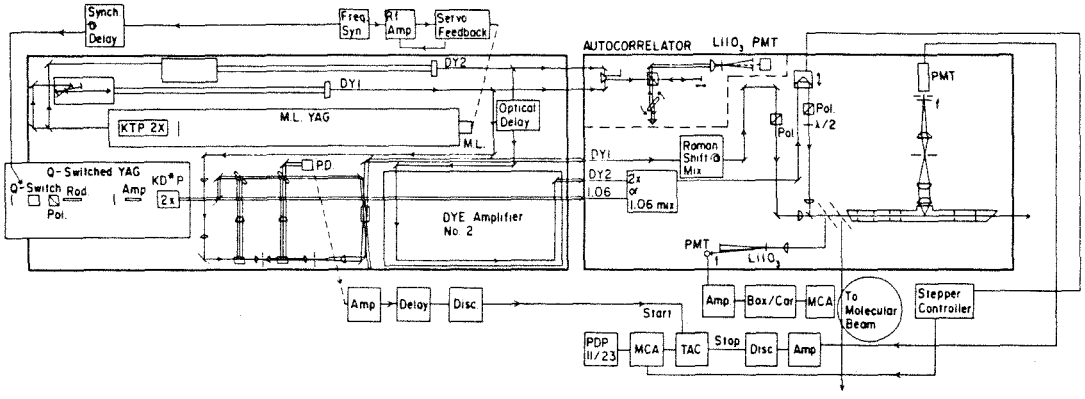

FIG. 2. The experimental arrangement. Three essential parts: (i) Laser system, oscillator, amplifiers, real-time pulse diagnostics; (ii) interferometer arrangement; (iii) gas phase bulb and the molecular beam apparatus. The abbreviated terms are explained in the text. The heavy borders represent the outlines of the optical tables. Amplifier 2 is essentially the same as amplifier number 1. The arrow labeled "to molecular beam" is in reference to the preceeding and subsequent papers in this series, and for peroxide experiments in progress.

fine étalon (40 GHz cw bandpass) as tuning elements. Output couplers of 30% transmissibility are used in both lasers to ensure good pulse formation via mode competition.[15] The output of the first dye laser (82 MHz, 6–7 ps Gaussian pulses, 50 mw average power, 1 nJ/pulse, approximately transform limited) is amplified in a three-stage (home-built) pulsed dye amplifier with a Q-switched Nd:YAG laser (20 Hz, 3.5 ns pulse, 200–250 mJ/pulse at 532 nm) as a pump source. The second dye laser's output (11 ps Gaussian pulses, 40 mw average power, approximately transform limited) is amplified in a separate, but essentially identical, three-stage dye amplifier pumped by the same Q-switched laser. The synchronization of the YAG Q switching and the arrival of the dye laser picosecond pulse at the amplifiers is suitably adjusted for maximum amplified power by way of electronic and optical delays. Each dye amplifier consists of two transversely pumped dye stages and a final counter propagating longitudinally pumped dye cell. The cells are isolated by spatial filters to discriminate against amplified spontaneous emission and to facilitate wavelength tunability. The optics design maintains the TEM_{00} mode of the synch-pump laser through the amplifier. In the third amplification stage, the longitudinal pumping causes the output mode to take on the "doughnut" transverse mode of the Q-switched laser. The picosecond beam diameter is increased in each succeeding dye stage to prevent nonlinear distortions (e.g., dielectric breakdown, self-phase modulation) from broadening the pulse in time or frequency. The linear group velocity dispersion, caused by the wavelength dependent change in the index of refraction of the optics and dye medium, contributes approximately 2 ps (assumed Gaussian), in convolution with the input pulse width, to the time duration of the amplified pulses. The output pulses of the dye amplifiers (20 Hz, 6.6 or 11.2 ps, 0.5 mJ/pulse) are injected into the optical arrangement for the delay line and are split off for pulse characterization.

The oscillator dye laser pulses and the amplified pulses are analyzed in time using background-free second harmonic generation (SHG)[16] and in frequency by monitoring the bandwidth. A real-time autocorrelator is used to aid in the adjustment of the dye laser cavity lengths and is also used to obtain signal-averaged autocorrelations for pulse analysis. This home-built spinning-block design also allows for the measurement of the cross correlation of the two dye lasers. The amplified pulse autocorrelations are acquired using a stepper motor variable delay interferometer which makes repetitive-scan signal averaging possible. It is found that the oscillator and amplified pulses are essentially equivalent in the present laser configuration, that is, the amplifier is not (appreciably) broadening or distorting the picosecond pulses in time or frequency. The acquired autocorrelations are deconvoluted with symmetric Lorentzian, Gaussian, or sech model functions for the pulse duration using a nonlinear least-squares fitting routine. It should be noted that such symmetric model functions are only a convenient approximation to the true pulse shape.[17] If a log plot of the autocorrelation data shows evidence for the existence of another component, an additional deconvolution is performed for the noise burst model[18]–coherence spike.[19] This precaution was unnecessary, however, for the present experimental arrangement of tuning elements. The oscillator and amplified pulse cross correlations may be obtained with the same experimental arrangements and their measurement involves only minor alignment adjustments. These cross correlations are deconvolved using the respective autocorrelation information and a symmetric model function to account for the pulse jitter.[20] It may be noted that the amplification process does not adversely affect the modeled jitter.

Figure 3 displays typical auto- and cross correlations obtained by background free sum frequency generation. The cross correlation is deconvoluted with a 6.6 ps Gaussian pulse (obtained from the autocorrelation of DL1) and yields a 11.5 ps Gaussian component. This second contribution is very similar to the 11.2 ps Gaussian pulse width obtained form the autocorrelation of the second dye lasser. The contribution from the cross-correlation jitter is <3 ps in this

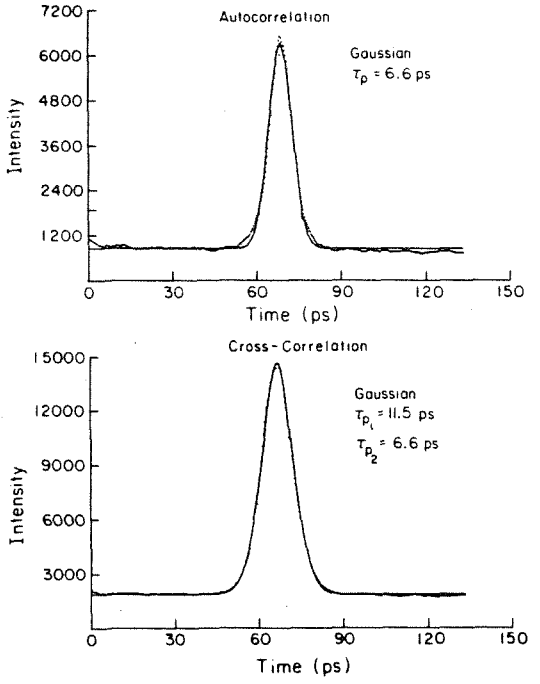

FIG. 3. Auto- and cross correlations of the amplified pulses. The correlation functions are generated by sum frequency generation, as seen in the lower portion of Fig. 2, utilizing the scanning interferometer arrangement of Fig. 2. The fitted autocorrelation pulse width is $\tau_p = 6.6$ ps FWHM Gaussian, cross correlation fitted pulse widths (Gaussian) are $\tau_{p_1} = 6.6$ ps and $\tau_{p_2} = 11.5$ ps which is very similar to the autocorrelation of DY2 (not shown) of 11.2 ps. The ratio of amplitudes for the contributions to the cross is equal to 1.

case. This value is small in comparison to the pulse widths, and is perhaps also (partially) due to the assumption that the pulse may be represented by a symmetric model function.

Bandwidth measurements are performed using a Spex 0.75 m monochrometer, which has 0.25 cm^{-1} spectral resolution at 600 nm for 20 μm slits. The pulse bandwidths are fit with a Gaussian functional form and are deconvoluted for the monochrometer resolution. It is found that the oscillator and amplified bandwidths for DL1 are equivalent and are 2.6 cm^{-1} at 607.5 nm while the bandwidth of DL2 is 2.8 cm^{-1} at 303.75 nm. This gives a pulse duration–bandwidth product of 0.50 for DL1, as compared to the transform limit of 0.441 for minimum uncertainty (Gaussian) pulses.[16]

B. Pump–probe arrangement

1. Visible pump–UV probe

The optical scheme, as represented in the remaining portion of Fig. 2, consists of an optical interferometer arrangement in which the amplified outputs of DL1 and DL2 enter the fixed and variable delay arms, respectively. The pump beam of 200 μJ pulse energy at the sample is focused to a 0.25–0.5 mm spot size. The probe light (DL2) is generated using a KDP crystal to frequency double the laser fundamental. The second harmonic beam enters the variable delay arm of the interferometer, which (usually) contains a beamsplitter, a corner cube on a stepper motor actuated translation stage and a zero degree retroreflector to double pass the beam through the scanning corner cube. This double pass arrangement facilitates long scans (2.5 ns) and ensures beam positioning accuracy when the arrangement is properly aligned. Figure 2 shows an arrangement for a single-pass through the corner cube. This is done for the purpose of enhanced visual clarity, and is an alternative experimental scheme. The delayed beam passes through the beamsplitter, is analyzed with a Glan–Taylor polarizer and is rotated by a half-wave plate. This optical arrangement allows making the relative pump–probe polarizations parallel or perpendicular for the various measurements. Placing the waveplate after the analyzer allows polarization changes to be made without significantly disturbing the beam overlap. This arrangement obtains extinction ratios of $\geq$20:1. The probe beam is focused separately from the pump beam to a diameter of 0.25–0.5 mm and is attenuated to $<0.25\,\mu J$ pulse energy. The beams are recombined with a dichroic reflector, are carefully adjusted to be collinear and propagate through the HOOH/LIF cell. Independent focusing enables one to position the pump and probe beam waists at the fluorescence cell viewing window and match the spot sizes. Chromatic aberation of these two (infinite conjugate ratio) beams does not allow one lens to do this effectively while maintaining a reasonable spot size.

The system response function is obtained by generation of the difference frequency signal[21] between the pump and probe beams under time delay conditions identical to those for a given experimental transient. The collinear beam condition employed satisfies[22] a k vector matching condition of the form $\Delta\bar{k} = 0 = \bar{k}_1 + \bar{k}_2 - \bar{k}_3$, where $\bar{k}_3$ represents the wave vector for the beam from DL2, $\bar{k}_1$ is that from DL1, and $\bar{k}_2$ is that associated with the difference frequency beam. This light is monitored slightly off-axis of the DL1 and DL2 beams since it cannot be preferentially selected by spectral or polarization discrimination methods. The extreme divergence of this beam results from the chromatic aberation of focusing into the nonlinear crystal with a single lens. The same interferometer as described above is used to generate the pump–probe cross correlations. The changes in the optical arrangement involve rotation of the half-wave plate and analyzer to produce perpendicular relative polarizations of the beams, appropriate attenuation of the pump and probe beams to avoid damaging the nonlinear crystal while maintaining the same relative time delay (i.e., time zero is not shifted), and inserting a plane mirror before the sample cell to direct the beams into a 1.5 mm $LiIO_3$ crystal. The difference frequency beam is monitored with a photodiode, and the signal is recorded as the delay-line scans over the identical range as for the corresponding experimental transient. The observed response functions are shorter (in time) than the corresponding cross correlations of the two visible beams since the pulse from DL2 has been frequency doubled. The shape of the second harmonic pulse is proportional to the square of the $\hat{e}$ field, causing the pulse duration (for a trans-

form limited pulse and no group velocity dispersion contribution) to become $\simeq\sqrt{2}$ shorter.

2. UV pump–UV probe

An alternative pump scheme was used which involves the same probe arrangement but differs in that the pump wavelength is 282 nm. This is done for the purpose of probing the dissociative electronic state for comparison with the direct overtone excitation scheme. The generation of this light involves inserting a methane Raman shifter in the path of DL1 (along with appropriate focusing and recollimating lenses), mixing the resultant anti-Stokes shifted light with the fundamental frequency in another KDP crystal (sum frequency generation). An appropriate set of dichroic beamsplitters and recombiners send this new pump beam along the fixed delay path of the formerly visible pump beam. Similar overlap and beam waist position criteria to those described above are used for lens and recombiner positioning. The response function for this UV pump scheme is not readily obtainable by difference frequency generation since this entails the detection of 3000 cm^{-1} light—we were not equiped with the necessary (e.g., Ge) detector.

Several other pump–probe schemes are possible—the essential difference lying in the method of generation of the specific frequencies of light required in the particular experiment of interest. The common factor remains the utilization of the scanning delay line interferometer.

C. Sample preparation and signal acquisition

There are several considerations involved in the design of the sample cell. Since HOOH catalytically decomposes on metal surfaces, the construction materials consist exclusively of glass and Teflon. A flowing vapor cell is necessary to replenish the sample in the observation region and to minimize the effects of wall decomposition. A capacitance manometer (MKS Instruments Baratron 222BA) is used to monitor the pressure and thereby regulate the rate of OH quenching[23,24] and ensure that the observed transients are not distorted by an extreme pressure condition. Finally, the cell must be designed to effectively discriminate against scattered laser light, in particular that which is derived from the probe beam. The pump light may be filtered (Corning 7-54) before the PMT detector. The probe light, however, is more troublesome in that the LIF is monitored for the resonance fluorescence—filtering is not possible. Extensive light baffling of the probe light within the cell was a feasible solution. As may be seen in Fig. 2, several black Teflon light baffles are incorporated into the cell.

The OH LIF is detected at right angles through a fused silica viewing window. The emission is collected and collimated with an $f/1$ plano-convex lens and focused with a $f/2$ lens onto a 2 mm slit. The transmitted light is refocused by an $f/1.5$ lens onto a 7.5 mm slit which is located just before the detecting high gain PMT (EMI 9635QB). The several slit aperatures further reduce the amount of scattered laser light and a filter (7-54) in front of the PMT removes essentially all of the visible beam scatter.

The HOOH sample (70%, FMC Corp.) is extensively degassed by repeated freeze–pump–thaw cycles before being used. The pressure in the cell is regulated by adjusting a Teflon needle valve which separates the sample holder from the cell's main body. The cell is actively pumped on (cryotrapped stokes pump) to establish HOOH flow through the fluorescence viewing region to prevent the accumulation of the photo- and wall dissociation products. Tuning into the $A\,^2\Sigma \leftarrow X\,^2\Pi_\Omega$ OH resonance transition of interest is most easily done using a (Bunsen) burner flame as an OH radical source.[24] The dye laser wavelength is adjusted while monitoring the LIF signal from the flame source with a filtered (7-54) PMT (Hamamatsu 1P28a).

The observed photoproduct OH LIF signal level is expected to be low because of several contributing factors; the absorpting cross section for this transition to the fourth overtone ($< 10^{-23}$ cm^2) and the sample number density are small. In addition, the picosecond pulse energy is $\simeq 1\%$ that of the nanosecond pulses used in Ref. 6. Therefore, less than one detectable event per laser pulse is anticipated, indicating the suitability of a single photon counting detection scheme. The Q-switched YAG pulse is monitored with a fast photodiode (H.P. 5082-4220), amplified in an inverting amplifier (H.P. 461A), discriminated (Ortec 473A), and used for the start input signal of a time-to-amplitude converter (Ortex 457 TAC). The output of the EMI PMT is amplified (Comlinear CLC100), passes through a 130 ns delay, is fed into a differential discriminator (Ortec 583), and is used as the stop pulse of the TAC. The delay serves to prevent the TAC from registering the scattered light events. The detection window for the TAC is adjusted to be 1 μs (duty cycle: 0.002%) to maximize the number of countable events and still maintain good discrimination with respect to the tube dark counts (< 100 events per second, uncooled). In this detection scheme the signal event rate must be less than the pulse repetition rate to avoid biased sampling problems, therefore, maximum experimental count rates were maintained to < 4 counts per second for this 20 pps laser system. For the case of uncorrelated photon statistics (Poisson), two photon biased sampling events would occur at most 6% of the time.

D. Signal processing

The signal is accumulated in an MCA (Tracor Northern 1706) whose channel advance is synchronized to the variable delay line stepper motor controller. The accumulated transient is transfered to a minicomputer (MDB PDP11/23 +) for storage and further processing. The maximum accumulated signal level in a given channel of the 512 channel memory is typically 250 counts per scan—only one quarter of this consititutes a background signal. Accordingly, a maximum S/N ratio for Poisson noise statistics is 13:1. Some of the experimental noise is systematic causing the S/N ratio to be somewhat less. The transients which are presented herein are data which have been smoothed using a three point Gaussian weighting function. This enhances the transient S/N but has no effect on the fitting parameters.

Transients are fit with a single or biexponential model function of the form

$$S_{\text{trans}} = \int_{-t_1}^{t_2} \{\alpha_1[e^{(-t/\tau_1)}] + \alpha_2[e^{(-t/\tau_2)}]\} \cdot I_{\text{resp}}(t)dt, \quad (1)$$

which includes convolution with the intergrated system response function, $I_{\text{resp}}(t)$. (See the preceeding paper[2] for additional details). A nonlinear least-squares curve fitting routine[25] is used for the analysis of the experimental data to extract the state lifetimes and preexponential factors. Pulse widths may be determined from auto and cross correlations by using a variation of this routine.

III. SPECTROSCOPIC PHENOMENOLOGY

This section will acquaint the reader with the essential nomenclature for the HOOH and OH systems which will be used in the subsequent sections of this paper.

Preparation of a pure local-mode (LM) state requires that several rather exacting experimental factors be simultaneously attained. The bandwidth of the laser must be broad enough to span all of the molecular eigenstates which contribute to the formation of the local-mode coherent superposition state. The bandwidth should, however, not be so broad that additional states which do not contribute to the superposition state of interest are optically excited. The pulse duration must be sufficiently short to prepare the desired state and to be able to measure the subsequent dynamical evolution (dephasing). Our use of the work "local-mode" (LM) state is to indicate that the pump laser is tuned within the absorption band of the OH stretch, identified by the use of the Birge-Sponer relationship, as a local mode with a fundamental frequency of 3701 cm^{-1} and a diagonal anharmocicity of -90.5 cm^{-1}.[6(a)]

The spectroscopy of HOOH at $v_{OH} = 5,6$, has been studied in Crim's group,[6(b)] and has built on the prelaser studies concerning the nature of the infrared absorption spectum of hydrogen peroxide.[9] Specifically, these developments include detailed modeling studies of the $v_{OH} = 5,6$ gas phase "predissociation" spectra,[6(b)] and have provided insight into the nature of the vibrational spectral features. Of particular interest to the work presented in this paper is the apparent success of adiabatically separating the OH stretch from the molecular torsional motion (in a manner analogous to the Born–Oppenheimer approximation), making possible the assignment of some of the more prominent spectral features. This has allowed the identification of three types of vibrational features (all of which have associated rotational structure) in the main fourth overtone absorption (i.e., predissociation) region, those due to: (1) pure overtone excitation; (2) hot band transitions involving the torsional motion; and (3) excitation features which include both O–O stretch (ν_3) and torsional hot bands. It should be reiterated that such high internal energy spectral features are prominent in the $v_{OH} = 5$ predissociation spectrum because the zero point of this transition is 1100 cm^{-1} below the D_0 value of HOOH. Hence, the transition features which presumably dominate the true absorption spectrum[26] are those which originate from appreciably populated ground state levels (Boltzmann distribution) and are not observed to be predominant in the fourth overtone predissociation spectrum.

The spectroscopy of the hydroxyl radical has been extensively studied[27] and is well understood, in contrast to the degree of knowledge of the overtone levels of HOOH. The dissociation products are formed in the two spin–orbit manifolds ($\Omega = \frac{1}{2}, \frac{3}{2}$) of the $X\,^2\Pi_\Omega^\Lambda$ electronic ground state and may undergo transitions to the two types of spin–rotation states (F_1 and F_2) of the $A\,^2\Sigma$ excited electronic state. The angular momentum quantum number N excludes the spin angular momentum ($S = \pm\frac{1}{2}$), and the total angular momentum is denoted by J, where $J = S + N$. Further characterization of these states is given by $\Lambda = (\pm)$, which describes orbital–rotation interactions. Because of the quasidegeneracy of the F states, the usual P, Q, and R transitions are further labeled according to the type of F levels (1 or 2) involved. The initial (in the $\Pi_{3/2}$ state) N quantum number is represented enclosed in the parentheses, e.g., $Q_1(1)$ for $N = 1$. For more details see the paper by Dieke and Crosswhite.[27] Since the spectral bandwidth of the probe laser is a few wave numbers in extent the e.g., $Q_1(1)$ and (the satellite branch) $Q_{21}(1)$ transitions are not distinguishable. This does not cause a problem in interpretation, however, because these transitions originate from the same Ω,N,Λ ground state level.

In performing polarization studies it is important to understand the degree of correlation between fragment angular momenta and the recoil velocity axis (this will not be detailed here). Time-integrated polarization experiments have been elegantly demonstrated on this and other related systems.[28] Only preliminary results of time-dependent polarization studies are presented herein. Relevant spectroscopic parameters of HOOH and OH are given in Table I.

IV. RESULTS

A. Fourth overtone predissociation studies

1. Pump wavelength and polarization dependences

Figure 4(a) shows an overtone pump OH product probe experimental transient for the $Q_1(1)$ transition (pump wavelength: 6142.5 Å). This transient was fit to a biexponential functional form, including a deconvolution for the response function; the resulting parameters are $\tau_1 = 80 \pm 10$ ps and $\tau_2 = 580 \pm 75$ ps with the value for the fraction, i.e., the ratio of the amplitude of the fast component to the total amplitude [see Eq. (1)], being 0.58. The transient in Fig. 4(b) is for a pump excitation wavelength of 6139 Å and the probe transition $Q_1(1)$, with fitted time constants of $\tau_1 = 54 \pm 7$ ps and $\tau_2 = 410 \pm 50$ ps, where $f = 0.37$. The notable features are that both transients exhibit quasibiexponential buildup behavior and that the values for the fraction differ considerably between these transients. The only essential difference in experimental conditions for the two measurements is the alteration of the pump wavelength. The variation in the fraction qualitatively follows the oscillations in the lifetimes—a smaller value for the fraction is seen in conjunction with longer time constants. It is interesting to note that a small change in the excitation energy results in dramatic changes in the transient behavior. This point will be analyzed in greater detail below and in the Discussion section. In general it has been found that each of the ob-

TABLE I. Spectroscopic constants used in calculations.[a]

Parameter	Value	Reference	Parameter	Value	Reference
		H_2O_2			
D_0(HO–OH)	49.6 kcal mol^{-1}	13	A''	10.063 cm^{-1}	6
D_0(HOO–H)	88.5 kcal mol^{-1}	44[b]	B''	0.8737 cm^{-1}	6
$r_{HOO-H,eq}$	0.965 Å	44	C''	0.8366 cm^{-1}	6
$r_{HO-OH,eq}$	1.462 Å	44	A'	8.74 cm^{-1}	6
ν_1	3599 cm^{-1}	44	B'	0.905 cm^{-1}	6
ν_2	1402 cm^{-1}	44	$h\bar{\nu}_0^0$	16250 cm^{-1}	6
ν_3	877 cm^{-1}	44	C_6	0.546 E6 cm^{-1} Å^6	
ν_4	c				
ν_5	3608 cm^{-1}	44			
ν_6	1266 cm^{-1}	44			
$V_{0,g}$	971.0 cm^{-1}	9	$V_{0,e}$	901.8 cm^{-1}	6
$V_{1,g}$	1093.4 cm^{-1}	9	$V_{1,e}$	903.5 cm^{-1}	6
$V_{2,g}$	546.7 cm^{-1}	9	$V_{2,e}$	835.6 cm^{-1}	6
$V_{3,g}$	− 56.4 cm^{-1}	9	$V_{3,e}$	84.0 cm^{-1}	6
$\chi_{0,eq}$	111.5°	6	$\chi_{5,eq}$	102°	6
$\alpha_{0,g}$	39.945 cm^{-1}	9	$\alpha_{0,e}$	35.0 cm^{-1}	6
$\alpha_{1,g}$	0.248 cm^{-1}	9	$\alpha_{1,e}$	0 cm^{-1}	6
$\alpha_{2,g}$	0.0433 cm^{-1}	9	$\alpha_{2,e}$	0 cm^{-1}	6
		OH			
ν	3735 cm^{-1}	44	$r_{OH,e}$	0.9710 Å	44

[a] The V_i are the torsional potential constants in the ground $V_{i,g}$ and excited $V_{i,e}$ states. $\chi_{i,eq}$ is the equilibrium torsional dihedral angle.
[b] See Ref. 44 for the original references of the listed parameters.
[c] These values are determined from the potential parameters, see the text and Appendix.

served transients corresponding to the $N = 1,2$ OH transitions may be modeled as a rising biexponential buildup of the OH photoproduct. All of the results to be reported are for parallel pump–probe polarizations, unless otherwise specifically indicated.

A more detailed analysis is presented in Fig. 5(a) which shows an expanded scan of the initial component of the 6142.5 Å pump $Q_1(1)$ probe transition. The system response function is also displayed to indicate the substantial difference between the fast buildup and the response. Both the transient and the cross correlation correspond to exactly the same scan range. The $t = 0$ of the response function is seen to occur substantially earlier than the half-maximal value of the transient signal level. This clearly illustrates that the fast component has a substantially longer lifetime than the duration of the system response. The response displayed in the figure is used in fitting the experimental transient. The fitted exponential lifetime for this initial portion of the quasibiexponential buildup [seen in Fig. 5(a)] is 75 ± 5 ps. This is in good agreement with the lifetime obtained from the long delay-time scans. The response function is determined to have a Gaussian functional form with, approximately, a 10 ps FWHM. The shape is actually slightly asymmetric reflecting the asymmetry of the oscillator pulse(s).

In addition to the greater portion of the data being for parallel pump–probe polarizations, several transients with perpendicular polarizations were obtained. Performing these $\parallel$ and $\perp$ polarization studies with the same experimental conditions yields a result *on the transients* (not yield) since identical parameter values, within the fitting errors, are obtained. Since the effective B constant $(\frac{B+C}{2})$ is about 0.86 cm^{-1} and $\langle J \rangle \approx 23$ for the molecules with sufficient energy to undergo dissociation, the period for the rotational motion associated with the largest moment of inertia is on the order of a picosecond or less. This is substantially faster than the most rapid observed rate of dissociation. Experiments using proper geometry for anisotropy detection[28] are in progress.

The effects of variations of the specific pump excitation wavelength on the $N = 1$ transient behavior are compiled in Table II. The different pump excitation energies ($h\nu_{pump}$) cause the prompt components of the biexponential rises to change in duration in a *nonmonotonic* fashion. The long components change in a similar manner but not necessarily by a uniformly proportional amount, the only exception to this trend being the transient associated with the $P_1(1)$ transition. It may be noticed that there is a strong correlation for the two lifetime components in that they become longer or shorter together. The table also lists the fraction. There is a correlation of the value of the fraction with the trends seen for the lifetimes; the smallest value for the fraction occurs in conjunction with the shorter time constants. The pump-energy selective dissociation rates as well as a predissociation spectrum adapted from Ref. 6 is shown in Fig. 6. This figure makes manifest the close correlation between the two time constants and the fraction at each excitation wavelength. It is not as straightforward to associate specific spectral features with the observed lifetimes. This issue of the transient dependence on the pump wavelength will be addressed more completely in the discussion section by comparing the ob-

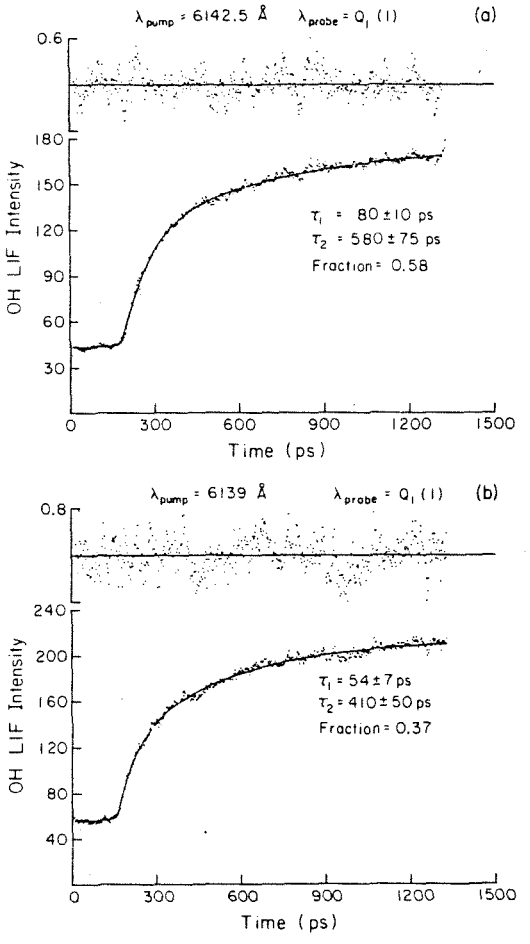

FIG. 4. Experimental results showing the ubiquitous biexponential behavior. The lifetimes and the fraction are indicated, the experimentally changed condition [between (a) and (b)] is the excitation wavelength. The residual for each transient shows the adequacy of a biexponential model function to simulate the behavior. Other transients, similar in form to those shown here, were obtained—the fitting parameters are given in Table II.

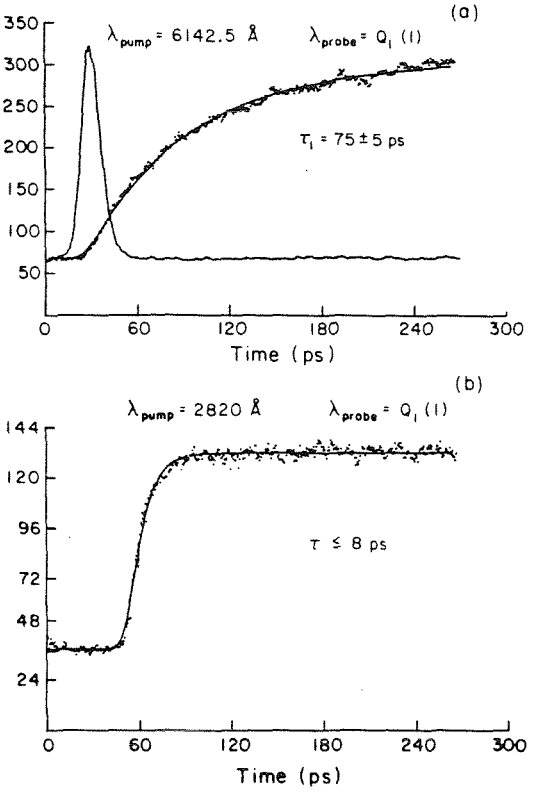

FIG. 5. Short component and the response function, (a). This corresponds to the fast component in Fig. 4(b). The response function is seen to be noticably shorter than the rise. A single exponential fit, using the same response is the fitted curve through the data. The UV–UV transient and the fitted single exponential are shown in (b). There is no biexponential behavior discernable in (b).

served behavior with the results of statistical rate/spectral model studies.

2. Probing different OH states

The results for the $N=2$ Q-branch transitions show markedly different behavior than the $N=1$ transitions for the same pump laser excitation wavelength. The short and the long lifetimes are somewhat different than the corresponding $N=1$ results, the long time constant having changed by a more significant amount. The most dramatic difference is found in the change in the value of the fraction from about 0.4 to more than 0.7 in both cases (the precision of the individual results is about ± 0.05). The experimental result is shown in Fig. 7. The difference between this $N=2$ result and the results shown in Fig. 4 are quite clear—the value for the fraction has changed significantly. The differ-

TABLE II. Dependence of experimental transient on excitation wavelength.

Probe transition	Pump λ (± 0.5 Å)	τ_1 (ps)[a]	τ_2 (ps)	Fraction
$Q_1(1)$	6011 Å	51(8)	515(75)	0.53
	6029 Å	45(7)	310(50)	0.35
	6038 Å	32(5)	240(40)	0.32
	6098 Å	35(5)	300(50)	0.41
	6129 Å	40(5)	300(50)	0.40
	6132 Å	83(10)	610(100)	0.61
	6139 Å	54(7)	410(50)	0.37
	6142.5 Å	80(10)	580(75)	0.58
	6144 Å	91(10)	600(100)	0.63
	6146 Å	80(10)	570(75)	0.63
	6149 Å	65(8)	430(50)	0.60
	6157 Å	60(7)	580(75)	0.58
	6160 Å	52(8)	510(75)	0.43
$R_1(1)$	6136 Å	50(8)	540(75)	0.30
	6144 Å	95(10)	650(100)	0.57
	6157 Å	50(8)	550(75)	0.59
$P_1(1)$	6163 Å	45(8)	700(100)	0.65
$Q_1(2)$	6140 Å	43(8)	350(50)	0.72
	6160 Å	50(8)	400(400)	0.72

[a] The error bars represent $\pm$ 1 standard deviation for the fitting parameters.

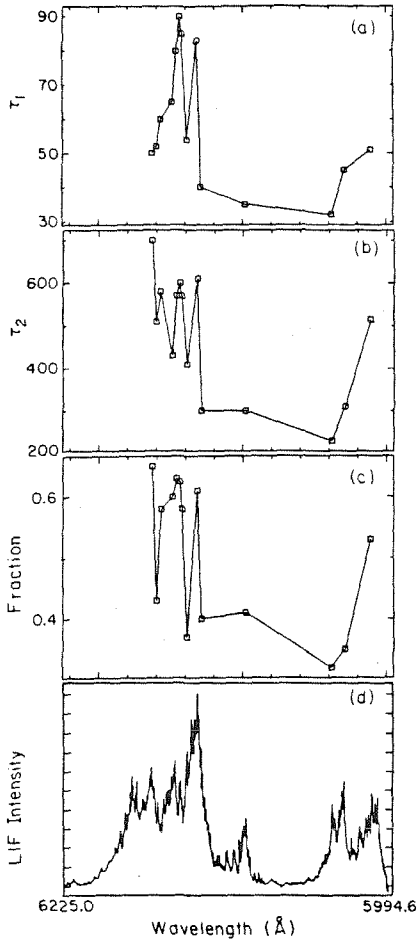

FIG. 6. The pump excitation wavelength dependent fluctuations in the short (a), and long (b), lifetimes (τ is in units of picoseconds) and the fraction (c). The predissociation spectrum [detecting $Q_1(1)$] of (d) is adapted from Ref. 6. The wavelength axes are all to the same scale. The fluctuations in the parameter values (also listed in Table II) may be examined for correlations.

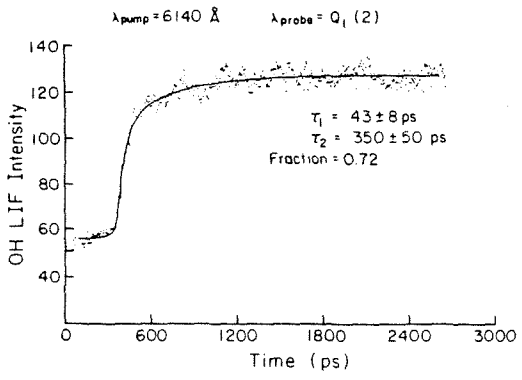

FIG. 7. Transient for $N = 2$. Probe is interrogating $Q_1(2)$. A biexponential fit gives the listed parameters. The time axis is twice that of Fig. 4(a). The excitation wavlengths for Fig. 4(a) and the present figure are the same ($\pm$ 1 Å). Only the probe transition is changed such that the OH fragment interrogated contains one quantum more rotational energy.

ence between the $Q_1(1)$ and the $Q_1(2)$ may be qualitatively understood in that some of those states closest to the barrier which form the $N = 1$ product may not be sufficiently energetic to form the $N = 2$ product.

In comparing the observed parameter of the Q-branch probe transitions with those for the R-branch transitions for the same pump wavelength, it is found that they are essentially equivalent, for the precision of the measurements. Within the limits of sensitivity of these experiments and for $N = 1$ there does not appear to be a Λ quantum number dependence for the time constants or fractions.

B. Diagnostic studies

1. Collison-free conditions

Several different control or diagnostic experiments must be performed to aid in the interpretation of the primary studies. Assurance that the results are collision-free for the duration of experimental interest (3 ns) is presented in Fig. 8(a). This figure shows a decay curve, for the $R_1(1)$ OH product transition (pump wavelenth: 6157 Å, pressure: 300 mTorr), which is the lifetime of the OH in the excited $A\ ^2\Sigma$ state. The transient, with a single exponential time constant of 424 ns, is shorter than the collision-free lifetime observed by others ($\tau \approx 800$ ns).[29] The collision period estimated from the hard sphere collisions is on the time scale of several nanoseconds (see Refs. 23 and 24 and references. cited therein). It has been previously observed that (ground state) rotational equilibration also takes place on a several hundred nanosecond time scale.[6(a)] The early-time deviation from a single exponential decay indicates the degree of over counting of the early bins, which may occur in single photon counting detection schemes. The TAC can process at most one event per laser shot. The pulse height distribution becomes skewed to early time when the event rate becomes too large. Since the OH lifetime signal was accumulated at the maximum pump–probe time delay, and hence maximum signal level, the small amount of over counting seen ($< 5\%$ of the total intergrated signal) has no significantly measurable (for the observed S/N) saturation effect on the transient. In general, the Baratron was used to monitor the cell pressure, which was maintained at $<$250 mTorr, ensuring a collision-free environment for all measurements. The decay of Fig. 8(a) is therefore a worst case condition in terms of mean time between collisions. The time scale being considered here is much longer than the pump–probe picosecond delay time scale.

2. Power dependence and two-photon processes

The power dependence of the OH LIF signal on the pump field intensity has been determined and Fig. 8(b) shows that the behavior is linear (the slope is equal to one within the experimental error). This is consistent with the picture that the fourth overtone is actually being interogat-

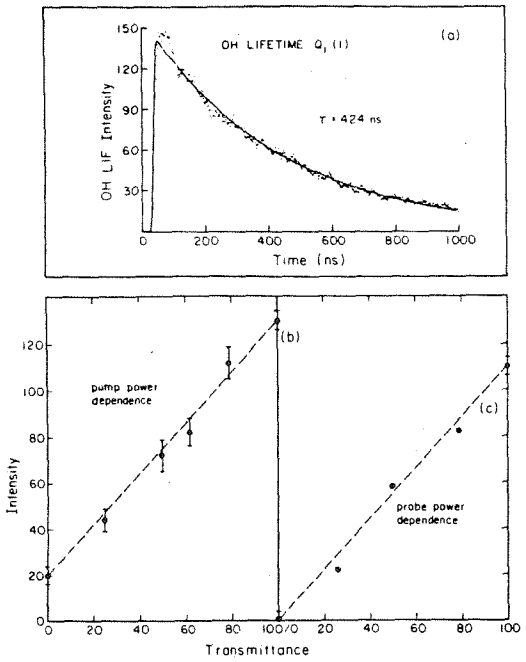

FIG. 8. Diagnostics. Top (a), shows the OH excited state lifetime. The transient was obtained at the maximum pump–probe delay setting and for a cell pressure of 300 mTorr. This decay is obtained by using the TAC in pulse-height analysis mode. The visible (pump) and UV (probe) power dependences are shown in (b) and (c), respectively. The linear trends are indicated by the dashed lines.

ed, and that the dynamics are not representative of some pumping scheme (e.g., two-photon to dissociation) which causes dissociation via a repulsive higher lying potential energy surfaces(s) of HOOH.[6,10] If the pump pulses are blocked, a steady state background (usually $\lesssim$25% of the total signal) remains. The background signal is reflected in the non-zero intercept in Fig. 8(b). This signal stems from the probe pulse interogation of a dissociative electronic state of HOOH and the same pulse probing the OH products formed.

A power dependence study of the probe field is performed to determine whether the behavior is consistent with the proposed mechanism of Fig. 1. The results of the UV beam intensity dependence study are presented in Fig. 8(c). The UV alone signal is subtracted from the total signal level at each point. This signal is time independent since it depends only on the presence of the probe pulse, and it does not contribute to the observed transient behavior. Furthermore, the pump–probe signal cannot be due to wall decomposition of HOOH since this would also result in a time independent signal. Blocking the probe beam shows that there is no observable signal from the pump field alone. The presence of this pump field only effect was examined at all of the different pump wavelengths used—such a two-photon signal has not been observed.

Verification that the LIF signal is due to OH is established by tuning the probe laser off-resonance of a specific $^2\Sigma \leftarrow {}^2\Pi$ OH transition and observing the signal disappear. Closing off the Teflon needle valve, which then isolates the HOOH reservior from the fluorescence viewing region of the cell, and evacuating the cell eliminates the LIF signal. The power dependence and other diagnostics show that the observed signal is consistent with the scheme of pump excitation of HOOH ($v_{OH} = 5$) and subsequent probe beam interrogation of the OH photodissociation product. This is further confirmed by the results of Sec. IV A 3. below.

3. Excited electronic state interrogation

The transient behavior which results from direct excitation of a dissociative electronic state of HOOH is useful for the interpretation of the constituent nature of the two components of the biexponential transient buildup. An alternative experimental arrangement is required for this study.[30] Since UV light of $\lambda \lesssim 300$ nm is required to make the transition with a reasonable absorption cross section[7] (in order to obtain a useful degree of enhancement), a Raman shifting method (involving CH_4) is employed to generate anti-Stokes shifted ($+2914\ cm^{-1}$) light of the fundamental frequency of DL1. The mixed light (anti-Stokes shifted plus fundamental) of 282 nm is generated as the new pump field, while the probe frequency is maintained in resonance with the $Q_1(1)$ OH transition. Figure 5(b) shows the resultant transient to be a single exponential rise which has a time constant of less than 8 ps—there is no long component present. Even though the pump wavelength is somewhat different than twice the frequency of the visible overtone pump field, it is seen that the transient shape and the single lifetime component differs substantially from those of Fig. 4. For the sake of making a clear distinction of the difference in the transient behavior due to visible or UV proton dissociation of HOOH, it may be recalled that Fig. 5(a) is an expanded view of the initial buildup of 6142.5 Å pump $Q_1(1)$ probe transient. The abscissa of the UV pump transient has the same scale calibration as Fig. 5(a) but the time-zero is different for the two plots. It is clear that the prompt reaction rates for overtone predissociation and direct dissociation are extremely different, especially when taking into account the fact that the response functions only differ by about 25% [see the rise of the signal in Fig. 5(b)].

It has been previously mentioned (Experimental section) that the response function for the UV-pump–UV-probe transient is not directly obtainable. A deconvolution of this transient with a (simulated) 9 ps Gaussian response yields, unlike all of the visible pump transients, a single exponential buildup with a lifetime of the same order as the response duration, that is $\tau \lesssim 8$ ps. This number is an upper-bound, and is consistent with earlier work[10,28] which deduces the lifetime from alignment experiments for excitations of 248 or 266 nm. Further studies, similar to those reported in Ref. 31 (femtosecond photofragment spectroscopy), are in progress to give more precise measurements for the HOOH excited electronic state lifetimes into specific Λ,N,Ω product states. The main conclusion to be reached from this study is that the time-dependent behavior of the

excited electronic state is quite different from that observed for direct overtone pumping and that this (along with the power dependences) is conclusive in showing that the (visible excitation) transients are not due to some sort of multiphoton effect of the pump field.

V. DISCUSSION

The preceding exposition of the overtone pump experimental results indicate three important observations. First, the product buildup rates are quasibiexponential. Second, these same rates (and the fraction) behave nonmonotonically with respect to changes in the pump wavelength. Third, the contribution of the dissociation time constants(s) to the linewidth (only 0.05–0.15 cm^{-1}) is several orders of magnitude less than the apparent width. This section will be devoted to gaining further insight into the significance of these observations and the dynamics which they reflect. The aim will be to determine the degree of applicability of statistical and nonstatistical theories in explanation of the results. The first part of the discussion will be concerned with the source of the biexponential transient behavior. The second portion of this section will be devoted to understanding the unique energy dependence of the transients. In the final part of the discussion, some remarks are made comparing the results of linewidth studies to the real-time measurements of IVR and reaction rate.

A. Quasibiexponential behavior

To begin the discussion suppose, for the moment, that the lack of available spectral information is such that spectral transition frequencies and states cannot be assigned. If the intramolecular dynamical behavior is considered to be statistical then the expected unimolecular reaction behavior is expected to conform to a single exponential decay rate. Conventionally, the averaged rate constant is related to the microcanonical rate constants $k(E_x)$ by the expression[32]

$$\langle k(T,E_x)\rangle = \frac{1}{Q}\int_0^\infty k(E+E_x)\,\rho(E)\cdot e^{(-E/k_BT)}dE, \quad (2)$$

where Q is the vibrational partition function, E refers to a given thermal energy, E_x is the excess vibrational energy, and $\rho(E)$ is the state density. In general, $k(E_x)$ may be evaluated using the RRKM expression or some variation thereof. In the simplest form $k(E_x) = A\,[\exp(-B/E_x)]$, where A and B are constants. The resultant rate of product formation is embodied in the single (average) exponential rate constant.

Two causes for the deviation of the experimental results from such single exponential behavior may now be realized. Firstly, the probability of mode occupation following the overtone excitation is no longer related to the internal temperature by a Boltzmann distribution. Secondly, the nonexponential behavior may stem from a division of the rovibrational phase space of the molecule.[32,33] The division creates two (or more) classes of initial states which are distinguishable by their associated reaction rate behavior. Our observation of biexponential behavior could, therefore, be related to nonstatistical behavior provided one exludes the effects of proper thermal averaging and thermal state distributions. In what follows, such effects will be carefully examined to elucidate the implications for the resultant behavior.

1. Thermally averaged rate

To begin, consider the microcanonical rate constant (k_{MC}) to be that which is defined by the well known RRKM expression

$$k_{MC}(EJ) = \frac{N^{\ddagger}_{E^*J}}{h\rho_{EJ}}, \quad (3)$$

where $N^{\ddagger}_{E^*J}$ is the state count in the critical configuration for the given model of the reaction with energy $E^* = E - E_0$ (for $J = 0$) above the critical energy for reaction, ρ_{EJ} is the state density in the reactant. The probability at time t of having formed a specific product from molecules excited to the fourth overtone level is obtained by averaging the microcanonical RRKM rates of reaction over the internal energy distribution, and may be expressed by

$$P_N(t) = \sum_{J=0}^{\infty}\int_o^\infty p_N(EJ)\cdot p^0_{EJ}\cdot\{1 - e^{[-k_{MC}(EJ)\cdot t]}\}dE, \quad (4)$$

which is then evaluated as a function of time to obtain the transient waveform. The original energy and J distributions, the associated Boltzmann distribution and state density are contained in p^0_{EJ}, while $p_N(EJ)$ is the probability that the system is in any of the final quantum states (product state distributions).

In performing the calculations for HOOH, the values for the microcanonical rate constants, $k_{MC}(EJ)$, were determined by combining the value for the number of states in the critical configuration ($N^{\ddagger}$) for a loose transition state, phase space theory (PST), calculation with the density of reactant states obtained from a direct state-count routine. The reader is referred to Table I for some details of the parameters used in the calculations (see Sec. V B below and the preceeding paper[2] for a discussion of PST).

Figure 9 displays the simulated transients [plot of Eq. (4) vs time] for the $N = 1$ and $N = 2$ OH product rotational levels as curves 1 and 4, respectively. The calculated behavior, as seen in curve 1, is qualitatively similar to the observed experimental behavior in that the calculated transient is nonexponential (quasibiexponential) in nature. Notice the rapid buildup behavior of $N = 2$ as compared to $N = 1$. The fitted lifetimes and fraction, as presented in Table III, show the same relative trends as the experimental $Q_1(1)$ and $Q_2(2)$ results. The fast and slow component lifetimes for the $N = 2$ transient are shorter than for $N = 1$ and the contribution of the fast component to the total amplitude becomes larger (i.e., the fraction increases). The calculation was performed for laser excitation energy of 16 255 cm^{-1} which is equivalent to the 0–0 transition frequency determined from a Birge–Sponer plot.[6] The barrier to dissociation is 1100 cm^{-1} above this value, so only molecules in the tail of the thermal distribution are potentially reactive. The OH product state distribution, which is obtained as a by-product of this calculation, is typically peaked at $N = 1$ and is (generally) a monotonically decreasing function of N. The experimentally measured product state distribution[6] is peaked at $N = 1$ and

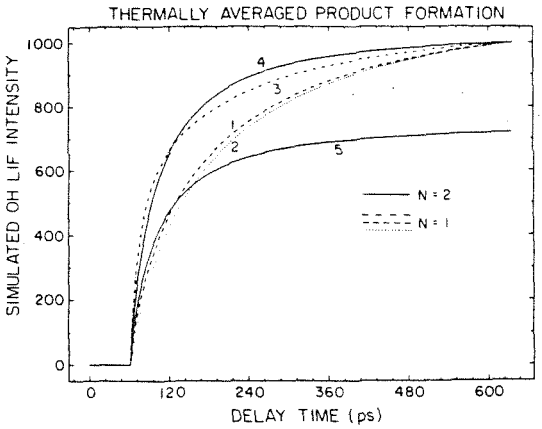

FIG. 9. Phase space theory (thermally averaged) calculation of product state probability vs time. Curve 1: $N = 1$, curve 2: $N = 1$ "cold" distribution, curve 3: $N = 1$ "hot" distribution, curve 4: $N = 2$. All four curves are normalized to the same final value to enhance the effect of different parameters on the calculated signal. Curve 5: $N = 2$ intensity, relative to $N = 1$. The time scale for all of the transients is half that of Fig. 4. This is done to aid the distinction of the curves near the breaks for the two components of the quasibiexponential behavior. The results of the biexponential model fitting are given in Table III.

P_N is also monotonically decreasing with increasing N. It is interesting that the thermal average of the microcanonical rates and distributions give qualitative trends which agree with the experimentally measured rates and product state distributions.

2. Nonstatistical perspective

It was suggested in our earlier communication[5] that a divided vibrational phase space may also account for the observed quasibiexponential product buildup dynamics. This is similar to the resultant behavior of a model advanced for IVR by Perry *et al.*[32] Marcus and Hase have recently indicated that nonexponential behavior could be explained if the phase space of the molecule were divided in a way representative of the directness with which a (classical) trajectory crosses the transition state to dissociation.[33] The *a priori* assumption is that the phase space of the system is noncommunicating on some portion of the time scale of the measurement, such that this non-RRKM behavior becomes manifest.

A two part divided phase space model yields a biexponential decay of reactant systems. For illustration, assume the following scheme (see Refs. 32, 33, and 39 for development of the model for the description of IVR and reactions):

TABLE III. Thermal averaged calculations.

Curve no.	Parameter	Energy (cm^{-1})	τ_1 (ps)	τ_2 (ps)	Fraction
1	($N = 1$)	16 250	46	270	0.36
2	cold	16 250	68	300	0.42
3	hot	16 250	23	225	0.48
4,5	($N = 2$)	16 250	38	215	0.59

$$N_2 \underset{k_2}{\overset{k_1}{\rightleftharpoons}} N_1 \xrightarrow{k_1} \text{products},$$

where N_1 and N_2 are the populations of the two subspaces. For the experimental results presented herein the implication of the observed biexponential product (OH) buildup is that the slow component is described by the RRKM rate while the fast component is determined by $k_2 + k_3$. A necessary conditon is that $(k_2 + k_3) \gg k_1$ and that the slower (RRKM) component is much different than the fast one, as discussed by Marcus.[33] This non-RRKM behavior is physically intuitive: at short times the phase space is divided and only the trajectories initiated in one portion thereof may cross the transition state, while at long times the system equilibrates and reaches the statistical limit behavior. The long time component observed in the present experiments falls in the range of 300 to 700 ps. In comparison, the fast component is 40–90 ps. It is therefore tempting to ascribe the biexponential transient behavior to nonstatistical effects, where the RRKM rates at these energies should be given by the values for the slow rise. Standard statistical calculations performed near the threshold yield values for the RRKM time constant close to the 300–700 ps range expected. Furthermore, at all energies of excitation the transient behavior is still biexponential and only the values of the rate constants change. One's exuberance must be restrained, however, because of the other possible explanations discussed herein.

In paper III,[34] the model of a divided phase space is used to account for the biexponential decay observed in the photodissociation of beam-cooled van der Waals molecules (this is interpreted as non-RRKM behavior). For that case the initial distribution (p^0_{EJ}) is very narrow (beam experiment). The thermal conditions of the present study, however, make the analysis more difficult. To fully examine the specifics of such non-RRKM behavior it is desirable to rigorously specify the initially prepared state and the internal energy. This last point constitutes the efforts of work in progress.

Recently reported classical trajectory studies[12] of the intramolecular and dissociation dynamics of hydrogen peroxide excited to the fifth overtone level—one quantum higher than the present study—show evidence for incomplete (vibrational) energy redistribution on the time scale of reaction. This is quite interesting and lends support to the aforementioned divided phase space model. These calculations showed that most of the vibrations are strongly coupled (on the time scale of the reaction). The exception being the OH oscillator which is initially unexcited. The exact nature of the division of the phase space must await more complete calculations which include rotation–vibration coupling and which are performed using a more refined (perhaps *ab initio*) potential energy surface. It would be interesting to perform these calculations for energies near the threshold. For comparison with theory experimental investigations for $v_{OH} = 6$ are in progress.

The next salient point to be understood is whether the nonmonotonic behavior of the rates with excess energy may be used to test for nonstatistical effects. An alternative issue is the effectiveness of statistical calculations (using the known spectral information) in simulating the same effects. These points shall be addressed in the following section.

B. Dependence of rates on photon energy

Coming to an understanding of fluctuations in the values of the reaction rates and fraction as a function of excitation energy is perhaps the more interesting of the two main issues which this Discussion section is intended to address. This is because the nonmonotonic behavior may reflect nonstatistical behavior. However, caution must be exercised since several explanations of the observed behavior are possible. These various interpretations will be investigated and the domain of their applicability examined, after discussing the effect of (conventional) thermal averaging.

1. Thermally averaged rates

To begin, assume that no transition frequency information is available. This implies transfering the ground state thermal distribution to the level of the fourth overtone. Consider the behavior which may be observed: (i) Sec. V A established that a quasibiexponential buildup behavior is to be expected; (ii) tuning the laser to greater energy (shorter wavelength) would have the effect of making the excited molecule acquire more internal energy, therefore, the expectation is for the reaction rates to increase monotonically with laser excitation energy. Intuitively, the state count in the transition state increases more rapidly than the state density (ρ_{EJ} changes by a factor of 3 over 2500 cm^{-1} beginning at 16 250 cm^{-1}) in the reactant for a given δE increase in the excitation energy. Therefore, the rate expression of Eq. (3) would be overall increasing with excitation energy. The expectation is for the rates to change monotonically with laser energy.

From the data for the initial component lifetime from Figs. 4 and 6 and Table II it may be seen that the behavior is hardly monotonic. Without invoking any further spectral knowledge concerning the fourth overtone it might be concluded that the behavior is nonstatistical. This conclusion, however, ignores the reality that excitation of different portions of an inhomogeneously broadened overtone band prepares different (in this case) initial distributions of states. The specifics of the excitation have a direct bearing on the subsequent unimolecular dynamics. Again, this nonstatistical mode-specific rate behavior may only be unequivocally demonstrated when the optical preparation is of a single (homogeneously broadened) spectroscopic state.

2. Effect of nonuniform state distribution

Now consider the resultant transient behavior, in the spirit of Eq. (4), for the case where the specific transition frequencies are still not known but the distribution of states excited to the fourth overtone level is non-Boltzmann. The idea is to examine the effect of enhancing (or diminishing) some portion of the tail of the probability distribution by generating the corresponding transient. In the thermally averaged calculation, the average J of reacting molecules is $\langle J \rangle = 23$ while the average reactant state energy above the 0–0 transition energy $\langle E \rangle \approx 1700\ cm^{-1}$ (recall that the barrier height with respect to this same reference is 1100 cm^{-1}). To simulate the effects of "hot" and "cold" nonthermal distributions, the (Boltzmann) distribution factor $\exp(-E/k_BT)$ was changed to $\exp^{[(\alpha - E)/k_BT]}$ with

$$\alpha = \begin{cases} 0, & E \leqslant 1600 \\ 500, & E > 1600 \end{cases} \text{ and } \begin{cases} 0, & E \leqslant 1600 \\ -650, & E > 1600 \end{cases}$$

for the hot and cold distributions, respectively. The values for α are expressed in units of cm^{-1}. The results are depicted in curves 2 and 3 of Fig. 9, and the fitted values are in Table III. Notice that by adjusting only the probability distribution the resultant transients (lifetimes as well as the fraction) are affected. One conclusion is that the specific variations in the distribution of optically prepared states may be the underlying cause of the experimentally observed fluctuations.

As a further illustration of the physical picture consider the model four level system—two ground states (1′ and 2′) optically coupled to two excited states. The latter two states (1 and 2) are sufficiently energetic to undergo reaction with rate constants k_1 and k_2. The corresponding absorption coefficients are ϵ_1 and ϵ_2. If the reaction proceeds exclusively to products in state m then a biexponential product buildup is observed with the aforementioned rates and fraction $\epsilon_1/(\epsilon_1 + \epsilon_2)$. Now cosider that the two excited levels of this four level system become two sets of levels with reaction rates $\{k_i\}_1$ and $\{k_j\}_2$ for reaction into the exclusive product quantum state m. Each absorption coefficient now refers to the respective set of levels. If there is no intersection of the two sets, and the members of each set are distributed such that the rates of one set are faster than the other, but within a set there is a distribution of rates, then preparation of one set or the other will result in a distribution of rates in the product buildup behavior. If both sets of states are prepared and if the difference in rates between the two sets is larger than the extent of the distributions within the sets, then a quasibiexponential transient behavior will be observed. The fraction will be essentially the same as before.

3. Effect of rotations

Variation of the J value for a given reactant energy can have a pronounced effect on the reaction rate especially near threshold. This is predicted by other statistical theories[35] as well. The conserved quantum numbers restrict the domain of the phase space (for the given E and J). The restriction imposed by J affects $N^{\ddagger}_{E^*J}$ and ρ_{EJ} differently, therefore, the rate varies with J. The implication is that this variation may have a strong influence on the observed rates of reaction because the average value of J may differ for various portions of the action spectrum for the fourth overtone. This point will be investigated more carefully in the following section.

4. Effect of combined spectral and thermal distributions

The focus of this section is to attempt to simulate the experimental biexponential and nonmonotonic behavior of the rates. This will be done by explicitly considering the spectral and E,J distributions of the initial excitation to the fourth overtone. Crim and co-workers[6(b)] have considered the spectral consequences of making an adiabatic separation, in the spirit of the Born–Oppenheimer approximation, of the rapid OH stretching motion from the low frequency torsional motion about the O–O bond. Implementation of this

method has allowed them to empirically fit the major features of the predissociation spectrum to: (i) hot band transitions of the torsional and/or O–O stretching mode; (ii) sequence band transitions; and (iii) combination bands of torsion with the $\Delta v_{OH} = 5$ overtone transition. It should be reiterated that these features would seem to be dominant in the predissociation spectrum since a zero-point transition to $v_{OH} = 5$ (as determined from the HOOH Birge–Sponer plot[6]) leaves the peroxide molecule 1100 cm^{-1} below the barrier to dissociation.

Using their recently reported torsional potential parameters[6(b)] and the analogous parameters for the ground state,[9] we have evaluated the transition frequencies from the initial and final eigenvalues (relevant to the $\Delta v_{OH} = 5$ transition), which were calculated as the solutions of a tridiagonal matrix of difference equations. The eigenvectors then were obtained using the same numerical routine and applied in the determination of the associated transition intensities. The time integrated intensity of product formation into a specific OH product state $N(\Omega = \frac{1}{2})$ is given by

$$I(E,J,K;N) = C\bar{\nu}A_{KJ}P'^{0}_{EJ}P_N|\langle v'\tau'|\hat{\mu}|v''\tau''\rangle|^2, \qquad (5)$$

where C is a constant ($\frac{8\pi^3}{3hc}$), $\bar{\nu}$ is the transition frequency in cm^{-1} units and τ is the torsional quantum number. The Boltzmann weighting factor for energy E and degeneracy terms are included in P'^{0}_{EJ}, P_N is the probability for formation of the OH product in state N, and A_{KJ} are the Hönl–London factors for (as an approximation[6]) ⊥ prolate symmetric top transitions.

Since the OH stretching and torsional motions are assumed to be separable, the transition moment may be decomposed into those portions with projections onto the stretch and torsional coordinates. The term for the square modulus can therefore be rewritten as $|\langle v'|\hat{\mu}|v''\rangle\langle\tau'|\tau''\rangle|^2$. This is in accord with the assumption of the OH overtone behaving as a LM state—that is $\hat{\mu}_{torsion} \sim 0$. It may now be seen that the intensity of hot band or combination transitions are dictated by the torsional mode overlap integral. The eigenvalues and therefore the transition frequencies indicate that there are three types of features in the fourth overtone band: (i) the spectral feature near 16 200 cm^{-1} (6173 Å) is enhanced by contributions from ν_3 (O–O stretch) hot band transitions; (ii) the region near 16 240 cm^{-1} (6158 Å) is enhanced by the presence of torsional hot band transitions; while (iii) the feature near 16 300 cm^{-1} (6134 Å) is most prominent because this is the region with the highest density of allowed transitions which have sufficient energy for dissociation. This is elaborated more explicitly by the values of $\langle J\rangle$ and $\langle E_{vib}\rangle$ listed in Table IV. The values for $\langle E_{total}\rangle$ as a function of laser excitation wavelength, which are not listed, fall in the range 1700 ± 100 cm^{-1} above the lowest rovibrational level of the fourth overtone.

A classical phase space theory is invoked in the calculation of the rates and product state distributions (PSD), and is combined with the above described spectral analysis. PST gives P_N for a given E and J. (The value of the C_6 parameter is 0.546×10^6 cm^{-1} $Å^6$.)[36] P_N is evaluated for each specific transition allowed within the simulated laser bandwidth. The relative intensities of the formation of product into the

TABLE IV. Calculated transient parameters including all spectroscopic transitions.

Probe trans.	Pump λ	τ_1 (ps)	τ_2 (ps)	Fract.	$\langle J\rangle$	$\langle E_{vib}\rangle$	No. trans.
$N=1$	6129	45	280	0.51	18.8	1040	185
	6132	60	270	0.22	17.6	1130	190
	6139	55	280	0.30	15.5	1310	180
	6142.5	100	315	0.43	15.5	1420	165
	6144	75	330	0.49	16.5	1455	150
	6146	85	300	0.57	17.0	1525	135
	6149	50	280	0.29	16.4	1620	120
	6157	45	290	0.39	16.3	1610	105
	6160	45	250	0.46	15.5	1630	110
	6163	30	350	0.87	16.2	1655	95

$N = 1$, 2, and 3 states as a function of excitation wavelength is obtained by summing Eq. (5) over all possible transitions and weighting each optical transition by the simulated laser bandwidth. This calculation allows for making a coarse-spectral-resolution comparison with the action (or predissociation) spectrum measured in Ref. 6. The agreement is good enough to be able to discern the major features observed in the experimental spectra for $N = 1$, 2, and 3. These results, which are highlighted in Table IV for different excitation energies, will be presented in more detail in another publication[37] (also see the Appendix). It suffices to say that the spectral simulation is faithful to the actual results and enhances the reliability of the simulated transients obtained below.

The time-dependent intensity of product formation into state N can be expressed, in analogy with Eq. (4), in a manner representative of the individual optically allowed transitions. Indexing these transitions by i and combining Eqs. (4) and (5) gives

$$P(N,t) = \bar{\nu}\sum_i M^i(A^i_{KJ})L(\delta,\bar{\nu})P^i_N \cdot P'^{0i}_{EJ}\cdot\{1 - e^{[-k_i(EJ)\cdot t]}\}, \qquad (6)$$

where $M^i = C|\langle v'|\hat{\mu}|v''\rangle|^2|\langle\tau'|\tau''\rangle_i|^2$, the laser bandwidth functional form $L(\delta,\bar{\nu})$ is Gaussian, FWHM: 3.0 cm^{-1}, P'^{0i}_{EJ} is the Boltzmann factor for the given E and J of the ith transition and $k_i(EJ)$ is the microcanonical rate for the ith transiton. For a simulated laser bandwidth of 3.0 cm^{-1} there are typically more than 100 possible optical transitions.

The form of the simulated transients are quasibiexponential rises (as opposed to single exponential), albeit there is a large diversity in the calculated behavior for the variously chosen transition energies $\bar{\nu}$ as listed in Table IV (see Fig. 10). There is some correlation between the experimentally measured fast component (Table II) and the transient value calculated here.[38] The correlation is achieved essentially independent of adjustable parameters, (i.e., there has been no fine tuning of the results) within the limits of the assumptions invoked in applying PST, in obtaining the density of states, and in only considering optical transitions involving the torsional and O–O stretching modes in determining the discrete transitions. The calculated long component lifetimes are about a factor of 2 to 3 faster than the measured

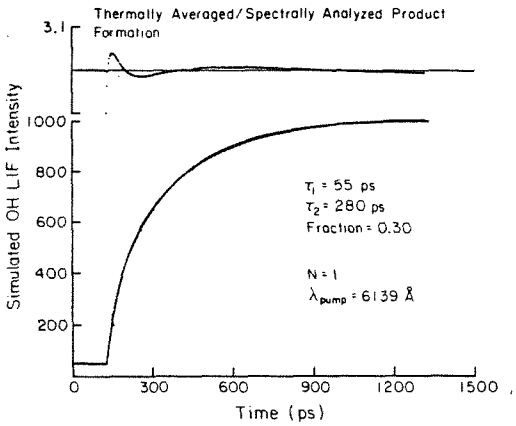

FIG. 10. PST calculation of product yield vs time, including all possible discrete transitions [Eq. (6)]. Excitation wavelength is 6139 Å, probe transition is for $N = 1$. The time scale is such as to facilitate comparison with the experimental results in Fig. 4. The residual, the difference between the data points and the fitting function, shows a damped increasing period oscillation which indicates that the simulated data is composed of more exponential components than just the two of the fitting function. (A linear predictor exponential fitting routine (Ref. 46), courtesy of Dr. M. Rosker, shows that there are approximately five significant components, in this case.) The biexponential model function, however, fits the overall shape of the transient allowing comparison to be made with the experimental data. The calculated transient was convoluted with a simulation of the response function (Ref. 45) to facilitate comparison with the experimental results. This is particularly important for the early time behavior (see the Experimental section).

values and show less correlation. It is expected that PST would yield lifetime results which are faster than the observed values. That the values differ by approximately a factor of 2 might not be surprising in that the transition state is being modeled as very loose. The question of the degree of "flexibility" of the transition state and its effect on the observed behavior (rates and product state distributions) is currently being investigated.[37]

A final remark about the dependence of $P(N,t)$ on N. In realizing the importance of considering discrete transitions for simulation of the experimental results, the question of the influence of the N quantum number on the observed OH product formation may be investigated. Analysis of the kinetics of reaction into the several product channels shows that if a single resonance is excited or reached by energy redistribution, then all products form with the same time constant (see paper I). While the rates are the same, the relative probabilities for the formation of specific product states do vary. In the present study it is not possible to excite a single resonance because of the wide distribution in E and J. The different energy and angular momentum constraints for the formation of the OH product in, e.g., $N = 2$ as compared to $N = 1$, for a distribution of reactant E and J values, changes the number of initial states which may correlate to this product. Such constraints will effect the product yield and the fraction and rates of the product buildup. This is most important in the case of a reaction which proceeds near threshold, it may not be a significant effect for sufficiently large E. Curve 5 of Fig. 9 shows the relative amplitude of the $N = 2$ thermal averaged product formation to be reduced in comparison with the $N = 1$ result. The fitting parameters are the same as curve 4, the exception being that curve 4 was normalized to the same final value (for the plotted range) as curve 1 to facilitate visual comparison.

C. Homogeneous linewidth and IVR: "T_1" and "T_2"

In a molecule with a complex level structure it is important to define the origin of homogeneous broadening in order to interpret the observed spectral results and their impact on predissociation dynamics. A simple model for HOOH, which yields the intrinsic linewidth contributions from the different time-dependent intramolecular processes, can be described as follows. An optically active mode (in this case the OH overtone state ϕ_s) couples to optically inactive bath modes, $\{\phi_l\}$, in the peroxide vibrational/rotational phase space. These states are in turn coupled to the dissociation "continuum" of OH product states (including translational motion). The coherent preparation of the molecular eigenstates (of the Hamiltonian $H = H_0 + V_{sl}$) with a transform limited laser pulse produces the initial zeroth-order state ϕ_s provided the laser bandwidth spans all relevant eigenstates. That is, the initially prepared superposition state in the diagonalized representation is

$$\Psi(0) \equiv \phi_s = \sum_n c_n |\psi_n\rangle,$$

where the ψ_n are the molecular eigenstates with the coefficients c_n. This initial nonstationary state ("packet") will evolve in time, the degree of evolution represented by $|\langle\phi_s|\Psi(t)\rangle|^2$. The time scale for this dephasing is determined by the degree of coupling and the extent of the energy spread of the ψ_n. Following the dephasing, the states evolve by energy relaxation (in this case by predissociation) which leads to a decrease of the HOOH population and concomitant increase in the OH population. This picture is similar to the description advanced for IVR[39] and multiphoton processes, where "T_1" and "T_2" type processes are described.[40] This model was used in paper I[2] to describe the predissociation of NCNO. The HOOH predissociation, however, occurs on the ground state potential energy surface—therefore, only vibrational energy redistribution is required.

With these ideas in mind, it may be understood that the action (or predissociation) spectrum linewidth, which is dominated by inhomogeneous effects, will have a more significant contribution from the dephasing behavior than from the energy relaxation effects. The value of this energy relaxation contribution is the Fourier transform of the rates of reaction measured in these experiments. The linewidth contributions from the dissociation vary from 0.05 to 0.15 cm^{-1} (assuming a Lorentzian line shape), as determined from the fast component of the biexponential buildup. This addition to the linewidth, which is due to population relaxation, is very small compared to the inhomogeneous apparent width of 200 cm^{-1}. Our experiments demonstrate that the OH-stretch overtone band is definitely inhomogeneously broadened to a resolution of < 10 cm^{-1}. Conversely, this gives an upper limit for the homogeneous broadening. These limits

for the inhomogeneous and homogeneous broadenings were established by measuring the rates of OH product appearance as the laser (bandwidth 3 cm^{-1}) was scanned within the main overtone band region (see Fig. 6). The results of a recent study of the action spectrum of jet-cooled HOOH by Butler *et al.*[41] is in agreement with the time-resolved results of Scherer *et al.*[5] in that these jet spectra for the $\Delta v_{OH} = 4$ and $\Delta v_{OH} = 6$ overtone transitions show sharp features which are much narrower than the apparent linewidth for the room temperature spectra.[6] The spectra reported therein show the linewidth (instrument limited) to be approximately 0.08 and 1.5 cm^{-1} for the transitions to the third and fifth overtones, respectively. The contribution of the population relaxation to the linewidth is not determined in their fifth overtone ($\Delta v_{OH} = 6$) results since time-resolved results are not yet available for this state.

The density of states of HOOH near threshold is about 10–200 depending on J. If ten states are effectively involved in the coupling, then the linewidth (due to energy relaxation) and level spacing are comparable. For higher densities the $\{|l\rangle\}$ manifold is essentially a quasicontinuum. This is especially the case considering that the linewidth due to dephasing could be much larger than the 0.05–0.15 cm^{-1} width. (It should be noted that the phase space is not necessarily composed of only a single $|l\rangle$ manifold; a requirement for obtaining nonstatistical behavior is that at least two subspaces are present, as discussed earlier, in Sec. V A 2.) In this limit of fast IVR, the measured picosecond transients give the predissociation rates.

Finally, the inhomogeneous width reported herein for a relatively small molecule might turn out to be general for large molecules. There is some evidence for inhomogeneous contributions to the LM transition in larger systems.[42] Further pump–probe experiments are in progress to obtain energy relaxation and dephasing rates for $v_{OH} = 6$ of HOOH (an other molecular systems) in a molecular beam to further understand the origin of homogeneous line broadening and IVR for high energy LM vibrational states.

VI. CONCLUSIONS

This paper, the second in the series, presents picosecond time-resolved studies of the overtone ($v_{OH} = 5$) initiated unimolecular reaction $HOOH + h\nu \rightarrow 2\,OH(D_0 = 49.6\ kcal\ mol^{-1})$ and provides a detailed account of our previously communicated results.[5] The primary findings reported here are: (a) the measurement of the homogeneous contribution(s) to the linewidth; (b) observation and analysis of quasibiexponential and nonmonotonic in pump wavelength behaviors; and (c) determination of the significant difference in the rate(s) of dissociation for overtone and repulsive state excitation.

(a) The OH local-mode transition to the fourth overtone ($v_{OH} = 5$) is inhomogeneously broadened. The apparent width is observed to be about 200 cm^{-1}, while the predissociation rate contribution to the *homogeneous* width is 0.05–0.15 cm^{-1}. The inhomogeneity of the spectra is evident from the results of picosecond experiments which examined the variation of the transient behavior as a function of the excess vibrational energy (for excitation within the LM absorption band) in HOOH. The homogeneous contribution is determined from real-time measurements of the actual rate of OH product formation. The energy relaxation time (T_1) is 30 to 100 ps while the pure dephasing time (T_2') is $\geq$0.5 ps.

(b) The time dependent behavior of OH product formation (for each of the product rotational states studied) is (i) quasibiexponential and (ii) nonmonotonic with respect to the pump laser wavelength. The experimental data is analyzed with two different perspectives in mind. First, the possibility of nonstatistical (non-RRKM) behavior is addressed and related to both of these observations; biexponential and nonmonotonic behaviors. In this case, a divided vibrational phase space is invoked and a simple kinetic model may be used to reproduce the biexponential behavior. Second, the initial thermal distribution and the inhomogenious nature of the spectral transitions within the laser bandwidth are incorporated into an analysis of the present studies. Considering the multitude of discrete transitions possible for a given laser bandwidth facilitates understanding the nonexponential and nonmonotonic behavior of the rates in the predissociation of HOOH at room temperature. Deciding whether these behaviors reflect nonstatistical dynamics or not must await the results of future beam experiments. Such molecular beam studies, similar in spirit to those of papers I and III, should allow for gaining an understanding of the photofragmentation in a state-to-state manner. Such measurements will also allow critical comparisons to be made with statistical theories and with the results obtained from the model calculations of Uzer, Hynes, and Reinhardt and others. Our goal in such experiments is to resolve the different timescales for IVR and predissociation, as discussed in the model given here.

(c) Experiments were performed wherein the OH fragments are produced following UV excitation of the peroxide, instead of reaction initiation by way of overtone (visible) excitation. The results indicate that, in constrast with the 30–100 ps buildup time (depending on pump wavelength) for the overtone predissociation, the UV initiated dissociation of HOOH may be modeled as a single exponential rise of $\leq$8 ps. This observation is consistent with the interpretation that the upper potential energy surface, reached via the UV excitation, is directly dissociative–repulsive in nature. These experimental results also provide a way (in addition to the other diagnostic experiments reported herein) to determine that the dynamics observed for the very weak absorption overtone transition are not due to a two-photon pump process.

ACKNOWLEDGMENTS

This research was supported by a grant from the National Science Foundation (CHE-8512887). Some additional support was provided by the Presidential Fund and the Keck Foundation. We thank Professor Rudy Marcus for many useful discussions concerning RRKM theory. We would like to thank Lutfur Khundkar for enlightening conversations regarding statistical theories. We thank Dr. Joseph Perry for his invaluable assistance during the formative period of this project and for his continued interest, and Dr.

Fuad Doany for his help in the initial state of this research. We are also grateful to Professor F. Crim for his help and interest throughout these studies, and Professor J. Troe for communicating results prior to publication. Finally, the early attempts to study overtone dynamics on the picosecond time scale (1981) involved the dedicated efforts and hard work of Mr. Joseph Perry and Dr. Eugene Ryabov, and this must be acknowledged here.

APPENDIX

The direct count method employed considers all of the bound torsional eigenstates, which are evaluated using the torsional potential parameters of Hunt *et al.*[9] and Dubal *et al.*[6] The torsional eigenvalues and eigenvectors are obtained by numerically solving the Schrödinger equation. The values for the terms of the kinetic energy prefactor $\alpha(\chi)$ and the potential $V(\chi)$ are given in Table I for the ground and $v_{OH} = 5$ torsional potentials. The issue of treating the hindered rotor levels above the torsional barrier was not considered here; only the torsional levels up to the (*cis*) barrier height are considered. Moreover, the issue of torsion–rotation interaction was ignored; this has the effect of maintaining the same values for the rotational constants for all states. The two rotational motions related to this prolate near symmetric top's B and C constants were treated as adiabatic rotations, whereby J is a constant of the motion and the K quantum number (the projection of J onto the figure axis) is not. Nuclear spin statistics and the OH $\Omega = \frac{1}{2}$ OH spin–orbit state were not included in the calculation. In our previous paper[5] we incorporated a different direct count algorithm (Hase–Bunker[43]) which gave qualitative agreement with the experimental results (i.e., it gave a biexponential form), but was quantitatively in poorer agreement than the present calculation. Our previous calculation postulated a somewhat tight transition state as opposed to the present calculation which invokes a loose transition state via PST.

Finally, it should be mentioned that the purpose of the present calculation has been to illustrate, in the simplest manner, the comparison between the predictions of standard statistical theories and our experimental results. A more complete theoretical treatment, which includes a modified treatment for the determination of the transition state will be given in Ref. 37.

[1]See for example, K. V. Reddy, D. F. Heller, and M. J. Berry, J. Chem. Phys. **76**, 2814 (1982); K. V. Reddy, R. G. Bray, and M. J. Berry, in *Advances in Laser Chemistry*, edited by A. H. Zewail (Springer, New York, 1978), p. 48.

[2]L. R. Khundkhar, J. L. Knee, and A. H. Zewail, J. Chem. Phys. **87**, 77 (1987), paper I in this series.

[3]See e.g., B. R. Henry, Acc. Chem. Res. **10**, 207 (1977); W. M. Gelbart, P. R. Stannard, and M. L. Elert, Int. J. Quant. Chem. **14**, 703 (1978); H. L. Fang and R. L. Swoford, J. Chem. Phys. **72**, 6382 (1980); M. L. Sage and J. Jortner, Adv. Chem. Phys. **47**, 293 (1981); M. S. Child and L. Halonen, *ibid.* **57**, 1 (1984); E. L. Sibert, W. P. Reinhardt, and J. T. Hynes, J. Chem. Phys. **81**, 1115 (1984).

[4]J. W. Perry and A. H. Zewail, J. Chem. Phys. **70**, 582 (1979); Chem. Phys. Lett. **65**, 31 (1979); J. Phys. Chem. **86**, 5197 (1982); J. Chem. Phys. **80**, 5333 (1984).

[5]N. F. Scherer, F. E. Doany, A. H. Zewail, and J. W. Perry, J. Chem. Phys. **84**, 1932 (1986).

[6(a)]T. F. Rizzo, C. C. Hayden, and F. F. Crim, Faraday Discuss. Chem. Soc. **75**, 223 (1983); T. F. Rizzo, Ph.D. thesis, University of Wisconsin (Madison), 1984. (b) H. R. Dubal and F. F. Crim, J. Chem. Phys. **83**, 3863 (1985); T. M. Ticich, T. R. Rizzo, H. R. Dubal, and F. F. Crim, J. Chem. Phys. **84**, 1508 (1986).

[7]L. T. Molina and M. J. Molina, J. Photochem. **15**, 97 (1981); J. J. Willman, D. F. Jennings, W. B. Olson, and A. Goldman, J. Mol. Spectrosc. **117**, 46 (1986); G. A. Khachkuruzov and I. N. Przhevalskii, Opt. Spectrosc. **36**, 172 (1974); **44**, 112 (1978); P. A. Giguere, J. Chem. Phys. **18**, 88 (1950).

[8]D. Cremer, J. Chem. Phys. **69**, 4440 (1978); R. Block and L. Jansen, *ibid.* **82**, 3322 (1985), and references therein.

[9]E. Hirota, J. Chem. Phys. **28**, 839 (1958); R. L. Redington, W. B. Olson, and P. C. Cross, *ibid.* **36**, 1311 (1962); R. L.Hunt, R. A. Leacock, C. W. Peters, and K. T. Hecht, *ibid.* **42**, 1931 (1965).

[10]G. Ondrey, N. van Veen, and R. Bersohn, J. Chem. Phys. **78**, 3732 (1983); S. Klee, K. Gericke, and F. J. Comes, *ibid.* **85**, 40, 4463 (1986).

[11]E. M. Evleth, J. Am. Chem. Soc. **98**, 1693 (1976).

[12]T. Uzer, J. T. Hynes, and W. P. Reinhardt, Chem. Phys. Lett. **117**, 600 (1985); J. Chem. Phys. **85**, 5791 (1986); see also the work of Ref. 47.

[13]H. Okabe, *Photochemistry of Small Molecules*, (Wiley, New York, 1978).

[14]H. Klann, J. Kuhl, and D. von der Linde, Opt. Commun. **38**, 390 (1981).

[15]A. Yariv, *Quantum Electronics*, 2nd ed. (Wiley, New York, 1975); G. R. Flemming, Adv. Chem. Phys. **49**, 1 (1982), and references therein.

[16]E. P. Ippen and C. V. Shank, in Topics in Applied Physics, edited by S. L. Shapiro (Springer, Berlin, 1977), Vol. 18, p. 83.

[17]D. von der Linde, Appl. Phys. B **39**, 201 (1986).

[18]H. A. Pike and M. Hersher, J. Appl. Phys. **41**, 4562 (1970).

[19]D. P. Millar and A. H. Zewail, Chem. Phys. **72**, 381 (1982); G. R. Flemming Adv. Chem. Phys. **49**, 1 (1982).

[20]J. M. Clemens, J. Najbar, I. Bronstein-Bronte, and R. M. Hochstrasser, Opt. Commun. **47**, 271 (1983).

[21]N. F. Scherer, J. W. Perry, F. E. Doany, and A. H. Zewail, J. Phys. Chem. **89**, 894 (1985).

[22]Y. R. Shen, *The Principles of Nonlinear Optics* (Wiley, New York 1984).

[23]I. S. McDermid and J. B. Laudenslager, J. Chem. Phys. **78**, 1824 (1982); K. H. Gericke and F. J. Comes, Chem. Phys. **65**, 113 (1982).

[24]G. P. Smith and D. R. Crosley, J. Chem. Phys. **85**, 3896 (1986); J. H. Bechtel and R. E. Teets, Appl. Opt. **18**, 4138 (1979).

[25]D. W. Marquardt, J. Soc. Ind. Appl. Math. **11**, 431 (1963); P. R. Bevington, *Data Reduction and Error Analysis for the Physical Sciences*, (McGraw–Hill, New York, 1969); D. P. Millar, Ph.D. thesis, California Institute of Technology, 1982.

[26]A true absorption spectrum, instead of the action spectrum, would be an asset to gaining a complete understanding of the transitions and transition frequencies for $v_{OH} = 4,5,6$.

[27]G. H. Dieke and H. M. Crosswhite, J. Quant. Spectrosc. Radiat. Transfer. **2**, 97 (1962); W. L. Dimpfl and J. L. Kinsey, *ibid.* **21**, 233 (1979); M. Alexander and P. Dagdigian, J. Chem. Phys. **80**, 4325 (1984).

[28]K. Gericke, S. Klee, F. Comes, and R. N. Dixon, J. Chem. Phys. **85**, 4463 (1986); M. P. Docker, A. Hodgson, and J. P. Simons, Chem. Phys. Lett. **128**, 264 (1986); P. Andersen, G. S. Ondrey, and B. Titze, J. Chem. Phys. **80**, 2548 (1984).

[29]See for example, J. A. Silver, W. L. Dimpfl, J. H. Brophy, and J. L. Kinsey, J. Chem. Phys. **65**, 1811 (1976).

[30]It would also be interesting to perform UV excitation experiments at twice the photon energy of that used in the overtone excitation, i.e., about 306 nm.

[31]N. F. Scherer, J. L. Knee, D. D. Smith, and A. H. Zewail, J. Phys. Chem. **89**, 5141 (1985).

[32]See J. W. Perry, N. F. Scherer, and A. H. Zewail, Chem. Phys. Lett. **103**, 1 (1983); L. R. Khundkar, R. A. Marcus, and A. H. Zewail, J. Phys. Chem. **87**, 2473 (1983).

[33]W. L. Hase, J. Phys. Chem. **90**, 365 (1986); R. A. Marcus, J. Chem. Phys. **85**, 5035 (1986).

[34]J. L. Knee, L. R. Khundkar, and A. H. Zewail, J. Chem. Phys. **87**, 115 (1987), paper III in this series.

[35]See paper I for references of RRKM, SACM, PST, and others. Also, we

were informed in a private communication (F. Crim) that the rate of reaction near threshold has a significant dependence on the J quantum number (determined from SACM calculations by Troe's group); work in progress.

[36]See J. O. Hirschfelder, C. F. Curtis, and R. B. Bird, *Molecular Theory of Gases and Liquids* (Wiley, New York, 1954); the value of C_6 was obtained by a similar procedure to that referenced in Ref. 6.

[37]N. F. Scherer, L. R. Khundkar, D. Wardlaw, R. A. Marcus, and A. H. Zewail (work in progress).

[38]The fraction of the amplitude of the fast component to the total amplitude is found to be fluctuating (see Tables II and IV). This may depend on the extent of the rotational energy contribution to the total energy of reaction. Additionally, Table IV shows that the contribution of vibrational energy to the total energy is the smallest near 6134 Å and largest neart 6160 Å (see the text and Ref. 6).

[39]P. M. Felker and A. H. Zewail, J. Chem. Phys. **82**, 2961, 2975, 2994 (1985).

[40]See e.g., N. Bloembergen and A. H. Zewail, J. Phys. Chem. **88**, 5459 (1984).

[41]L. J. Butler, T. M. Ticich, M. D. Likar, and F. F. Crim, J. Chem. Phys. **85**, 2331 (1986).

[42]M. C. Chung and R. N. Zare, J. Chem. Phys. **82**, 4791 (1985).

[43]W. L. Hase and D. L. Bunker, program QCPE-234, Caltech, Pasadena, CA 91125.

[44]D. M. Wardlaw and R. A. Marcus, J. Chem. Phys. **83**, 3462 (1985).

[45]The calculated transients, of the form $P(N,t)$, Eq. (6), are convoluted with a Gaussian pulse to produce transients for comparison with the experimental results. The procedure is similar to that of Eq. (1) except that the transients here are rising exponentials.

[46]H. Barkhuijsen, R. DeBeer, W. M. M. J. Bovee, and D. Van Ormonolt, J. Magn. Reson. **61**, 465 (1985).

[47]B. G. Sumpter and D. L. Thompson, J. Chem. Phys. **86**, 2805 (1987); John S. Hutchinson, *ibid.* **85**, 7087 (1986), and references therein.

CHAPTER VI.

Picosecond Photofragment Spectroscopy IV. Perturbed Fragment Spectroscopy of the Overtone Initiated Unimolecular Reaction: H_2O_2 (ν_{OH}=6) → [HO-OH]*→2OH

6.1 INTRODUCTION

Much of condensed phase chemical reaction dynamics, that is "traditional chemistry," occurs on the ground electronic potential energy surface.[1] Simple bimolecular processes include a reaction step, which involves some type of bond-breakage. The fact that the (complex) reaction dynamics occur in, for example, a liquid environment, will tend to complicate detailed investigation of the role of intramolecular energy redistribution in the reaction process. The study of model or prototype bond-fission reactions under isolated gas phase conditions would serve to reduce the complexity causally related to the multi-body collisional reaction environment.[2]

A prototype molecular system for the study of ground potential energy surface (PES) bond fission would satisfy several desired criteria. First, the photo-excitation step optically prepares an initially well-defined state. Second, the reaction product fragments may be readily detected by sensitive spectroscopic techniques such as Laser Induced Fluorescence[3] (LIF) or Multi-Photon Ionization[4] (MPI). Third, the dissociation dynamics should be sufficiently simple (few relevant degrees of freedom) such that an effective PES may be obtained for the actual bond-fission process. This will yield insight into the simple fragment bimolecular recombination dynamics, i.e., the reverse reaction. Finally, it may be desirable to concieve of a means to probe the reaction transient intermediate configurations that lie between the initially prepared state and the final product states.

The overtone pump initiated unimolecular dissociation of hydrogen peroxide has been chosen as a molecular system that satisfies the aforementioned criteria. Numerous spectroscopic investigations of the ν_{OH}=4, 5, 6 OH-stretching levels have been performed by Crim and co-workers.[5-8] They have demonstrated that the reaction dynamics for the fourth and fifth overtone levels (ν_{OH}=5,6) do occur on the ground electronic PES. This implies that Intramolecular Energy Redistribution (IVR) from the OH stretch to the O-O stretch coordinate must be occuring prior to

actual dissociation. Their study of the third overtone[8b] energetically prohibits dissociation on the ground PES. Rather, the IVR process follows the pulsed laser excitation to the overtone level. A second photon, of the same or different wavelength, pumps the system to the electronically excited continuum. The actual dissociation dynamics occur on the repulsive excited electronic surface.

Previous studies from the Caltech group[9] have directly probed the dynamics of photo-induced ground state vibrational predissociation[10] associated with fourth overtone excitation of HOOH. These researchers found that the dissociation rates ranged from 30 to 600ps and did not increase in a monotonic fashion with increasing photolysis energy. It was demonstrated that a consideration of the distribution of states that underly the excitation laser bandwidth gave semi-quantitative agreement with the measured results. The state-dependent rates, which were weighted by a Boltzmann factor and by the excitation Franck-Condon factors, were obtained from a classical count Phase Space Theory (PST) calculation. The extensive thermal averaging reduced the sensitivity of the pump-probe experiment to state specific dynamics. However, it is not totally possible to rule out some type of no-statistical, divided phase space, condition could give an effective bi-exponential rise in the OH product concentration. Finally, these authors inferred the homogeneous linewidth to be less than $10cm^{-1}$. Such a (Lorentzian) spectral width would correspond to a 3.6ps dephasing time. Dephasing, in this context, refers to the decay of the initially prepared OH-stretch state vector. In a zeroth order picture, this occurs by way of energy transfer to other intramolecular degrees of freedom.

This chapter describes the dynamical results obtained for the overtone induced vibrational predissociation of HOOH when pumping ν_{OH}=6. The present reaction conditions energetically allow all molecules to react, which is contrary to the reaction dynamics of the fourth overtone level. In the latter case only those molecules with at least $1100cm^{-1}$ thermal energy may form the OH product. The fifth overtone lies $1570cm^{-1}$ above the D_o(=49.7kcal/mole) of the O-O bond. Therefore, the initial ground state modes with the highest occupation number will, in general, contribute

most significantly to the absorption and action spectra. Therefore, the dynamics will occur with, on the average, more energetic molecules in the ν_{OH}=6 vs. ν_{OH}=5 case. Moreover, a larger fraction of the energy for reaction will obtain from the laser excitation; less available energy will come from other thermally excited modes. Implementation of the previously developed picosecond pulse overtone-pump and LIF-probe method should allow for more critical study of the promptness of the IVR process in comparison with the rate of molecular bond fission. It will also be of interest to demonstrate the spectroscopic manifestations of (non-nascent) perturbed fragment absorption of the OH photoproduct.

Section 6.2 of this chapter consists of a brief experimental exposition. Section 6.3 describes the experimental results and provide a discussion for the interpretation of the observations. The significant new observations and interpretations will be summarized and focused, along with some ideas for future studies, in the conclusion section, 6.4.

6.2 EXPERIMENTAL SECTION

The experimental apparatus consists of essentially three parts. First, the tunable picosecond pulse generation and amplification system. Second, the optical scanning delay line, second harmonic generation optics and the low light scatter HOOH gas cell. Third, the electronic signal detction and processing equipment. A considerable fraction of this apparatus has been described in the Experimental chapter of this thesis and also in Ref. 9 (cf. Chapter 5). Therefore, the briefest possible outline will suffice, except for the somewhat more detailed elaboration of the features unique to the present endeavor.

The picosecond pulse generation scheme consists of a mode-locked Nd:YAG laser synchronously pumping a length-matched linear cavity dye laser. A mixed gain/saturable absorber (R6G/DQOCI) provided the dye laser gain and enhanced (passive) mode-locking. The 3ps FWHM Gaussian output pulses had a spectral

bandwidth of .5cm^{-1}, indicating nearly transform limited pulse formation conditions.

Pulse amplification was done in two separate dye amplifiers pumped by the 532nm and 354.8nm harmonics of a 20Hz pulsed Q-switched Nd:YAG laser. The first amplifier consists of four dye gain stages, and the dye mixture R640/CV670 was used as the gain medium. The 0.5mJ 3.5ps pulse output was split 80:20 with the 20% proceeding to an optical rrangement for frequency doubling and thus facilitated LIF detection of the $^2\Sigma \leftarrow {}^2\Pi$ OH transition.

The remaining 80% of the 616nm beam is focused into a cell of nanopure water to generate an optical continuum. The continuum pulse is temporally and spectrally processed in a quadruple pass arrangement through a 1800 l/mm hoographic grating and f=25cm cylindrical lens optical set-up. The details of the design are presented in Chapter 2 of this thesis. Th spectral bandpass is 2.5Å FWHM at 528nm. This frequency is chosen to allow for single photon resonant pumping of the $\Delta\nu_{OH}$=6 transition in HOOH.[7]

The spectrally selected continuum pulse is amplified from about 2nJ to 0.3mJ pulse energy and has a 4ps FWHM Gaussian temporal width. The second amplifier is a three-stage design where the gain medium is coumarin 522 (Exciton Chemical) dissolved in ethanol. The 355nm third-harmonic of the Q-switch YAG was employed in pumping the coumarin dye stages. Transverse pumping of the first two dye gain stages allowed for uniform amplification without imparting significant structure on the transverse mode profile of the 528nm beam. The final, longitudinally pumped amplification stage does impart a trnsverse multi-mode profile, which consists of several concentric TEM_{10^*} modes.[11] This type of structured transverse mode profile will limit the beam waist when focusing into the gas cell.

The two beams enter the arms of a scanning delay-line interferometer, with the 616nm light in the variable delay arm. This 616nm light is focused into a 1mm KDP crystal and the second harmonic light (at 3078.5Å for the H $Q_1(1)$ transition) is recollimated and focused into the gas cell with a 1 meter plano-convex lens.

The pump beam, at 528nm, is focused into the gas cell using a 0.8 meter plano-convex lens. The pump and probe beams are recombined on a dichroic reflector and propagate collinearly through the gas cell. The beams are independently focused to allow for matching the positions and diameters of the pump and probe beam waists. The beam waists are both about 150μm with the pump being slightly larger (~10%). The collinear copropagation of the two laser beams allows for imaging more than a 1cm optical path onto the 2'' optical area of the single photon counting photomultiplier tube.

The measured signal due to one pump phoon and one probe photon is quite weak and is on the order of 1 count per second. The photon counting signal acquisition electronics are the same as those used in the ν_{OH}=5 experiments of Chapter 5.

The laser pump-probe response function was obtained by difference frequency generation[12,13] of the 308 and 528nm pulses. The 738nm light was spectrally filtered with a red-pass cut-off filter and monitored with a silicone pin-photodiode. The difference frequency generation in KDP allows or obtaining the experimental t=0 and the pump-probe pulse cross-correlation that is the instrument response function of the two-color laser apparatus. The temporal system response is 5.5ps FWHM. The good temporal synchronization of the pump and probe pulses is obtained by way of selecting the pump pulse from the optical continuum, which is in turn generated from the fundamental of the probe pulse.

6.3 RESULTS AND DISCUSSION

Figure 1 show a schematic outline of the conceptual idea of the relevant intramolecular and rection dynamics. The picosecond pulse excitation projects hydrogen peroxide molecules to the level of the fifth overtone. These molecules then proceed to redistribute the vibrational energy, which is initially localized in the OH-stretch,[14] to the other molecular degress of freedom. The observable reaction dynamics obtain when sufficient vibration excitation becomes localized in the O-O

stretching coordinate to satisfy the energy threshold of the bond dissociation energy. Subsequent dynamics may include angular fragment interactions on the way to forming the nascent OH products. Generally, the OH LIF is monitored for the nascent $R_1(2)$ fragment. The possibility of monitoring the spectrally perturbed OH product will be discussed below.

Figure 2 shows the rise of the OH LIF intensity plotted vs. pump-probe delay time. The observed signal is enhanced above a background level obtains from the probe alone. The probe alone signal results from UV photon absorption by HOOH to the dissociative electronic surface followed by absorption of a second UV photon by the OH reaction product. The 1+1 pump-probe enhanced signal obtains for pulse excitation to the fifth overtone level and probe pulse electronic excitation of the OH product. The signal rises to a plateau level because the OH photoproduct is not removed by recombination nor does the K=2 ($R_1(2)$ transition) OH population change via collisional (de)-activation on the 35ps timescale. The experimental curve is obtained for 527nm excitation with 0.1mJ pulse energy. The probe intensity at 207nm is attenuated to less than $1\mu J$/pulse.

The figure also shows the integral of the pump-probe cross-correlation (solid line). It is seen that the integrated response function rises more promptly than the unimolecular reaction data. A simple single exponential fit, including convolution with the system response function, yields a lifetime of 2.1±0.5ps with a phenomenological time shift between the data and the response of $\Delta\tau$=0.45ps. The time shift obtains from the minimization of the sums of the squares of the deviations between the actual data and the fitted curve. The fitting algorithm is a nonlinear least squares method developed by Marquardt.[15] This fit to the data is shown in Figure 3a.

The obvious differences between the data and the fit of Figure 3a could be improved on by conidering the rise to be a biexponential rising function convoluted with the system response function. The fitting procedure minimized χ^2 for the parameters $\tau_1 = 0.7 \pm 0.5$ps, $\tau_2 = 1.9 \pm 0.75$ps and $\Delta\tau$, the phenomenological shift,

of 0.25ps. Figure 3b shows the resultant fit, which is clearly a better approximation to the actual dynamics than Figure 3a. The fitted curve appears to capture the essential dynamics of nascent OH appearance. However, the idea of an additional temporal shift should still be considered.

6.3.1 Review of Theoretical Studies of HOOH Vibrational Predissociation

Classical trajectory studies by Uzer *et al.*[16] have developed an insight into the intramolecular paths for energy flow from the initially prepared OH-stretch local mode into the other molecular degrees of freedom. The general conclusion, as exhibited by the ensemble aveaged probability of populating the HOO bend and O-O stretch zeroth-order motions, is that the energy flow proceeds from the local mode initially into combination excitation of OH stretch (with fewer quanta) and HOO-bend quanta. The vicinal bending motion couples into both the O-O stretching mode and the distal bend. The initial decay of population out of the local mode is calculated[16] to occur in a time period of 0.5ps. However, the IVR process is not complete on the 5ps timescale of the calculation. They[16] estimate a dissociation lifetime of 6ps. These authors did not observe any fast and direct (nonstatistical) energy flow to produce O-O bond fission. Therefore, no reaction product arises from the calculation in the first 0.5ps following the initiation of the dynamics.

Sumpter et al.[17] have examined intramolecular energy flow in HOOH for ν_{OH}=6 initial excitation. Their force field does not contain any mode couplings (potential coupling) and does not allow for large amplitude motions as the bonds are extended due to IVR. They observed[17] slow energy flow out of ν_{OH}=6 and did not see any dissociation on a 5ps timescale. Moreover, the restricted nature of their potential is in disagreement with the observed experimental dynamcs as may be seen in Figures 2 and 3.

A statistical analysis of the HOOH $\rightarrow$ 2OH unimolecular reaction has been carried out using the Statistical Adiabatic Channel Model (SACM).[18] The model allows for the calculation of reaction rates for different values of total available

energy and total angular momentum. The reactant lifetime for initial energy of 1600cm^{-1} above the dissociation threshold gives τ_J=3.2, 5.6, 10.0ps for J=0, 10, and 40, respectively. For an excess energy of E_{xs}=2000cm^{-1} and J=0, 10, 40, the lifetimes are τ=2.7, 3.7, and 6.7ps, respectively. The state averaging for the initial reactant thermal population distribution and for overtone transitions within the present laser bandwidth will primarily yield ν_{OH}=6 (E,J) values, which are in this range. The experimental excess energy (energy above the reaction threshol) is about 1600cm^{-1} for the $\Delta\nu_{OH}$=6 excitation.

Finally, two quantum mechanical studies are relevant to present dynamical unimolecular reaction results. The model study by Hutchinson[19] considers the process of state preparation, IVR, and unimolecular reaction. He finds that reaction yield following 0.1 to 10ps pulsed overtone excitation is a sensitive function of pulse duration and spectral detuning fro the "eigenstate" resonances. His model contains two modes, one being the overtone and the other related to the dissociating mode. He makes the observation that an inverse relation exists between the absorption line-width and the transition moment for any eigenstate. A state with a large transition moment has narrow width and is thus long lived. A state with a large projection on the pure overtone state (which carries the transition strength) has proportionally less dissociative character than a state with a projection onto fewer quanta of the high frequency (OH-stretch) mode state but more quanta projected onto the dissociative mode. The above statement is quantitatively demonstrated in numerical calculations. The conclusion to be drawn from this quantal study is that multiple eigenstate excitation could possibly result in a multiexponential-like rate of product formation.

The second quantum study[20] specifically treats the fifth overtone vibrational predissociation dynamics. The investigation uses the potential surface developedin Ref. 16 to evaluate the dissociation transition probability from a given initial state (considering quanta of various combinations in the five vibrational modes). It is found that the probability for direct dissociation from the fifth overtone state to the

O-O continuum is too small to lead to the magnitude of the OH product observed in experiment. The transition amplitude for dissociation becomes significant if the O-O stretching mode is relatively highly excited. It is necessary to include IVR dynamics in the analysis of the HOOH molecular reaction dynamics. The authors[20] map out a series of vibrational combination levels that are nearly isoenergetic with the initial $|6,0,0,0,0>$ state (i.e. six quanta in the overtone stretching mode only). They calculate the time dependent dynamics of population flowing into each of the ten combination levels relevant to the dynamics. The analysis obtains by way of a master equation for the reduced density matrix (ignoring the O-O contiuum).

6.3.2 Two-Step Kinetic Analysis

The dynamical behavior, oserved in the quantal study of Ref. 20, is reminiscent of the time dependence of the simple kinetic scheme

$$A \xrightarrow{k_1} B \xrightarrow{k_2} C, \tag{1}$$

where A represents the initially prepared state and B represents some intermediate configuration through which the reaction passes to attain the configuration of the final product(s) C. It is parenthetically noted that the dynamical evolution presented in Ref. 20 is about two orders of magnitude slower than that measured in Figure 3 and the aforementioned relevant references (i.e. 8, 16-18).

The idea of mode mixing and/or IVR is certainly relevant even for the ease of local mode excitation. Minton et al.[21] have reported a detailed study of mode mixing for the $3000cm^{-1}$ first C-H stretch excited mode of several organic molecules. The have seen that the degree of state mixing from the pure C-H stretch mode with the other degrees of freedom is J dependent and scales linearly with J. They determined that about 70 rovibrational states must couple to the zeroth order optically active mode to obtain significant statistical dilution. They note that this criterion is met for a coupled state spread of the zeroth order optically active model of about $0.05cm^{-1}$.

The mixed state-eigenstate picture can be combined with the common theme of the aforementioned theoretical treatments. It appears that the short time energy flow may be mode specific but is insufficient to induce reaction. Allowing more time for energy flow, in the content of the zeroth order picture, will allow for reaction to occur, but the reaction events (moniored by individual classical trajectories, for example) will obtain with quasi-random occurrence. Several alternative pathways may contribute to the observable reaction dynamics. Therefore, he reaction competes poorly with IVR, and the reaction rates obtained from dynamical calculations are close to statistical predictions.

The two-step kinetic scheme described in Eqn. (1) is a well known and solvable system of coupled differential equations. The temporal behavior of the concentrations of the reaction products may be evaluated by sequential integration of the differential equations that describe the time rate of change of A, B, and C. The mass conservation principle must also be observed; that is, $\mathrm{A}_\circ = \mathrm{A}(t=0) = \mathrm{A}(t)+\mathrm{B}(t)+\mathrm{C}(t)$. The temporal dynamics of the intermediate configuration is given by [22]

$$\mathrm{B}(t) = \mathrm{A}_\circ \cdot \frac{k_1}{(k_2 - k_1)} \cdot \left\{\exp\left(-k_1 t\right) - \exp\left(-k_2 t\right)\right\} \tag{2}$$

while the temporal behavior of the formation of the nascent OH product concentration is given by[22]

$$\mathrm{C}(t) = \mathrm{A}_\circ \left[1 \; - \; \frac{1}{(k_2 - k_1)} \cdot \left\{k_2 \exp\left(-k_1 t\right) - k_1 \exp\left(-k_2 t\right)\right\}\right]. \tag{3}$$

The proper dynamics must include a convolution of Eqns. (2) or (3) with the measured system response function.

The two-step kinetic scheme postulates that the intermediate configuration, denoted by B, is the exclusive route for completing the reaction. In light of the discussion of the previous subsection, it is plausible to consider that the configuration B corresponds to the O-O stretch mode. In particular, this configuration is where O-O stretch mode has acquired sufficientvibrational excitation to allow for

obtaining a significant probability amplitude for product formation. The implication is that k_1 then represents the rate of IVR from the initially prepared local mode to the sufficient energization of the reactive coordinate. The rate k_2 would refer to the actual dissociation (HO-OH separation) process. This scenario explains the dynamical evolution in terms of a zeroth order vibrational state description. An alternative eigenstate description might consider overtone (mixed state) dephasing to be the k_1 process and the proper phasing of the energy in the O-O coordinate (including the continuum levels) to be related to the k_2 process. A fit of Eqn. (3) to the data of Fig. 2 yields the two lifetimes $1/k_1 = \tau_1 = 0.6 \pm 0.4$ps, $\tau_2 = 2.4 \pm 0.8$ps, and an induction period of 1.35ps. The fitted curve is not shown because it is visually indistinguishable from the biexponential-plus-time-shift result of Fig. 3b.

The physical interpretations of the two-step kinetic analysis and the successful rising biexponential fitting are rather different. The kinetic model analysis has bee discussed in the previous paragraph. The latter process might arise from two different types of reaction behavior. The first is that the reaction proceeds via two distinct routes along a path which is directly dissociative and along a path which requires more extensive IVR to create significant probability in a configuration which may proceed to dissociation. The second mechanistic option is that the initial distribution of rovibrational (zeroth order) states that are prepared by laser excitation results in a distribution of reaction rates that may be simulated by a biexponential fit.

It may be possible to better discern between these two reaction mechanisms by obtaining time resolved reaction data at an excitation wavelength different than that for the 5265Å value above. Fig. 4 shows the dynamics of the OH product formation for 4Å pump pulse bandwidth excitation at 5274Å. This excitation wavelength is in the middle of the ν_{OH}=6 overtone band.[7] The displayed integral of the response function is a (nearly symmetric) Gaussian of 5.8ps FWHM. The curve is fit with a single exponential function convoluted with the system response function. Minimization of the χ^2 parameter gives $\tau = 3.4 \pm 0.8$ps and the temporal shift is

$\Delta\tau$=0.55ps. This finding is both qualitatively and quantitatively different than the results presented in Figs. 2 and 3. The longer, essentially single exponential, lifetime may be interpreted as originating from states wherein the E and J distribution is somewhat narrower than the distribution that produced the results presented in Figure 2, and analyzed in Figure 3.

These measurements do not rule out the possibility that a reaction process of the form described in Eqn. (1) underlies initial state specific dynamics. However the spectral conjestion problems which were clearly demonstrated in Chapter V and Ref. 9 could be masking the underlying subtle IVR or mixed initial state evolution. It is more conservative to interpret the observed dynamics in terms of a model that evaluates the reaction behavior for a distribution of E and J. The distribution obtains from many rovibrational transitions which fall within the pump laser bandwidth.

6.3.3 Perturbed Fragment Spectroscopy in Overtone Induced Predissociation

The probe laser frequency may also be tuned from resonance in an attempt to come into resonance with the transition frequency of the incipient OH fragment. If the fragment is being perturbed by its conjugate reaction partner, an off-resonant absorption may come about. The probe is tuned to $R_1(2)$+5cm^{-1}, the blue of the $R_1(2)$ transition. The resultant transient for 5272Å excitation pulse wavelength is presented in Fig. 5a. The system response function, measured by difference frequency generation is given in Fig. 5a, and is well fit by an 8.5ps FWHM Gaussian response function. The distinguishing feature of Fig. 5a is the transient enhanced signals which occurs near the t=0 value obtained from the response function measurement.

Qualitatively similar transient features have been seen in the (direct) electronic dissociation dynamics of ICN when the probe pulse is tuned to longer wavelengths than the resonance frequency of the nascent CN product.[23] The dynamical behavior has been interpreted as occuring from the transiently-shifted fragment absorption frequency. The shifted absorption arises from the perturbing presence of the partner

photofragment. Zewail[24] has termed this pump-probe method of "transition state spectroscopy" because the spectroscopically observed fragment is neither reactant nor nascent product. Rather, for reactions occuring without barriers the fragment is in transition to assuming the product energy configuration.

A more closely related result has been described in Chapter IV of this thesis. The HOOH molecule may be induced to dissociate following electronic state excitation. The two hydroxyl radical products acquire angular motion during the dissociation. This motion becomes the angular momentum of the nascent products. Moreover, the hydroxyl species have permanent dipole and quadrupole moments. The relative motion of the OH radicals will sample spatial configurations that contribute additional attractive, neutral, or repulsive energy by way of the multipole interactions. The detection of OH radicals with a given value for the final angular momentum implies that the incipient radical obtains a spatial orientational probability distribution described by the spherical harmonic of order J_i for fragment i. The nature of the interaction and the (associated) perturbed fragment spectrum will, therefore, depend on the rotational angular momentum of the spectroscopically labeled fragment and the associated distribution of correlated partner fragments. Under such circumstances a blue shifted broadening of the $R_1(2)^*$ perturbed absorption indicates: (1) that the long range multipolar interactions are more attractive for a ground state OH than an electronically excited OH, and/or (2) that the repulsive OH-OH interactions could be more significant fr the electronically excited OH than for ground state OH.

The data of Fig. 5a could be modeled with a molecular response which is the sum of Eqns. (2) and (3). It has been previously argued that such reaction dynamics are consistent with a model wherein the final product fragments C would pass through the spectrally perturbed configuration B. (This configuration for B is different than the case described in the previous subsection.) The relative amplitudes of the B and C signals would depend on the fragment resonance time in the spectrally selected region of the potential surface (as compared to the pulse duration) and the

excitation Franck-Condon factors. Therefore, the total amplitudes from the signals from B and C are not necessarily equivalent even though each samples the same number of fragments.

A simplified case for dynamical fitting is obtained if it is assumed that $k_1 \gg k_2$. The resultant limiting expression used to obtain the fit shown in Fig. 5b, is given by

$$S_{OH}(t) = b \cdot \exp(-k_2 t) + c \cdot \left[1 - \exp(-k_2 t)\right]. \tag{4}$$

where $S_{OH}(t)$ denotes OH signal intensity at a given time t. $S_{OH}(t)$ must be convoluted with the measured system response function to take into account the observed finite risetime of the signal. The fitted lifetime is 3.1±1.3ps, and the ratio b/c=3.1 and a phenomenological temporal shift of 0.55ps obtains. It is assumed that the relevant experimental signal levels for the B and C configurations of the kinetic scheme of Eqn. (1), where B≡OH* and C≡OH, are represented by b and c, respectively. The larger value for the B-configuration amplitude compared to C results from detuning the probe frequency off the nascent OH resonance even though the "lifetime" of the former is similar to the probe pulse duration.

A separate estimate may be made for the time of existence of the spectrally perturbed fragment. It may be assumed that the F.C. factors for the optical transitions associated with B and C are the same and that the detuned probe spectral intensity on resonance is about a factor of eight reduced from the peak probe spectral intensity. Given that the probe pulse duration is about 4.0ps FWHM and a $5cm^{-1}$ spectral width, the fragment should exist in the spectroscopically selected perturbed configuration for about 1ps.

The only concern about the nature of the origin of the transient signal of Fig. 5a is that some higher order (e.g. χ^3) matter-radiation interaction[25] may be the source of the observable effect. Comparison of the system response function and the time delay position of the peak amplitude of the transient feature shows that the OH-LIF signal obtains after the t=0 position. This indicates[26] that the molecular dynamical processes are of finite temporal duration and that the matter radiation

interaction is a simple sequential step process. By contrast, the dynamics associated with the term "coherence-spike"[25,26] are instantaneous on the picosecond time scale and would result in the OH-LIF signal, obtaining a maximal value prior to the t=0 time delay position.

In light of the discussion of the previous paragraph,, a more comprehensive functional form would be a better approximation to the actual dynamics. In particular the assumption of $k_1 \gg k_2$ should be relaxed. Unfortunately, the quality of the present data does not allow for convergence of the fitting algorithm when k_1 is included in the parameter list. Otherwise, the k_1 that could be extracted would be related to the intramolecular dynamics, including IVR and the initial O-O bond stretching behavior. More complete fitting models that consider quasi-biexponential dynamical behavior as observed for Fig. 2 should perhaps also be implemented. A suggested experiment is to monitor the dynamics of population of the O-O stretching mode.

Crim and coworkers[5] have shown that photodissociation spectra of HOOH may be obtained when exciting the third overtone level, even though the absorbed photon energy is about 4000cm^{-1} below the D_o of the O-O stretching mode. The action spectrum is more similar to the fifth overtone band than to the fourth. They reason that a second photon is being absorbed by those molecules initially pumped to the third overtone level. The second photon causes the vibrationally energetic molecule to undergo an electronic transition to the dissociative excited state. They observe significant OH population in the ν=1 level, which is not populated from one-photon excitation to the excited electronic surface.

The reaction dynamics associated with excitation to the fifth and fourth overtone levels studied in this and the previous chapters, respectively, do not produce detectable amounts of the ν_{OH}=1 product.[6,7] It is proposed that the IVR dynamics may be observed in an experiment that monitors the OH(ν=1) signal while simultaneously strongly pumping the overtone transition. The resultant signal will reflect

the IVR dynamics because it is probable that vibrational energy migration into the O-O coordinate enhances the excitation cross-section to the dissociative level.

Transfer of vibrational energy into the O-O stretch mode produces greater probability amplitude for longer internuclear separations. The distended bond correlates with lower potential energy in the ^1A_u lowest energy excited state.[27] It is to be expected that the vibrational overlap integral (F.C. factor) to be larger for O-O mode vibrationally excited HOOH molecules. This is because the vibrational energy-induced larger amplitude motion tends to more closely resemble the dissociating species than larger amplitude motion in the OH-stretch coordinate. (c.f. the case of F.C. factors for I_2 in Ref. 28). The resultant total 1+1 photon energy is also less than the onset of significant one photon absorption cross-sections from the HOOH vibrational ground state level.[29,30] Independent 1+1 wavelengths may also be employed.

6.4 CONCLUSIONS

Direct time-resolved measurements of the vibrational predissociation dynamics following excitation of the fifth overtone of HOOH have been measured. The rate of formation of the OH product is more than the order of magnitude more rapid than the dynamics observed for the OH formed following fourth overtone excitation. This larger rate of product formation presumably obtains from both the larger average amount of energy available for reaction and the smaller average angular momentum of the HOOH reactant.

Single or biexponential product build-up waveforms are observed for different pump-pulse photolysis wavelengths. It can be argued that the ν_{OH}=6 action spectrum is inhomogeneously broadened by way of spectral conjection in the excitation process. The intrinsic homogeneous Lorentzian linewidth may be estimated to be less than 30cm^{-1}; that is, the overtone dephasing rate is slower than 0.15ps. This conclusion is in general agreement with the IVR results of some classical dynamics calculations. Moreover, the measured 2-4ps lifetime for product formation is in good

agreement with the reaction rate(s) estimated by statistical unimolecular reaction models, dynamical calculations and action spectrum linewidth measurements.

The complex dynamics of product formation have been interpreted by various models and kinetic analysis. A unique interpretation of the dynamics will require a more direct probing method for the IVR dynamics which are implicit in the observed reaction behavior.

Finally, transient "peak-like" features become evident in the pump-probe LIF signal if the detection wavelength is tuned away from the nascent OH product electronic resonance. It has been argued that the transient feature obtains from OH fragment absorption during the period when the target OH is perturbed by the proximity of the partner reaction product. The transient feature obtains when the electronic resonance frequency of the perturbed OH falls within the probe laser bandwidth. The OH product is not yet of a nascent configuration, but because the spectral detuning is a small value (a few cm^{-1}) the perturbation is of moderate amplitude. It is suggested that the interaction is due to a long range affect because of the few (1-2) picosecond timescale during which the perturbation allows for spectroscopically monitoring the incipient product. Others[31] have invoked the electrostatic repulsions of the OH bond dipoles to account for the opening of the OOH angles to values larger than those between the oxygen bonding hydrides. The multipolar interactions are then clearly also significant for the vibrational predissociation dynamics.

A new pump-pump and LIF probe method was suggested to directly observe IVR dynamics. The observation would not be dependent on dynamics. The direct measure of the intramolecular dynamics would greatly improve the ability to understand the overall ground state reaction dynamics.

The observation and the unambiguous origin of such transient absorption features argues for the utility of time-resolved spectroscopic methods in the elucidation of potential energy surface features, which were heretofore not very accessible. Further study of the perturbed fragment spectrum and dynamical evolution should

allow for the determination of the significance of exit channel angular interactions in determining, for example, the rotational product state distribution. Such angular forces are difficult to quantify in statistical analysis of the unimolecular reaction dynamics.[32]

REFERENCES

1. J.T. Hynes, Ann. Rev. Phys. Chem. **36**, 573 (1985); G.W. Robinson and W.A. Jalenak, Laser Chem. **3**, 163 (1983); T. Fonseca, J.A.N.F. Gomes, P. Grigolini and F. Marchesoni, Adv. Chem. Phys. **62**, 389 (1985).

2. To obtain an insight into the range and depth of possible studies of gas phase reaction dynamics, see for example *The Theory of Chemical Reaction Dynamics*, C.D. Clary ed., (NATO ASI Series, Series C, vol. 170, D. Reidel Publishing, Boston, 1985).

3. See for example, R. Altkorn and R.N. Zare, Ann. Rev. Phys. Chem. **35**, 265 (1984); C.H. Greene and R.N. Zare, J. Chem. Phys. **78**, 6741 (1983).

4. See for example J. Berkowitz, *Photoabsorption, Photoionization and Photoelectron Spectroscopy*, (Academic Press, New York 1979); S.H. Lin, H.L. Selzle, K.O. Bornsen and E.W. Schlag, J. Phys. Chem. **92**, 1469 (1988).

5. M.D. Likar, A. Sinha, T.M. Ticich, R.L. Vander Wal and F.F. Crim, Ber. Bunsenges. Phys. Chem. **92**, 289 (1988).

6. T.M. Ticich, T.R. Rizzo, H.R. Dubal and F.F. Crim, J. Chem. Phys. **84**, 1508 (1986).

7. T.R. Rizzo, C.C. Hayden and F.F. Crim, J. Chem. Phys. **81**, 4501 (1984); H.R. Dubal and F.F. Crim, *ibid.*, **83**, 3863 (1985).

8. (a). L.J. Butler, T.M. Ticich, M.D. M.D. Likar and F.F. Crim, J. Chem. Phys. **85**, 2331 (1986); (b) X. Luo, P.T. Rieger, D.S. Perry and T.R. Rizzo, *ibid.*, **89**, 4448 (1988).

9. N.F. Scherer and A.H. Zewail, J. Chem. Phys. **87**, 97 (1987); N.F. Scherer, F.E. Donay, A.H. Zewail, and J.W. Perry, *ibid.*, **84**, 1932 (1986).

10. G. Herzberg, *"Molecular Spectra and Molecular Structure III. Electronic Spectra and Electronic Structure of Polyatomic Molecules"*, (Van Nostrand Reinhold Co., New York 1966).

11. W. Demtröder, *"Laser Spectroscopy"*, (Springer-Verlag, Berlin, 2nd ed., 1982), p.243

12. N.F. Scherer, J.W. Perry, F. Doany, and A.H. Zewail, J. Phys. Chem. **89**, 894 (1985); see also Chapter 5.

13. Y.R. Shen, *"The Principles of Nonlinear Optics"*, (Wiley, New York 1984).

14. L. Halonen, J. Chem. Phys. **86**, 3115 (1987); M.S. Child and L. Halonen, Adv. Chem. Phys. **57**, 1 (1984); J.W. Perry, D.J. Moll, A. Kupperman and A.H. Zewail, J. Chem. Phys. **82**, 1195 (1985); R.H. Page, Y.R. Shen and Y.T. Lee, Phys. Rev. Lett. **59**, 1293 (1987).

15. D.W. Marquardt, J. Soc. Ind. Appl. Math. **11**, 431 (1963); P.R. Bevington *"Data Reduction and Error Analysis for the Physical Sciences"*, (McGraw-Hill, New York, 1969); D.P. Millar, Ph.D. Thesis, Caltech, 1982.

16. T. Uzer, J.T. Hynes and W.P. Reinhardt, J. Chem. Phys. **85**, 5791 (1986); *ibid.*, Chem. Phys. Lett. **117**, 600 (1986).

17. B.G. Sumpter and D.L. Thompson, J. Chem. Phys. **82**, 4557 (1985); **86**, 2805 (1987).

18. L. Brouwer, C.L. Cobos, J. Troe, H.R. Dübal and F.F. Crim, J. Chem. Phys. **86**, 6171 (1987).

19. J.S. Hutchinson, J. Chem. Phys. **85**, 7093 (1985).

20. K. Nishikawa and S.H. Lin, Chem. Phys. Lett. **149**, 243 (1988).

21. T.K. Minton and J.D. McDonald, Ber. Bunsenges. Phys. Chem. **92**, 350 (1988).

22. G.M. Fleck, *"Chemical Reaction Mechanisms"*, (Holt, Reinhardt and Winston, New York, 1971); D.V. Roberts, *"Enzyme Kinetics"*, (Cambridge University Press, Cambridge, 1977); (b) See also Chapters IV and VII of this thesis.

23. M. Dantus, M.J. Rosker and A.H. Zewail, J. Chem. Phys. **89**, 6128 (1988); M.J. Rosker, M. Dantus and A.H. Zewail, *ibid.*, 6113; see also L.R. Khundkar, Ph.D. Thesis, Caltech 1988.

24. R. Bersohn and A.H. Zewail, Ber. Bunsenges. Phys. Chem. **92**, 373 (1988); R.B. Bernstein and A.H. Zewail, J. Chem. Phys., in press (1988).

25. T.F. Heinz, S.L.Palfrey and K.B. Eisenthal, Opt. Lett. **9**, 359 (1984); M.W. Balk and G.R. Fleming, J. Chem. Phys. **83**, 4300 (1985).

26. E.P. Ippen and D.V. Shank in *"Ultrashort Light Pulses"*, S.L. Shapiro ed., (Springer-Verlag, Berlin, 1984) p. 111; see also B.I. Greene in *"Ultrafast Phenomena IV"*, D.H. Auston and K.B. Eisenthal eds., p. 308 (1984); N.F. Scherer, J.W. Perry, F.E. Doany and A.H. Zewail, J. Phys. Chem. **89**, 894 (1985).

27. E.M. Evleth, J. Am. Chem. Soc. **98**, 1637 (1976).

28. J. Tellinghuisen, Adv. Chem. Phys. **60** p.299 (1985).

29. C.L. Lin, N.K. Rohatgi and W.B. DeMore, Geophys. Res. Lett., **5**, 113 (1978).

30. R. Bersohn and M. Shapiro, J. Chem. Phys. **85**, 1396 (1986).

31. J.E. Carpenter and F. Weinhold, J. Phys. Chem. **92**, 4306 (1988); **92**, 4295 (1988).

32. R.A. Marcus, J. Chem. Phys. **85**, 5035 (1986).

FIGURE CAPTIONS

1. A schematic outline of the relevant intramolecular and reaction dynamics. A picosecond pulse excites HOOH to the ν_{OH}=6 level; The excitation is followed by molecular energy redistribution, in particular vibrational energy. The dissociation proceeds via the O-O stretch coordinate. The OH product is detected as an asymptotically free species or while still perturbed by the partner product.

2. OH LIF intensity plotted vs. pump-probe delay time. The data is obtained for 5265Å excitation and probe pulse wavelength of 3070.3Å. The detection is of the $R_1(2)$ OH product. Also shown is the integral of the system response function obtained by difference frequency generation.

3. (a) A single-exponential nonlinear least squares fit to Figure 2. The fitting includes convolution with the system response function. This yields a lifetime for OH formation of τ=2.1±0.5ps with $\Delta\tau$=0.45ps. (b) A nonlinear least squares biexponential fit to Figure 2, also including convolution with the system response function. The fitted lifetimes are τ_1=0.7±0.5ps, τ_2=1.9±0.75ps, and $\Delta\tau$=0.25ps.

4. Time-resolved reaction data for an excitation at 5274Å with 4Å pump pulse bandwidth, showing somewhat different dynamics for the formation of the OH product. The detection is again for the $R_1(2)$ rotational transition. The single exponential fitted curve yields τ=3.3±0.9ps and $\Delta\tau$=0.53ps.

5. (a) The reaction transient for 5272Å excitation with the probe tuned from resonance to $R_1(2)+5cm^{-1}$. Also shown is the 8.5ps FWHM Gaussian cross-correlation obtained by difference frequency generation. The experimental zero of time is established by the response function. The experimental transient behavior obtains from the off-resonance probing. (b) Shows the same data but including a fitted curve, which is the convolution of both a single exponential rise and single exponential decay with the system response function. The lifetimes for the two dynamical responses are held equal to one another and have a value of 3.1±1.2ps and $\Delta\tau$=0.59ps. The ratio of the relative amplitudes (as descibed in the text), is b/c=3.1.

Perturbed Fragment Spectroscopy for Vibrational Ground-State Predissociative Reactions

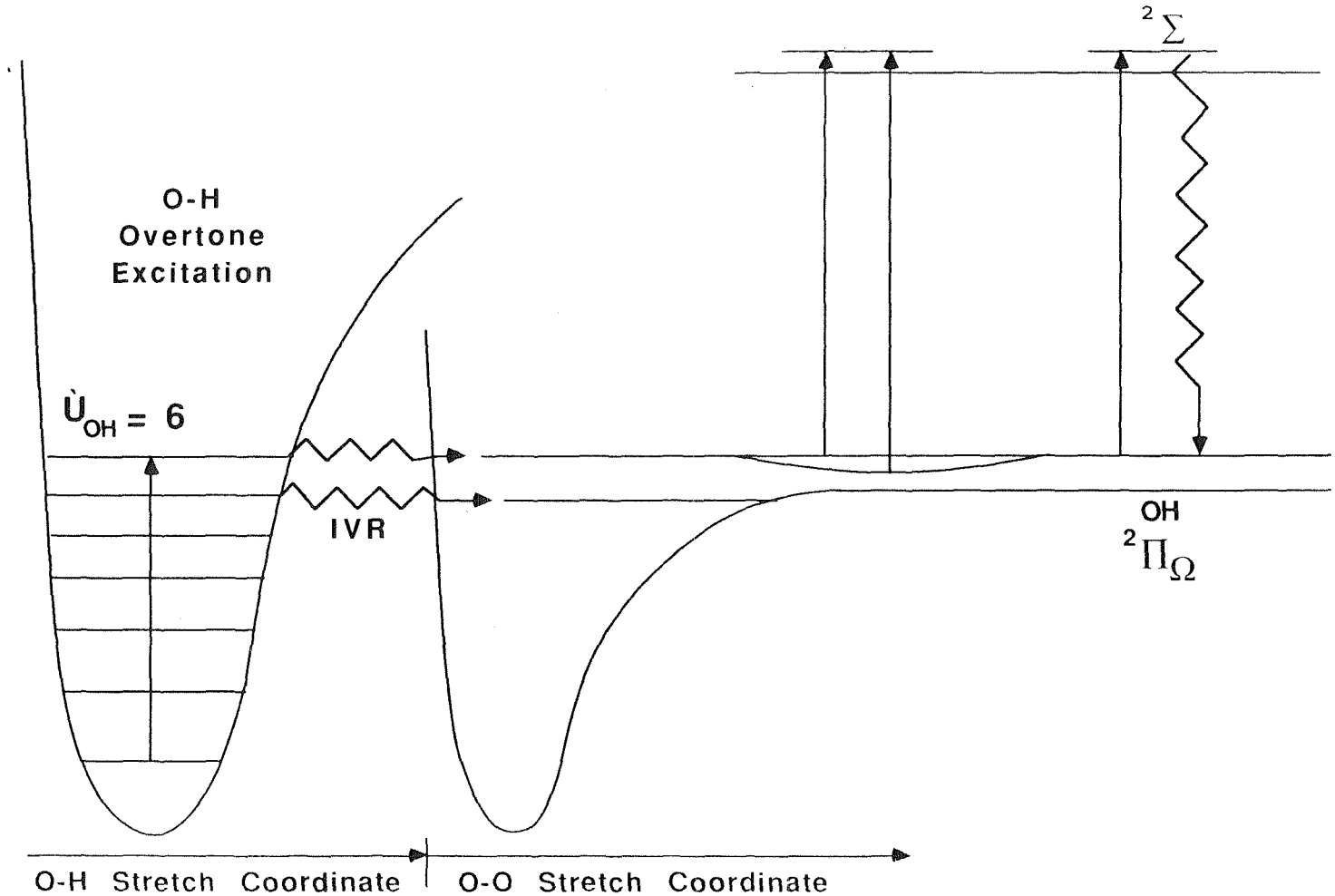

Figure 1.

Figure 2.

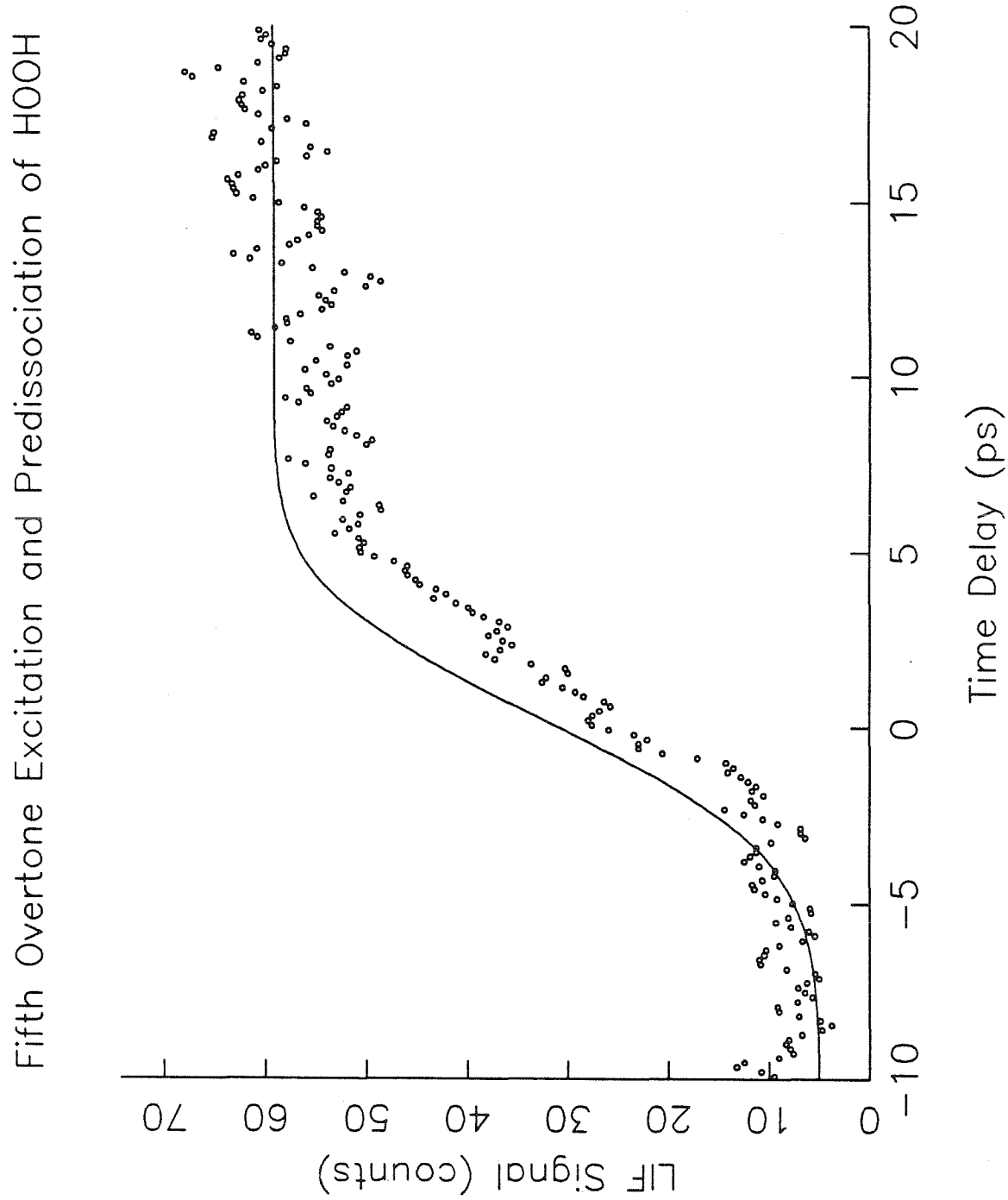
Fifth Overtone Excitation and Predissociation of HOOH
LIF Signal (counts)
0
10
20
30
40
50
60
70
−10
−5
0
5
10
15
20
Time Delay (ps)

Figures 3a and 3b.

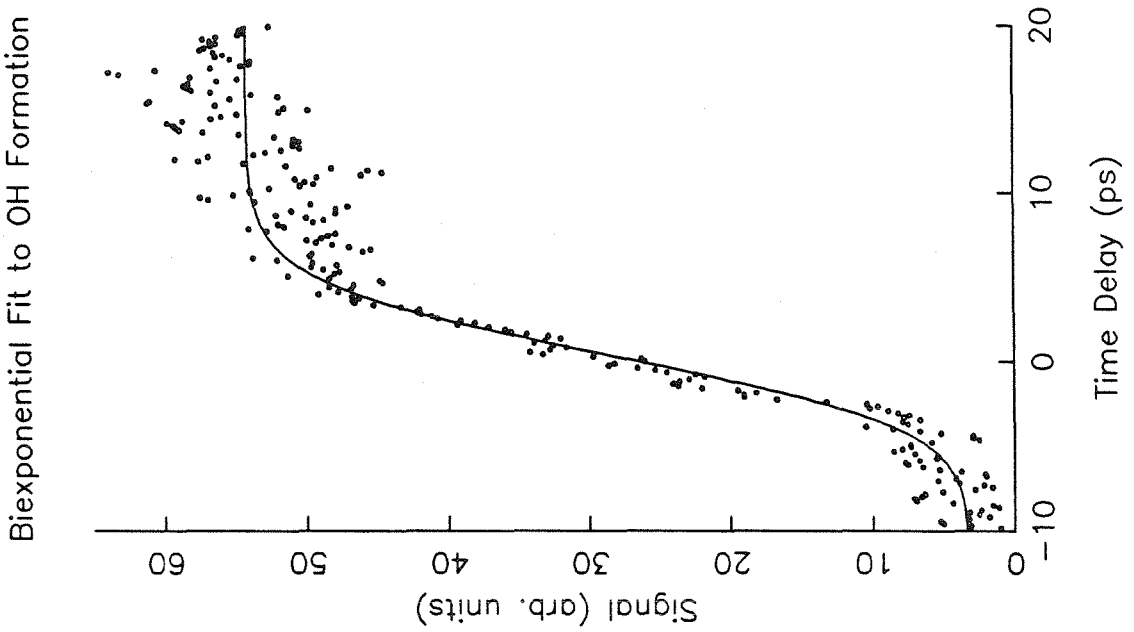

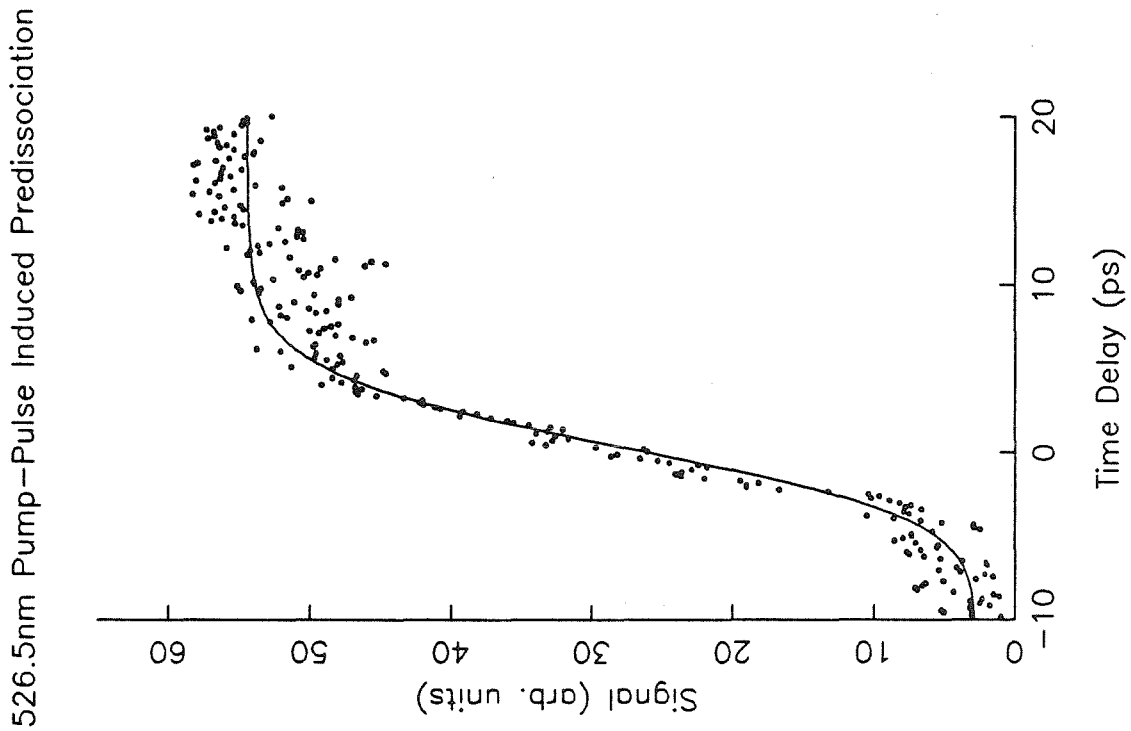

Figure 4.

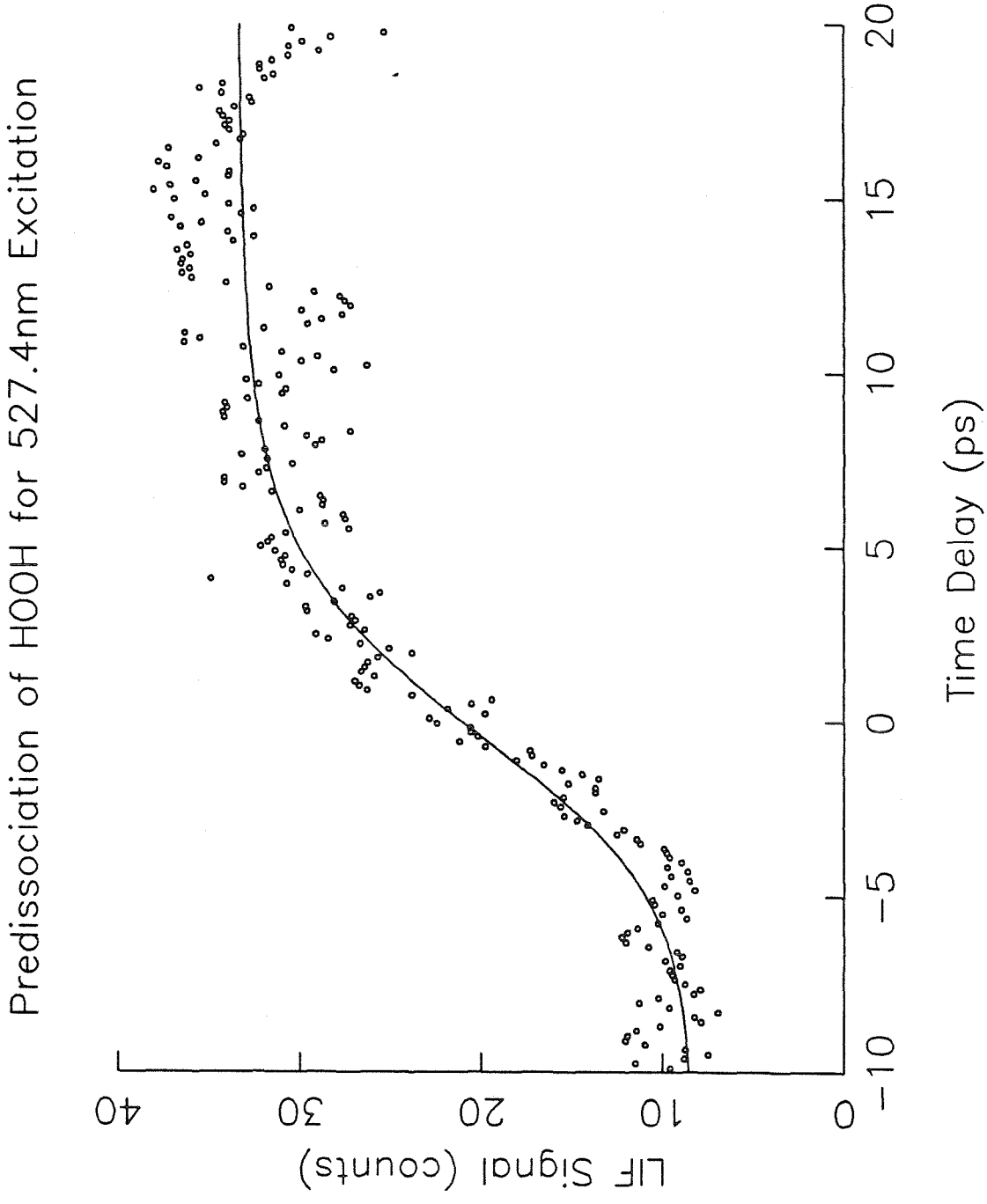
Predissociation of HOOH for 527.4nm Excitation
LIF Signal (counts)
0
10
20
30
40
-10
-5
0
5
10
15
20
Time Delay (ps)

Figures 5a and 5b.

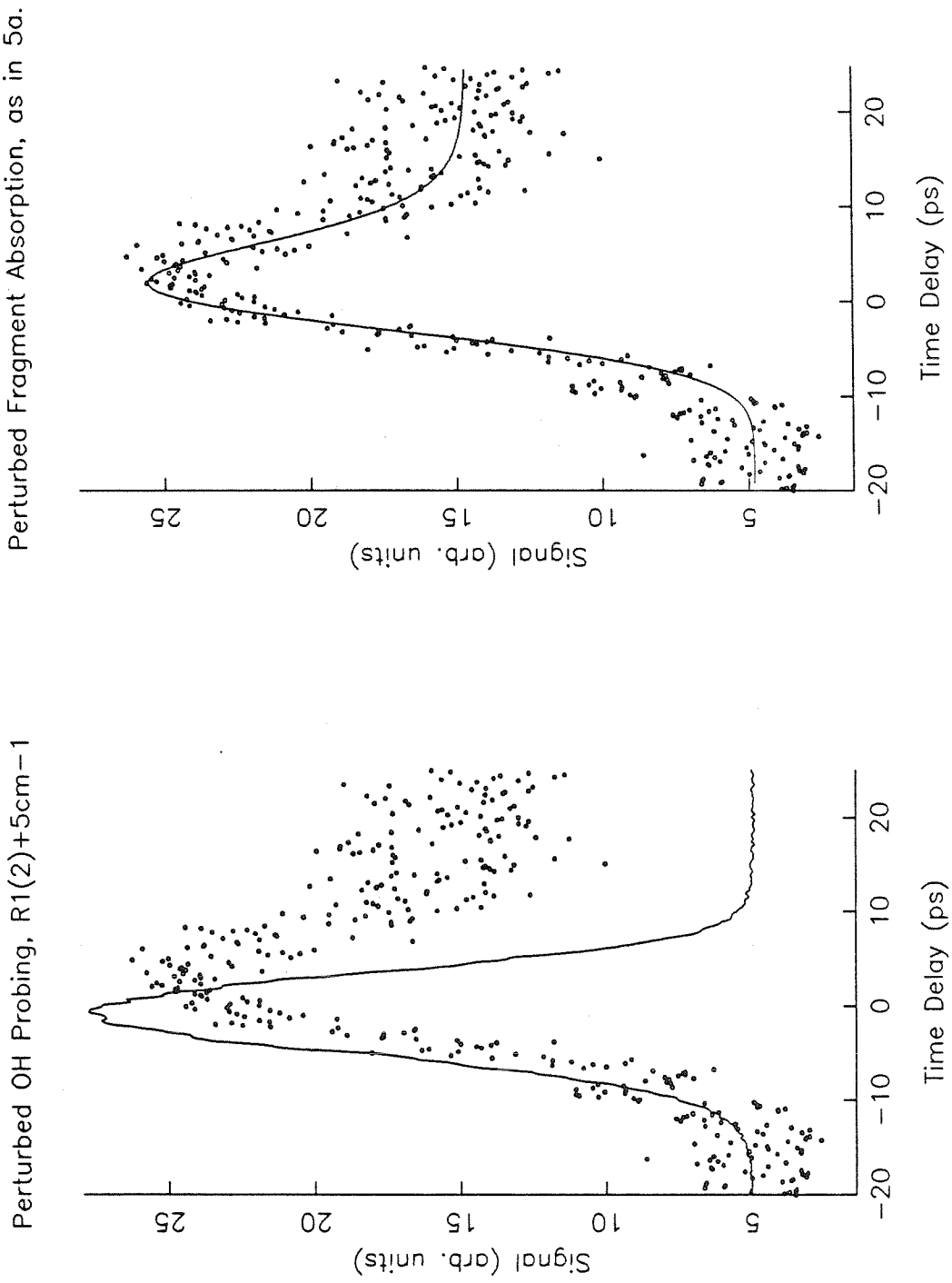

CHAPTER VII.

Time-Resolved Study of the Dynamics of Product Formation in the Oriented Bimolecular Reaction $IH\text{-}OCO + h\nu \rightarrow [HOCO]^{\dagger} \rightarrow OH + CO$.

7.1 INTRODUCTION

Detailed analysis of chemical reaction dynamics requires restriction of the initial parameter space to understandable and treatable dimensions. Ideally, a subject reaction could be studied in a state-to-state specific manner.[1] Such well defined experimental conditions could, in the case of unimolecular reactions, yield observable quantities related to the matrix elements that couple the reactant state with the product state. Analogous specificity for a bimolecular reaction study could obtain the state-to-state reaction cross-sections. Both types of experimental studies would provide a rigorous data base to assess the validity of various models of the molecular dynamics.[2] The extra complication, yet potentially larger information content, of bimolecular reactions, in comparison to unimolecular reactions, requires the development of a means to restrict the new and unique aspects of these reactions. The new degrees of freedom include the internal states of the independent reactants and the relative orientation of the reactants (angular relation and impact parameter).[3]

Highly state-selective experimental studies of unimolecular reactions are possible in the case of predissociative reactions; the intrinsic line-width (associated with lifetime broadening) must remain narrower than the state density for some initial energy. Such studies have been performed for van der Waals molecular (dimer) decomposition,[4] and high overtone initiated dissociation on ground electronic state surfaces.[5] Electronically excited state van der Waals predissociation has also been studied in a ro-vibrational state specific manner.[6] This type of predissociation does not involve electronic curve crossing, rather only vibrational energy redistribution.

A larger number of experimental efforts have been performed on the level of energy-to-state specificity, since the domain of this category includes photo-initiated reaction on purely repulsive potential energy surfaces.[7] Such energy specific experiments have investigated the energy dependence of product state distributions,[8] angular correlations of the products,[9] and the time-resolved measurement of the rate of product formation.[10–13] The initial reactant state may be specified, to some degree, provided that the lifetime-broadening/state-density criterion is met. This is

not possible in the case of direct dissociation, but is a possibility for predissociation reactions.

Predissociative reactions wherein the electronically excited reactant state (symmetry) does not directly correlate to the product state, sometimes occurs when the products are formed in their ground electronic state.[14] Such a predissociative mechanism requires introduction of an intermediate, such as the high lying and densely spaced ro-vibrational levels of the ground electronic state, which are iso-energetic with the photo-selected level in e.g., S_1. This S_1-S_o internal conversion essentially reduces initial state selectivity to a monochromatic energy condition.[10] Some exceptional cases, such as the investigations of formaldehyde predissociation by Moore and Field and coworkers,[15] have shown propensities for maintaining knowledge of the initial state through the traversal of the intermediate levels and projected on to products.

Performing highly detailed studies of bimolecular reactions may allow for greater control of the reactant(s) initial states, but the nature of such reactions typically necessitates the averaging over (or control of) additional experimental degrees of freedom. Reactant state selection might be afforded in a fashion similar to the unimolecular case, e.g., jet cooling, or photoselection.[16] Crossed-beam crossed-laser scattering geometries have allowed atom-diatom reactants to be aligned.[17] Such experiments allow for selecting reactants with some distribution of b and θ and studying the reaction behavior originating from the initially photo-excited state. In this situation only those reactants that absorb a photon will undergo the bimolecular reaction and be detected as a product. Photoselection allows for obtaining alignment (or specifying $|M_J|$) of the diatom.

A most elegant method for initial M_J state selection makes use of the first order Stark effect indigenous to symmetric top molecules.[18,19] Electrostatic selection of $|\, J, K, M_J\rangle$ states (possibly used in conjunction with laser photoexcitation) allows for the study of <u>oriented</u> crossed beam reaction behavior. The orientational distribution of reactants is therein consistent with the M_J orientational (spherical harmonic)

probability distributions. This method provides spectroscopic control of reactant orientation but does not restrict the impact parameter.

The utilization of non-covalent intermolecular forces in the formation of unique van der Waals (vdW) complexes allows for the study of chemical bonding and dynamics.[20] Soep[21] and Wittig[21] and coworkers have more recently conceived of using such weakly bound (i.e., relative to covalent interactions) complexes to orient the individual reactants of the bimolecular system. The degree of reactant relative orientation, which is essentially equivalent to the molecular/intermolecular zero-point motion, results from the cooling of internal degrees of freedom and the formation of the vdW complex in free-jet expansions. Wittig has termed the reaction occuring subsequent to pulsed laser photolysis of one of the reactants as proceeding under "precursor geometry limited" (PGL) conditions.[22] In essence, this term refers to the orientation of the reactants obtained from the constrained monomer motions of the complex. The restricted motion results from the attractive dispersion, electrostatic, and/or hydrogen bonded interaction of the van der Waals complex.[23]

The method of obtaining reactant orientation through weak intermolecular interactions is unique in that the impact parameter of the reactants has also been restricted. This is done in a fashion that is independent of the limitation imposed simply by energy and angular momentum constraints for reaction. The latter constraints dictate the range of impact parameters that (potentially) will allow for reaction in a crossed-beam study. At least in a conceptual sense, it appears that the vdW-created PGL conditions will allow for obtaining the most constrained initial reactant conditions possible for a bimolecular reaction. This is done while simultaneously maintaining the individual molecular identity of the two reactant species. The restricted monomer orientations allow for the study of specific dynamics through unique portions of (at least) the entrance channel portions of the reaction potential energy surface.

A fundamentally significant effect results from dictating the proximity constraint by the 2-4Å vdW bond length of the precursor monomers. Photoexcitation of one of the constituents to directly dissociative levels (i.e., purely repulsive PES)

makes possible the rather accurate determination of the instant of initiation, or the 'time-zero,' of the reaction.[24] The application of ultrafast pump-probe methods facilitates a direct time-resolved study of the progress of the reaction from precursors through intermediates and finally to products. The information obtained from a study of reaction rates as a function of effective or available energy will serve as a useful comparison to the results of dynamical calculations on model potential energy surfaces. Such reaction rate studies are also directly complementary to measurements of scalar and vector (asymptotic) quantities intrinsic to the specific reaction and reaction dynamics.

Radakrishnan et al.[22] studied the Product State Distributions (PSDs) of OH following the photodissociation of the vdW-PGL complex BrH-OCO, wherein the H-atom acquires sufficient potential and kinetic energy by photoabsorption and dissociation of HBr to commence reaction. This work is a more restrictive analysis of the important bulk gas phase reactions

$$OH + CO \xrightarrow{k_1} H + CO_2 \tag{1.1}$$

and the reverse reaction

$$H + CO_2 \xrightarrow{k_2} OH + CO \tag{1.2}$$

The authors of this study assumed a reactant internal energy well in excess of the 102 kJ/mole endoergic threshold. Comparison of the PGL-complex reaction PSD with that obtained from a room temperature study of a gas mixture of HBr and CO_2 showed that the PGL reaction obtained significantly colder product than the unoriented reaction. This result is quite intriguing in that one possible interpretation would say that the reaction proceeds with some remembrance of the initial reaction conditions, that is, a restricted set of reactant orientations and impact parameters.

With the realization that the proximal location of the two reactants should allow for a rather unambiguous determination the time zero for the photoinitiated

bimolecular reaction, it became clear that time resolved studies could significantly enhance the understanding of the reaction mechanism. We have previously given a preliminary report of the direct measurement of the overall reaction rate.[24] The purpose of the presentPpaper is the presentation of the results of a comprehensive study of reaction rate as a function of laser excitation energy. The present study is of the photoinitiated reaction of the IH-OCO vdW-complex over the wavelength range 263-231nm. The tunable photolysis photon obtains corresponding to H-atom translational energies of 13200-18500 cm^{-1} for the $I(^2P_{3/2})$ product and a 9400-11500cm^{-1} range for the H atom associated with the $I(^2P_{1/2})$ product channel. The analysis of the time-resolved rate of OH production utilizes a kinetic model, which accounts for the formation and (assumed) statistical unimolecular dissociation of a reaction intermediate. The systematic model analysis allows for obtaining significant insight into the overall reaction mechanism. Experimental evidence for the unprecedented degree of experimental control afforded by the constrained reaction initial conditions will be shown. This evidence takes the form of reaction channel specific dynamics and the observation of effects that may be interpreted as originating from a reactive scattering resonance.

7.2 BACKGROUND

One principal attraction afforded in studying van der Waals oriented bimolecular reactions is the reduced domain of the initial collision conditions. Such restricted initial conditions may allow for examination of dynamical properties not obtainable or observable under less selective reaction conditions. Moreover, the proximity of the monomer moieties, taken in conjunction with the restricted set of initial reaction configurations, allows for meaningful direct time-resolved measurement of the reaction dynamics. The essential and unique aspect of the oriented complex is that the monomer-monomer (reactant) separation is well defined and the close proximity limits the transversal along the reaction coordinate of the entrance channel

region to 2-3Å. To date, such direct time-monitoring of the progress of a gas phase bimolecular reaction has not been possible.

The motivation to control the reaction impact parameter and relative (reactant) orientation distribution results from the desire to obtain more detailed knowledge of the reactive PES. State selection[25] in the reactants of a typical bimolecular reaction still allows for a distribution of the c.m. energy and reaction angular momentum. This energy distribution results from the unconstrained collision configurations that proceed to product formation. Laser photoselection[17] may be used to restrict the collision orientational distribution but will not directly restrict the distribution of impact parameters. For molecules that exhibit first order Stark effect, electrostatic potential fields may be used to orient (as opposed to align) one, and in principle both, reactant(s).[18,26] This action will reduce the collisional orientational distribution and select a "heads vs. tails" reaction orientation for an asymmetric[14] reactant. Electrostatic focusing, however, will not selectively restrict the impact parameter distribution. Moreover, none of these techniques address the issue of obtaining the "time-zero" of reaction, and therefore will not allow for a meaningful time-resolved study.

Two research groups have pioneered the idea of using the van der Waals attractive forces holding the two monomeric constituents (reactants) in close (but weakly bound) proximity of each other. Soep and coworkers[21] have studied the reaction of vdW trapped Hg·Cl_2 by laser excitation, Hg-Cl_2 + hν $\rightarrow$ $Hg^+ \ldots Cl_2^-$ $\rightarrow$HgCl* + Cl. The completion of this reaction is monitored by observing luminescence from HgCl*. The vdW complex provides the initial geometric configuration that allows for direct absorption into the Hg^+Cl^-:HgCl curve crossing region.

The work of Buelow, Radhakrishnan,[22] and other members of the Wittig group[27,28] have used the oriented complex to study collision-induced atom transfer-decomposition reactions. These studies[22] proceed by way of reactive scattering of H (or D) and OCO, and detection of the outcome of the reaction by Laser Induced Fluorescence (LIF) of the OH (OD) reaction product. The results of this research, however, did not conclusively answer the question of whether orientation-selective

behavior is being observed. The ambiguity resulted from obtaining OH PSD at only one excitation energy. The Wittig group has extended these PGL reaction studies to the BrH-OCS system.[28] Different PSDs and products have been obtained. When changing BrH to HSH, and presumably forming the 'bidentate' attachment to the two oxygens of CO_2, a dramatically changed PSD is measured.[27] Several explanations may qualitatively account for the much 'colder' observed PSD. However, the absence of additional measurements, obtained while changing a controllable experimental parameter for the same molecular system, precludes a definitive answer to the question of the existence of unique reaction behavior under PGL conditions.

The previous studies only partially explored the unique properties of these XH-OCO vdW complexes. Direct time-resolved measurements would take advantage of the proximity of the hydrogen atom to the oxygen and the steeply repulsive XH (X-halogen) excited state potential surface. The light mass of the H-atom allows for efficient conversion of the photolysis photon energy into H-atom translational energy. Terminal hydrogen atom velocities obtained for halogen-hydride direct dissociation are approximately 200Å/ps. Because the H-O separation is only 2-3Å, it may be assumed that the motion of the H atom from the X-species to the oxygen would certainly occur on the order of 100fs. (This may be intuitively judged by the comparison of the H and CN masses and the measured ICN photodissociation time.[12]) The knowledge of the time of reaction initiation, or time-zero, of the bimolecular reaction is accurate to within this period of time. This is the time uncertainty intrinsic to this reaction method.

The experimental studies described in this chapter have been designed to take advantage of both orientation specificity and reactant proximity factors. Combining the measurement of time-resolved dynamics with the idea of monitoring this reaction evolution into specific product states and performing these studies at several different reaction energies might allow for a unique and unambiguous interpretation of the essential aspects of the reaction behavior. The chosen reaction complex, IH-OCO, satisfies the requirements for undertaking an effective and meaningful

time-resolved bimolecular reaction study. Figure 1 shows the overall concept of the experimental pump-probe scheme for study of the reaction.

The HI moiety was chosen for the XH-OCO complex to facilitate frequency tuning studies. The broad absorption band[29] of HI with a maximum near 220nm allows for large variations of initial H-atom kinetic energy. Moreover, the large 7600cm^{-1} I($P_{3/2}$ - $P_{1/2}$) spin orbit splitting[29] makes possible the study of OH photoproducts, which are energetically allowed ($\triangle H_o$=102kJ/mole) and correlate exclusively to the I($P_{3/2}$) products. The generation of wavelengths in the range of 270-220nm may be done by several different means and with essentially continuous coverage of this spectral range. Finally, the A-band absorption region of HI is continuous from 280nm to beyond 220nm.[29] The smaller energy separation between the red edge of this band and the dissociation energy of HI into its atomic constituents (D_o=296 kJ/mole) as compared to the HBr case allows for more extensive studies in the region of low H-atom translational energies.

7.2.1 Reaction Kinetics

Several experimental studies of the binary gas phase reaction

$$OH + CO \rightleftharpoons CO_2 + H$$

have been perfor med under differing conditions of temperature and pressure.[30-32] These measurements of the reaction rate show non-Arrhenius behavior. Smith and Zellner[30] postulated that the reaction proceeds by way of an intermediate configuration, disposed between the reaction entrance and exit channel Transition State (TS) conformations. Subsequent buffer gas quencher studies[31] have shown results consistent with an energetically (relatively) stable species. Smith[30b] also demonstrated that adabatic correlation rules for the spin and orbital symmetry of the H(^{2}S) and CO_2($^1\Sigma_g^+$) products must arise from the $^2A'$ state. The OH($^2\Pi$) and CO($^1\Sigma^+$) correlate with such a state and another. It was further argued[30b] that the postulated electronic ground state configuration of the HOCO intermediate is of $^2A'$

symmetry. Therefore, the bimolecular reaction proceeds on the ground electronic surface throughout.

A representation of the OH+CO→products[30b] reaction scheme for the collisional buffer gas studies is presented in Figure 2a. The course of the reaction is clearly presented, and an additional path for $[HOCO]^{\dagger}$ reaction involves collisional quenching with a buffer gas species, with rate constant k_c. The present review of the kinetic analysis follows the more complete treatment of Ref. 30. Invoking the steady state approximation for $[HOCO]^{\dagger}$ under a fixed set of pressure, temperature and buffer gas [M] conditions make possible the determination of a reaction rate constant. It is also possible to equate $\frac{-d[OH]}{dt}$ with the sum of the rates of formation of H and CO_2 and stabilized HOCO. This is expressed as

$$\begin{aligned} -\frac{d[OH]}{dt} &= k_{obs} \cdot [OH][CO] \\ &= \frac{k_a \cdot (k_b + k_c[M])}{k_a + k_b + k_c[M]} \cdot [OH][CO] \end{aligned} \tag{2.1}$$

Assume that $k_b \gg k_{-a}$, then the low pressure result for the rate of OH disappearance is $\frac{-d[OH]}{dt} = k_a[OH][CO]$. This expression also does not depend on pressure which is contrary to the findings of experimental measurements.[30,31] The overall rate expression when $k_{-a} \geq k_b$ does give an [M], buffer gas pressure, dependence.

Further studies[32] consider the variation of the P, T and [M] parameters, thereby allowing for the extraction of the unimolecular rate and equilibrium constants $k_{uni,a}$(T,P) and k_a(T) for $[HOCO]^{\dagger} \rightleftharpoons$ OH+CO. It is also possible to evaluate the unimolecular rate constant $k_{uni,b}$(T,P) for $[HOCO]^{\dagger} \rightleftharpoons CO_2$+H as well as the equilibrium constant K_b(T). Finally, the overall bimolecular rate constant k_{bi}(T,P) for the overall reactant to product process OH+CO→ CO_2+H may be obtained. Such a multiparameter analysis has been recently carried out.[32] The large number of parameters to be extracted from the available data or modelled by RRKM calculations may only be successfully assigned because of the availability of independent information about HOCO.

These independent measurements are of the HOCO structural parameters obtained in a matrix-isolation environment.[33] Jacox and coworkers have photolyzed H_2O/CO matrices and have analyzed the newly appearing IR freatures. The new absorption features were found to be consistent with the HOCO moiety. These absorption measurements obtain the bond lengths and vibrational frequencies of the HOCO radical. The frequencies are shifted due to interactions with the medium, but the authors estimate these shifts to be small ($\sim 30 cm^{-1}$).

The elucidation of the aforementioned structural constants for the common reaction intermediate of Eqns. (1.1) and (1.2) and of Figure 2a are useful in the study of the two unimolecular reactions originating from $[HOCO]^{\dagger}$. Analysis of the bimolecular reaction was carried out by way of two-channel RRKM calculations for the unimolecular decomposition of $[HOCO]^{\dagger}$ to the reactants or to products. In addition, the deactivation of $[HOCO]^{\dagger}$ was evaluated by calculating the effective collisional frequency, $\beta\omega$, where β is the value of the collisions which result in stabilization of the intermediate. The dynamics of the salient reaction must be contrasted with the Arrhenius temperature-dependent behavior observed for simple bimolecular reactions, which do not proceed via some stable intermediate configuration. A general representation of this (simple) rate behavior is given by

$$k(T) = A \cdot T^{\beta} \cdot \exp(-c/T) \tag{2.2}$$

This expression will fail to explain the observed pressure dependence of the reaction. Larson, *et al.*[32] have extended the Troe formalism,[34] which accounts for temperature and pressure dependences of unimolecular reaction rates, to the presently relevant case of bimolecular reaction through an intermediate configuration. The essential findings are obtained by fitting the aforementioned reaction rate constants ($k_{uni,i}$) for zero and infinite pressure (in the buffer gas [M]) to the modified Arrhenius expression. It will suffice to summarize these results and extract the information which is relevant to the present experimental effort.

Following the method of Ref. 32, it is found that the rate of OH formation, from the unimolecular process described by $k_{uni,a} = k_{-a} \cdot [\mathrm{HOCO}]^{\dagger}/[\mathrm{HOCO}]$ is given by

$$k_{uni,a} = \frac{K_c \cdot \beta\omega \cdot k_{-a}}{\beta\omega + (k_{-a} + k_b)/[\mathrm{M}]} \tag{2.3}$$

The rate of formation of CO_2, from $k_{uni,b} = k_b \cdot [\mathrm{HOCO}]^{\dagger}/[\mathrm{HOCO}]$, is given by

$$k_{uni,b} = \frac{K_c \cdot \beta\omega \cdot k_b}{\beta\omega + (k_{-a} + k_b)/[\mathrm{M}]}. \tag{2.4}$$

Therefore, the small [M] and high pressure limit of the unimolecular rate constants may be expressed, respectively, by

$$k^{\infty}_{uni,a} = K_c \cdot k_{-a} \tag{2.5a}$$

$$\frac{k^{\circ}_{uni,a}}{[\mathrm{M}]} = K_c \cdot \beta\omega \cdot \frac{k_{-a}}{(k_{-a} + k_b)} \tag{2.5b}$$

$$k^{\infty}_{uni,b} = K_c \cdot k_b \tag{2.5c}$$

$$\frac{k^{\circ}_{uni,b}}{[\mathrm{M}]} = K_c \cdot \beta\omega \cdot \frac{k_b}{(k_{-a} + k_b)} \tag{2.5d}$$

The temperature-dependent collisional deactivation equilibrium constant is written as the ratio of the unimolecular reaction rates over the collisional deactivation rate,

$$K_c(T) = \frac{k^{\circ}_{uni,a} + k^{\circ}_{uni,b}}{\beta\omega \cdot [\mathrm{M}]} \tag{2.6}$$

The two temperature dependent rate constants simply follow from Eqns. (2.5) and (2.6) to give

$$k_{-a}(T) = \frac{k^{\infty}_{uni,a}}{K_c} \tag{2.7a}$$

and

$$k_b(T) = \frac{k^{\infty}_{uni,b}}{K_c} \tag{2.7b}$$

Fitting the experimental data to the modified Arrhenius equation, Eqn. (2.2), results in the empirical evaluation of Eqns. (2.5);

$$k^{\infty}_{uni,a} = 10^{12.77} \cdot \mathrm{T}^{0.53} \exp(-1710/\mathrm{T}) \ \mathrm{sec}^{-1}, \tag{2.8a}$$

$$\frac{k^{\circ}_{uni,a}}{[\mathrm{M}]} = 10^{23.34} \cdot \mathrm{T}^{-1.89} \exp(-1775/\mathrm{T}) \ \mathrm{cm}^3/\mathrm{mol} \cdot \mathrm{sec}, \tag{2.8b}$$

$$k^{\infty}_{uni,b} = 10^{12.24} \cdot \mathrm{T}^{0.307} \exp(-1657/\mathrm{T}) \ \mathrm{sec}^{-1}, \tag{2.8c}$$

$$\frac{k^{\circ}_{uni,b}}{[\mathrm{M}]} = 10^{26.36} \cdot \mathrm{T}^{-3.024} \exp(-1765/\mathrm{T}) \ \mathrm{cm}^3/\mathrm{mol} \cdot \mathrm{sec}. \tag{2.8d}$$

These results are put into Eqns. (2.7) and plotted in Figure 2b. The figure clearly shows that the thermal rate constant for reaction of $[HOCO]^{\dagger}$ to form OH+CO is larger than the reaction producing $H+CO_2$. This observation is consistent with the results of Smith and co-workers,[30,31] as discussed above, that is, $k_{-a}(T) \geq k_b(T)$.

The molecular beam conditions of the present experimental study are not identical to the (canonical) bulb reaction results just presented. Quantitative extrapolation of the thermal rate constants to the jet-cooled, hence microcannonical, environment is not straightforward.[35] However, it is sufficient to notice that the temperature-dependent behavior of the individual unimolecular reactions will support the assumption that the titled vdW precursor reaction proceeds primarily to the formation of OH+CO. It will be concluded that decay of $[HOCO]^{\dagger}$ will not proceed as readily to the $H+CO_2$ reactants as toward the detectable product(s). The idea of a preferred directionality to the reaction is one of the primary conclusions to be drawn from these kinetic studies. The other essential information concerns the TS energies and configurations. This latter point will be examined in greater length in subsection III.

7.2.2 H+CO_2 *Reactive Scattering and Kinematics*

In contrast to the kinetic studies of the previous subsection, the present discussion will concentrate on the salient aspects of the reverse reaction

$$H + CO_2 \rightarrow OH + CO.$$

The measurements of this process all have a common feature, which is that the large barrier to reaction precludes significant product formation at room temperature collisional conditions. However, it is possible to obtain ballistic H-atoms, from the one photon photolysis of HX(X=Br,I), which are sufficiently energetic to cause reaction.

The pre-laser study of Eqn. (1.2) culminated with the reaction yield and threshold energy study performed by Oldershaw and Porter.[36] They photolyzed HI and HBr in mixture with CO_2 (and similar experiments with N_2O) and observed the product yield as a function of initial relative kinetic energy. The nearly monoenergetic H-atoms thus created allowed for an accurate determination of the reaction energy. The HI absorption spectrum, and associated range of H-atom translational energies, is sufficiently large to span the region of the reaction threshold and the range 100kJ/mole above threshold. The CO product was detected, following a fixed irradiation time, by mass spectroscopic or gas chromatographic methods. Considering the 296 kJ/mole HI dissociation energy and converting the H-atom translational energy to the relevant center-of-mass (c.m.) frame, results in a reaction threshold of 106±6kJ/mole. This is to be compared with a reaction enthalpy of $\triangle H_o$=102kJ/mole, or 25.5kcal/mole vs. 24kcal/mole.

A significant advance in experimental sensitivity was achieved through the use of laser pulsed photolysis of HBr combined with LIF detection of the OH reaction product.[37] These authors observed a rotationally and vibrationally hot OH product; K≤16 in $\nu'' = 0$ and the $\nu'' = 0, 1, 2$ states are populated. It is also noted that the OH LIF signal rises to a maximum value about 100nsec after the photolysis laser (λ_{pump}=193nm) firing. This delayed rise stems from the finite distance the H-atom

travels before encountering a CO_2 molecule (estimated to be about 1mm for the experimental pressures).

Improved probe laser spectral resolution and single collision reaction conditions (about 50mtorr pressure and 100nsec pump-probe delay) have allowed Kleinermans *et al.*[38] to quantitatively measure the OH rotational PSD. The experiments were done for 60 and 44kcal/mole relative kinetic energies. The PSD corresponding to the lower energy reaction is narrower than that obtained for the 60kcal case. Also, the PSD obtained at the lower collision energy peaks at K=6,7 while the other peaks near K=9,10. The authors compare the PSDs with plots of rotational surprisals, I=ln(P°/P) where P is the experimental distribution. Using a rigid-rotor harmonic oscillator expression for P° shows that the experimental PSD is colder than expected from democratic energy partitioning considerations. Moreover, these authors report a non-statistical population of the λ-doublet states as probed by the R and Q-branch transitions. These authors also postulate that the reaction proceeds through an intermediate configuration. They conclude that the HOCO complex decays with forces acting preferably *in* the C-O-H plane. They also speculate that the orbital angular momentum, **L**, of the reactive collision stays relatively constant (in-plane rotation of HOCO) for higher energy collisions. Out of plane rotations and changes in **L** become more significant with decreasing collision energy. The authors did not make more quantitative estimates of these effects.

The aforementioned discussion has been for energetics of the relative kinetic motion. This term refers to the relative translational energy of the reacting species. The laboratory kinetic energy of the H-atom obtains from conservation of linear momentum, where the velocity scales by $\frac{m_X}{m_{HX}}$, therefore $v_H = \frac{m_X}{m_{HX}} \cdot v_{cm}$. The laboratory kinetic energy is, $E_H = \frac{1}{2} m_H v_H^2$, given by $E_H = \frac{m_X}{m_{HX}} \cdot E_{tr}$, where E_{tr} is the c.m. translational energy of X and H, $E_{tr} = \frac{1}{2}\mu v_{cm}^2$. Vector addition of $\hat{v}_H$ and $\hat{v}_{OCO}$, in the limit where $\hat{v}_H \gg \hat{v}_{OCO}$, extends this expression to

$$E_{rel} = \left(\frac{m_{OCO}}{m_{HOCO}}\right) \cdot \left(\frac{m_X}{m_{HX}}\right) \cdot E_{tr}. \qquad (2.9)$$

In the case of sequential dissociation of HI and subsequent interaction of H with CO_2, $E_{rel} = 0.970 \cdot E_{tr}$.

7.2.3 Structure of the IH-OCO *van der Waals Precursor*

The analogue species XH-OCO (X=F,Cl) were first studied by Klemperer and co-workers using the method of rf and microwave Molecular Beam Electric Resonance (MBER) spectroscopy.[39,40] These authors determined that the equilibrium structure of the complex is linear, and that the average angle for the HX-bend off the c.m.-to-c.m. axis to be $\langle\gamma_{XH}\rangle(\equiv \arccos \mid \langle\cos^2\gamma\rangle \mid^{1/2}) = 25°$ in both cases. Because the C and O constituents do not exhibit a nuclear spin, it was not possible to measure γ_{CO_2}, but was argued that $\langle\gamma_{OCO}\rangle$ lies in the range of 5-10°. The vdW dimer bend force constants (k_γ, in units mdyne·Å) is evaluated as 0.022 and 0.011mdyne·Å for the HF and HCl species, respectively. The stretch force constants have about the same orders of magnitude as the bend force constant and are surprisingly weak, especially because the induced dipole moment is rather large (0.45 and 0.60Debye in the HF and HCl complexes). It may be concluded that the overall zero-point geometry of the vdW complex will preferentially constrain any photo-initiated reaction to end on attack. This assertion is true if the HBr and HI species are structurally similar to the HF and HCl species.

Early ab initio work by Kollman[41] on CO_2-HF compared the energetics of hydrogen bonding and Lewis acid-base interaction. The structure expected for H-bonding is more end-on, H directed at oxygen. The acid-base structure is T-shaped and HF acts as a Lewis base. The H-bonded case was found to be the energetically favored structure. Sapse *et al.*[42] have also performed ab initio calculations, using the Gaus-80 program, to determine the FH-OCO binding energy, which varies from 1733cm^{-1} to 1015cm^{-1}, depending strongly on the number of basis functions used in the calculation. The equilibrium structure $\theta_{OCO} = 178°$, $\theta_{HF} = 185°$ is not strongly affected by the choice of basis. The more recent calculations by Reed *et al.*[43] also predicted the near collinear equilibrium configuration and a 1140cm^{-1} binding energy.

Recent IR laser absorption experiments,[44] which probe the $\nu_1 = 1$ HF stretch region in a jet-cooled expansion, provide new information about the bending potential and the equilibrium structure. Analysis of the IR measurements determined that the ν_6 complex bending mode frequency is $10 \pm 5 cm^{-1}$. This corresponds to the bend (hindered rotation) of the CO_2 moiety of the vdW complex. It is agreed that a postulated linear excited state geometry, with small amplitude zero-point motion of the intermolecular CO_2 bend coordinate, is inconsistent with their measurements of the complex asymmetry (c.f. B-C rotational constants). Fitted spectra suggest a vibrationally averaged nonlinear geometry in the upper state. A similar, though smaller magnitude effect, is expected in the zero-point level. One interpretation of their direction absorption results assume a bent vdW-complex geometry wherein the bending angle increases from 26.5° to 31.3° on ν_1 excitation. These authors speculate that enhanced off-axis attraction accounts for the increase in the vibrationally averaged bending angle upon ν_1 excitation.[44]

The IR absorption spectrum of a co-deposition of Ar, CO_2, and HF at 12K shows[45] an HF librational mode frequency of $313 cm^{-1}$. It is estimated[45] that the isolated gas phase frequency would be about $300 cm^{-1}$. The lack of an observed splitting in the degenerate librational mode, as observed in this study, shows that the complex has a linear equilibrium structure. This HF bending (librational) mode is to be considered distinct from the observation of the previous paragraph.

Finally, rather definitive electrostatic - ab initio calculations of the FH- and ClH-OCO vdW-complex structures, energies and potential surface have been performed by Dykstra.[46] The calculated bending potential surface for HF and CO_2 is relatively flat with respect to the intermolecular bending motion. Moreover, this PES shows that the two moieties bend in a 'concerted fashion'[46] and thereby follow each other. It is determined that juxtaposition of dipole-quadrupole (cf. L shaped structure) and quadrupole-quadrupole (cf. linear structure) interactions account for the weak bend potential. This explains how a strongly bound complex, as inferred from the large induced dipole moment,[39] can exhibit large amplitude bending motions. The speculation by Nesbit is quantitatively manifest in these $\mu - \Theta$ vs. $\Theta - \Theta$

interactions. The Θ_{HF}-Θ_{OCO} interaction strength decreases with increasing bending angle whereas μ_{HF}-Θ_{OCO} increases with bend motion. Effectively, the second interaction acts to exert a bending force on the complex.

A linear cut through the two dimensional contour diagrams for the vdW complex potentials[46] is given in Figure 3a. The cut is chosen to proceed through the major axis of the, essentially, elliptical lowest energy contours for HF and HCl with CO_2. This cut represents the potential for the concerted bend motion of the two moieties. Because the cut passes through the $\theta_{HF} = \theta_{OCO}$ minimum, the cut is fully expressed by $\theta_{HF} = \alpha \cdot \theta_{OCO}$. In the HF case α=1.4. The choice of the major axis cut of the 2-dimensional PES also allows for the best (simple) approximation or measure of the area of the full two dimensional phase space. Dykstra[46] states that the smaller stabilization energy for the HCl compound is less than that obtained for HF and results primarily from the smaller permanent dipole moment of HCl.

Analyzing the calculated HF and ClH-OCO vdW surfaces and using the idea that the dipole moment of the HX moiety primarily dictates the form of the potential, allows for obtaining HBr and HI surfaces by extrapolation. Incorporating the dipole moments of Ref. (47) and continuing the HF to HCl trend (ratio of the value of the potential for a specific angle for the FH- vs. ClH moieties) facilitates calculation of the HBr and HI curves of Figure 3b. These curves are rough estimates of the 'major-axis' linear PES. Figure 3a for HF and Figure 3b for HI also show the best harmonic approximation of the zero-point energy level of 150 and 31cm^{-1}, respectively. Figure 4a gives $P(\theta)$ and $P(\theta) \cdot \sin\theta$ for the zero point, gaussian wavefunctions, $P(\theta) = |\Psi_{HI}|^2$. The finding gives an approximate idea of the angular probability distribution for the IH-OCO moiety. The quantity is a gaussian function for $P(\theta)$.

The last step required in specifying the reaction initial conditions is the structural geometry of the vdW complex. Dykstra[46] has indicated that the equilibrium values for the monomer-monomer centers-of-mass separation, $R_{c.m.}$, results primarily from the chosen values for the atomic radii. The calculation of the vdW-molecular structure, in particular $R_{c.m.}$, considers the known structures of FH and

ClH-OCO and extrapolates to the HBr and HI complexes. The extrapolation is done by geometrically constructing the known structures of HF and HCl with OCO using the appropriate atomic vdW radii and scaling up the $R_{c.m.}$ value accordingly for HBr and HI cases. The HF thru IH-OCO complexes are also shown with van der Waals radii in Figure 5. Table 1 lists the parameters for the atomic and XH species used to obtain the result of Figures 3-5. Table 2 lists the quantities used to calculate the bend potential (for a limited geometry) of the XH-OCO species. The evaluation of the R_{cm-cm} distance follows from simply adding the values of R_{XH}, R_{vdW} and R_{OC}.

7.2.4 Reaction Potential Energy Surface and Dynamics

Several reports concerning the energetics and structure of various configurations along the H+CO_2 reaction coordinate have been discussed in the preceeding subsections. It has been demonstrated that the thermal kinetic studies monitor a reaction, which proceeds through an energetically stable intermediate configuration, this being the HOCO radical.[30-32] The kinetic studies[30] have obtained the minimum reaction barriers, and associated TST studies have postulated a cis-like H-OCO TS while the unimolecular dissociation occurs via a trans-like HOCO configuration.

Direct spectroscopic measurements of the HOCO radical have only been performed in matrix isolation environments.[33] The IR spectrum of HOCO trapped in a H_2O:CO matrix[33b] showed that the moiety exists as both cis and trans conformers. The vibrational potentials are found to be only weakly perturbed by the matrix medium and allow for accurate assignment of five of the vibrational fundamentals of each of the two stereoisomers. Spectral evolution suggested that the HOCO photodecomposed to produce CO_2 (and presumably H) when the sample was irradiated in the 2000-3000Å spectral region.[33b] The discrete electronic band system, however, has not been defined. A more recent Ar-matrix IR absorption study of

the trapped HOCO radical shows that the t-HOCO conformation is the more stable stereoisomer.[33a] This study clearly demonstrates that the t-HOCO photochemically decomposes when the matrix sample is irradiated. In particular, it is claimed that the absorption/reaction threshold occurs at 300nm excitation energy. There is presently no other information concerning the PES of the electronically excited HOCO PES.

An ab initio configuration interaction study of the two HOCO ground state conformers has determined the t-HOCO configuration to be more stable than c-HOCO by 3.3±0.5 kcal/mole.[48] The calculations also predict the intramolecular rotational barrier (isomerization) to lie 10.1kcal above the trans isomer. The preferred stability of the trans species results from the smaller lone-pair bonding orbital vs. lone-pair lone-pair interaction. Finally, the barrier to interconversion of t-HOCO to HCO_2, formyl radical, is 34kcal/mole.

Schatz *et al.*[49] have calculated the PES for H+CO_2 inelastic collisions and for reactive scattering leading to the OH+CO products. Figure 6b presents a schematic representation [49] of the energetics and critical configurations of the overall (title) reaction. The ab initio points were developed into a continuous surface by way of many body expansions. They used surface fitting methods to optimize the values of PES features (or dynamical observables) for better agreement with experimentally determined results. Tests of the accuracy (and refinements) of portions of the H+OCO PES were made by performing quasiclassical trajectory-Fourier Transform (QCT-FT) action calculations to obtain the CO_2 ro-vibrational populations. The calculated values were compared to the experimental measurements of Flynn and co-workers.[50] The form of the potential surface was deficient, however, in that the QCT-FT analysis did not quantitatively reproduce the experimental CO_2 ro-vibrational distributions. It is not clear how these problem features, presumably repulsive H-OCO interactions, might influence comparisons between calculation and experimental results of vdW-precursor oriented reactions. The calculated PSD from reactive trajectories is, however, in reasonable quantitative agreement with the experiment.[38,22]

This globally fitted and semiempirically optimized PES shows[49] that a $H+CO_2$ reactive encounter leads to the formation of the HOCO intermediate by way of a cis-like transition state configuration. The TS configuration requires that the CO_2 bend angle be significantly larger than the zero-point maximal bend displacement, 21° vs. 5°. It is this configurational change that could make the "effective"[49] barrier to reaction larger than the 1.12eV cis saddle point energy. Most of the reactive trajectories (> 70%) are seen to pass through the HOCO intermediate complex. Collisions that are end-on tend to produce rotationally colder CO_2 (inelastic) than side-on collisions do. Finally, it is observed that the measured[38] and calculated[49] reactive cross-section for OH product formation are in good agreement with a value of $1Å^2$. The calculations also show that the forward reaction cross-section is comparable with the calculated $HOCO^{\dagger} \rightarrow H+CO_2{}^*$, reverse reaction, cross section. The reaction cross section is about 30 times smaller than the inelastic scattering cross section.

The finding about the comparable unimolecular reaction cross-sections is in agreement with the thermal rates of the forward and reverse reaction provided that the branching ratio (that is the branching fraction[3]) favors the OH+CO product. This could be expected because the density of states in the HO-OC TS is larger than the density of states in the H-OCO TS. The last point obtains from the lower frequency complex-mode which leads to rotational (and orbital) motion of both the OH and CO products.

The PSD of PGL[22] van der Waals reactants have been studied by Wittig and co-workers.[22,27–29] They have reported the results of PSD measurements for the BrH-OCO reactant system. Reactions performed under bulk and PGL conditions show OH PSDs that are colder than those predicted by simple model calculations. The PGL reaction obtains the colder of the two PSDs. Hence, the deviation between the statistical model Prior distribution and the experimental PSDs is larger in the case of the jet-expansion study. Their study[22] at one photolysis wavelength does not provide enough information to distinguish between several alternative explanations of the apparent selectivity of PSDs from PGL conditions.

Four causes of the selective behavior might be considered for the studies described in the previous paragraph. (These four potential explanations were originally elaborated in Ref. 22.) Firstly, the high relative translational energy is significantly larger than the energy of the minimum reaction pathway and may, therefore, cause the reaction to proceed via a direct mechanism rather than through the HOCO intermediate. This would allow the more constained PGL reaction to result in a rotationally colder product. Secondly, because both the $Br(^2P_{3/2})$ and $Br(^2P_{1/2})$ spin orbit products are energetically reactive channels, it is possible that the less energetic H-atom channel (cf. $Br(^2P_{1/2})$) is more favored and will be preferentially enhanced. Thirdly, (re)collisions of OH with the Br "spectator" will result in rotational cooling of the OH product. Finally, the smaller than expected OH rotational excitation may result from the small separation of the OH center of mass and the C-O bond axis, the dissociation axis, hence only a small torque results from a given magnitude imparted force. The significant conclusion is that the PGL reaction conditions do obtain a unique observable result when compared with the observed behavior from the bulk bimolecular reaction.

More recently, Wittig and co-workers have proposed[28b,27] that multibody interactions in the PGL entrance channel result in deviations between the PSD obtained from a statistical model calculation and the experimental PSD data. The explanation implies that the energy made available for HOCO unimolecular decomposition is overestimated in assuming that the reaction proceeds sequentially with HX photolysis followed by H-OCO collision. Even though this idea is quite reasonable in nature, their evidence for substantiation only corroborates rather than uniquely defines this as the correct explanation. The domain of their experimental measurements is not extensive enough, that is, not enough parameters for the XH-OCO system have been varied, to allow them to conclude that an energy defect in the HOCO intermediate causes the colder PGL-PSD.

Schatz and co-workers[51] have recently performed QCT calculations for the BrH-OCO system. The overall force field follows from their previous H+OCQ studies.[49] Determination of the overall PES required addition of the relevant HBr electronic

surfaces and the Br-O and Br-C two body potentials. The vdW -H-O- bond was fixed to a previously estimated value of 2.2Å. These calculations were performed at 2.6 and 1.9eV of excess energy and did not account for the approximately 15% photoexcitation of the $Br(^2P_{1/2})$ reaction channel. The trajectories were sampled over a distribution of initial HBr orientations relative to the linear equilibrium geometry. It was found that the OH product formed only for initial reactant orientations displaced within 15° of the linear configuration when b=0. The dynamical reaction probability, $P_r(\theta)$, and $P_r(\theta) \cdot \sin\theta$ are plotted in Figure 4b. These values may be compared with the present IH-OCO complex orientational probabilities of Figure 4a. It was also observed that at least 70% of the reactive trajectories at 2.6eV pass through the HOCO intermediate configuration. They observe[59] that a potentially rotationally hotter OH product resulting from the direct O-C insertion mechanism is cooled due to secondary collisions with the nearby Br atom. However, neither the complex nor direct mechanisms result in OH rotational distributions that are significantly colder than those obtained from the bulk reaction. This disagreement with the experimental PSD results is attributed to deficiencies in the assumed PES. Finally, the HOCO unimolecular decay lifetimes were found to be about 0.3ps at 2.6eV and 0.4ps at 1.9eV.

More recent calculations indicate[52] that several factors contibuted to the above mentioned disagreement of theory with the experiment. Firstly, the vdW bond length obtained from Ref. 22 was 0.1 to 0.2Å too short. This actually necessitated a non Born-Oppenheimer (non-vertical) simulated optical excitation. This is a physically unrealistic approximation. Stretching the vdW bond slightly acts to reduce the degree of H-OCO repulsive interaction at the equilibrium Br-H separation and allows for making a vertical excitation to the $HBr(^1\Pi)$ excited state. Secondly, some aspects of the H-OCO repulsive interaction have recently been refined.[52] The combination of these two corrections cause the dynamically calculated PSDs to qualitatively reproduce the experimentally observed[22] trend of colder OH distribution for PGL vs. bulk conditions. Moreover, the corrections also seem to yield less energetic HOCO by transferring more energy into Br and HOCO translational energy

with respect to the complex center of mass. It has been learned[52] that the QCT calculations show an induction period in the appearance of the OH product. This last point was not reported in the earlier publication.[51]

Finally, the findings of a preliminary investigation of the time-resolved dynamics of the IH-OCO system were reported.[24] The picosecond (photolysis) pump pulse and OH LIF probe experiments, performed at 239nm=2.0eV available energy, gave a 5.0±2.0ps lifetime for the total time of reaction. That includes the HI photolysis, formation of HOCO, dissociation of HOCO and formation of spectroscopically observable (unperturbed by CO or I) OH. The long lifetime was rationalized as consistent with a reaction that occurs through a long-lived HOCO intermediate configuration. It was not possible to provide a quantitative explanation for the much longer than statistical reaction lifetime. The single-photon-counting (OH LIF photon) capability developed for this preliminary report provides the groundwork for the present comprehensive experimental effort. The idea of this previous study, and the concept of the present studies is schematically illustrated in Figure 6a.

7.3 EXPERIMENTAL SECTION

The experimental design was implemented with several objectives and constraints in mind. The objectives included: (1) obtaining the ability to measure directly the real-time dependence of concentration of the OH product; (2) maintaining simultaneously the ability of sufficient temporal resolution and the capability of spectrally resolving the OH ($^2\Sigma \leftarrow {}^2\Pi$) electronic transitions for OH formed in a single specific rotational state; (3) developing of a continuously tunable excitation (pump) laser light source that may be scanned over a large wavelength range, thus facilitating pump energy dependence studies of the reaction dynamics; (4) enhancing the information obtainable from each time-resolved bimolecular reaction scan by measuring the laser system (time) response function in such a way that the t=0 of the reaction is obtained without ambiguity; and (5) allowing for sufficient control of

the reactant gases and *in-situ* diagnostics of the molecular and complexed-molecule composition of the free-jet expansion.

Mutual attainment of the first two desired objectives is of course restricted to obeying the Heisenberg uncertainty relation $\Delta t \cdot \Delta \nu$=0.441 (for Gaussian envelope pulse). The spectral resolution necessary to satisfy the second item is dictated by the spacing of the aformentioned OH electronic transitions for adjacent values of the K-quantum number for the ground state product. Isolating on Q-branch transitions, it may be seen that an upper limit frequency bandwidth of 10 cm^{-1} is obtained.[53] In the case of Gaussian pulse shapes, this allows for 1.0 ps pulse durations (FWHM). The experimental results reported herein were obtained with an amplified synchronously pumped dye laser system. The dye laser/amplifier scheme that was employed, allowed for obtaining near optimal frequency and temporal conditions. This was facilitated by essentially continuous control of the laser spectral bandwidth and minimizing gain saturation in the amplification.

7.3.1 Pulse Formation, Amplification and Continuum Generation

The essentials of this laser oscillator and amplifier apparatus have been previously described[54] so a more terse elaboration will suffice here. The pulse generation and amplification arrangement is shown in Figure 5a. The output of an actively modelocked $Nd^{+3}YAG$ laser was frequency doubled to produce an 82MHz output of 10nJ, 80ps 532nm pulses. These pulses synchronously pump a cavity length matched ($\Delta l = 1 - 3\mu m$) dye laser. The dye medium was a mixture of R6G dye and DQOCI saturable absorber. The dye laser gave pulse autocorrelations of 4.3 ps FWHM, as measured by a home-built spinning block design autocorrelator. This results in a Gaussian pulse width of 3ps FWHM. A two plate birefringent filter was used as the cavity tunning element. Operationally, the dye laser was run in a fashion which restricted the temporal pulse duration by the limited spectral bandwidth while obtaining favorable conditions for good mode locking. These oscillator pulses were monitored on a continuous basis with the spinning block autocorrelator.

The principle fraction of the dye laser beam intensity was injected into a four-stage pulsed dye amplifier pumped by a 20Hz, 300 mJ/pulse Q-switched YAG laser. The first two stages were optically separated by either a 25μm diamond spatial filter or a 200 μm thick dye jet of 5×10^{-4}M Malachite Green (MG) in ethylene glycol. The second and third stages were separated by a 50μm diameter diamond-pinhole spatial filter. The spatial filter acts to reduce the amount of amplified spontaneous emission (ASE) intrinsic to the present pulsed dye-amplifier design. The first three stages were transversely pumped with increasing fractional amounts of the 532nm Q-switched YAG output. The fourth stage was longitudinally pumped by the remaining 50% of the 532 beam. The picosecond beam diameter was matched to the size of the YAG transverse beam diameter. The input pulse energy was increased from 0.5nJ to 0.3mJ, for a gain of nearly 10^6.

The MG Dye absorber jet was employed in most of the experimental measurements. The saturable absorber reduced the amount of pulse broadening to less than 25%; even less pulse width broadening could be obtained for lower amplification gain factors. The absorber jet was also somewhat more effective than the spatial filter in reducing the ASE that originates in the first stage. The dye in the amplifier stages was a mixture of R640/CV670 in about a 10-15:1 ratio. The solvent was methanol in all stages, and the concentration of the dye was about $2\text{x}10^{-4}$ M in the first two stages and $5\text{x}10^{-5}$ in the last two. The dye mixture was used in an energy transfer mode to obtain enhanced gain near 619nm when the $Q_1(6)$ transition was probed.

The amplified picosecond pulse is split by an 80% reflectance beam splitter, where the transmitted 20% of the beam will be frequency doubled and used as the probe beam. The majority of the light is focused into a cell of nanopure (e.g., filtered and deionized) water and results in the creation of an optical continuum.[55] The optical continuum is obtained when a sufficiently intense optical field interacts with the medium third-order nonlinear susceptibility. The spectral continuum is produced to allow for good pump-probe laser pulse synchronization with a minimum

of relative timing jitter. The continuous frequency light source is to be used as the seed light pulse for a second amplifier.

The white-light continuum is obtained in the following fashion. A half-waveplate rotates the plane of polarization of the light source entrant on the continuum cell to the horizontal. The horizontal polarization enhances the reflection or transmission efficiency of the optics that are to follow. An f=8cm lens focuses the beam into a 2cm cell of water. The optical continuum beam is recollimated with a 6cm achromat lens and is analyzed with a polarizer, which is set to transmit only horizontally polarized light. Self Phase Modulation (SPM), known to be a significant (and presently desired) mechanism in continuum generation,[56] should maintain the same polarization of light as the entrant beam. Extensive optical manipulation of this light source is required for spectral bandpass selection, limited pulse shaping and finally amplification to the 0.1-0.25mJ level. A portion of these manipulations is shown in Figure 7a.

Following the polarizer, the beam is diffracted by an 1800 lines/mm ruled diffraction grating and is directed into a cylindrical lens (f=15 cm) placed 20 cm after the grating face. A variable aperture slit is positioned at the focal plane of the cylindrical lens. A normal incidence mirror, located immediately after the slit, retroreflects the spectrally selected beam back onto the grating but displaced ~2cm below the level of entrant beam. The resultant spectrally selected pulse, with a 3Å FWHM bandwidth, has approximately equal temporal duration as the pulse exiting the first amplifier. The pulse energy of this spectrally selected portion of the optical continuum varies from about 25nJ near the center frequency to less than 0.5nJ at 470nm. These pulse energies are sufficient to be injected into, and serve as a seed for a second dye amplifier. This second amplifier is pumped with either the second or third harmonic of the Q-switched YAG laser. The three stage amplifier, with the last stage being longitudinally pumped, could obtain amplification factors of $\sim 2 \times 10^4 - 5 \times 10^5$ depending on the pump wavelength, amplifier dye and initial spectrally selected continuum picosecond pulse energy.

It has been shown[57] that the introduction of a lens of focal length longer than its separation from the grating face will allow for the introduction of positive group velocity dispersion (GVD) on the exiting beam, causing a positive linear chirp to be introduced in the pulse temporal behavior. Treacy[58] has shown that a grating pair arrangement introduces negative GVD. This latter arrangement has been applied to pulse recompression following dispersion in an optical fiber.[59] The present arrangement introduces negative GVD and acts to compensate for approximately 0.5 ps of pulse broadening. Such temporal dispersion arises from the dispersion of the index of refraction in the glass lenses, suprasil dye cells and the dye medium of the amplifier. In particular this negative GVD will act to offset some of the positive GVD introduced by the second amplifier.

7.3.2 Pump-Probe Scheme

The time-resolved experimental studies were performed over the wavelength range 265-230nm. It is possible to amplify 530-474nm light using the 355nm YAG pump and several dyes (coumarins: 522, 500, 481, 480, 460; Exciton Chemicals) in polar and nonpolar solvents (ethanol, hexane, cyclohexane). Second harmonic generation allowed for essentially continuous coverage of the wavelengths 265-237nm. The frequency doubling was performed using a 4mm (thickness) β-barium borate (β-BBO; CSK Co.) crystal placed slightly after the beam waist of a 1m focal length lens. This second harmonic light was used as the experimental pump beam and initiated the reaction by causing the HI moiety to dissociate. The higher energy portion of the wavelength range (238-230nm) was studied with pump light obtained by doubling the 613-587nm ouput from the second amplifier in a KDP crystal and mixing this doubled light with the 1.064μm fundamental of the YAG laser in a type II KD*P crystal. The various frequencies were dispersed using a Pellin-Broca prism, and this 'doubled-and-mixed' beam was used as the pump light for initiation of the reaction.

A schematic outline of the experimental arrangement is shown in Chapter 2 of this thesis. The 20% remainder of the beam from the first amplifier is used

to form the probe beam. The visible pulse propagates through a variable delay line stepper motor/worm gear translation stage (10μm/step resolution) to obtain the timing delay between the pump and probe pulses. The beam is then focused (f=40cm) into a 1mm KDP crystal, recollimated with a 20cm suprasil lens and sent toward the molecular beam apparatus. A waveplate ($\lambda/2$) is used to adjust the relative pump-probe polarizations. Focusing into the thin nonlinear crystal, and in particular placing the crystal within a confocal length of the position of the beam waist, causes the second harmonic beam transverse profile to become much less structured than the entrant fundamental beam.

The pump and probe beams are independently focused into the molecular beam apparatus. A 150μm diamond pinhole inside the chamber and on the axis defined by the molecular jet orifice and the skimmer, but positioned orthogonal to the direction of the jet expansion, is used to overlap the pump and probe light beams. A 0.75m plano-convex (plcx) lens is used to focus the pump beam and a 1m plcx lens focuses the probe light. This arrangement allows the beam waists of the pump and probe light to be independently adjusted and matched to the axis of the free jet expansion. Both laser beams show significant diffraction from the 150μm pinhole. The pump and probe beams are combined by a dichroic reflector (coated to allow for 80-90 % transmission of the probe light) and propagate collinearly through the molecular beam apparatus. The pump pulse energy is 5-10μJ (25cm^{-1} FWHM bandwidth), and the probe pulse energy is attenuated to be $\leq$ 1μJ with a 6cm^{-1} FWHM spectral width.

7.3.3 Molecular Beam and Sample Characterization

The molecular beam apparatus consists of a pulsed nozzle apparatus, vacuum chamber and pumping apparatus and an electronics unit to provide an electrical pulse to the valve in synchrony with the Q-switched laser firing. This arrangement is depicted in Figure 7b. The vacuum chamber is constructed of two cylindrical chambers separated by a 1.7mm opening tapered cone Ni electroformed skimmer. The skimmer allows for differential pumping of the two chambers, with nominal

experimental pressures of 2×10^{-4} torr and 4×10^{-6} torr obtained in the primary and secondary chambers, respectively. Each volume is pumped with a 6″ diffusion pump (Varian VHS-6) and is isolated from the pump via LN_2 cryobaffles. The baffles effectively eliminate backstreaming of pump oil. The primary chamber, which handles >95% of the gas load, is arranged with the nozzle, laser entrance and exit (light baffle) ports, and the LIF collection optics and the 150μm pinhole on three mutually orthogonal axes. The second chamber also has three such mutually orthogonal axes; one defined by the now skimmed molecular beam, the second contains the entrance and exit optical ports for the laser light (not used in this study), and the third consists of an electron ionization time of flight mass spectrometer (EI-TOFMS), described below.

The nozzle assembly in the primary chamber is of Kel-f and Teflon coated metal construction. The generic valve design has been described before,[60] so the elaboration here will be brief. The valve is a solenoid-plunger design, wherein a current pulse energizes the solenoid coil, which, in turn, induces a metal piston to be retracted. The piston pulls a Viton tipped Vespel plunger to expose the orifice opening. The valve is closed by the action of a small spring, which forces the Vespel/Viton plunger to seal the opening. All of the exposed metal surfaces have been coated with a 0.001″-0.002″layer of Teflon to prevent the catalytic decomposition of the HI in the nozzle plenum just prior to expansion. The orifice is a 1/16″ thick strainless steel disk (held to the Vel-f nozzle body by a screw-on cap) with a 500μm hole. The screw cap contains a 45° conical aperture centered on the orifice position. The 2mm deep conical extension acts to enhance the cooling and cluster forming efficiency during the early collisional portion of the expansion.

The nozzle open-time is controlled by the magnitude (voltage) and temporal duration of the electrical pulse to the solenoid (120V, 550-600μsec). The resultant open-time, as measured by the EI-TOFMS varies from 600-800μsec. The time-delay between the firing of the electric pulse and the laser firing is adjusted to optimize the amount of the desired vdW molecule at the time of the arrival of the laser

pulses. The pulsed nozzle controller is triggered by a monitor pulse from the Q-switched YAG, which comes 3.3msec prior to laser Q-switching. The controller is adjusted to generate an appropriate internal timing delay. The adjustment is made by optimizing the 1+1 molecular complex (IH-OCO) signal observed by EI-TOFMS.

The traditional problem of identification of the 1:1 complex (neutral) vs. ion evaporation during the drift period was partially addressed by monitoring the relative peak intensities in rich HI, CO_2 mixtures. The relative peak intensities of the 1:1, 1:2, and 2:1 complexes were recorded for electron impact energies varying from 20 to 70eV. It was found that the relative peak intensities did not change over the 20-40eV range. That is, fragmentation of the ion (2:1 or 1:2) does not produce the 1:1 signal at sufficiently low impact energies. This is consistent with the observations of the HF:OCO studies.[39]

7.3.4 Gas Mixture and Beam Characterization

A sample handling and dynamic flow gas mixing apparatus was constructed to allow for flexability and efficiency in the adjustment of the relative constituent gas concentrations. The nozzle expansions were performed with helium as a carrier gas. Even though there is a large mass differential between He and CO_2 and HI, the small polarizability of He is advantageous in that the propensity to form larger aggregate complexes is diminished. The high purity He and CO_2 were premixed to a 4% concentration of CO_2. The exact concentration was adjusted to allow for only slight ($\sim$ 5%) dimerization of CO_2 in a pure He-CO_2 expansion at the operational backing pressure conditions. The HI (Matheson) was purified just prior to use by cold-trapping, removing the disproportionated I_2 and pumping the H_2. The HI and He-CO_2 gas flows passed through separate flow meters (Matheson rotameters # 600, 601, 602) and were combined just after the meters. The expansion pressure (1700-2100 torr) was adjusted primarily with the He+CO_2. The HI regulated pressure was greater on the inlet side of the associated flow meter. A micro-adjustable needle valve allowed for dynamic regulation of the HI concentration in the mixture. The positive-pressure across the valve allowed for continuous and steady HI flow. This

type of a flow scheme relies on stable pressures of the constituent gases; adequate stability was maintained with a two-state regulator on the He+CO_2 tank and a two-stage corrosive gas regulator on the HI lecture bottle.

The composition of the gas flow was only coarsely adjusted with the flow meters. The actual composition was adjusted while monitoring via the EI mass spectrum of the amount of HI-OCO^+ vs. HI-$(OCO)_2{}^+$ and $(HI)_2$-OCO^+ ions from vdW complexes. The ratio of the desired complex to the higher mass clusters was always optimized to obtain at least a value of 10:1. This required adjusting the HI composition to 1.5% of the total as monitored by the rotameters and in EI-TOFMS. The dynamic mixing required flow rates of 50-100cc/min to facilitate ease of adjustment. The entire entrained gas flow passed through a final -15°C (glycol-dry ice) trap just before entering the nozzle plenum. All subsequent surfaces contacted by the gas mixture were constructed of inert plastic materials.

The second vacuum chamber contains the EI-TOFMS, which is shown in Figure 7b and in greater detail in Chapter 2. The spectrometer consists of a pulsed electron gun juxtaposed with several voltage grids, a TOF field-free drift region (1 meter length) a grounding grid and the box and grid design ion detector. The electron gun consists of a filament in a Faraday cup and an extraction (gate) grid. DC power supply provides 3.5-4.0 amps of current to the tungsten coiled wire (0.005″) filament, and the room temperature voltage drop across the filament is approximately 1 Ω. The Faraday cup is held at the potential of the low-side of the filament, which (along with the covering extraction grid) serves to "store" the electrons. The gate grid is held several volts below the filament potential, and is pulsed 20-30V above the filament potential for about 1 μsec to extract the electrons.

The electron beam is subsequently accelerated to a nominal 50 eV energy, which is the potential difference between the filament and repeller/accelerator grids. The repeller grid is pulsed to the accelerator voltage about 0.75μsec before the beginning of the gate pulse. This serves to create a field-free region between the repeller and accelerator grids; the crossing-region of the electron and molecular beams.

Subsequently, the repeller is returned to 150V above the (positive)accelerator grid voltage 0.25μsec following the end of the gate pulse.

The drive electronics for producing the gate pulse and to pulse the voltage of the repeller grid are obtained from a discrete transistor design.[61] Briefly stated, the original gating pulse input obtains from a pulse generator, triggered by a fast photodiode, which is monitoring the Q-switched Nd:YAG laser pulse. This optical/electrical synchronization allows for producing the electrical pulse coincident in time with the optical pulses (and spectroscopic experiment). This 2μsec duration trigger pulse is input to the two electronic control circuits. In the case of the gate circuit, the amplified trigger pulse is used to rapidly switch a 30-40V pulse into a 2μF, 600V rated capacitor. This capacitor induces this pulse onto the DC (nominal) voltage of the gate. The second circuit obtains the repeller pulse. The design acts to subtract the pulse feature (2μsec duration, 150V amplitude) from the nominal 550V bias of the repeller. This is effected by switching a high voltage capable MOSFET. This discrete device can hold-off 600V, and with the present circuit design, is able to transiently switch up to $\sim$180V in a few tens of nanoseconds.

The repeller, accelerator and ground grids are located directly above the electron gun, and all of the grid spacings are about 3cm. The grid voltages have been chosen in accord with obtaining first order space focusing.[62] The grounding grid is followed by two parallel, vertically oriented electrodes which, when properly biased, act to deflect the ions of a given mass-range toward the detector. These deflection plates serve to remove the transverse velocity component of the ions, which are obtained from the translational velocity of the molecules in the skimmed expansion. A second grounded grid, located 1 meter above the first, defines the end of the field-free region of the TOF drift tube. The ion detector cathode, at 3000V, follows the grounding grid, and accelerates the ions to energies sufficient to initiate the electron cascade through the 18 dynode detector.

The 50Ω terminated output is fed into a 500MHz (PAR model 115) 10$\times$ wideband amplifier. The output is entrant on a Boxcar integrator/averager unit (PAR model 164, 162 averager), which produces an output voltage proportional to the

current monitored in the 50nsec integrator gate width. The voltage output is fed to a voltage-to-frequency converter (VFC), and the signal is stored in a multichannel analyzer (MCA, Tracor Northern). The time delay position of the boxcar gate may be swept in time to scan a mass-spectrum, higher mass species arriving at the detector later in time than the lighter ions. Alternatively, the output of the $\times 10$ amplifier is fed into a transient digitizer (Lecroy), which serves to simultaneously sample 1000 sequential 40 or 80 nsec time intervals and digitize the analog voltage signal of the entire mass-spectrum (or a selected portion thereof) every laser shot. The parallel data collection expedites the diagnostic exercise.

The mass resolution using either of the data acquisition methods described, expecially in the boxcar detection scheme, is approximately 4 amu at 127 amu. The detection resolution at the mass of the desired complex, m/e=172, is about 6 amu for good peak separation. The mass spectral feature assigned to the desired complex is sometimes seen convolved with the $(CO_2)_4$ species - four mass units larger. This broadened double peak is obtained from a slightly too-rich CO_2 concentration and results, with two discernable peaks, at the 172 and 176 m/e positions.

A large dynamic range is inherently required to observe the CO_2 and HI signals, the 1:1 complex and the even more evanescent signal corresponding to the larger undesired clusters, the later two at a few millivolt signal level. This implies that the HI signal level is about 100 mV, the CO_2 level is 300-400mV and the He peak is saturating the detection/amplification system at a level in excess of 2V. Figure 7c shows a graph of the amplitude of several vdW complexes plotted against the nozzle backing pressure. The signals are normalized to the HX parent peak height. The two sets of samples have the same relative composition He:CO_2:HX of 94.5:4.0:1.5 for both HBr and HI. The slopes of the lines indicate that the BrH-OCO complex forms more easily than the IH-OCO complex. This is to be expected in light of the results associated with Figure 3.

7.3.5 LIF Signal Detection

The experimental signal is monitored by Laser Induced Fluorescence (LIF) of the OH product with the probe laser tuned to the $X\,^2\Sigma \leftarrow A\,^2\Pi$ electronic transition.[53] The fluorescence emission is monitored at right angles to the laser and molecular beam axes. The laser, focused to a 150μm beam waist diameter, intersects the molecular beam at x/D=40-45; that is, 40-45 nozzle diameters downstream (D=0.5mm). The emission is collected by a 2″ diameter plcx f/1 suprasil lens. The lens is positioned to collimate the emission. This now collimated emission passes through a 2″ diameter 3/8″ thick suprasil window, which forms the vacuum seal along this optical path. The collimated light next passes through a 12nm FWHM interference filter (Andover) centered at 308nm. Another plex lens (f/1.5, 2″ diameter) focuses the entrant light onto an adjustable slit, which is set to maximize the signal throughput and minimize any scattered laser light. The necessity of detecting resonance fluorescence implies that the light which is scattered from other portions of the chamber cannot be discriminated against by spectral filtering. Other filters, instead of the interference filter, may be placed between this f/1.5 lens and the slit. This placement minimizes the amount of filter fluorescence (from these cut-off or bandpass filters Schott WG-320 and UG-11, respectively), which could reach the detector. Another f/1.5 lens recollimates the emission that passes through the slit, and a final f/1.5 lens, which is permanently mounted inside the PMT housing, focuses the emission onto the photocathode of a signal photon counting PMT (Amperex XP2020). The PMT is mounted in a thermoelectrically cooled housing (Products for Research model).

The nominally 50Ω terminated output is amplified in a wide band amplifier (PAR model 115, DC-500MHz) and sent to a constant fraction differential discriminator (PAR model). The discriminated pulse is fed to the stop input of a Time to Amplitude Converter (Canberra, TAC). The start pulse for the TAC is obtained from a fast photodiode (HP), which monitors the Q-switched YAG laser pulse, and is amplified and inverted (TeK), then fed to a constant fraction discriminator (PAR).

The TAC output is passed to the MCA, which accumulates the signal in synchrony with the stepper motor (delay line) advance. This signal detection arrangement is appropriate for time correlated single photon counting detection.[63] The MCA stores one count for every detected photon event, and because the channel position of the MCA is synchronized to the delay line step advance, the signal events are recorded for the appropriate pump-probe relative time delay. Typical accumulation times are 3 seconds per channel and the scans are repeated 15-20 times depending upon the signal level and the enhancement over the probe beam alone background.

The gated detection (1μsec gate) obtained with the TAC and the low repetition rate of the laser amplifier reduce the dark count rate to less than 1 count in 10 seconds. This is quite important when it is considered that the experimental signal level is about 1 count per second, on the average. These extremely small signal levels necessitate long experimental runs to obtain a sufficiently good S/N ratio to provide the desired accuracy in data analysis.

7.4 RESULTS

A complete description of the time-dependence of OH product formation for the titled reaction requires obtaining an accurate measurement of the "time-zero" of the reaction and the correct system response function. These quantities are essential for the determination of the proper (kinetic) model description of the dynamical behavior. Additional diagnostic experimental measurements are necessary to verify that the observed LIF signals reflect the dynamics of the titled reaction. The purpose of this section is to describe the results of direct measurements of the bimolecular reaction and how these results are analyzed using companion system response function data. The primary goal herein will be to provide convincing evidence to substantiate the claim that the observed dynamical behavior can be rationalized only by a model analysis, which requires the reaction to proceed via an intermediate species (presumably HOCO) of measurable lifetime.

The transient waveform for the formation of the OH photoproduct in different rotational quantum states is an approximately exponentially rising function, which asymptotically approaches some final value for the signal level. A representative scan for the photoinitiated collision of the H and OCO precursors and the observed formation of the OH photoproduct in the lowest energy (238nm photolysis wavelength) rotational quantum state is shown in Figure 8a. The small open circles are the total amount of signal measured in a given channel (~400 channels displayed) at a given pump-probe relative time delay. The ordinate lists the actual number of counts accumulated in a given detector channel with a temporal width of 0.0667ps. The dashed line in the same figure is obtained by monitoring the same quantum state of the OH product formed in the photoinitiated dissociation of HOOH at the same photolysis wavelength (identical pump-probe reaction conditions).[64-66] The $HOOH \xrightarrow{h\nu} 2OH$ results are taken as the system response function. Using the HOOH photodissociation measurements as the system response function implies that the HOOH dissociation dynamics occur on a <200 femtosecond timescale (beyond the detection limit of the experimental apparatus). This assertion will be justified in the following subsection.

The important feature to be noted in comparing these two signal waveforms is that the product formed from the vdW oriented precursor reaction shows a definite time − shift between the inflection points of the two rising curves. A direct measure of this shift value gives a crude estimate of the lag − time between the initiation of the reaction and the observation of the photoproduct. The other notable feature is the difference in the slopes of the response and bimolecular reaction data sets. In particular, it may be seen that the response function rises more steeply than the reaction data. It may be preliminarily stated that a satisfactory accounting of both of these observable differences between the bimolecular reaction dynamics and the (assumed) system response function will lead to a proper description of the underlying dynamical behavior. Before proceeding further it is important to demonstrate that the HOOH data is an adequate representation of the system response function.

7.4.1 System Response Function

An ideal measurement of the pump-probe pulse system response function would be performed *in situ* with the primary experiment. We have chosen the method of one photon (pump) photodissociation of HOOH and one photon (probe) LIF of the OH product.[64–66] The study of the HOOH system is performed with the identical optical alignment and delay conditions to those used for the vdW complex oriented reaction. The optical paths for the bimolecular experiment and response function measurement are identical. Moreover, the optimal pump-probe beam overlap is typically obtained using the bulb (300K, 100mtorr) HOOH direct dissociation reaction. There is no need to change the optical alignment in proceeding to the bimolecular reaction study. The HOOH photodissociation and OH LIF response function method does, however, have some negative aspects. This scheme does not allow for monitoring the system response function simultaneously with the experiment and over the extended time interval of the signal collection. The HOOH response studies are performed under 50mtorr gas phase bulb collisionless reaction conditions. The bimolecular reaction, on the other hand, proceeds under free-jet expansion conditions into an ambient pressure of order 10^{-4} torr. These intrinsic deficiencies may be compensated for. For example, the HOOH response transient is obtained before and after each bimolecular experiment. Systematic degradation of the system response function would be made manifest through this contrasting data. The signal obtained from the HOOH direct dissociation and LIF detection is large enough to allow the signal to be integrated and averaged in a Boxcar signal averager (PAR model 162, 164). The response function scans were, therefore, obtained in about an hour, each. The associated S/N ratio is about 10× better than that of the bimolecular data.

The potentially most significant and possibly intrinsic problem with the method may be that the HOOH dissociation and OH formation is not sufficiently rapid to be termed "instantaneous" on the present experimental timescale. Figure 8b shows a comparison of the time dependence of the HOOH reaction with a true pump-probe

pulse cross-correlation obtained by difference frequency generation of the pump (234nm) and probe ($Q_1(1)$) pulses in a crystal of KD*P with type II phase matching. The instantaneous response obtained from the nonlinear mixing results from the rapid ($\sim 10^{-15}$ sec) response of the crystal medium to the convolution of the pump and probe E-fields.[67] The figure shows that the difference frequency response may be convolved with a single exponential function with lifetime $\tau_{HOOH} = \pm 200$fs, for which the convolved response is indistinguishable from the difference frequency data. Such a small response is well within the intrinsic error of the 4.5 ps gaussian response, which is obtained from the experimental pulse cross-correlation. Care was taken to insure that the pump and probe optical paths were equivalent in the HOOH and difference frequency studies. The equivalence facilitates the determination of the value of any lag-time between the inflection points of the two data sets. The induction period is not discernable in the present results. Therefore, the HOOH $\rightarrow$ 2OH photodissociation behavior may be considered to be a good approximation, for the present pump and probe pulse durations, of the instrument response function.

For several reasons, the HOOH response method has been used to analyze the bimolecular results presented in this paper. Firstly, as mentioned before, the HOOH dissociation allowed for optimization of the pump and probe beam overlap under time delay conditions that were identical to those used in the bimolecular reaction. Secondly, because the signal from the IH-OCO $\rightarrow$ OH reaction was accumulated by photon counting at such low laser system repetition rates (20Hz), it was much easier to maximize reproduceably the obtainable signal with the *in situ* HOOH response. Thirdly, the OH LIF signal could be optimized for on-resonance $^2\Sigma \leftarrow {}^2\Pi$ electronic transitions and facilitate probe wavelength tuning to the $Q_1(1)$ and $Q_1(6)$ transitions. Finally, the HOOH dissociation may be used as a reference over the entire ($\sim$6000 cm^{-1}) initial photon energy range used in this study. By contrast, several nonlinear crystals and IR detectors would be required to span the range of the difference frequency light.

Even though the results of Figure 8b do not obtain the time rate of HOOH dissociation very accurately, it is possible to estimate an upper limit of the lifetime

for OH formation at τ <200fs. This is the case for the presently used 8cm^{-1} probe pulse bandwidth and LIF of the $Q_1(1)$ OH product. Analysis of asymptotic reaction product alignment measurements for the value(s) of the product anisotropy parameter obtained from the angular distribution of the OH product,[65,66] result in estimates for the lifetime of 60fs; this is the time during which HO-OH interactions could affect the orientational distribution of the products. Finally, a simple (classical) calculation of the time integration of particle motion on the exponential repulsive surface[68] of HOOH shows that ~100fs are required to obtain an O-O internuclear separation of 7Å. It may be concluded that the method of using HOOH to obtain the system response function is reasonable provided that the bimolecular reaction dynamics occur on a somewhat longer timescale (τ >400fs, for example).

Finally, the response method serves another useful purpose. The low count rates of the bimolecular reaction study preclude the possibility of measuring the power law dependence of the OH product. Because the detected photoproduct is the same for both reactions the power dependence is performed for the HOOH reaction. Figure 9a shows a logarithmic plot of the signal against a decrease in the optical density obtains a reasonably straight line with slope of 0.95 ± 0.1 for $Q_1(1)$ detection and 238nm excitation. This is consistent with the idea that a single probe photon induces the LIF of the OH product. A similar result is obtained when the $Q_1(6)$ transition is probed. The linear intensity dependence shows that the electronic transitions are not being saturated in the probing process. Therefore, the LIF intensity is proportional to the number density of the ground electronic state OH product obtained from the reaction.

7.4.2 Kinetic Model Analysis

Having established the validity of the HOOH photodissociation response method, these response functions may now be used in an analysis of the experimental results. A first attempt at understanding the dynamics of product formation is

to attempt to fit the bimolecular data with the model function for the observable signal S(t)

$$S(t) = \int_0^t \left[\int_{-\infty}^{t'} R(t'') \cdot \exp\left[-k(t' - t'')\right] dt'' \right] dt' + \Delta\tau' \qquad (3.1)$$

where R(t) is the HOOH response function to be convolved with the exponential rate (k) of product formation. The integration over t'' is for convolution. The quantity $\Delta\tau'$ is an independently adjustable time-shift parameter, which may be held fixed or allowed to float in accord with a measure that determines the goodness of fit. Holding the time-shift fixed at zero and fitting the data of Figure 8 with the displayed response results in a lifetime, $\tau' = 1/k'$, of 2.9 $\pm$ 0.6 ps. A physical interpretation of the analyzed lifetime might conclude that this time constant represents the slow decay of the [HOCO]† intermediate.

We previously reported[24] on preliminary findings for the same (title) reaction, monitored by the rate of OH product formation. The preliminary account, using a method of 1+1 ionization[54,12a] of p-n butyl aniline[69,70] for the response function, obtained a lifetime of 5$\pm$2 ps via single exponential fit without lag-time. Comparison of the present lifetimes and that reported in Ref. 24 with the $\sim$ 2×10^{-13} sec lifetime expected from an RRKM calculation shows a large discrepancy. The parameters for the PES and TS configurations of the calculation are obtained from Ref. 49. Although perfect agreement is not to be expected, the magnitude of the disagreement between experiment and simple theory suggests that Eqn. (3.1) requires $\Delta\tau' \neq 0$.

The aforementioned model with the shift held fixed implicitly assumes that the process of [HOCO]† formation is very prompt. This assumption, however, presupposes the physical (kinetic) mechanism of the reaction. A first approach at broadening the scope of the analysis of the information contained in the experimental data involves allowing the time-shift to float freely. The shift parameter is evaluated in a fashion consistent with minimizing the value of χ^2 in the nonlinear least

squares fitting. The result for the same data set (Figure 8a) yields a lifetime of 0.9 $\pm$ 0.3 ps and a shift $\Delta\tau' = 0.75$ ps. Moreover, the χ^2 value has been diminished by about 50%. The shorter value for the lifetime thus obtained is more in accord with the value expected from a simple (statistical) calculation of the unimolecular dissociation rate. This description, however, loses a sound physical basis because the single exponential model representation only phenomenologically accounts for the observed time-shift behavior. Moreover, the nontrivial value for the shift is at odds with the idea that only one measurable lifetime is observed in the experimental data. This deficiency in the examination of the reaction dynamics via a simple kinetic model give compelling evidence for the existence of an intermediate species. Further analysis is required to determine if the shift behavior may be related to information about the formation of $[HOCO]^{\dagger}$.

It will be assumed that a kinetic analysis is an adequate description of this restricted geometry bimolecular reaction. Extension of the previous simple analysis leads to invocation of a model which accounts for both the bimolecular dynamics leading to formation of the intermediate species and the subsequent unimolecular-like decay of this intermediate. Consider the kinetic model:

$$A \underset{}{\overset{k_1}{\rightleftharpoons}} B \overset{k_2}{\rightleftharpoons} C \tag{3.2}$$

where A is the van der Waals restricted geometry reactant, B is the $[HOCO]^{\dagger}$ intermediate and C is the OH (implicitly CO) final product. It follows from the isolated conditions of the free jet expansion that the recombination of OH and CO will not occur. The absence of a spectator mass, which could remove a sufficient amount of translational energy and reverse the velocity vectors, diminishes the likelihood of recombination. Therefore, the $C \overset{k_{-2}}{\rightarrow} B$ reaction will not be a significant factor in the overall reaction dynamics.

Additional simplification of the kinetic behavior may be obtained if it becomes possible to estimate the relative magnitude of k_{-1} compared to k_2 and k_1. Several

studies of the dynamics of the reverse reaction

$$OH + CO \overset{k_{-2}}{\rightleftharpoons} HOCO \overset{k_{-1}}{\rightarrow} H + CO_2 \tag{3.3}$$

have been performed at a range of temperatures. Analysis of the measured thermally averaged rate constants k_{-1}, k_2, and k_{-2} and model TST and RRKM calculations have allowed for making some general assumptions about these rate constants. The preliminary section of this paper summarized the results of temperature and pressure dependence studies by Smith[30] and coworkers[31] and Golden and coworkers.[32] The temperature and pressure dependence of the OH + CO → H + CO_2 reaction is analyzed with a method described by a modified Arrhenius rate expression for reactions that proceed via bound intermediates.[32] It is shown that the thermal rate constant for HOCO → OH + CO_2 is much smaller than that associated with HOCO → OH + CO. Specifically, $k_{-1}(T)<k_2(T)$, and it can be inferred that the microcannonical unimolecular reaction rate behavior relevant to the present study is similar; that is, $k_{-1}(E)<k_2(E)$.

The previously assumptions and independent measurements may be used to reduce the complexity of Eqn. (3.2), which, therefore, reads

$$A \xrightarrow{k_1} B \xrightarrow{k_2} C \tag{3.4}$$

with the same designations for A, B, and C. The kinetic equation behavior for the formation of C in either Eqn. (3.2) or (3.4) is of a standard form.[71] The differential equations that express the time dependent change of the constituent populations are

$$-\frac{d[A]}{dt} = k_1 \cdot [A] \tag{3.5a}$$

$$\frac{d[B]}{dt} = k_1 \cdot [A] - k_2 \cdot [B] \tag{3.5b}$$

$$\frac{d[C]}{dt} = k_2 \cdot [B] \tag{3.5c}$$

Material conservation gives the relation A_o=A+B+C. The initial conditions, at t=0, are A=A_o, B=C=0. The simplification of the kinetic model of Eqn. (3.2) to Eqn. (3.4) facilitates a straightforward solution of the set of Eqns. (3.5). Sequential integration of Eqns. (3.5) allows for the evaluation of A(t) and B(t), where A=[A], etc. Appropriate use of the mass conservation and population initial conditions results in an expression for C(t). The observable kinetic rate expression is found to be

$$[\mathrm{OH}] = \mathrm{A}_o\left\{1 + \left(\frac{k_2}{k_1 - k_2}\right)\cdot \exp\left(-k_1 t\right) - \left(\frac{k_1}{k_1 - k_2}\right)\cdot \exp\left(-k_2 t\right)\right\} \qquad (3.6)$$

where A_o refers to the t=0 number density for the reactants. This is the expression which will be used as the model equation for the nonlinear least squares fitting of the time-resolved data. The term [OH] implicitly depends on the pump wavelength and specific OH ($\nu = 0$) K=1,6, that is $Q_1(1)$ or $Q_1(6)$, rotational state which is probed. The data fitting can obtain additional information about the reaction dynamics besides the rate constants for reaction. The additional insight is in reference to the 'induction-period'. This may be understood to be the delayed build-up of the final product due to the finite time of formation and/or reaction (dissociation) of the complex intermediate.

This induction-period refers to the time interval between t=0 and the inflection point in the rise of the OH product. The point of inflection in the rise of the product, denoted by C in the kinetic scheme, may be found by solving for the roots of $d^2\mathrm{C}/dt^2 = 0$ or, equivalently, $-k_2 \cdot d\mathrm{B}/dt = 0$. The expression for B and $d\mathrm{B}/dt$ were obtained in the course of solving for C(t) and are given by

$$[\mathrm{B}] = [\mathrm{HOCO}]^{\dagger} = \mathrm{A}_o \cdot \left(\frac{k_1}{k_2 - k_1}\right)\cdot \left[\exp\left(-k_1 t\right) - \exp\left(-k_2 t\right)\right] \qquad (3.7)$$

and

$$\frac{d[\mathrm{B}]}{dt} = \mathrm{A}_o \cdot \left(\frac{k_1}{k_2 - k_1}\right)\cdot \left[k_2 \exp\left(-k_2 t\right) - k_1 \exp\left(-k_1 t\right)\right] \qquad (3.8)$$

It is seen that the inflection point in the rise of OH occurs at the time when the population of $[HOCO]^{\dagger}$ reaches a maximum; $\frac{d^2C}{dt^2} = -k_2\frac{dB}{dt} = 0$. The lag-time may be obtained from Eqn. (3.8) and is found to be

$$\Delta\tau = \frac{\ln(k_1/k_2)}{(k_2 - k_1)}. \tag{3.9}$$

Figure 9b schematically summarizes the overall dynamics accounted for by the present kinetic model. This figure is for $k_1 = 2k_2$, the associated induction period, but illustrates this induction time for the case of an instantaneous system response time.

7.4.3 Experimentally Observed Dynamics

The solid line in Figure 8a shows a fit to the data for the time-dependent formation of the OH product using the sequential reaction scheme. Visually, the fitted result is similar in appearance to that of the model Eqn. (3.1), but the χ^2 parameter has been improved by another 15%. The improvement in the goodness-of-fit parameter is perhaps to be expected in that additional fitting parameters have been introduced. However, the more complete kinetic scheme requires a close coupling of the two rate constants by way of the relative amplitude factors $\left(\frac{k_1}{k_1-k_2}\right)$, etc. Such restrictions on the independence of the individual fitting parameters mandates the physical resonableness of the model to the actual dynamical behavior measured in the experiments. Making unphysical adjustments, such as switching $\frac{k_1}{k_1-k_2}$ for $\frac{k_2}{k_1-k_2}$, for example, in the kinetic fitting model typically precluded obtaining any convergence in the fitting parameters.

Figure 10 shows the large contrast in the bimolecular reaction results for photoinitiated dissociation with 263nm (10a) and 241nm (10b) pump pulses. The figures also show that HOOH response functions obtained for the same pump-probe laser pulse conditions as the bimolecular reaction data. The response functions are similar for the two data sets and thereby emphasize the difference in the measured reaction behavior. The figures also show the best fit to the data using Eqn. (3.6) and

convoluting with the respective response functions. The lifetimes $\tau_1=1/k_1$ and $\tau_2=1/k_2$ and the induction period are summarized in Figures 12 and 13.

The symmetric form of Eqn. (3.6) leads to the interchangability of the k_1 and k_2 fitted rates. The fitting procedure typically ascribes the larger rate to the initial step of the reaction (c.f. k_1). It is, however, possible that the unimolecular decomposition of the intermediate will be assigned the faster rate of reaction by the fitting procedure. The ambiguity as to which rate is faster can be solved with a reasonable degree of assurance by examining the dynamical behavior observed in QCT studies.[51] Presentations of the reactive trajectories[52] clearly show that the formation of the HOCO intermediate occurs more quickly than the subsequent unimolecular decay. The data fitting analysis was performed in a self-consistent fashion in that the first rate component (i.e., k_1) was always fit with the larger rate constant.

Temporal signals for the reaction product were obtained at several wavelengths while monitoring the $Q_1(1)$ OH electronic transition. Additional measurements at various pump wavelengths were made while detecting the $Q_1(6)$ product. The principal idea was to make manifest the consistent or systematic differences which may be observed when comparing the $Q_1(6)$ results with the $Q_1(1)$ measurements at a given photolysis pulse wavelength. Individual data sets (bimolecular reaction results vs. HOOH response) for $Q_1(1)$ or $Q_1(6)$ detection are shown in Figures 11a-h. The K=1 vs. K=6 results for a given photolysis wavelength are to be compared. The $Q_1(6)$ data generally show noticeably more prompt OH formation than the $Q_1(1)$ results. The only exception to this trend is for 256nm excitation, which is considered a low energy excitation data set. The lifetimes and other characteristic parameters are summarized in Figures 12 and 13.

Figures 12a,b summarizes the $\tau_1=1/k_1$ and $\tau_2=1/k_2$ values for the different pump pulse wavelengths for both $Q_1(1)$ and $Q_1(6)$ detection. The values are plotted against the energy made available to the HI moiety of the vdW-reactant complex. Many of the data points are the averaged value of several independent measurements. The D_e° (energy of formation) of HI has been subtracted and the energy

imparted to the H-atom has been converted to relative center of mass motion with respect to I and OCO. This calculation of the translational energy in the c.m. frame has been performed by serially considering each pairwise correction according to Eqn. (2.9). Effective three-body corrections have not been considered. In light of the proximity of the two monomer reactant species it may be prudent to consider such multibody collisions. This point will be addressed in the Discussion section below. The $Q_1(1)$ and $Q_1(6)$ data were obtained in back-to-back experimental runs, interspersed only by their respective response function measurements. It may be observed from the data and figures that the reaction dynamics for K=1 and K=6 are approximately equivalent at the lower excitation energies. The concept of equivalent rates of product formation in a photo-initiated unimolecular reaction,[10] under essentially microcanonical conditions, should hold when both of these rotational product states are energetically accessible. Such microcanonical reaction conditions are to be expected if the restricted sampling of relative angle of (bimolecular) interaction and impact parameter is not a significant factor.

Figure 12 shows that the values for τ_1 and τ_2 at a given energy are usually within a factor or two of one another. It is expected that the rate of formation of the intermediate species would be rather prompt, while the subsequent unimolecular decay (c.f. k_2) would be somewhat retarded, by comparison. The relatively small magnitude for the difference in the τ_1 and τ_2 time constants may result from the large amplitude motions required to form HOCO from H+OCO (see the Discussion section). Another general observation is that both τ_1 and τ_2 decrease essentially monotonically with increasing available energy.

The last point, which concerns the monotonicity of the lifetime or rate with energy, is understandable for the unimolecular reaction behavior associated with the decay of the intermediate $[HOCO]^\dagger$ to form the OH product. The formulation of the statistical rate constant from RRKM theory is

$$k_{\mathrm{RRKM}} = \frac{\mathrm{N_{MC}}^{\ddagger}(\mathrm{E,J})}{\rho_{\mathrm{MC}}(\mathrm{E,J}) \cdot h} \qquad (3.10)$$

where MC denotes the microcanonical reaction condition. It can be seen that for a given increase in energy the change in the microcannonical state count in the critical configuration, $N^{\ddagger}_{MC}(E,J)$, will generally rise more rapidly than the density of states of the reactant, $\rho(E,J)$. This conclusion is reasoned from the relative proximity ($\triangle E$) to the respective zero-point levels. It has been shown by Levine and Bernstein[3] that the reaction cross section (hence the rate) of a bimolecular reaction, which involves a reaction barrier, increases monotonically with collision energy, for energies above the threshold to reaction. More quantitative analysis of the shape of these curves is left for the Discussion section.

The induction associated with the lifetimes (inverse rate constants) of Figure 12 is presented in Figure 13a. It may be seen that this lag-time also decreases essentially monotonically with increasing available energy. The significant reduction of the induction period serves to emphasize the rapidly decreasing overall reaction time with increasing energy. This summary of the lag-time between the initiation of the reaction and the appearance of the desired OH product will be of use when comparing the present experimental period with the results of future dynamical calculations.[52] The observation of the induction period, which is an intrinsic characteristic of the two-step kinetic analysis in that it reflects the dynamics of the intermediate species, is inconsistent with a reaction that proceeds directly from reactants to (spectroscopically observable) products.

It should be parenthetically noted that these experimental measurements are equally sensitive to OH products that form via the HOCO intermediate as those that are formed by way of a more direct reaction route, bypassing the HOCO species. It is not presently possible to estimate the fraction of the product OH, which is formed via a direct mechanism at a given energy. The model equation, Eqn. (3.6), does not explicitly account for product formation from two distinct reaction mechanisms; complex vs. direct. It will be inferred that only a small fraction of the reactive encounters actually proceed by the H-atom direct insertion mechanism. This estimation stems from the result of the QCT studies.[51]

7.4.4 Relative Reaction Probability

Figure 13b is a plot of the relative reaction probability. This quantity is obtained by normalizing every data set to the pump and probe light intensities, transmission characteristics of the collection optics and to the gas phase absorption coefficient data of Ref. 29. The results have not been normalized to account for the branching ratios in the formation of $I(^2P_{3/2})$ and $I(^2P_{1/2})$, this ratio being an excitation energy dependent quantity.[72] The relative reaction probability is plotted against the energy made available to the IH-OCO species, with consideration given to the D_o° (HI; $^2P_{3/2} \Rightarrow$ 296kJ/mole) and the pairwise hydrogen - c.m. relative velocity. The most evident features to be noticed are the two steeply rising regions of the reaction probability at high and low energy and the more slowly rising region of connection. A vertical line has been drawn in the figure that represents the measured threshold for the room temperature gas-phase (bulb) $H+CO_2$ reaction[36] 106kJ/mole=8876cm^{-1}. plus the 7603 cm^{-1} energy of the $I(^2P_{3/2}$-$^2P_{1/2})$ spin-orbit splitting.[72] The energy of this vertical line should represent the threshold for the formation of the OH product in the lowest rotational quantum state and the formation of I in the $^2P_{1/2}$ state. This conclusion is made while assuming that all other things remaining the same for comparison with the lower energy reaction results that correlate to the $I(^2P_{3/2})$ product.

The rise and plateau behavior at lower energies may be understood by considering two separate contributions to the product yield into the K=1 $OH(^2\Pi_{3/2})$ state. Firstly, it is known that the branching ratio for formation of the $^2P_{3/2}$ vs. $^2P_{1/2}$ product is decreasing with increasing energy,[72] especially in this wavelength range. The value at 248nm photolysis wavelength is about 50%. Secondly, the relative probability of forming the lowest energy product decreases in comparison to the formation of higher lying product states at energies sufficiently above a given reaction threshold. This is because the product state distribution curve becomes bell-shaped, and the absolute flux into the lowest quantum state may begin to decrease.

A spike-like feature may be seen at the 240 nm ($1.648\times10^4 cm^{-1} = E_{avail}$) position of Figure 12b. The enhanced reaction probability at this energy is a statistically significant deviation from the general trend of the curve as represented by the neighboring data point. The reduced magnitude of the error bars near this feature reflect the multiple (independent) measurements that contributed to the displayed result. Arguments that elucidate the nature of this locally enhanced reaction probability are presented in the Discussion section. It will presently suffice to say that the underlying reaction promoting behavior occurs quite near the threshold of the $I(^2P_{1/2})$ reaction channel. Figure 12b also shows data points (open circles), which refer to the formation of the OH product in the K=6 rotational state. Even though there are fewer data points for this higher energy final product state it does appear that the increase in reaction probability is a somewhat more smoothly rising function than that observed for $Q_1(1)$ LIF detection. Note that the $Q_1(1)$ and $Q_1(6)$ relative reaction probabilities are not normalized with respect to one another.

7.4.5 Limitations of the Kinetic Analysis

A final note must be made concerning an additional aspect of the reaction dynamics. The aforementioned reaction rate (lifetime) measurements and the associated induction period required the phenomenological introduction of a small time-shift. This was necessary for obtaining the minimum value for χ^2, that is, the best measure of the goodness of the fit. The magnitude of this shift is small but is perhaps significant at the lowest studied reaction energies. The shift feature is physically distinct from the induction behavior. These results are also plotted in Figure 13a as time-shift vs. E_{avail}. The maximum magnitude of the time-shift is 0.63ps at 263nm. The underlying physical significance of the observed deviation from the kinetic analysis stems from two particular effects, (i) the method of performing such pump-probe experiments and (ii) the reaction behavior actually described and accounted for by (statistical and kinetic equation) reaction rate constants.

Consideration of the detection of the reaction products brings about a concern about effects that are ascribed to perturbed-product fragments.[64] The term

perturbed-product refers to the optically detected fragment (cf. OH), which interacts with the partner photoproduct in the course of separation and eventually becomes the nascent product. The effect is spectroscopically observable in photoinitiated unimolecular dissociation on directly repulsive potential surface(s)[12,73,11] (e.g., ICN,CH_3I, HOOH). The manifestation of the process is that the perturbed photoproduct is detected (e.g. ionization,[73] LIF[11,12]) off the nascent product electronic transition wavelength. In principle this allows for probing phtofragments during the course of the dissociation.[74] This effect has also been observed for reactions that undergo unimolecular dissociation on the ground electronic surface.[75] This latter observation in HOOH dissociation may be associated with spectroscopic probing of one OH radical while the partner OH is still nearby. Such probing may be taking place in the exit channel region where long range multipolar interactions may persist for (experimentally) significant periods of time (0.25-1.0ps)[75] for the relative translational energy of these reactions ($\sim$ 2000-5000cm^{-1}).

These "off-resonance" effects have not been observed for the present bimolecular reaction study. The lack of the observable effect may stem from several causes. The small dipole moment of the CO partner fragment may not produce a sufficiently large interaction in the course of dissociation. The 2.5Å vdW bond length and the extension of the I-HOCO(c.m.) separation to about 10Å during the 1-2ps reaction period will also act to minimize the I-OH interaction. Lack of observation of this effect may also result from differences in the PES for HOOH unimolecular dissociation[76] and HOCO dissociation. Loose vs. tight TS configurations may affect the spectral form or magnitude of the perturbed fragment spectrum.

Secondly, the rate equation description used herein only considers the reaction dynamics from the reactant phase space region to the transition state configuration,[76] that is, from the $[HOCO]^{\dagger}$ energetic intermediate to the saddle point configuration [HO–CO]. The time required for the OH to become sufficiently removed from the perturbing associated photoproduct and come into resonance with the probe pulse bandwidth may be significant in the case of small relative translational energies of the fragments. It is expected that the time delay, in proceeding

from the TS configuration to the spectroscopically observable product configuration, should be measurable. Such an effect lies outside the realm of description of the overall rate equation analysis and has, presently, been summarized simply as a phenomenological time shift. Neglect of this additional shift does adversely affect the goodness of the fit for the low energy data in the range of 263-247 nm.

7.5 DISCUSSION

The aim of this section is to deal more completely with some of the issues of interpretation that were mentioned and defined in the results section. It is necessary to devote more time to the analysis of the more subtle features observed in the summary of the reaction lifetimes τ_1 and τ_2 (Figure 12) and the spike-like feature in the relative reaction data (Figure 13b). The desire is to make a coherent and convincing case that: (i) the titled reaction indeed proceeds via the $[HOCO]^\dagger$ intermediate species; (ii) that both the threshold and moderate reaction energy dynamics have been measured in the time-resolved studies; (iii) that two major channels contribute to the formation of the OH product; and (iv) finally that these results show that these vdW intra-complex bimolecular reactions display unique dynamical features that are intrinsic to the proximity and constrained geometry of the oriented reactants.

7.5.1 Deviation From Statistical Unimolecular Decomposition

The first observation to be addressed is the energy dependence of the reaction rate, k_2. This behavior corresponds to the decomposition of the $[HOCO]^\dagger$ reaction intermediate to form the spectroscopically observable OH product. The τ_2 data of Figure 12b have been replotted as $1/\tau_2 \equiv k_2$ in Figure 14. The several additional curves plotted in this figure are the results of statistical unimolecular reaction model calculations. The energy threshold for the calculations as well as the relevant parameters for the energetic intermediate, the unimolecular transition state

(critical configuration) structural parameters and associated energetics are summarized in Tables 3,4,5. The variety of calculation conditions were chosen to obtain a diverse sampling of the range of reaction rates expected for reasonable statistical unimolecular reaction conditions. The plotted RRKM[76] results are from a standard calculation without free rotations in the critical configuration. These calculations conserve angular momentum throughout and at the level of the average value for the 10°K initial conditions of the experimental reaction. The RRKM #1 results are calculated with the values for the frequencies and energy parameters obtained from Ref. 49. Zero-point energy corrections have been included to make the fitted PES energies more like the actual experimental conditions.

The parameters of Table 4 and RRKM #2 curve in Figure 14 are from the gas-phase kinetic studies discussed above.[32] The barrier at 13030cm^{-1} above the HOCO monimum energy configuration is about the same as the asymptotic energy for the separated fragments of 12980cm^{-1}.[51] The HOCO frequencies are from matrix isolation studies[33] and the parameters for the critical configuration are obtained from RRKM modelling of the thermal reaction data.[32]

The model curve RRKM #3 in Figure 14 obtains from the studies of Smith et al.[30,31] The study does not provide HOCO parameters; so these have been estimated according to the prescriptions which these authors applied to obtaining the parameters for the critical configuration. Thereforem, the curve is shown more for demonstrating the range of RRKM rate behavior which is possible.

It may be concluded that the large discrepancy between the measured unimolecular reaction rates and the results of a variety of model statistical calculations cannot be brought into resonable agreement simply by adjusting the structural aspect (tight vs. loose) or location of the critical configuration. The presently discussed reaction rates are relevant for the decomposition of the [HOCO]† intermediate. Therefore, any unusual dynamical features observed in k_2 will become manifest if a restricted or altered value for $\langle J \rangle$ is obtained, or if the effective energy in [HOCO]† is significantly different than expected. The expected relatively small range of statistical rates[2,34] for different finite $\langle J \rangle$ values discounts the possibility

that angular momentum conservation (for rotationally hot vs. cold reagents) may fully account for the observed discrepancy of Figure 14. The unimolecular reaction barrier of 22-23kcal/mole above the free H+CO_2 energy has been obtained from several different experimental studies[30-32] and from recent ab-initio calculations[49,51]. It is reasonable to assume that the close agreement of several reports of the energy of the critical configuration preclude ascribing the deviation between the experimental and theoretical results in Figure 14 to uncertainty in the reaction barrier height.

An alternative explanation postulates that a reaction bottleneck,[77] which prevents the $[HOCO]^{\dagger}$ from dissociating in a statistical fashion, may account for the deviation. Such an interpretation is fraught with conjecture and will not easily yield a sound and defensible explanation. Although not implausible, the idea of a bottleneck to reaction will not be considered further here.

A simpler explanation for the deviation of the experimentally observed reaction rate from the simple statistical model rate may be formulated. Consider that the total amount of energy which is actually available for reaction is less than the total energy imparted to the vdW reaction complex by the pump photon. An explanation for the origin of this energy deficit is illustrated in Figure 15. The idea of this figure is the construction of an effective "linear" PES of the entrance channel region of the overall reaction PES. It will be useful to gain an appreciation for the (qualitative) partitioning of the reaction energy between H-atom kinetic and the H-atom interaction energy with both partner species (i.e. I and OCO).

The horizontal axis in Figure 15 is labeled as the reaction coordinate, and refers to the internuclear separation of hydrogen from iodine. The distance is given in units of bohr radii. This distance may be related to the distance of hydrogen from the center of mass of CO_2 when the I-atom and CO_2 relative translational motion is fixed during the period of the H-atom attack. The vertical axis is expressed in cm^{-1} units of energy above the dissociation energies for HI→H+I($^2P_{3/2}$), and the CO_2 moiety. The curve labeled A in Figure 15a is obtained from Schatz *et al.*[49] and is a linear cut through the H-OCO potential (interaction) surface. The ab-initio

PES represents the minimum energy reactive surface; the geometry of the CO_2 is adjusted to minimize the potential energy for each value of (r,ϕ) describing the approach of H to the CO_2 c.m. The linear-cut represents an approach geometry of 35° between the O-O axis of CO_2 and the line connecting H with the CO_2 c.m. The curve labeled B in Figure 15a is the HI $^1\Pi$ repulsive electronic state.[72] This potential surface correlates to the I($^2P_{3/2}$) product.

The relative positioning of the HI and HOCO potential surfaces (coordinate scales) is consistent with the results of the calculation (given in the Background section) for the center of mass separation of the IH and OCO species in the IH-OCO vdW complex. Curves A and B are therefore positioned in a configuration corresponding to the interfragment separation, which exists at the t=0 point of the reaction. Curve C of Figure 15a represents a linear cut through the potential contours for H-atom attack on CO_2 with the CO_2 bending angle held fixed at 175°.[52] The plotted curve is a linear cut taken at a C-O-H angle of 25°. The 175° bend represents CO_2 at the maximum of the zero-point displacement from the linear equilibrium configuration.

Figure 15b is simply a linear addition of curves A and B, and C and B shown along with curve B. These simply additive linear cuts of the PES represent the minimum and maximum energy reaction paths that could exist at the reaction t=0. The curves are not completely representative of the true PES because the I-M (M=O,C) two body and I-H-A (A=O,C) three body (dispersion) interactions have not been taken into account. The effective PESs of Figure 15b will, however, suffice for obtaining a physical picture of the photo-initiated reaction dynamics and for making semi-quantitative comparisons with the experimental results.

The portion of the effective (minimum energy) PES for the "bimolecular" aspect of the reaction is represented in Figure 15b. The energy scale of Figure 12 may be transposed to Figure 15 to visualize the energy for reaction initiation. The effective PES is initially repulsive (between I and H), and the surface supports a minimum along this reaction coordinate. The minimum is bounded by a rise, which forms the minimum energy barrier to the initial portion of the reaction. The IH

(repulsive) potential energy is converted into kinetic energy as the reaction proceeds from the repulsive Franck-Condon region to the coordinate position, which corresponds to the local shallow minimum point of the effective PES.

It can be seen that of the two simply additive linear potential surfaces of Figure 15b, only the PES for equilibrated H-OCO shows a well that corresponds to the configuration of the HOCO intermediate. The 175° additive surface is, by contrast, purely repulsive. Because at t=0 the H is not strongly interacting with CO_2, the bend angle is expected to be close to 180°. Hence, reactions that proceed via formation of the reaction intermediate require a CO_2 bending conformational change.

In the case of a 2eV excitation (41616cm^{-1}-24990cm^{-1}) about 1eV of potential energy is converted into kinetic energy of the H-atom motion at the internuclear separation of the local minimum. However, inspection of the energetics of the two curves A and B, which constitute the minimum energy reaction path PES, shows that the H-atom is already encountering a strong repulsive interaction with OCO at this H-OCO separation. The reaction is now in a coordinate region of mutual pairwise repulsion of I and H and also H and OCO. The dynamics have evolved to the point where the iodine and OCO are, effectively, mutually repelling each other. The mediator of this heavy-mass fragment repulsive interaction is the relatively light H atom. The mutual repulsion causes the I-atom to obtain more kinetic energy in the center-of-mass frame than would be expected from the simple picture of a two-step sequential reaction.

In this picture of mutual interaction and considering a classical view of the dynamics, the I and H separate and the H-atom, with the maximal amount of kinetic energy at the configuration of the local minimum, interacts with the OCO. The multi-body reaction scheme described, apportions a greater portion of the total available energy to the translational motion of the iodine product. The OCO fragment, and hence the HOCO intermediate, will also obtain more kinetic energy in the center of mass frame of the vdW complex. In general, however, it is not known how much energy will be converted into internal excitations of the OCO. The present

discussion for dynamical evolution on the minimum energy PES will not allow for further adaptation or accommodation by CO_2, provided internal excitations are ignored. Therefore, conservation of the c.m. motion requires the HOCO to be accelerated in proportion to the ratios of the I atom to vdW complex masses.

A simple calculation, which considers I and HOCO to be hard spheres (no energy accommodation into internal degrees of freedom) would reduce the energy available for the HOCO reaction by 27%. It is expected that this would be the elastic half-collision limiting condition. In reality, the internal degrees of freedom of the CO_2 would certainly accomodate some portion of this 27% maximal energy defect. Also, the finite steepness (or repulsive character) of the interaction potentials would also make the actual dynamics less impulsive and allow for more internal excitation of CO_2.

Such a termolecular reaction mechanism also implies that the energy distribution of the HOCO may not be quite as narrow as would have been assumed for the simpler sequential bimolecular behavior. The jet-cooled conditions of the present study minimize the thermal mode occupation contributions to the energy uncertainty. However, the termolecular situation may lead to a large internal energy spread because the distribution of initial impact parameters and fragment relative angular orientations would create a range of energy lost to the linear translation of the I-atom. A simple line-of-centers picture for the reactant c.m. energy would scale the energy of the collision encounter by $\cos\theta$ where $\theta = \frac{b^2}{d^2}$. The reaction impact parameter is b and d is the sum of the hard-sphere reactant radii. However, for the exclusively small-angle reactive collision configurations of Ref. 51 the reaction energy distribution is quite narrow.

Reasonable agreement between the experimental (K=1) k_2 rate-values and the RRKM #2 curve is obtained if the experimental E_{avail} value is scaled downward by a constant value of 15%. The rescaling factor is shown by the horizontal arrows of Figure 14. This scaling factor is certainly empirical but does clearly show that the $[HOCO]^{\dagger}$ reaction intermediate has less energy available for reaction than would be predicted from a straight-forward bimolecular process. The same figure indicates

that the values for the $Q_1(6)$ data should be rescaled by the same percentage. The only notable difference between the $Q_1(1)$ and $Q_1(6)$ results occurs in the intermediate energy range from 16000cm^{-1} to 18000cm^{-1}. This will be discussed below.

Wittig and coworkers[28b] have conjectured that the decreased available energy is the cause of the deviation of their experimental PGL PSD of OH from the PSD resulting from the bulk H+OCO reaction. Both distributions differ from the PSD obtained from a prior statistical calculation.[22,78] Earlier studies[22] with the BrH-OCO system did not allow this group to uniquely discriminate between the alternative explanations of: (1) constrained angular momentum conditions from the precursor geometry limited reaction conditions; (2) termolecular entrance channel effects, which reduce E_{avail} for product formation; (3) a kinematic bias caused by the small separation between the axis for unimolecular dissociation (along the -CO- bond) and the -OH center of mass; and (4) the presence of product formation from the $Br(^2P_{1/2})$ channel, or some combination of these effects. Certainly the energetics of their study allowed for product formation via (4) in addition to the $Br(^2P_{3/2})$ channel.

Their qualitative justification for attributing the colder PSD obtained for the PGL reaction studies to an energy defect mechanism completely neglects a plausible alternative interpretation. The bulk reaction results allow for, and via the angular dependence of the H-OCO potential[49] energetically prefer, an enhancement of the reaction probability for somewhat broadside (as opposed to end-on) H atom attack. Such a side-on geometry is not as readily obtained in the vdW geometry limited reaction conditions. Hence, the bulk reaction will proceed with a greater average angular momentum than the beam reaction.

The preference for a side-on attack geometry can be inferred from Figure 16. This figure reproduces the plots of Figure 15b and adds two more linear-cut effective surfaces. The additional linear cuts are for a CO_2 bend angle of 160°. One is for symmetric C-O bond lengths of $2.2a_o$ and the other for asymmetric C-O bond lengths of $2.2a_o$ and $2.4a_o$. The H-atom approach angle is about 30° to the CO_2

c.m. and O-O internuclear axis. Both of these simple additive linear PES curves show a local minimum, which identifies the cis-HOCO configuration. Moreover, the approach angle for all of the curves of Figure 16 are for a minimum energy path to form HOCO.

The t=0 H-C separation (H to center of mass) was estimated in the Background Section to be $6.96a_o$ ($\equiv$3.68Å). The plot of $P(\theta)\sin\theta$ in Figure 4b and the reaction probability from Ref. 51 indicate that $\theta = 9°$ is the median H-atom initial approach angle for reactive encounters. The collision angular momentum for a 100Å/ps approach velocity (taking into account that half of the H-atom energy is not converted into kinetic energy at the minimum entrance channel energy of Figure 15b) is obtained from the expresseion $mvr \cdot \sin\theta$ to be 57amu-Å^2/ps. The angular frequency of the HOCO may be obtained from $L_z = \omega \cdot I_z$, for the angular momentum along an axis perpendicular to the plane of the HOCO intermediate. The moment of inertia, which is perpendicular to the plane, is calculated from the HOCO structural data of Refs. 33 and 49 to be 47amu-Å^2. This gives a HOCO angular velocity of 1.21rad/ps. The bulk gas phase reaction, for the 3.68Å collision radius, and for $\langle\theta\rangle$ of 60° and for the full 200Å/ps impact velocity, yields an angular momentum of 600amu-Å^2/ps. The relation $E_{rot} = I\omega^2 \sim B \cdot J^2$ for rotation about a single axis allows for estimation of the quanta of rotational excitation obtained in the beam and bulb studies. This gives J_{max}=4 for the indicated beam geometry and $< J > \simeq 40$ for the gas phase bulb reaction. Clearly, this large difference in the rotational excitation for the bulb vs. beam studies could enhance the rotational excitation of the OH product.

The product state distribution obtained from high J reactant would be enhanced in the high K quantum numbers of the OH product. The interpretation of the product state distributions[22] calls for associating the high J with the bulb results while low $\langle J \rangle$ results would correspond to the beam studies for a given energy. This point will be examined further in another publication wherein the PSDs obtained under bulk and beam conditions at several wavelengths for the IH-OCO reaction are analyzed.[79] *The important point to be made here is that the present*

time-resolved experiments more clearly discriminate between the several explanations listed above for the observed experimental behavior. This is especially the case when the dynamical behavior is studied over a range of molecular system energies.

7.5.2 $Q_1(1)$ *and* $Q_1(6)$ *Probing and* $[HOCO]^\dagger$ *Dissociation*

The lifetime behavior observed while monitoring the reaction dynamics into the two different rotational product states was shown in Figures 12a and 12b. As was anticipated in the Results section, the low energy reaction rates (lifetimes) are similar for the formation of the OH product in the two rotational quantum states. The higher energy results show a divergence in the rates of reaction where the $Q_1(1)$ rate (lifetime) is observed to be smaller (longer) than that for $Q_1(6)$. Figure 12a shows the unimolecular reaction results (τ_2 vs. E_{avail}) for K=1 and K=6 state detection. Good agreement exists at low energies, but the reaction lifetime results differ at intermediate excitation energies. Such a difference in the time of product formation could be explained if (i) the reaction conditions are not microcannonical, or (ii) if distinct product channels, and the associated times of reaction, preferentially correlate the reactants with different products. The combined observations of the close agreement of the low energy lifetimes results, the sudden onset of the divergence for the reaction rates and subsequent highest energy coalescence of the $Q_1(1)$ and $Q_1(6)$ rates may all be accounted for by a common cause. This interpretation argues that a new reaction channel opens up near the 242 nm pump photon wavelength.

If the reaction had involved a large distribution of reaction initial conditions (and available energy), a large associated distribution of microcanonical rates of intermediate (unimolecular) decay to products would be obtained. A large internal energy distribution in the HOCO intermediate does not afford an *a priori* expectation that the similar dynamical behavior observed at the extremes of the studied energy range in $Q_1(1)$ and $Q_1(6)$ detection would be very different than the intermediate energy regime. A broad distribution of (available) energy in the intermediate complex would tend to enhance the rate of formation of the more energetic product

in contrast to the lower energy product[10] (apart from considerations of the OH and CO product state correlations[66]).

The more plausible interpretation, which explains the product state dependent reaction rate behavior, requires invocation of a secondary reaction channel. The nature of the additional reactive channel is illustrated by the curves of Figure 17a. The source of the curves is the same as Figure 15a. Curve B represents the $^3\Pi_o{}^+$ PES for HI dissociation correlating to the $I(^2P_{1/2})$ product state.[72] The asymptotic energy of this curve is displaced $7603cm^{-1}$ from curve B of Figure 15a, the $I(^2P_{3/2})$ product. The curves in Figure 17b are the linear sum of curve C and the $^3\Pi_o{}^+$ potential energy surface and curves B and A. Several features are notable when comparing the minimum energy reaction paths for the $I(^2P_{3/2})$ and $I(^2P_{1/2})$ channels (i.e. Figure 15b and Figure 17b). Firstly, the entrance channel minima for both of these simply additive potential sufaces occur at about 2eV potential energy, This entrance channel barrier defines the minimum energy required to allow for the formation of the HOCO intermediate. Assuming that the $I(^2P_{3/2})$ and $I(^2P_{1/2})$ products do not strongly interact with HOCO (strong spin-orbit interaction) it is expected that the overall reaction will proceed (in the $I(^2P_{1/2})$ channel) under conditions where the available energy satisfies the requirement

$$E_{rt} = E_{h\nu} + D_o(HI;\ P_{1/2}) \geq 8870cm^{-1} \tag{4.1}$$

where E_{rt} denotes the relative translational energy. This threshold excitation energy, as deduced from Ref. 49, is reached at the level of the 242nm pump wavelength, assuming purely bimolecular collision behavior obtains. It may be noticed from Figure 12a that the unimolecular lifetime (τ_2) for the dissociation of the $[HOCO]^\dagger$ intermediate shows a sudden discontinuity in the trend of decreasing lifetime with increasing excitation energy just above this threshold energy. This effect is emphasized when contrasting the K=1 and 6 lifetime data near these threshold excitation energies. It is seen that the two sets of data separate around this energy, and the

K=1 data deviate more from the rate behavior predicted by the RRKM model, as shown in Figure 14.

7.5.3 Reaction Dynamics on Surfaces Correlating to $I(^2P_{3/2})$ *and* $I(^2P_{1/2})$

The effect of OH product arising from reaction on two distinct potential surfaces may be analyzed by considering the following model for the unimolecular rate behaviors. The method decomposes the dynamics from two reaction channels, which contribute to the overall time rate of formation of a common product. Begin by considering the two-channel unimolecular dynamics given by Eqn. (4.2),

$$\mathrm{B} \xrightarrow{k_2} \mathrm{C}\ ;\quad \mathrm{I}(P_{3/2}) \tag{4.2a}$$

$$\mathrm{B}' \xrightarrow{k_2'} \mathrm{C}\ ;\quad \mathrm{I}(P_{1/2}) \tag{4.2b}$$

The two channel model analysis may be related to the observed (experimental) rate $k_{2,obs}$ by equating

$$\begin{aligned}\frac{d[\mathrm{C}]}{dt} &= k_2[\mathrm{B}] + k_2'[\mathrm{B}'] \\ &= k_{obs} \cdot \{[\mathrm{B}] + [\mathrm{B}']\}\end{aligned} \tag{4.3}$$

The total population is related to A_o from Eqn. (3.6). The mechanism for formation of the intermediate is not of importance for this analysis so long as it is prompt. It is therefore postulated that $a \cdot [\mathrm{A}_o] = [\mathrm{B}]$ and $(1-a) \cdot [\mathrm{A}_o] = [\mathrm{B}']$ at t=0. Therefore, $\frac{-d[\mathrm{B}]}{dt} = k_2 \cdot [\mathrm{B}]$ and $[\mathrm{B}] = a \cdot [\mathrm{A}_o] \cdot \exp(-k_2 t)$. On appropriate substitution into Eqn.(4.3), it is found that

$$a \cdot k_2 \exp(-k_2 t) + (1-a) \cdot k_2' \exp(-k_2' t) = k_{obs} \cdot [a \exp(-k_2 t) + (1-a) \exp(-k_2' t)]. \tag{4.4}$$

The expression will be satisfied if, at t=0,

$$k_2' = \frac{k_{obs} \cdot (1-a) \cdot k_2}{a \cdot k_2 - k_{obs}}. \tag{4.5}$$

The values for a and $(1-a)$ may be obtained from the plot of the relative reaction efficiency if the low energy portion of the curve of Figure 13b is extended (extrapolated). The value for $(1-a)$ is the fractional value of the product formed via the second channel. The value for the fraction is obtained by dividing the magnitude of the products formed by the second channel by the total (relative) product formed. The values for k_2 are obtained from the $Q_1(6)$ reaction results. This last point requires somewhat more discussion. This rationalization withstanding, the rate constant for product formation via the second reaction channel may be evaluated from the set of experimentally measured rate constants and product yield.

It is necessary to justify the assumption that the $Q_1(6)$ data correspond (strictly) to reaction product formed on the PES correlated with the $I(^2P_{3/2})$ product. In contrast, the $Q_1(1)$ results, at energies greater than 242nm obtain from the sum of the two proposed reaction channels. The argument has already been made for interpreting the $Q_1(1)$ results in the intermediate energy range as arising from a dual reaction channel model. However, the $Q_1(6)$ product threshold lies about $720cm^{-1}$ higher in energy, from E_{rot} = J(J+1)·B. It is expected that the PSDs for these well-above threshold excitation energies are peaked near K=7. By contrast, the product population from the $I(^2P_{1/2})$ channel will be peaking at lower K values for reaction energies near threshold. The product will preferentially form in K=1 for energies very close to threshold. Therefore, the fractional contribution to the OH in K=6 from this near threshold channel may not be significant for much of the range of intermediate energies studied. The PSD from the $I(^2P_{3/2})$ channel has reduced population in $Q_1(1)$ (vs. $Q_1(6)$) and the $I(^2P_{1/2})$ channel could contribute effectively to this lower rotational level. The relative reaction efficiency curves of Figure 12b show the sharp onset of the second channel when probing the $Q_1(1)$ transition. There is insufficient information to discern if a similar onset is observed in the $Q_1(6)$ probing near 238nm. (As a reminder, the $Q_1(1)$ and $Q_1(6)$ reaction yield curves are not normalized to each other.) The higher energy $Q_1(6)$ data of Figure 13b do not show a similarly rapid increase in the product yield as observed for $Q_1(1)$.

It is concluded that the $Q_1(6)$ data may be taken as representative of the unimolecular rate(s) associated with the $I(^2P_{3/2})$ reaction channel. The idea is now to remove this fractional component of the total observed rate, thereby obtaining the reaction dynamics associated with the $I(^2P_{1/2})$ reaction channel. A smooth curve is interpolated through the $Q_1(6)$ k_2 reaction rate data and treated as the "k_2" input for Eqn. (4.5). The results of the analysis according to Eqn. (4.5) are presented in Figure 18a along with (unshifted) $Q_1(1)$ and $Q_1(6)$ curves of k_2. The extrapolated reaction rates are quite small when compared with the $Q_1(1)$ and $Q_1(6)$ data of the same figure. This is expected since the HOCO unimolecular decomposition is occuring for internal energies close to threshold.

Figure 19 shows a curve of the reaction rates obtained from the RRKM models along with the (energy shifted) $I(^2P_{1/2})$ data from Figure 18. The threshold for the RRKM rates has been obtained by taking the $7603cm^{-1}$ spin-orbit splitting energy into consideration for the energy scaling. The model curves for RRKM #1 and #2 are in reasonable agreement with the deconvolved reaction rates for the $I(^2P_{1/2})$ channel. This is in contrast with the large energy shift required to allow for agreement between the PST rates and the experimental $I(^2P_{3/2})$ results (at low energy). Moreover, the deconvolved rates actually are faster than the rates from model #2. The best fit (logarithmic) curve through the data points falls between the two calculated curves. The large uncertainty in the extrapolated data for the rates of decomposition on the $I(^2P_{1/2})$ correlated surface does not allow for making a definitive comparison with the model calculations. The reasonable agreement hints that the energy defect behavior observed for the $I(^2P_{3/2})$ dynamics in Figure 14 and explained in Figures 15 and 16 is not significant for the present reaction channel. The present data are also in agreement with a reaction threshold of about $9000cm^{-1}$.

A physically intuitive explanation for the observed experimental data and the PST results may be elucidated by examining the simple PES diagrammed in Figure 17b and comparing with the analogous effective potential surfaces of Figure 15b.

The $^3\Pi_o^+$ is more steeply repulsive than the $^1\Pi$ surface and the $^3\Pi_o^+$ surface asymptotes to the final energetic value at smaller I-H separation. The H+OCO interaction potential is assumed to be the same for each of the two channels. Therefore, reactions that proceed on the surface correlated to the $I(^2P_{1/2})$ product will allow for the conversion of nearly all of the total available (potential) energy to H-atom translational energy. This is in sharp contrast with the dynamics anticipated for the PES correlating with the $I(^2P_{3/2})$ channel for a given H-atom position and interaction with CO_2. The idea of contrasting dynamical behavior is best understood through the examination of the IH potential energy which remains at the position of the internuclear separation of the minimum of Figures 15b and 17b. The reaction which proceeds via the $I(^2P_{3/2})$ channel still shows a residual potential energy of about 1eV (shown as a horizontal arrow in Figure 15b) while the $I(^2P_{1/2})$ channel has less than 0.2eV of I-H potential energy remaining. The H-atom interaction with $I(^2P_{1/2})$ is only a small fraction of the total available energy, at positions along the reaction coordinate where the H-atom interacts strongly with OCO.

7.5.4 Analysis of the Bi-(Ter-)molecular Reaction Step

The discussion has, up to this point, not considered the τ_1 lifetime data displayed in Figure 12a. Several authors have proposed methods for the calculation of rates and cross-sections for bimolecular reactions.[3,80] The complicated dynamics, which the previous discussion has argued to occur in the initial step of the overall reaction, and the time dependent variation of the effective PES (as seen in the dynamically evolving PES of Figure 16) limits the utility of a more detailed TST[2,76] or PST[2] analysis. The complexity of the dynamical reaction behavior necessitates a more precise (e.g. QCT) reaction simulation or a more general consideration of individual portions of the overall dynamical behavior.

A line-of-centers model has been formulated to allow for intuitive modelling of the bimolecular reaction cross-section.[3] The model expression is

$$\sigma_R(E_{trans}) \begin{cases} = \pi d^2 \cdot (1 - E_o/E_{trans}) & ; E_{trans} > E_o \\ = 0 & ; E_{trans} \leq E_o \end{cases} \qquad (4.6)$$

where E_o is the reaction threshold energy, E_{trans} is the relative translational energy of the collision partners and d is the largest value of the impact parameter (b_{max}) for which reactions may occur. For the moment this expression will not be extended to include the angular dependence of the opacity function,[81-83] hence and angle-dependent reaction cross-section.[81,82] The expression for the reaction cross-section, Eqn. (4.6), may be combined with the simple expression for the bimolecular reaction rate:

$$k_{bimol} = \sigma_R \cdot v \tag{4.7}$$

The quantity v is the reactant relative velocity, and $v = \sqrt{2E_{trans}/\mu}$.

The reaction cross-section of Eqn. (4.6) may be substituted in Eqn. (4.7). Rearrangement of the substituted form gives

$$k\sqrt{E_{trans}} = \pi d^2 \sqrt{2/\mu} \cdot (E_{trans} - E_o). \tag{4.8}$$

The results of the plot of the experimental bimolecular reaction rate times $\sqrt{E_{trans}}$ vs. E_{trans} are presented in Figure 20. The experimental k_1 data, both unscaled and rescaled to account for the previously observed energy defect, are presented.

Figure 20a and 20b each contain two linear best fits to the low and high-energy data (i.e. results for wavelengths longer than 240nm and results at 240nm and shorter). The observed zero-crossing point for the unscaled data occurs at 11226cm^{-1} and the 15% rescaled data yields a threshold value of 9544cm^{-1}. In the case of a simple two-step reaction process, where H dissociates from I and where H attacks OCO. Under such circumstances, which are also the proper conditions for usage of Eqn. (4.8), the expected threshold for the bimolecular reaction step is 1.1eV (=8873cm^{-1}).

The slopes for the low-energy best fit linear approximation are 0.0367×10^{12} and 0.0398×10^{12}sec^{-1} cm^3 (cm^{-1})$^{0.5}$ for the full and 15% reduced available energy, respectively. The slopes, represented by $\pi d^2\sqrt{2/\mu}$, may be evaluated to give the distance, d, of the H-OCO separation for the barrier position for $\mu_{H-OCO} = 1.624\times 10^{-24}$gram.

The higher energy data linear fits need to be deconvolved to obtain the threshold and cross-section for the bimolecular reaction step which is correlated to the $I(^2P_{1/2})$ product. This has not been performed so the indicated vaues for the threshold and slope are lower approximations to the true values. The indicated but fit linear approximation is a poor approximation to the data because the fraction of the signal which arises from the $I(^2P_{1/2})$ channel increases with increasing excitation energy. A deconvolution which is similar to the k_2-rates would be required.

The close agreement obtained between the PST rates and the $Q_1(1)$-$I(^2P_{1/2})$ rates deduced exclusively from experimentally observed quantities substantiates several aspects of the dual reaction channel interpretation presented above. First, a simple and physically reasonable picture is able to qualitatively account for and explain the energy defect observed in the low energy reaction rate measurements. Second, this same physical model may be extended to explain the observed onset of a second distinct reaction channel. Manifestations of the second channel are evident in the relative reaction probability and reaction rate results. Third, the same model accounts for the reasonable agreement between the experimental and theoretical unimolecular reaction rates, obtained from experiments and PST model calculations. Finally, and perhaps most significantly, the agreement of the unimolecular reaction rates and the self consistent interpretation (through a simple kinetic model) of all of the IH-OCO vdW-complex reaction results solidifies the basic premise that the present reaction proceeds via a bi- or ter-molecular process to form a reaction intermediate, which in turn reacts via a unimolecular dissociation to the observed product.

7.5.5 The Evolution of the Reactant Entrance Channel PES

The previously discussed experimental observations have shown evidence for the complexity of the initial "bi-molecular" step of the reaction for the restricted domain of precursor configurations leading to products. The significant complication results from two sources. First, the H-atom may simultaneously experience the presence of the I and OCO species through primarily repulsive interactions. This

effect complicates the simple two body picture of a bimolecular reaction and makes this a multibody interaction problem. Second, the potential energy surface for the H+OCO interaction is quite complicated because this PES depends strongly on the configuration (and motion) of the CO_2 bend angle and bond length(s).

The additional points, which concerns the dual channel reaction mechanism, has been made manifest through the reaction rates observed and ascribed to the dynamics on potential surfaces correlating with the $I(^2P_{3/2})$ and $I(^2P_{1/2})$ products. The significance of these observations is the contrasting dynamical reaction behavior, which may be studied in a single oriented binary reaction complex. The two distinct entrance channel surfaces initiate the overall reaction in manifestly different ways; the contrast being of a reaction proceeding almost adiabatically (loosely speaking) as opposed to impulsively. The same reactant relative geometrical configurations obtain in both cases, that is, the distributions in b and θ are the same for both channels. More detailed studies and analysis allow for making a detailed comparison of the specific types of entrance channel features that tend to dominate or lead to unique reaction dynamics. The manifestations of unique dynamical behavior will be addressed further in the following subsection.

The strong dependence of the H-OCO interaction potential on the CO_2 internal configuration is demonstrated in Figures 21 and 16. The figures show simple additive effective potential surfaces constructed from the $^1\Pi$(Fig. 16) and $^3\Pi_o$(Fig. 21) HI repulsive excited states with linear cuts through the full H+CO_2 PES, as calculated by Schatz and coworkers.[49,51] The cuts are made at a fixed angle H-c.m.(CO_2) approach geometry as described for Figures 15 and 16. The $HI(^3\Pi_o^+)$ PES is also shown beginning in the left-hand portion of Figure 21 as curve A. Curve B corresponds to the everywhere equilibrated H+OCO interaction surface added to curve A. Curve C represents the interaction potential when CO_2 is at its near equilibrium geometry. This PES does not show a minimum which can be ascribed to the configuration of the HOCO reaction intermediate. In other words, the potential surface for equilibrium CO_2 geometry ($\theta_{OCO} = 175°$) is essentially purely repulsive. This is the effective PES which exists at the reaction t=0. However, curve D, which

is a 160° bend, begins to show a local minimum associated with HOCO. The local minimum of curve B associated with the cis-HOCO configuration is shifted and of higher energy than the equilibrum configuration of the HOCO species. The final curve labeled E is obtained from the addition of the linear cut through the 160° O-C-O angle asymmetric bond length (0.1Å stretch of the viscinal C-O bond to $2.4a_o$) H+OCO potential surface with curve A. The cis-HOCO saddle point geometry is $\theta_{OCO} = 159°$, $\theta_{HCO} = 143°$, and $R_{CO} = 2.52a_o$ vs. $R_{eq.CO} = 2.2a_o$ at the saddle point.

The potential curves of figures 16 and 21 demonstrate that the CO_2 must change its geometric configuration in order for the reaction to proceed. The "lingering" presence of the H-atom will force the CO_2 to adapt in relation to the proximity and position of the H and OCO. In some sense, the presence of the H-atom causes the CO_2 to change its geometry adiabatically with proximity as measured by the H-CO_2 c.m. distance and approach angle. The accommodation of the H-atom by CO_2 will also depend on conditions that favor longer duration proximal interactions of these two species. The accommodation is primarily affected by CO_2 bending and rotation of OCO to decrease θ_{HOC} from 180° in the vdW-complex equilibrium configuration toward $\theta_{OCO} = 159°$ for the equilibrated configuration.

The present experiment observes only those H and OCO encounters leading to the formation of the OH product. The detected signal is associated with those few interactions of H and OCO where the impact parameter, initial H-atom approach geometry, and the phase of the CO_2 motion and H-atom movement are all favorably disposed. The effect of the H-atom on the CO_2 may be approximately viewed as a nuclear response to an instantaneous force analogous to the Born-Oppenheimer approximation. The H-OCO collisional encounter encourages the OCO to change geometry to accomodate the hydrogen, but the hydrogen will not exist in the unstable configuration between I and OCO for very long.

Even though each effective PES does not show a well, which corresponds to the HOCO intermediate geometry, each curve does display a local minimum near $R_{IH} = 3.50 - 3.75a_o$ The well in the entrance channel region of the linear-cut

reactive PES can be thought of as harmonic for sufficiently small excitation energy, especially for the 175° CO_2 geometry curve B. The H-atom dynamics in such a well may be thought of as the motion of a wavepacket along this coordinate. This picture is somewhat accurate and descriptive if the time duration of the excitation pulse is sufficiently short and if the H-atom motion is significantly more rapid than the associated separation or internal motion (bending) of the I and CO_2 moieties.

The rapid motion of the H-atom species ($\nu_{max} \approx$100Å/ps) implies that the capture of H by CO_2 must occur in a few tens of femtoseconds. Attainment of the proper configuration for hydrogen capture requires some OCO bending (ν_{bend}=707cm^{-1})[9] and a rotation of the CO_2 or an angular (lateral) migration of the H-atom to near the saddle point geometry. Obtaining accurate information of the time required for the CO_2 to transform some of the relative c.m. translational energy into internal motion (CO coordinate stretch and bend) involves performing a dynamical calculation. Short of this task, it is possible to estimate the time period of OCO librational motion. This may be judged to be a limiting factor of attaining the proper reaction configuration. Nesbitt and coworkers estimated the OCO librational frequency to be 10±5cm^{-1} for the HF(ν=1) state.[44] This quantity is also assumed for the unexcited IH-OCO moiety. The angular displacement of HI from the vdW complex principle axis is seen in Figure 4a, (and is assumed to be similar for OCO) is limited to less than 1 radian. The displacement required for adequate bending displacement is a quarter-period of motion, $\sim \pi/2$. This corresponds to a CO_2 hindered rotation time of about 1ps. This is rather long compared to the desired timescale for adaptation by rotation.

Excitation of the internal degrees of freedom of CO_2 will reduce the translational energy of the H-atom and prolong the period of time it spends in close proximity with OCO. Such internal excitation will also enhance the OCO bend to sample configurations further removed from the linear equilibrium geometry. This bending motion might aid the accommodation dynamics. A bending motion period will be completed in less than 50fs. Such internal motion is on the desired timescale.

The transverse H-atom motion in IH-OCO has not been directly measured but is presumed to be weakly bound. The approximate extrapolation from the XH-OCO potential curves calculated by Dykstra,[46] shown in Figure 3b, limits the transverse bond energy to less than $300cm^{-1}$. Moreover, the potential surface along this transverse coordinate is broad as well as shallow. The low energy for dissociation along this coordinate will only slightly hinder the H-atom from leaving the interaction region but it may move the H-atom closer to the saddle point HOC angular configuration. In other words, the transverse escape of the H-atom will bring it closer to the $\theta_{HOC} = 143°$ geometry, and hence the configuration to form cis-HOCO.

The present experimental study has resolved reaction rates for initial conditions averaged over a range of θ and b. It is perhaps satisfactory to consider the interaction potential to be in some static and best approximation form, which will vary with H-atom translational energy.

In summary, it appears that the key factors desirable for reaction are: (1) optimization of both the H+OCO c.m. impact energy and the collision geometry; (2) having a proper phasing of the OCO bend, the vicinal OC stretch and the H-atom attack (both in time and orientation), in other words, to optimize the conditions of T-V energy transfer; and (3) to prolong the time of H and OCO interaction thereby allowing more time for process (2) to occur.

7.5.6 Evidence for Dynamical Resonance(s) in the Reaction Entrance-Channel

The reduced dimensionality potential curves (linear cuts through the multidimensional PES) of Figure 21 are suggestive of the presence of quasi-bound state(s) in the reaction entrance channel. Any type of long-lived resonance in the entrance channel could be manifested in some of the experimental observables. In a dynamical sense, a resonance feature corresponds to wavepacket motion of one or more periods of oscillation; classically analogous to chattering motion.[84] The wavefunction associated with a resonance has a finite probability amplitude in the region of the effective potential curve with significant H-OCO repulsive interaction. Some

probability will persist until either the hydrogen atom has escaped from the region localized between the I and OCO or that the I and OCO separate sufficiently to cause the probability amplitude to go to zero.

The floppiness of the reaction complex will cause significant deviations from an assumed linear equilibrium geometry. Recent work by Dykstra[46] on the FH- and ClH-OCO complexes has shown that the angular motions of both species will be large, and that the XH moiety will undergo greater magnitude excursions. The scaling of the moments of inertia would predict that the majority of the zero point angular motion occurs in the hydrogen halide. It may be inferred from Ref. 46 that the monomer fragments undergo large amplitude concerted bending. Therefore, the collisions which lead to reaction are those in which H collides with the vicinal oxygen. In other words, the H-atom impact which causes reaction occurs with a relatively small distribution of impact parameters and relative fragment angles. This should be taken in contrast with the gas phase bulb H+OCO reaction wherein neither the impact parameter nor the relative angle of attack is *a priori* restricted.

Of course, the concept of a colinear 1-dimensional resonance feature may not obtain under conditions of higher dimensionality.[85] The most productive arguments for deciding whether such features actually exist is to examine the experimental data for observable manifestations.

The conspicuous features of the relative reaction efficiency and the τ_2 reaction time for product formation correlated with the $I(^2P_{1/2})$ spin-orbit excited channel at the 240nm excitation wavelength, shown in Figures 13b and 12b, respectively, require further examination. The relative reaction probability for $Q_1(1)$ detection, as displayed in Figure 13b, shows a prominent spike at the 16497cm^{-1} position. The behavior shows that the reaction probability has suddenly increased by a statistically significant amount, as compared to the immediately adjacent points (241 and 239nm).

Such an increase in the product yield at an energy which is about 300cm^{-1} above the energetic threshold for the $I(^2P_{1/2})$ channel can obtain from various causes. Firstly, the available reaction energy may be essentially resonant with an

excited state of the HOCO intermediate. Second, since the entrance channel barrier is not much higher than the exit barrier energy (for the case of the entrance channel saddle point H-OCO configuration), the $I(^2P_{1/2})$ channel reactants may be nearly isoenergetic with the low quantum states of the reaction products. This fortuitious circumstance may result in an enhanced continuity condition from reactants to products. Third, a resonance feature may exist in the entrance channel region of the PES correlated with the $I(^2P_{1/2})$ product. The enhancement of the reaction product follows from the "longer lived" reacting configuration, which allows CO_2 a greater opportunity to attain a favorable configuration for accomodating the H-atom and forming HOCO.

The other statistically significant unusual reaction dynamical behavior is observed in the prolonged lifetime of the HOCO intermediate formed via the $I(^2P_{1/2})$ reaction channel. The effect is manifest in Figure 12b and in the extrapolated rates of Figure 19. Since the reaction of the $[HOCO]^\dagger$ complex occurs by way of unimolecular decay, very few reasonable interpretations exist to explain the sudden slowing of the unimolecular reaction. The first explanation calls for the existence of phase space bottlenecks[77] to unimolecular dissociation, as such dynamical features have been invoked to account for the retarded decay of I_2He van der Waals species.[77] Alternative interpretations of slower than statistical reaction rates have called for trapped trajectories in the reaction transition state region.[86] Quasi-periodic trajectories have been found in the unimolecular dissociation of CCH at energies far above threshold.[87] A second, somewhat more reserved explanation for the reduced reaction rate, which does not explicitly require a breakdown in statistical unimolecular decay models, may be considered. The more "conventional" idea is that the HOCO intermediate obtains less energy than expected for the given photolysis wavelength. The analysis of the previous subsections showed that this energy-defect effect is a significant factor in explaining the discrepancy between the measured and calculated values of k_2. This effect is especially significant when the reaction occurs on the PES correlated with the $I(^2P_{3/2})$ product.

There is no *a priori* reason to rule out the first explanation for the selectively enhanced reaction yield except to say that such a controversial description of the dynamics would require additional experimental observations for some sort for corroboration. However, a more objective decision can be made by considering the simultaneous consistency of two mechanisms (one for the enhanced yield and the other for the prolonged lifetime) in explaining both of the unusual experimental observations. The first explanation (of resonant HOCO formation) given for the enhanced reaction yield cannot be reconciled with the decreased rate of unimolecular decay. At best, the unimolecular decay rate predicted by this explanation would not be significantly changed. Actually, resonant formation of an HOCO excited state would tend to increase the rate of HOCO dissociation, since the termolecular effects, which decrease the energy available for HOCO reaction, would be minimized. It seems unlikely that the enhanced reactivity to a preferred resonant mode of HOCO would yield such a dramatic and selective result given the high density of states in HOCO at these reactant energies.

The second explanation of adiabaticity between the initial reactant states and the low energy product states is difficult to justify in light of the limited amount of experimental and theoretical knowledge about the state-to-state cross sections for this system. The inconsistency again seems to be that the reaction rate would increase when the reaction passage to the K=1 product formation is enhanced. This implies that the matrix elements coupling of the reactants and specific products, at a specific (low) total system energy, are singularly large. This type of speculation is, however, difficult to defend and cannot presently be verified. If the proposed explanation of the reaction mechanism were more of a direct as opposed to statistical nature then an enhanced K=1 product yield might obtain but only with an associated enhanced rate of unimolecular reaction.

The most reasonable explanation of the simultaneously observed enhanced reaction yield, into the K=1 product, and decreased reaction rate is the third. The formation of the HOCO intermediate is enhanced by some feature in the entrance channel portion of the overall reaction-PES. The feature, as argued in the previous

subsection, would results in a greater product yield if the H-atom interacted for a longer period of time with the CO_2. This persistent interaction allows more time for the H-OCO potential to change from a form like curve C of Figure 21 to curve B by way of D and E. Moreover, the increased time of residence of the H-atom between the I and OCO species would increase the efficacy of the termolecular mechanism for imparting energy into translation of the iodine product and into c.m. translation of the HOCO intermediate. Only the energy imparted to the internal degrees of freedom of HOCO and the overall rotational energy of the HOCO are available for unimolecular decay of HOCO. The reduced rate of unimolecular decay of HOCO into OH and CO is consistent with a statistical reaction model in which there is less energy available for reaction than expected.

A simple approximation to the entrance channel PES is to consider the low energy portion of the well to be harmonic. The zero-point level of such a harmonic well is located at energy $\frac{1}{2}\hbar\omega$. This simulation of the near equilibrium portion of the well of curve C of Figure 21 is shown in Figure 22, along with the position of the zero-point feature at the 4000cm^{-1} zero point level. This picture is certainly a very simplified view of the actual multidimensional time-dependent PES. Hydrogen atom motion along the transverse coordinate would act to destroy the collinear (iodine c.m. to CO_2 c.m.) resonance feature. It has, however, been argued that some transverse motion of the H-atom is required to reach or force an optimal geometry for reaction. Such motion is similar to H-atom migration as opposed to elastic scattering.

The fact that the energy level of the zero-point feature in Figure 22 lies slightly above the extrance channel minimum energy barrier is quite significant. *This zero-point level also occurs at virtually the identical energy as the 240nm excitation energy; the energy for the anomalously enhanced lifetime and reaction yield behaviors.* The energetic location of the resonance may change during the time course of the reaction, as the effective PES evolves from curve C to E of Figure 21 and finally lead to HOCO formation. However, even a short lived resonance feature may be sufficient to produce the observed dynamical effects.

Several theoretical investigations[88-90] have found evidence of resonance features in the prototypical heavy-light-heavy reaction $IH + I' \rightarrow [IHI]^{\dagger} \rightarrow I + HI'$. Earlier results by Babamov and Marcus[88] and others for collinear systems (b=0) have been shown that several resonances (bound levels) may obtain. More recent 3-dimensional quasi-quantal calculations[89,90] show that all but the lowest resonance features are destroyed when other reaction degrees of freedom are allowed for the H-L-H systems. The significant conclusion is that symmetric H-atom transfer still allows for the existence of a stable reaction resonance in 3-dimensions. This result obtains even though the transverse motion is only weakly hindered.

Valentini and co-workers have recently reported the direct experimental observation of dynamical resonances in the $H+H_2$ reaction.[91] The dynamical behavior attributed to the resonances was observed under state-to-state bimolecular reaction conditions, with the H-atom translational energy obtained via the photon-induced dissociation of HI. The manifestation of the dynamical resonances is by way of the enhanced product partial cross sections. They extracted cross-section information following the calibration of their instrument sensitivity. It is interesting that the resonance features obtain even though the unconstrained gas phase bulb reaction conditions allow for large impact parameter collisions. They argue, however, that the small magnitudes of reaction cross-sections $\sigma(\nu' = 1, j')$ and $\sigma(\nu' = 1)$ suggest that only partial waves of small l (orbital angular momentum) are important. It is predicted that $\sigma(\nu' = 1)$=0.1Å implies that only partial waves less than or equal to l=4 are important.

The constrained initial reactant geometry of the present vdW-precursor experiment will reduce the number of partial waves that contribute to the formation of the reaction product. The present observation of the enhanced reaction yield, as seen in Figure 13b, is analogous to the enhanced partial cross section results for $H+H_2$.[91] However, the results for Ref. 91 result from a dynamical Feshbach resonance tantamount to doing vibrational spectroscopy of the reaction TS region.[92] The results of the present oriented bimolecular reaction are being attributed to a somewhat different dynamical effect. The present resonance feature is conceptually

more similar to a shape resonance.[84] The unique structure of the oriented complex allows for the formation of a (linear-cut) metastable well and an associated bound state. The dynamical resonances of Ref. 91 would be more analogous to the observation of reaction promoting modes of the HOCO intermediate of the current work.

The presently studied IH-OCO species is a H-L-H atom transfer reaction. Schatz has shown[51] that the angle dependent probability of reaction is only non-zero only for small (non-zero) approach angles when the impact parameter b=0. These calculations were performed for the H-O initial internuclear separation for the BrH-OCO vdW precursor. The larger H-O separation for the IH case should further restrict the extent of the non-zero angular probability distribution, $P(\theta) \cdot \sin\theta$ (cf. Figure 4b). Therefore, the present reaction would be expected to form HOCO only in the case of nearly collinear initial conditions.

It should be noted that the observed jump in the reaction probability could be obtained by simply doubling the number of H-atom collisions with OCO on the surface correlated with the $I(^2P_{1/2})$ product, and at 240nm excitation energy. Classical trajectory calculations at 1.9 and 2.6eV have not shown evidence for reactive trajectories proceeding via a "chattering" effect in the entrance channel. However, the present experiment has obtained evidence for a reactive resonance at about 1eV energy on the $I(^2P_{1/2})$ correlated surface. Although the width of the resonance feature observed in Figures 12b and 13b is not well defined, the upper limit can be inferred to be less than 200cm^{-1} FWHM. In the case of a Gaussian lineshape this would correspond to a lifetime of 75fs or greater for the H-atom between I and OCO (cf. with the linewidths observed in Ref. 91, and the therein inferred resonance lifetime of 10-30fs).

7.5.7 Limitations of the Kinetic Rate Equation Analysis

The concept of a reaction rate equation is useful for analyzing or modelling data that are a measure of the reaction behavior obtained under conditions considerably longer than characteristic vibrational or reconfiguration periods.

Recent experiments, which directly time resolve the dynamics of photoinduced bond breakage[12,64] and unimolecular reaction,[75] show evidence for the reaction to progress through one or a series of intermediate configurations before the reaction product comes into resonance with the probe laser bandwidth. The photodissociation studies directly observe an induction period between the time of photolysis and the appearance of the final unperturbed or nascent product. Moreover, probe laser tuning studies have shown that the dissociating fragment proceeds through correlated reaction fragment spectrally perturbed configurations.[64] Such perturbed fragment spectroscopy conditions obtain when the first and second derivatives of the potential function with respect to the reaction coordinate variable have a negative and positive value, respectively. Such perturbations have recently been described by a classical formalism that infers potential features from the time shift and the spectral shift of the time resolved data.[93]

The observation of a transient (nascent resonance detuned) absorption feature in the ground electronic surface unimolecular dissociation[75] case, in which $\frac{dV}{dr}$ is primarily positive and $\frac{d^2V}{dr^2}$ is negative in value, has a different significance. This observation is important because it demonstrates that the system may pass through the reaction transition state (saddle point) region and still be a transient species thatis becoming the nascent product. This result was independently, and subsequently, predicted in Ref. 93.

In summary, it may be said that reaction is the process wherein the reactant moieties evolve from an initial configuration through a (continuous) series of spectroscopically distinct intermediate perturbed fragment configurations on the way to the product. Alternatively, a unimolecular reaction is traditionally considered as the evolution from the reactant configuration to the coordinate position of the transition state. This evolution is described by the reaction rate in the form of the rate of loss of reactant population. However, the previous studies[12,64,75] have shown that the "transition state" configuration is not spectroscopically identical to that of the final product. Rather, the reaction proceeds from the TS configuration through

other spectroscopically distinct forms, which are neither TS or the unperturbed product, and hence to the final product state.

The present study of the titled bimolecular reaction has also shown some deficiencies in the analysis of the reaction data with a simple two-step kinetic model treatment. The discrepancy arises when examining the lowest energy data (obtained at wavelengths 263-247nm). The interpretative dilemma is that an empirical time-shift (shown in Figure 13a) is required in addition to the induction period. The latter is an intrinsic property of the kinetic model of Eqn. (3.6). The value of the empirical time-shift is obtained from the nonlinear least squares fit to the data, and appears directly in the process of minimizing the χ^2 goodness-of-fit parameter. It is observed, for all cases in this excitation range, that a non-zero empirical time-shift is required to obtain the best fit to the data. The lowest curve of Figure 13a summarizes the values for this shift. The higher energy values all have an empirical time-shift of less than 200fs. Admittedly, such small values for the time shift are well within the intrinsic uncertainty of the system time resolution for the 3.5-4.5ps FWHM response functions and the HOOH photodissociation method for obtaining the system response function. The values obtained for the time-shift at the lowest energy points are, however, significant.

In light of the previous discussion, the observed time-shift could result from the finite amount of time required for the reaction to proceed from the TS configuration(s) (entrance and exit channels) to the configuration of either the $[HOCO]^{\dagger}$ intermediate or the OH+CO final products. The potential surface from the TS of the entrance channel to the $[HOCO]^{\dagger}$ configuration is exoergic, and generally repulsive in form. The time resolved studies of photoinitiated dissociation have shown that a time delay will be associated with the final state formation. This is saying that the time dependent decay rate of [A(t)] is not precisely the same as the rate of formation of [B], but rather is associated with $[B(t-\Delta\tau)]$. The second TS lies in the region of the rising PES leading from $[HOCO]^{\dagger}$ to OH+CO. Since fragment multipolar (dispersion) interactions are long range and extend beyond the estimated position of the TS,[49] the OH product will be perturbed by the partner

fragment(s) in the exit channel separation region, which is located between the TS and nascent OH+CO configurations. Since the OH was being probed on-resonance, such fragment-fragment interactions will perturb the (transitioning) OH* energy levels away from the nascent $Q_1(1)$ optical transition.[51] Therefore, additional time is required for OH* to become OH(K=1) and be resonant with the $Q_1(1)$ transition within the probe laser bandwidth.

It is known that an induction time exists for the process of photoinitiated dissociation of HOOH and the formation of nascent OH. This delay time has not been measured, and the earlier comparison with the time response (cf. Figure 8b) obtained via difference frequency generation does not show a discernable time shift (to within about 200fs). If anything, the time-shift intrinsic to the response function method[64] will reduce the magnitude of the shift observed for the bimolecular reaction. This is an implicit consideration for the overall data analysis procedure. However, the measured uncertainty of the time shift for the higher energy data points is also of the same magnitude.

Even though a kinetic model analysis has been used throughout this presentation, it is clear that application of a rate equation model to high (intrinsic) time resolution studies must be done with care. Dynamical calculations, classical or quantal, will certainly be a more complete reflection of all aspects of the reaction dynamics. Moreover, such dynamical calculations would allow for the best comparison with the present time-resolved measurements. The intrinsic complications of performing such calculations for this 5-atom problem preclude a direct comparison at this time for the many energies studied herein. Hence, a model analysis at least serves the purpose of allowing for future quantitative comparison by adequately recording the measured dynamical information.

7.6 CONCLUSION

The thrust of the present chapter has been to elucidate essential features of bimolecular reactions, as probed by time resolved spectroscopic methods. The direct

study of bimolecular reactions has been investigated for a unique class of PGL precursor dimer complexes. The well defined proximity of the monomeric reactants in these vdW-complexes facilitates the undertaking of meaningful time-resolved measurements.

Photolysis wavelength tuning experiments and LIF detection of the OH product for the titled reaction have provided significant information concerning the reaction mechanism. A two-step kinetic rate equation analysis is the minimum degree of model complexity required for self-consistent analysis of the reaction behavior. The analysis, done in conjunction with an associated measure of the laser system response function, implies the existence of a reaction intermediate. The HOCO radical intermediate is judged to have a stabilized configuration, as compared to the H+OCO TS and the OH+CO products. The lifetimes for the HOCO unimolecular decay to the OH+CO products is analyzed to be somewhat longer than the rates obtained from RRKM and PST statistical rate theories.

It is argued that the longer than expected HOCO lifetime obtains from multibody, termolecular reaction entrance channel conditions. The multibody interactions obtain from simultaneous interactions of the H-atom with the I-atom and the OCO molecule. This effectively amounts to I–OCO repulsive interaction resulting in additional energy being put in I-atom and (H)OCO c.m. translational motion and less into the H+OCO interaction. The energy defect appears to scale as approximately 15% of the maximal amount of energy available for reaction.

Closer inspection of the k_2 rates shows a sudden decrease in the unimolecular decay rate of the HOCO intermediate at 240nm excitation energy. It is argued that this is caused by the onset of a second reaction channel. The energy for the onset suggests that this second and distinct reaction channel correlates to the HI($^1\Pi$) excited electronic surface and to the I($^2P_{1/2}$) product. The combined information from the $Q_1(1)$ and $Q_1(6)$ time resolved measurements and the relative reaction yield is used to evaluate the k_2' rates associated with the I($^2P_{1/2}$) product.

The k_1 reaction rate results for the bimolecular reaction step leading to HOCO formation may be compared with simple collision models. The bimolecular reaction

threshold calculated from the collision model are in reasonable agreement with the known value of 1.1eV so long as the energy available for reaction is corrected by the 15% amount observed for the k_2 rates.

The overall observed reaction dynamics are consistent with the behavior expected of a bimolecular reaction. However, the multibody interactions in the entrance channel region complicate the simple reaction picture. Some of the complications are most dramatically manifest at the 240nm excitation region in the plots of the k_2 reaction rates and the relative reaction probability. It is argued that the sharply diminished reaction rate and increased reaction yield both result from a long-lived resonance feature in the entrance channel region. Such a resonance in the I-H-OCO metastable (linear cut) well is unique to the presently employed vdW-complex oriented-reagents initial conditions. The relatively sharp resonance feature implies that the energy broadening (a measure of the microcanonical energy conditions) does not contribute greatly to the assumed less than $200cm^{-1}$ resonance linewidth. This implies that the reaction conditions on the PES that correlate with the $I(^2P_{1/2})$ product are accurately termed bimolecular in nature. This conclusion is confirmed by the close agreement obtained between the calculated and measured (analyzed) k_2' reaction rates. The physical basis for the observation arises from the steeply repulsive $^1\Pi$ HI electronic surface. The steep repulsion minimizes the I–OCO mutual repulsion, which is observed for the less repulsive $^3\Pi$ HI surface and $I(^2P_{3/2})$ product.

This observation has profound implications for controlling reaction rates and yields in such vdW-force oriented reaction precursors. The types of entrance channel resonances observed are unique to such complexes and will not obtain under normal gas phase conditions. It is, however, expected that such resonance behavior could be of importance in condensed phase reactions.[94] Such "intermolecular" resonance behavior and the associated unique initial conditions implicitly afford control of the reaction rates and product yield. This serves to demonstrate that steric effects have a pronounced importance in dictating the mechanism and time course (evolution)

of bimolecular reactions. This conclusion is consistent with the observation and conclusions of other studies of sterically controlled reactions.[18,19]

The present study elucidates the behavior and reaction dynamics and degree of reaction control that may be obtained for the general class of bimolecular reactions that result with PGL initial conditions. The study of the energy dependence of the reaction observables has allowed for gaining significant insight into the dynamics of the IH-OCO system. Other PGL reactions could also be studied at several available energies and in a time resolved fashion.

The study of vdW-complex systems which, unlike the present system, form an equilibrium structure orientation directed at the configuration of reaction minimum would allow for directly accessing the reaction intermediate. The reaction control obtained via unique entrance channel effects would thereby be traded-off with reaction control, or reaction memory, obtained from the more direct nature of the subsequent reaction. Qualitatively different PSDs have been observed for the H_2S-CO_2 system,[27] where the complex structure may be cyclical with a bidentate attachment. Reaction initiation from this initial structure presumably projects the H-atom more directly at the configuration appropriate for the formation of HOCO.

It is perhaps remarkable to consider that such a simple vdW dimer complex may embody the essential differences of bimolecular reactions studied in the gas phase and in condensed phases. The reactant orientational initial conditions affect or impart control on the subsequent course of the reaction in a time period of about 200fs, or so. This is a time scale sufficiently short that it is conceivable that the orientational selectivity will obtain even under liquid-like reaction conditions.[95] This prospect would allow for obtaining considerable insight into the nature of condensed phase reaction dynamics from the study of comparatively simple gas phase vdW-dimers.

Future studies should extend the present method and measured results to conditions of better time resolution and the probing of other aspects of the reaction dynamics. Operationally, such undertakings should be done with a more capable experimental apparatus that allows for data collection at higher repetition rates, or

at least more signals per laser pulse. Higher time resolution still has to be balanced against the desire to monitor individual rotational quantum states of the OH product. However, a 1.5ps system response function may still simultaneously satisfy these requirements.

The most important subsequent study would be to probe the HOCO intermediate. Very little is known about the nature of the electronically excited state except that the absorption of the HOCO certainly occurs in the 280-300nm range (and at higher energies).[33] Perhaps 1+1 or 1+2 photon resonance enhanced ionization could be used to probe the absorption spectrum of HOCO and the reaction dynamics. Such time-resolved probing has been shown to be effective in detecting and following the time course of a reaction; see for example Ref. 10 and references therein. Alternatively, one-photon absorption by HOCO may lead to enhanced OH production in the $^2\Pi$ and $^2\Sigma$ states. If the latter obtains, then the signature for HOCO absorption would be chemiluminescence from the $^2\Sigma$ excited electronic state.

It is also of interest to probe the dynamics for formation of the OH(ν'=1) product vs. the ν'=0 product observed in the present study. Time-resolved alignment studies at energies below and above the I($^2P_{1/2}$) channel onset could show behaviors that afford insight into the planarity of the HOCO formation and dissociation.

Deuterium isotopic substitution studies, DI vs. HI, would further establish the role of the entrance channel dynamics on subsequent behavior. The slower D-atom motion would allow more time to establish conditions favorable for reaction. The magnitude of the energy defect should also be somewhat affected because the D (vs. H) would spend more time "between" the iodine and OCO.

Frequency resolved studies would be quite complementary to the time-resolved studies. Measurement of PSDs at several wavelengths should show the I($^2P_{1/2}$) threshold and provide additional insight into the entrance channel specificity, which is translated to the reaction product. High resolution studies of the Doppler spectrum of the OH product[65] would give information on the partitioning of energy in the products.

Continuous scanning of the pump wavelength and specific OH product state detection will more clearly map out any unusual dynamical effects that occur in the entrance channel and at later times during the course of reaction.

Operatioanlly, higher reactant number densities and longer molecular beam-laser beam overlap could be achieved with planar nozzle expansion methods. The asymetric flow of the expansion would act to concentrate the molecular flow in a shape more similar to the laser beam profile.

The success of the present experimental effort and the insights gained into the mechanism of the titled reaction inaugurates a new method for the time-resolved study of bimolecular reactions. The dynamical stereospecific reaction behavior, as observed in the rate of product formation and product yield, indicate the selectivity afforded by the PGL reaction conditions and selectivity of the state-resolved/time-resolved experimental method. Aspects of the methods of probing the reaction dynamics near the TS regions[93] should be fruitful in the elucidation of greater detail of bimolecular reaction mechanisms.

7.7 REFERENCES

1. S.R. Leone, Ann. Rev. Phys. Chem. **35**, 109 (1985); J.C. Polyani, Science **236**, 680 (1987); H.O. Pritchard, J. Phys. Chem. **89**, 3970 (1985).

2. D.M. Wardlaw and R.M. Marcus, Adv. Chem. Phys. **00**, 000 (1988); S.J. Klippenstein, Ph.D. Thesis, Caltech 1988.

3. R.D. Levine and R.B. Bernstein, *Molecular Dynamics and Chemical Reactivity*, (Oxford Press, 1987 Oxford).

4. D.J. Nesbitt, Chem. Rev. **88**, 843 (1988); K. Janda, Adv. Chem. Phys. **60**, 201, (1985).

5. L.J. Butler, T.M. Ticich, M.D. Likar, and F.F. Crim, J. Chem. Phys. **85**, 2331 (1986); X. Luo, P.T. Reiger, D.S. Perry, and T.R. Rizzo, J. Chem. Phys. **89**, 4448 (1988).

6. R.E. Miller, Science **240**, 447 (1988); G.E. Ewing, J. Phys. Chem. **91**, 4662 (1987).

7. H. Reisler and C. Wittig, Ann. Rev. Phys. Chem. **37**, 307 (1986); R. Bersohn, IEEE J. Quant. Elect. **QE-16**, 1208 (1980).

8. H. Reister and C. Wittig, Ann. Rev. Phys. Chem., **37**, 307 (1986); R. Bersohn, J. Phys. Chem. **88**, 5145 (1984).

9. P.L. Houston, J. Phys. Chem. **91**, 5388 (1987); P. Andersen, G.S. Ondrey, B. Titze and E.W. Rothe, J. Chem. Phys. **80**, 2548 (1984), see also D.R. Hershbach, Farad. Disc. Chem. Soc. **55**, 241 (1973); R.N. Zare and D.R. Hershbach, Proc. IEEE *January*, 173 (1963).

10. L.R. Khundkar, J.L. Knee and A.H. Zewail, J. Chem. Phys. **87**, 77 (1987).

11. N.F. Scherer and A.H. Zewail, J. Chem. Phys. **87**, 97 (1987).

12. N.F. Scherer, J.L. Knee, D.D. Smith and A.H. Zewail, J. Phys. Chem. **89**, 5141 (1985); M.J. Rosker, M. Dantus and A.H. Zewail, J. Chem. Phys. **89**, 6113 (1988); **89** 6128 (1988).

13. T.S. Rose, M.J. Rosker and A.H. Zewail, J. Chem. Phys. **88**, 6672 (1988); T.S. Rose, M.J. Rosker and A.H. Zewail, J. Chem. Phys. to be submitted.

14. F.F. Crim, Annu. Rev. Phys. Chem. **35**, 657 (1984).

15. C.B. Moore and J.C. Weisshaar, Ann. Rev. Phys. Chem **34**, 525 (1983); C.E. Hamilton, J.L. Kinsey and R.W. Field, Annu. Rev. Phys. Chem. **37**, 493 (1986); see also, J.A. Blazy and D.H. Levy, J. Chem. Phys. **76**, 4328 (1982).

16. See, for example, J.H. Ling and K.R. Wilson, J. Chem. Phys. **65**, 881 (1976); D.A. Case, G.M. McClelland and D.R. Hershbach, Mole. Phys. **35**, 541 (1978).

17. Y.T. Lee, Science **236**, 793 (1987); C.T. Rettner and R.N. Zare, J. Chem. Phys. **77**, 2416 (1982). See also C.H. Greene and R.N. Zare, J. Chem. Phys. **78**, 6741 (1983), R. Altkorn, R.N. Zare and C.H. Greene, Mole. Phys. **55**, 1 (1985).

18. K.H. Kramer and R.B. Bernstein, J. Chem. Phys. **42**, 767 (1965); S.E. Choi and R.B. Bernstein, J. Chem. Phys. **83**, 4463 (1985); S. Stolte, K.K. Chakravorty, R.B. Bernstein and D.H. Parker, Chem. Phys. **71**, 353 (1982).

19. D.H. Parker, H. Jalink and S. Stolte, J. Phys. Chem. **91**, 5427 (1987), and references therein.

20. A.C. Legon and D.J. Millen, Acc. Chem. Res. **20**, 39 (1987); E.J. Goodwin and A.C. Legon, J. Chem. Phys. **87**, 2426 (1987), for vibrational dynamics see M.P. Casassa, Chem. Rev. **88**, 815 (1988).

21. C. Jouvet and B. Soep, Chem. Phys. Lett. **96**, 426 (1983); C. Jouvet,-M. Boivineau, M. Dural and B. Soep, J. Phys. Chem. **91**, 5416 (1987).

22. S. Buelow, G. Radhakrishnan, J. Catanzarite and C. Wittig, J. Chem. Phys. **83**, 444 (1985); G. Radhakrishnan, S. Buelow and C. Wittig, J. Chem. Phys. **84**, 727 (1986); S. Buelow, G. Radhakrishnan and C. Wittig, J. Phys. Chem. **91**, 5409 (1987).

23. A.D. Buckingham, P.W. Fowler and A.J. Stone, Int. Rev. Phys. Chem. **5**, 107 (1986); A.D. Buckingham, P.W. Fowler, and J.M. Hutson, Chem. Rev. **88**, 963 (1988).

24. N.F. Scherer, L.R. Khundkar, R.B. Bernstein and A.H. Zewail, J. Chem. Phys. **87**, 1451 (1987).

25. D.P. Gerrity and J.J. Valentini, J. Chem. Phys. **79**, 5202 (1983); *ibid.* **83**, 2207 (1985).

26. S.R. Gandhi, T.J. Curtiss and R.B. Bernstein, Phys. Rev. Lett. **59**, 2951 (1987); S.E. Choi, Ph.D. Thesis, UCLA 1987.

27. J. Rice, G. Hoffmann and C. Wittig, J. Chem. Phys. **88**, 2841 (1988).

28. D. Häusler, J. Rice and C. Wittig, J. Phys. Chem. **91**, 5413 (1987); b) C. Wittig, S. Sharpe and R.A. Beaudet, Acc. Chem. Res. bf 21, 341 (1988).

29. B.J. Huebert and R.M. Martin, J. Phys. Chem. **72**, 3046 (1968); G. Herzberg, *Spectra of Diatomic Molecules*, (Van Nostrand, New York, 1950); C. Moore, NBS Tables, XXX (19xx).

30. I.W.M. Smith and R. Zellner, J. Chem. Soc. Faraday II, **69**, 1617 (1973); (b) I.W.M. Smith, Chem. Phys. Lett. **49**, 112 (1977).

31. J. Brunning, D. WynDerbyshire, J.W.M. Smith and M.D. Williams, in press (1987).

32. C.W. Larson, D.H. Stewart and D.M. Golden, Int. J. Chem. Kinetics, in press (1987); D.M. Golden, J. Phys. Chem. **83**, 108 (1979).

33. (a) M.E. Jacox, J. Chem. Phys. **88**, 4598 (1988); (b) D.E. Milligan and M.E. Jacox, J. Mol. Spect. **46**, 460 (1973).

34. J. Troe, J. Phys. Chem. **83**, 114 (1979); *ibid.,* Ber. Bunsenges. Phys. Chem. **87**, 161 (1983).

35. L.R. Khundkar, R.A. Marcus and A.H. Zewail, J. Phys. Chem. **87**, 2473 (1983).

36. G.A. Oldershaw and D.A. Porter, Nature **223**, 490 (1969).

37. C.R. Quick and J.J. Tiee, Chem. Phys. Lett. **100**, 223 (1983).

38. K. Kleinermans and J. Wolfrum, Chem. Phys. Lett. **104**, 157 (1984); K. Kleinermans, E. Linnebach and J. Wolfrum, J. Phys. Chem. **89**, 2525 (1985).

39. F.A. Baiocchi, T.A. Dixon, C.H. Joyner and W. Kemperer, J. Chem. Phys. **74**, 6544 (1981).

40. R.S. Altman, M.D. Marshall and W. Klemperer, J. Chem. Phys. **77**, 4344 (1982).

41. P.A. Kollman, J. Am. Chem. Soc. **99**, 4875 (1977).

42. A.M. Sapse and J.M. Howell, J. Chem. Phys. **78**, 5738 (1983).

43. A.E. Reed, F. Weinhold, L.A. Curtiss and D.J. Pochatko, J. Chem. Phys. **84**, 5687 (1986).

44. C.M. Lovejoy, M.D. Schuder and D.J. Nesbitt, J. Chem. Phys. **86**, 5337 (1987).

45. L. Andrews and G.L. Johnson, J. Chem. Phys. **76**, 2875 (1982).

46. C.E. Dykstra, J. Chem. Phys., in press (1988); *ibid.*, Acc. Chem. Res., in press (1988).

47. P.G. Jasien and W.J. Stevens, Chem. Phys. Lett. **180**, 127 (1986).

48. A.D. McLean and Y. Ellinger, Chem. Phys. **94**, 25 (1985).

49. G.C. Schatz, M.S. Fitzcharles and L.B. Harding, Farad. Disc. Chem. Soc., **84**, 359 (1987).

50. G.W. Flynn and R.E. Weston Jr., Ann. Rev. Phys. Chem **37**, 551 (1986); J.A. O'Neill, J.Y. Cai and G.W. Flynn, J. Chem. Phys. **84**, 50 (1986); S.A. Hewitt, J.F. Hershberger, G.W. Flynn and R.E. Weston Jr., *ibid.*, **87**, 1894 (1987).

51. G.C. Schatz and M.S. Fitzcharles, NATO Workshop ASI series (1987), in press.

52. G.C. Schatz, private communication (August and October 1988).

53. H.M. Crosswhite and G.H. Dicke, J. Quant. Spect. Radit. Trans. **2**, 97 (1964); (b)I.L. Chidsey and D.R. Crosley, *ibid.*, **23**, 187 (1980); (c)W.L. Dimpfl and J.L. Kinsey, *ibid.*, **21**, 233 (1979).

54. Experimental Details Chapter, N.F. Scherer Ph.D. Thesis, Caltech 1989.

55. T. Jimbo, V.L. Caplan, Q.X. Li, Q.Z. Wang, P.P. Ho and R.R. Alfano, Opt. Lett. **12**, 477 (1987); R.L. Fork, C.V. Shank, C. Hirlmann, R. Yen and W.J. Tomlinson, Opt. Lett. bf 8, 1 (1983).

56. R.R. Alfano, L.L. Hope and S.L. Shapiro, Phys. Rev. A, **6**, 433 (1972); C.X. Li, T. Jimbo, P.P. Ho and R.R. Alfano, Appl. Opt. **25**, 1869 (1986).

57. O.E. Martinez, IEEE J. Quant. Elect. **QE-23**, 59 (1987).

58. E.B. Treacy, *ibid.*, **QE-5**, 454 (1969).

59. B. Nikolaus and D. Grischkowsky, Appl Phys. Lett.**42**, 1 (1983); W.J. Tomlinson, R.H. Stolen and C.V. Shank, J. Opt. Soc. Am. **B1**, 139 (1984).

60. B.W. Keelan, J.A. Syage, J.F. Shepanski and A.H. Zewail, Proc. Int. Conf. Lasers (STS, McLean, VA, 1985), p. 718.

61. L.R.Khundkar, Ph.D. Thesis, Caltech (1988).

62. W.C. Wiley and I.H. McLaren, Rev. Sci. Inst. **26**, 1150 (1955).

63. D.V. O'Connor and D. Phillips, *Time-Correlated Single Photon Counting*, (Academic Press, New York, 1984).

64. N.F. Scherer, Ph.D. Thesis, Caltech (1989); Chapter 4.

65. S. Klee, K. Gericke and F.J. Comes, J. Chem. Phys. **85**, 40 (1986); **85**, 4463 (1986).

66. K.H. Gericke, A.U. Grunewald, S. Klee and F.J. Comes, *ibid.* **88**, 6255 (1988).

67. Y.R.Shen, *The Principles of Nonlinear Optics*, (Wiley, New York, 1984).

68. E.M. Evleth, J. Am. Chem. Soc. **98**, 1637 (1976); R. Bersohn and M Shapiro, J. Chem. Phys. **85**, 1396 (1986).

69. See Chapter 2 in N.F. Scherer, Ph.D. Thesis, Caltech (1989).

70. The 1+1 ionization method has been shown to give equivalent results with the HOOH direct dissociation. Ref. 54 gives a superposition of a HOOH response and a 1+1 ionization response taken under the same experimental conditions. It is expected that the 1+1 ionization response is essentially instantaneous provided that rapid IVR behavior does not occur.

71. G.M. Fleck, *Chemical Reaction Mechanisms*, (Holt, Rinehardt, New York, 1971).

72. R.D.Clear, S.J. Riley, and K.R. Wilson, J. Chem. Phys. **63**, 1340 (1975);- R. Schmiedl, H. Dugan, W. Meier and K.H. Welge, Z. Phys. A. **304**, 137 (1982).

73. L.R. Khundkar and A.H. Zewail, Chem. Phys. Lett. **142**, 426 (1987).

74. A.H. Zewail and R.B. Bernstein, Chem. & Engr. News, Special Report, **66**, 24 (1988).

75. N.F. Scherer, Ph.D. Thesis, Chapter 6, Caltech (1989); ν_{OH}=6.

76. R.A. Marcus, private discussions; R.A. Marcus, J. Chem. Phys. **20**, 359 (1952); P. Pechukas,Annu. Rev. Phys. Chem. **32**, 159 (1981); D. Truhlar, Annu. Rev. Phys. Chem. **35**, 159 (1984).;The fundamental assumption of RRKM theory, which is that IVR is effectively complete on the timescale of other dynamical processes, may not be fulfilled on the present experimental timescale. This point should be kept in mind when making comparisons with any statistical reaction rate theories.

77. S.K. Gray and S.R. Rice, J. Chem. Phys. **86**, 2020 (1987).

78. R.D. Levine, in *Atom-Molecule Collision Theory*, R.B. Bernstein ed., (Plenum, New York, 1969).

79. N.F. Scherer, E.D. Potter and A.H. Zewail, to be published. (1989).

80. A.G. Urena, Mole. Phys. **52**, 1145 (1984).

81. R.D. Levine and R.B. Bernstein, Chem. Phys. Lett. **105**, 467 (1984); **132**, 11 (1986).

82. S.E. Choi and R.B. Bernstein, J. Chem. Phys. **85**, 150 (1986).

83. I.W.M. Smith, J. Chem. Edu., **59**, 9 (1982).

84. For example see *Resonances in Electron-Molecule Scattering, van der Waals Complexes and Reactive Chemical Dynamics*, D.G. Truhlar ed., (ACS Symposium Series 263; American Chemical Society, Washington, D.C., 1984).

85. E. Pollak, J. Chem. Phys. **78**, 1228 (1983); I. Last and M. Baer, J. Chem. Phys. **86**, 5534 (1987).

86. E. Pollak, in *Theory of Chemical Reaction Dynamics*, ed. M. Baer, CRC Press, Boca Raton, FL. 1985.

87. R.J. Wolf and W.L. Hase, J. Chem. Phys. **73**, 3379 (1980); I. Hamilton and P. Brummer, *ibid.* **82**, 1937 (1985); R.M. Hedges and W.P. Reinhardt, J. Chem. Phys. **78**, 3964 (1983); W.L. Hase, J. Phys. Chem. **90**, 365 (1986).

88. V.K. Babamov and R.A. Marcus, J. Chem. Phys. **74**, 1790 (1981).

89. D.C. Clary and J.N.L. Connor, Chem. Phys. Lett. **94**, 81 (1983).

90. E. Pollak, *ibid.*, **94**, 85 (1983).

91. J.C. Nieh and J.J. Valentini, Phys. Rev. Lett. **60**, 519 (1988).

92. A. Kuppermann, in *Potential Energy Surfaces and Dynamics Calculations*, ed. by D.G. Truhlar, (Plenum, New York, 1981), p. 374; P.G. Hipes and A. Kuppermann, Chem. Phys. Lett. **133**, 1 (1987).

93. R.B. Bernstein and A.H. Zewail, J. Chem. Phys., inpress (1989).

94. R.Alimi, R.B. Gerber and A. Apkarian, J. Chem. Phys. **89**, 174 (1988).

95. G.R. Fleming, *Chemical Applications of Ultrafast Spectroscopy*, (Oxford, New York, 1987).

TABLE 1.

Parameters for XH-OCO Geometries[a]

X	Radius (Å)	R_{XH-OCO} (Å)	R_{H-X} (Å)	R_{XH-OCO}(Calc.) (Å)
F	1.58	1.91	-	-
Cl	1.84	2.14		-
Br	2.00	-	1.48	2.32
I	2.15	-	1.608	2.50

[a] Bond length of O−C=1.163Å.

TABLE 2.

Additional Parameters for Reactant Complex Geometry

vdW Complex	$R_{cm.-cm.}$ (Å)	HX Dipole Moment (Debye)	Force Const. (Bend) (mdyne·Å)	E_{ZP}[a] (Bend) (cm^{-1})
FH-OCO	4.078	1.82	0.023	111
ClH-OCO	4.629	1.08	0.013	59
BrH-OCO	4.960	0.82	0.010	46
IH-OCO	5.270	0.45-0.5	0.0061	32

[a] denotes zero point energy.

TABLE 3.

Energetics for Bimolecular Reaction[a]

RRKM #1 - Standard Calculation

Quantity	HOCO (trans)	H–OCO (cis saddle pt.)	HO–CO (saddle pt.)
R_{OH} (a_o)	1.95	2.91	1.81
R_{CO} (a_o)	2.80	2.52	4.75
$R_{CO'}$ (a_o)	2.20	2.20	2.15
θ_{HOC} (deg)	124.8	143.2	112.3
$\theta_{OCO'}$ (deg)	127.1	158.6	165.2
Energy (eV)	-0.63	1.10	0.93

HOCO Frequencies (cm^{-1})	HOCO Moments of Inertia (amu·Å^2)	HO–CO Saddle Pt.[b] (cm^{-1})	HO–CO Moments of Inertia (amu·Å^2)
3770	56.3	3578	115
1890	2.3	1928	1.02
1181	58.6	401	116
1098		284	
791		137	
612		(107)[c]	

[a] from References 49,51.

[b] Barrier Energy above *t*-HOCO minimum = 11800cm^{-1} having included zero-point energy corrections.

[c] No internal rotation in critical configuration.

TABLE 4.

RRKM #2[a]

HOCO Frequencies (cm^{-1})	HOCO Moments of Inertia (amu·Å^2)	HO–CO Saddle Pt.[b] (cm^{-1})	HO–CO Moments of Inertia (amu·Å^2)
3456		3456	99.24
1833	47.2	1900	95.66
1260	2.50	900	3.58
1080	49.7	425	
615		175	
615		-	

[a] Conditions from Reference 32.
[b] Barrier Energy above *t*-HOCO minimum = 13030cm^{-1}.
[c] No internal rotations in critical configuration.

TABLE 5.

RRKM #3[a]

HOCO Frequencies (cm^{-1})	HOCO Moments of Inertia ($amu \cdot Å^2$)	HO–CO Saddle Pt.[b] (cm^{-1})	HO–CO Moments of Inertia ($amu \cdot Å^2$)
3456	43.8	3501	61.55
1833	3.9	2009	
1261	47.8	860	4.28
1077		314	65.75
615		270	0.864[c]
472			

[a] Conditions from References 30,31.
[b] Barrier Energy above t-HOCO minimum = 13260cm^{-1}.
[c] No internal rotations in Critical configuration.

FIGURE CAPTIONS

1. Schematic potential energy surfaces that are relevant to the chemical dynamics of $IH - OCO \xrightarrow{h\nu} I + [HOCO]^{\dagger} \rightarrow I + OH + CO$.

2a. Kinetic equations for a gas phase study of the rate of OH+CO formation which is one of three different routes for $[HOCO]^{\dagger}$ to decay.

2b. Lifetime of $[HOCO]^{\dagger}$ vs. temperature is plotted to study the temperature dependence of the rate of HOCO formation of $H+CO_2$ and OH+CO. The rate for the former process is significantly slower than the latter reaction path

3a. The angular potential energy curves obtained from linear cuts ($\theta_{HX} = \alpha \cdot \theta_{OCO}$, where X=F or Cl) through the two dimensional contour diagrams for the FH-OCO and ClH-OCO vdW complex potentials, respectively. α denotes a constant for the cut to pass through the lowest energy at each θ_{HX} configurations.

3b. The angular potentials for BrH-OCO and IH-OCO van der Waals complex extrapolated from Figure 3a by considering the ratios of the halogen radii.

4a. The probability amplitude $P(\theta)$ and $P(\theta) \cdot \sin\theta$ are plotted as a function of angle for the zero-point motion of HI in the potential IH-OCO, illustrated in Figure 3b.

4b. Plot of the angular dependence of the reaction probability $P(\theta)$, and $P(\theta) \cdot \sin\theta$ for BrH-OCO from classical trajectory studies with impact parameter b=0.

5a. Diagram for the FH-OCO complex, whose structure has been measured and calculated by ab initio techniques. The relative size and configuration are drawn to realistic values with a constant scaling factor.

5b. Diagram of the structure of the IH-OCO van der Waals complex as extrapolated from Figure 5a by considering the ratio of halogen radii.

6a. Reaction scheme for pump-probe studies of the oriented bimolecular reaction H+OCO via the photolysis of HI in the van der Waals complex IH-OCO

6b. Reaction energy diagram which indicates the important barrriers to reaction and minimum energies for the different configurations and transition-state regions for HOCO.

7a-b. (a) Diagram of the continuum spectral selection method; (b) Molecular Beam Apparatus; For further details, see Chapter 2.

7c-d. The EI signals of the vdW complex BrH-OCO and IH-OCO (normalized to BrH signal and IH signal, respectively,) are plotted as a function of the backing pressures.

8a. Rate of OH formation in IH-OCO oriented bimolecular reaction. The excitation wavlength 238nm is used to phytolyze IH-OCO→I+H-OCO; the OH product (formed from the dissociation of $[HOCO]^{\dagger}$) in the lowest rotational quantum state $Q_1(1)$ is detected via LIF. o; Experimental data, +; System Response function obtained from direct dissociation of HOOH at the same photolysis wavelength, and −; Curve-fit to the two-step kinetice model (described

in Eqn. (3.6)) which is convolved with the response function shown in the figure. The values used to obtain the curve-fit are k_1=1.27ps^{-1}, k_2=0.95ps^{-1}, and $\Delta\tau$=0.95ps.

8b. Comparison of the time-dependence of the HOOH reaction with a true cross-correlation obtained by difference frequency generation.

9a. Log-log plot of the OH LIF signal against a decrease in the optical density for 238nm excitation and $Q_1(1)$ detection. A reasonably straight line (with a slope of 0.95±0.1) is consistent with that a single probe photon induces the LIF of the OH product.

9b. Schematic diagram for the time dependance of the populations of the A,B and C configurations of the two-step kinetic model described by Eqn. (3.2).

10. (a) Plots for 263nm excitation and Q1(1) detection, in which the fitted-curve is obtained for k_1=0.623ps^{-1}, k_2=0.38ps^{-1}, and $\Delta\tau$=2.27ps; (b) Plots for 241nm Excitation and Q1(1) detection, in which the fitted curve is obtain for k_1=1.93ps^{-1}, k_2=1.13ps^{-1}, and $\Delta\tau$=0.75ps; For further details, refer to the captions for Figures 9a-b or the text.

11. (a) Plots for 256nm excitation and Q1(1) detection; (b) Plots for 256nm excitation and Q1(6) detection; (c) Plots for 240nm excitation and Q1(1) detection; (d) Plots for 240nm excitation and Q1(6) detection; (e) Plots for 236nm excitation and Q1(1) detection; (f) Plots for 236nm excitation and Q1(6) detection; (g) Plots for 234nm excitation and Q1(1) detection; (h) Plots for 234nm excitation and Q1(6) detection; for further details refer to the captions for Figures 9a-b or the text.

12a. Time of HOCO formation $\tau_1(\equiv 1/k_1)$ is presented for the different pump pulse wavelength for both $Q_1(1)$ and $Q_1(6)$ detection. The τ_1-values are actually plotted against the energy made available to the HI-moiety of the vdW reactant complex IH-OCO.

12b. HOCO lifetime $\tau_2(\equiv 1/k_2)$, in which k_2 denotes the dissociation rate of HOCO to OH and CO, is presented for the different pump pulse wavelength for both $Q_1(1)$ and $Q_1(6)$ detection. The τ_2-values are plotted against the energy made available to the HI-moiety of the vdW complex IH-OCO. For further details with respect to the spike-like feature for 240nm excitation wavelength (which correlates to E_{avail}=16480cm^{-1}), see text.

13a. Summary of the induction periods associated with the lifetimes of Figure 12. The monotonic decrease in the induction period is observed with increasing available energy. Also shown in the figure is the small time-shift parameter values, that were used to minimized χ^2 for each data point.

13b. Normalized relative reaction probability for the formation of OH for Q1(1) and Q1(6) detection. The results have not been normalized to account for the branching ratios in the formation of I($^2P_{3/2}$) and I($^2P_{1/2}$), and also the plots for $Q_1(1)$ and $Q_1(6)$ are not normalized to each other.

14. The $[HOCO]^{\dagger}$ dissociation rate $k_2(\equiv 1/\tau_2)$,, τ_2-values corresponding to those presented in Figure 12b, to form the observable OH product have been plotted as a function of the available energy for both $Q_1(1)$ and $Q_1(6)$ detections. Also the figure contains plots of the reaction rates obtained from the RRKM calculations without free rotations in the critical configuration. The RRKM #1 (open squares), RRKM #2 (closed circles), and RRKM #3 (closed squares) curves correspond to RRKM calculations results obtained for the values of frequencies and energies reported in Ref. 49, Refs. 32-33, and Refs. 30-31, respectively. The numerical values of frequencies and energies are listed in Table 3, Table 4, and Table 5, respectively.

15a. Potential energy surfaces, describing various interactions between constituents in van der Waals complex IH-OCO, are presented for a fixed center-of-mass separation of IH and OCO. The curve A (closed circle) is a linear cut through the equilibrated PES of H-OCO at 35° with respect to a line going through the CO_2 c.m. and kept parallel to O-O axis of the equilibrated CO_2 configuration. The curve B (dots) is the HI repulsive electronic state $^1\Pi$. The curve C (open squares) represents a linear cut through the PES of H-OCO (with CO_2 bening angle fixed at 175°) at a C-O-H angle of 25°.

15b. The potential energy curves in this figure represent a simple addition of curves A and B of Figure 15a (closed squares), a simple addition of curves C and B of Figure 15a (open squares), and the HI repulsive electronic surface $^1\Pi$ (dots).

16. Four effective potential curves of IH-OCO plotted against H-I distance. The plots show the change of the barrier to reaction and the formation of the HOCO well depending on the particular IH-OCO configurations obtained for different H-atom approach directions to various CO_2 geometry. The three curves shown in dots, open squares, and closed squares are reproduced from Figure 15b. The remaining two curves are obtained by simple additions of the curve B of Figure 15a and 30°-linear cuts of HOCO potential energy surfaces corresponding to CO_2 bend angle of 160° with symmetric C-O bond lengths (open triangles) and with asymetric C-O bond lengths (small squares), respectively.

17a. Same as that of Figure 15a, except here the curve B represents the $^3\Pi_o{}^+$ repulsive electronic PES of HI dissociation correlating to the $I(^2P_{1/2})$ product state.

17b. Simple additive potential surfaces of Curve A and Curve C with Curve B of Figure 17a, respectively.

18. HOCO dissociation rates, k_2 are plotted for $Q_1(1)$ products correlating to the $I(^2P_{3/2})$ reaction channel, $Q_1(6)$ product correlating to the $I(^2P_{1/2})$ reaction channel, and $Q_1(1)$ product correlating to $I(^2P_{1/2})$ reaction channel. $Q_1(1)$ data for $I(^2P_{1/2})$ reaction chnnel is rescaled to reflect the $7603cm^{-1}$ spin-orbit splitting energy.

19. Curves of HOCO dissociation rates obtained from the RRKM models. The open square, closed circle, and the closed square corresponds to RRKM #1, RRKM #2, and RRKM #3 curves of Figure 14, respectively, with threshold

energy rescaled for the 7603cm^{-1} spin-orbit splitting. The open circles are data points for $Q_1(1)$ product correlating to the excited $I(^2P_{1/2})$ reaction channel, and the solid line going through the points represents the best (logarithmic) fit to the data.

20a. Plot of k_1 vs. E_{tr} for the low energy data points and its best linear fit. An equivalent plot for the data of 15% reduced avaiable energy is also presented. The plots show the entrance channel threshold values of 10657cm^{-1} and 9058cm^{-1} for the full and 15% rescaled data, respectively. Furthermore, $\triangle t = 5 \times 10^{-3}$ps and 4.2×10^{-3}ps, and a=1.35×10^{-2} and 1.13×10^{-2} are obtained for the full and 15% rescaled data, respectively.

20b. Reaction probabilities for the values of a obtained in Figure 20a are plotted against the available translational energy. The linear dependence of the probability on the kinetic energy follows from assigning $\triangle t$ to be a constant.

21. Simply additive potential surfaces which hint at the time dependance of the effective potential surface. The individual curves are for various OCO geometries and clearly show a one-dimensional well in the entrance channel region.

22. The simply additive potential surface for the entrance channel region considering only the IH repulsive surface and the H-OCO interaction potential for nearly-equilibrium geometry OCO (175^o O-C-O bending mode)

Figure 1

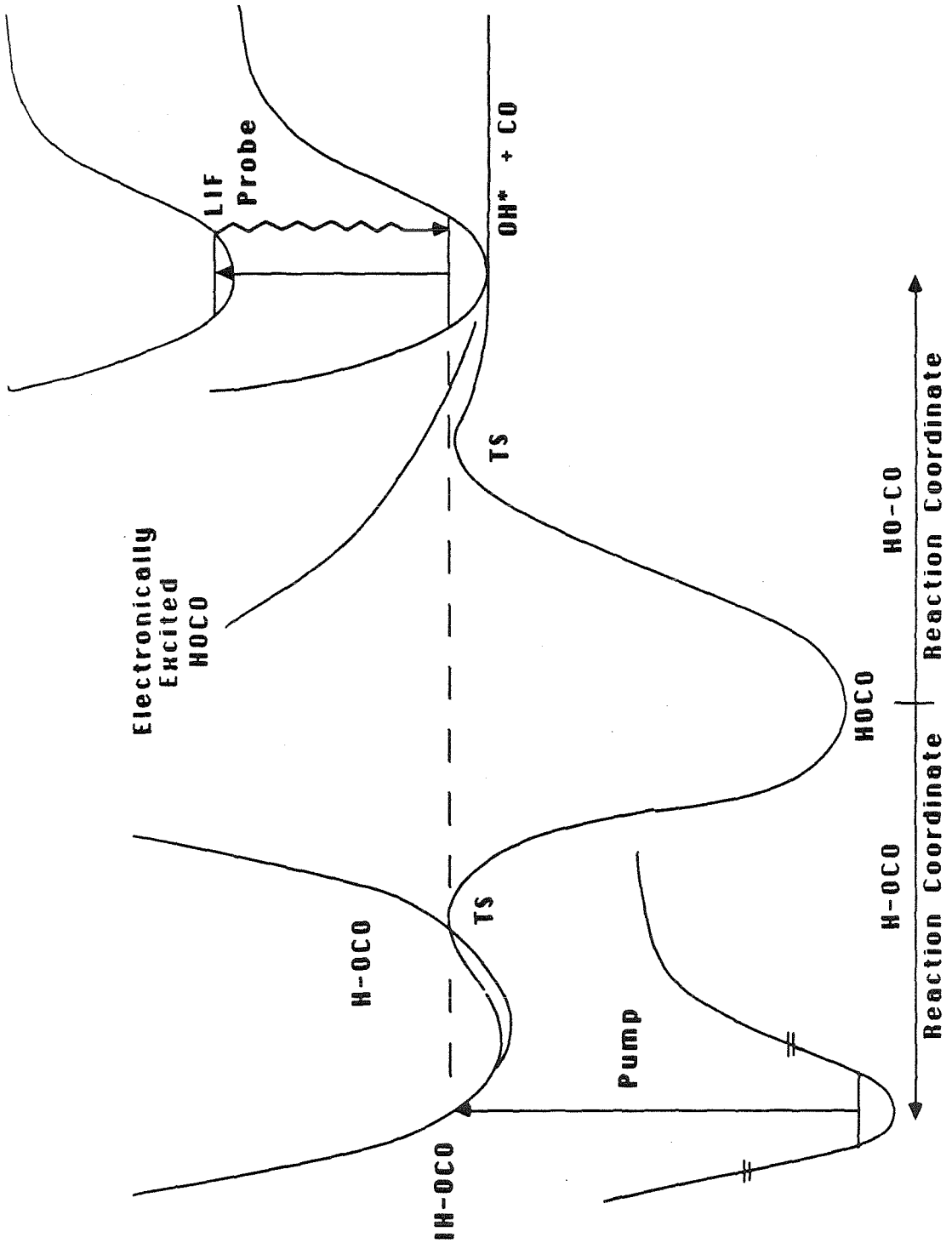
LIF
Probe
OH* + CO
TS
Electronically
Excited
HOCO
HO-CO
HOCO
H-OCO
TS
H-OCO
Pump
IH-OCO
Reaction Coordinate
Reaction Coordinate

Figures 2a, 2b.

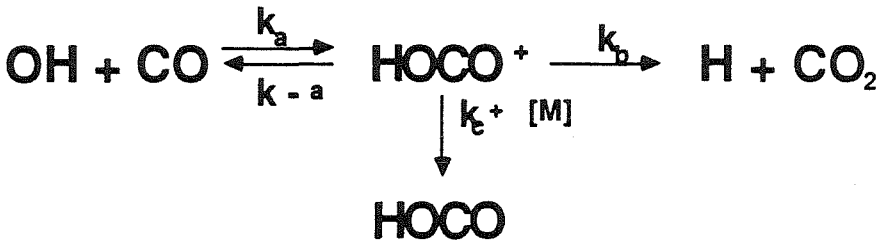

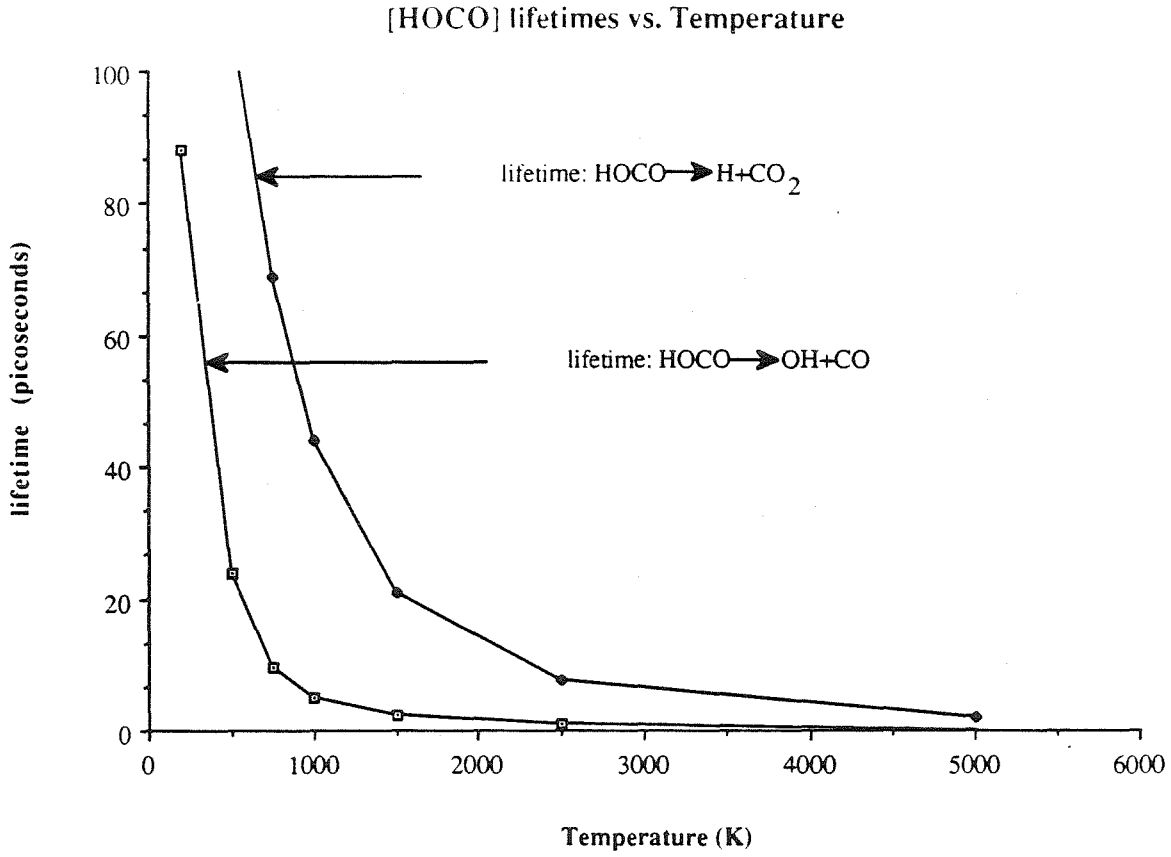

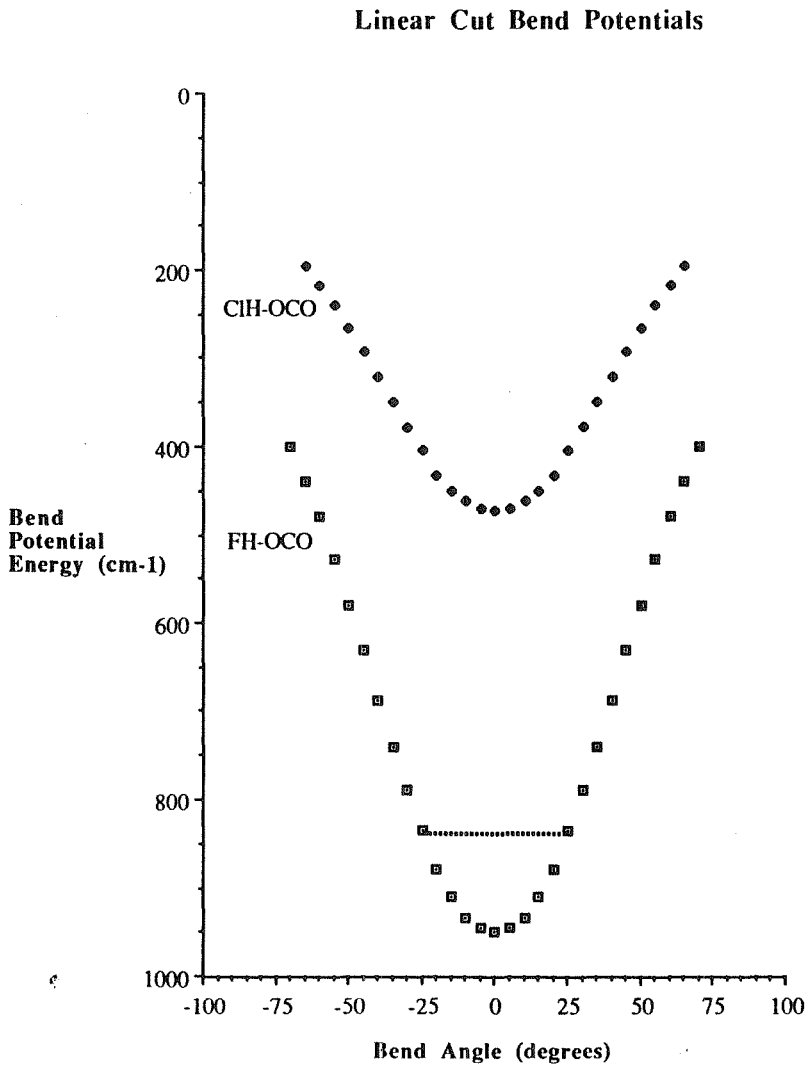

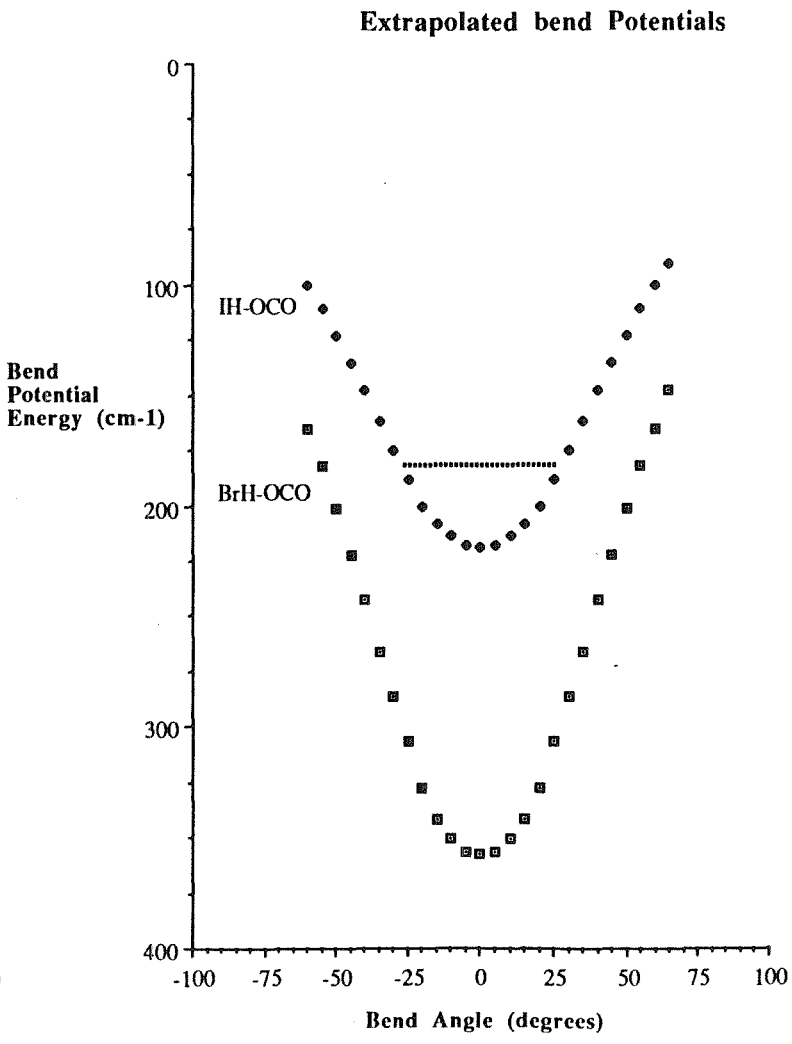

Figures 3a, 3b.

Figures 4a, 4b.

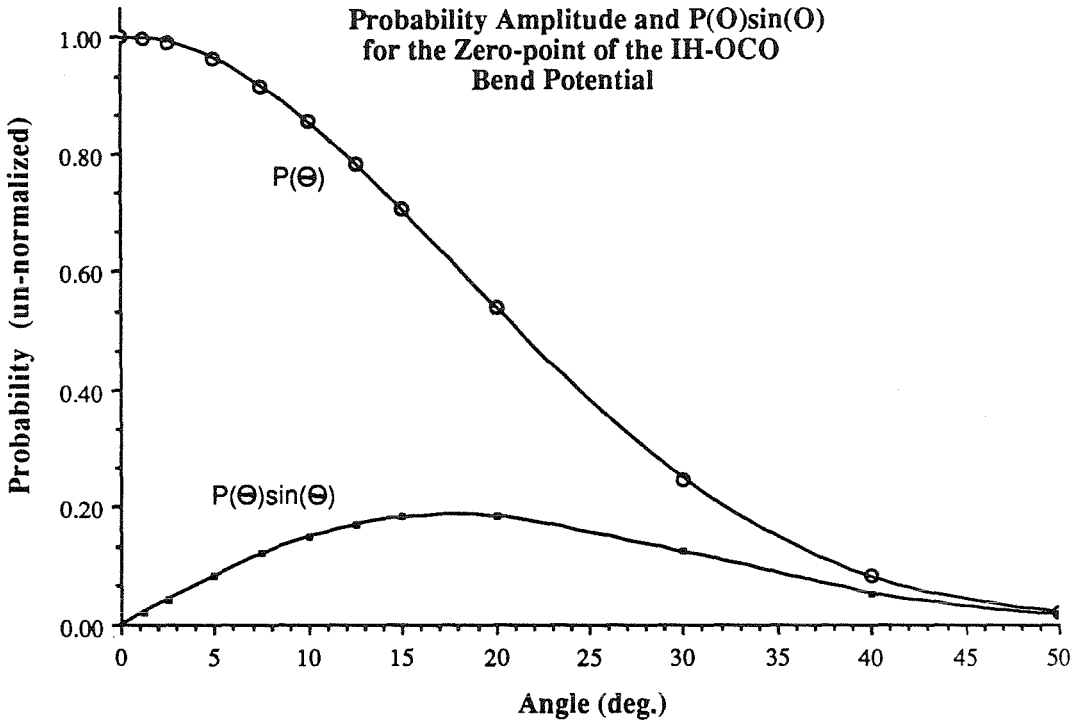

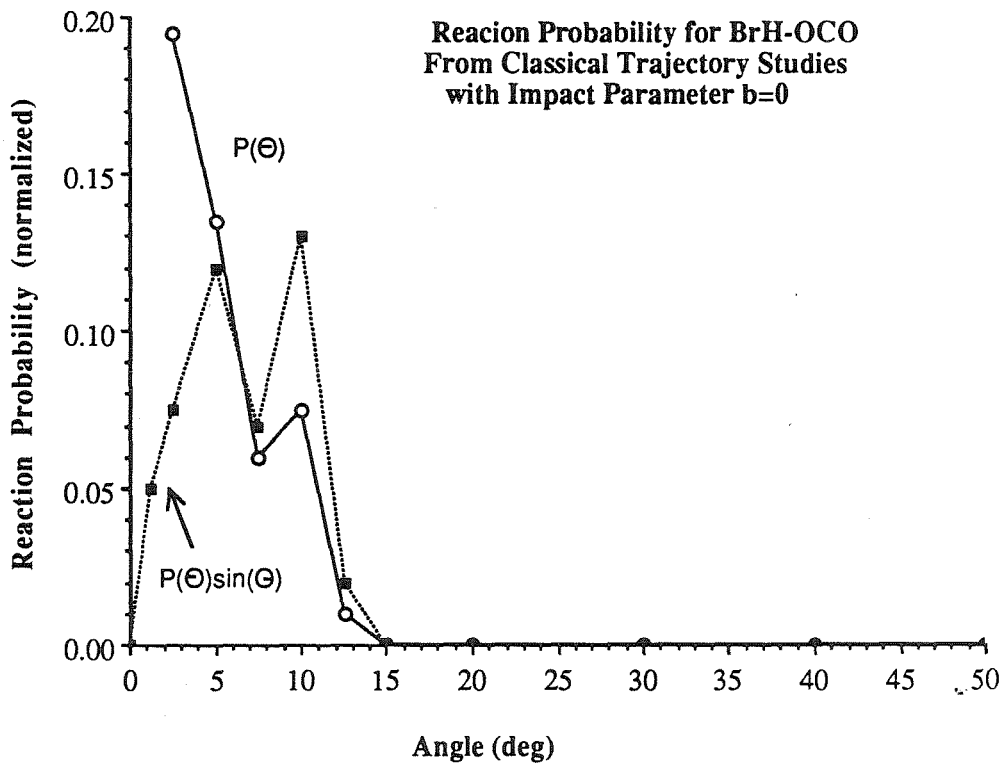

Figures 5a, 5b.

FH-OCO van der Waals Complex

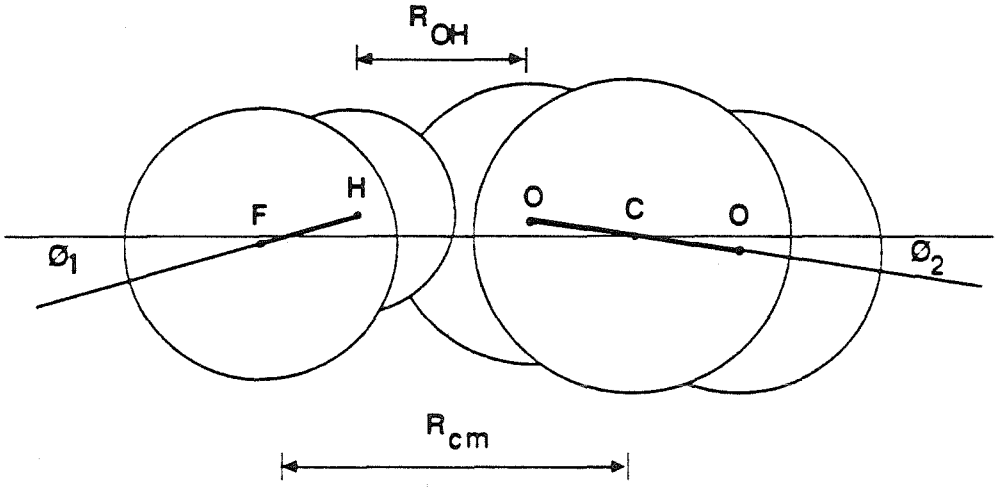

IH-OCO van der Waals Complex

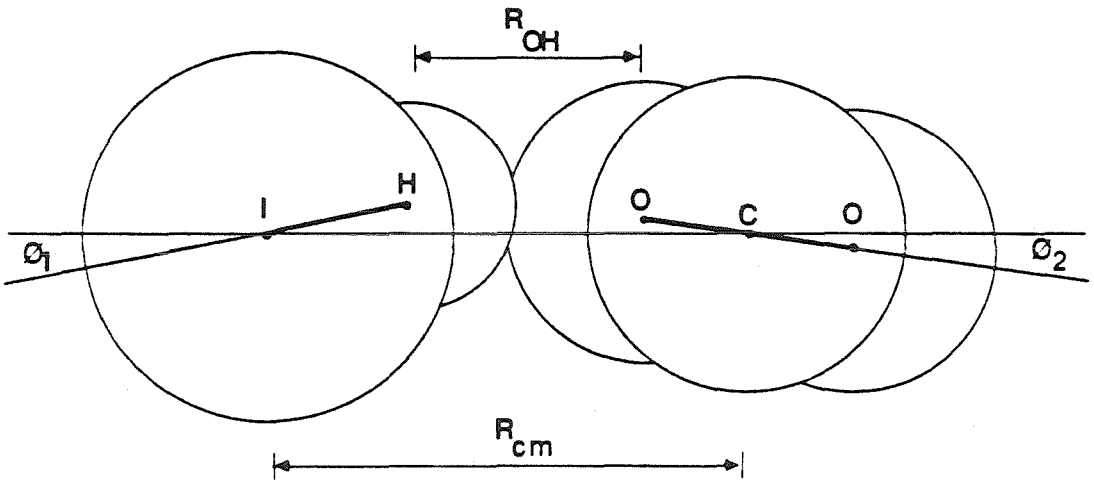

Figurea 6a, 6b.

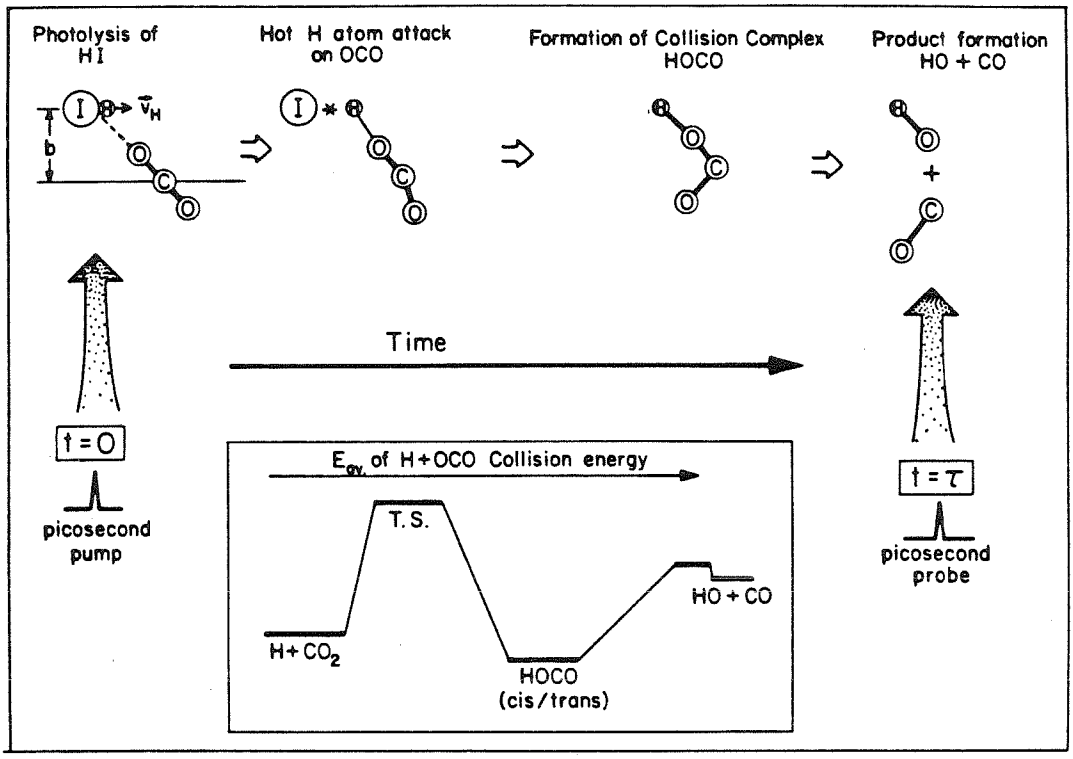

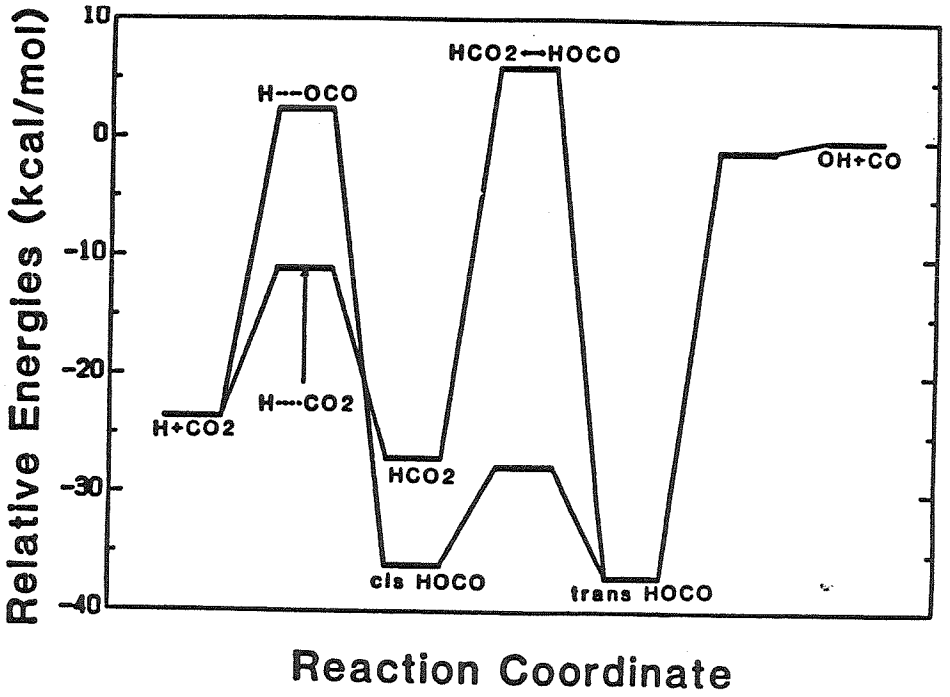

Figures 7a, 7b.

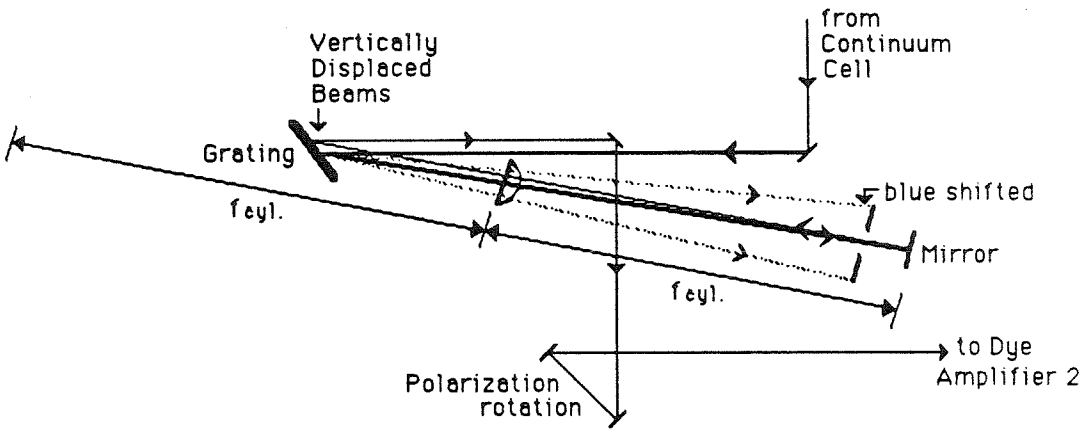

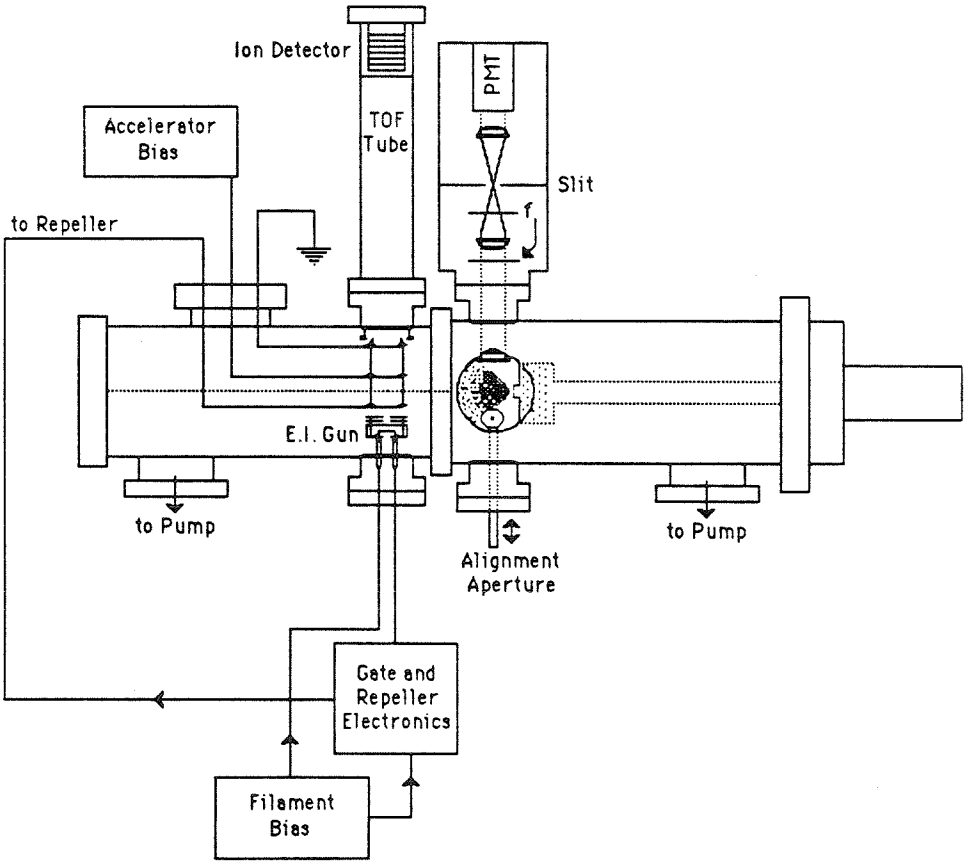

Figures 7c, 7d.

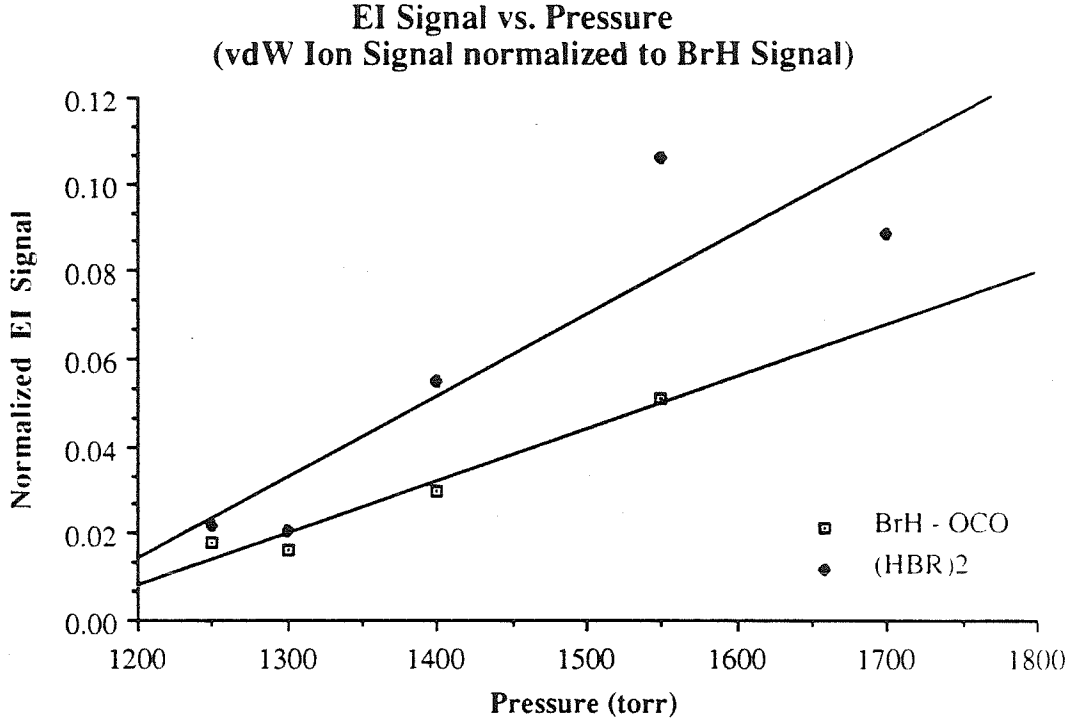

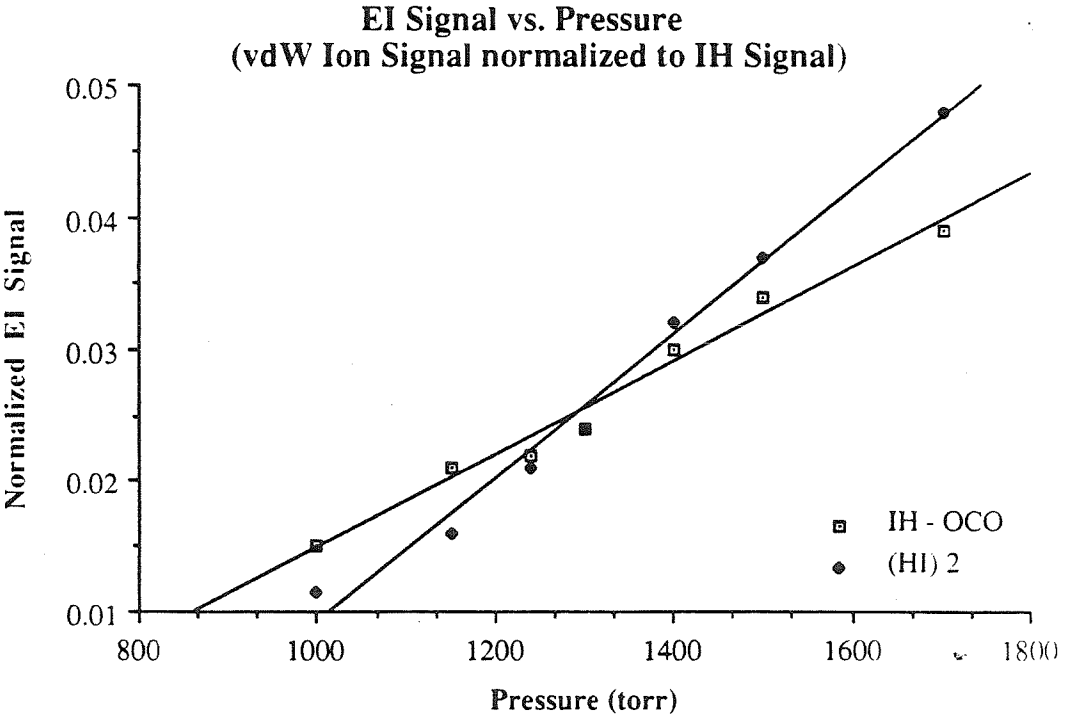

Figures 8a, 8b.

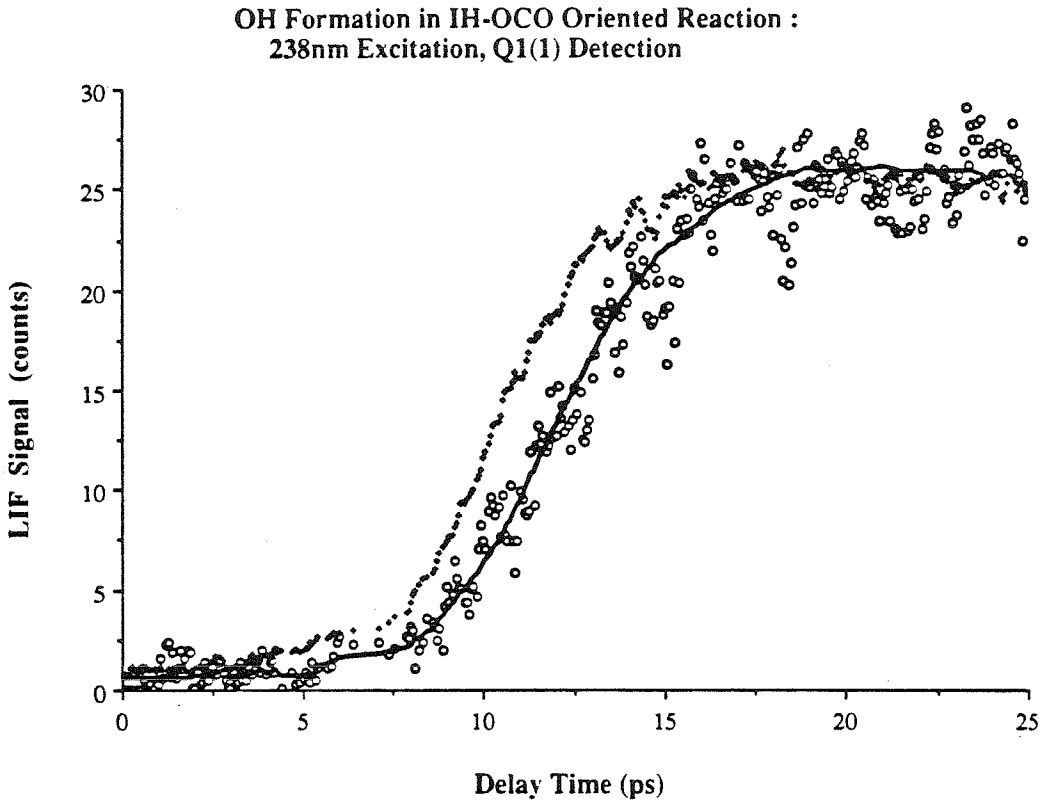

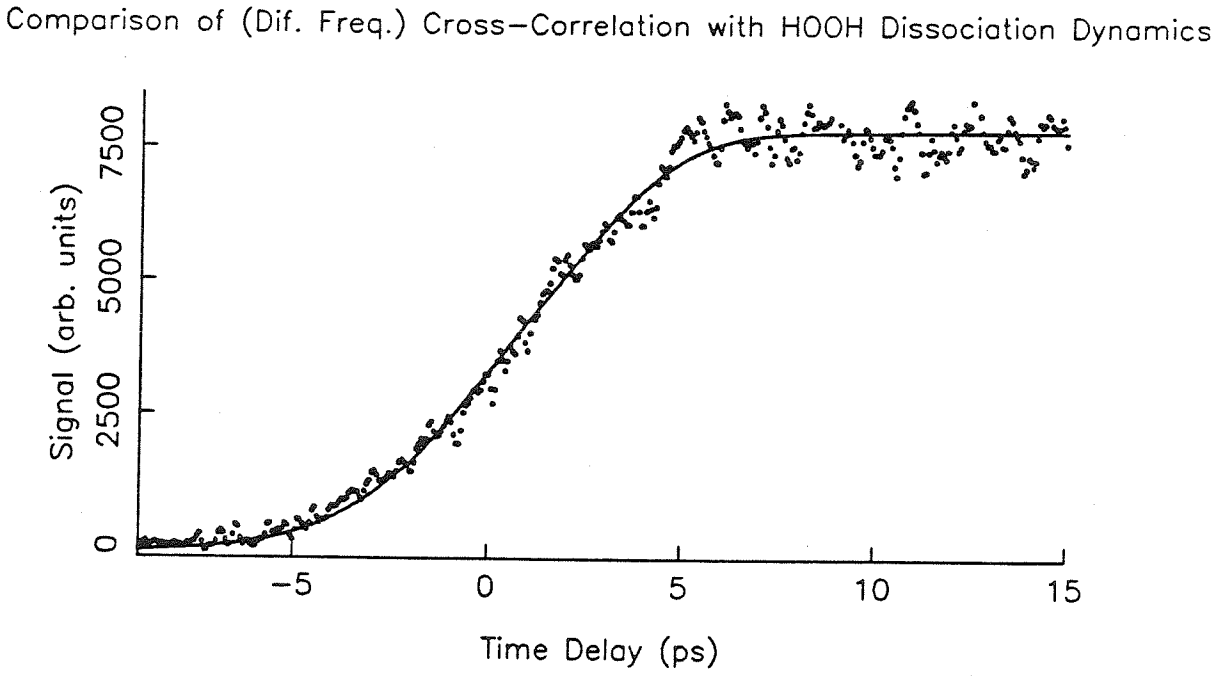

Figures 9a, 9b.

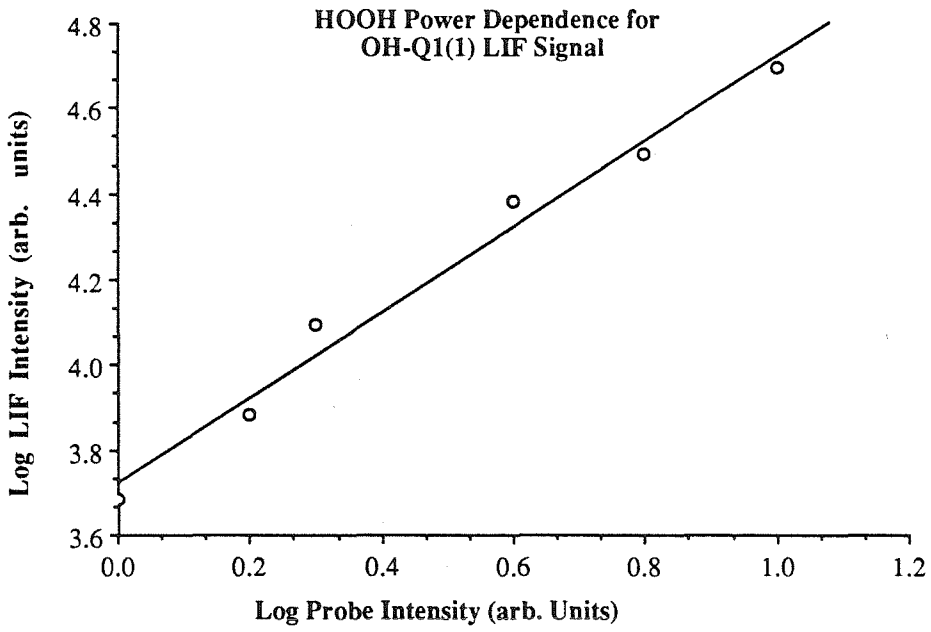

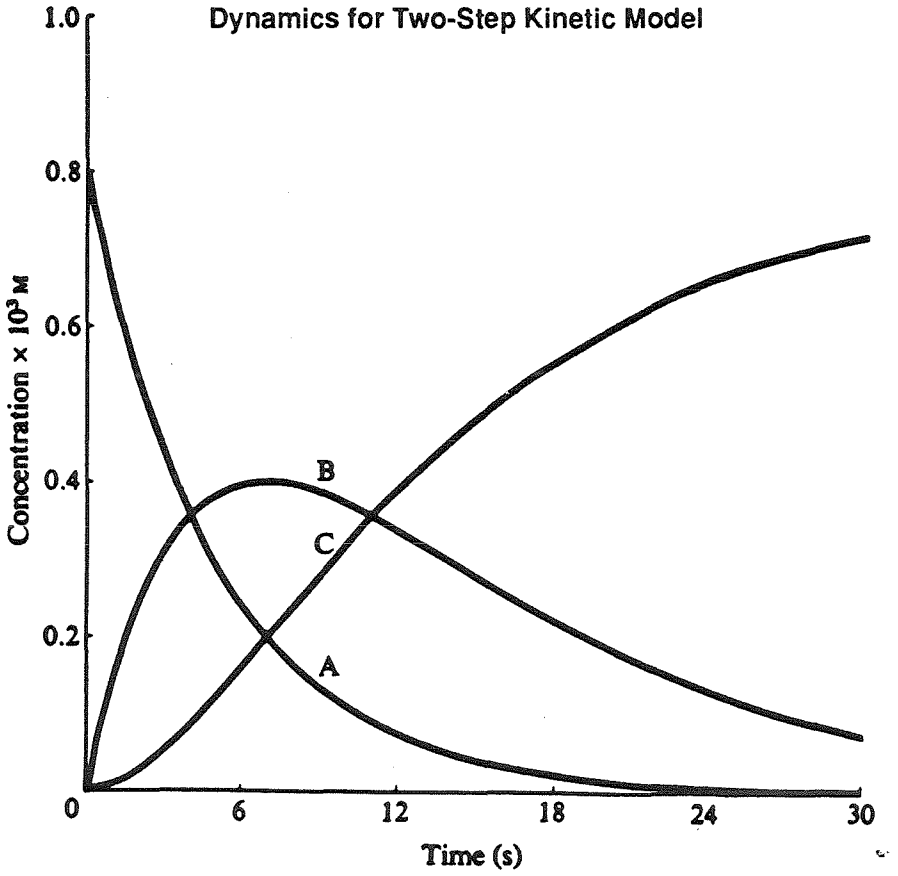

Figures 10a, 10b.

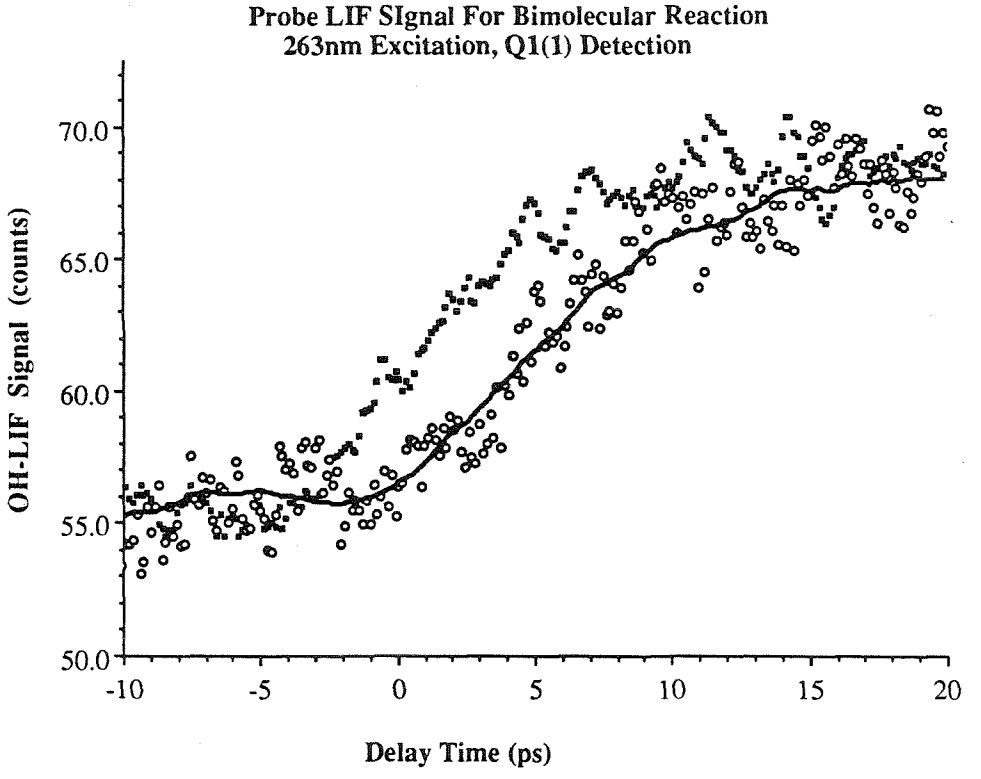

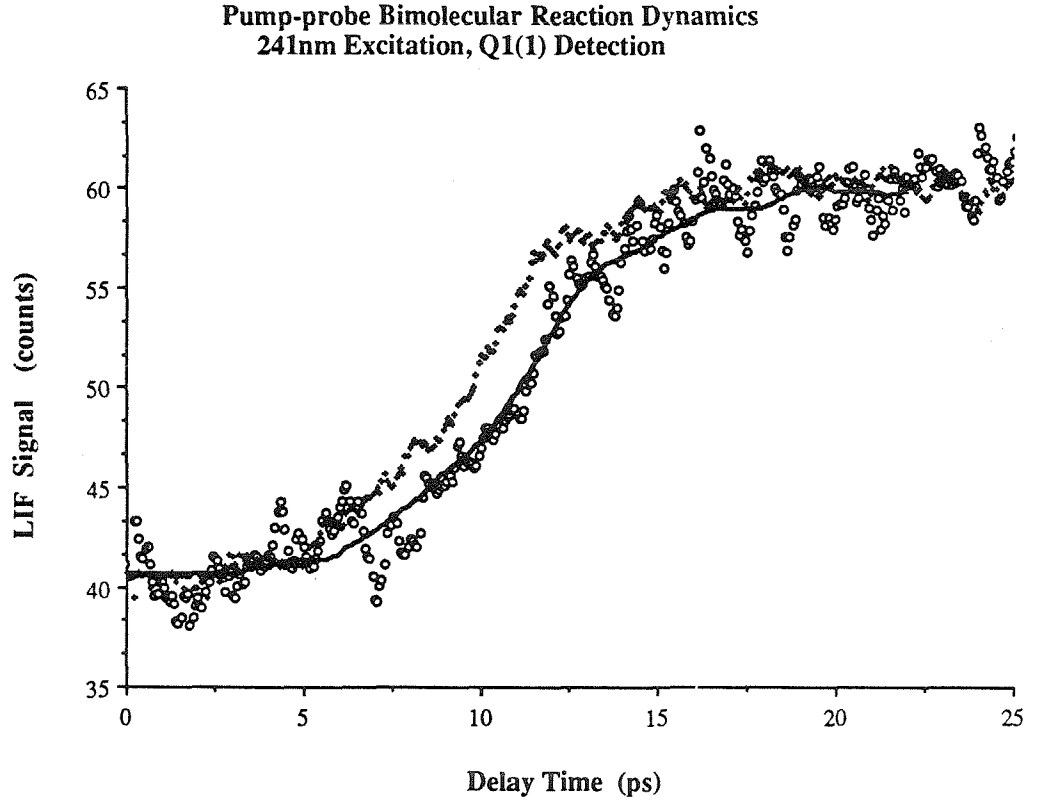

Figures 11a, 11b.

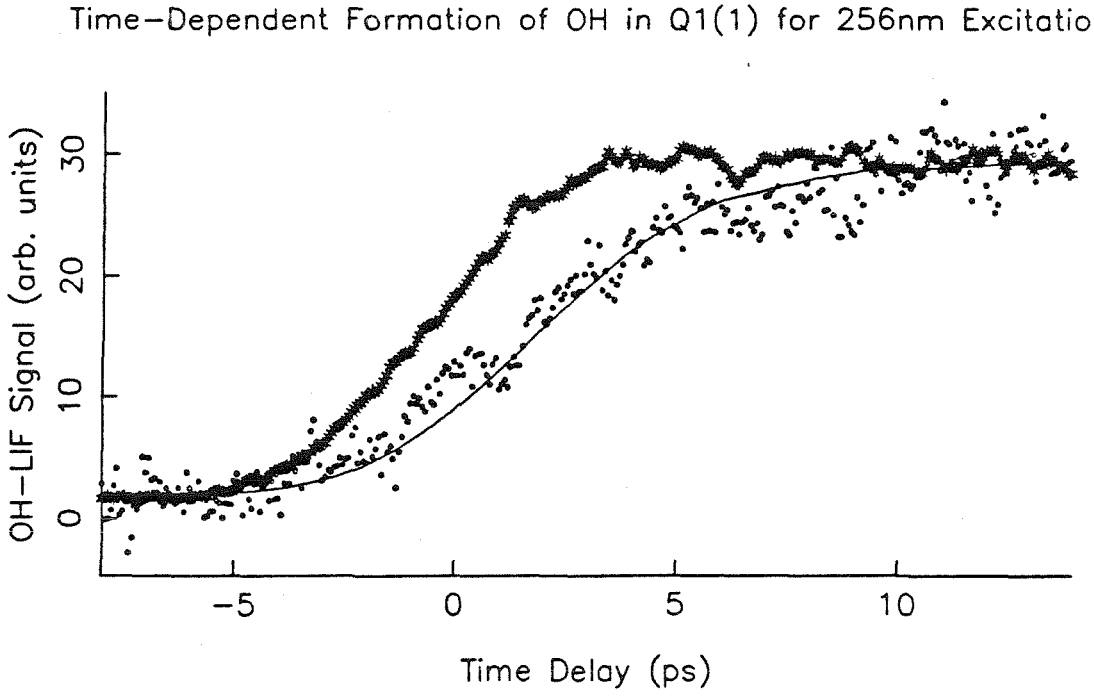

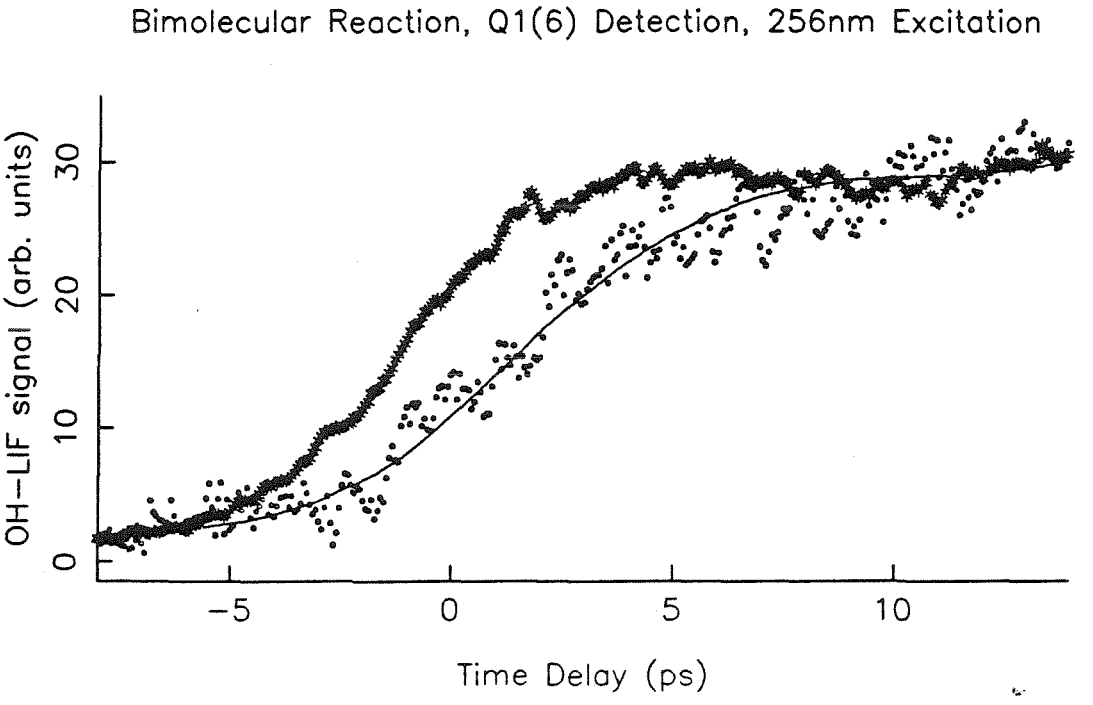

Figures 11c, 11d.

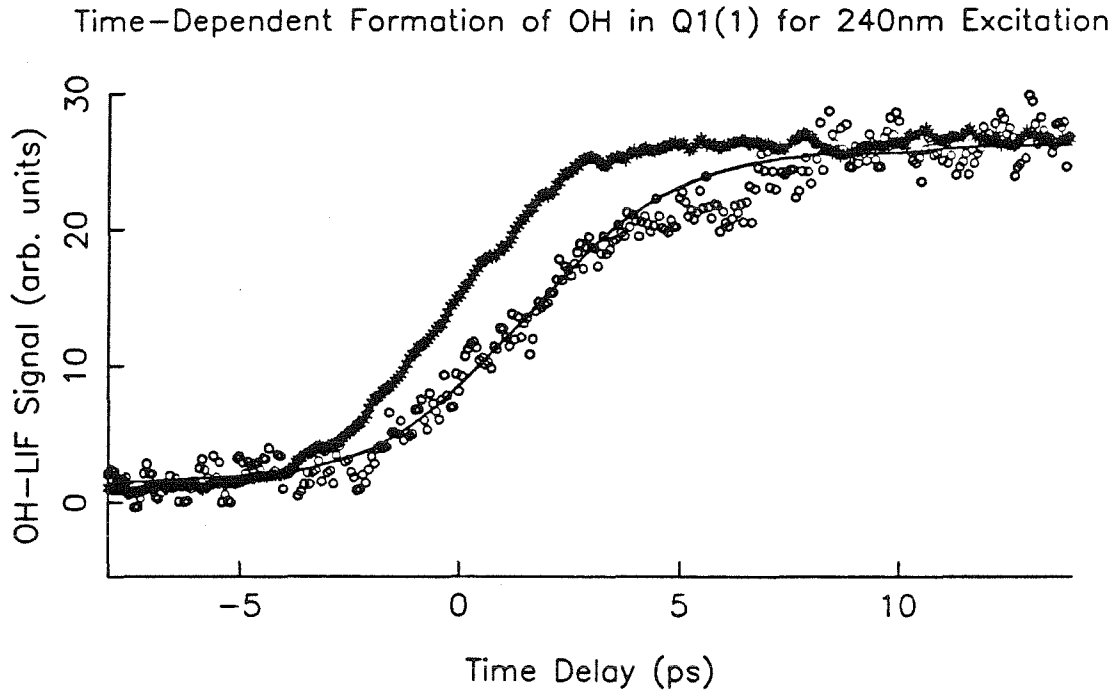

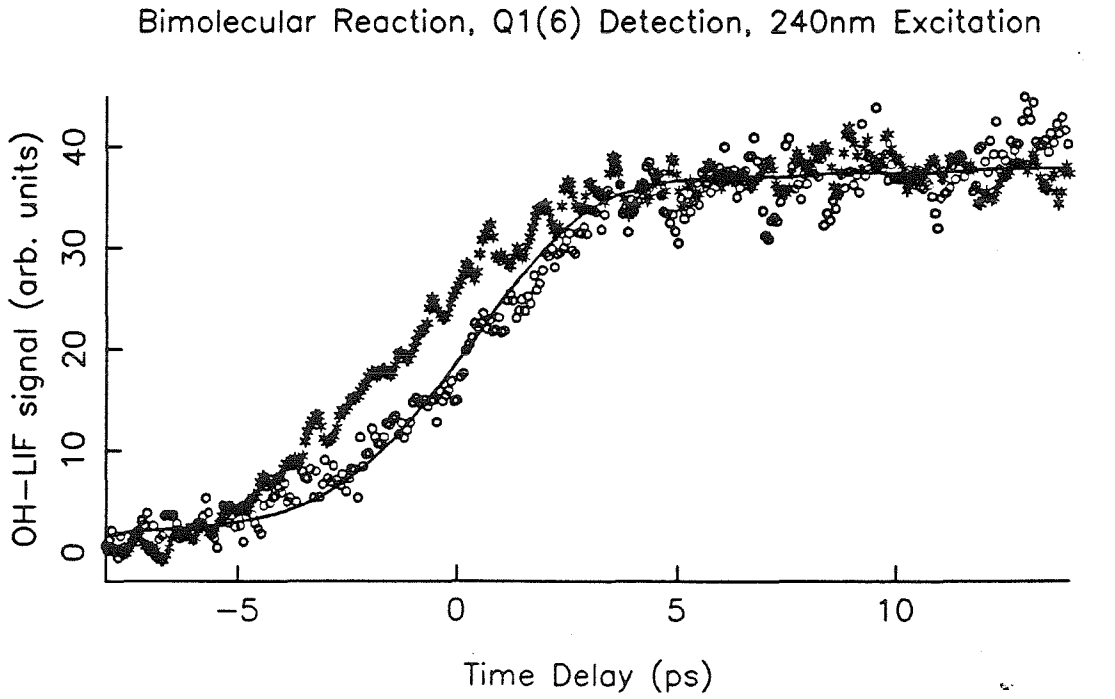

Figures 11e, 11f.

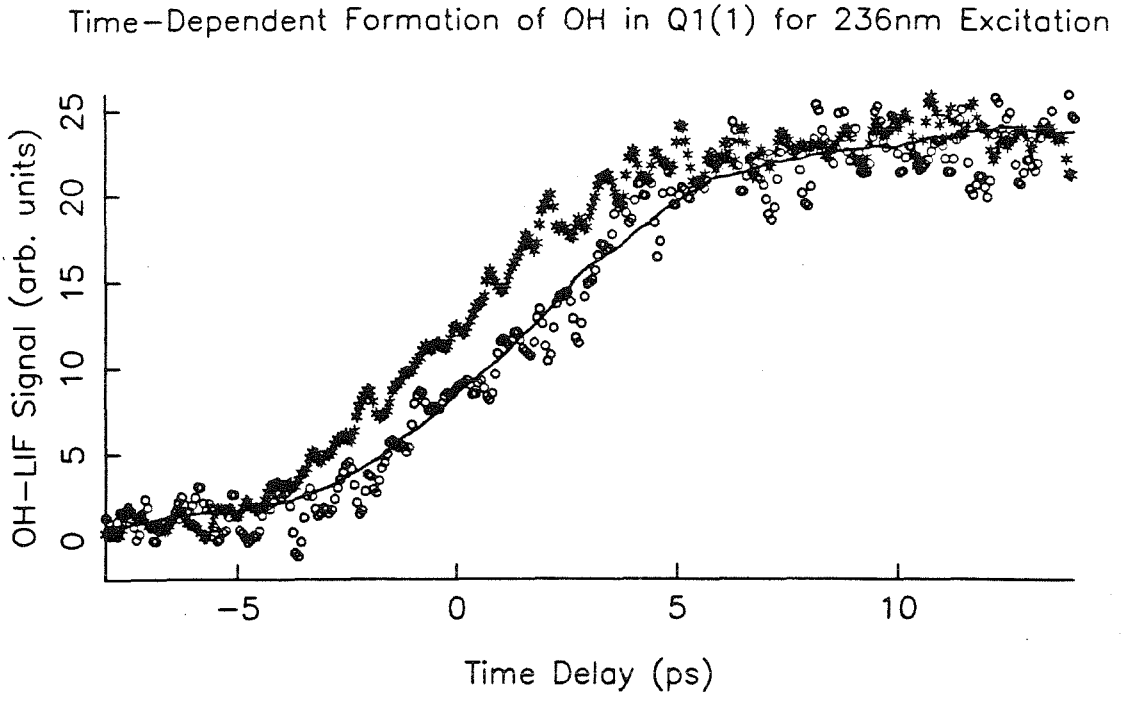

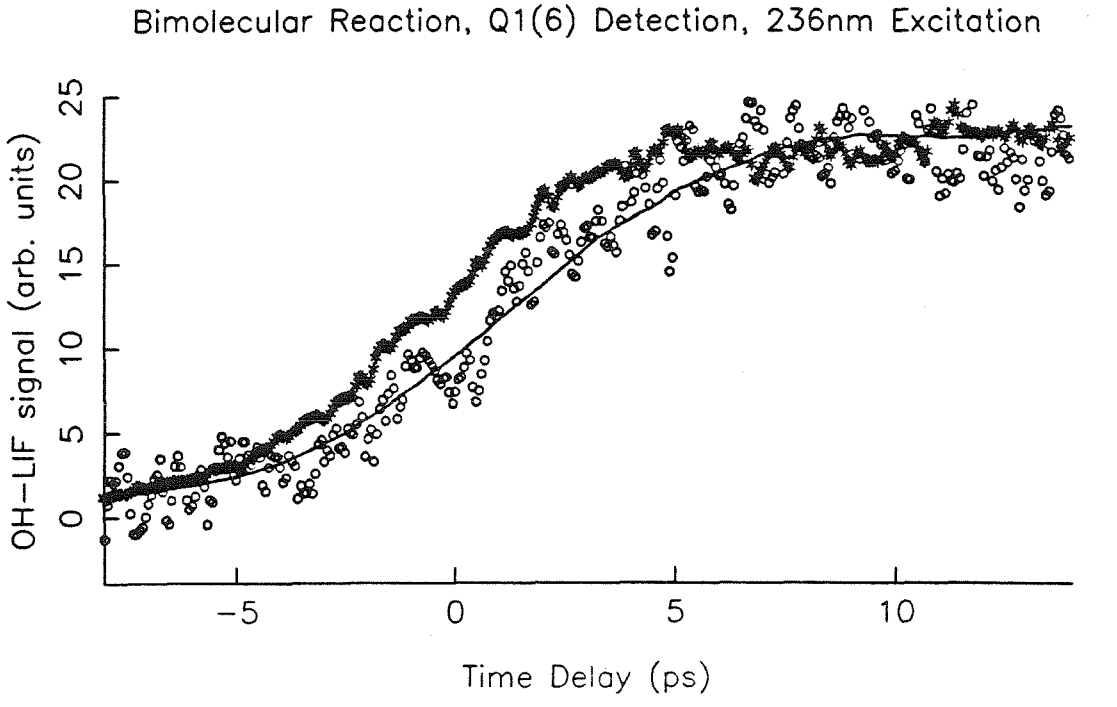

Figures 11g, 11h.

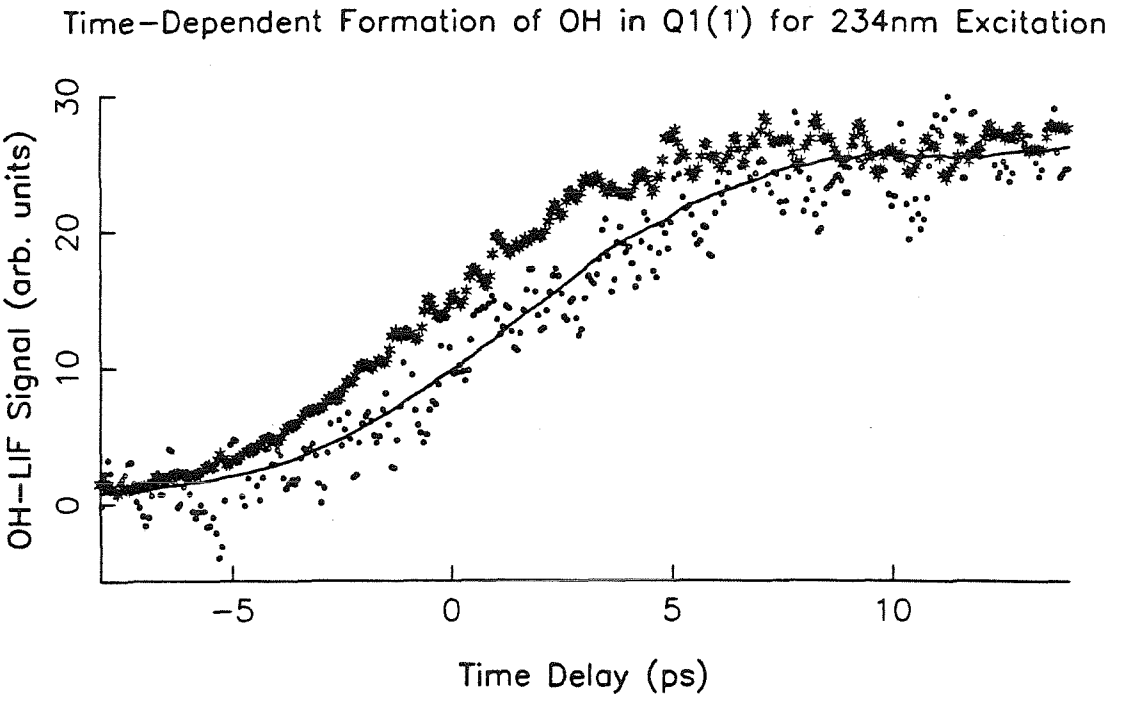

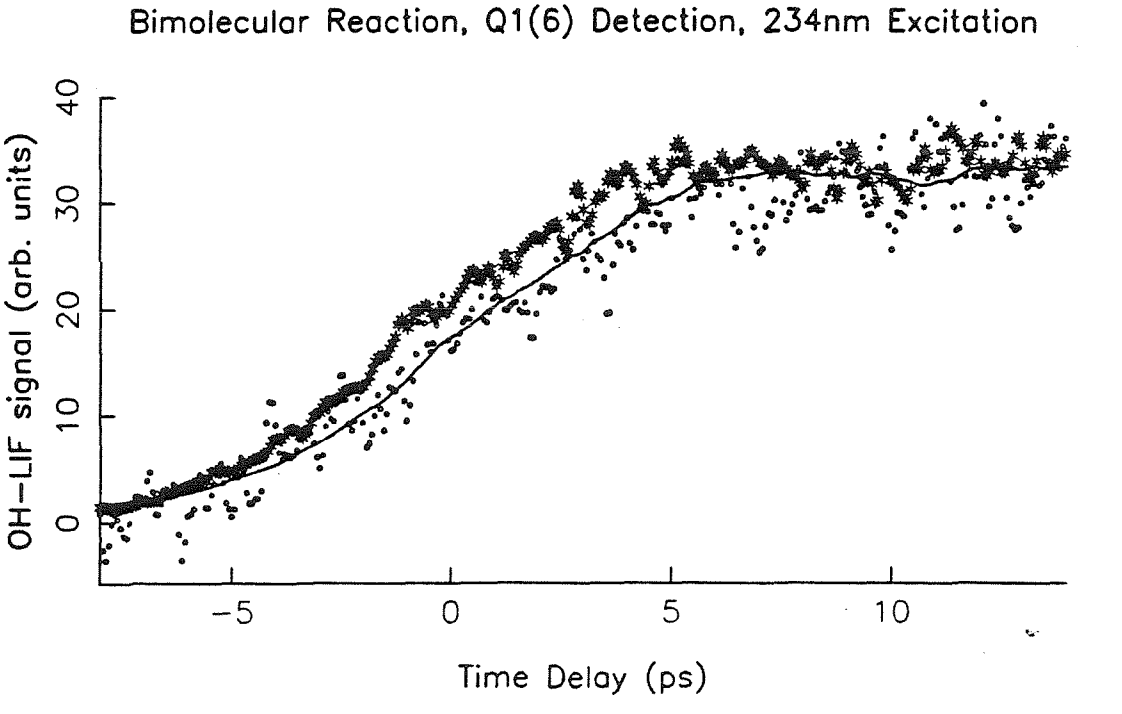

Figures 12a, 12b.

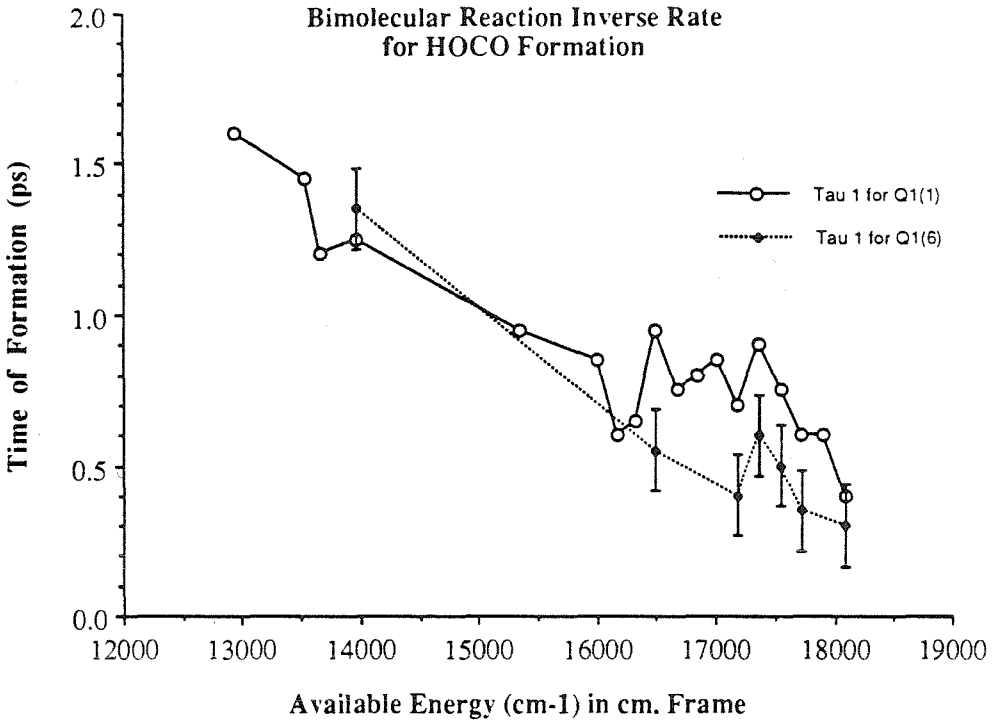

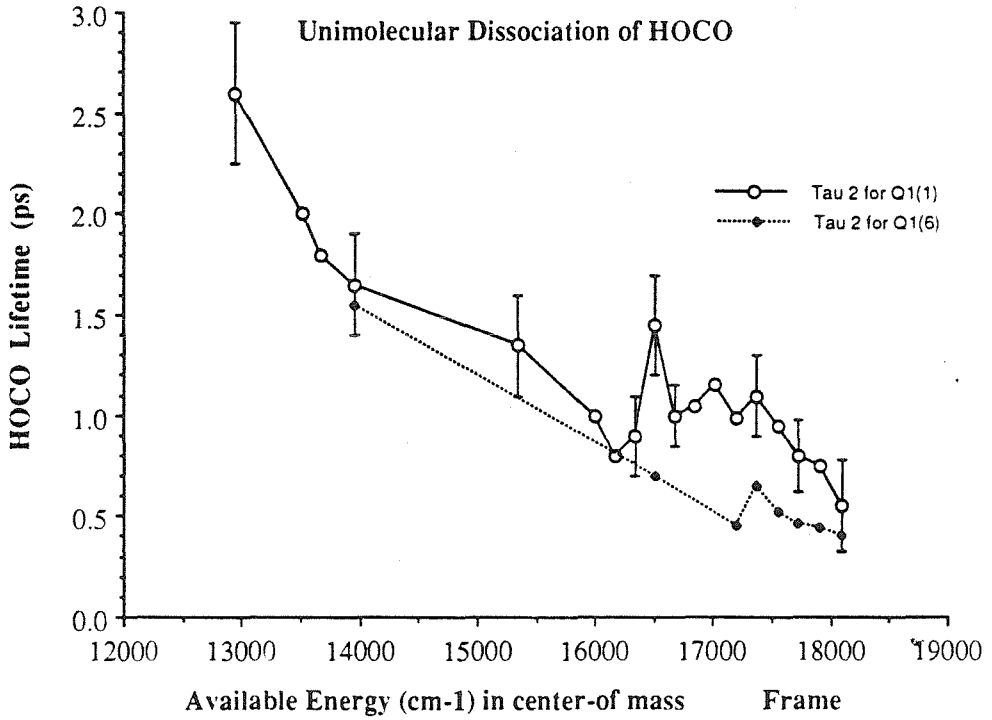

Figures 13a, 13b.

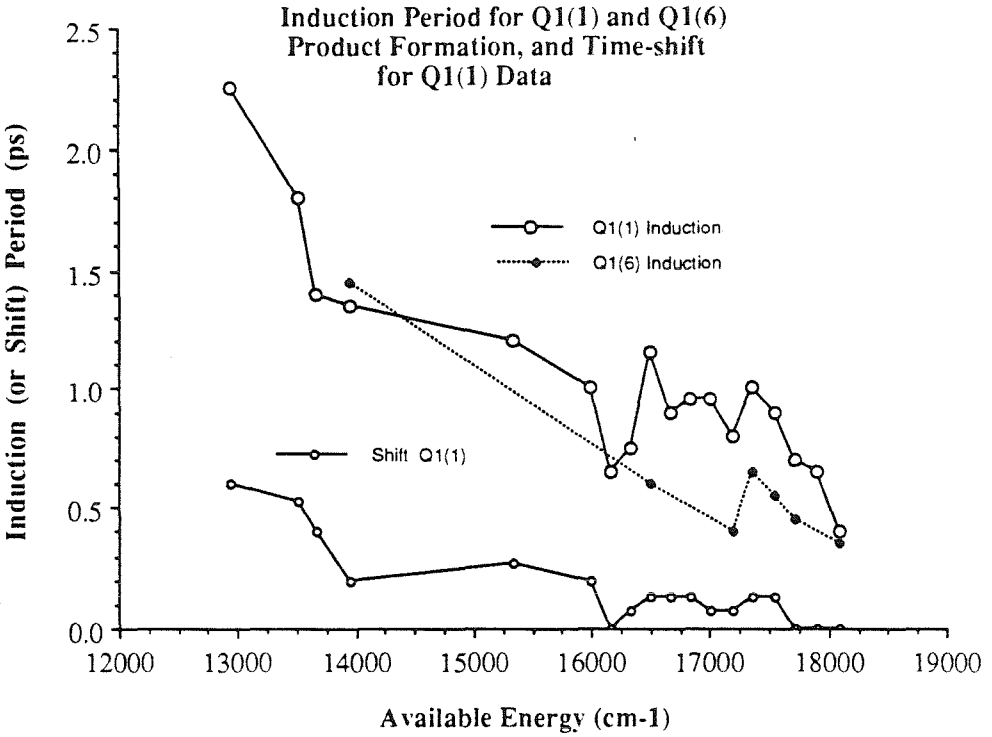

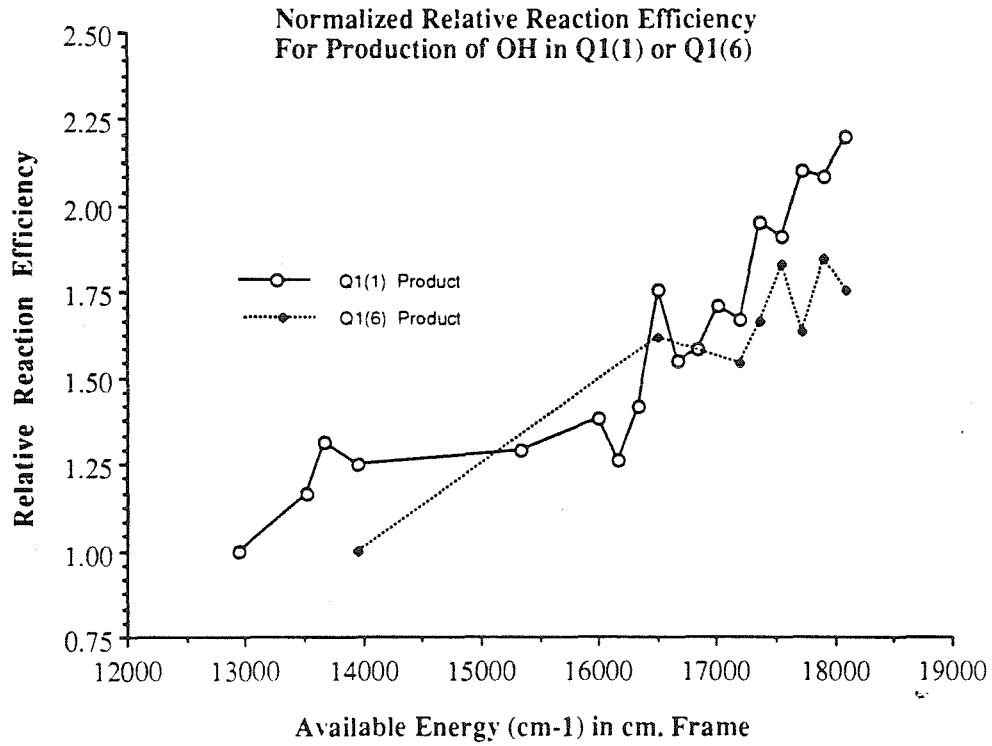

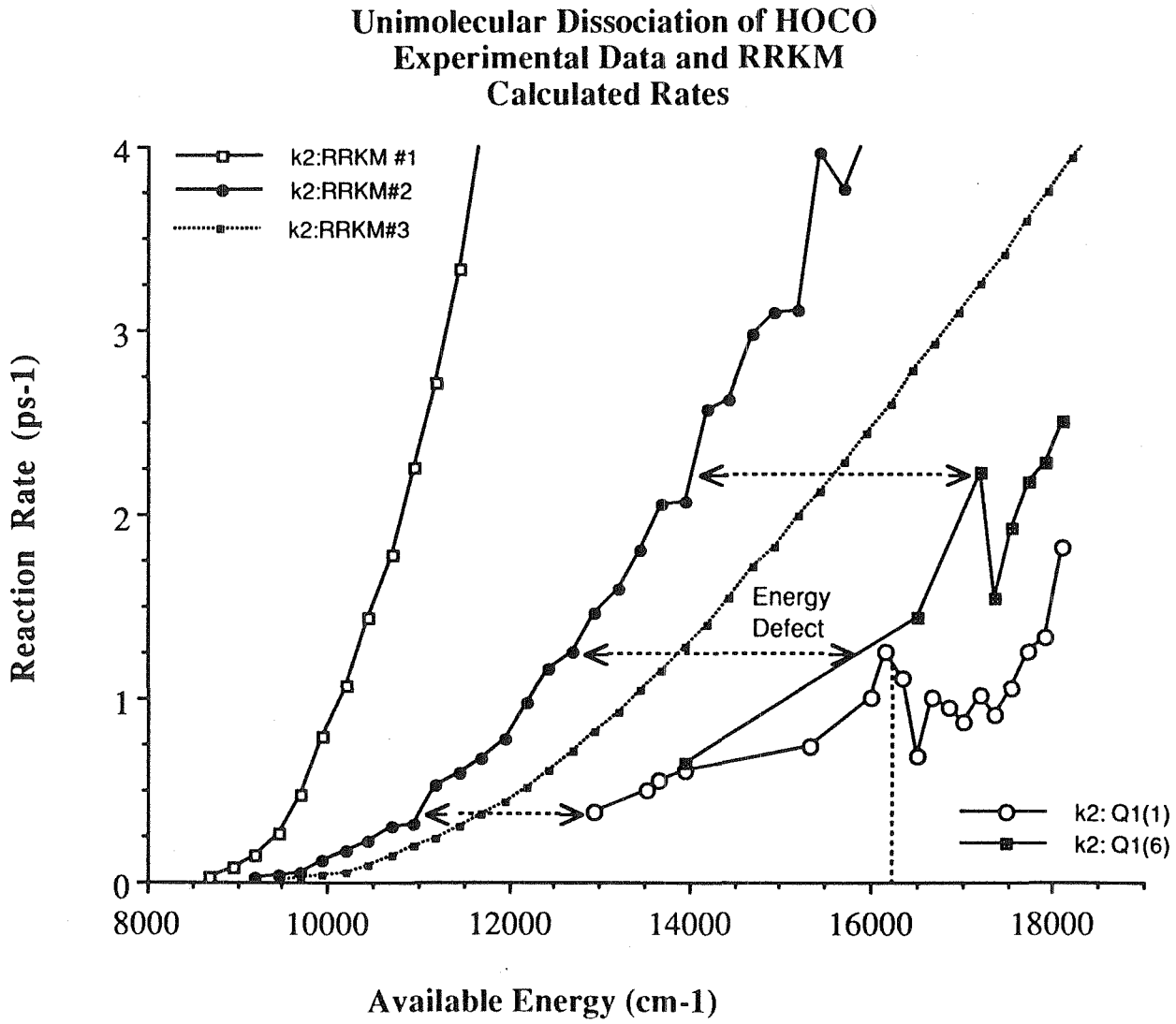
Unimolecular Dissociation of HOCO
Experimental Data and RRKM
Calculated Rates
k2:RRKM #1
k2:RRKM#2
k2:RRKM#3
Energy
Defect
k2: Q1(1)
k2: Q1(6)
Reaction Rate (ps-1)
Available Energy (cm-1)
0
1
2
3
4
8000
10000
12000
14000
16000
18000

Figure 14.

Figures 15a, 15b.

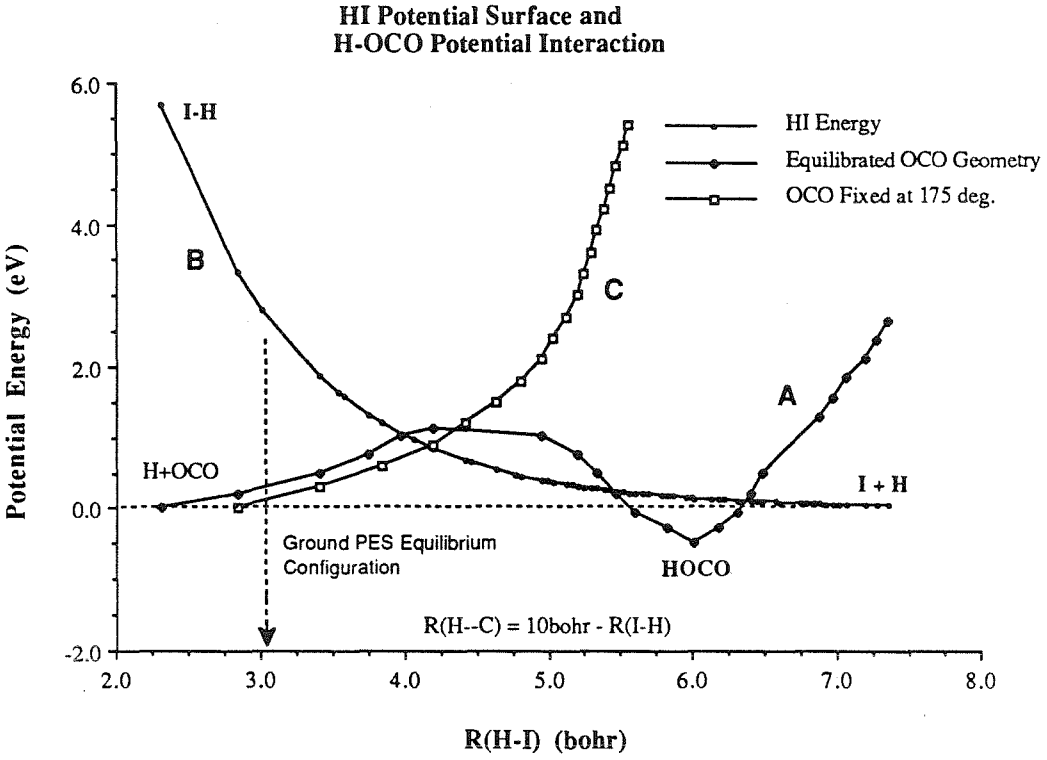

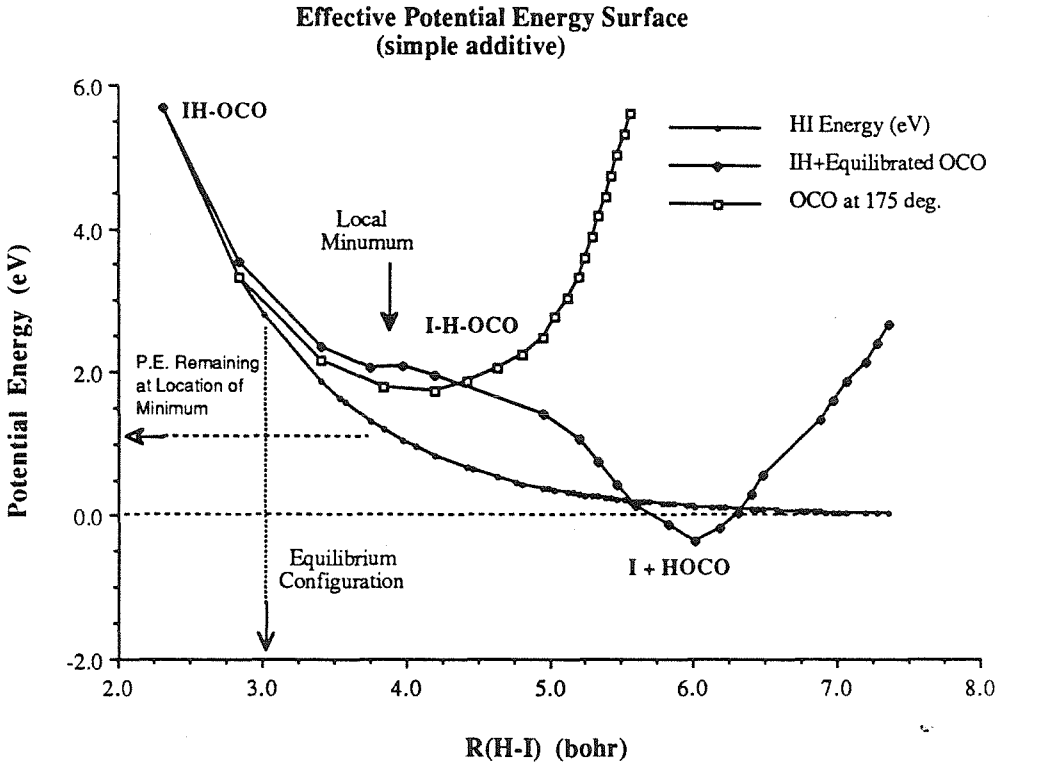

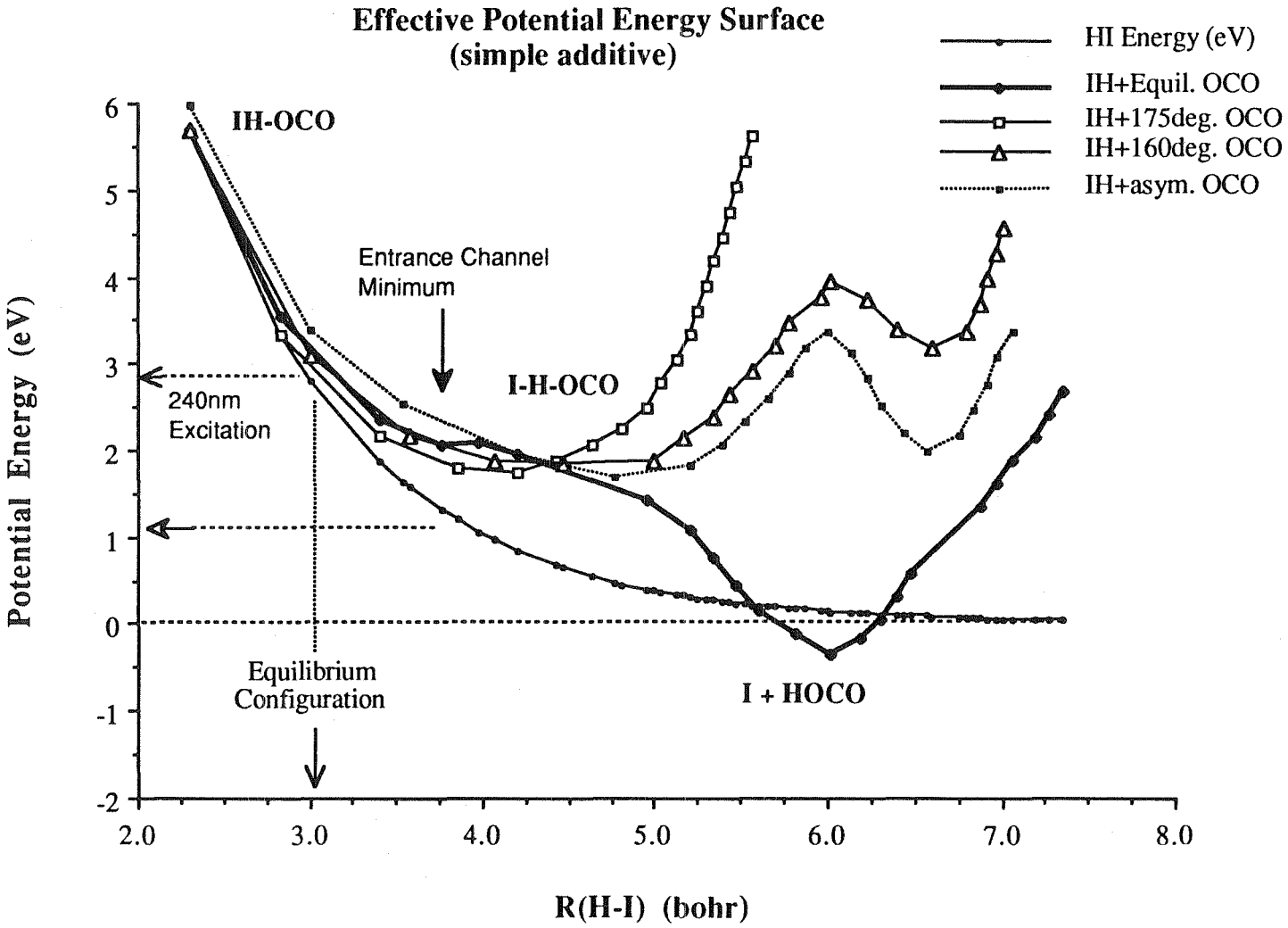
Effective Potential Energy Surface
(simple additive)
HI Energy (eV)
IH+Equil. OCO
IH+175deg. OCO
IH+160deg. OCO
IH+asym. OCO
IH-OCO
Entrance Channel
Minimum
I-H-OCO
240nm
Excitation
Equilibrium
Configuration
I + HOCO
Potential Energy (eV)
R(H-I) (bohr)
6
5
4
3
2
1
0
-1
-2
2.0
3.0
4.0
5.0
6.0
7.0
8.0

Figure 16.

Figures 17a, 17b.

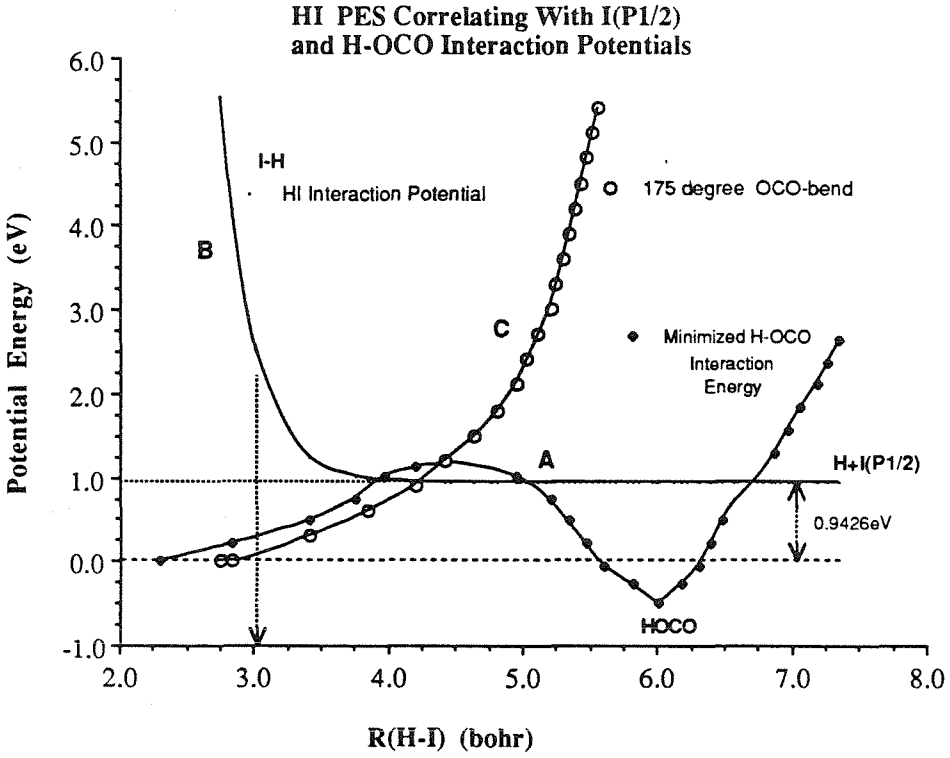

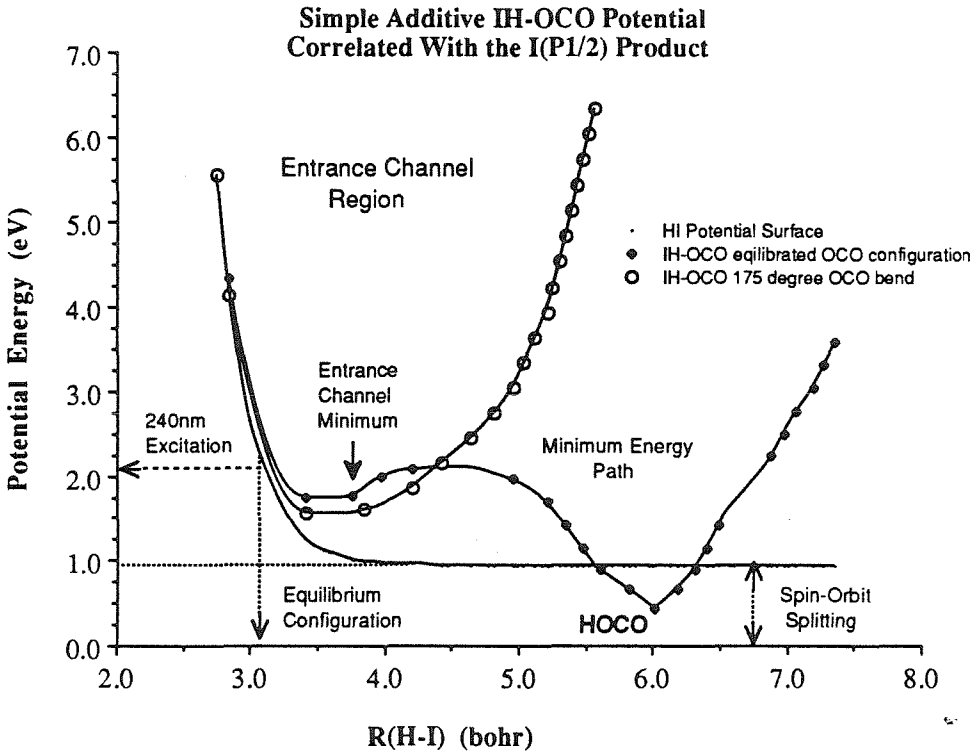

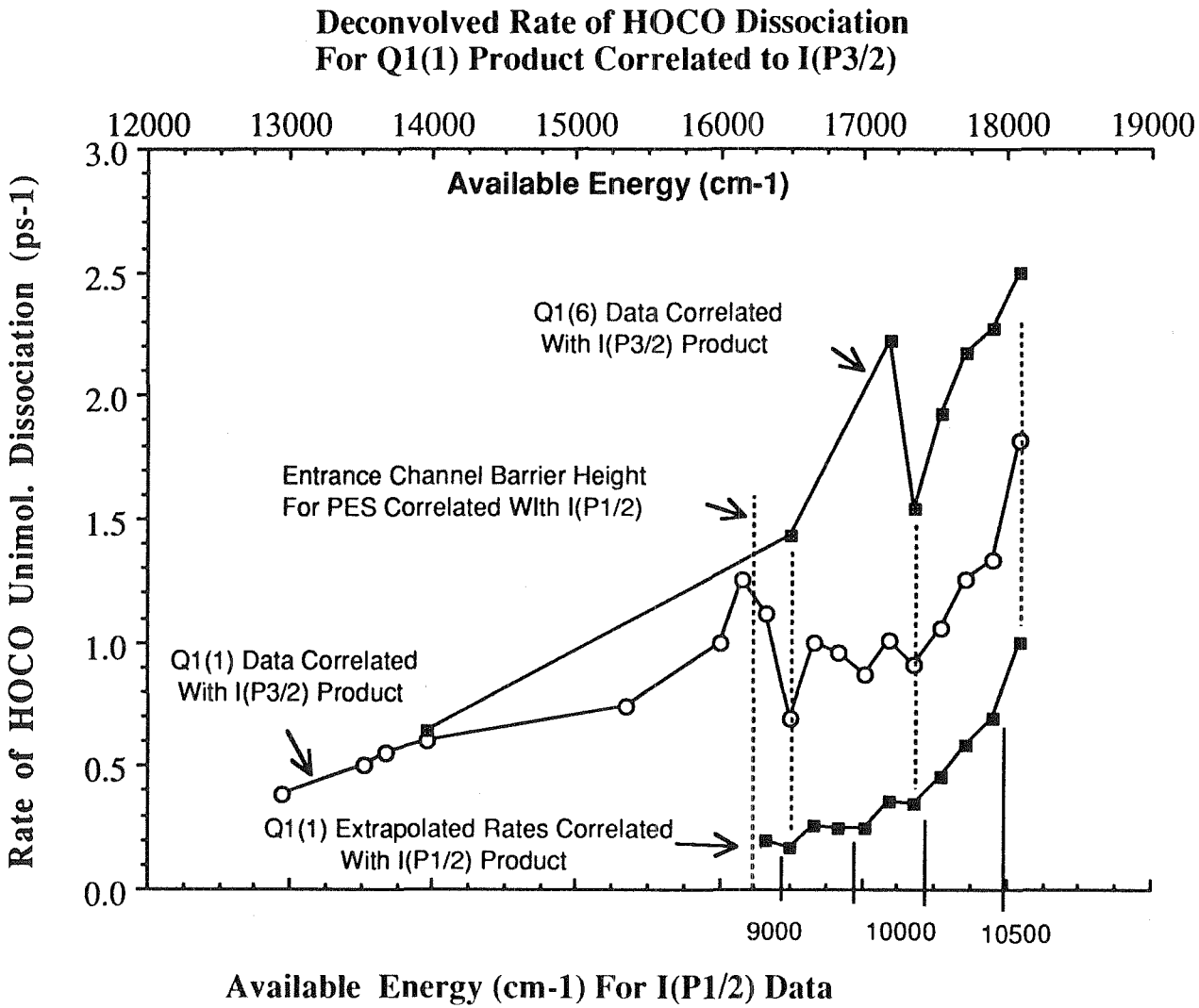
Deconvolved Rate of HOCO Dissociation
For Q1(1) Product Correlated to I(P3/2)
12000
13000
14000
15000
16000
17000
18000
19000
Available Energy (cm-1)
3.0
2.5
2.0
1.5
1.0
0.5
0.0
Rate of HOCO Unimol. Dissociation (ps-1)
Q1(6) Data Correlated
With I(P3/2) Product
Entrance Channel Barrier Height
For PES Correlated WIth I(P1/2)
Q1(1) Data Correlated
With I(P3/2) Product
Q1(1) Extrapolated Rates Correlated
With I(P1/2) Product
9000
10000
10500
Available Energy (cm-1) For I(P1/2) Data

Figure 18.

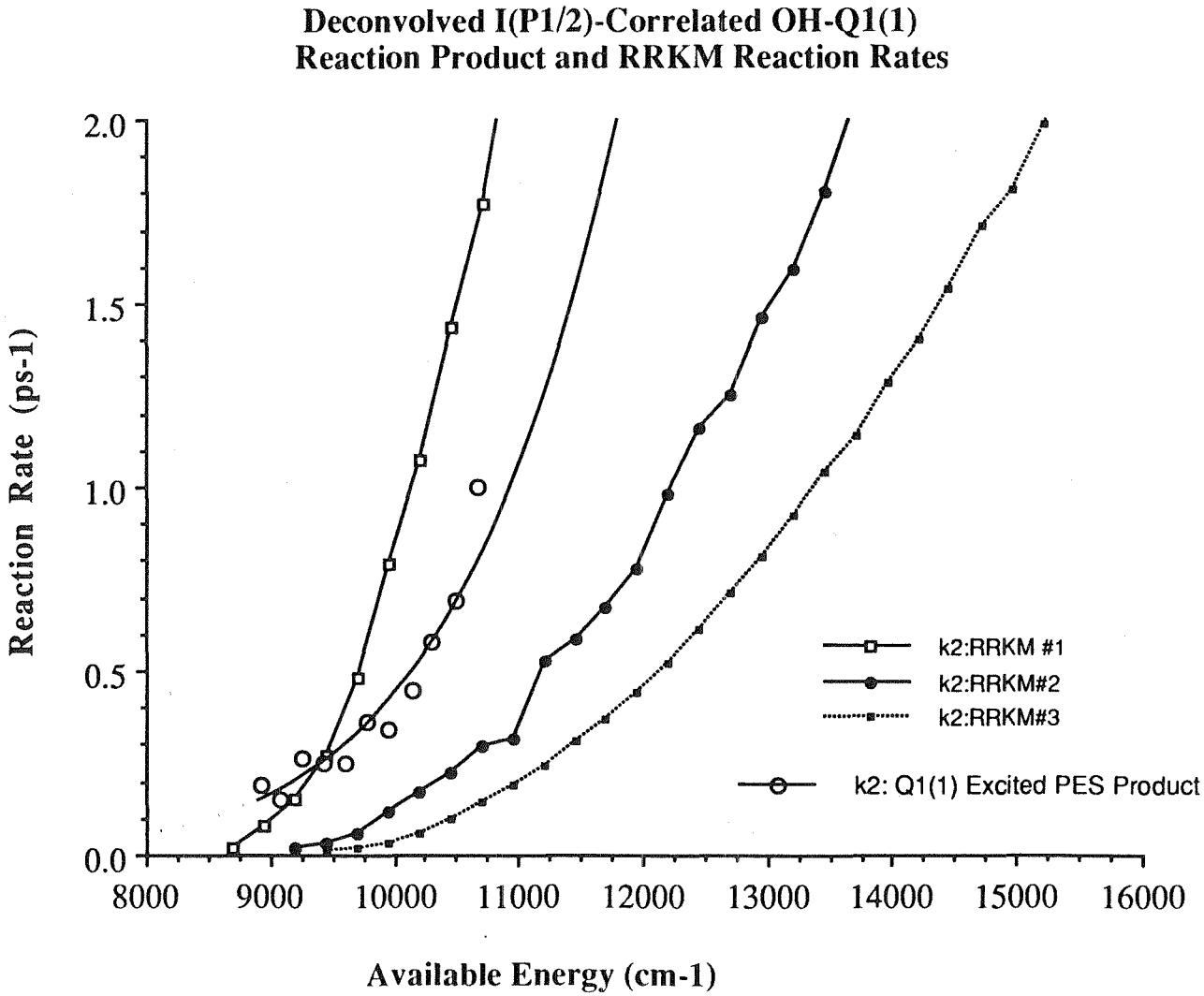
Deconvolved I(P1/2)-Correlated OH-Q1(1)
Reaction Product and RRKM Reaction Rates
Reaction Rate (ps-1)
2.0
1.5
1.0
0.5
0.0
8000
9000
10000
11000
12000
13000
14000
15000
16000
Available Energy (cm-1)
k2:RRKM #1
k2:RRKM#2
k2:RRKM#3
k2: Q1(1) Excited PES Product

Figure 19.

Figures 20a, 20b.

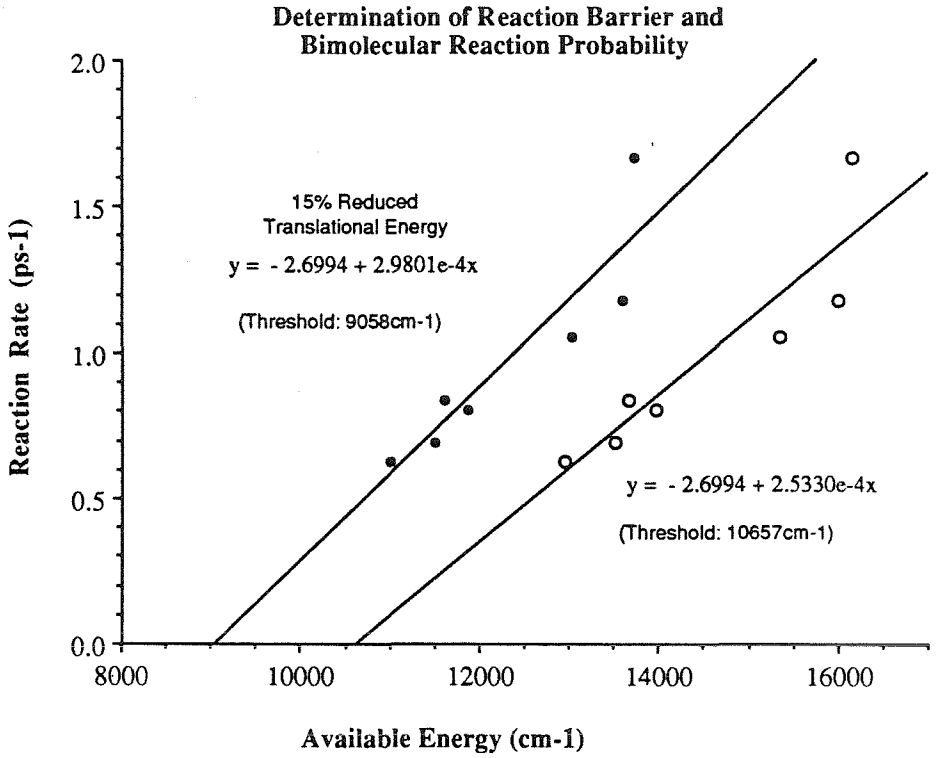

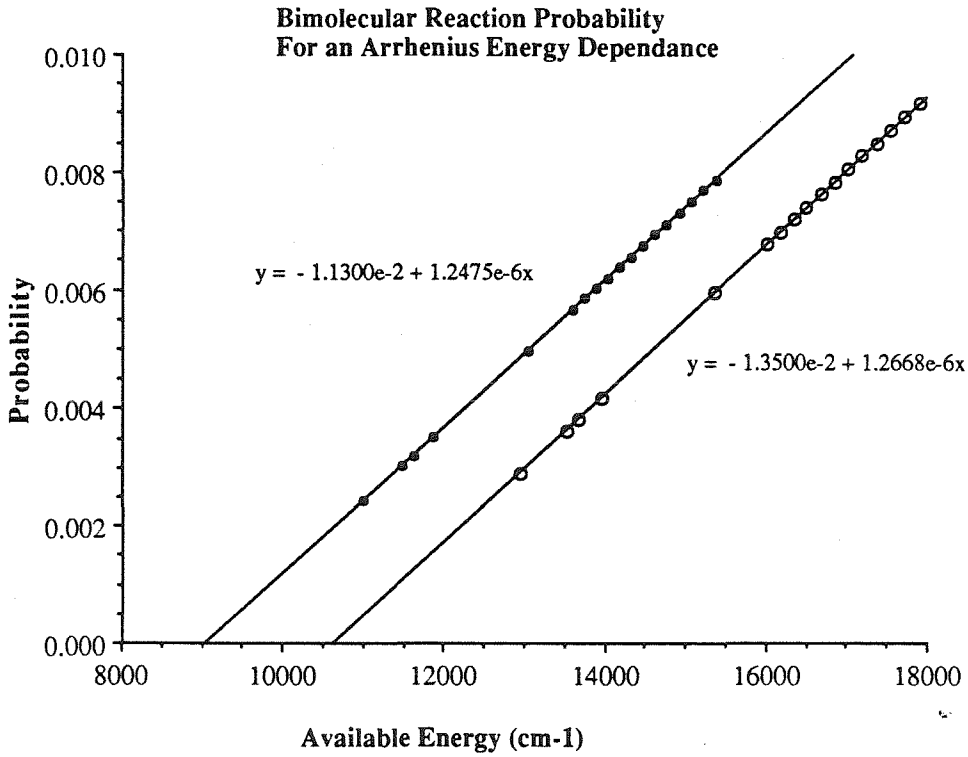

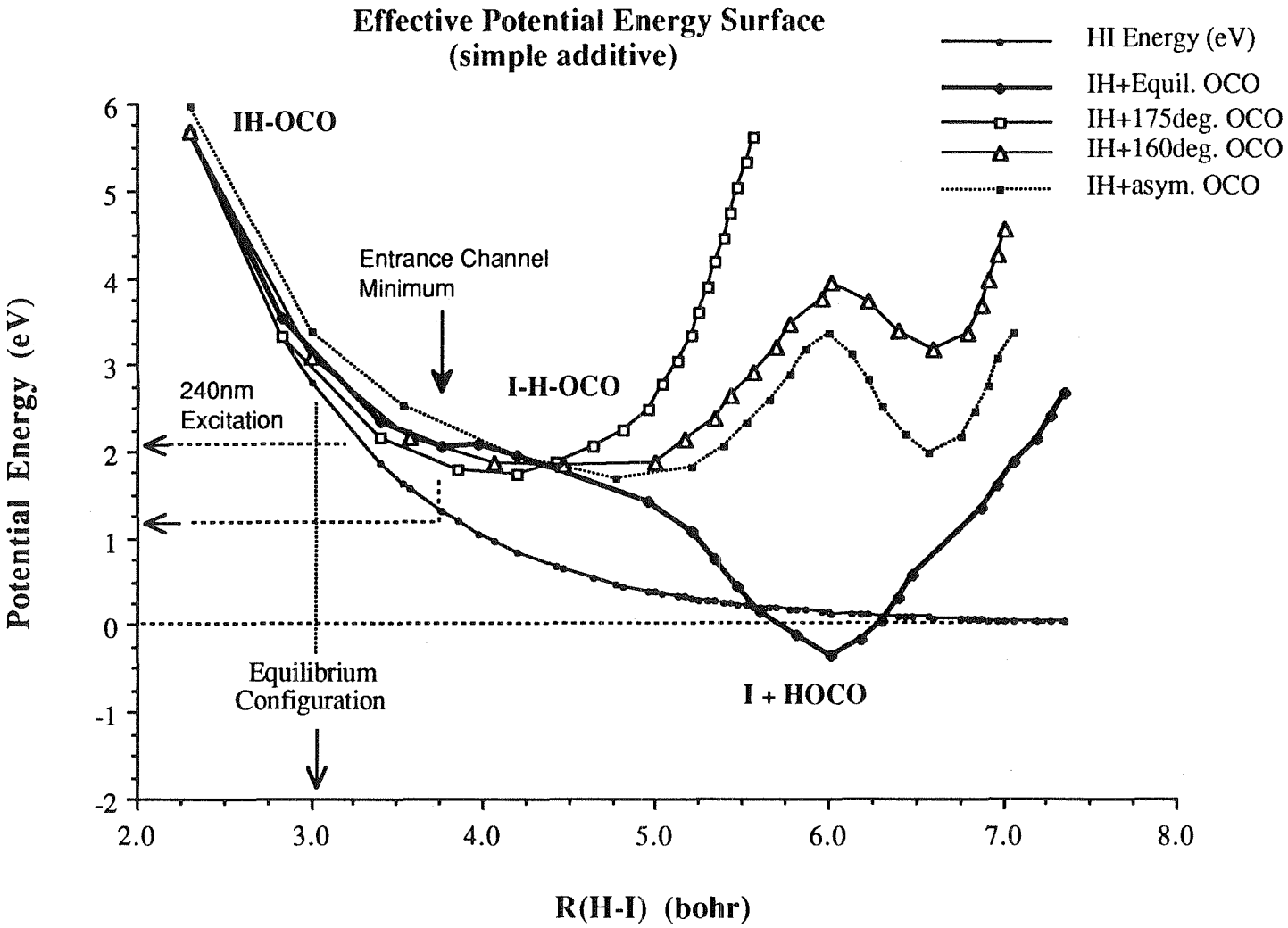
Effective Potential Energy Surface
(simple additive)
HI Energy (eV)
IH+Equil. OCO
IH+175deg. OCO
IH+160deg. OCO
IH+asym. OCO
IH-OCO
Entrance Channel
Minimum
I-H-OCO
240nm
Excitation
Equilibrium
Configuration
I + HOCO
Potential Energy (eV)
R(H-I) (bohr)
6
5
4
3
2
1
0
-1
-2
2.0
3.0
4.0
5.0
6.0
7.0
8.0

Figure 21.

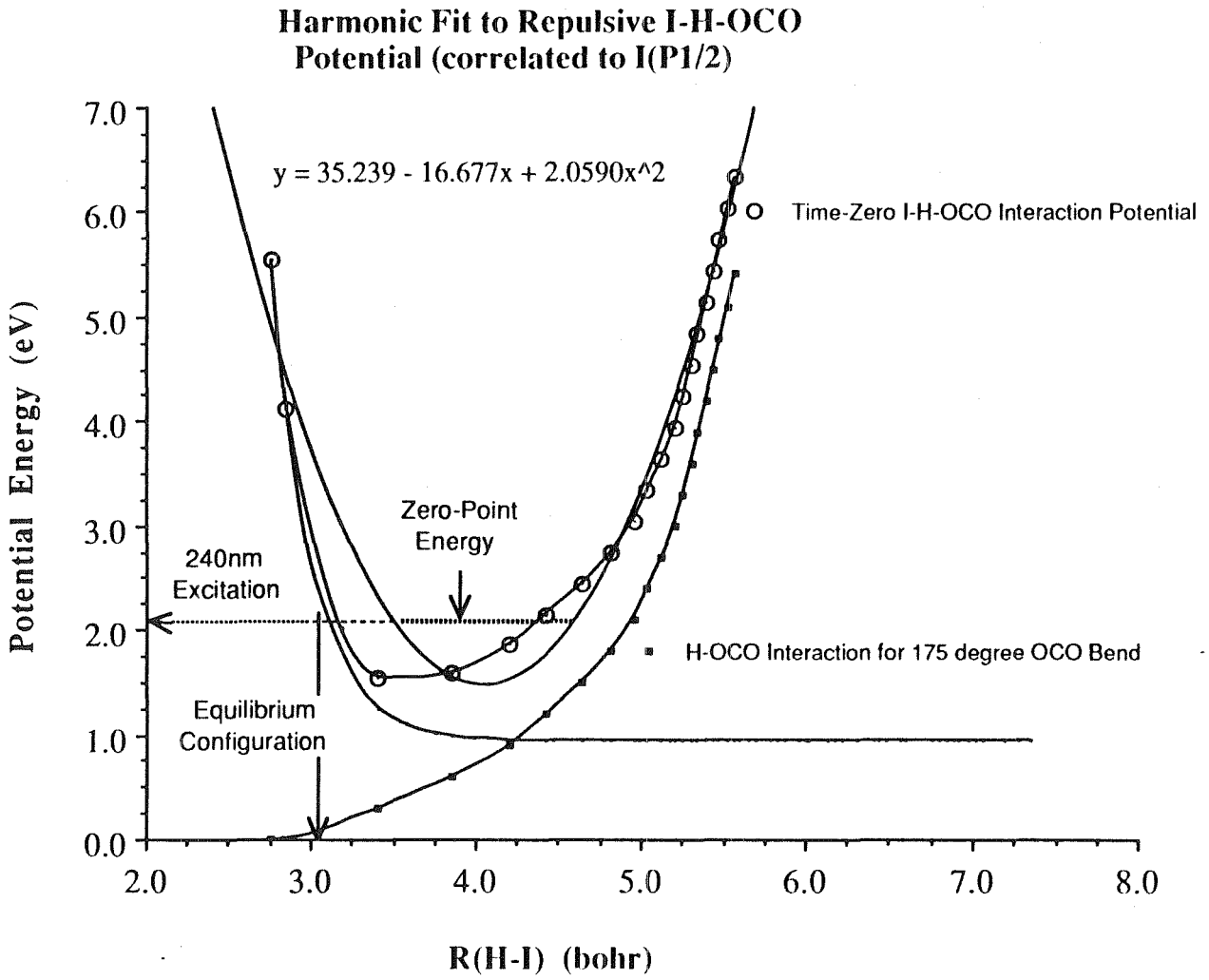
Harmonic Fit to Repulsive I-H-OCO Potential (correlated to I(P1/2)
y = 35.239 - 16.677x + 2.0590x^2
Time-Zero I-H-OCO Interaction Potential
H-OCO Interaction for 175 degree OCO Bend
Zero-Point Energy
240nm Excitation
Equilibrium Configuration
Potential Energy (eV)
R(H-I) (bohr)
7.0
6.0
5.0
4.0
3.0
2.0
1.0
0.0
2.0
3.0
4.0
5.0
6.0
7.0
8.0

Figure 22.

Published in The Journal of Physical Chemistry, **91, 6478 (1987).

APPENDIX A.

Sub-Doppler Measurement of Excited State Rotational Constants and Rotational Coherence by Picosecond Multiphoton Ionization Mass Spectrometry

N. F. Scherer, L. R. Khundkar, T. S. Rose and A. H. Zewail[†]

A. A. Noyes Laboratory of Chemical Physics,[‡]
California Institute of Technology Pasadena, California 91125

[†] John Simon Guggenheim Foundation Fellow

[‡] Contribution Number: 7605

ABTRACT

A method is presented here for one-photon sub-Doppler measurement of excited-state rotational constants and coherence of large polyatomic molecules. The method, which relies on the concept of purely rotational coherence in molecules, utilizes (polarized) picosecond pump-probe multiphoton ionization (MPI) *mass spectrometry. It offers improved temporal resolution (pulse width limited) and is applicable to weakly of non-fluorescing molecules. The present implementation in a molecular beam provides measurements of the rotational constants in the excited* (S_1) *state of trans-stilbene and gives information on the direction of the relevant transition moments involed. From the coherence decay of the initially prepared state we obtain the dephasing time, which we discuss in relation to experiments involving vibrational/rotational energy redistribution.*

A.1 INTRODUCTION

Recent publications[1,2] from this group have reported on the phenomenon of purely rotational coherence and its application to sub-Doppler time-resolved measurements of excited state rotational constants in large isolated molecules. The technique is based on the following realization. A coherent and polarized picosecond pulse can form a coherent superposition of JK levels in a given vibronic manifold, even at finite rotational temperatures. This induced coherence or alignment in the ensemble of molecules decays on the picosecond time scale, but rephases again at a time determined by the rotational constant of the molecule in the excited vibronic state. These recurrences have been observed on the (analyzed) fluorescence of a number of molecules.[1-3] Because the total fluorescence is unmodulated, analyzing the time-resolved fluorescence for polarization *parallel* and *perpendicular* (to the direction of the initial excitation) gives identical recurrences (time period) but with opposite phases.

The important features of this technique are (a) it provides sub-Doppler spectroscopic resolution with one photon excitation; (b) the recurrences (time periods

and shape) give the rotational constants (with high accuracy) and provide information on the the molecular geometry and transition moment direction; and (c) it is particularly valuable when applied to large molecules, since the smaller the rotational constant the larger the time interval between the recurrences. This time-resolved high-resolution feature (recurrences) of the technique should be complimentary to measurements involving high resolution frequency-resolved spectra.[4-6] The time evolution of the initial coherence, on the other hand, is important to questions dealing with rotational-vibrational couplings, as discussed by Nathanson and McClelland,[7] by Hochstrasser and coworkers,[8] and by this group.[1,2,9] This last point will be discussed later.

In the previous time-resolved fluorescence studies of stilbene, stilbene-He, stilbene-Ar, and fluorene,[1-3] the rotational constants were measured to an accuracy as high as one part in 700. For example, for stilbene in S_1, where[2]

$$E/h(J', K') = \frac{1}{2}(B' + C')J'(J' + 1) + [A' - \frac{1}{2}(B' + C')]K'^2$$

the measured B′+C′ is 0.5132±0.0007GHz.[2] For fluorene[3] and fluorene-Ar, the values of B′+C′ are respectively 1060.2±4.3 and 878.7±2.3MHz,[10] which is in excellent agreement with the high-resolution spectral results of Meerts et al.[6] In these experiments, the temporal resolution was typically 40-70ps nd was determined by the response function of the time-correlated single-photon-counting apparatus.[2]

To extend the technique to more general cases (*e.g.*, larger rotational constants), better time resolution is desired. Furthermore, it is advantageous to have the method be applicable to cases where the molecules of interest do not (or weakly) fluoresce. Picosecond pump-probe MPI mass spectrometry[9,11] in a molecular beam is one idea for achieving such optimum, pulse width limited, time resolution. Such an "absorption" method does not depend on detecting the fluorescence emission from the excited state, thus fulfilling the second objective.

In this letter, we report on the observation of purely rotational coherence and sub-Doppler rotational spectra of stilbene in a (skimmed) molecular beam using

picosecond pump-probe MPI mass spectrometry. The time resolution is improved to 3-5ps. The predicted recurrences (coherence) are observed, and the measured rotational constant(s) are in excellent agreement with previous fluorescence results.[1,2]

A.2 THE PICOSECOND PUMP-PROBE METHOD

The scheme of the experimental method is similar to that employed in Refs. 9 and 11 and is illustrated in Figure 1. A coherent, *polarized* ($\widehat{e}_1$) picosecond pulse (duration $\approx$ 5ps) is used as a "pump" to coherently prepare rotational levels of the stilbene molecules in the S_1 state. The treatment of this coherent preparation of states is given in ref 1 and 2. A second *analyzing* ($\widehat{e}_2$) picosecond pulse, delayed in time, probes the initially formed coherence (alignment) by absorption from S_1 to S_4, followed by ionization from S_4. The probe wavelength is adjusted to ensure resonance with the known absorption[12] ($S_4 \leftarrow S_1$) of the molecule in this region. Both the pump and probe pulses are spatially overlapped (after the skimmer) in the molecular beam and the ion signal is mass-selectively monitored as a function of the delay time between the two pulses.

These absorption (and resonant ionization) experiments are conceptually the same as the fluorescence experiments[1,2] (Figure 1; $\widehat{e}_2'$ detection). The possible exception is that the transition moment direction for the probe ($S_1 \leftarrow S_0$ vs. $S^+ \leftarrow S_4 \leftarrow S_1$) could be different, in particular not be parallel. Therefore, comparison of the recurrences in fluorescence and absorption will give information on the symmetry of the intermediate S_4 state. The key point to be made is that both experiments monitor the time-evolution of the prepared state; the time interval between recurrences gives the rotational constant(s) while the shape of the waveform provides information on the direction of the transition moment, the initial temperature, and asymmetry.[1,2] As will be shown below, the observed recurrences in the pump-probe experiments are identical (time spacing and polarization characteristics) to those observed in fluorescence experiments. This illustrates the feasibility of employing pump-probe methods for sub-Doppler measurements of the rotational constants and

rotation coherence of the excited state. It appears that, in this case, the transition moment for fluorescence ($S_1 \rightarrow S_0$) and MPI ($S^+ \leftarrow S_4 \leftarrow S_1$) are similarly parallel.

A.3 EXPERIMENTAL SECTION

The picosecond pulse generation/amplification scheme and molecular beam apparatus have been fully described in other publications.[13] Therefore, only a brief description will follow. The output of a mode-locked Nd:YAG laser is frequency doubled giving a train of 532nm pulses, each of which is <80ps in duration and about 10nJ in energy. This beam is split and used to synchronously pump two dye lasers, DL1 and DL2. The tuning element of DL1 is a two-plate birefringent filter (BRF) while that in DL2 is a three-plate BRF. The two resultant pulse trains (DL1, 4ps; DL2, 6-7ps pulse duration) are each amplified in two three-stage dye amplifiers. The dye amplifiers are pumped by a Q-switched Nd:YAG laser. The independent dye lasers and amplifiers facilitate independent wavelength tunability.

The output beams from the two dye amplifiers enter the arms of a scanning delay line interferometer. The beam corresponding to DL1 passes through a fixed delay and a calcite polarizer and arrives at the dichroic beam combiner. The amplified pulses of DL2 enter the variable delay line which is set up in a double-pass configuration to allow for longer scans ($\leq$2.5ns). The beam is reflected by a visible reflecting/UV transmitting dichroic mirror, passes through a KDP crystal (frequency doubler), 7-54 visible absorbing filter, a corner-cube mounted on a stepper-motor-actuated translator and is (retro-)reflected by a normal incidence mirror. This last optic causes the now second harmonic beam to propagate back through all of the above mentioned optics and be transmitted by the dichroic mirror. The polarization of this UV beam can be rotated by a 1/2 wave plate and analyzed with a Glan-Taylor calcite polarizer. The intensity is adjusted by attenuating the beam with quartz neutral-density filters. The UV pump and visible probe beams are recombined with an appropriate dichroic beam combiner such that they propagate in a collinear fashion through the molecular beam apparatus. A fused silica lens

(f=50cm) is used to focus both laser beams and adjust the location of the beam waists relative to the molecular beam axis.

Stilbene was puchased from Pfaltz & Bauer, >97%. The sample is heated in the pulsed valve of the skimmed molecular beam apparatus to 124°C, mixed with the He carrier gas (80 psi) and is expanded through a 0.5mm diameter orifice. The beam is skimmed 3cm downstream, while the laser intersects the molecular beam approximately 12cm from the nozzle. The ions are analyzed with a time-of-flight (TOF) mass spectrometer. The ion current is amplified and signal averaged in a boxcar integrator/averager with the gate set for the parent ion mass (m/e=180). The lens position is adjusted to minimize the saturation due to the pump field alone. The pump and probe beam intensities are also adjusted to maximize the enhancement (by the probe) and to eliminate signals from other fragment species. Enhancement ratios of better than 20:1 are readily obtained for pump and probe per pulse energies of <1 and 250μJ, respectively.

A.4 RESULTS AND DISCUSSION

A.4.1 Rotational Constants and Rotational Coherence.

Figure 2a shows the ion signal plotted as a function of time for parallel pump and probe $\hat{e}$-field polarizations. The excitation populates the vibrationless level of the first excited singlet state (32234 cm^{-1}).[14] The notable features are the sharp spike on the rising edge, a negative and positive recurrence. (The analysis is performed on the raw data since (Gaussian) smoothing would diminish the sharpness of the observed features and affect the interpretation.) The overall decay (Figure 2a) of the signal may also be fitted to a single exponential of 2.4±0.4ns, which is in agreement with the stilbene S_1 lifetime of 2.7ns.[14] The three (sharp) features are clearly resolved. The system response function of the present experiments is significantly shorter ($\leq$ 10 ps) than that of fluorescence experiments ($\simeq$ 40-70 ps)

and allows for more precise measurements of the rotational constants and coherence decay parameters.

To obtain the excited state rotational constants the time intervals of the recurrences must be determined. The interval from t=0 to the negative recurrence and from the negative to the positive recurrence for the experimental results are 960 ± 15 and 965 ± 10ps, respectively. This spacing compares well with the value reported in ref. 2 and may also be obtained from a full transient simulation to be 974 ± 10ps. Numerical simulations[2] previously applied to fluorescence studies may be used to determine the rotational temperature of stilbene in the molecular beam and the asymmetry parameter, as shown in Figure 2b. The simulation is performed for excitation of a parallel-type transition and emission for a parallel-type transition. This is represented by $(\|, \|)$. Parallel laser $\hat{e}$-field and fluorescence analyzer polarizations are denoted by $\hat{e}_2' \parallel \hat{e}_1$. The $\hat{e}_2 \parallel \hat{e}_1$ configuration for pump-probe is equivalent to $\hat{e}_2' \parallel \hat{e}_1$ for pump-fluorescence detection. A 2.7ns state lifetime is included in the simulation, as is a convolution of the 10.5ps (experimental) system response function. Comparison of Figure 2b to the experimental result shows a strong similarity in the aforementioned initial decay and recurrence (spacing = 974 ± 2ps) behavior.

The calculation is performed with the values for the ro-tational constants (A′=2.68GHz, B′=0.273GHz, C′=0.240GHz) determined in ref. 2. The rotational energy levels in S_0, S_1 (and implicitly, for comparison with experiment, in S_4) are described by the standard expression for near-symmetric top molecules. The molecular temperature is the other parameter to be varied. A temperature of 2K gives the best agreement between simulated and experimental results.

The results of a $\hat{e}_2 \perp \hat{e}_1$ experiment (not shown) exhibit a single exponential decay ($\tau = 2.4 \pm 0.3$ps) and recurrences. These (two) sharp features are analogous to the partial recurrences in the $\hat{e}_2 \parallel \hat{e}_1$ case except that the phase (positive/negative) is *opposite* and the amplitude is reduced. This is understood in that for an isotropically detected distribution of rotors, $I_{54.7^0} = I_{\|} + 2I_{\perp}$, which gives an unmodulated population decay signal.

The decay of the anisotropy of the ensemble of rotors prepared by laser excitation to the S_1 state is most prominently seen in a plot of the (rotational) anisotropy

$$r(t) = \frac{I_{\|}(t) - I_{\perp}(t)}{I_{\|}(t) + 2I_{\perp}(t)}.$$

This *r(t)* can be constructed from measurements of $I_{\|}(t)$ *and* $I_{\perp}(t)$, individually convoluted with the system response function. The experimental plot of the rotational anisotropy for the long time scan is shown in Figure 3a. (The signal prior to t=0 fluctuates severely and has been removed from Figure 3a for visual clarity.) The figure shows the case ($\|, \|$), and $I_{\|}$ corresponding to $\hat{e}_2 \parallel \hat{e}_1$. The corresponding rotational anisotropy plot for the simulated results for the ($\|, \|$) case are presented in Figure 3b, (T=2°K). There is good agreement between the experimental and simulated results. For more details, the reader is referred to the full treatment of *r(t)* in ref. 1 and 2.

A.4.2 Temporal Resolution of the Initial Decay and Recurrences.

Changing the delay-time scan conditions to higher resolution allows for more detailed study of the three specific features of Figure 2a and 3a. Such focused scans facilitate better S/N for each of the recurrence features. Figure 4a shows a "magnified" view of the recurrence which occurs at approximately 2-ns. The phase (positive/negative) of the recurrence changes with the relative polarization between the pump and probe. This phenomenon has been observed in fluorescence experiments[1,2] for parallel and perpendicular relative polarizations of the laser and the analyzer. The magnitude of the recurrence shown for the parallel configuration is twice as large as that for the perpendicular orientation. Part b of this figure also displays the *r(t)* plot of the results of part a. (Notice that several of the small oscillatory features nearest the main recurrence feature are also observed in the individual parallel and perpendicular transients.) The narrow feature superimposed on the *r(t)* results of Figure 4b is the 10.5-ps, Gaussian system response function.

A time-enhancement of the same positive recurrence obtained from simulation (including convolution of the response function) is presented in Figure 4c. The additional small oscillations near the recurrence are strongly influenced by the temperature and rotational constant parameters. These small-amplitude features, as well as the decreased amplitude of the recurrence (0.19 vs. 0.4), reflect the asymmetry of the stilbene molecule in the S_1 electronic state. The departure from a symmetric top molecule gives rise to incommensurate frequency components in the molecular rotation. Thus, the molecule may be viewed as exhibiting irregular motion, and the resulting temporal width can be used to obtain information on the asymmetry parameter.

In previous work,[2,9] and initial decay (dephasing) of coherence was reported for stilbene in a molecular beam. Here, we povide better temporal resolution and a more detailed experimental analysis of this initial dephasig. The results are presented in Figure 5a. The system response function for this experimental *r(t)* decay is 7ps, Gaussian. The experimental results, which are represented in this figure, were obtaied by using a slightly different dye laser arrangement than exployed in the other portions of this paper.[15] A simulation is presented in Figure 5b. The wings of the simulation response function were truncated at 1% of the maximum value.

The results of a numerical comparison of the width of the initial decay feature with the subsequent recurrence features for both experimental and simulated *r(t)* transient features are presented in Table I. For simplicity, the initial feature and subsequent recurrences were taken to be single and double-sided Gaussians, respectively. This facilitates the deconvolution with the known response function. The widths of the features increase proceeding to later time. For consistency in comparing experimental and numerical results,the same procedure of deconvolution and determination of the width is applied to both. Note that in the case for symmetric tops twice the dephasing width equals the width of the first positive recurrence. The additional width in the subsequent recurrences of the asymmetric top illustrates the

contribution of incommensurate Fourier components of the beat envelope and the corresponding partial spatial realignment of the transition moments.

A.4.3 Resonant Probe State and Transition Moment Direction.

The selectivity for the observed rotational coherence effects stems from the S_4 intermediate state. This conclusion is derived from the results of previous work[9] and from an intuitive assumption that probe excitation high into the ionization continuum may reduce such selectivity. Probing directly (one UV photon) to the *threshold* of the ion may yield sufficient selectivity for both the rotational and vibrational coherence behavior in S_1. There is reason to believe that the transition moment for the ion$\leftarrow S_1$ excitation is somewhat different from that of $S^+ \leftarrow S_4 \leftarrow S_1$. This is concluded on the basis of experiments involving probing via. a $S^+ \leftarrow S_1$ transition.[17] The good agreement between the experimental and theoretical results presented here implies that the transition moment for $S^+ \leftarrow S_4 \leftarrow S_1$ is quite well approximated as being parallel to the $S_1 \leftarrow S_0$ transition moment.

Since the S_4 electronic state has not been ro-vibrationally analyzed in free-jet expansions, it is not clear whether overlapping rovibrational states are being probed. This condition was tested by changing the probe wavelength by greater than $\pm$5nm, independent of the pump. The tuning of the probe did not change the resultant transients. This may be a result of the essentially featureless nature of the absorption which may imply a quasi-continuous distribution of (vib-)rotational states. The data presented herein were obtained for a probe wavelength of 594nm, which is near the center of the $S_4 \leftarrow S_1$ absorption band.[12] Of course the electronic transition moment is characteristic of the entire vibrational/rotational envelope.

The pump and probe bandwidths could have an effect on the amplitude and width of the experimentally observed initial decay and recurrences. The finite spectral bandwidth of the excitation places an upper limit on the frequency components which contribute to the signal. Since the excitation pulse is nearly transform limited, and the bandwidth is larger than that used in the fluorescence experiments, more detailed features are observed, i.e. higher frequency Fourier components are

added. Furthermore, changing of the probe laser bandwidth, which is analogous to changing the slit width on the monochromator in fluorescence, will affect the number of oscillatory terms adding to $I_{\|}(t)$ or $I_{\perp}(t)$, and the amplitude of recurrences. The bandwidth issue was investigated by using various tuning elements in the two dye lasers. For example, the combination of a two-plate BRF in DL1 and a three-plate BRF in DL2 yields a probe bandwidth which is approximately equal to the pump laser bandwidth (and also gives a good system response function). If three-plate BRF filters are used in both lasers, the amplitude of the recurrences is diminished.

A.4.4 Purely Rotational Coherence and IVR Measurements.

In the dissipative IVR regime[14] one observes a quasi-biexponential decay, the first component of which is due to intramolecular dephasing on the picosecond time scale. Interprettion of such decays requires the separation of the effect of rottional coherence from that of vibrational coherence.

In stilbene, a quasi biexponential decay has been observed in picosecond fluorescence[14] and MPI[9] experiments. The fluorescence experiments (e.g., upon excitation of the molecule to $E_{vib} = 1249\ cm^{-1}$), showed that, depending on detection polarization, the fast lifetime and the fast-to-slow intensity ratio of the decays take on different values.[2] The recurrences associated with rotational coherence were also observed.[2] In the MPI experiments, a strong polariztion dependence of the initial fast components was observed and interpreted as being cused by a form of vibrationa/rotational coupling in the isolated molecule.[9] The initial dephasing[2] associated with rotational coherence issimply give by $\tau_d^{-1} = \alpha\ kT \cdot [(B+C)/2]^{\frac{1}{2}}$ where α is a constant and T is the temperature. At the rotational temperature of interest (2K), $\tau_d \sim 17ps$.[2] This contribution of purely rotational coherence to the overall decay is, therefore, pronounced at early time. It is reasonable to conclude that the transients observed in our earlier MPI experiments[9] reflect both the rotational coherence and the possible loss of coherence due to vibrational/rotational interactions.

The data on purely rotationl coherence reported here agrees with the earlier (polarized) pump-probe photoionization experiments[9,18] on beam-cooled stilbene. It is also consistent with the bulb fluorescence experiments[8] which showed the existence of polarization-dependent transients on a similar time scale (<10ps). Other more recent measurements[8] deduced a somewhat longer rotational relaxation time (48ps for silbene in a bulb, but as shown later[8] this number corresponds to population decay and not to rotational coherence. Clearly, IVR and purely rotational coherence are both important elements to be taken into consideration for interpretation of the dynamics[19] of excited polyatomic molecules.

A.5 CONCLUSIONS

The reported experimental observation of purely rotational coherence by use of (polarized picosecond pump-probe MPI mass spectrometry shows that it is possible to make one-photon sub-Doppler measurements of the rotational constants of large molecules in their excited states. For molecular beam of *trans*-stilbene, we have determined the rotational recurrences to be 963 $\pm$ 10ps, and the rotational constants in the first excited state to be A′=2.68GHz, B′=0.273GHz, and C′=0.240GHz.[20] The recurrences give B′ + C′ directly, and the individual rotational constants are determined from simulation of the observed waveform of the transients, as prescribed by Baskin et al.[2,3]

Dephasing times have also been measured and related to the rotational coherence of the excited levels. The relationship of this coherence decay to the rotational temperature and the direction of transition moments are discussed. The relevance of rotational anisotroy ot IVR measurements is also addressed.

The sensitivity of the pump-probe method is discussed in relation to fluorescence detection methods.[1,2] The improved time resolution of pump-probe method (limited only by the pulse width of the laser) should now make the technique more general and applicable to sub-Doppler measurements of non-fluorescing molecules. Future directions are to include (i) the use of threshold probing to the ionization

oevel for zero Stark fields, which may yield sensitivity analogous to that of resonance fluorescence detection; (ii) use of the same techniques for the detection of vibrational coherence, as done in the fluorescence methods;[19] (iii) use of the high temporal resolution to fully resolve the initial decay of the coherence (dephasing), especially at high internal molecular energies. This will provide the information necessary to seperate the effect of vibrational/rotational coupling on intramolecular dephasing from the contribution due to purely rotational coherence, a point which must now be taken into consideration in analyzing the dephasing of isolated molecules.[2,7-9]

Acknowledgement. We thank Mr. Spencer Baskin and Dr. Peter Felker for enlightening discussions. The computer simulations done here benefited from these discussions and from the work presented in ref. 1 and 2. This work was supported by a grant from the National Science Foundation (DMR-8521191).

Registry No. *trans*-Stilbene, 103-30-0.

REFERENCES

1. P.M. Felker, J.S. Baskin and A.H. Zewail, J. Phys. Chem. **90**, 724, (1986); J.S. Baskin, P.M. Felker, and A.H. Zewail, J. Chem. Phys., **84**, 4708, (1986); J. S. Baskin, D. Semmes and A. H. Zewail, J. Chem. Phys., **85**, 7488 (1986).

2. P.M. Felker and A.H. Zewail, J. Chem. Phys., **86**, 2460 (1987); J.S. Baskin, P.M. Felker and A.H. Zewail, J. Chem. Phys., **86**, 2483, (1987).

3. J. S. Baskin, and A. H. Zewail, to be published.

4. E. Reidle, H. J. Neusser and E. W. Schlag, J. Phys. Chem., **86**, 4847 (1982); ibid. J. Chem. Phys., **80**, 4686 (1984).

5. B. J. van der Meer, H. Th. Jonkman, J. Kommandeur, J. Laser Chem., **2**, 77 (1983); B. J. van der Meer, H. Th. Jonkman, J. Kommandeur, W. L. Meerts and W. A. Majewski, Chem. Phys. Lett., **92**, 565 (1982).

6. W. L. Meerts, W. A. Majewski and W. M. Herpen, Can. J. Phys., **62**, 1293 (1984).

7. G.M. Nathanson and G.M. McClelland, J. Chem. Phys., **81**, 629, (1984); ibid. **84**, 3170, (1986).

8. D. K. Negus, D. S. Green and R. M. Hochstrasser, Chem. Phys. Lett., **117**, 409 (1985); A.B. Meyers, P.L. Holt, M.A. Pereira and R.M. Hochstrasser, Chem. Phys. Lett., **130**, 265, (1986); A.B. Meyers and R.M. Hochstrasser, J. Chem. Phys., **85**, 6301, (1986).

9. N.F. Scherer, J.F. Shepanski and A.H. Zewail, J. Chem. Phys, **81**, 2181, (1984); J.W. Perry, N.F. Scherer and A.H. Zewail, Chem. Phys. Lett., **103**, 1, (1983); N.F. Scherer, J.W. Perry, F.E. Doany and A.H. Zewail, J. Phys. Chem., **89**, 894, (1985).

10. The relation $\tau_r^{-1} = B' + C'$ is exact only for a symmetric top. It has been found that the asymmetries of fluorene and fluorene-Ar are sufficiently large to cause deviations from this simple relation. A more detailed analysis is underway to determine the correction ot τ_r^{-1} required to obtain improved values of $B' + C'$.

11. J.L. Knee, F.E. Doany and A.H. Zewail, J. Chem. Phys., **82**, 1042, (1985); L.R. Khundkar and A.H. Zewail, J. Chem. Phys. **82**, 4715, (1985).

12. B.I. Greene, R.M. Hochstrasser and R.B. Weisman, Chem. Phys., **48**, 289, (1980)

13. N.F. Scherer and A.H. Zewail, J. Chem. Phys., **87**, 97, (1987); J. L. Knee, L.R. Khundkar and A.H. Zewail, van der Waals. J. Chem. Phys., **87**, 115, (1987).

14. J.A. Syage, Wm.R. Lambert, P.M. Felker, A.H. Zewail and R.M. Hochstrasser, Chem. Phys. Lett., **88**, 266, (1982);J.A. Syage, P.M. Felker, A.H. Zewail J. Chem. Phys., **81**, 4685 (1984); ibid. **81**, 4706 (1984); B.W. Keelan and A.H. Zewail, J. Phys. Chem. **89**, 4939, (1985); P.M. Felker, Wm.R. Lambert, A.H. Zewail, J. Chem. Phys., **82**, 3003 (1985).

15. The probe laser (DL1) was hybrid mode-locked using a single dye jet.[16] A saturable absorber jet was used in the associated dye amplifier. In both cases the saturable absorber dye DQOCI was employed. The resultant 2.5-ps pulse from DL1 was transform limited, having a bandwidth of about 4 cm^{-1}. The cross-correlation between the dye lasers was 7ps in width and Gaussian in shape.

16. G.A. Mourou and T.Sitzer II, Optics Comm., **41**, 47 (1982).

17. N.F. Scherer and A.H. Zewail, unpublished results. In a preliminary UV pump - UV probe experiment the t=0 feature appears for orthogonally polarized pump-probe $\hat{e}$-fields. The parallel polarization transient does show less evidence for such a spike. More careful UV/UV experiments are needed before a definite statement can be made.

18. The anisotropy reported in ref 9 for 0,0 excitation was reduced in value when compred with the present result. This is probably due to a lower S/N ratio and larger response time in the early experiments. It should be noted that the coherent signal only ~15% of the total (Figure 2a) and much more careful determination of t=0 is needed for poorer S/N experiments.

19. Wm. R. Lambert, P. M. Felker and A. H. Zewail, J. Chem. Phys., **75**, 5958 (1981); P. M. Felker and A. H. Zewail, J. Chem. Phys., **82**, 2961 (1985); P. M. Felker and A. H. Zewail, J. Chem. Phys., **82**, 2975 (1985); P. M. Felker and A. H. Zewail, J. Chem. Phys., **82**, 2994 (1985); Wm. R. Lambert, P. M. Felker and A. H. Zewail, J. Chem. Phys., **82**, 3003 (1985).

20. As noted in Ref. 2, these rotational constants are preliminary values. Further refinements of these values are forthcoming.[3]

TABLE I.

Values for the Widths of the Dephasing and Recurrence Features(Picoseconds)

Type of Result	Near t=0	Negative Recurrence	Positive Recurrence
experimental	19	50, gaussian	70
simuln (asym)	17[a]	54	77
simuln (sym top)	17[a]	34	34
response func	7	10.5	10.5

[a] Determined by considering only the decay for a δ-function response, and is not the actual width displayed in the figure.

FIGURE CAPTIONS

1. Schematic of the picosecond pump-probe MPI rotational coherence experiment. The pump pulse creates a superposition of rotational states in S_1. The probe pulse, in analogy with fluorescence detection (dashed lines), promotes the system from S_1 to S_4 (or S_n). The same probe pulse continues the excitation into the ionization continuum.

2. (a) Experimental time-resolved curve for parallel polarization. Several features of this decay curve ($\tau = 2.4 \pm 0.4$ns) are notable. The spike at time=0 is far above the level of the remainder of the curve. Subsequent negative and positive sense recurrences appear at time intervals of 960±15 and 965±10ps. The system response function is a 10.5-ps Gaussian. (b) Numerical simulation of purely rotational coherence for parallel pump and detection (probe) polarizations. The simulated curve is obtained for rotational constants A=2.68GHz, B=0.273GHz, C=0.240GHz, temperature 2.0K; response of 10.5-ps includes a 2.7-ns decay. Similar features as in Figure 2 (initial spike, negative and positive recurrences) are also seen. The interval spacing is 974-ps. In the top figure the zero of time is determined from the response function.

3. (a) Anisotropy (*r(t)*) of rotational coherence. This figure shows the initial decay of this anisotropy and the negative and positive recurrences. The system response is 10.5-ps. (b) Shows the *r(t)* obtained from a numerical simulation using the previously listed parameters. The "width" of the features are listed in Table I. The data are normalized to the 0.4 value at the peak.

4. Exapnded view of the rotational recurrence features. (a) Shows the experimental data for parallel and perpendicular relative polarizations for the positive (~2-ns) recurrence feature. (b) Shows the experimental *r(t)* for the same recurrence and includes the experimental response function on the same time scale. (c) Shows the simulation for the recurrence. The general shape of the simulated result is very similar to the experimental, even to the extent that some of the smaller oscillatory features near the main peak are present in both.

5. Decay of the anisotropy. A 7-ps system response is used in both parts. The experimental *r(t)* decay is obtained by determining the earliest data channel for which there exists an event. The numerical simulation shows the same behavior for the sharply decaying portion of the feature but an initial "lag" is present. The *r(t)* value has a value of 0.4 as soon as the signal (of the parallel and perpendicular components) is above zero, but this depends on the truncation of the wings of the Gaussian response function. The discrepancy lies in that the experimental signal to noise ratio at these early channels is low. As an approximation of this effect, the response used in the simulation was truncated at 1% of the peak amplitude. A truncation at 10% would correspond more closely to the experimental result.

Figure 1.

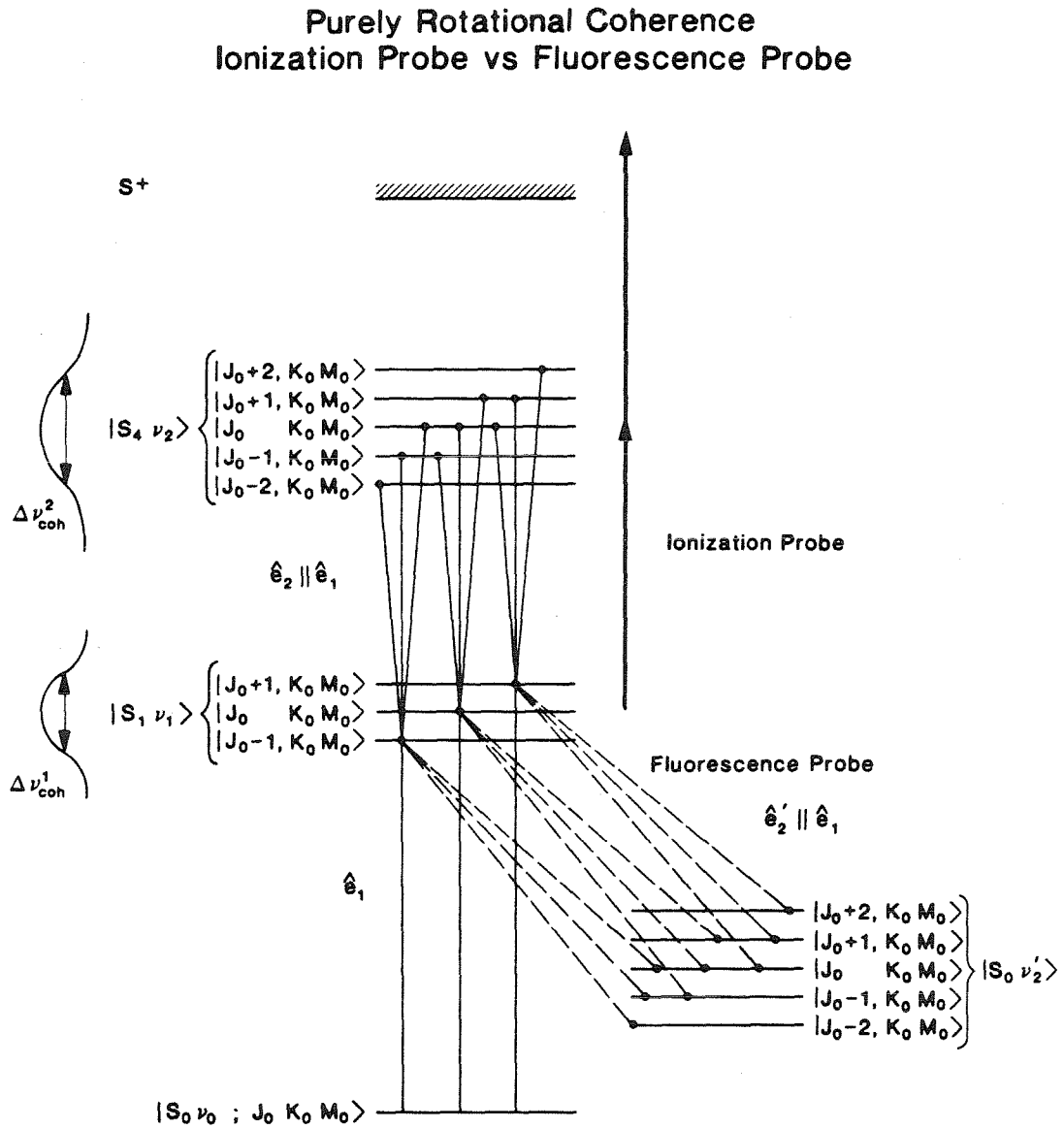
Purely Rotational Coherence
Ionization Probe vs Fluorescence Probe
S+
|S4 ν2⟩
|J0+2, K0 M0⟩
|J0+1, K0 M0⟩
|J0 K0 M0⟩
|J0−1, K0 M0⟩
|J0−2, K0 M0⟩
Δν²coh
ê2 ∥ ê1
Ionization Probe
|S1 ν1⟩
|J0+1, K0 M0⟩
|J0 K0 M0⟩
|J0−1, K0 M0⟩
Δν¹coh
Fluorescence Probe
ê2′ ∥ ê1
ê1
|J0+2, K0 M0⟩
|J0+1, K0 M0⟩
|J0 K0 M0⟩
|J0−1, K0 M0⟩
|J0−2, K0 M0⟩
|S0 ν2′⟩
|S0 ν0 ; J0 K0 M0⟩

Figures 2a,b.

Rotational Coherence via Picosecond MPI (Parallel Polarization)

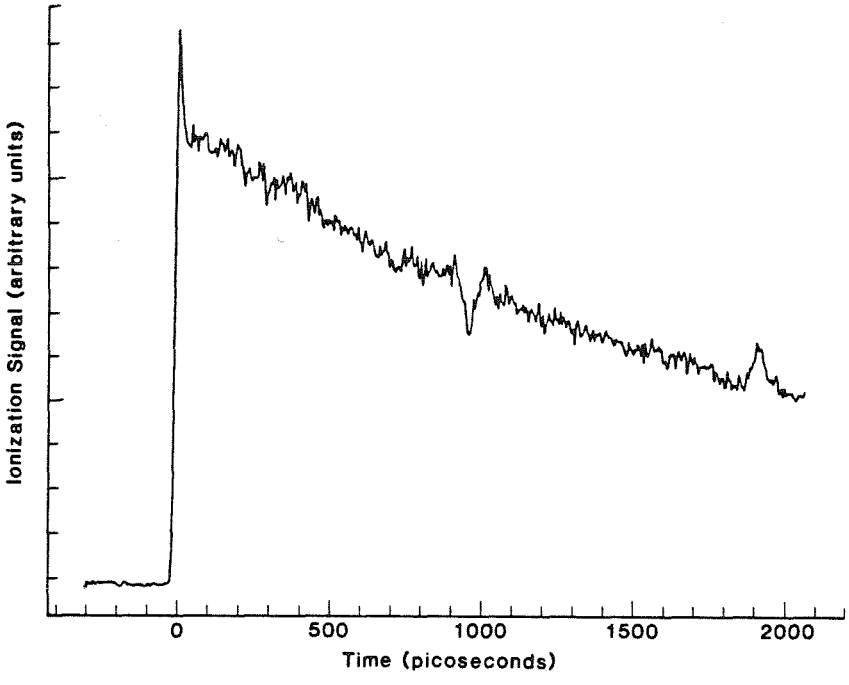

Parallel Decay Simulation, 2.0 K, 10.5ps Response

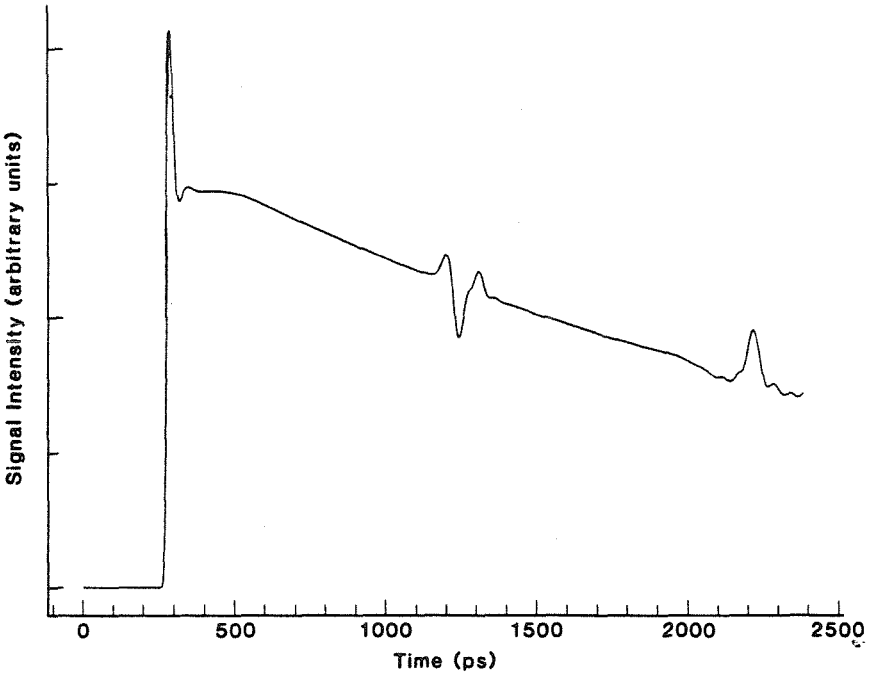

Figures 3a,b.

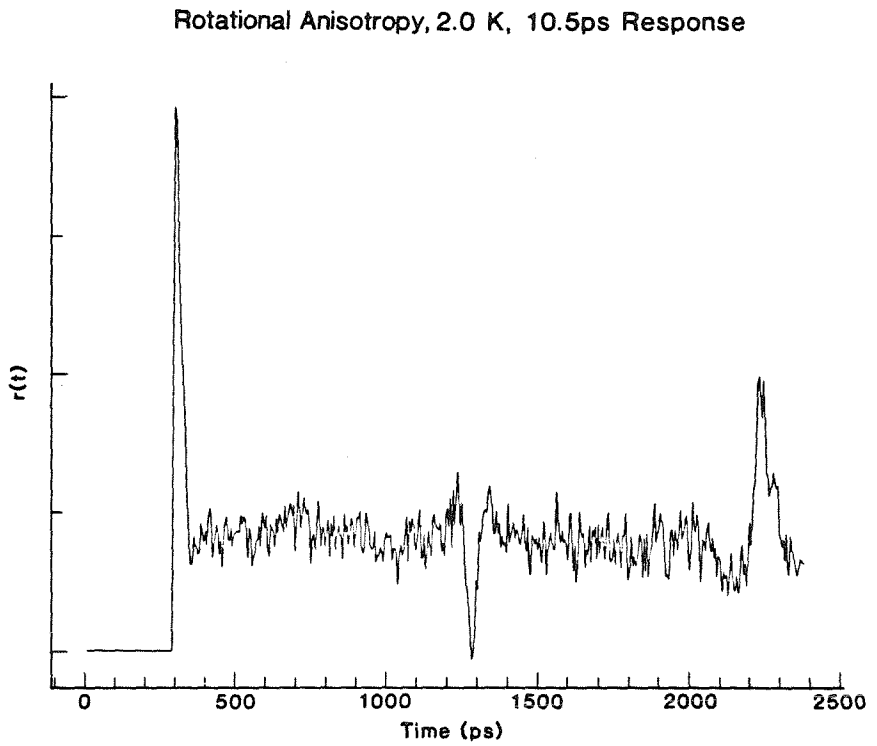
Rotational Anisotropy, 2.0 K, 10.5ps Response
r(t)
0
500
1000
1500
2000
2500
Time (ps)

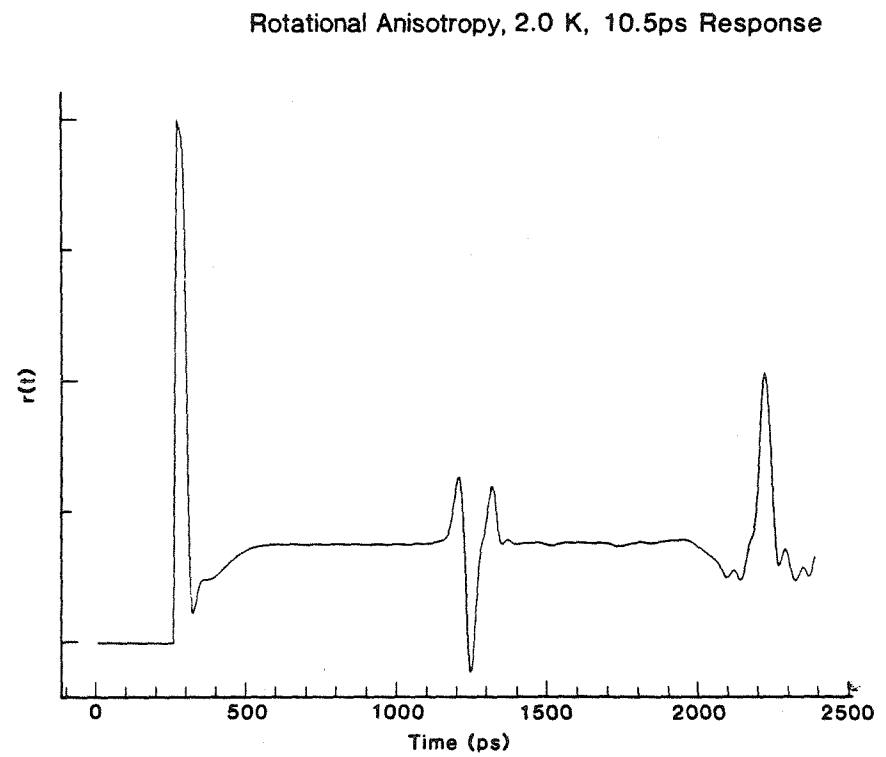
Rotational Anisotropy, 2.0 K, 10.5ps Response
r(t)
0
500
1000
1500
2000
2500
Time (ps)

Figures 4a,b,c.

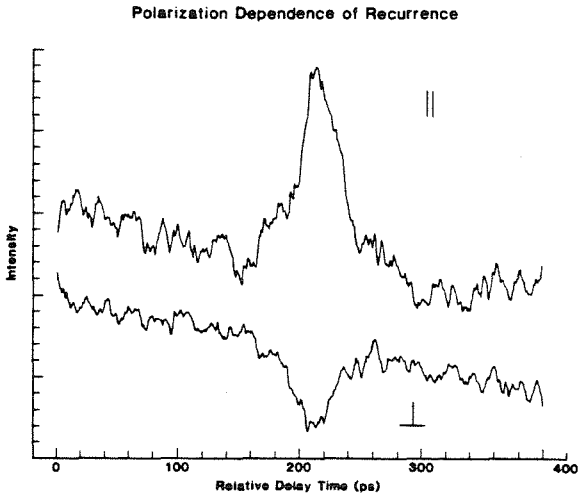

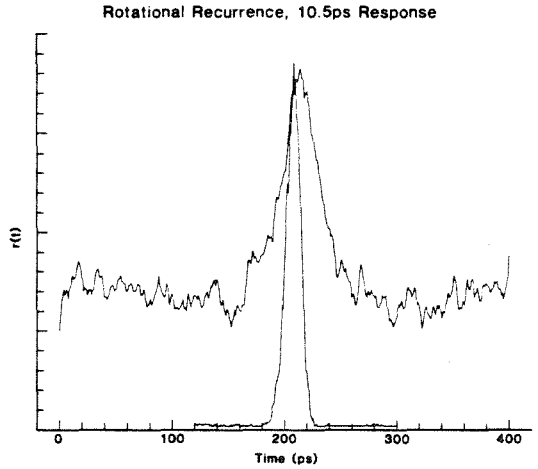

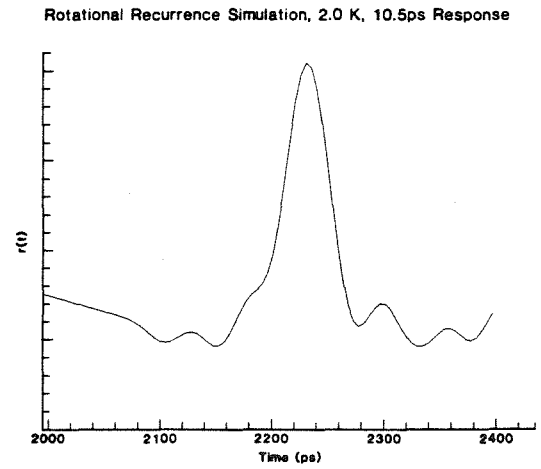

Figures 5a,b.

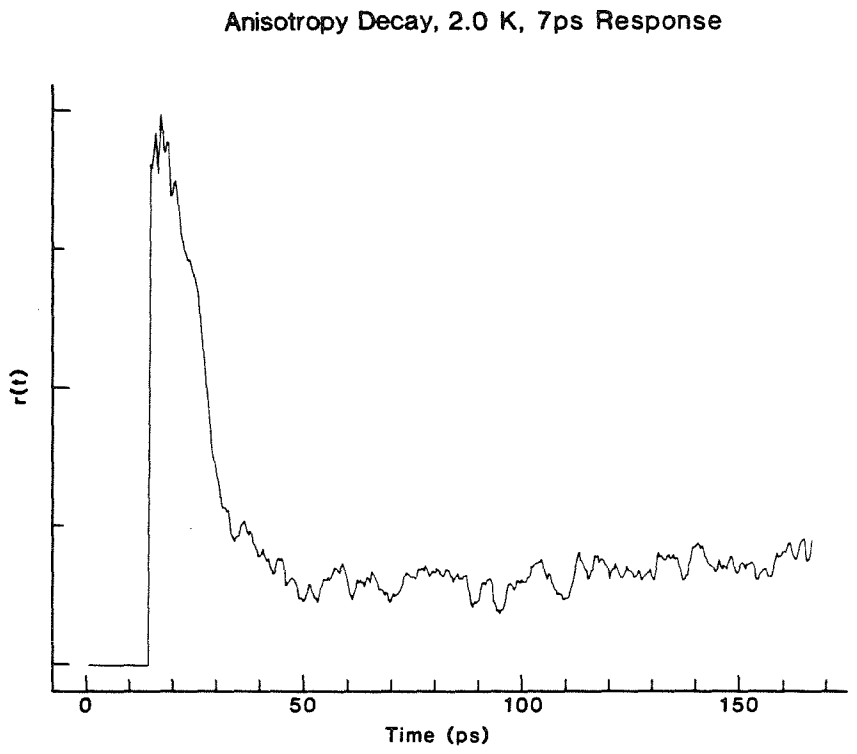
Anisotropy Decay, 2.0 K, 7ps Response
r(t)
0
50
100
150
Time (ps)

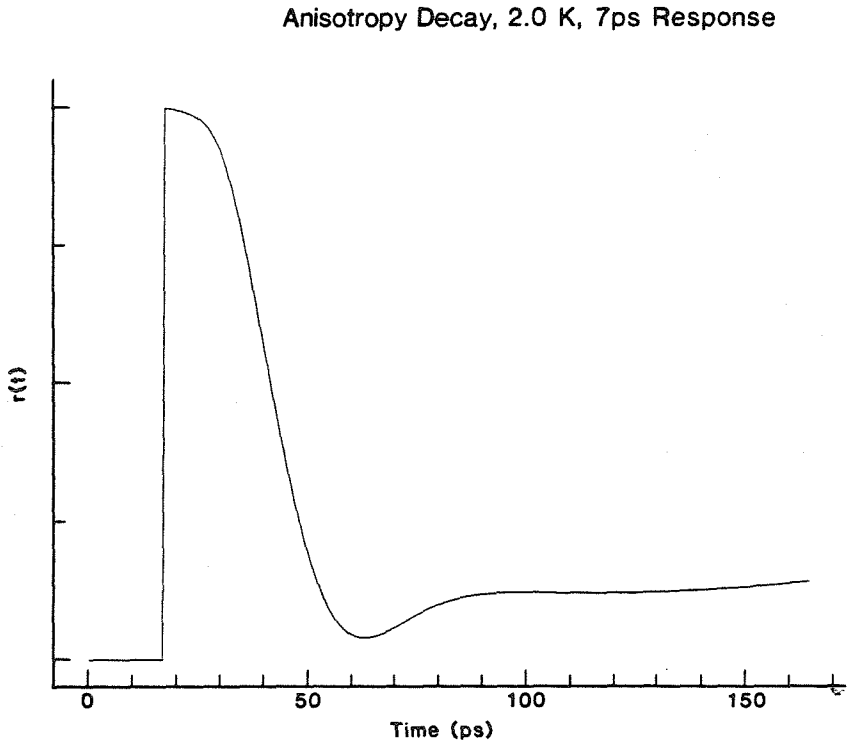
Anisotropy Decay, 2.0 K, 7ps Response
r(t)
0
50
100
150
Time (ps)

Epilogue

"First, my fear; then my curtsy; last my speech.
My fear, is your displeasure,
my curtsy, my duty
and my speech, to beg your pardon."

Shakespear
(from epilogue to the second part of
Henry IV)